Astrophysics of Galaxy Clusters and Groups with eROSITA

Yunus Emre Bahar

München 2024

Astrophysics of Galaxy Clusters and Groups with eROSITA

Yunus Emre Bahar

Dissertation
der Fakultät für Physik
der Ludwig-Maximilians-Universität
München

vorgelegt von
Yunus Emre Bahar
aus Antalya, Türkei

München, den 03.09.2024

Erstgutachter: Prof. Dr. Kirpal Nandra
Zweitgutachter: PD Dr. Klaus Dolag
Tag der mündlichen Prüfung: 15.10.2024

Contents

List of Figures

List of Tables

Zusammenfassung

Diese Dissertation untersucht nicht-gravitative astrophysikalische Phänomene, die die physikalischen Eigenschaften von Galaxienhaufen und -gruppen formen. Die Auswirkungen dieser Prozesse werden durch Messungen der physikalischen Eigenschaften von Galaxienhaufen und -gruppen mithilfe von Röntgenbeobachtungen von eROSITA eingegrenzt. Diese Eingrenzungen werden durch den Vergleich der eROSITA-Messungen mit den Vorhersagen des einfachen sphärischen Kollaps-Szenarios und den Vorhersagen kosmologischer hydrodynamischer Simulationen kontextualisiert. Die in dieser Dissertation präsentierten Ergebnisse bieten einen umfassenden Überblick über die Populationseigenschaften von Galaxienhaufen und -gruppen und dienen als Maßstab zur Aufschlüsselung der nicht-gravitativen Mechanismen, die kosmische Strukturen prägen. In dieser Dissertation konzentrieren wir uns zunächst auf die Röntgen-Skalierungsrelationen von Galaxienhaufen und -gruppen. Wir kalibrieren sieben Röntgen-Skalierungsrelationen, wobei wir Selektionseffekte und die Halo-Massenfunktion berücksichtigen, anhand von eROSITA-Beobachtungen von 265 Galaxienhaufen und -gruppen, die im eFEDS-Feld entdeckt wurden. Die Stichprobe wird durch Anwendung von Auswahlverfahren gewonnen, die in eROSITA-Simulationen reproduzierbar sind, sodass die resultierende Stichprobe eine gut definierte Selektionsfunktion hat. Eine Bayessche Methodik wird verwendet, um die Relationen zu berechnen, wobei eine benutzerdefinierte Selektionsfunktion und eine kanonische Halo-Massenfunktion einbezogen werden, um Selektionseffekte und die Massenverteilung der Halos zu berücksichtigen. Unsere Ergebnisse zeigen signifikante Abweichungen vom selbstähnlichen Modell und stimmen gut mit Simulationen überein, die Modelle für nicht-gravitative Mechanismen enthalten, sowie mit aktuellen Studien, die Selektionseffekte berücksichtigen. Unsere Ergebnisse legen nahe, dass nicht-gravitative Prozesse den physikalischen Zustand von Haufen und Gruppen erheblich beeinflussen. Unsere Studie erweitert die Skalierungsrelationen auf den Parameterraum niedriger Masse und geringer Leuchtkraft mithilfe von eFEDS-Beobachtungen. Sie demonstriert eROSITAs Fähigkeit, Emissionen des Intrahaufen-/Intragruppenmediums hinaus bis zu r_{500c} mit Belichtungen in der Tiefe der Himmelsdurchmusterungen zu messen und Skalierungsrelationen über einen breiten Massen-Leuchtkraft-Rotverschiebungsbereich einzugrenzen. Zweitens konzentrieren wir uns auf die Auswirkungen des AGN-Feedbacks auf die Entropie und die charakteristische Gas-Temperatur von Galaxiengruppen, die in SRG/eROSITAs erster Himmelsdurchmusterung (eRASS1) entdeckt wurden. Wir analysieren eRASS:4-Beobachtungen von 1178 Galaxiengruppen aus dem eRASS1-Galaxienhaufen- und -gruppenkatalog. Wir teilen die Stichprobe in 271 Teilproben auf, basierend auf den physikalischen und statistischen Eigenschaften der Gruppen, und analysieren gemeinsam ihre Röntgenbeobachtungen nach einem Bayesschen Ansatz. Durch

dieses Verfahren extrahieren wir durchschnittliche thermodynamische Eigenschaften, einschließlich der Elektronendichte, Temperatur und Entropie, an drei charakteristischen Radien (von den Kernen bis zu den Außenbereichen) sowie die durchschnittliche integrierte Temperatur innerhalb von r_{500c} für die 271 Teilproben. Wir erzielen die genauesten Eingrenzungen mit unvergleichlicher statistischer Präzision bezüglich der Auswirkungen des AGN-Feedbacks, indem wir die durchschnittliche Entropie und charakteristische Temperatur der größten in Röntgenstudien verwendeten Anzahl an Galaxien-Gruppen messen. Wir quantifizieren auch die Auswirkungen verschiedener Systematiken auf unsere Messungen und berücksichtigen ihre Auswirkungen im Gesamtfehlerbudget. Wir stellen fest, dass die Entropie mit der Temperatur einer Potenzgesetzbeziehung bei höheren Temperaturen des Intragruppenmediums (IGrM) folgt, während bei kühleren ($T < 1,44$ keV) IGrM-Temperaturen eine leichte Abflachung beobachtet wird. Wir vergleichen unsere Ergebnisse mit kosmologischen hydrodynamischen Simulationen (MillenniumTNG, Magneticum, OWL) und finden, dass unsere Entropiemessungen im Kern unter den Vorhersagen der Simulationen liegen. In der mittleren Region und den Außenbereichen stimmen unsere Messungen gut mit den Vorhersagen der Magneticum-Simulationen überein. Unsere Messungen werden genauere AGN-Feedback-Implementierungen in numerischen Simulationen ermöglichen. Zukünftige eROSITA-Surveys werden Entropiemessungen auf noch kühlere IGrM-Temperaturen ausdehnen und ermöglichen die Überprüfung der AGN-Feedback-Implementierungen in diesem Parameterraum. Abschließend untersuchen wir in dieser Dissertation die Profile von thermodynamischen Eigenschaften der von eROSITA selektierten Galaxiengruppen. Frühere Studien deuten auf signifikante Unterschiede zwischen den Profilen der thermodynamischen Eigenschaften von Gruppen und Haufen hin, da Gruppen flachere Gravitationspotentiale haben und daher empfindlicher auf nicht-gravitative Prozesse reagieren. In unserer Studie messen wir die Dichte-, Temperatur-, Entropie- und Druckprofile von 1178 Galaxiengruppen mithilfe von eROSITA-Beobachtungen. Die in dieser Studie verwendete Stichprobe ist identisch mit der unserer zweiten Studie und hat daher eine gut definierte Selektionsfunktion. Wir erhalten genaue Eingrenzungen für die durchschnittlichen skalierten thermodynamischen Profile von röntgenhellen Gruppen, indem wir thermodynamische Profile mit den Vorhersagen des selbstähnlichen Modells normalisieren. Beim Vergleich der skalierten Profile mit früheren Messungen von Haufen und Gruppen stellen wir fest, dass die skalierten Dichteprofile von Gruppen signifikant unter den skalierten Dichteprofilen von Haufen liegen. Unser Befund bestätigt frühere Studien, die darauf hindeuten, dass Gruppen innerhalb von r_{500c} baryonenarm sind. Wir stellen auch fest, dass die skalierten Entropieprofile von Gruppen bei allen Radien erheblich höher sind als die von Haufen, was die größere Auswirkung von AGN auf das IGrM im Vergleich zum ICM unterstreicht. Wir vergleichen unsere Messungen mit den Vorhersagen aus strahlungsfreien hydrodynamischen Simulationen, die als Referenz dienen, und stellen fest, dass die nicht-gravitativen Prozesse die skalierten Dichte- und Druckprofile von Gruppen verringern, während sie die skalierten Entropie- und Temperaturprofile erhöhen. Darüber hinaus wenden wir unsere Selektionsfunktion auf Simulationen (Magneticum, MillenniumTNG) an, die verschiedene AGN-Feedback-Modelle enthalten, und vergleichen unsere Ergebnisse mit deren Vorhersagen. Wir stellen fest, dass Magneticum unsere Messungen in den mittleren Radien und Außenbereichen am besten reproduziert, während unsere Messungen im Kern besser mit MillenniumTNG übereinstimmen. Wir stellen außerdem fest, dass unsere Entropiemessungen unter den Vorhersagen der Simulation im Kern und über

deren Vorhersagen in den Außenbereichen liegen, was darauf hindeutet, dass die überschüssige Entropie, die vom zentralen AGN im Kern eingeführt wird, in den aktuellen AGN-Feedback-Implementierungen nicht effizient auf größere Radien übertragen werden kann.

Abstract

This thesis investigates non-gravitational astrophysical phenomena shaping the physical properties of galaxy clusters and groups. The impact of these processes is constrained by measuring the physical properties of galaxy clusters and groups using X-ray observations of eROSITA. The constraints are contextualized by comparing the eROSITA measurements with the predictions of the simple spherical collapse scenario and the predictions of cosmological hydrodynamical simulations. The results presented in this thesis provide a broad view of the population properties of galaxy clusters and groups and serve as a benchmark for unraveling the non-gravitational mechanisms governing cosmic structures.

In this thesis, we first focus on the X-ray scaling relations of galaxy clusters and groups. We calibrate seven X-ray scaling relations, accounting for selection effects and the halo mass function, using eROSITA observations of 265 galaxy clusters and groups detected in the eFEDS field. The sample is obtained by applying selection procedures that are reproducible in eROSITA simulations such that the resulting sample has a well-defined selection function. A Bayesian framework is employed to fit the relations, incorporating a custom selection function and a canonical halo mass function to account for selection effects and the mass distribution of halos. Our results show significant deviations from the self-similar model, aligning well with simulations that include prescriptions for non-gravitational mechanisms and recent studies considering selection effects. Our findings suggest that non-gravitational processes significantly influence the physical state of clusters and groups. Our study extends scaling relations to low-mass, low-luminosity parameter space using eFEDS observations. It demonstrates eROSITA's capability to measure intracluster/intragroup medium emission out to r_{500c} with survey-depth exposures and constrain scaling relations across a broad mass-luminosity-redshift range.

Second, we focus on the effects of AGN feedback on the entropy and characteristic temperature of galaxy groups detected in SRG/eROSITA's first All-Sky Survey (eRASS1). We analyze eRASS:4 observations of 1178 galaxy groups from the eRASS1 galaxy clusters and groups catalog. We divide the sample into 271 subsamples based on the physical and statistical properties of the groups and jointly analyze their X-ray observations following a Bayesian approach. Through this procedure, we extract average thermodynamic properties, including electron number density, temperature, and entropy, at three characteristic radii (from cores to outskirts) as well as the average integrated temperature within r_{500c} for the 271 group bins. We achieve the tightest constraints with unparalleled statistical precision on the impact of AGN feedback by measuring the average entropy and characteristic temperature of the largest group sample used in X-ray studies. We also quantify the impact of various systematics on our measurements and include their

impact to their total error budget. We find that entropy increases with temperature following a power-law relation at higher intra-group medium (IGrM) temperatures, while a slight flattening is observed in cooler ($T < 1.44$ keV) IGrM temperatures. We compare our results with cosmological hydrodynamic simulations (MillenniumTNG, Magneticum, OWL), and find that our entropy measurements at the core lie below the predictions of simulations. At mid-region and outskirts, we find that our measurements align well with the predictions of the Magneticum simulations. Our measurements will facilitate more accurate AGN feedback implementations in numerical simulations. Future eROSITA surveys will extend entropy measurements to even cooler IGrM temperatures, enabling the testing of AGN feedback implementations in this parameter space.

Lastly, in this thesis, we explore the thermodynamic property profiles of eROSITA-selected galaxy groups. Previous studies suggest significant differences between the profiles of thermodynamic properties of groups and clusters due to groups having shallower potential wells and, therefore, being more sensitive to non-gravitational processes. In our study, we measure the density, temperature, entropy, and pressure profiles of 1178 galaxy groups using eROSITA observations. The sample used in this study is identical to the one employed in our second study and, therefore, has a well-defined selection function. We obtain tight constraints on the average scaled thermodynamic profiles of X-ray bright groups by normalizing thermodynamic profiles with the self-similar model predictions. Comparing scaled profiles with previous cluster and group measurements, we find that the scaled density profiles of groups are significantly below the scaled density profiles of clusters. Our finding confirms previous studies suggesting groups to be baryon depleted within r_{500c}. We also find that the scaled entropy profiles of groups are considerably higher than clusters at all radii, highlighting AGN's more significant impact on the IGrM compared to the ICM. We compare our measurements with predictions of the non-radiative hydrodynamical simulations, which serve as baselines, and found that the non-gravitational processes decrease groups' scaled density and pressure profiles while increasing the scaled entropy and temperature profiles. Furthermore, we apply our selection function to simulations (Magneticum, MillenniumTNG) that include different AGN feedback models and compare our results with their predictions. We find that Magneticum reproduces our measurements the best at the intermediate radii and outskirts, while our measurements at the core agree better with MillenniumTNG. We further find that our entropy measurements lie below the predictions of simulation at the core and above their prediction at the outskirts, suggesting the excess entropy introduced by the central AGN at the core cannot be efficiently carried to larger radii in the current AGN feedback implementations.

Chapter 1

Introduction

1.1   Galaxy Clusters and Groups

Charles Messier was among the first to notice the clustering of nebulae (at the time, the term
"nebulae" was used to describe extended objects in the sky, including galaxies). While cata-
loging extended objects in his search for comets, he found that the positions of nebulae are not
isotropically distributed in the sky(Messier, 1781). Around the same time, F. William Herschel,
aided by his sister Caroline Herschel, also noticed the clustering of nebulae while cataloging ob-
jects that exhibit diffuse emission during his investigation of double stars (Herschel, 1785, 1802).
In the 20th century, Edwin Hubble discovered that the (optical) light from the spiral and ellipti-
cal "nebulae" comes from stars, and hence, similar to the Milky Way, these nebulae are galaxies
(Hubble, 1926). This revealed the true nature of these objects and brought a new perspective for
understanding their physics. With a better understanding of the individual galaxies, astronomers
began to study the properties of the larger structures these galaxies form. Fritz Zwicky analyzed
velocity measurements of the galaxies in the Coma cluster (Hubble and Humason, 1931) and
found that the total mass of Coma, calculated from the velocity dispersion measurements of the
members via assuming virial equilibrium, is ~ 400[1] times larger than the sum of the masses
of the individual galaxies (Zwicky, 1933). Based on this, Zwicky postulated that to match the
orbital velocities of its member galaxies, clusters should host significant amount of "undetected"
matter, which he named Dunkle Materie (dark matter in English). A similar measurement carried
out by Sinclair Smith on the Virgo cluster confirmed the findings of Zwicky such that the total
mass predicted by the velocity dispersion measurements are ~ 200[2] times higher than the sum
of the masses of the galaxies (Smith, 1936). These measurements mark the first evidence that
galaxy clusters are not only aggregations of galaxies rotating around the common center of mass
but more massive and complex dark matter reservoirs with deep potential wells.

Efforts to catalog the objects in the optical sky continued during the rest of the 20th century.
George O. Abell performed a systematic search for nearby ($z < 0.2$) galaxy clusters that host

---

[1]It is later shown by future work that employing updated values for H_0 and stellar masses of galaxies result in a
reduction of the ratio, yet they found that the mismatch persists.

[2]See footnote 1.

large numbers of member galaxies (>30) using photographic plates. As a result of these efforts, he compiled a catalog containing most of the nearby galaxy clusters, which is still widely used today (Abell, 1958; Abell et al., 1989). The knowledge of the physics of these objects significantly changed once again with the discovery of the X-ray emission produced by the hot plasma composing the intra-cluster medium (ICM). The detection of the brightest central galaxy of the Virgo cluster (M87) by Byram et al. (1966) marks the first discovery of an X-ray source that is linked with a galaxy cluster. Cavaliere et al. (1971) proposed that many of the extragalactic X-ray sources are related to the emission from ICM and the independent detection of the X-ray emission from Coma with the Uhuru satellite (Gursky et al., 1971; Kellogg et al., 1972) and an Aerobee 150 rocket (Meekins et al., 1971) strengthened their hypothesis. Since the discovery of the X-ray emission from clusters and groups, X-ray observations have proven to be one of the most reliable ways to detect them, with tens of thousands of clusters having been detected over the course of the history of X-ray astronomy (e.g., Bulbul et al., 2024).

The discovery of the hot plasma in galaxy clusters and groups in X-rays accounted for some part of the missing mass in galaxy clusters. Nevertheless, it was soon understood that the hot dilute gas in X-rays is not enough to explain the discrepancy. Therefore, the mismatch between the total mass and the sum of baryonic mass remained. On the contrary, the detection of hot gas in galaxy clusters and groups further proved that clusters and groups are required to have deep potential wells. In fact, later studies confirmed that only $\sim 10-20\%$ of the mass in clusters is in the form of baryonic matter, and the remaining $\sim 80-90\%$ is in the form of dark matter (Ettori, 2015; Lovisari et al., 2015; Chiu et al., 2018; Mantz et al., 2022).

The discovery of the hot plasma in galaxy clusters and groups brought a new perspective to the physics of gaseous haloes and provided astronomers new grounds for detecting and investigating their physical properties. Sunyaev and Zeldovich (1970) proposed that the inverse Compton scattering of low-energy cosmic microwave background (CMB) photons should leave Doppler boosting imprints in the CMB spectrum as they pass through intra-cluster/group medium (ICM/IGrM). This phenomenon is called the Sunyaev-Zel'dovich (SZ) effect (Sunyaev and Zeldovich, 1970, 1972), and it traces the integrated thermal gas pressure along the line of sight. Since the proposal of this phenomenon, thousands of galaxy clusters have been detected through the thermal SZ effect (e.g., Hilton et al., 2021).

Around the same time, Willson (1970) reported the discovery of the first extended radio emission from clusters by analyzing the One-Mile Telescope observations of the Coma cluster. This provided the first evidence of magnetic fields on large scales. Later studies revealed that galaxy clusters and groups exhibit two types of extended radio emission: radio relics and radio haloes. Radio relics are elongated polarised radio structures that are not associated with any optical counterparts, and radio haloes are relatively faint polarized diffuse structures centered around the peak of the X-ray emission from ICM/IGrM. Later studies also confirmed that the radio emission originates from the interaction of the relativistic populations of electrons (also known as cosmic ray electrons) with the magnetic fields in the ICM/IGrM (see van Weeren et al., 2019, for an extensive review on the origin of the extended radio emission from clusters). In 2010, Finoguenov et al. (2010) provided the first evidence for the association between the radio relics and X-ray shocks that confirmed the theory that the radio relics are manifestations of the plasma getting (re-)accelerated by the ICM/IGrM shocks Ensslin et al. (1998). On the other side,

Figure 1.1: A composite image of the SMACS 0723.3–7327 cluster using *Chandra* (X-ray) and JWST (IR). The image is created by overlaying the *Chandra* image of the ICM (blue) over the JWST image of the galaxies and stars (RGB). Credit: X-ray: NASA/CXC/SAO; IR (Webb): NASA/ESA/CSA/STScI

the radio haloes are thought to originate from the (re-)accelerated relativistic electrons by strong turbulence in ICM/IGrM whose correlation with X-ray radio properties have been reported in many studies (e.g. Liang et al., 2000; Govoni et al., 2001; Yuan et al., 2015; Pasini et al., 2022).

Einstein's general theory of relativity (Einstein, 1916) predicts the direction of the light to be changed as it passes through gravitational potential wells. Chwolson (1924) was the first to publish on this effect, and 55 years later Walsh et al. (1979) discovered the first lensed object by noticing a pair of quasars (0957+561 A and B) showing remarkably similar features to each other. They conclude that this may be due to the light from the quasar being lensed, such that we are seeing two images of the same object at different sky positions. Owing to their large masses, two of the most suitable objects to significantly bend the light are galaxy clusters and galaxy groups. Through geometric reconstruction, the mass profiles of the gravitational lens can be inferred by measuring the distortion of the shapes of the background objects. This provides a relatively direct and robust way to measure the masses of galaxy clusters and groups, which otherwise is very challenging due to the "dark" nature of the dark matter (Hoekstra et al., 2013). For galaxy clusters and groups, two types of lensing are relevant: strong and weak lensing. The strong lensing analysis is based on investigating multiple appearances or significant distortions of the shapes of a few background objects close to the direction of the lens, whereas the weak lensing analysis is based on statistical treatment of the small distortions of the shapes of background galaxies in larger regions on the sky. Both of these techniques are used to determine the mass profiles of galaxy clusters at different radial scales. The weak lensing technique is used more often to investigate the mass profiles in population studies (e.g., Chiu et al., 2022; Grandis et al., 2024b; Kleinebreil et al., 2024). This is because the applicability of the strong lensing technique is limited to the clusters and groups able to reproduce significant distortions of the images of the background objects close to the center of the lens. It is therefore used more often for the analysis of individual objects or relatively smaller samples (e.g., Sand et al., 2002; Monna et al., 2017; Mahler et al., 2023).

A composite image of a galaxy cluster (SMACS 0723.3–7327) obtained by combining the observations of the highest resolution X-ray and infrared telescopes is shown in Fig. 1.1. The imprints of the three main components of galaxy clusters and groups (galaxies, ICM, and dark matter) are evident in this image. The infrared (IR) emission from member galaxies is shown in yellow, X-ray emission from ICM is shown in blue, and the infrared emission from the lensed background galaxies, whose shapes are distorted by the dark matter potential well, is shown in orange. Having remarkable multi-wavelength properties in X-ray, optical/infrared, microwave, and radio bands, galaxy clusters and groups are widely used to investigate astrophysical phenomena at large scales and the properties of the universe as a whole, e.g., cosmological studies.

1.1.1   X-ray Emitting Plasma

X-ray emitting hot gas makes up $10 - 20\%$ of the mass in galaxy clusters and groups. According to the standard cosmological model, this gas is the end product of the surrounding baryonic matter accreting onto the largest density peaks in clumps of various sizes. Through the accretion process, the gas first gets heated up by accretion shocks. Subsequently, it gets compressed adiabatically and thermalized at electron number densities of $n_{\mathrm{e}} \approx 10^{-4} - 10^{-3}$ cm^{-3}

($\rho \approx 10^{-28} - 10^{-27}$ gr cm^{-3}) and temperatures of $kT \approx 0.5 - 10$ keV under the influence of the evergrowing potential well (Kravtsov and Borgani, 2012). The hot gas predominantly consists of hydrogen (H) and helium (He) ions, along with a minor proportion (<1%) of heavier elements like iron (Fe). At these temperatures, most of the elements, except the heaviest ones, are fully ionized.

Hot dilute plasma at these temperatures and densities shines brightly in X-rays through four emission mechanisms: thermal bremsstrahlung (free-free), line emission (bound-bound), recombination (free-bound), and two-photon emission (2q). Thermal bremsstrahlung, recombination, and two-photon emission make up the spectral continuum, whereas the line emission appears as spectral bumps at given energies over the continuum. The emission from the thermal bremsstrahlung mechanism dominates the spectral continuum for gas at $kT > 1$ keV such that the contributions of the recombination and two-photon processes to the continuum are relatively small. However, at $kT < 1$ keV, the contribution of the recombination process to the continuum becomes non-negligible (see Fig. 6 in Boehringer and Werner, 2009).

Emission from the thermal bremsstrahlung mechanism arises from the electromagnetic interaction of the free electrons and the ionized nuclei in collisionally ionized optically thin plasma. The emissivity of an electron in hot plasma scattered by an ion (X_j) with an effective charge Q_{X_j}, at frequency ν, can be formulated as

$$\epsilon_{\nu,j}^{ff} = \frac{32\pi e^6}{3m_e c^3} \left(\frac{2\pi}{3m_e k}\right)^{1/2} Q_{X_j}^2 g_{ff}(Q_{X_j}, T, \nu) n_e n_{X_j} T^{-1/2} e^{-h\nu/kT} \tag{1.1}$$

where m_e is the electron mass, c is the speed of light, k is the Boltzman constant, g_{ff} is the gaunt factor, n_e is the electron number density, n_{X_j} is the ion number density, T is the temperature of the plasma and h is the Planck constant. The gaunt factor takes into account the quantum mechanical corrections and the impact of distant scatterings as a function of the effective charge of the ion, frequency, and temperature (Karzas and Latter, 1961). The temperature and frequency dependence of the gaunt factor is relatively weak such that it slowly decreases with increasing frequency and temperature (e.g., see Fig. 1 in Kellogg et al., 1975). It can be seen from Eq. 1.1 that at lower photon energies ($h\nu << kT$), the emissivity scales with temperature as $\epsilon_{\nu}^{ff} \propto T^{-1/2}$ whereas, at higher energies ($h\nu \gtrsim kT$), the exponential term takes over and the emissivity drops exponentially, $\epsilon_{\nu}^{ff} \propto e^{-h\nu/kT}$ as a function of energy. The photon energy where the turnover takes place ($h\nu = kT$) is called the cut-off energy and is used to determine the temperature of the plasma. Eq. 1.1 can be further integrated over frequency to find the total power emitted by hot plasma through thermal bremsstrahlung per unit volume as

$$\epsilon_j^{ff} \approx \frac{32\pi e^6}{3hm_e c^3} \left(\frac{2\pi k}{3m_e}\right)^{1/2} Q_{X_j}^2 \overline{g_{ff}}(Q_{X_j}, T) n_e n_{X_j} T^{1/2} \tag{1.2}$$

where $\overline{g_{ff}}$ is the frequency averaged gaunt factor.

Recombination radiation is the second component of the spectral continuum and arises due to the free electrons getting recaptured by the ions in the plasma. The emissivity of the free-bound

recombination process for ion X at the jth ionization state (X_j), can be calculated as

$$\epsilon_{\nu,j}^{fb} = \frac{h^4}{c^2} \left(\frac{2}{\pi \left(m_{\text{e}}k\right)^3} \right)^{1/2} n_{\text{e}} n_{X_{j+1}} \sum_l \frac{\omega_{l,X_j}}{\omega_{gs,X_{j+1}}} a_{\nu,X_j}^l \nu^3 T^{-3/2} e^{-(h\nu - \chi_{l,X_j})/kT} \qquad (1.3)$$

where the summation over l goes over all energy levels of X_j, $\omega_{gs,X_{j+1}}$ stands for the statistical weight of the ground state of the ion undergoing recombination (X_{j+1}), ω_{l,X_j} stands for the statistical weight of the lth energy level of ion X_j, a_{ν,X_j}^l stands for the photoionization cross-section of ion X_j and χ_{l,X_j} is the ionization potential for the lth energy level of ion X_j (Osterbrock, 1974; Sarazin, 1986).

The third and last component of the spectral continuum is the emission from the two-photon process. The radiation through this mechanism arises due to the electrons at the $2s$ metastable states gradually transiting to the $1s$ state of hydrogen-like and helium-like ions. Direct transition from the $2s$ state to the $1s$ state is forbidden due to the conservation of angular momentum. However, in hot ICM/IGrM, these electrons can get collisionally excited to higher energy states and gradually transit to the $1s$ state through non-forbidden transitions (Spitzer and Greenstein, 1951). The emission resulting from this process is called two-photon emission and contributes to the overall spectral continuum from clusters and groups in relatively small amounts. The emissivity of the two-photon decay of H I can be calculated as

$$\epsilon_\nu^{2q} = \frac{1}{4\pi} n_{\text{e}} n_{\text{p}} \alpha_{2s}^{\text{eff}} g_\nu \left(1 + \frac{n_{\text{p}} q_{2s,2p}^p + n_{\text{e}} q_{2s,2p}^e}{A_{2s,1p}} \right)^{-1} \qquad (1.4)$$

where n_{p} is the number density of protons, α_{2s}^{eff} is the effective recombination coefficient to the $2s$ level, g_ν is the spectral distribution of H I, $q_{2s,2p}^p$ and $q_{2s,2p}^e$ are the the collisional transition rates and $A_{2s,1p}$ is the transition probability of the two-photon decay (Osterbrock, 1974).

The last component of the ICM/IGrM spectra is the line emission. Line emission arises as a result of an electron releasing energy while moving from a higher bound energy state to a lower one. Bound energy states are quantized as a consequence of the discrete nature of quantum mechanics; hence, photons emitted through the line emission mechanism are at fixed energies. For this reason, unlike the three components described above (thermal bremsstrahlung, recombination radiation, and two-photon process), photons emitted through the line emission mechanism are not part of the spectral continuum. The electrons generating the line emission can be excited to high energy states through various mechanisms: collisional excitation, inner shell ionization (through collision or photoelectric effect), recombination (dielectric or radiative), or photon absorption. Among these mechanisms, collisional excitation stands out as the most important one (Kaastra et al., 2008). The emissivity of collisionally excited (ce) line emission for an ion X_j in a hot plasma at the low electron density limit can be calculated as

$$\int \epsilon_{\nu,j}^{line(ce)} d\nu = \frac{h^3}{4} \left(\frac{2}{\pi^3 m_{\text{e}}^3 k} \right)^{1/2} \frac{\Omega(T) B}{\omega_{gs,X_j}} \nu n_{\text{e}} n_{X_j} T^{-1/2} e^{-\Delta E/kT} \qquad (1.5)$$

where ν is the frequency of the photon emitted during the transition, $\Omega(T)$ is the collision strength, B is the branching ratio, and ΔE is the energy difference between the ground and the excitation level (Osterbrock, 1974; Sarazin, 1986).
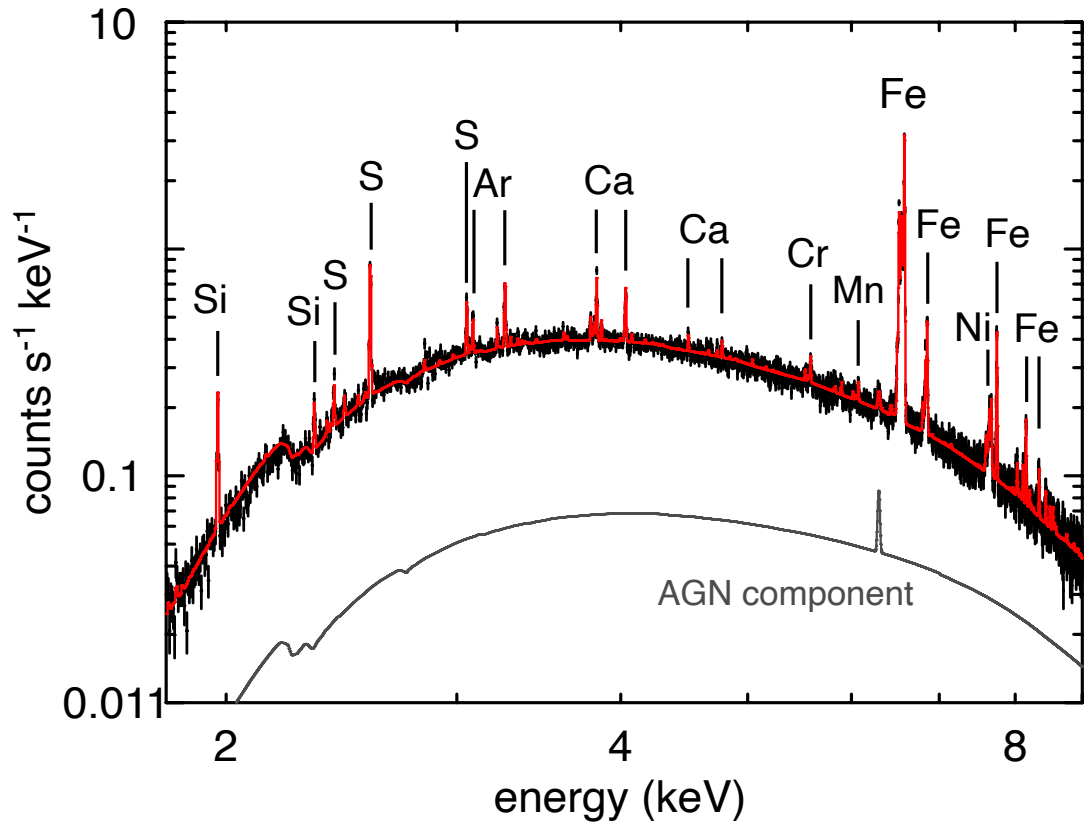
Figure 1.2: X-ray spectrum of the hot gas ($kT \sim 4$ keV) at the core of the Perseus cluster measured by Hitomi's X-ray micro-calorimeter. Black data points represent the measurements, the red line represents the modeled spectrum, and the grey line represents the contribution of an AGN (NGC 1275) within the field of view to the total spectrum. Figure taken from Hitomi Collaboration et al. (2017).

The strength of the emission lines above the spectral continuum depends on the gas temperature and the abundance of the metals responsible for creating these lines. It is often assumed that metals in galaxy clusters and groups have abundance ratios close to the solar values. In fact, this is confirmed by measuring the strength of the emission lines from the Perseus cluster with the high-resolution X-ray micro-calorimeter onboard the Hitomi satellite (Hitomi Collaboration et al., 2017; Simionescu et al., 2019). The Hitomi spectrum of the core of Perseus exhibiting a large variety of emission lines from different elements is shown in Fig. 1.2. In general, there is a broad agreement that the metallicity[3] of galaxy clusters and groups is at the $Z \approx 0.3 \, Z_\odot$ level outside the core region ($r > 0.2 r_{500c}$) and gradually increases to the levels of $Z \approx 0.7 \, Z_\odot$ within the core region ($r < 0.2 r_{500c}$) (see Fig. 4 in Gastaldello et al., 2021, and the references therein). Some of the strongest lines from clusters residing at the high-temperature parameter space ($kT > 2$ keV) can be listed as iron-K (Fe-K) lines at ~ 6.7 keV, sulfur (S) lines at ~ 2.5 keV, silicon (Si) lines at ~ 1.85 keV, magnesium (Mg) lines at ~ 1.4 keV, iron-L (Fe-L) complex at $\sim 0.7 - 1.2$ keV and oxygen (O) lines at ~ 0.65 keV. The strongest lines residing above 1.8 keV can easily be seen in the Hitomi spectrum of the hot gas ($kT \sim 4$ keV) at the core of Perseus cluster in Fig. 1.2. In the lower-temperature parameter space ($kT < 2$ keV), fewer of the metals in the intra-group medium can get fully ionized; therefore, the strength of emission from these ions, hence their contribution to the total flux, increases. Through this dependence, the relative strengths of emission lines can be used to trace the temperature of the ICM/IGrM.

The total emissivity of clusters and groups is the sum of the emissivities of the four emission processes described above; therefore, can be written as

$$\epsilon_\nu = \epsilon_\nu^{ff} + \epsilon_\nu^{fb} + \epsilon_\nu^{2q} + \epsilon_\nu^{line} \tag{1.6}$$

where the first three are responsible for the spectral continuum, and the last one is the emissivity of the bound-bound line emission mechanism. One can notice that all four emission mechanisms are proportional to the number density of electrons (n_e) and the number density of the ions (n_{X_j}). Hence, the total emissivity of an emission mechanism from a collisionally ionized hot gas can be obtained by summing over the ions, X, and ionization states, j.

$$\epsilon_\nu = n_e n_p \sum_{X,j} \left(\frac{n_X}{n_p} \right) \left(\frac{n_{X_j}}{n_X} \right) \left(\frac{\epsilon_{\nu,j}^{ff} + \epsilon_{\nu,j}^{fb} + \epsilon_{\nu,j}^{2q} + \epsilon_{\nu,j}^{line}}{n_e n_{X_j}} \right) \tag{1.7}$$

where the first term in the sum is the ratio between the number density of element X and the number density of proton/hydrogen, and the second term is the ionization fraction, $f(X_j, T) = n_{X_j}(T)/n_X$. The result of the summation is called the cooling function, $\Lambda_{ep,\nu}$, and it is a function of frequency (ν), temperature (T) and metallicity (Z). Hence, the total emissivity of galaxy clusters and groups can be written as

$$\epsilon_\nu = \frac{dE}{dt dV d\nu} = n_e n_p \Lambda_{ep,\nu}(T, Z). \tag{1.8}$$

Furthermore, emissivity can be further integrated over ν at a given band, $\nu_0 - \nu_1$ such that the total energy emitted per unit time from a unit volume of collisionally-ionized diffuse plasma, can

---

[3]Metallicity is defined as the abundance of elements heavier than helium

be calculated as

$$\epsilon_{\nu_0 - \nu_1} = \int_{\nu_0}^{\nu_1} \epsilon_\nu d\nu = \frac{dE}{dt dV} = n_e n_p \Lambda_{ep}(T, Z) \tag{1.9}$$

where $\Lambda_{ep}(T, Z)$ is the band-averaged cooling function expressed in units of erg s^{-1} cm^3 in the cgs (centimeter-gram-second) system. Lastly, the surface brightness of galaxy clusters and groups at a given band can be calculated by integrating the power emitted per unit volume ($\epsilon_{\nu_0 - \nu_1}$) along the line of sight as

$$S_X = \frac{1}{4\pi(1 + z)^4} \int n_e n_p \Lambda_{ep} dl. \tag{1.10}$$

One should note that the $(1+z)^4$ term above should be replaced with $(1+z)^3$ when S_X is calculated in detector units (cnts s^{-1} cm^{-2} arcsec^{-2}).

Two spectral fitting codes that are often used to extract spectral information from clusters and groups are `Xspec` (Arnaud, 1996) and `SPEX` (Kaastra et al., 1996, 2020). The biggest difference between these two codes is that they use different atomic codes and tables. `Xspec` uses the AtomDB atomic database (Foster et al., 2012) to calculate the APEC (Astrophysical Plasma Emission Code) model, an updated version of the Raymond-Smith model (Raymond and Smith, 1977; Smith et al., 2001), for collisionally-ionized diffuse plasmas whereas `SPEX` uses the SPEX-ACT atomic database to calculate the CIE (Collisional Ionisation Equilibrium model), an updated version of the MEKAL model (Mewe et al., 1985, 1986; Liedahl et al., 1995). Both APEC and CIE models include the contribution from the four emission mechanisms described above, whereas different atomic code implementations and the use of different atomic databases result in some differences. Initially, the difference between the two models was relatively significant; hence, they could lead to different conclusions about the emission from the plasma (e.g., Kim, 2012). The codes calculating these models, as well as the atomic tables used by these codes, have been significantly updated since they were first introduced. Over time, the spectral models produced by the two codes with the same input have shown a converging trend. The current versions of APEC and CIE models using the latest atomic databases, AtomDB v3.0.9 and SPEX-ACT v3.8.0, are in relatively good agreement (e.g., see Fig. 1 in Gastaldello et al., 2021, for the evolution of the Fe-L complex produced by using APEC and CIE models). Although abundance measurements of individual elements can exhibit discrepancies (e.g., up to $\sim 20\%$ level for Fe for plasma at $kT < 2$ keV with *XMM-Newton*), the temperature measurements obtained from the two codes agree relatively well (Mernier et al., 2020). Throughout this thesis, the relative abundances of elements are fixed to the solar metal abundance ratio measurements presented in Asplund et al. (2009), and the temperature of galaxy clusters and groups are measured by fitting X-ray spectra using the APEC model in `Xspec` that uses the AtomDB atomic database. Given the good agreement between the temperature measurements with the two plasma codes, the choice of a particular code has negligible impact on our findings. The photon flux model (APEC) of collisionally ionized optically thin plasma for gas having a metallicity $Z = 0.3Z_\odot$, at a redshift $z = 0$, having an APEC normalization $\frac{10^{-14}}{4\pi(D_A(1+z))^2} \int n_e n_H dV = 1$ and at various temperatures is shown in Fig. 1.3. The photon flux model of thermal bremsstrahlung emission from the same plasma is also plotted for reference using the BREMSS model in `Xspec`. It can be seen that, at all temperatures, emission from the thermal bremsstrahlung mechanism is responsible for the
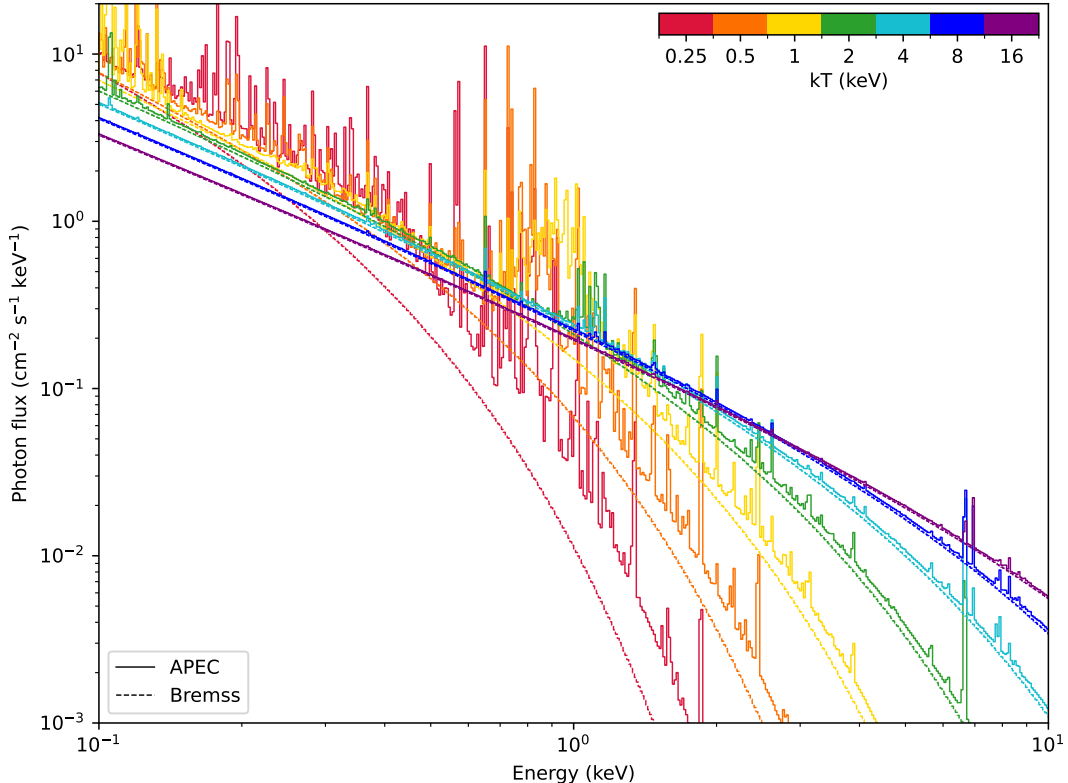
Figure 1.3: Photon fluxes from collisionally-ionized hot plasma as a function of photon energy. Fluxes are calculated using APEC and BREMSS models implemented in `Xspec` assuming a metallicity of $0.3Z_\odot$, an APEC normalization of one at a redshift of 0 and at various temperatures. The temperature of the plasma is shown by the color of the lines where red corresponds to the lowest temperature ($kT = 0.25$), and purple corresponds to the hottest temperature ($kT = 10$). Solid lines represent the overall emission from the plasma calculated by using the APEC model, and the dashed lines represent the contribution of the thermal bremsstrahlung component calculated by using the BREMSS model.

overall shape of the spectral continuum. Furthermore, it can be noticed that, as the temperature of the plasma increases, the gas becomes almost fully ionized; hence the APEC model matches very well with the BREMSS model. At lower temperatures, as the ionization fractions of metals decreases, contributions from both the line emission and other emission mechanisms involving metals (recombination radiation and two-photon process) become more significant.

In practice, the observed ICM/IGrM spectrum looks different than the photon flux model shown in Fig. 1.3 due to various observational factors. First of all, observations are made with an X-ray telescope (e.g., with eROSITA Predehl et al., 2021) that has finite energy resolution and sensitivity that is a function of photon energy (see Sect. 1.5 for more details on X-ray instruments, particularly eROSITA). This can be taken into account while analyzing X-ray observations by folding in the instrumental response before comparing it with the observed spectra. Furthermore, the observed clusters and groups are not at a redshift of 0, and the X-rays emitted by ICM/IGrM pass through absorbing material in the interstellar medium (ISM) of our own Galaxy before reaching the telescope. The former results in the source spectra being redshifted, and the latter results in some parts of the spectra being suppressed by the absorbing material. During spectral analysis, redshifting of the spectra can be corrected by a procedure called "K correction" (Hogg et al., 2002), and absorption of X-rays by the Milky Way can be accounted for by using absorption models such as TBABS (Wilms et al., 2000b). In addition, the source spectra from galaxy clusters and groups may not look as "clean" as in Fig.1.3 given that there are various background and foreground components, such as the galactic foreground (e.g., Bulbul et al., 2012; Ponti et al., 2023), the local hot bubble (e.g., Yeung et al., 2023), the cosmic X-ray background (due to unresolved X-ray sources; e.g., Cappelluti et al., 2017) and the detector background (due to cosmic rays depositing energy in the X-ray detectors; also referred as the particle background or non-X-ray background, NXB) superimposed with the spectra of the hot plasma. During the spectral analysis, these components can be accounted for by either subtracting or co-fitting spectra extracted near the source region (local background spectra). Lastly, the hot gas in galaxy clusters and groups often is not at a single temperature but is made up of plasma at different temperatures. This can be accounted for during the spectral analysis by using a plasma emission model that includes a distribution of temperatures, such as GADEM[4]. Nevertheless, obtaining robust fits to these multi-temperature models requires deep, high-quality data, which are often not available. Another alternative to this is splitting clusters or groups into smaller regions where the temperature can be assumed to vary less and deprojecting temperature profiles through deprojection schemes calibrated through simulations (e.g., Mazzotta et al., 2004; ZuHone et al., 2023). However, this technique also requires deep observations; hence, it is observationally expensive. For these reasons, when moderate signal-to-noise observations are available for galaxy clusters and groups, the spectra are often fitted with a single-temperature plasma model (e.g., Liu et al., 2022a; Bulbul et al., 2024).

---

[4]https://heasarc.gsfc.nasa.gov/xanadu/xspec/manual/XSmodelGadem.html

1.1.2 Physical Properties of Clusters and Groups as a Function of Radius

In the previous section, it was shown that the strength of the emission from the hot plasma in galaxy clusters and groups depends on several physical properties: the density of electrons (n_e), the density of protons (n_p), and the cooling function $\Lambda_{ep,\nu}(T, Z)$ (see Eq. 1.9). These properties vary as a function of radius as a consequence of the underlying dark matter potential well and other non-gravitational effects such as active galactic nuclei (AGN) feedback. It is crucial to investigate the radial dependence of the physical properties of galaxy clusters and groups to achieve a comprehensive understanding of the physical state of the cluster or group. For this purpose, analytical models are often used to model the physical properties of galaxy clusters and groups as a function of radius.

Dark matter mass and baryonic mass stand out as perhaps the most frequently utilized physical attributes of galaxy clusters and groups. Their measurements are not only of astrophysical interest but also hold significant importance for cosmology studies, given the close relation between the mass distribution of haloes and cosmology (Allen et al., 2011).

A commonly used analytical formulation for the dark matter distribution of galaxy clusters and groups is obtained by Julio Navarro, Carlos Frenk, and Simon White using N-body simulations of dark matter particles. They found that the shape of the dark matter density profiles shows remarkable similarity in a wide mass and cosmology range. The analytical formula they came up with is called Navarro-Frenk-White (NFW) profile (Navarro et al., 1996, 1997) and is given by

$$\rho_{\mathrm{DM}}(r) = \frac{\rho_0}{\frac{r}{r_s}\left(1 + \frac{r}{r_s}\right)^2} \tag{1.11}$$

where ρ_0 is the normalization of the profile and r_s is the scale radius. The model can also be equivalently expressed by two other parameters often used in the literature, halo mass (M_Δ) and concentration (c_Δ), by replacing r_s with

$$r_s = \frac{r_\Delta}{c_\Delta} \tag{1.12}$$

and ρ_0 with

$$\rho_0 = \frac{M_\Delta}{4\pi\left(\frac{r_\Delta}{c_\Delta}\right)^3}\frac{1}{\ln(1 + c_\Delta) - \frac{c_\Delta}{(1+c_\Delta)}}. \tag{1.13}$$

where the term r_Δ in the equations above is defined as the radii within which the average density of the halo becomes Δ times the critical density of the universe (ρ_c[5]) and is related to M_Δ as

$$M_\Delta = \Delta\,\rho_c\frac{4}{3}\pi r_\Delta^3 = \Delta\,\rho_{c,0}E(z)^2\frac{4}{3}\pi r_\Delta^3. \tag{1.14}$$

In the equation above, $\rho_{c,0}$ is defined as the critical density at a redshift of zero, $\rho_{c,0} \equiv \rho_c(z = 0)$, and $E(z)$ is defined as $E(z) \equiv H(z)/H_0$ where H_0 is the Hubble constant.

---

[5]The critical density of the universe is defined as $\rho_c \equiv 3H^2(z)/(8\pi G)$ where $H(z)$ is the Hubble parameter and G is the gravitational constant.

X-ray and optical observations later independently confirmed that the dark matter density of galaxy clusters and groups follow an NFW profile (e.g., Pointecouteau et al., 2005; Okabe et al., 2013). There are extensions to the NFW profile in the literature that provide more degrees of freedom, including a more generalized version of the NFW profile (gNFW) or the Einasto (1965) profile. Nevertheless, to date, the canonical NFW is still being widely used (e.g., Chiu et al., 2022; Grandis et al., 2024b).

Similar to the dark matter density profiles, galaxy clusters and groups exhibit remarkably similar baryonic matter/gas density profiles. A simple yet very versatile analytical formula for the gas density profile is the β profile (Cavaliere and Fusco-Femiano, 1976). The β profile is formulated as

$$\rho_{\text{gas}} = \rho_0 \left(1 + \left(\frac{r}{r_c} \right)^2 \right)^{-3\beta/2} \tag{1.15}$$

where ρ_0 is the normalization, r_c is the core radius and β is a free parameter for the exponent. The analytical form of the profile is motivated by the density distribution that arises from solving the hydrostatic equilibrium equation with the following assumptions: the hot gas in galaxy clusters and groups is isothermal and is in hydrostatic equilibrium, the typical atomic velocities are similar to the velocities of the galaxies in galaxy clusters and groups ($\sigma_r^2 \sim kT/\mu m_{\text{p}}$, where σ_r is the velocity dispersion of galaxies and μ is the mean molecular weight) and that the King (1962) approximation holds for the density profile of galaxies. Once the hydrostatic equilibrium equation is solved with these assumptions, the analytical formula provided in Eq. 1.15 is obtained where $\beta = \mu m_{\text{p}} \sigma_r^2 / kT$ (see Sarazin, 1986, for the full derivation). Furthermore, using the fact that $\rho_{\text{gas}} = n_e \mu_e m_{\text{p}}$, where μ_e is the mean molecular weight per electron, Eq. 1.15 can be rewritten for electron number density as

$$n_e = n_0 \left(1 + \left(\frac{r}{r_c} \right)^2 \right)^{-3\beta/2}. \tag{1.16}$$

It is well-established in the literature that the gas in galaxy clusters and groups is neither isothermal nor fully in hydrostatic equilibrium (e.g., see Lau et al., 2009; Ghirardini et al., 2019). For these reasons, the β profile proves to be insufficient for adequately describing the density profiles of galaxy clusters and groups throughout the entire radial range. Nevertheless, using the β profile for modeling the emission from galaxy clusters and groups at a given band has various advantages, even though it fails to describe the density profile with high precision. Perhaps the greatest advantage it has over more complicated models is the fact that the surface brightness profile of the ICM/IGrM from a gas following the β model can also be expressed analytically. The analytical form of the surface brightness profile of the gas following the β model is obtained as follows.

The surface brightness of hot gas with an arbitrary gas distribution is calculated by integrating the emission along the line of sight by following Eq. 1.10. The n_{p} term in Eq. 1.10 can be written in terms of n_e as

$$n_{\text{p}} = n_e \frac{\mu_e}{\mu_{\text{p}}} \tag{1.17}$$

where μ_p is the mean molecular weight per proton. Using this, the Eq. 1.10 can be rewritten as

$$S_X = \frac{1}{4\pi(1+z)^4}\frac{\mu_e}{\mu_p}\int n_e^2 \Lambda_{ep} dl. \tag{1.18}$$

Furthermore, by assuming the band averaged cooling function does not depend on radius (e.g., for an isothermal gas), substituting n_e with the analytical form of the β model (Eq. 1.16) and applying a change of variable ($dl = dr^2/2\sqrt{r^2 - b^2}$), the surface brightness of the gas can be expanded as

$$S_X = \frac{1}{4\pi(1+z)^4}\frac{\mu_e}{\mu_p}\Lambda_{ep} n_0^2 \int_{b^2}^{\infty}\left(1+\left(\frac{r}{r_c}\right)^2\right)^{-3\beta}\frac{1}{\sqrt{r^2-b^2}}dr^2 \tag{1.19}$$

where b is the projected radius from the center of the cluster or group. The solution to the integral on the right is presented in Gradshteyn and Ryzhik (1980, equation 2 of 3.196), using which the surface brightness profile can be written as

$$S_X = S_0\left(1+\left(\frac{b}{r_c}\right)^2\right)^{-3\beta+0.5} \tag{1.20}$$

where S_0 is

$$S_0 = \frac{1}{4\pi(1+z)^4}\frac{\mu_e}{\mu_p}\Lambda_{ep} n_0^2 r_c B(3\beta - 0.5, 0.5) \tag{1.21}$$

and B is the beta function[6] that forces $\beta > 1/6$ (Ettori, 2000). Given that the surface brightness profile resulting from the β density profile can be written in an analytical form, it is relatively easy to deproject emission from galaxy clusters and groups to measure their density profiles by assuming the distribution of the gas follows the β profile.

However, the β profile fails to accurately represent the shapes of the density profiles of many galaxy clusters and groups due to its low degree of freedom. For this reason, in most science cases, more complex density profiles are often preferred. After the β model, one of the most commonly used profiles with a higher degree of freedom is the Vikhlinin profile (Vikhlinin et al., 2006). Its functional form is obtained by applying substantial modifications to the β model. These modifications are motivated by the observed cuspiness at the cores and the steeper profiles observed at larger radii ($r > 0.3r_{200c}$). The square of the Vikhlinin electron number density profile presented in Vikhlinin et al. (2006) can be written as

$$n_e^2(r) = n_0^2\left(\frac{r}{r_c}\right)^{-\alpha}\left(1+\left(\frac{r}{r_c}\right)^2\right)^{-3\beta+\alpha/2}\left(1+\left(\frac{r}{r_s}\right)^3\right)^{-\epsilon/3} + n_{02}\left(1+\left(\frac{r}{r_{c2}}\right)^2\right)^{-3\beta_2}. \tag{1.22}$$

The right-most additive β model term is added by Vikhlinin et al. (2006) to provide extra degrees of freedom to model the emission from the cores of galaxy clusters and groups. However, for most studies, the signal-to-noise and/or resolution are not enough to fit this many free parameters. Therefore, it is common to drop the extra β model, after which the expression becomes

$$n_e^2(r) = n_0^2\left(\frac{r}{r_c}\right)^{-\alpha}\left(1+\left(\frac{r}{r_c}\right)^2\right)^{-3\beta+\alpha/2}\left(1+\left(\frac{r}{r_s}\right)^3\right)^{-\epsilon/3}. \tag{1.23}$$

---

[6]The beta function is defined as $B(a,b) = \frac{\Gamma(a)\Gamma(b)}{\Gamma(a+b)}$ and the gamma function (Γ) is defined as $\Gamma(y) = \int_0^{\infty} x^{y-1}e^{-x}dx$

The formula above without the extra β term is called the modified Vikhlinin profile and is perhaps the most common form of the Vikhlinin profile used in the literature (e.g., Maughan et al., 2008; McDonald et al., 2013; Ghirardini et al., 2019, 2021). In this formulation, the first two multiplicative terms (after the normalization) describe the core and the intermediate regions, and the third multiplicative term describes the outskirts of the clusters and groups. If needed, the model can be further simplified by dropping one of the radius parameters as $r_s = r_c$, such as been done in Liu et al. (2022a). The disadvantage of the modified Vikhlinin profile compared to the β profile is that the surface brightness profile of a gas following the Vikhlinin profile does not have an analytical form. Hence, to de-project the emission, the Vikhlinin profile is required to be integrated numerically. This, especially, adds considerable computation time when fitting X-ray images through the forward modeling approach. Nevertheless, thanks to the advancements in algorithmic optimization, code parallelization, and central processing unit (CPU) efficiency, calculating the projection integral numerically to fit X-ray images with the modified Vikhlinin profile remains feasible.

Throughout this thesis, the modified Vikhlinin profile is used to model and deproject the electron density profiles of galaxy clusters and groups, given its ability to accurately model the surface brightness emission from ICM/IGrM at large radii (Vikhlinin et al., 2006).

1.2   Scaling Relations

Scaling relations are mathematical expressions connecting the physical properties of gaseous haloes at different mass scales and redshifts. Given the connection they form between haloes in different evolutionary states, they are crucial tools for understanding the evolution of the large-scale structure. The exact form of these relations depends on two things: non-gravitational processes (e.g., AGN feedback, stellar feedback, galactic winds, and radiative cooling) and cosmology (e.g., cosmological model and its parameters).

Scaling relations are versatile tools and of interest in various astrophysical and cosmological studies. Two broad science themes stand out in studies utilizing scaling relations: (i) Quantifying the impact of non-gravitational physics in galaxy clusters and groups (e.g., Puchwein et al., 2008; Lovisari et al., 2015; Giles et al., 2016), and (ii) constraining cosmological properties of the universe by constructing the mass distribution of galaxy clusters (e.g., Mantz et al., 2015; Bocquet et al., 2019, 2024; Ghirardini et al., 2024).

In addition, well-calibrated scaling relations provide means to estimate physical properties that are observationally more challenging and/or expensive to measure (such as total mass or temperature) from observables that are easier to obtain, for instance, X-ray luminosity (e.g., Mantz et al., 2016; Bulbul et al., 2019; Chiu et al., 2022; Grandis et al., 2024b). This aspect of scaling relations is frequently used in galaxy cluster and group science, given that observational resources are often limited.

Kaiser (1986) derived simple forms of these relations by making three key assumptions: (i) Gaseous haloes are formed by the peaks in the initial density field collapsing under the influence of gravity in an Einstein–de Sitter Universe ($\Omega_m = 1$ and $\Omega_\Lambda = 0$), (ii) the power spectrum of the density fluctuations can be expressed as a power-law, and (iii) additional scales are not intro-

duced by the astrophysical mechanisms governing the physical properties of the halo. In such conditions, the gravitational collapse, as well as the resulting haloes, are scale-free (Kravtsov and Borgani, 2012). The model encapsulating the aforementioned assumptions and their consequences is called the Kaiser model (or the self-similar model), and the resulting relations are called self-similar scaling relations.

1.2.1 Self-similar Model

The Kaiser model predicts that the clusters forming via the scale-free collapse of the initial density peaks are "self-similar" (see Böhringer et al., 2012, for a review on the self-similarity of galaxy clusters). This implies that galaxy clusters at different masses and redshifts are simply scaled versions of each other such that their physical properties are connected to each other with appropriate mass and redshift scaling (Lovisari and Maughan, 2022).

In this section, the mass and redshift dependence of the self-similar scaling relations and their derivations are presented for seven observables: gas mass (M_{gas}), temperature (T), bolometric X-ray luminosity (L_{bol}), soft-band X-ray luminosity (L_X), Y_X, entropy (S) and pressure (P).

In addition to the three key assumptions of the Kaiser model mentioned in the last paragraph of the previous section, Kaiser assumed that clusters are spherically symmetric and the gas within the haloes is in hydrostatic equilibrium (Kaiser, 1986; Kravtsov and Borgani, 2012). Given these assumptions, the gas mass of the halo can be calculated out to an overdensity radius r_Δ as

$$M_{gas} = 4\pi\mu m_p \int_0^{r_\Delta} n_e r^2 dr = M_\Delta f_{gas} \propto M_\Delta \tag{1.24}$$

where f_{gas} is the gas mass fraction within r_Δ. In the final proportionality, f_{gas} is omitted based on the assumption in the Kaiser model that f_{gas} is independent of both z and M_Δ (Giodini et al., 2013).

Furthermore, the hydrostatic equilibrium equation of the gas compressed and heated under the influence of the dark matter potential well can be written as (Sarazin, 1986)

$$\frac{dP}{dr} = -\rho_g g = -\rho_g \frac{GM(<r)}{r^2}. \tag{1.25}$$

where g is the gravitational acceleration and G is the gravitational constant. Using the ideal gas law, $P = nkT = \rho_g kT/\mu m_p$, the equation above can be rewritten as

$$M(<r) = -\frac{kT}{G\mu m_p} \left(\frac{d\ln\rho_g}{d\ln r} + \frac{d\ln T}{d\ln r} \right) r. \tag{1.26}$$

If the gas is assumed to be isothermal, its temperature would be constant at all radii such that $d\ln T d/\ln r = 0$. Hence, the equation above can be simpified as

$$M(<r) = -\frac{kT}{G\mu m_p} \frac{d\ln\rho_g}{d\ln r} r. \tag{1.27}$$

Furthermore, the ρ_g term can be substituted with β density profile (Eq. 1.16), from which the relation between the mass and temperature can be calculated as

$$M(< r) = \frac{3\beta kTr}{G\mu m_p} \frac{(r/r_c)^2}{1 + (r/r_c)^2}. \tag{1.28}$$

Note that at large radii ($r >> r_c$), the equation approaches $M(< r) = 3\beta kTr/G\mu m_p$ which is equal to the mass temperature relation of a self-gravitating singular isothermal sphere (SIS), as long as $\beta = 2/3$ (Shapiro et al., 1999; Voit, 2005). For both the gas distributed as prescribed by the β model and the SIS, the relation between temperature, mass, and radius at large radii can be expressed as

$$T \propto M(< r)/r. \tag{1.29}$$

It should be further noted that the same relation can be obtained by assuming the isothermal gas is in virial equilibrium (e.g., see Lovisari et al., 2020). At an overdensity radius r_Δ, the r and $M(< r)$ terms in the equation above can be substituted using Eq. 1.14 such that the relation between T, M_Δ, z and Δ becomes

$$T \propto M_\Delta^{2/3} E(z)^{2/3} \Delta^{1/3}. \tag{1.30}$$

The bolometric X-ray luminosity (L_{bol}) is defined as the energy emitted per unit of time across the bolometric X-ray band ($0.01 - 100$ keV). It can be calculated by integrating $\epsilon_{0.01-100 \text{ keV}}$ [7] over the volume as

$$L_{\text{bol}} = \int \epsilon_{0.01-100 \text{ keV}} dV \propto \int n_e^2 \Lambda_{\text{ep}}^{\text{bol}} dV. \tag{1.31}$$

where $\Lambda_{\text{ep}}^{\text{bol}}$ is the band averaged cooling function for the bolometric X-ray band. Assuming thermal bremsstrahlung dominates the emission from the collisionally ionized hot plasma (see Sect. 1.1.1), L_{bol} within r_Δ can be rewritten using Eq. 1.2 as

$$L_{\text{bol}} \propto \int n_e^2 T^{1/2} dV \propto \rho_g^2 T^{1/2} r_\Delta^3 \propto M_{\text{gas}}^2 T^{1/2} r_\Delta^{-3}. \tag{1.32}$$

The relation can be further simplified by substituting r_Δ using Eq. 1.14 and M_{gas} using Eq. 1.24 such that the M_Δ, z and Δ dependence of L_{bol} becomes

$$L_{\text{bol}} \propto M_\Delta^{4/3} E(z)^{7/3} \Delta^{7/6}. \tag{1.33}$$

Similarly, the soft-band X-ray luminosity (L_X) in the canonical soft X-ray band ($0.5 - 2$ keV) can be written as

$$L_X = \int \epsilon_{0.5-2 \text{ keV}} dV \propto \int n_e^2 \Lambda_{\text{ep}}^X dV. \tag{1.34}$$

where Λ_{ep}^X is the band averaged cooling function for the $0.5 - 2$ keV band. As long as the ICM is sufficiently hot ($kT > 2$keV), the band averaged cooling function is insensitive to T in the soft

---

[7]See Eq. 1.9 for the definition of $\epsilon_{\nu_0-\nu_1}$

X-ray band (Eckert et al., 2016; Lovisari et al., 2021) therefore, the relation for L_X can be written as

$$L_X \propto \rho_g^2 r_\Delta^3 \propto M_{gas}^2 r_\Delta^{-3}. \tag{1.35}$$

Lastly, by substituting r_Δ and M_{gas} using Eqs. 1.14 and 1.24, the relation between L_X, M_Δ, z and Δ can be written as

$$L_X \propto M_\Delta E(z)^2 \Delta. \tag{1.36}$$

Kravtsov et al. (2006) introduced the parameter Y_X as a proxy for the total thermal energy of the ICM. It is defined as $Y_X \equiv M_{gas}T$ such that M_{gas} is proportional to the number of particles in the system and T is proportional to the average kinetic energy; therefore, their multiplication is proportional to the total thermal energy of the gas. It is inspired by the Sunyaev Zel'dovich (SZ) observable Compton-y parameter (Y_{SZ}), and similar to that, it is a low scatter mass indicator (Kravtsov et al., 2006). Employing the definition introduced above and using the Eqs. 1.24 and 1.30, the M_Δ, z and Δ dependence of Y_X can be written as

$$Y_X \propto M_{gas}T \propto M_\Delta^{5/3} E(z)^{2/3} \Delta^{1/3}. \tag{1.37}$$

Another useful quantity for studying the hot gas in galaxy clusters and groups is entropy S. It depends on the structure of ICM/IGrM and is closely connected to the thermodynamic history (Voit, 2005). It is defined as $S \equiv kT/n_e^{2/3}$ and the M_Δ, z and Δ dependence of it can be derived using Eqs. 1.14, 1.24 and 1.30 as

$$S \equiv kT n_e^{-2/3} \propto T \rho_{gas}^{-2/3} \propto T M_{gas}^{-2/3} r_\Delta^2 \propto M_\Delta^{2/3} E(z)^{-2/3} \Delta^{-1/3}. \tag{1.38}$$

Lastly, pressure is a key thermodynamic quantity that prevents the gas from collapsing under the deep dark matter potential well. To first order, clusters are in hydrostatic equilibrium. Hence, the pressure of the hot gas is tightly connected to the mass distribution of the halo via the hydrostatic equilibrium equation (see Eq. 1.25). Pressure of ICM/IGrM is defined as $P \equiv n_e kT$ and the M_Δ, z and Δ dependence of it can be derived by using Eqs. 1.14, 1.24 and 1.30 as

$$P \equiv n_e kT \propto T \rho_{gas} \propto T M_{gas} r_\Delta^{-3} \propto M_\Delta^{2/3} E(z)^{8/3} \Delta^{4/3}. \tag{1.39}$$

1.2.2 Deviations from Self-similarity in Observations

Testing the predictions of the self-similar model with the observations of galaxy clusters and groups is essential for advancing our understanding of the complex baryonic physics governing gaseous halos. Achieving a better understanding of the scaling relations is also key for using galaxy clusters and groups as cosmological probes (Allen et al., 2011). In this subsection, we present observational evidence of the deviations from the self-similar model. The observational results presented in this section are selected based on their relevance to this thesis, with the goal of laying the groundwork for the studies presented in the following Chapters. Furthermore, the theoretical perspective on the deviations of galaxy clusters and groups from self-similarity is presented and discussed in the next subsection.

The $L - T$ relation, which connects X-ray luminosity and temperature of galaxy clusters and groups, is both the first and most extensively studied scaling relation (e.g., Mitchell et al., 1977, 1979; Mushotzky, 1984; Pratt et al., 2009; Maughan et al., 2012; Lovisari et al., 2015; Giles et al., 2016; Molham et al., 2020). This is due to the fact that both of these observables can be obtained almost independently from the X-ray observations (Giodini et al., 2013). When Kaiser (1986) formulated self-similar relations, there were already indications from early studies (Mitchell et al., 1977, 1979) that the observed $L - T$ relation has a steeper slope than the one predicted by the self-similar model (the self-similar model predicts a slope of 2 for the $L_{bol} - T$ relation and a slope of $3/2$ for the $L_X - T$ relation). Subsequent studies confirmed indications of a steep $L - T$ relation and got to a consensus of a slope of ~ 3 for the $L_{bol} - T$ relation and a slope of ~ 2.5 for the $L_X - T$ relation (Giodini et al., 2013). The temperature of the gas in galaxy clusters and groups is a good proxy of the underlying potential well (e.g., see Borgani et al., 2002) whereas, L is highly sensitive to non-gravitational feedback mechanisms as it has a strong dependence on the density of the gas, $L \propto n_e^2$ (see Sect. 1.3 for details on the feedback processes). Therefore, the significant mismatch between the observed slope of the $L - T$ relation with the prediction of the self-similar model indicates that the non-gravitational mechanisms, such as AGN feedback, impact the gas distribution of galaxy groups differently than the gas distribution of clusters (Donahue and Voit, 2022).

Similar to the $L - T$ relation, the $S - T$ relation also provides valuable insights into the heating and cooling history of the halo. Entropy is a direct tracer of the feedback (Voit, 2005); hence, studying the $S - T$ relation allows constraining the feedback mechanisms acting on galaxy clusters and groups. Ponman et al. (1999) investigated this relation in their pioneering study and found excess entropy compared to the similarity relation (obtained from non-radiative hydro-dynamic simulations) for haloes at the low-temperature/low-mass parameter space. Subsequent research, which employed a more accurate analysis that moved beyond isothermality assumptions and investigated the temperature of the ICM/IGrM as a function of radius, confirmed the excess entropy (Mahdavi et al., 2005; Finoguenov et al., 2007). Around the same time, Johnson et al. (2009) and Sun et al. (2009) investigated the $S - T$ relation for groups and concluded that the entropy excess is more prominent in galaxy groups compared to clusters. Sun et al. (2009) also investigated the radial dependence of the $S - T$ relation and found that the agreement between observations and the self-similar haloes in non-radiative hydrodynamic simulations (Voit, 2005) improves as the measurement radii increases. This is also in agreement with the findings of Pratt et al. (2009) for galaxy clusters. Lastly, Panagoulia et al. (2014) investigated nearby galaxy clusters and groups and found that the shape of the entropy profiles of massive haloes can be described well with a broken power law.

As shown above for the $L - T$ and $S - T$ relations, there are numerous observational studies in the literature indicating scaling relations of galaxy clusters and groups deviate from the self-similar predictions (e.g., Pratt et al., 2009; Lovisari et al., 2015; Giles et al., 2016; Bulbul et al., 2019; Chiu et al., 2022). These deviations are attributed to the departures from the simplistic assumptions inherent in the Kaiser model. While many studies report these deviations, some studies find that high-mass galaxy clusters exhibit results consistent with self-similarity (e.g., Mantz et al., 2016; McDonald et al., 2017). Regardless of how representative the self-similar model is, it holds significance as it provides a baseline for comparing the observed scaling rela-

tions and quantifying the impact of non-gravitational processes.

Given the impact of non-gravitational processes on the properties of gaseous haloes is yet not fully constrained, scaling relations are required to be calibrated using observations to get their true form and dependencies. Scaling relations cannot be calibrated by directly fitting power-law models to the measurements due to observational biases (Lovisari and Maughan, 2022). Robust calibration of the scaling relations can only be obtained by fully taking into account the selection effects and the mass function, as in recent studies (Mantz et al., 2016; Giles et al., 2016). A detailed prescription of the calibration process of the X-ray scaling relations by taking into account the selection effects and the mass function is presented in Chapter 2.

1.2.3   Deviations from Self-similarity from the Theoretical Perspective

The self-similar model predicts power-law scaling relations. The form and the relations are a consequence of the set of assumptions of the Kaiser (1986) model. In this subsection, the validity of the list of assumptions of the Kaiser model will be examined, and the consequences of deviations from these assumptions on the scaling relations will be discussed.

One of the first assumptions made to derive self-similar relations is that, even though the normalizations of the T and ρ_{gas} profiles scale with mass (M), their shape is independent of M (Kravtsov and Borgani, 2012). This assumption is used to derive self-similar relations for M_{gas} and T (Eqs. 1.24 and 1.30) however, numerical simulations have shown that even in purely self-similar models, the shape of the matter density profile, $\rho(r)$ has a mass dependence (e.g. the concentration mass relation in Navarro et al., 1997). Furthermore, the same simulations also have shown that the mass dependence of the shape of ρ differs in various cosmologies. According to the latest cosmology constraints obtained by combining the eROSITA and Planck results, our universe can be described well with a Lambda Cold Dark Matter (ΛCDM) model with $\Omega_{\Lambda} = 0.68$, $\Omega_m = 0.32$ and $\sigma_8 = 0.82$ (Planck Collaboration et al., 2020; Ghirardini et al., 2024). This is very different than the simple Einstein-de Sitter model ($\Omega_{\Lambda} = 0$ and $\Omega_m = 1$) assumed in the Kaiser (1986) model. Therefore, even in the case of simple spherical collapse (without any non-gravitational physics), the shapes of the T and ρ_{gas} profiles being mass dependent, as well as this dependence not being the same for ΛCDM and Einstein-de Sitter cosmologies, poses challenges to the self-similar relations.

Besides assuming the shapes of the profiles to be independent of halo mass and cosmology, Kaiser (1986) assumed scaling relations to be purely shaped by gravity and thermodynamics. In the self-similar model, non-gravitational astrophysical phenomena are assumed to be negligible; therefore, their impact on the scaling relations is ignored. Nevertheless, clusters and groups are subject to various astrophysical phenomena that have a non-negligible impact on these relations throughout their formation and evolution (e.g., see Sect. 1.3). In general, the non-gravitational phenomena have two effects on the scaling relations: they alter the relation and add scatter. One would notice that the self-similar relations presented in the previous section are in the form of power law proportionalities, whereas, considering the diverse nature of these objects, some scatter is expected between observables. A significant proportion of this scatter comes from the sum of the impact of non-gravitational phenomena on the properties of ICM/IGrM.

It has been shown by independent studies in the literature that galaxy clusters and groups are

not in full hydrostatic equilibrium as assumed in the self-similar scenario (e.g., see Ettori et al., 2013; Salvati et al., 2018; Pratt et al., 2019; Eckert et al., 2019; Gianfagna et al., 2021, and the references therein). This is theorized to be due to the turbulence and/or bulk motions providing additional (non-thermal) pressure support to the ICM/IGrM whose amount varies from halo to halo. The objects deviating from the hydrostatic equilibrium assumption in different amounts both introduce scatter and contribute to the change in the exponents of the relations.

Furthermore, the self-similar model ignores the astrophysical mechanisms that supply additional non-gravitational energy to the system, such as AGN feedback, stellar feedback, and galactic winds, as well as the processes that subtract energy from the system, such as radiative cooling. Modern cosmological hydrodynamical simulations such as Magneticum[8] (Hirschmann et al., 2014), MillenniumTNG[9] (Hernández-Aguayo et al., 2023; Pakmor et al., 2023) and the OverWhelmingly Large Simulations (OWL simulations, Schaye et al., 2010) include prescriptions of these processes to reproduce observations and the resulting scaling relations show significant deviations from self-similarity (e.g, Le Brun et al., 2014; Biffi et al., 2014; Pakmor et al., 2023; ZuHone et al., 2023). Even though prescriptions of non-gravitational phenomena are included in all modern cosmological hydrodynamical simulations, there are implementation differences as well as uncertainties on the strength of the feedback mechanisms (see Sect. 1.3 for the description and discussion of the feedback mechanisms). These differences result in discrepancies between the physical properties of gaseous haloes in different simulations (e.g., see Fig. 15 in Eckert et al., 2021). Observations allow us to test the models implemented in these simulations, thereby putting constraints on both the implementation and the assumed feedback model parameters (e.g, Le Brun et al., 2014).

Lastly, Kaiser (1986) assumed gaseous haloes to be spherically symmetric. Whereas there is a plethora of observational and theoretical evidence that neither the dark matter distribution nor the gas distribution is fully symmetrical (e.g., Oguri et al., 2010; Umetsu et al., 2018; Chua et al., 2019; Ghirardini et al., 2022; Campitiello et al., 2022). This is due to the fact that morphologies of gaseous haloes can depend on various factors, such as their merging history and the directions of the filaments connecting them to the cosmic web. The diversity of the morphologies of gaseous haloes introduces large amounts of scatter to the scaling relations (e.g., Pratt et al., 2009; Lovisari et al., 2020) as well as poses challenges to the validity of the assumed radial hydrostatic equilibrium equation (Eq. 1.25) and to the spherical mass definition (e.g. in Eq. 1.24) in the self-similar model.

1.3 Feedback

In the context of galaxies, galaxy groups, and galaxy clusters, the word "feedback" is used as an umbrella term to describe self-regulating processes providing energy to their surroundings. Feedback is introduced as an essential mechanism necessary to explain the observed properties of gaseous halos. The need for feedback in a cosmological context is initially motivated by four observational findings (i) the observed relation between the mass of the central supermassive

---

[8]http://www.magneticum.org
[9]https://www.mtng-project.org
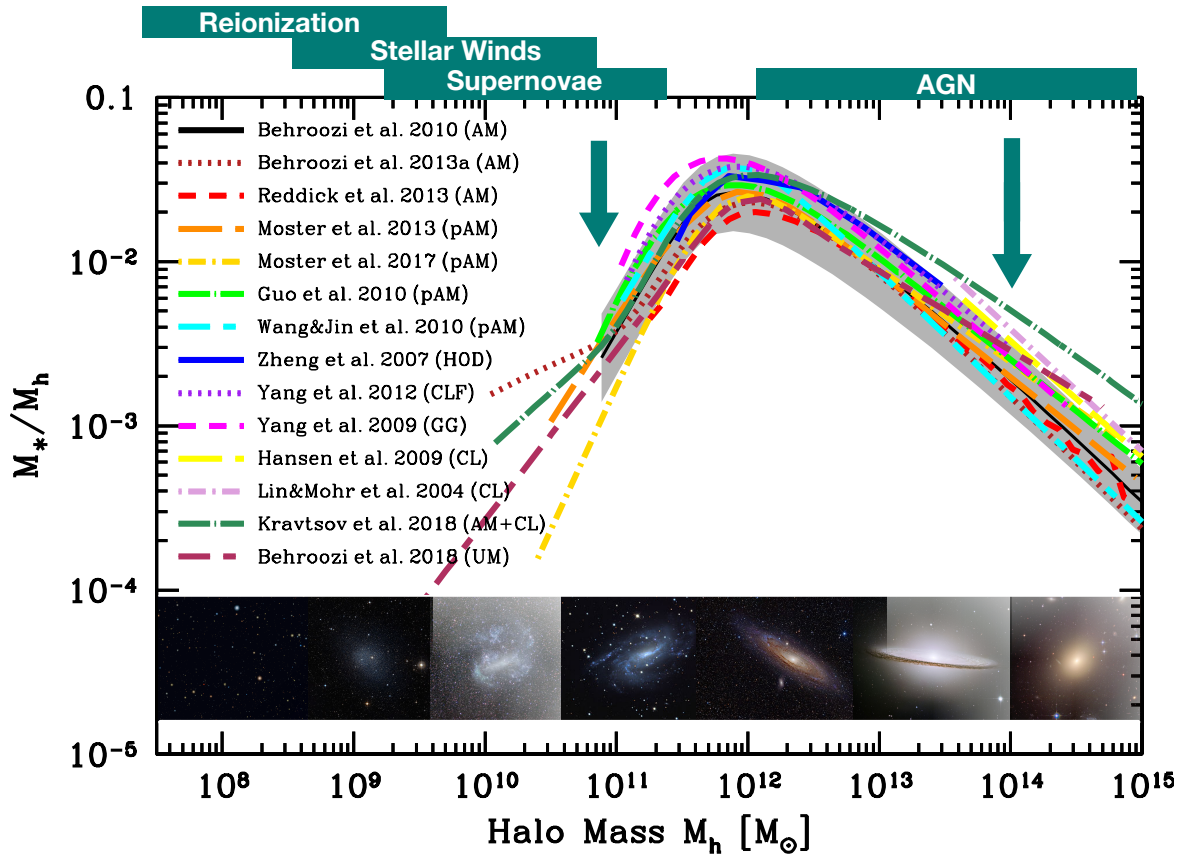
Figure 1.4: Measurements of stellar-to-halo mass ratios (M_*/M_h) of central galaxies (at $z = 0.1$) compiled by Behroozi et al. (2019). At the top of the figure, approximate mass ranges where the annotated feedback processes are most influential are shown with green rectangles. Green arrows indicate reduced star formation efficiency at the high and low mass end of the parameter space. At the bottom panel, images of example galaxies are shown that are hosted by haloes at the corresponding mass range. Plot adapted from Wechsler and Tinker (2018).

black hole and the bulge properties (the $M_{BH} - \sigma$ relation Magorrian et al., 1998; Ferrarese and Merritt, 2000; Gebhardt et al., 2000), (ii) the lack of catastrophic cooling flows around massive galaxies (Binney and Tabor, 1995; Ciotti and Ostriker, 1997; Peterson et al., 2003), (iii) the excess entropy at the cores of galaxy groups (Ponman et al., 1999; Lloyd-Davies et al., 2000; Ponman et al., 2003), and (iv) the requirement of an additional mechanism to reproduce the observed stellar mass/luminosity function in semi-analytical models and hydrodynamical simulations (Blanchard et al., 1992; Benson et al., 2003; Croton et al., 2006; Hopkins et al., 2006).

Initially, stellar winds and supernovae (stellar feedback) are considered to be the sources of feedback required to explain observations. These mechanisms were able to explain some of the observational findings for the low-mass galaxies (stellar masses $< 10^{10}$ $M_\odot$), such as the inefficiency of galaxy formation at the low-mass end of the stellar mass/luminosity function (Harrison and Ramos Almeida, 2024). However, it soon became clear that the stellar feedback alone is not sufficient to explain the stellar mass/luminosity function at the high mass end (Menci and Cavaliere, 2000; Bower et al., 2001), as well as the hot gas properties of the massive gaseous haloes (Kay et al., 2003; Valdarnini, 2003; Nagai et al., 2007b). Given the observed co-evolution of the mass of the central supermassive black hole and the bulge properties, feedback from the central black hole (AGN feedback) emerged as an attractive solution to explain the observational findings for giant ellipticals, galaxy groups, and galaxy clusters (Eckert et al., 2021). In fact, over time, the energetics and kinematics of AGN feedback proved to be sufficient to explain the higher mass end of the mass/luminosity function as well as the hot gas properties of massive gaseous haloes and became a crucial component of modern cosmological hydrodynamic simulations (Springel et al., 2005; Di Matteo et al., 2005).

One of the best ways to visualize the impact of AGN feedback on gaseous haloes at different mass scales is by looking at the stellar-to-halo mass ratio as a function of halo mass. Observational results compiled by Behroozi et al. (2019) for stellar-to-halo mass ratios of central galaxies at $z = 0.1$ are presented in Fig. 1.4. In this figure, the approximate mass ranges where the feedback processes are most influential are also shown at the top panel. As indicated by the green arrows, overall, feedback processes reduce the star formation efficiency (also see Fig. 1 of Harrison, 2017). The degree of this reduction varies with the mass scale and, therefore, depends on which feedback mechanism is dominant. It can be seen from Fig. 1.4 that the gaseous haloes of interest in this thesis ($M_h > 5 \times 10^{12}$ $M_\odot$) fall within the mass range where feedback from AGN primarily determines the baryonic properties. Consequently, in this thesis, we primarily focus on the feedback from AGN.

1.3.1 AGN Feedback

AGN feedback is a crucial mechanism in high-mass halos for regulating bulge properties, preventing cooling flows, accounting for the excess entropy, and controlling star formation activity (Harrison and Ramos Almeida, 2024). Accretion onto black holes is the most efficient process for converting rest mass into energy (Werner et al., 2019). Silk and Rees (1998) introduced a relatively simple model for AGN feedback where AGN regulates the accretion flow (thereby also controls the feedback) through winds created by radiation. In this model, the feedback mechanism couples the properties of the central black hole and the galactic bulge and, establishes the

$M-\sigma$ relation. They further argued in their paper that depending on the accretion rate, the release of gravitational potential energy from AGN can approach or even exceed the binding energy of the host galaxy. King (2003) refined the model proposed by Silk and Rees (1998) by modeling outflows as momentum-driven wind bubbles. This led to model predictions for the $M_{BH} - \sigma$ relation that are in better agreement with observations compared to those of Silk and Rees (1998). Croton et al. (2006) then extended these ideas by incorporating a two-mode feedback model. They introduced the "quasar mode feedback" (also called wind mode feedback or thermal feedback), which arises from AGN with radiatively efficient disks operating at high accretion rates, and the "radio mode feedback" (also called jet mode feedback or kinetic feedback), which arises from AGN with radiatively inefficient disks operating at low accretion rates (Hlavacek-Larrondo et al., 2022).

Quasar mode feedback is inspired by observations of high-redshift AGN that convert most of the accretion energy into radiation and wind (e.g., Russell et al., 2010; Siemiginowska et al., 2010; O'Sullivan et al., 2012), and the radio mode feedback is inspired by radio observations exhibiting feedback signatures around powerful jets, such as X-ray shocks and cavities (e.g., McNamara et al., 2005; Kirkpatrick et al., 2009; Randall et al., 2015). The quasar mode feedback in numerical simulations is often modeled as isotropic energy release to the surroundings of the supermassive black hole, whereas the implementation of the radio mode varies from one simulation suite to another. In the modern cosmological hydrodynamical simulations, the radio mode feedback is either modeled as isotropic thermal feedback with an increased efficiency (e.g., see Hirschmann et al., 2014) or as kinetic feedback where the central supermassive black hole releases kinetic energy rather than thermal energy to its surroundings (e.g., see Pillepich et al., 2018; Weinberger et al., 2017).

The most direct observational evidence of AGN feedback arises from its interaction with its surroundings. During this interaction, AGN can manifest itself in various forms, such as bubbles/cavities, shocks, sound waves, and winds Hlavacek-Larrondo et al. (2022). A well-known example of these phenomena is the sound waves (ripples) observed in the X-ray images of the Perseus cluster (Fabian et al., 2003; Sanders and Fabian, 2007). These ripples were generated by the central AGN, operating in the radio mode, which inflated small bubbles and produced weak shocks. After the bubbles were created, they moved outwards due to buoyant forces and produced distinct X-ray features of Perseus. Similar ripples have also been observed in the Abell 2052 (Blanton et al., 2011) and Centaurus (Sanders et al., 2016) clusters. Additionally, the literature contains numerous examples of larger bubbles and stronger shocks that often exhibit cavities inflated by radio jets (e.g., McNamara et al., 2005; Kirkpatrick et al., 2009; Randall et al., 2015). To form these cavities, AGN should overcome the local pressure. Therefore, if cavities are present (or detectable), they can be used to put lower limits on the mechanical power of the AGN (Eckert et al., 2021). Like cavities, shocks are characteristic AGN feedback features with energy levels comparable to the cavities (Liu et al., 2019). A collage of images of galaxy clusters and groups that exhibit prominent radio mode AGN feedback signatures, including shocks and cavities, is shown in Fig. 1.5.
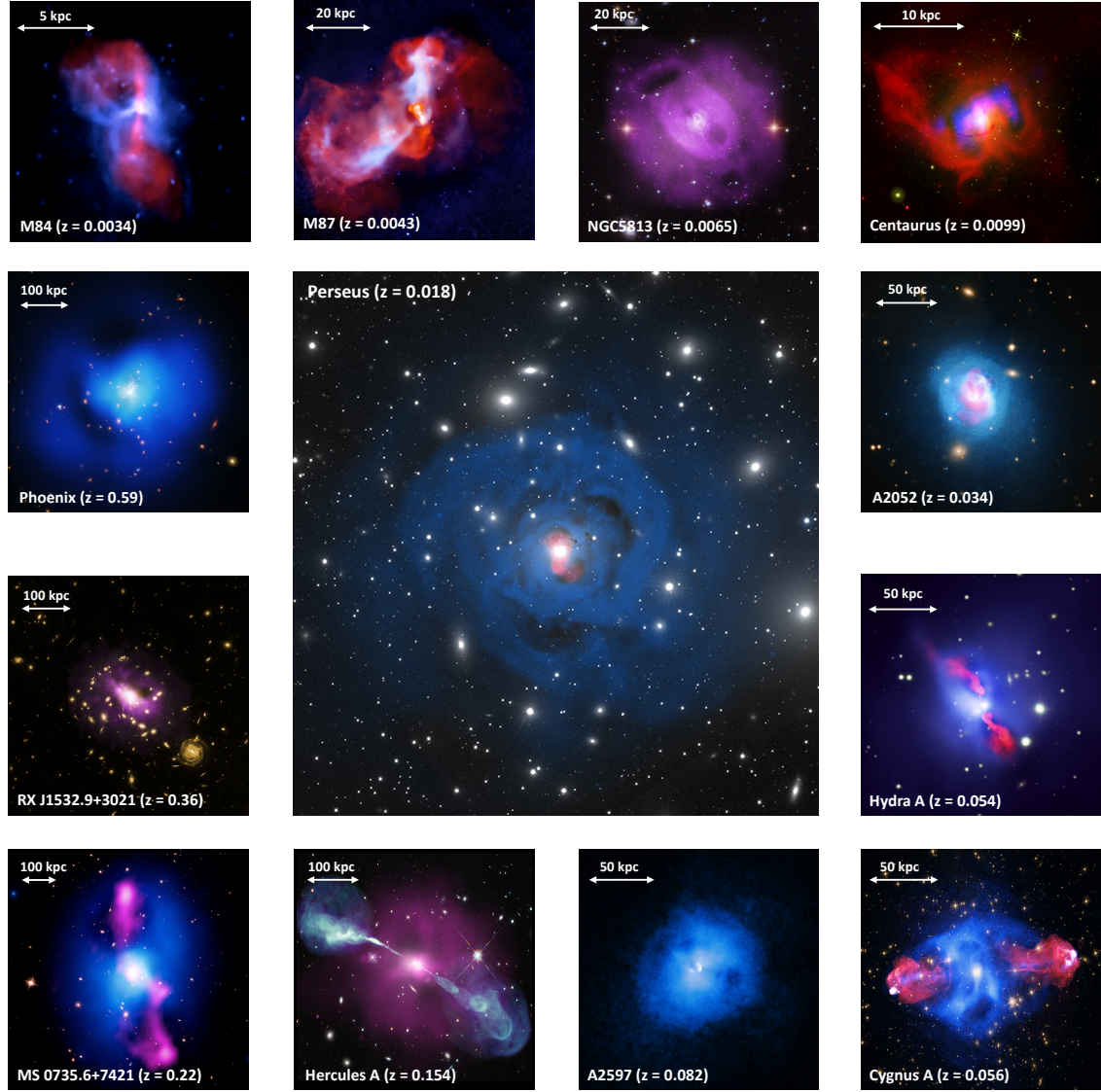
Figure 1.5: A collage of images of galaxy clusters and groups that exhibit prominent radio mode AGN feedback signatures (McNamara et al., 2005; Nulsen et al., 2005; Finoguenov et al., 2008; Kirkpatrick et al., 2009; Werner et al., 2010; Blanton et al., 2011; Hlavacek-Larrondo et al., 2013; Randall et al., 2015; McDonald et al., 2015; Sanders et al., 2016; Tremblay et al., 2018). Plot taken from Hlavacek-Larrondo et al. (2022).

1.4 Galaxy Groups

There is no universal definition of galaxy groups in the literature; however, there is a broad agreement that their masses range between $5 \times 10^{12} M_\odot < M_{500c} < 10^{14} M_\odot$ and/or they have less than 50 member galaxies. The parameter space they live in connects relatively smaller objects, such as giant ellipticals, with large ones, such as massive clusters. Given that they are abundant and have substantial mass, they can be considered as the building blocks of the large-scale structure. In fact, at low redshift, the halo mass density function (in log-space) peaks at the group mass regime (Eckert et al., 2024). Given their role in forming large-scale structures, it is crucial to have a good understanding of their properties in order to achieve a comprehensive picture of the Universe.

They are particularly interesting objects for investigating non-gravitational mechanisms since their potential wells are not as deep as clusters; therefore, the impact of these mechanisms is more prominent. This puts them to a unique place in the mass parameter space such that their binding energy is comparable to the energy supplied by the central AGN (Eckert et al., 2021). This allows groups to retain a majority of their gas content while their gas gets heavily impacted by the central engine (Eckert et al., 2024).

The hot plasma in galaxy clusters and groups is in a delicate balance of heating and cooling. Cooling takes place through emission, and the heating is supplied by various objects or events such as AGN, supernovae, or galactic winds. Earlier simulations tried to reproduce observations by including prescriptions of supernovae (SNe) feedback; nevertheless, the heating supplied by SNe proved to be insufficient for stopping the gaseous haloes in the universe from catastrophically cooling via cooling flows and producing overly massive central galaxies (e.g., Borgani et al., 2004; Nagai et al., 2007a). In light of these attempts to reproduce observations, the prescription of an extra source for heating, AGN, is implemented in simulations. Nevertheless, given the uncertainties about the energy output of AGNs and their interactions with the surrounding gas, different AGN feedback implementations in simulations result in significant mismatches between their predictions at various scales (e.g., see Ni et al., 2023; Grandis et al., 2024a).

Given the vulnerability of IGrM to non-gravitational processes, the impact of these mechanisms can be constrained well by measuring the thermodynamic properties of the gas in galaxy groups. Furthermore, the physics of these mechanisms can then be constrained by comparing these measurements with the predictions of simulations with different subgrid physics prescriptions (see Oppenheimer et al., 2021, for a comparison between the predictions of simulations at the galaxy group scale). The coupling between the central AGN and the surrounding hot gas is often probed through the two main X-ray observables: temperature and density. In a broad sense, the central AGN in galaxy clusters and groups releases energy through two mechanisms. It heats the surrounding gas (thermal feedback) and gives gas kinetic energy (kinetic feedback) (Weinberger et al., 2017). These processes result in the surrounding gas being heated and pushed away. Therefore, as a consequence of the feedback, the temperature of the gas increases, and its density decreases. The observable that traces the combination of these properties the best is entropy ($S \equiv kT/n_e^{2/3}$). It keeps a record of the thermodynamic history and is responsible for determining the structure of the hot gas (Voit, 2005). As the potential wells of groups are shallower than clusters, the deviation of their entropy profiles from the self-similar entropy profile (Voit,
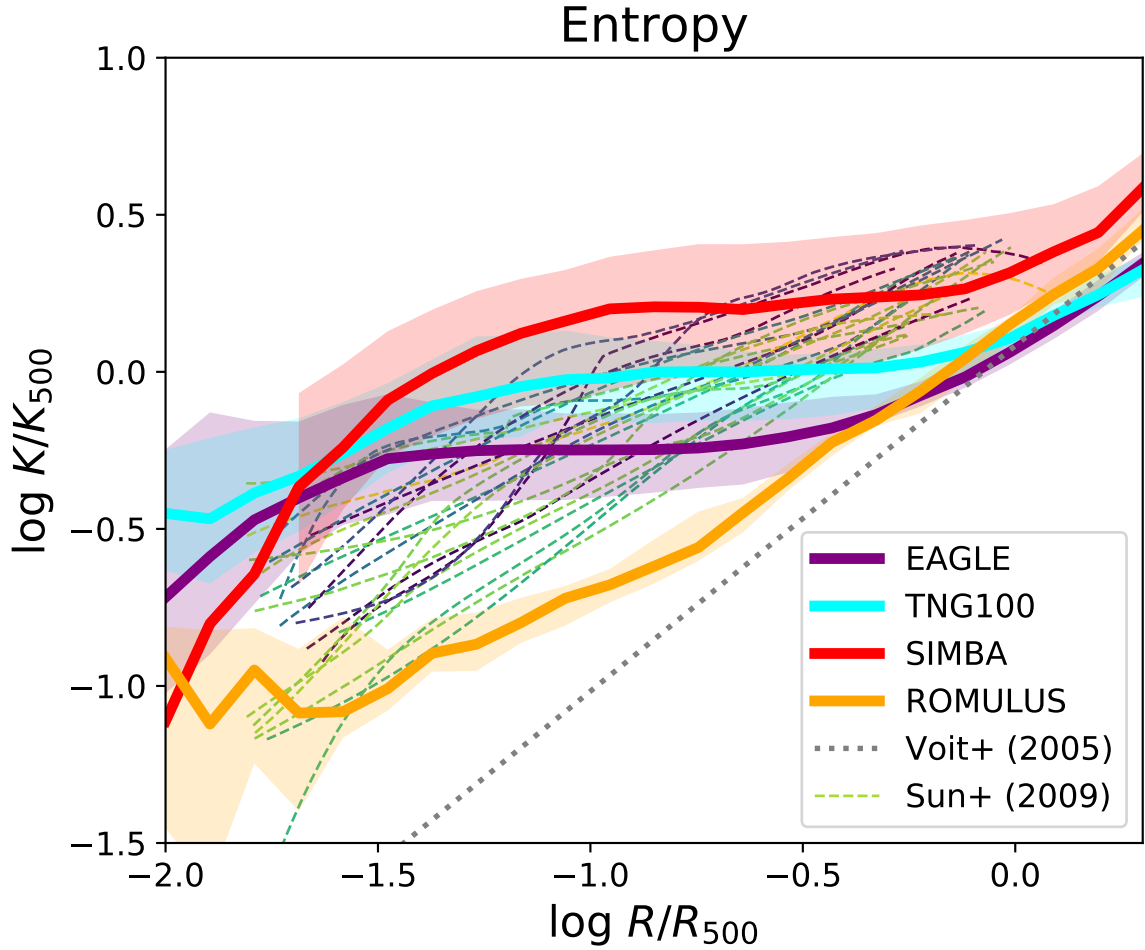
Figure 1.6: Scaled entropy profiles of galaxy groups as a function of dimensionless radius. Entropy is scaled with adiabatic entropy predicted from the mass of the halo (see Eq. 7 in Sun et al., 2009), and the x-axis is scaled with r_{500c}. Predictions of various simulations are shown with solid lines in various colors, and their scatter is shown as shaded regions. The baseline profile obtained from non-radiative simulations is shown with grey dotted lines (Voit, 2005), and the *Chandra* measurements of nearby galaxy groups are shown with dashed lines Sun et al. (2009). Plot taken from Oppenheimer et al. (2021).
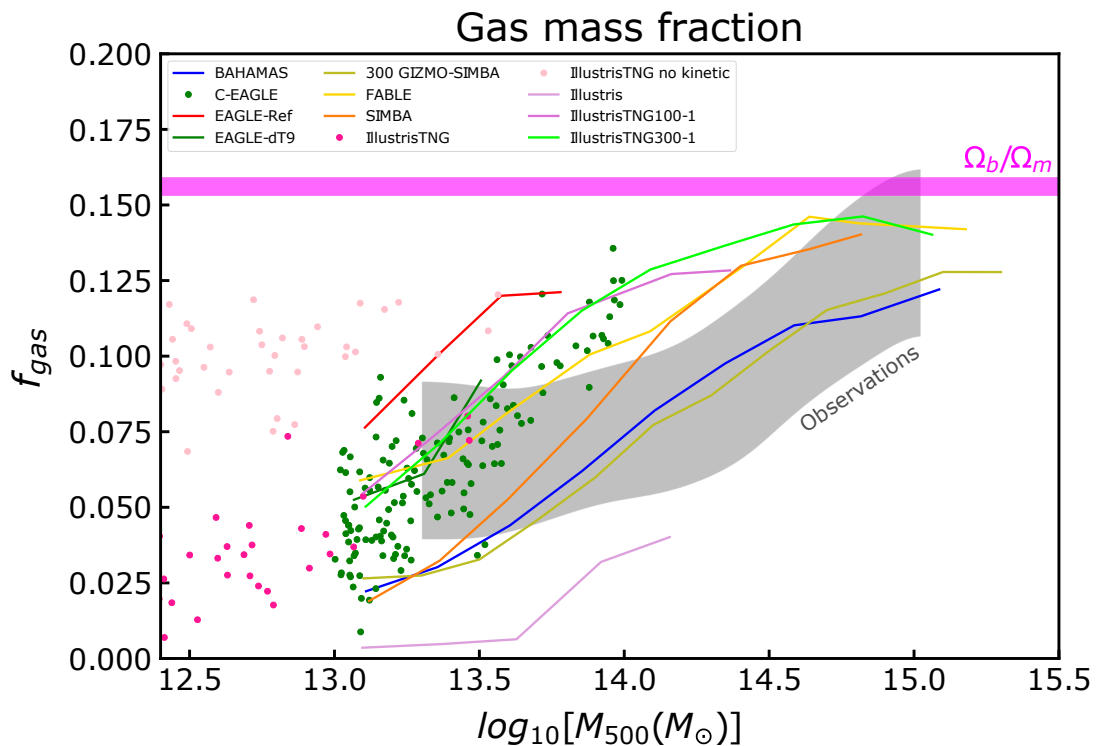
Figure 1.7: Gas mass fraction as a function of halo mass. The universal baryon fraction is shown as a shaded area in magenta. Predictions of various modern hydrodynamic simulations are shown as solid lines and scatter points in different colors. The parameter space covering a compilation of observations is shown as a shaded region in grey (see Fig. 7 in Eckert et al., 2021, for the list of observations used to derive the shaded region). Plot adapted from Eckert et al. (2021).

2005) extends to larger radii (e.g., see Fig. 5 in Le Brun et al., 2014). A comparison between the group entropy profiles of Sun et al. (2009) with the predictions of modern hydrodynamic simulations is shown in Fig. 1.6.

Another key physical property for quantifying the impact of AGN feedback is the gas mass fraction ($f_{gas} \equiv M_{gas}/M$) within an overdensity scale Δ. Gas mass fraction is highly relevant for X-ray studies given that M_{gas} can be directly measured by integrating the electron density profile (see Eq. 1.24), and M can also be measured using X-rays assuming hydrostatic equilibrium (see Eq. 1.26). Observations have shown that the gas mass fraction within r_{500c} gradually decreases from values close to the cosmic baryon fraction (Ω_b/Ω_m) to $f_{gas} \sim 0.06$ (see grey shaded area in Fig. 1.7). Simulations suggest that this may be due to a significant portion of the IGrM gas being carried to outer regions by the central AGN, which is harder for clusters given the deeper potential well (Gaspari et al., 2012; Le Brun et al., 2014). Similar to entropy, predictions of simulations with different AGN feedback prescriptions are significantly different for the gas mass fraction (see the lines and data points for simulations in Fig. 1.7). Robustly measuring gas mass profiles of groups and comparing the measurements with simulations with different AGN feedback implementations allow constraints on the burstiness and energetics of the AGN feedback prescriptions (Le Brun et al., 2014).

It should be noted that when comparing observations with the predictions of simulations, the selection effects should be accounted for. The gas properties, such as the electron density profile or the temperature profile, can be highly correlated with the detection probability of groups in X-rays (e.g., see Eckert et al., 2011; Rossetti et al., 2017). Ideally, to have a fair comparison, it should be ensured that the compared samples were subject to similar selection; if this is not possible, either the selection effects should be modeled, or observables that are not a strong function of the selection probability should be chosen while comparing with simulations (Gelman et al., 2014).

Another approach to constrain the impact of non-gravitational processes on IGrM is through measuring scaling relations between integrated quantities and comparing the relations with the predictions of the simulations and/or the predictions of the self-similar model. As discussed extensively in Sect. 1.2, the form and the exact relation between the integrated properties of clusters and groups are determined by the thermodynamic histories (heating/cooling) of the gaseous haloes. The self-similar model predicts the $L_X - T$ and $L_X - M$ relations to flatten at the group regime due to the change of the temperature dependence of the band averaged cooling function at the IGrM temperatures (see Fig. 6 in Donahue and Voit, 2022). Nevertheless, recent observations suggest that galaxy groups scale not very different than galaxy clusters (Lovisari et al., 2021). This can be explained well by the increased impact of AGN feedback on the integrated properties of the group scale haloes (Puchwein et al., 2008). Similar to entropy and gas mass fraction, AGN feedback prescription can be tested by robustly calibrating scaling relations (by taking into account the selection effects and the mass function) and comparing them with the predictions of the state-of-the-art cosmological hydrodynamical simulations.

The hot gas in galaxy groups also holds significance due to its metal content. A significant portion of metals produced in galaxies residing in clusters and groups are expelled into the surrounding hot atmospheres, ICM/IGrM (Gastaldello et al., 2021). The detection of Fe-K line emission in the spectra of Perseus, Coma, and Virgo clusters by Ariel 5 and OSO8 space
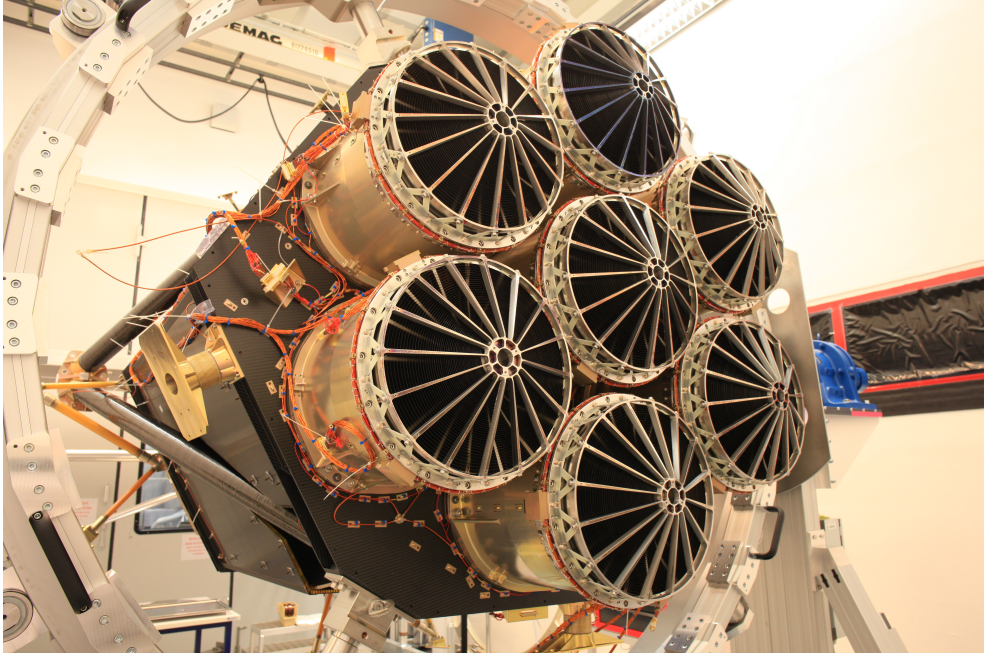
Figure 1.8: Front view of eROSITA showing the seven mirror assemblies. Image taken from Predehl et al. (2021).

telescopes marks the first indication that the hot atmospheres of gaseous haloes are enriched by metals (Boehringer and Werner, 2009). The ratio between the iron present in ICM/IGrM to the iron contained in the galaxies can get up to 10 (Renzini and Andreon, 2014; Ghizzardi et al., 2021). The hot gas in galaxy groups has a temperature of $kT < 2$ keV. As the temperature of the gas decreases, heavy elements get recombined, and the fraction of fully ionized metals decreases. This results in the strength of the emission from metals (line emission and free-bound emission) becoming comparable to the emission from the thermal bremsstrahlung mechanism at $kT = 1 - 2$ keV and surpassing it at $kT < 1$ keV (see the right panel of Fig. 1 in Lovisari et al., 2021). This makes the emission highly sensitive to the metal content and hence makes galaxy groups uniquely suited objects for studying the metal content of hot atmospheres (Gastaldello et al., 2021).

1.5   eROSITA

The extended ROentgen Survey with an Imaging Telescope Array (eROSITA; Merloni et al., 2012; Predehl et al., 2021) is an X-ray telescope that was launched on the 13th of July 2019 on board the Spectrum-Roentgen-Gamma (SRG) mission to perform all-sky survey observations from the second Lagrange point (L2). eROSITA is the primary instrument attached to the SRG observatory and is built under the responsibility of the Max Planck Institute for Extraterrestrial Physics (MPE) in Germany. It shares SRG with another X-ray telescope, Mikhail

Pavlinsky ART-XC (Pavlinsky et al., 2021), that has complementary instrumental characteristics to eROSITA at higher energies and was built by the Russian Space Research Institute, IKI. eROSITA was designed and built to perform the most sensitive and sharp complete survey of the X-ray sky following the success of its predecessor ROSAT (1990 – 1999; Truemper, 1982).

eROSITA is an imaging telescope that is made up of seven co-aligned identical X-ray telescope modules (TMs) that are arranged in a hexagonal configuration. It is sensitive to X-ray photons over a large energy range (0.2 – 8 keV). Seven identical mirror assemblies (one for each TM) are mounted to the instrument that consists of 54 Wolter-I (Wolter, 1952) type mirror shells (Friedrich et al., 2008; Arcangeli et al., 2017). An image of the seven mirror assemblies is shown in Fig. 1.8, and a schematic view of the instrumental configuration of the eROSITA telescope is shown in Fig. 1.9. The average on-axis spatial resolution of the mirror assemblies is 18″ Half-Energy Width (HEW), and the average spatial resolution over the field of view is about 30″ HEW.

Each telescope module contains a charge-coupled-device (CCD) camera at the focal plane that has 384×384 pixels without any chip gaps. The pixels in each CCD cover a physical area of 28.8 mm × 28.8 mm that corresponds to a field of view of $1°03 \times 1°03$. The eROSITA CCDs are significantly improved versions of the EPIC-pn CCDs of *XMM-Newton*. The former CCDs are equipped with a framestore area that almost fully prevents the occurrence of out-of-time events. The information in the image area is transferred to the framestore area in 0.115 ms, and the read-out process takes place in 9.18 ms. Overall, the eROSITA CCDs have a nominal integration time of 50 ms.

In addition to its large field of view and good spatial resolution, eROSITA also stands out with the energy resolution and sensitivity of its CCDs. The in-orbit calibration tests show that for single-pixel events, the energy resolution is close to the theoretical limit (Dennerl et al., 2020). In terms of sensitivity, the total on-axis effective area of eROSITA (including all 7 TMs) is slightly higher than *XMM-Newton* (pn + MOS) in the soft X-ray band (0.5–2 keV). At the harder energies (> 2 keV), eROSITA response exhibits a sharp drop due to an absorption edge at 2.2 keV attributed to the gold M-shell, after which eROSITA's hard band sensitivity is substantially lower. Despite that, eROSITA's on-axis effective area at the hard X-ray band (2 − 10 keV) is slightly larger than *Chandra* and significantly surpasses that of ROSAT. Nevertheless, the greatest strength of eROSITA is its efficiency in performing large-area surveys. One of the parameters that quantify this efficiency is called grasp, which is defined as the product of effective area and field of view. It is a metric for evaluating the surveying capabilities of instruments and is often used to compare the effectiveness of X-ray telescopes in mapping large regions in the sky. eROSITA's unprecedented grasp significantly outperforms all the previously built X-ray instruments between the 0.2–4 keV energy band. A comparison between the effective area and the grasp of eROSITA, *Chandra*, *XMM-Newton*, and ROSAT is shown in Fig. 1.10.

eROSITA's primary science goal, which has driven the design decisions, includes detecting 100,000 galaxy clusters and groups out to high redshifts ($z > 1$), providing high-quality X-ray observations to investigate their physical properties, and constrain cosmology by testing cosmological models including Dark Energy (Predehl et al., 2021). To fully accomplish the primary science objective within the SRG mission's lifespan, eight all-sky X-ray surveys were planned to be conducted with eROSITA that correspond to four years of survey observations (Merloni et al.,
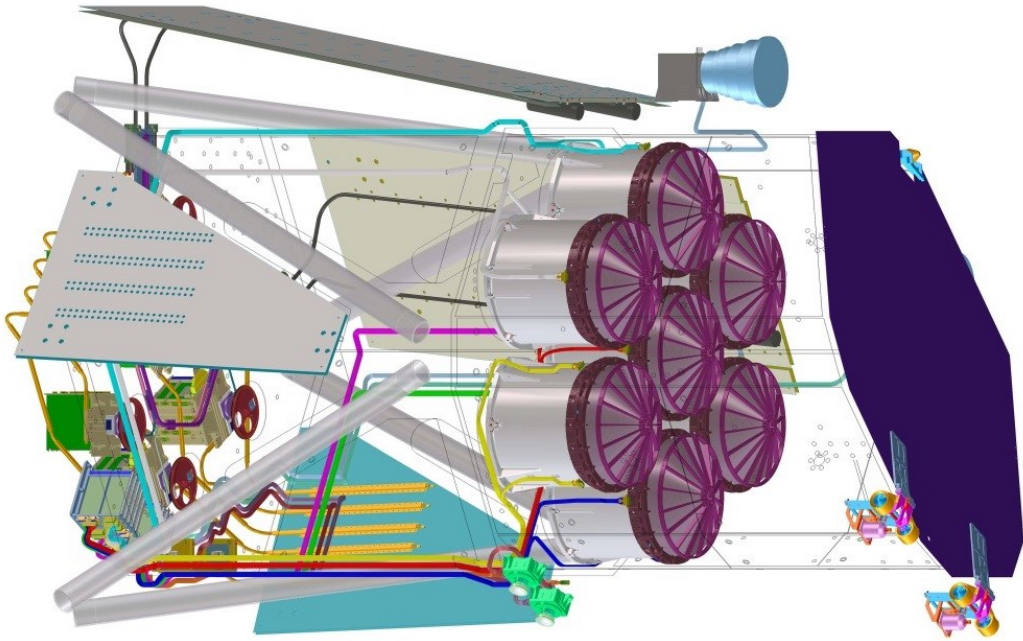
Figure 1.9: Schematic view of eROSITA's telescope layout. From left to right, seven camera assemblies, including camera, electronics box, and filter wheel; seven mirror assemblies, including, mirrors and electron deflector; and front cover. Figure adapted from Predehl et al. (2021).

2012). During its operations time in addition to tens of thousands of galaxy groups, eROSITA is predicted to detect millions of AGNs. Furthermore, eROSITA's survey observations also include sources from other astrophysical species, such as X-ray binaries, active stars, supernova remnants, and the warm-hot circumgalactic medium of the Milky Way.

The all-sky survey observations eROSITA performs are called eROSITA all-sky surveys (eRASS) and are performed by the spacecraft rotating continuously around an axis pointing towards the vicinity of the Sun. With this observing strategy, eROSITA draws large circles on the sky and scans the full sky in six months. This observing strategy results in exposure inhomogeneities in the sky such that exposures around the ecliptic poles are larger than the exposures in equatorial regions (see Fig. 16 in Predehl et al., 2021).

The scientific utilization rights of eROSITA data are shared equally between German and Russian eROSITA consortia according to an inter-agency agreement signed in 2009 (Merloni et al., 2024). Under this agreement, the German eROSITA consortium (eROSITA-DE) has rights to the scientific exploitation of the Western Galactic hemisphere ($359.9442° > l > 179.9442°$), and the Russian consortium has the rights for the eastern Galactic hemisphere ($-0.05576° < l < 179.9442°$) that are splitted by the line passing through the Galactic poles and Sgr A*.

Since its launch, eROSITA has completed Calibration and Performance Verification (CalPV) observations and ~ 4.5 all-sky surveys. On the 26th of February 2022, the survey operations
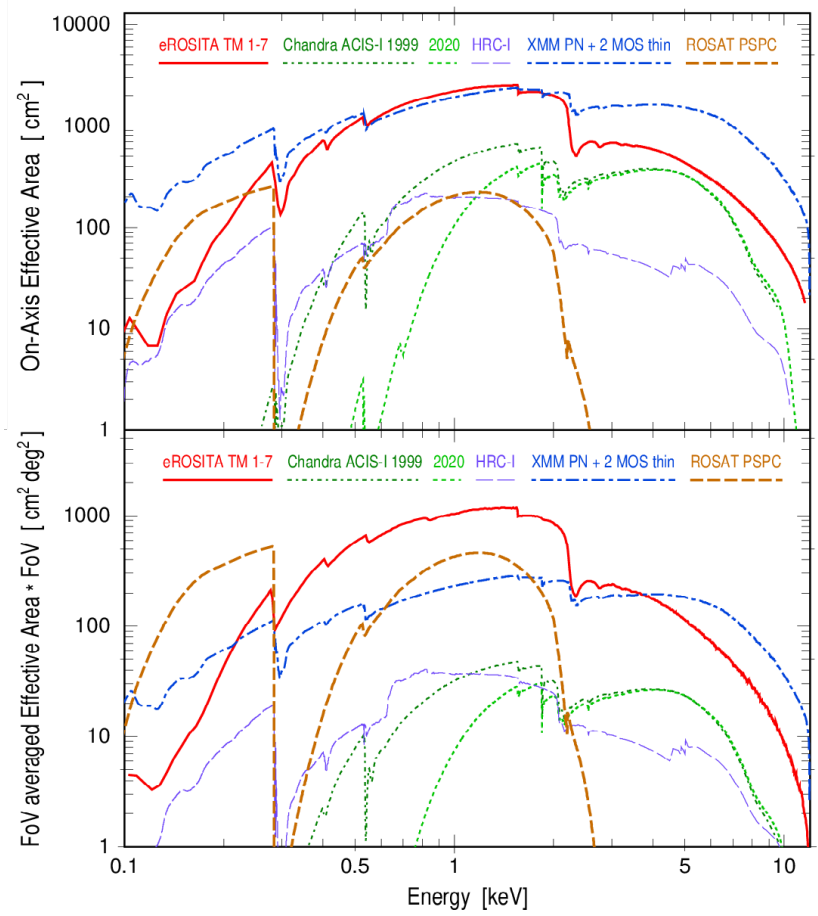
Figure 1.10: *Top:* Comparison between the on-axis effective area of eROSITA with *Chandra* ACIS-I (1999 and 2020), *Chandra* HRC-I, *XMM-Newton*, and ROSAT. *Bottom:* Comparison between the field of view averaged grasp (field of view averaged effective area × field of view) of eROSITA with *Chandra* ACIS-I (1999 and 2020), *Chandra* HRC-I, *XMM-Newton*, and ROSAT. Figure adapted from Predehl et al. (2021).
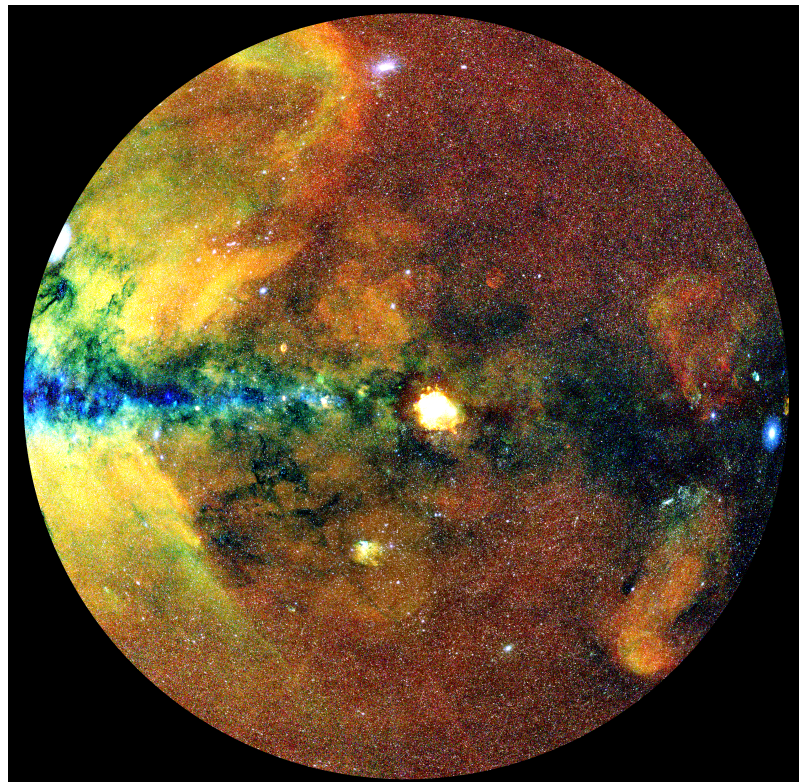
Figure 1.11: RGB exposure corrected X-ray image of the Western Galactic hemisphere obtained from eRASS1 observations. The red color represents the X-ray intensity in the 0.3–0.6 keV energy band, the green color represents the X-ray intensity in the 0.6–1 keV energy band, and the blue color represents the X-ray intensity in the 1–2.3 keV energy band. Credit: Jeremy Sanders (MPE)

were paused, and eROSITA was put in safe mode[10]. The completion of the remaining planned all-sky survey observations by eROSITA is uncertain.

On the 28th of June 2021, the eROSITA-DE consortium made their CalPV observations publicly accessible and gave astronomers a glimpse of the eROSITA's rich dataset. The data release includes the observations of eROSITA's first mini-survey, eROSITA Final Equatorial Depth Survey (eFEDS). X-ray catalogs of various astrophysical pieces detected in the eFEDS field are also published as part of the data release campaign (e.g., Liu et al., 2022a,b; Brunner et al., 2022). Furthermore, on the 31st of January 2024, the eROSITA-DE consortium released the Western Galactic hemisphere of the first all-sky survey (eRASS1) observations along with a catalog of extended and point sources detected in these observations (Merloni et al., 2024). Exposure-corrected X-ray image of the Western Galactic hemisphere using publicly available eRASS1 observations is shown in Fig. 1.11. Galaxy clusters and groups in the main eRASS1 catalog (Merloni et al., 2024) are optically confirmed (Kluge et al., 2024), and the final eRASS1 galaxy clusters and groups sample with their physical properties are presented in Bulbul et al. (2024).

1.6   Outline of the Thesis

The thesis starts with an introduction in Chapter 1 that provides an overview of the key concepts and background information essential for understanding the research presented in the subsequent Chapters. First, a general introduction to galaxy clusters and groups is presented in the Chapter, highlighting the properties of the X-ray-emitting plasma and the physical properties of galaxy clusters and groups as a function of radius. The introduction then advances to scaling relations by providing an overview of the predictions of the self-similar model and then discussing the causes and consequences of the deviations from self-similarity. Then, a more detailed overview of the astrophysics of the galaxy groups is presented, which are the cosmological species investigated deeply in the following Chapters, and finally, the introduction Chapter finishes with an overview of eROSITA, the X-ray space telescope whose observations are employed in all the subsequent Chapters of this thesis.

In Chapter 2, the first eROSITA study on the X-ray scaling relations of galaxy clusters and groups is presented. The Chapter begins with a brief overview of the eFEDS observations and the scaling relation studies in the literature. Then, a summary of the analysis procedures conducted on the eFEDS observations to extract the X-ray observables of the clusters and groups used in the scaling relations calibration is presented. This is followed by a detailed description of the Bayesian modeling and fitting framework utilized in the study. Then, the best-fit relations for seven X-ray scaling relations, $L_X - T$, $L_{bol} - T$, $L_X - M_{gas}$, $L_{bol} - M_{gas}$, $L_X - Y_X$, $L_{bol} - Y_X$, and $M_{gas} - T$, are presented and are compared with the previous results in the literature. Lastly, the eROSITA measurements are compared with the predictions of the self-similar model, and the impact of non-gravitational mechanisms on integrated physical properties of ICM/IGrM is constrained.

---

[10]https://www.mpe.mpg.de/7856215/news20220303

The work presented in Chapters 3 and 4 employs this final eRASS1 galaxy clusters and groups sample. For the X-ray analysis, however, a deeper, stacked version of the first four eROSITA all-sky survey observations (eRASS:4[11]) are used.

In Chapter 3, constraints on the impact of AGN feedback in galaxy groups obtained from the all-sky survey observations of eROSITA are presented. The Chapter begins with a brief overview of the eRASS observations and the AGN feedback studies in the literature for groups. Then, the galaxy group sample used in the study is introduced, and the key physical properties of the sample are presented. This is followed by a detailed description of the initial X-ray data reduction procedure and the Bayesian imaging and spectral analysis procedures applied to the eRASS observations of the groups. Later, various systematics that may impact the measurements reported in this study are discussed, and their impact is quantified to be included in the total error budget. Then, the entropy measurements obtained from these procedures at three characteristic radii are presented as a function of integrated temperature, and the results are compared with the previous findings in the literature. The eROSITA measurements are compared with the baseline predictions of the OWL Simulations, and the constraints on the impact of AGN on IGrM are reported. Lastly, the measurements are compared with three modern cosmological hydrodynamical simulations with different AGN feedback implementations: Magneticum, MillenniumTNG, and the OWL Simulations, and the strengths and weaknesses of these simulations in reproducing the observations of galaxy groups are discussed.

In Chapter 4, thermodynamic profiles of galaxy groups measured with eROSITA are presented. It begins with a brief overview of the studies in the literature investigating thermodynamic profiles for galaxy clusters and groups. Then, the measurements of four key X-ray observables: (i) electron density, (ii) temperature, (ii) entropy, and (iv) pressure are presented, and the mass dependence of these profiles is examined. Furthermore, the scaled thermodynamic profiles are obtained by normalizing them with the self-similar scales, and the mass trends after the removal of these scales are discussed. The scaled profiles are then compared with the previous measurements from the literature on galaxy clusters and groups, and the similarities/differences between the profiles of clusters and groups are discussed. Later, the profiles are compared with the baseline predictions of the non-radiative cosmological hydrodynamic simulations, through which the impact of non-gravitational processes is constrained. The measurements are also compared with the predictions of various runs of the cosmo-OWL simulations that include different model parameters for their AGN feedback implementation. Lastly, the scaled profiles are compared with the predictions of the Magneticum and MillenniumTNG simulations, and the agreement/disagreement between these simulations and the eROSITA measurements are discussed.

Finally, in Chapter 5, a summary of the thesis as well as an outlook of future studies is presented.

Throughout this thesis, we adopt a flat ΛCDM cosmology using the Planck Collaboration et al. (2016) results, namely $\Omega_m = 0.3089$, $\Omega_b = 0.0486$, $\sigma_8 = 0.8147$, and $H_0 = 67.74$ km s^{-1} Mpc^{-1}. Quoted error bars correspond to a 1-σ confidence level unless noted otherwise.

---

[11]Throughout this thesis, colon, :, is used to indicate cumulative/stacked eROSITA all-sky surveys observations. The number written after the colon indicates the number of stacked all-sky survey observations starting from the first.

Chapter 2

The eROSITA Final Equatorial-Depth Survey (eFEDS): X-ray Properties and Scaling Relations of Galaxy Clusters and Groups

The physical properties of the hot gas in galaxy clusters and groups are shaped by the underlying mass distribution and non-gravitational processes acting on large scales. Scaling relations link these properties and provide insights into how they vary across halos of different masses and redshifts. In the absence of non-gravitational effects, the masses of gaseous halos are expected to obey so-called self-similar scaling relations between X-ray observables. The impact of non-gravitational processes on the hot plasma can be constrained by quantifying any deviations from these self-similar relations. Scaling relations can also be used to probe the evolution of large-scale structure, estimate observables of clusters and groups, and constrain cosmological parameters through cluster number counts. In this Chapter, we investigate the scaling relations between X-ray observables of the clusters detected in the eFEDS field using SRG/eROSITA observations, taking into account the selection effects and the halo mass distribution. We extract five X-ray observables (L_X, L_{bol}, T, M_{gas}, Y_X) within r_{500c} for a sample of 542 clusters and groups. We then use these observables to calibrate seven X-ray scaling relations, based on a secure subsample consisting of 265 clusters with less than 10% contamination. We define this subsample such that the selection procedure is reproducible in simulations; therefore, the sample has a well-defined selection function. We fit the relations in a Bayesian framework which incorporates a selection function (derived from simulations) and a canonical halo mass function to account for selection effects and the mass distribution of dark matter halos. We present the best-fit scaling relations obtained through this fitting procedure, along with comparisons with previous measurements from the literature. Additionally, in this Chapter, we compare the best-fit scaling relations with the self-similar scaling relations and discuss the observed deviations. From this comparison, we find that the best-fit slopes significantly deviate from the self-similar model at a $> 4\sigma$ confidence level. Our results are, however, in good agreement with cosmological simulations that incorporate non-gravitational physics, as well as with the recent observational studies that

account for selection effects. The study presented in this Chapter extends the scaling relations to the low-mass, low-luminosity galaxy cluster and group regime. Our work demonstrates the ability of eROSITA to measure emission from the intracluster medium out to r_{500c} at depths equivalent to the equatorial regions of the final eROSITA all-sky survey and constrain the scaling relations over a wide mass-luminosity-redshift range.

The results presented in this Chapter have been published in Bahar et al. (2022), for which I performed the majority of the work and analysis. Dr. Ang Liu and Dr. Vittorio Ghirardini provided the best-fit parameters of the electron density profiles and the X-ray observables within the overdensity radius r_{500c}, and Dr. Nicolas Clerc provided the selection function used to calibrate the scaling relation.

2.1   Introduction

Galaxy clusters, which are formed by the gravitational collapse of the largest density peaks in the primordial density field, represent the largest virialized objects in the Universe. Embedded in the cosmic web, they evolve and grow through mergers and by accreting smaller subhaloes via the surrounding large-scale structure (e.g., Kravtsov and Borgani, 2012). The number counts of clusters of galaxies as a function of redshift and their mass is a powerful cosmological probe that is orthogonal and complementary to other cosmological geometrical experiments (e.g., Pillepich et al. 2012; Mantz et al. 2015; Schellenberger and Reiprich 2017; Pacaud et al. 2018, see also Pratt et al. 2019 for a review). Additionally, based on the current Lambda cold dark matter (ΛCDM) cosmological model, galaxy clusters are among the structures formed most recently and, therefore, capture the formation history and the growth of the structure in the Universe.

Well-established scaling relations between cluster mass and observables provide a way forward for cosmological investigations using clusters of galaxies. Accurate estimates of cluster total masses are crucial ingredients for exploiting the cluster number counts as cosmological probes. However, measurements of masses of individual clusters through multi-wavelength (X-ray, optical, weak lensing, and radio) observations can be expensive for larger cluster samples. Scaling relations aid this problem, and bridge cluster number counts with cosmology. On the other hand, the scaling relations between observables and their evolution allow us to constrain intracluster medium (ICM) physics and theoretical models based on gravitational collapse (e.g., Kaiser, 1986; Ascasibar et al., 2006; Short et al., 2010; Capelo et al., 2012). Kaiser (1986) modeled the formation of clusters as scale-free collapses of initial density peaks and derived relations between ICM properties that result in clusters at different redshifts and masses being scaled versions of each other. This is known as the self-similar model and it is discussed extensively in Chapter. 1. Other non-gravitational physical processes, such as radiative cooling, turbulence, galactic winds, and AGN feedback that affect the formation and evolution of these objects throughout cosmic time, may have imprints on these relations. In observational studies, these imprints are quantified by measuring deviations from the self-similar scaling relations (see Subsect. 1.2.2). Clusters of galaxies, owing to their deep potential well, are less prone to these non-gravitational processes, while the intra-group gas in galaxy groups can be significantly impacted by non-gravitational physics (e.g., Tozzi and Norman, 2001; Borgani et al., 2002; Babul

et al., 2002; Puchwein et al., 2008; Biffi et al., 2014; Barnes et al., 2017).

The majority of the baryonic content of the clusters is in the form of X-ray-emitting hot ionized plasma, the ICM. Being in the fully ionized state and reaching up to 10^8 Kelvin in temperature, the ICM emits primarily in X-rays through thermal Bremsstrahlung, offering an opportunity to measure physical properties of the ICM to establish scaling relations between these properties and mass, and to constrain their evolution over cosmic time (see Sect. 1.1.1 for details on the X-ray-emitting plasma its emission mechanisms). The scaling relations between X-ray observables and mass have been extensively explored for massive clusters in the literature, selected in various ways by the large-area, multi-wavelength surveys (e.g., Mantz et al., 2010b; Bulbul et al., 2019). However, samples including a sufficient number of uniformly selected groups covering the low-mass, low-redshift, and low-luminosity range with adequate count rates are limited. Studies of the scaling relations of galaxy groups and clusters spanning a wide mass, luminosity, and redshift range with large-area surveys with a well-understood selection will improve our understanding of the interplay between galaxy evolution, AGN feedback, and gravitational processes in these deep potential wells. XMM-*Newton*'s largest observational program XXL (Pierre et al., 2011) served as a bridge between narrow and deep observations (e.g., CDF-S, Finoguenov et al., 2015) and very wide, moderately deep observations (e.g., RASS, Ebeling et al., 1998) by populating the intermediate parameter space with detected clusters. Most recently, the extended ROentgen Survey with an Imaging Telescope Array (eROSITA, Merloni et al., 2012; Predehl et al., 2021) carried out its eROSITA Final Equatorial-Depth Survey (eFEDS) observations and provided numerous cluster detections that span a large mass–redshift space. eROSITA on board the Spectrum-Roentgen-Gamma (SRG) mission continues to detect large numbers of clusters spanning a wide range of redshift and mass since its launch in 2019. It will provide sufficient statistical power to place the tightest constraints on these scaling relations for probing their mass and redshift evolution.

eFEDS was performed during eROSITA's calibration and performance verification phase (Predehl et al., 2021; Brunner et al., 2022; Liu et al., 2022a). eFEDS, the first (mini)survey of eROSITA, is designed to serve as a demonstration of the observational capabilities of the telescope to the scientific community. The survey area is located at (approximately) $126° <$ R.A. $<$ $146°$ and $-3° <$ Dec. $< +6°$ and covers a total of $\sim140 \deg^2$. The exposure time of the survey area is mostly uniform with average vignetted and unvignetted exposure times of ~ 1.3 and ~ 2.2 ks, respectively (Brunner et al., 2022). The eFEDS area is also covered in survey programs of other telescopes such as the Hyper Supreme-Cam Subaru Strategic Program (HSC-SSP; Aihara et al., 2018), DECaLS (Dark Energy Camera Legacy Survey, Dey et al., 2019), SDSS (Sloan Digital Sky Survey, Blanton et al., 2017), 2MRS (2MASS Redshift Survey, Huchra et al., 2012), and GAMA (Galaxy And Mass Assembly, Driver et al., 2009). These observations are used to optically confirm the detected clusters and measure their redshifts (Klein et al., 2022). In addition to the optical confirmation and redshift determination, HSC-SSP observations are also used in measuring the weak lensing mass estimates of the detected clusters. The observables presented in this Chapter are measured using r_{500c}[1] values inferred from the weak lensing measurements

---

[1] r_{500c} is the overdensity radius within which the density of the cluster is 500 times the critical density of the Universe at the cluster's redshift.

presented in Chiu et al. (2022).

In this Chapter, we provide X-ray properties of the 542 galaxy clusters and groups in the full eFEDS-extent-selected sample (Liu et al., 2022a) in two apertures ($r < r_{500c}$ and $0.15r_{500c} < r < r_{500c}$). Additionally, we investigate the scaling relations between core-included ($r < r_{500c}$) X-ray observables in a subsample of 265 galaxy clusters and groups with a lower level of contamination by non-cluster detections. The study presented in this Chapter expands the scaling relation studies to the poorly explored mass (6.86×10^{12} M$_\odot$ $< M_{500c} < 7.79 \times 10^{14}$ M$_\odot$), luminosity (8.64×10^{40} erg s^{-1} $< L_X < 3.96 \times 10^{44}$ erg s^{-1}), and redshift ($0.017 < z < 0.94$) ranges with the largest number of galaxy groups and clusters, paving the way for similar studies using the eROSITA All-Sky survey (eRASS) observations. We note that the scaling relations between X-ray observables and weak lensing masses have already been published in our companion paper, Chiu et al. (2022). The selection function employed in this Chapter is based on the realistic full-sky simulations of eROSITA and is fully accounted for in our results (Comparat et al., 2020). Throughout this Chapter, T stands for the temperature of the intra-cluster/group medium, L_X stands for soft-band ($0.5 - 2.0$ keV) X-ray luminosity, L_{bol} stands for the bolometric luminosity calculated in the $0.01 - 100$ keV energy band, and the errors correspond to 68% confidence levels.

2.2   Data Analysis

2.2.1   Data Reduction and Sample Selection

The eFEDS observations were performed by eROSITA between 4 and 7 November 2019. The observation strategy allowed the eFEDS field to be surveyed nearly uniformly with a vignetted exposure of $\sim$ 1.3 ks, which is similar to the expected vignetted exposure of the final eROSITA All-Sky Survey (eRASS:8) at the equatorial regions. Initial processing of the eFEDS observations was carried out using the eROSITA Standard Analysis Software System (`eSASS`, version `eSASSusers_201009`, Brunner et al., 2022). In this Chapter, we present only an outline of the source detection and preliminary data reduction procedures. We refer the reader to Brunner et al. (2022) and Liu et al. (2022a) for a more detailed explanation of these steps. We first applied filtering to X-ray data, removing dead time intervals and frames, corrupted events, and bad pixels. Images created in the $0.2 - 2.3$ keV band using all available telescope modules (TMs) are passed to eSASS source-detection tools in order to perform the source detection procedure and provide extension and detection likelihoods. After applying a detection likelihood ($\mathcal{L}_{det}$) threshold of 5 and an extension likelihood ($\mathcal{L}_{ext}$) threshold of 6, we obtained 542 cluster candidates in the eFEDS field (Brunner et al., 2022). The physical properties of these clusters, such as soft-band and bolometric luminosities, and ICM temperature measurements within a physical radius of 300 kpc and 500 kpc are provided in Liu et al. (2022a).

We used realistic simulations of the eFEDS field (Liu et al., 2021) in order to measure the contamination fractions of samples with different $\mathcal{L}_{det}$ and $\mathcal{L}_{ext}$ cuts. According to these simulations, the eFEDS cluster catalog, which consists of 542 clusters, has a contamination fraction of $\sim$20%. This is a relatively high contamination rate for statistical studies. In order to avoid significant bias caused by the non-cluster sources present in the sample (e.g., AGNs and spu-
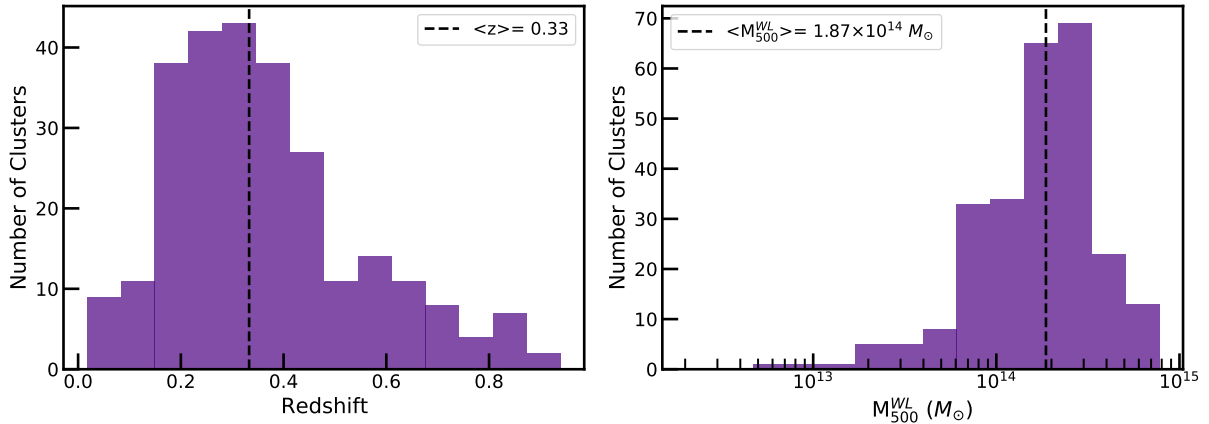
Figure 2.1: *Left*: Redshift histogram of the $\mathcal{L}_{det} > 15$, $\mathcal{L}_{ext} > 15$ sample used in this Chapter. *Right*: Weak lensing calibrated total mass (M_{500c}^{WL}) histogram of the $\mathcal{L}_{det} > 15$, $\mathcal{L}_{ext} > 15$ sample used in this Chapter excluding upper limit measurements. Medians of the measurements are marked with dashed lines. The overdensity radii r_{500c} within which we measure the X-ray observables in this Chapter are calculated from the mass measurements presented in this figure. The mass measurements of the full sample ($\mathcal{L}_{det} > 5$, $\mathcal{L}_{ext} > 6$) is presented in Chiu et al. (2022).

rious sources), we applied $\mathcal{L}_{det} > 15$ and $\mathcal{L}_{ext} > 15$ cuts that give us a sample of 265 clusters with an expected contamination fraction of 9.8%. The final sample covers a total mass range of (6.86×10^{12} M$_\odot$ < M_{500c} < 7.79×10^{14} M$_\odot$, a luminosity range of 8.64×10^{40} erg s^{-1} < L_X < 3.96×10^{44} erg s^{-1}, and a redshift range of ($0.017 < z < 0.94$). The redshift and mass histograms of this final subsample are shown in Fig 2.1. Consisting of 68 low-mass (< 10^{14} M$_\odot$) galaxy groups, our study extends the scaling relation studies to the low-mass range with one of the largest group samples detected uniformly to date.

2.2.2 X-ray Observables within r_{500c}

In this Chapter, we provide X-ray properties of eFEDS clusters within the overdensity radius r_{500c} that are extracted following the X-ray imaging and spectral analysis procedures described in Ghirardini et al. (2021) and Liu et al. (2022a). In this section, we also provide an overview of these procedures; however, for a more detailed description, we refer the reader to the aforementioned references.

The measurements of r_{500c} employed in this Chapter are obtained from the weak lensing calibrated cluster masses presented in our companion paper, Chiu et al. (2022). The mass calibration in Chiu et al. (2022) is obtained using the eFEDS observations of the same cluster sample used in this Chapter, which enables the r_{500c} measurements to be self-consistent. Mass estimates are obtained by jointly modeling the eROSITA X-ray count-rate (η) and HSC shear profile (g_+) as a function of cluster mass (M_{500c}) and obtaining a scaling relation between $\eta - M_{500c} - z$. After obtaining the mass estimates, r_{500c} measurements are calculated by $r_{500c} = \left(\frac{3}{4\pi}\frac{M_{500c}}{500\rho_c}\right)^{1/3}$ where ρ_c

is the critical density at a given redshift and cosmology. We refer the reader to Chiu et al. (2022) for a more detailed description of the HSC weak-lensing mass calibration analysis.

In this Chapter, X-ray spectra of clusters are extracted within r_{500c}, both core-included ($r < r_{500c}$) and core-excised ($0.15r_{500c} < r < r_{500c}$), using the eSASS code srctool. The background spectra are extracted from an annular region that is $4 - 6$ r_{500c} away from the clusters' centroid. We fit the X-ray spectra with an absorbed APEC thermal plasma emission model (Smith et al., 2001; Foster et al., 2012) to represent the ICM emission. The fitting band of $0.5 - 8$ keV was used for TMs 1, 2, 3, 4, and 6, and a more restricted band of $0.8 - 8$ keV was used for TMs 5 and 7 in the spectral fits due to the light leak noticed during the commissioning phase (see Predehl et al., 2021). The Galactic hydrogen absorption is accounted using the TBABS model (Wilms et al., 2000a), where the column density n_H used is fixed to $n_{H,tot}$ (Willingale et al., 2013a), estimated at the position of the cluster center. The metallicity of the clusters is fixed to 0.3 $Z_\odot$, adopting the solar abundance table of Asplund et al. (2009). The background spectra and spectra are simultaneously fit to account for the background in the total spectra as described in detail by Ghirardini et al. (2021). The background spectra are modeled with a set of APEC and power-law models representing instrumental background based on the filter-wheel closed data (see Freyberg et al., 2020)[2], cosmic background (local bubble, galactic halo, and emission from unresolved AGNs). The best-fit values and standard deviations of the ICM temperatures (T) are measured using the Markov chain Monte Carlo (MCMC) method within Xspec (version 12.11.0k).

We extract images and exposure maps in the $0.5 - 2.0$ keV energy band to obtain cluster density profiles. We model the two-dimensional distribution of photons by projecting the Vikhlinin et al. (2006) density model. Point sources are either modeled or masked depending on their fluxes; see Ghirardini et al. (2021) for further details. The cosmic background contribution is added to the total model as a constant. The resulting total image is finally convolved with eROSITA's vignetted exposure map, while the instrumental background model is folded with the unvignetted exposure map. A Poisson log-likelihood in MCMC is used to estimate best-fit cluster model parameters. Finally, the electron density (n_e) profile of the gas is obtained by measuring the emissivity using the temperature information recovered from the spectral analysis. Best-fit parameters of clusters to the Vikhlinin et al. (2006) electron density profile model are presented in Table A.1 in the Appendix. In order to obtain luminosity profiles, $L_X(r)$ and $L_{bol}(r)$, we calculated conversion factors from count rate to luminosity in soft ($0.5 - 2.0$ keV) and bolometric ($0.01 - 100$ keV) energy bands.

The gas mass (or ICM mass) of the clusters enclosed within r_{500c} is computed by integrating the gas electron density assuming spherical symmetry:

$$M_{\rm g} = \mu_e m_p \int_0^{r_{500c}} n_e(r) 4\pi r^2 dr, \qquad (2.1)$$

where n_e is the number density of electrons, m_p is the proton mass, and $\mu_e = 1.1548$ is the mean molecular weight per electron calculated using the Asplund et al. (2009) abundance table (Bulbul et al., 2010). Lastly, Y_X is calculated by multiplying the gas mass ($M_{\rm gas}$) with the gas temperature

---

[2]https://erosita.mpe.mpg.de/edr/eROSITAObservations/EDRFWC/

(T) as

$$Y_\mathrm{X} = M_\mathrm{gas} \cdot T, \tag{2.2}$$

which is introduced by Kravtsov et al. (2006) as a low scatter mass estimator.

We note that in our analysis, uncertainties in r_{500c} measurements are fully propagated using the MCMC chains, and the redshift errors are neglected. We use the single temperature in our calculations as the survey data do not have sufficient depth to recover the temperature profiles as a function of radius. For all eFEDS clusters, we provide the core-included ($r < r_{500c}$) X-ray observables within r_{500c}, including T, L_X, L_bol, M_gas, and Y_X as well as the core-excluded X-ray observables extracted between $0.15 r_{500c} - r_{500c}$ (T_cex, $L_\mathrm{X,cex}$, $L_\mathrm{bol,cex}$) in Table A.2 in the Appendix. eROSITA's field-of-view-averaged point spread function (PSF) half-energy width is $\sim 26''$ which is comparable to the cores ($0.15 r_{500c}$) of the majority of clusters. This has a mild effect on the $L_\mathrm{X,cex}$ measurements because we deconvolve the surface brightness profiles with the PSF and use the best-fit core-included temperatures for the emissivity. However, given the limited photon statistics, only a first-order PSF correction is applied to the T_cex measurements where the flux changes at different energies are compensated by assuming the spectrum to be similar over the whole of the source. Therefore, we advise the reader to approach T_cex measurements with caution.

In this Chapter, we focus on the scaling relations between X-ray observables, namely $L - T$, $L - M_\mathrm{gas}$, $L - Y_\mathrm{X}$, and $M_\mathrm{gas} - T$. The scaling relations between observables and cluster mass (M_{500c}) obtained from weak-lensing observations are already provided in the companion paper by Chiu et al. (2022). Although we provide measurements of the core-excluded observables in Table A.2 in the Appendix, we only utilized the core-included observables in our scaling relations analysis. The reasons for this are twofold, and are related to the selection function, and the decrease in the statistics. Our selection function is built using the core-included observables from the simulations of eROSITA sky (Comparat et al., 2020). Constructing selection functions with the core-excised observables relies on modeling the PSF accurately in simulations. Our imaging analysis and spectral fits account for the PSF spilling, but this analysis is not available yet in simulations. As a workaround, one could model the relation between the core-excised and core-included observables (e.g., $P(Y_\mathrm{X,cex}|Y_\mathrm{X})$), but a significant fraction of eFEDS clusters populate a previously poorly explored parameter space and such an approach requires a good understanding of the surface brightness profiles of these clusters. Secondly, when the core is excised, the temperature measurements become either loose or lost due to the decrease in photon statistics. This affects the reliability of the X-ray observable measurements used in our fits and may lead to biased constraints on the scaling relations. A full analysis with the core-excised observables will be carried out for the clusters detected in the eRASS observations, where we have a larger sample of clusters with a higher depth around the ecliptic poles.

2.3 Modeling and Fitting of the Scaling Relations

We model the scaling relations and the likelihoods for different pairs of observables in a similar manner with minor tweaks. Therefore, in this section, we present the general form of the scaling relations and the structure of the likelihood for two hypothetical observables: X and Y.

2.3.1   General Form of the Scaling Relations

Kaiser (1986) derived simple forms of scaling relations, namely self-similar relations, by assuming gravitational interactions to be the driving force of the evolution of groups and clusters. These relations suggest that the observables of clusters follow these simple power-law relations. Departures from these relations are often interpreted as a result of non-gravitational physical processes, such as radiative cooling, galactic winds, and AGN feedback that can have a significant impact on the distribution of baryons in the ICM and energy budget of the system (Bhattacharya et al., 2008; McCarthy et al., 2010; Fabjan et al., 2010; Bulbul et al., 2016; Giodini et al., 2013; Lovisari et al., 2020).

In this Chapter, we use a relation that takes into account the power-law dependence and the redshift evolution of the form

$$Y = A \, Y_{\mathrm{piv}} \left(\frac{X}{X_{\mathrm{piv}}} \right)^{B} \left(\frac{E(z)}{E(z_{\mathrm{piv}})} \right)^{C} , \qquad (2.3)$$

where Y_{piv}, X_{piv}, and z_{piv} are the pivot values of the sample, and A, B, and C are the normalization, power-law slope, and redshift evolution exponent, respectively. The redshift evolution is modeled using the evolution function, which is defined as $E(z) = H(z)/H_0$ where $H(z)$ is the Hubble-Lemaître parameter and H_0 is the Hubble constant.

2.3.2   Likelihood

In our fits to the scaling relations, we take into account various observational and physical effects by adding the relevant components to the corresponding likelihood function similar to the method presented in Giles et al. (2016) for the XXL clusters. The joint probability function in terms of the measured values $(\hat{X}, \hat{Y})$ of the true values of the observables X and Y is given by

$$P(\hat{Y}, \hat{X}, Y, X, I | \theta, z) = P(I|Y, z) P(\hat{Y}, \hat{X}|Y, X) P(Y|X, \theta, z) P(X|z), \qquad (2.4)$$

where $P(I|Y, z)$, also known as the selection function, is the probability of a cluster being included (I) in our sample, $P(\hat{Y}, \hat{X}|Y, X)$ is the two-dimensional measurement uncertainty, $P(Y|X, \theta, z)$ is the modeled $Y - X$ relation, and the $P(X|z)$ term is the cosmological distribution of the observable X. The variable θ in the scaling relation term marks the free parameters of the scaling relation, such as A, B, C, and the scatter $\sigma_{Y|X}$. We note that in this Chapter, correlations between the measurement uncertainties of observables X and Y are fully considered using the MCMC chains. We also note that the cosmological parameters are frozen throughout our analysis. More than 65% of the clusters in our sample have spectroscopic redshifts, and the remaining clusters have photometric redshift measurements using the high signal-to-noise-ratio HSC data, which provides uncertainties of the order of 0.3% (see Klein et al., 2022). Therefore, we assume that the errors on the redshifts have negligible effects on our measurements, that is, $z = \hat{z}$. The variance in exposure time due to the overlapping regions and the missed observations due to malfunctions of telescope modules (TMs) (see Brunner et al., 2022, for details) are accounted for by using the exposure time (t_{exp}) at the X-ray center of each cluster when calculating $P(I|Y, z)$.

We model the $Y - X$ relation such that the observable Y is distributed around the power-law scaling relation log-normally. The assumption of the log-normal distribution of X-ray observables is widely used in the literature (e.g., Pacaud et al., 2007; Giles et al., 2016; Bulbul et al., 2019; Bocquet et al., 2019). The scaling relation term $P(Y|X, \theta, z)$ in Eq. 2.4 then becomes

$$P(Y|X, \theta, z) = \mathcal{LN}\left(\mu = A \ Y_{\text{piv}}\left(\frac{X}{X_{\text{piv}}}\right)^B \left(\frac{E(z)}{E(z_{\text{piv}})}\right)^C, \sigma = \sigma_{Y|X}\right). \tag{2.5}$$

To obtain the cosmological distribution of the observable X ($P(X|z)$), that is, the expected distribution of X as a function of redshift given a fixed cosmology and an assumed $X - M$ scaling relation, we convert the Tinker et al. (2008) mass function to a Tinker X function using weak-lensing mass-calibrated scaling relations reported in Chiu et al. (2022) obtained from the same cluster sample used in our study. This conversion is applied such that the intrinsic scatter of the $X - M$ relation is taken into account by the following equation:

$$P(X|\theta_{\text{WL}}, z) = \int_M P(X|M, \theta_{\text{WL}}, z)P(M|z)dM, \tag{2.6}$$

where θ_{WL} is the best-fit result of the weak-lensing mass-calibrated scaling relation $X - M_{500c}$. We note that the form of the $X - M$ relation presented in Chiu et al. (2022) is different than the form we use in our $Y - X$ relation. Hereafter, we do not include the θ_{WL} term in $P(X|\theta_{\text{WL}}, z)$ because it is fixed throughout the analysis. After properly defining all the terms in the joint distribution in Eq. 2.4, we marginalize over the nuisance variables (X, Y) in order to get the likelihood of obtaining the measured observables ($\hat{X}$, $\hat{Y}$, I). The final likelihood of a single cluster then becomes

$$P(\hat{Y}, \hat{X}, I|\theta, z) = \int \int_{Y,X} P(I|Y, z)P(\hat{Y}, \hat{X}|Y, X)P(Y|X, \theta, z)P(X|z)dYdX. \tag{2.7}$$

To avoid significant bias in the results due to the assumed cosmological model and the exact form of the $X - M$ relation, we do not use the observed number of detected clusters as data, but instead, we take it as a model parameter. In the Bayesian framework, this corresponds to using a likelihood that quantifies the probability of measuring $\hat{X}_i$ and $\hat{Y}_i$ observables given that the cluster is detected. Such a likelihood can be obtained using the Bayes theorem, where the likelihood for the ith cluster becomes

$$\mathcal{L}(\hat{Y}_i, \hat{X}_i|I, \theta, z_i) = \frac{P(\hat{Y}_i, \hat{X}_i, I|\theta, z_i)}{\int \int_{\hat{Y}_i, \hat{X}_i} P(\hat{Y}_i, \hat{X}_i, I|\theta, z_i)d\hat{Y}_i d\hat{X}_i}. \tag{2.8}$$

Lastly, the overall likelihood of the sample is obtained by multiplying the likelihoods of all clusters

$$\mathcal{L}(\hat{Y}_{\text{all}}, \hat{X}_{\text{all}}|I, \theta, z) = \prod_i^{\hat{N}_{\text{det}}} \mathcal{L}(\hat{Y}_i, \hat{X}_i|I, \theta, z_i), \tag{2.9}$$

where $\hat{Y}_{\text{all}}$ and $\hat{X}_{\text{all}}$ are the measurement observables of all clusters in the sample and $\hat{N}_{\text{det}}$ is the number of detected clusters in our sample.

This form of the likelihood is similar to those used in the literature; see, for example, Mantz et al. (2010a). The most fundamental difference is the goal of our study, which is to fit the scaling relations at a fixed cosmology rather than simultaneously fitting scaling relations and cosmological parameters. Using this likelihood allows us to avoid including terms that have a strong dependence on cosmology, such as those in Mantz et al. (2010b), namely the probability of not detecting the model-predicted, undetected clusters, $P(\bar{I}|\theta)$, possible ways of selecting $\hat{N}_{\text{det}}$ clusters from the total sample N, $\binom{N}{\hat{N}_{\text{det}}}$, and the prior distribution of the total number of clusters in the field, $P(N)$ (see Mantz, 2019, for the use of these parameters). Another benefit of using this likelihood is it allows the results to be less sensitive to the accuracy of the normalization of the $X - M$ relation and therefore, makes our analysis more robust for the goal of our study.

2.3.3   Modeling the Selection Function

The selection function model adopted here, $P(I|Y, z)$ in Eq. 2.7, is similar to that described in Liu et al. (2022a). It relies on multiple mock realizations of the eFEDS field (Liu et al., 2021). The simulations faithfully reproduce the instrumental characteristics of eROSITA and features induced by the scanning strategy (exposure variations, point-spread function, effective area, and the grasps of the seven telescopes.) Realistic foreground and background models are associated with a full-sky light-cone N-body simulation assuming the Planck-CMB cosmology. These sources include stars, active galactic nuclei (AGN), and galaxy clusters. The method to associate AGN spectral templates to sources is derived from abundance-matching techniques. For clusters and groups, the association between a massive dark matter halo and an emissivity profile drawn from a library of observed templates depends on the mass, redshift, and dynamical state of the halo. In particular, relaxed halos are associated with gas distributions with higher central projected emission measures. The steps leading to the AGN and cluster simulations are extensively described in Comparat et al. (2019, 2020). The SIXTE engine (Dauser et al., 2019) serves in converting sources into event lists, while the eSASS software (Brunner et al., 2022) is used to process those lists and to deliver source catalogs.

The next steps are identical to those in Liu et al. (2022a), except for the definition of an extended detection which assumes $\mathcal{L}_{\text{det}} > 15$ and $\mathcal{L}_{\text{ext}} > 15$. In particular, pairs of the simulated and detected sources are looked for in the plane of the sky, accounting for their relative positions, their extents, and favoring association between bright sources in cases of ambiguity. Securely identified matches are flagged as a successful detection.

The modeling of the detection probabilities involves interpolation across the multi-dimensional parameter space describing galaxy cluster properties, which includes their intrinsic soft-band or bolometric luminosity, their redshift, the local exposure time, and, optionally, the central emission measure. Other parameters are marginalized over, making the assumption that their distributions are correctly reflected in the simulations. To this end, we make use of Gaussian Process classifiers, a class of nonparametric models that capture the variations of the detection probability under the assumption that the covariance function (kernel) is a squared exponential function. One advantage of using such models rather than the multi-dimensional spline interpolation, for

example, is a more appropriate mathematical treatment of uncertainties, particularly in poorly populated areas of the parameter space. Two-thirds of the simulated clusters are used for training the classifiers, and the remaining third provides the material to test the performance of the classifiers and to assess their behavior on a realistic population of halos. In particular, we check that systems assigned a given detection probability by the classifier display a detection rate with a value close to that probability; in such cases, the classifier is said to be well-calibrated.

These models are designed to emulate the whole chain of computationally expensive steps needed in performing an eFEDS end-to-end simulation (Liu et al., 2021). It is worth noting that such selection functions have a range of applicability that is set by the simulation.

In order to demonstrate the representativeness of the selection function, we model the luminosity distribution of the $\mathcal{L}_{\text{det}} > 15$, $\mathcal{L}_{\text{ext}} > 15$ clusters and compare it with the observed cluster distribution. We model it as $P(I, L_X, z) = P(I|L_X, z)P(L_X|z)P(z)$ where we calculate $P(L_X|z)$ using Eq. 2.6 and the best-fit $L_X - M$ relation presented in Chiu et al. (2022). For the redshift distribution, we assume the comoving cluster density to be constant within our redshift span ($0 < z < 0.9$) so that $P(z)$ is proportional to the comoving volume shell $dV_c(z) = \frac{c}{H_0} \frac{(1+z)^2 d_A(z)^2}{E(z)} \Omega_s dz$ (Hogg, 1999) where c is the light speed, H_0 is the Hubble constant, $d_A(z)$ is the angular diameter distance, and Ω_s is the solid angle of the eFEDS survey. A comparison between the distribution of the luminosity measurements for the cluster sample with $\mathcal{L}_{\text{det}} > 15$, $\mathcal{L}_{\text{ext}} > 15$ selection and our model predicted by our selection function is shown in Fig. 2.2. The figure visually demonstrates the consistency of the luminosity distribution with redshift predicted from the selection function (plotted as the background color) and measurements from the eFEDS data (white data points and white contours).

2.3.4 Fitting

We fit scaling relations using the MCMC sampler package `emcee` (Foreman-Mackey et al., 2013) with a likelihood described in Sect. 2.3.2. Before we fit the real data, we validate our fitting code on simulated clusters. For the tests, we generate mock X-ray observables of a sample of 265 clusters corresponding to the same number of clusters in the sample selected with the criteria of $\mathcal{L}_{\text{det}} > 15$ and $\mathcal{L}_{\text{ext}} > 15$. Using the observed redshifts as priors, we sample the observables, X and Y, from a bivariate distribution of the form

$$P(Y, X, I|\theta_{\text{sim}}, z) = P(I|Y, z)P(Y|X, \theta_{\text{sim}}, z)P(X|z), \tag{2.10}$$

where $P(Y|X, \theta_{\text{sim}}, z)$ is the scaling relation term including intrinsic scatter and θ_{sim} is the input scaling relation parameters for the simulated clusters. We then scatter the X and Y observables to mimic observational uncertainty and assign conservative error bars to model our observable measurements. We then run our fitting code on the simulated clusters with 100 walkers for 10000 steps and compare the best-fit θ values with the input parameters (θ_{sim}). We find that the fitting code successfully recovers all input parameters with a deviation within one sigma, validating the performance and the accuracy of the code.

After the test run, we fit the X-ray scaling relations using the eFEDS measurements using flat priors for all scaling relation parameters; $\mathcal{U}(-4, 4)$ for the normalization (A), $\mathcal{U}(-10, 10)$ for
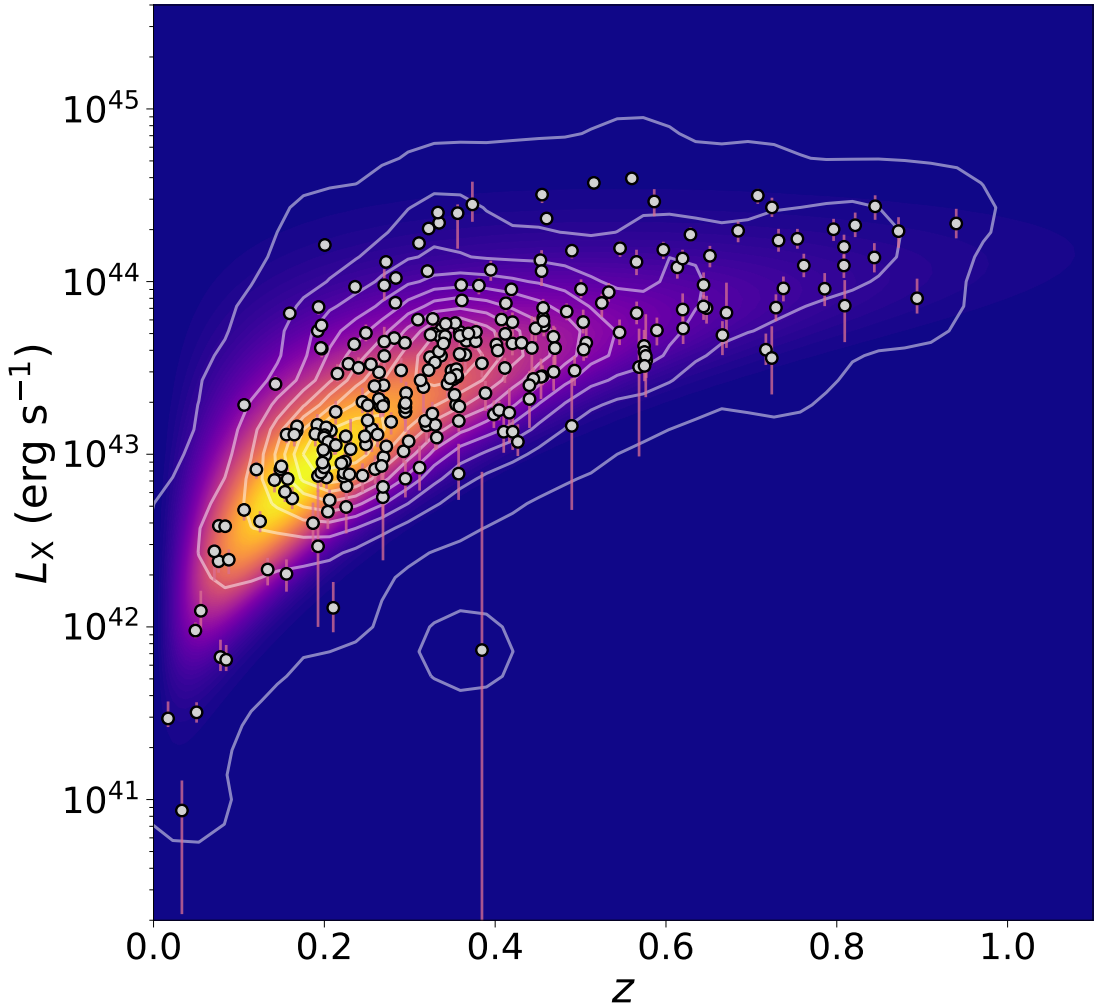
Figure 2.2: Soft band $(0.5 - 2.0 \text{ keV})$ X-ray luminosity and redshift measurements of the clusters in the eFEDS field that satisfies the $\mathcal{L}_{\text{det}} > 15$ and $\mathcal{L}_{\text{ext}} > 15$ condition. Luminosities are measured within apertures of r_{500c}. White solid curves are smoothed contours of the $L_X - z$ data points, and the color is proportional to the PDF of the hypothetical $L_X - z$ distribution modeled as $P(I, L_X, z) = P(I|L_X, z)P(L_X|z)P(z)$ (see Sect. 2.3.3 for the description of the model).

Table 2.1: Median values of observables measured for the $\mathcal{L}_{\mathrm{det}} > 15$, $\mathcal{L}_{\mathrm{ext}} > 15$ clusters.

Parameters	Median/Pivots
L_{X}	3.20×10^{43} erg s^{-1}
L_{bol}	9.49×10^{43} erg s^{-1}
T	3.26 keV
M_{gas}	1.04×10^{13} M$_{\odot}$
Y_{X}	3.75×10^{13} M$_{\odot}$ keV
z	0.33

Notes. These values are used as pivot values of observables in Eq. 2.3

Table 2.2: Self-similar expected model parameter values of scaling relations of the form $Y = A\, Y_{\mathrm{piv}} \left(\frac{\mathrm{X}}{X_{\mathrm{piv}}} \right)^{B} \left(\frac{E(z)}{E(z_{\mathrm{piv}})} \right)^{C}$

Relation			
Y	X	B_{self}	C_{self}
L_{X}	T	3/2	1
L_{X}	M_{gas}	1	2
L_{X}	Y_{X}	3/5	8/5
L_{bol}	T	2	1
L_{bol}	M_{gas}	4/3	7/3
L_{bol}	Y_{X}	4/5	9/5
M_{gas}	T	3/2	-1

Table 2.3: Best-fit parameters of the scaling relations

| Relation | | Best fit parameters | | | | | | | |
| | | Free redshift evolution | | | | Self-similar redshift evolution | | | |
Y	X	A	B	C	$\sigma_{Y\|X}$	A	B	$C = C_{self}$	$\sigma_{Y\|X}$
L_{X}	T	$0.91^{+0.16}_{-0.15}$	$2.89^{+0.14}_{-0.13}$	$1.59^{+0.86}_{-0.93}$	$0.78^{+0.08}_{-0.07}$	$0.89^{+0.16}_{-0.15}$	$2.93^{+0.12}_{-0.12}$	1	$0.80^{+0.07}_{-0.07}$
L_{X}	M_{gas}	$0.89^{+0.02}_{-0.02}$	$1.10^{+0.03}_{-0.02}$	$1.44^{+0.25}_{-0.26}$	$0.30^{+0.02}_{-0.02}$	$0.88^{+0.02}_{-0.02}$	$1.07^{+0.02}_{-0.02}$	2	$0.30^{+0.02}_{-0.02}$
L_{X}	Y_{X}	$1.20^{+0.04}_{-0.04}$	$0.83^{+0.02}_{-0.02}$	$1.50^{+0.33}_{-0.35}$	$0.29^{+0.03}_{-0.03}$	$1.20^{+0.04}_{-0.04}$	$0.83^{+0.02}_{-0.02}$	$8/5$	$0.29^{+0.03}_{-0.03}$
L_{bol}	T	$1.02^{+0.14}_{-0.14}$	$3.01^{+0.13}_{-0.12}$	$2.69^{+0.74}_{-0.78}$	$0.70^{+0.07}_{-0.06}$	$0.96^{+0.15}_{-0.14}$	$3.13^{+0.12}_{-0.12}$	1	$0.76^{+0.07}_{-0.06}$
L_{bol}	M_{gas}	$0.86^{+0.03}_{-0.03}$	$1.19^{+0.03}_{-0.03}$	$1.86^{+0.29}_{-0.30}$	$0.32^{+0.02}_{-0.02}$	$0.86^{+0.02}_{-0.02}$	$1.16^{+0.02}_{-0.02}$	$7/3$	$0.31^{+0.02}_{-0.02}$
L_{bol}	Y_{X}	$1.12^{+0.03}_{-0.03}$	$0.90^{+0.02}_{-0.02}$	$1.83^{+0.27}_{-0.28}$	$0.28^{+0.02}_{-0.02}$	$1.12^{+0.03}_{-0.03}$	$0.90^{+0.02}_{-0.02}$	$9/5$	$0.28^{+0.02}_{-0.02}$
M_{gas}	T	$0.83^{+0.13}_{-0.13}$	$2.41^{+0.11}_{-0.11}$	$0.21^{+0.74}_{-0.79}$	$0.67^{+0.07}_{-0.06}$	$0.77^{+0.13}_{-0.12}$	$2.47^{+0.11}_{-0.10}$	-1	$0.72^{+0.06}_{-0.06}$

Notes. Fitted relation is of the form $Y = A\, Y_{\mathrm{piv}} \left(\frac{X}{X_{\mathrm{piv}}} \right)^{B} \left(\frac{E(z)}{E(z_{\mathrm{piv}})} \right)^{C}$ with a log-normal intrinsic scatter $\sigma_{Y|X}$ (in natural log). Pivot values of the observables are provided in Table 2.1. Each relation is fitted twice; first leaving the redshift evolution exponent (C) free and second with a redshift evolution exponent fixed to the corresponding self-similar value (see Table 2.2 for the self-similar exponents). Details of the modeling and the fitting of the scaling relations can be found in Sect. 2.3. Errors are 1σ uncertainties calculated from the second half of the MCMC chains.

the slope (B), $\mathcal{U}(-10, 10)$ for the redshift evolution exponent (C), and $\mathcal{U}(0.1, 3.0)$ for the scatter ($\sigma_{Y|X}$). The median values of the observables are used as the pivot values in our fits and are provided in Table 2.1.

In total, we perform two fits for each scaling relation. The first fits are performed with free redshift evolution exponents, C, and in the second fits, the parameter C is fixed to the self-similar values. The self-similar expectations are given in Table 2.2 for all scaling relations investigated in this Chapter. The best-fit parameters of these seven relations can be found in Table 2.3. We provide our results and comparisons with the literature in Section 2.4.

2.4   Results

Scaling relations between X-ray observables are tools for understanding the ICM physics for various mass scales and the evolution of the ICM with redshift, while the relations between observables and cluster mass are used for facilitating cosmology with cluster number counts. In this section we examine the $L - T$, $L - M_{\mathrm{gas}}$, $L - Y_{\mathrm{X}}$, and $M_{\mathrm{gas}} - T$ scaling relations, using both L_{X} and L_{bol}, and provide extensive comparisons with the literature. Owing to the high soft-band sensitivity of the eROSITA, we were able to include a large number of low-mass, low-

luminosity clusters in our study, down to the soft band luminosities of 8.64×10^{40} ergs s^{-1} and masses (M_{500c}) of 6.86×10^{12} M$_\odot$. In the eFEDS field alone, we detect a total of 68 low-mass groups with $M_{500c} < 10^{14}$ M$_\odot$ that are fully included in our analysis. eROSITA is revolutionary in both ICM studies and cosmology in this regard as it extends cluster samples to much lower luminosities and lower masses than ever reached before. We first describe our method and lay the groundwork with the eFEDS sample with this study, and will push the mass and luminosity limits down with our ongoing work on the eRASS1 sample. One other important aspect is the fact that the eROSITA group and cluster samples are uniformly selected, and the selection function is well understood with the help of our full-sky eROSITA simulations.

There are several complications in comparing scaling relation results in the literature with our results. These are linked to the form of the fitted scaling relations, the energy band of the extracted observables, and the assumed cosmology, and the instrument calibration also varies from one study to another. To overcome these difficulties, we apply corrections before we compare them with our results. In these comparison plots, we use the self-similar redshift evolution as the common reference point and convert the observables accordingly. The standard energy band we use in this Chapter for the extraction of observables is the $0.5 - 2.0$ keV band. To convert normalizations of scaling relations involving luminosities obtained in the $0.1 - 2.4$ keV energy band ($L_{0.1-2.4}$), we faked an unabsorbed APEC spectrum within Xspec and calculated a conversion factor of 1.64 for a cluster that has a temperature of 3.26 keV, an abundance of 0.3 $Z_\odot$, and a redshift of 0.33. These redshift and temperature values are the median values of our sample (see Table 2.1). Changing the temperatures and redshifts affects the conversion factor by a few percent, which is consistent with the findings of Lovisari et al. (2020). We, therefore, applied the same conversion factor to all other works using the $0.1 - 2.4$ keV energy band. Lastly, we convert the relations assuming a dimensionless Hubble constant of 0.6774, which is the value we use in this Chapter. The corrections are only applied to the normalizations, and therefore, the slopes and redshift evolution exponents of previously reported relations remain unchanged.

Another challenge in comparisons of scaling relations involving the ICM temperature is the calibration differences between various X-ray telescopes. It has been shown that calibration differences between *Chandra* and XMM-*Newton* are dependent on the energy band and can be as large as a factor of two for hot clusters with temperatures > 10 keV in the soft band ($0.7 - 2$ keV) (Schellenberger et al., 2015). However, this difference is small, namely of 10%–15% in the full $0.7 - 7$ keV band for low-temperature clusters (< 4 keV), to which we are sensitive in the eFEDS observations. Our preliminary calibration studies with eROSITA showed that, in general, eROSITA temperatures are in good agreement with *Chandra* and XMM-*Newton* temperatures (Sanders et al., 2021; Veronica et al., 2021; Iljenkarevic et al., 2021; Whelan et al., 2021). Turner et al. (2021) recently cross-matched the eFEDS cluster catalog (Liu et al., 2022a) with the XMM-*Newton* Cluster Survey (XCS, Romer et al., 2001) sample and found luminosities of 29 cross-matched clusters to be in excellent agreement. They also compared the temperatures of 8 clusters that were measured with both telescopes and found XMM measurements to have slightly higher temperatures on average. In order to better understand the instrumental differences, more extensive studies should be performed with a cluster sample containing a larger range of temperatures using the survey data. Temperature offsets resulting from calibration differences will be further investigated in future eROSITA projects.
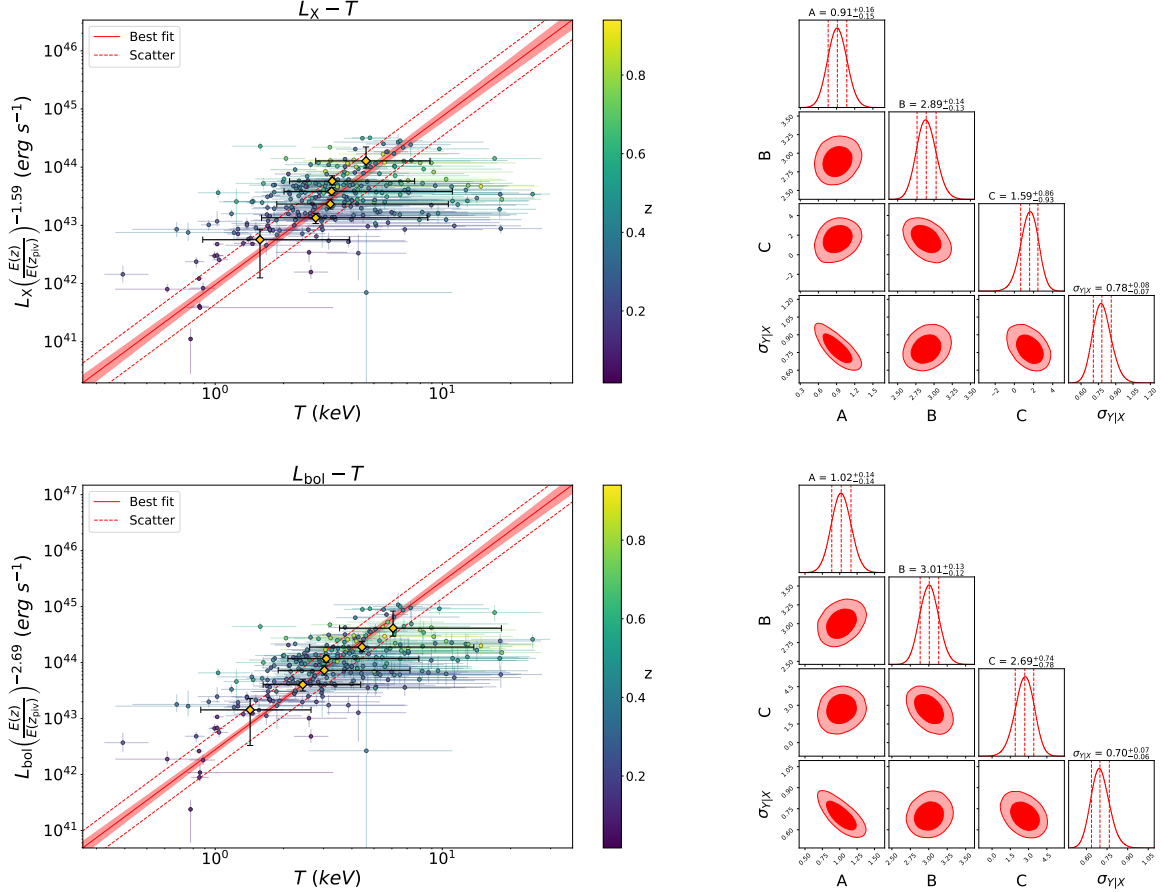
Figure 2.3: $L - T$ scaling relations and the posterior distributions of the scaling relations parameters. *Left:* Soft band $(0.5 - 2.0 \text{ keV})$ X-ray luminosity (L_{X}), bolometric $(0.01 - 100 \text{ keV})$ luminosity (L_{bol}), temperature (T), and redshift (z) measurements of the $\mathcal{L}_{\text{det}} > 15$, $\mathcal{L}_{\text{ext}} > 15$ sample and the best-fit scaling relation models. The light-red shaded areas indicate 1σ uncertainty of the means of the log-normal models (see Eq. 2.5), and dashed red lines indicate the best-fit standard deviations $(\sigma_{L|T})$ around the mean. Orange diamonds indicate median temperature measurements obtained from clusters between luminosity quantiles. *Right:* Parameter constraints of the $L_{\text{X}} - T$ and $L_{\text{bol}} - T$ relations obtained from the second half of the MCMC chains. Marginalized posterior distributions are shown on the diagonal plots, and the joint posterior distributions are shown on off-diagonal plots. Red dashed vertical lines indicate the 32nd, 50th, and 68th percentiles, and contours indicate 68% and 95% credibility regions.

2.4.1 $L_X - T$ and $L_{bol} - T$ Relations

The two main observables from X-rays, luminosity, and temperature, reflect different but complexly related features of the ICM in clusters. On one hand, luminosity is proportional to the square of the electron density, and therefore, it is highly sensitive to the distribution of the hot gas. On the other hand, the temperature is related to the average kinetic energy of the baryons in the ICM. Both luminosity and temperature are subject to gravitational and non-gravitational effects in a different manner, and this makes their relation nontrivial (see Giodini et al., 2013, for a more detailed discussion). Hence, a better understanding of the $L - T$ relation will shed light on the history of the heating and cooling mechanisms of clusters.

In the self-similar scenario (Kaiser, 1986), the relation between luminosity, temperature, and redshift follows

$$L_X \propto T^{3/2} E(z) \tag{2.11}$$

and

$$L_{bol} \propto T^2 E(z). \tag{2.12}$$

However, a plethora of studies report steeper $L_X - T$ ($B \sim 2.5$) and $L_{bol} - T$ ($B \sim 3.0$) relations compared to their self-similar predictions (e.g., Pratt et al., 2009; Eckmiller et al., 2011; Maughan et al., 2012; Hilton et al., 2012; Kettula et al., 2015; Lovisari et al., 2015; Zou et al., 2016; Giles et al., 2016; Molham et al., 2020).

Our best-fit results for the $L_X - T$ relation are presented in Table 2.3 where we report a slope of $B = 2.89^{+0.14}_{-0.13}$, a redshift evolution dependence of $C = 1.59^{+0.86}_{-0.93}$, and a scatter of $\sigma_{L_X|T} = 0.78^{+0.08}_{-0.07}$. The best-fit model is shown in Fig. 2.3. In general, our results agree well with studies that account for the selection biases. A comparison of our results with some others can be found in Fig. 2.4. Our best-fit slope is significantly steeper at a $\sim 11\sigma$ confidence level than the self-similar expectation ($B_{self} = 3/2$). Our relation is slightly steeper than the slopes reported for the XXL sample, $B = 2.63 \pm 0.15$ (Giles et al., 2016), and the combined Northern ROSAT All-Sky Survey (NORAS) plus ROSAT-ESO Flux Limited X-ray Survey (REFLEX) samples, $B = 2.67 \pm 0.11$ (Lovisari et al., 2015), but all three agree well within 1.3σ. We note that these latter authors fully account for selection effects in their analysis, and both of these latter samples are the most similar to the eFEDS sample because they also contain a significant fraction of low-mass clusters. Our slope is also slightly steeper than the slopes found in Eckmiller et al. (2011) ($B = 2.52 \pm 0.17$) and Kettula et al. (2015) ($B = 2.52 \pm 0.17$) but is consistent with both within 1.7σ. The slope of $B = 2.24 \pm 0.25$ reported in Pratt et al. (2009) is 2.3σ shallower than our results. Our best-fit redshift evolution for the $L_X - T$ relation is in agreement with the self-similar scenario ($C_{self} = 1$) and with Giles et al. (2016) within 1σ. Furthermore, our redshift evolution also agrees well with most of the other results because of the large error bars which indicate the redshift evolution could not be constrained, as well as other parameters. When we fix the evolution term to the self-similar value, we find a steeper slope of ($B = 2.93 \pm 0.12$). This slope is $\sim 4\sigma$ away from the slope reported in Migkas et al. (2020) ($B = 2.38 \pm 0.08$) if their temperature correction is taken into account. Our best-fit intrinsic scatter for the $L_X - T$ relation agrees very well with Pratt et al. (2009) ($\sigma_{L_X|T} = 0.76 \pm 0.14$) whereas it is in 3σ tension with Giles et al. (2016) ($\sigma_{L_X|T} = 0.47 \pm 0.07$). Lovisari et al. (2015) ($\sigma_{L_X|T} = 0.56$) and Eckmiller
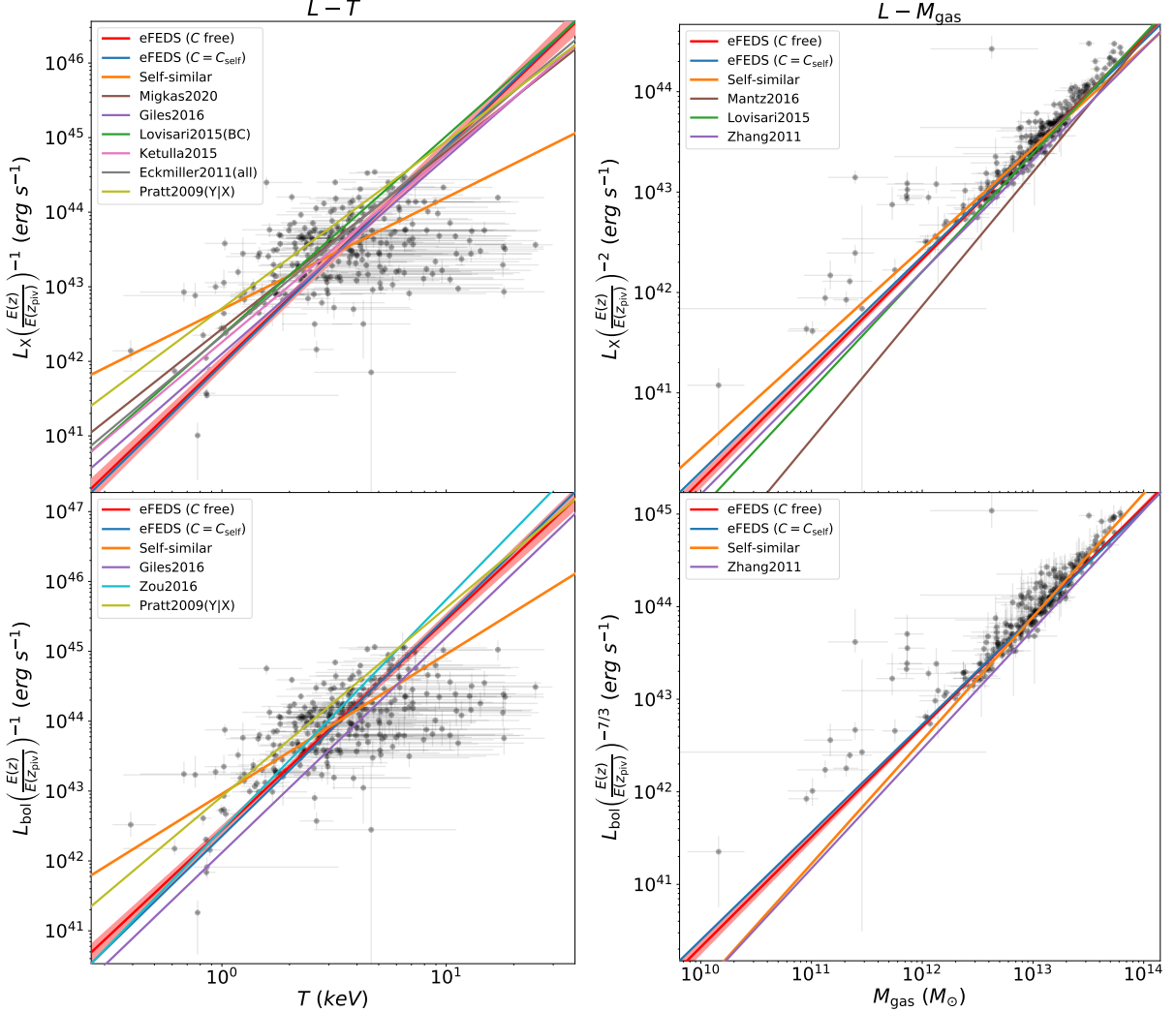
Figure 2.4: Comparison between our best-fit $L - T$ and $L - M_{\text{gas}}$ relations, the self-similar model and other studies in the literature (Pratt et al., 2009; Eckmiller et al., 2011; Zhang et al., 2011; Kettula et al., 2015; Lovisari et al., 2015; Mantz et al., 2016; Giles et al., 2016; Zou et al., 2016; Migkas et al., 2020). Grey circles are the eFEDS clusters. In order to achieve consistency, a cosmology and energy band conversion is applied to the previously reported results (see Sect. 2.4 for the details).

et al. (2011) ($\sigma_{L_X|T} = 0.63$) also reported slightly smaller intrinsic scatter results compared to our findings, but a statistical comparison cannot be made because of the lack of error bars in their scatter measurements.

For the $L_{bol} - T$ relation, we find a slope of $B = 3.01^{+0.13}_{-0.12}$, a redshift evolution term of $C = 2.69^{+0.74}_{-0.78}$, and a scatter of $\sigma_{L_{bol}|T} = 0.70^{+0.07}_{-0.06}$. Both the slope and the redshift evolution are steeper than the self-similar expectation of $B_{self} = 2$ at a 8.5σ level and $C_{self} = 1$ at a 2σ level. Due to the temperature dependence of the X-ray emissivity, the $L - T$ scaling relation involving the bolometric luminosity is expected to be steeper than that of the soft-band luminosity for the same cluster by a factor of $\propto n_e^2 T^{0.5}$. The slope in this case agrees very well with Giles et al. (2016) ($B = 3.08 \pm 0.15$), Zou et al. (2016) ($B = 3.29 \pm 0.33$), and Pratt et al. (2009) ($B = 2.70 \pm 0.24$). When we fix the redshift evolution to the self-similar value, we obtain a steeper slope of $B = 3.13 \pm 0.12$. Our best-fit slope with fixed redshift evolution is also consistent with the slopes in Giles et al. (2016) and Zou et al. (2016) within uncertainties, whereas Migkas et al. (2020) found a slope that is shallower by 4.5σ ($B = 2.46 \pm 0.09$). Maughan et al. (2012) ($B = 3.63 \pm 0.27$), however, found a steeper slope than both the self-similar model and our results when they included the cluster cores. Maughan et al. (2012) reported that when they limit their sample to relaxed cool core clusters, they find a much shallower slope of $B = 2.44 \pm 0.43$, indicating that the discrepancy observed here could be due to their samples being heavily affected by the selection effects, which we take into account by using realistic simulations in our analysis. The intrinsic scatter of the $L_{bol} - T$ relation is lower compared to the best-fit value of our $L_X - T$ relation, but they agree within the error bars. Pratt et al. (2009) reported $\sigma_{L_{bol}|T} = 0.73 \pm 0.14$, which is consistent with our results for the $L_{bol} - T$ relation within uncertainties. Our best-fit intrinsic scatter is slightly higher than the findings reported in Zou et al. (2016) ($\sigma_{L_{bol}|T} = 0.47 \pm 0.11$) and Giles et al. (2016) ($\sigma_{L_{bol}|T} = 0.47 \pm 0.07$), but within 1.8 and 2.5σ statistical uncertainty, respectively.

2.4.2 $L_X - M_{gas}$ and $L_{bol} - M_{gas}$ Relations

Luminosity and gas mass are two tightly related observables because of their mutual dependence on electron density, and therefore, a strong correlation is expected between them. Measurement of their correlation whilst taking into account selection effects and the mass function with a large sample allows us to test the theorized relation between these observables. According to the self-similar model, they are connected as

$$L_X \propto M_{gas} E(z)^2 \tag{2.13}$$

and

$$L_{bol} \propto M_{gas}^{4/3} E(z)^{7/3}. \tag{2.14}$$

Our best-fit results for the $L_X - M_{gas}$ and $L_{bol} - M_{gas}$ relations are provided in Table 2.3 and in Fig. 2.5. A comparison of these results with previous work is shown in Fig. 2.4. We report a slope of $B = 1.10^{+0.03}_{-0.02}$, a redshift evolution term of $C = 1.44^{+0.25}_{-0.26}$, and a scatter of $\sigma_{L_X|M_{gas}} = 0.30 \pm 0.02$. The slope is in tension with the self-similar expectation at a 5σ level, but the redshift evolution is consistent with the self-similar model within 2σ confidence for the
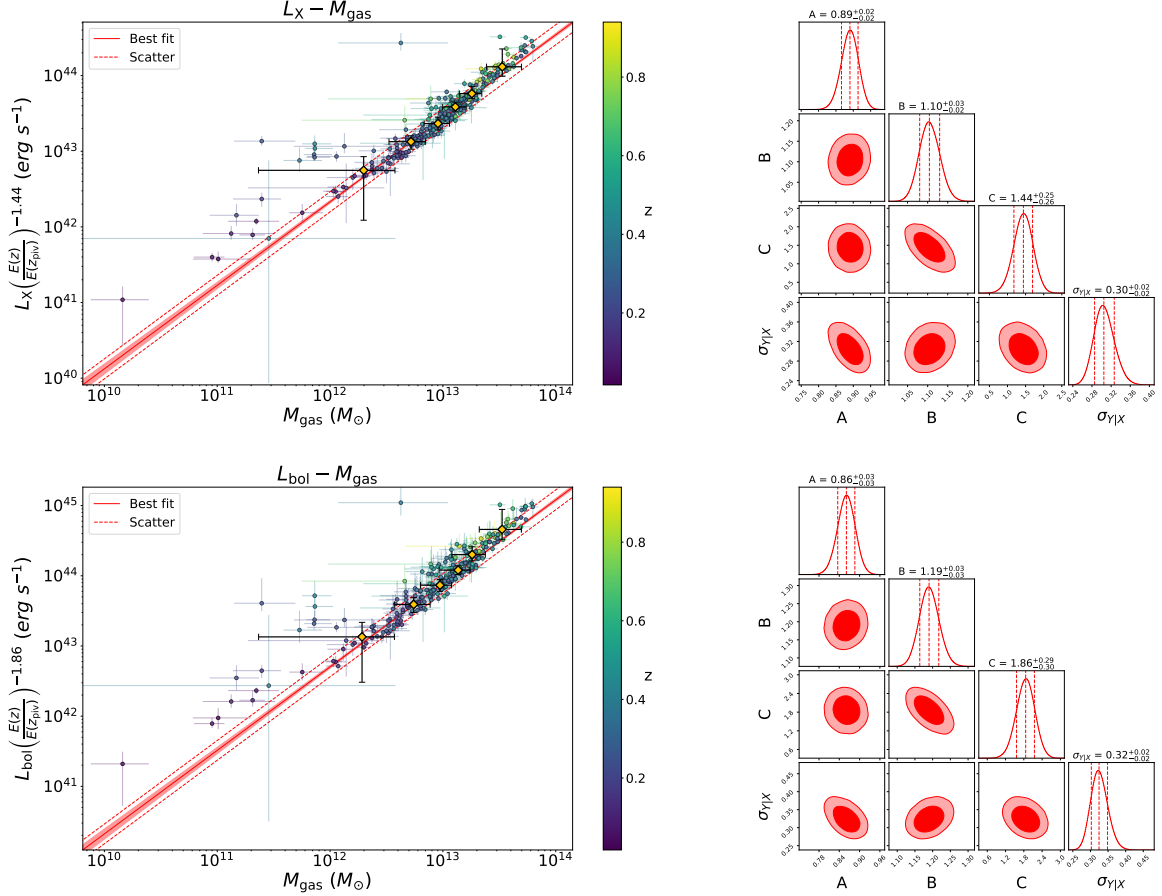
Figure 2.5: $L - M_{gas}$ scaling relations and the posterior distributions of the scaling relations parameters. *Left:* Soft band $(0.5 - 2.0$ keV) X-ray luminosity (L_X), bolometric $(0.01 - 100$ keV) luminosity (L_{bol}), gas mass (M_{gas}), and redshift (z) measurements of the $\mathcal{L}_{det} > 15$, $\mathcal{L}_{ext} > 15$ sample and the best-fit scaling relation models. The light-red shaded areas indicate 1σ uncertainty of the means of the log-normal models (see Eq. 2.5), and dashed red lines indicate the best-fit standard deviations $(\sigma_{L|M_{gas}})$ around the mean. Orange diamonds indicate median gas mass measurements obtained from clusters between luminosity quantiles. *Right:* Parameter constraints of the $L_X - M_{gas}$ and $L_{bol} - M_{gas}$ relations obtained from the second half of the MCMC chains. Marginalized posterior distributions are shown on the diagonal plots, and the joint posterior distributions are shown on off-diagonal plots. Red dashed vertical lines indicate the 32nd, 50th, and 68th percentiles, and contours indicate 68% and 95% credibility regions.

$L_X - M_{gas}$ relation. When we fix the redshift evolution to the self-similar value, the slope does not change significantly ($B = 1.07 \pm 0.02$). Zhang et al. (2011) obtained a slope of $B = 1.11 \pm 0.03$ from the 62 clusters in the HIFLUGCS sample, which is consistent with our measurements. Their slope for the cool-core clusters ($B = 1.09 \pm 0.05$) is similar to what they found for their whole cluster sample, but the best-fit slope for their noncool-core clusters is steeper ($B = 1.20 \pm 0.06$). Lovisari et al. (2015) studied the scaling properties of a complete X-ray-selected galaxy group sample and found the slope of the $L_X - M_{gas}$ relation for galaxy groups to be $B = 1.02 \pm 0.24$, which is slightly shallower than but still consistent with the result they obtained for more massive clusters, $B = 1.18 \pm 0.07$. Both of these measurements are consistent with our slope. Conversely, a flux-limited sample of 139 clusters compiled from the ROSAT All-Sky Survey catalog has a steeper slope with $B = 1.34 \pm 0.05$ for the $L_X - M_{gas}$ relation (Mantz et al., 2016). The result of these latter authors is more than 4σ away from our measurement. This discrepancy might be due to the fact that the Mantz et al. (2016) sample is dominated by massive, luminous clusters (their lowest luminosity system is about as bright as our most luminous systems), while the eFEDS sample is composed of low-mass clusters and groups. There are not many studies in the literature reporting intrinsic scatter of the $L_X - M_{gas}$ relation. Therefore, we were only able to compare our results with those of Zhang et al. (2011), who found $\sigma_{L_X|M_{gas}} = 0.14 \pm 2$, which is significantly lower (5.5σ) than our results.

On the other hand, we find the best-fit parameters of the slope, the evolution term, and the scatter of the $L_{bol} - M_{gas}$ relation to be $B = 1.19 \pm 0.03$, $C = 1.86^{+0.29}_{-0.30}$, and $\sigma_{L_{bol}|M_{gas}} = 0.32 \pm 0.02$, respectively. Similarly, the slope is $\sim 5\sigma$ away from the self-similar model, while the redshift evolution is fully consistent with the model. This relation has received much less attention in the literature. Zhang et al. (2011) found a slope of $B = 1.29 \pm 0.05$ when they fitted their whole sample. Their reported slope is less steep for cool-core clusters ($B = 1.24 \pm 0.05$) relative to the noncool-core clusters ($B = 1.42 \pm 0.06$). The slope of the whole sample is fully consistent with our measurements within 2σ. Similar to the $L_X - M_{gas}$ relation, we could only compare our best-fit intrinsic scatter for the $L_{bol} - M_{gas}$ relation with the results of Zhang et al. (2011), who report $\sigma_{L_{bol}|M_{gas}} = 0.21 \pm 2$, which is in 4σ tension with our results.

One additional point is that there is a noticeable deviation around the gas mass of $\sim 10^{12}$ $M_\odot$ in Fig. 2.5. The low-mass groups tend to show higher luminosity relative to the mass determined from the scaling relations. The slope and normalization of this power-law relation are mostly governed by the higher mass clusters. The low-mass groups would prefer a shallower $L_X - M_{gas}$ power-law slope relative to the high-mass clusters. This observed trend is fully consistent with the $L_X - M_{gas}$ relation reported by Lovisari et al. (2015), who similarly observed the relation getting shallower at the group scale but within error bars.

2.4.3 $L_X - Y_X$ and $L_{bol} - Y_X$ Relations

The accurate mass indicator, Y_X, first introduced by Kravtsov et al. (2006), shows a low intrinsic scatter with mass and has a tight relation with the Sunyaev Zel'dovich (SZ) effect observable Compton-y parameter, Y_{SZ} (e.g., Maughan, 2007; Benson et al., 2013; Mantz et al., 2016; Bulbul et al., 2019; Andrade-Santos et al., 2021). Because of this strong correlation, scaling relations involving Y_X can be used as a connection in multi-wavelength studies of galaxy clusters. Numer-
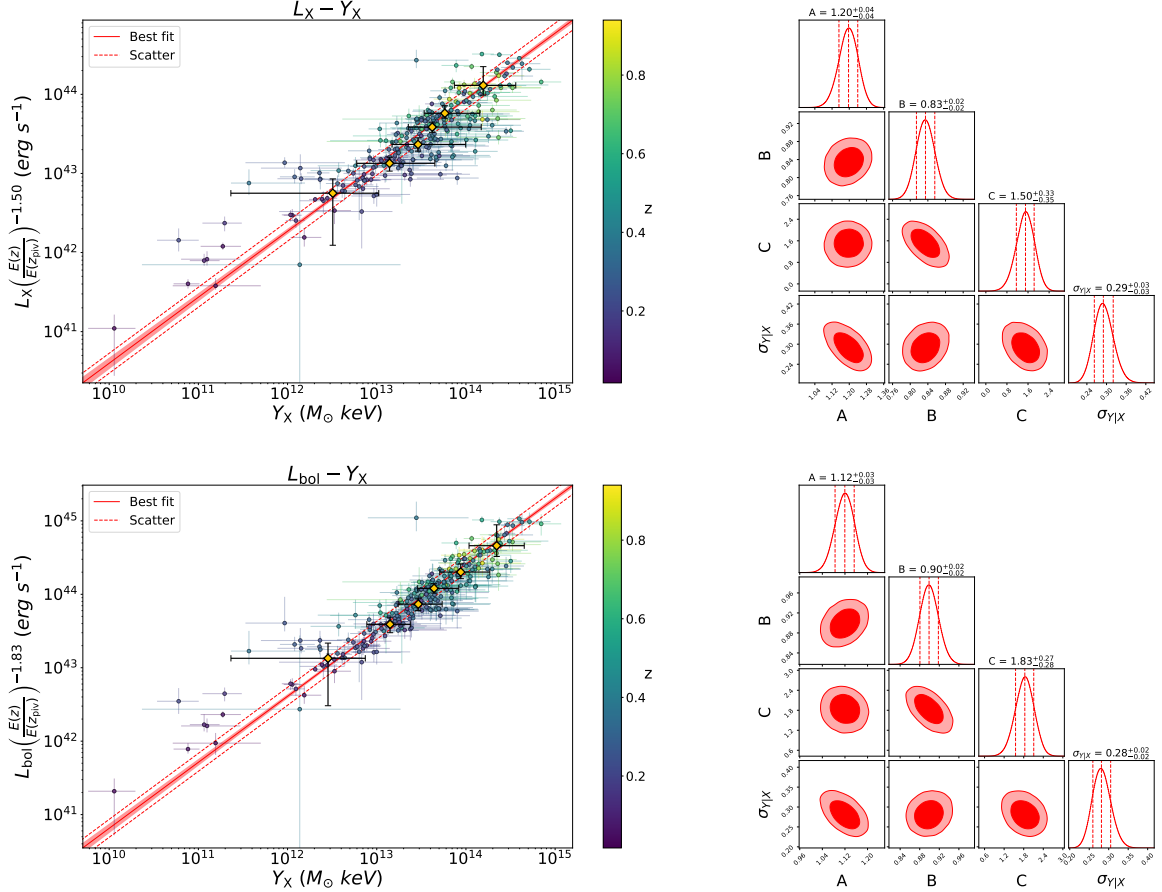
Figure 2.6: $L - Y_X$ scaling relations and the posterior distributions of the scaling relations parameters. *Left:* Soft band ($0.5 - 2.0$ keV) X-ray luminosity (L_X), bolometric ($0.01 - 100$ keV) luminosity (L_{bol}), Y_X, and redshift (z) measurements of the $\mathcal{L}_{det} > 15$, $\mathcal{L}_{ext} > 15$ sample and the best-fit scaling relation models. The light-red shaded areas indicate 1σ uncertainty of the means of the log-normal models (see Eq. 2.5), and dashed red lines indicate the best-fit standard deviations ($\sigma_{L|Y_X}$) around the mean. Orange diamonds indicate median Y_X measurements obtained from clusters between luminosity quantiles. *Right:* Parameter constraints of the $L_X - Y_X$ and $L_{bol} - Y_X$ relations obtained from the second half of the MCMC chains. Marginalized posterior distributions are shown on the diagonal plots, and the joint posterior distributions are shown on off-diagonal plots. Red dashed vertical lines indicate the 32nd, 50th, and 68th percentiles, and contours indicate 68% and 95% credibility regions.
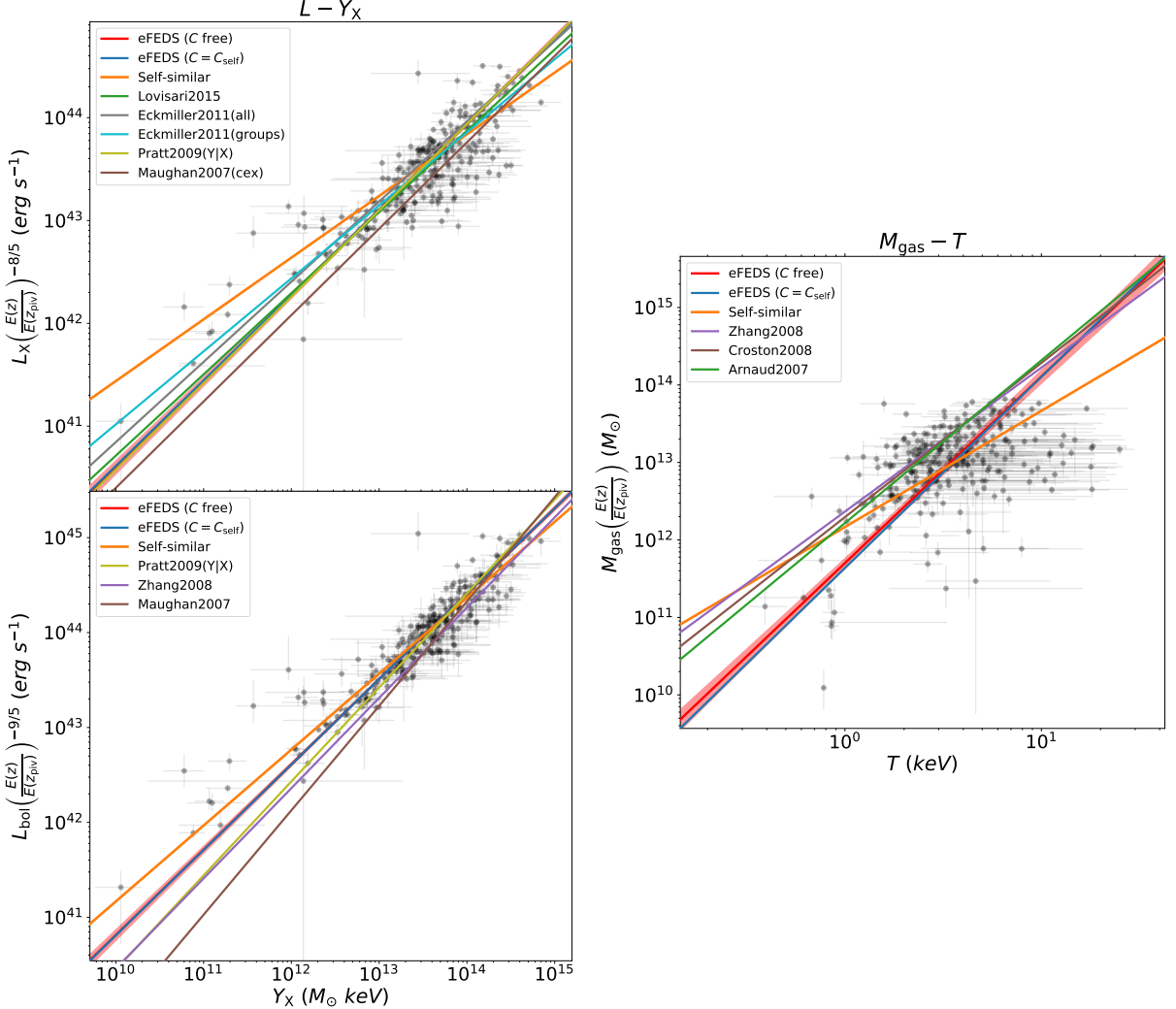
Figure 2.7: Comparison between our best-fit $L - Y_X$, and $M_{gas} - T$ relations, the self-similar model and other studies in the literature (Maughan, 2007; Arnaud et al., 2007; Croston et al., 2008; Zhang et al., 2008; Pratt et al., 2009; Eckmiller et al., 2011; Lovisari et al., 2015). Grey circles are the eFEDS clusters. In order to achieve consistency, a cosmology and energy band conversion is applied to the previously reported results (see Sect. 2.4 for the details).

ical simulations suggest that non-gravitational effects have a small influence on this mass proxy compared to other X-ray observables (Nagai et al., 2007a).

According to the self-similar model, luminosity is expected to depend on Y_X and redshift as

$$L_X \propto Y_X^{3/5} E(z)^{8/5} \tag{2.15}$$

and

$$L_{bol} \propto Y_X^{4/5} E(z)^{9/5}. \tag{2.16}$$

Our results for the best-fit $L_X - Y_X$ relations are listed in Table 2.3 and plotted in Fig. 2.6, while a comparison with the literature is provided in Fig. 2.7. We find a slope of $B = 0.83 \pm 0.02$, a redshift evolution exponent of $C = 1.50^{+0.33}_{-0.35}$, and an intrinsic scatter of $\sigma_{L_X|Y_X} = 0.29 \pm 0.03$ for the $L_X - Y_X$ scaling relation. Our slope for the $L_X - Y_X$ relation is 11.5σ steeper than that predicted by the self-similar model. The redshift evolution of the $L_X - Y_X$ relation is slightly shallower than the self-similar expectation but is consistent within the uncertainties. Our slope is consistent with the results presented in Maughan (2007) ($B = 0.84 \pm 0.03$) and with that of Lovisari et al. (2015) ($B = 0.79 \pm 0.03$). Our results for the same relation are within 1.8σ statistical uncertainty of the HIFLUGCS+groups sample of Eckmiller et al. (2011) and within 2.2σ of their groups-only sample. These latter authors find slopes of $B = 0.78 \pm 0.02$ and $B = 0.71 \pm 0.05$ for the HIFLUGCS+groups and groups only samples, respectively, where the latter is within $\sim 2\sigma$ from the self-similar expectation. Our best-fit intrinsic scatter is in good agreement (1.5σ) with the findings of Pratt et al. (2009) ($\sigma_{L_X|Y_X} = 0.41 \pm 0.07$). Eckmiller et al. (2011) ($\sigma_{L_X|Y_X} = 0.46$) and Lovisari et al. (2015) ($\sigma_{L_X|Y_X} = 0.51$) report higher values for the intrinsic scatter of the $L_X - Y_X$ relation, but these measurements are presented without error bars and therefore a statistical comparison with our findings cannot be made.

For the $L_{bol} - Y_X$ relation, we find a slope of $B = 0.90 \pm 0.02$, a redshift evolution exponent of $C = 1.83^{+0.27}_{-0.28}$, and an intrinsic scatter of $\sigma_{L_{bol}|Y_X} = 0.28 \pm 0.02$. The slope shows a 5σ deviation from self-similarity. Maughan (2007) find an even larger deviation from the self-similarity, measuring a slope of $B = 1.10 \pm 0.04$. Also, in Zhang et al. (2008) and Pratt et al. (2009), the authors reported steeper slopes of $B = 0.95 \pm 0.08$ and $B = 1.04 \pm 0.06$ where the former agrees well with our results within statistical uncertainties whereas the latter is 2.2σ higher. Numerical simulations show a similar scenario. Biffi et al. (2014) reports this slope to be $B = 0.94 \pm 0.02$, which is also slightly steeper than our results and significantly steeper than the self-similar value. Our redshift evolution for the $L_{bol} - Y_X$ relation is consistent with the self-similar prediction within the uncertainties. A similar redshift evolution was measured in Maughan (2007), with $C = 2.2 \pm 0.1$, which is $< 1.5\sigma$ away from our finding. Our best-fit intrinsic scatter for the $L_{bol} - Y_X$ relation is slightly smaller (1.5σ) compared to the value reported in Pratt et al. (2009) ($\sigma_{L_{bol}|Y_X} = 0.38 \pm 0.06$). Maughan (2007) reported a similar value ($\sigma_{L_{bol}|Y_X} = 0.36 \pm 0.03$) for the intrinsic scatter that is in 2.2σ tension with our best-fit value.

2.4.4 $M_{gas} - T$ Relation

$M_{gas} - T$ and $L_X - T$ relations are conjugates of each other because of the tight correlation between M_{gas} and L_X. However, we still expect to see differences as M_{gas} has a linear dependence on
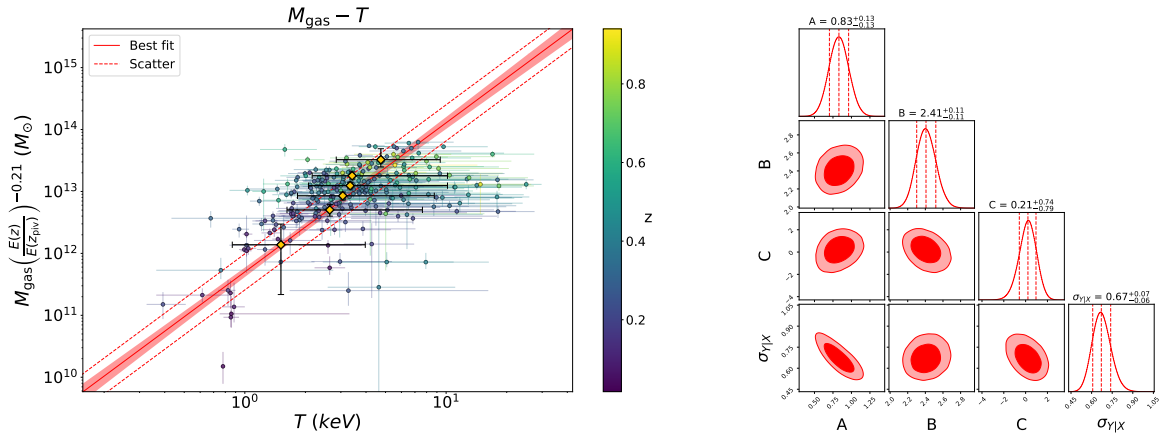
Figure 2.8: $M_{\text{gas}} - T$ scaling relation and the posterior distributions of the scaling relation parameters. *Left:* Gas mass (M_{gas}), temperature (T), and redshift (z) measurements of the $\mathcal{L}_{\text{det}} > 15$, $\mathcal{L}_{\text{ext}} > 15$ sample and the best-fit scaling relation models. The light-red shaded area indicates the 1σ uncertainty of the mean of the log-normal model (see Eq. 2.5), and dashed red lines indicate the best-fit standard deviations ($\sigma_{M_{\text{gas}}|T}$) around the mean. Orange diamonds indicate median temperature measurements obtained from clusters between gas mass quantiles. *Right:* Parameter constraints of the $M_{\text{gas}} - T$ relation obtained from the second half of the MCMC chains. Marginalized posterior distributions are shown on the diagonal plots, and the joint posterior distributions are shown on off-diagonal plots. Red dashed vertical lines indicate 32nd, 50th, and 68th percentiles, and contours indicate 68% and 95% credibility regions.

electron density, whereas L has a quadratic dependence. We fit the $M_{\mathrm{gas}} - T$ relation following the similar framework as in the sections above with minor changes. We use the L_{X} flavored selection function by converting M_{gas} to L_{X} because we do not have a selection function involving M_{gas} from simulations. This one-to-one conversion, in principle, should not introduce a large bias to our results because L_{X} and M_{gas} are tightly correlated, and the scatter between them is relatively low.

Based on the self-similar model, gas mass and temperature should be related to each other via

$$M_{\mathrm{gas}} \propto T^{3/2} E(z)^{-1}. \tag{2.17}$$

Our results for the $M_{\mathrm{gas}} - T$ relation are listed in Table 2.3 and shown in Fig. 2.8. We obtain a slope of $B = 2.41 \pm 0.11$, a redshift evolution exponent of $C = 0.21^{+0.74}_{-0.79}$, and a scatter of $\sigma_{M_{\mathrm{gas}}|T} = 0.67^{+0.07}_{-0.06}$. Our slope is 8.3σ steeper than the self-similar model. We find a positive redshift evolution, which is expected to be negative in the self-similar case, but our result agrees with the self-similar prediction within 1.5σ statistical uncertainty. A comparison of our results with the literature is given in Fig. 2.7. In general, the slope of the $M_{\mathrm{gas}} - T$ relation reported in the literature is close to ~ 1.9, which is steeper than the self-similar expectation. Reported slopes in the literature show a dependency on the mass range of the parent sample. For instance, Arnaud et al. (2007) reports a slope of 2.10 ± 0.05 based on the XMM-*Newton* observations of ten relaxed nearby clusters. Consistently, Croston et al. (2008) found 1.99 ± 0.11 using the 31 clusters in the REXCESS sample, and Zhang et al. (2008) obtained 1.86 ± 0.19 with XMM-*Newton* data for 37 LoCuSS clusters. These slopes are shallower than the results reported here, with a 2.5σ difference. The discrepancy could be due to the different selection of the samples compared here.

We find a factor of approximately two difference when we compare our best-fit normalization results with those of Arnaud et al. (2007) and Croston et al. (2008) at their pivot temperature value (5 keV). To investigate this difference and test our results, we reconstructed the $M_{\mathrm{gas}} - T$ relation using our best-fit $L_{\mathrm{X}} - T$ and $L_{\mathrm{X}} - M_{\mathrm{gas}}$ relations, which are in agreement with the most recent studies in the literature taking into account the selection effects. We obtain a relation of

$$M_{\mathrm{gas}} = 1.02 \, M_{\mathrm{gas,piv}} \left(\frac{T}{T_{\mathrm{piv}}} \right)^{2.63} \left(\frac{E(z)}{E(z_{\mathrm{piv}})} \right)^{0.14}. \tag{2.18}$$

The normalization, slope, and evolution terms are $< 2\sigma$ away from the best-fit $M_{\mathrm{gas}} - T$ relation, which indicates that our results for the $M_{\mathrm{gas}} - T$ relation would be in good agreement with the previous results if the selection effects were taken into account. We argue that the observed discrepancy arises due to the combined effect of two main differences between our analyses and the other analyses reported in the literature for the same relation. The first difference is that we include selection effects in our work, and therefore, measure a steeper slope for the $M_{\mathrm{gas}} - T$ relation compared to the previously reported results. Our steeper slope agrees well with previous findings because M_{gas} is a very good L_{X} proxy, and many studies, including ours, show that the best-fit slope of the $L_{\mathrm{X}} - T$ relation is found to be steeper when the selection effects are taken into account. The second difference is that our sample includes a larger fraction of low-mass clusters compared to the other samples. If the cluster populations were similar, we would not observe such a difference in normalization even if the slopes did not match. Therefore, in our case,

the populations and the slopes being different combine and result in the observed mismatch. Additionally, using a converted flavored selection function might have also contributed to the discrepancy, but its effect is expected to be much smaller because the relation between L_X and M_{gas} is tight and the scatter is low.

2.5 Discussion

Slopes of the scaling relations between X-ray observables studied in this Chapter show deviations from the self-similar model by $4 - 11.5\sigma$ confidence levels. These deviations are often attributed to the departures from the assumptions in the self-similar (Kaiser, 1986) model in the literature. We discuss two potential reasons for the observed discrepancy in the eFEDS sample in this section.

The most commonly proposed explanations in the literature for the departures from self-similarity challenge two major assumptions in the model. First, clusters are assumed to have a spherically symmetric gas distribution that is in hydrostatic equilibrium. Secondly, physical processes are primarily driven by the gravitational force, and the other effects are negligible in shaping the observed physical state of clusters. Observational data and numerical simulations indicate that both of these assumptions may not hold, and this can lead to departures from the self-similar expectation. non-gravitational processes such as AGN feedback, galactic winds, and star formation introduce extra energy to the system, heat the gas, and increase the entropy in the core (e.g., Voit, 2005; Walker et al., 2012; Bulbul et al., 2016). AGN feedback, in particular, can play an important role in shaping gas physics, especially in low-mass clusters and groups that dominate the eFEDS extended source sample. AGN activity can expel gas to the outskirts for lower mass haloes because of their shallower potential wells. As the larger fraction of gas is removed from the centers of low-mass haloes, their luminosity decreases (e.g., Puchwein et al., 2008). The most massive clusters with deeper potential wells, higher total mass, and the ICM temperature are less affected by the non-gravitational effects. When the clusters and groups are fit together, the lower luminosity of the groups and low-mass clusters leads to a steeper slope of the $L_X - T$ scaling relations when the cores are included. This result is consistent with numerical simulations (Puchwein et al., 2008; Schaye et al., 2010; Biffi et al., 2014; Truong et al., 2018; Henden et al., 2018, 2019), and the observational data in the literature (Eckmiller et al., 2011; Maughan et al., 2012; Pratt et al., 2009; Zou et al., 2016; Giles et al., 2016; Migkas et al., 2020; Lovisari et al., 2021). Another proposed reason for the steeper slope is the use of the overdensity radii r_{500c}, which are based on X-ray masses calculated under the assumption of hydrostatic equilibrium(see Lovisari et al., 2021, for discussion). If the radius r_{500c} is biased low because of the unaccounted-for non-thermal pressure in the ICM, the luminosity extracted in this radius would be lower. The temperatures are less impacted by this effect because of large uncertainties. However, in this Chapter, we use the overdensity radii r_{500c} reported in Chiu et al. (2022) that are obtained from the HSC weak lensing measurements uniformly for groups and clusters in the eFEDS sample. We argue that the (mass-dependent) hydrostatic equilibrium bias and radius of extraction do not have a major effect on our results and cannot explain the steeper slope of the $L_X - T$ scaling relations. The $M_{gas} - T$ relations should be affected by the AGN feedback similarly

but less severely than the $L_X - T$ relation because of the linear dependence of M_{gas} on the number density of electrons, i.e., $M_{\mathrm{gas}} \propto n_e$ while $L_X \propto n_e^2$ through X-ray emissivity. The expected steepening in $M_{\mathrm{gas}} - T$ should be less prominent as a result of this effect. This is fully consistent with our results, assuming that the discrepancy is attributed to non-gravitational effects. Another important issue in comparing various results in the literature is the calibration differences between X-ray telescopes. The number density and luminosity measurements are expected to be consistent between X-ray telescopes, namely *Chandra* and XMM-*Newton* (Bulbul et al., 2019); however, significant band-dependent disagreements have been reported for cluster ICM temperature measurements (Schellenberger et al., 2015). Given that the reported discrepancies between X-ray instruments are small in the soft X-ray band where the temperature measurements of most of our clusters lie, we do not expect that the slope differences are due to these calibration effects.

For $L_X - Y_X$ and $L_X - M_{\mathrm{gas}}$ scaling relations, the effect of Malmquist bias, i.e., preferential sampling of bright objects, can clearly be seen and is often prominent in X-ray-selected samples. We note that these biases and selection effects are fully accounted for in our selection function and, therefore, should not bias our best-fit scaling relations. We observe mild deviations from the self-similar model on both scaling relations in low M_{gas} and Y_X regimes. The mass proxy Y_X shows low intrinsic scatter with cluster mass in the literature (Kravtsov et al., 2006; Eckmiller et al., 2011; Bulbul et al., 2019). As the ICM temperature scales with total mass, we expect to see a similar trend with low-scatter in the $L_X - Y_X$ scaling relations. Indeed, the $L_X - Y_X$ scaling relations show a tight correlation for massive clusters. Along the lines of what we observe, as the group scales dominate the sample, the intrinsic scatter becomes larger. We find that the departures from the self-similarity are significant for both of the relations, which is consistent with the results reported in the literature and numerical simulations (Eckmiller et al., 2011; Biffi et al., 2014; Lovisari et al., 2015).

The self-similar model predicts cosmology-dependent redshift evolution for the scaling relations between observables and cluster mass. This dependence is introduced through the overdensity radius (and the critical density), which is inversely related to the evolution of the Hubble parameter with redshift z, $E(z) = H(z)/H_0$. We do not find significant departures from the self-similar evolution with redshift in any of our relations. All show self-similar redshift evolution $< 2.5\sigma$ confidence level. There are contradictory reports in the literature as to the evolution of scaling relations. Some studies report self-similar redshift evolution with redshift (Giodini et al., 2013), while some studies report no evolution (Maughan, 2007; Pacaud et al., 2007). Larger samples covering a wide redshift range will be available with the eRASS catalogs, which can be used to constrain the redshift evolution of scaling relations and test the self-similar model.

In this Chapter, we investigate the scaling relations between X-ray observables of the galaxy clusters and groups by fully modeling the selection effects. Our method of obtaining the selection function relies on realistic simulations of the eROSITA observations. This is the most robust way of modeling the selection effects as long as the simulated population of sources is representative of the observed sample. The advantage of this method lies in the fact that the same detection and reduction methods are applied to both simulated observations and the eROSITA data self-consistently (Clerc et al., 2018; Comparat et al., 2020). In these simulations, cluster surface brightness profiles are created by making use of the previously measured profiles of cluster and group samples that span a wide range of mass and redshift; they use X-COP, SPT, XXL,

and HIFLUGCS cluster samples. This method allows the profiles to be consistent with the observations, except in the low-L, low-z regime, where we probe a mass and redshift space that is poorly explored by previous X-ray observations. This led to a slight excess in the number of detected simulated clusters by the pipeline in this parameter space, the presence of which is barely visible in Fig. 2.2. The mild difference does not have any effect on our best fitting relations because our likelihood takes the redshift (z) and detection (I) information of clusters as given, $\mathcal{L}(\hat{Y}_{\mathrm{all}}, \hat{X}_{\mathrm{all}} | I, \theta, z)$, such that in our analysis, the shape of $P(I|L_{\mathrm{X}}, z)$ as a function of L_{X} is more important than the relative normalizations at different redshifts, $P(I|z) = \int P(I|L_{\mathrm{X}}, z) P(L_{\mathrm{X}}|z) dL_{\mathrm{X}}$.

Following our analysis of the eFEDS observations, this less populated mass–luminosity range will be filled with eFEDS clusters, and therefore, surface brightness profiles of simulated clusters at these regimes will be improved for modeling the selection function for the future eRASS observations.

We also test our method by comparing the model-predicted number of detected clusters (N_{det}) and the number of clusters in our observed sample ($\hat{N}_{\mathrm{det}}$) as also presented in Giles et al. (2016). However, we find that comparing the predicted and observed cluster numbers is not informative because the predictions have large uncertainties driven mostly by the propagated errors from our scaling relation analysis and the weak-lensing mass-calibrated scaling relation analysis of Chiu et al. (2022). To give an example, we compare the observed number of detected clusters for the $\mathcal{L}_{\mathrm{det}} > 15$, $\mathcal{L}_{\mathrm{ext}} > 15$ sample (265) with the model-predicted number for the $L_{\mathrm{X}} - T$ relation similar to the Giles et al. (2016). We calculated N_{det} as

$$N_{\mathrm{det}} = \int \int \int_{L_{\mathrm{X}}, T, z} P(I|L_{\mathrm{X}}, z) P(L_{\mathrm{X}}|T, \theta_{L_{\mathrm{X}}T}, z) \frac{dn}{dT} \frac{dV_{\mathrm{c}}}{dz} dL_{\mathrm{X}} dT dz, \qquad (2.19)$$

where $\frac{dV_{\mathrm{c}}}{dz}$ is the differential comoving volume shell spanning a solid angle of $\Omega_{\mathrm{eFEDS}} = 140/(180/\pi)^2$, $\frac{dn}{dT}$ is the temperature function calculated as described in Sect. 2.3.2, and $\theta_{L_{\mathrm{X}}T}$ is the best-fit parameters of the $L_{\mathrm{X}} - T$ relation. While calculating N_{det}, first we only propagate the errors of the best-fit parameters ($\theta_{L_{\mathrm{X}}T}$) using MCMC chains and a pivot value of $M_{\mathrm{piv}} = 1.4 \times 10^{14} M_{\odot}$, which is the median of the eFEDS sample. We find the model-predicted number of detected clusters to be $N_{\mathrm{det},\mathrm{L_xT}} = 301.2^{+42.5}_{-49.4}$. When we further propagate both the uncertainties of $\theta_{L_{\mathrm{X}}T}$ and the best-fit weak-lensing mass-calibrated scaling relation parameters ($A_\chi, B_\chi, \gamma_\chi$), we find the new measurement to be $N_{\mathrm{det},\mathrm{L_xT}} = 309.3^{+134.2}_{-86.1}$. In this case, the observed number of clusters is consistent with the predicted number of clusters within the uncertainties. The difference in the absolute values might be due to the selection function or the cosmology-dependent normalization of the mass function. In this Chapter and in the eROSITA simulations (Comparat et al., 2020), the Planck cosmology (Planck Collaboration et al., 2016) and the Tinker et al. (2008) mass function are used. Larger samples of clusters of galaxies became available through the eROSITA All-Sky observations (Bulbul et al., 2024), and provide sufficient statistics to constrain cosmology simultaneously with the scaling relations (Ghirardini et al., 2024).

Decreasing the scatter is of significant importance in reducing the systematic error on the constraints of cosmological parameters through cluster counts. Cool-core and relaxed clusters are reported to show less scatter on the scaling relations relative to the mergers (Vikhlinin et al., 2009; Mantz et al., 2010b). The dynamical states of the eFEDS clusters and groups were presented in

Ghirardini et al. (2022). The dynamically relaxed clusters make up 30 to 40% of this sample, and therefore, using them reduces the statistical power of our measurements. Additionally, the use of the relaxed cluster in the scaling-relation fits requires a selection function characterized in terms of these morphological parameters and a dynamical-state-dependent mass function (e.g., Seppi et al., 2021). This form of selection function is not available yet. We, therefore, leave this work to future studies of the eRASS data.

2.6   Conclusions

The eFEDS is of a similar depth to the final eROSITA All-Sky Survey in Equatorial regions. In this field, a total of 542 galaxy clusters and groups are detected as extended X-ray sources (Liu et al., 2022a; Klein et al., 2022). In addition, 346 more clusters are found in the point source catalog that were misclassified due to the sizable PSF of eROSITA (Bulbul et al., 2022). In this Chapter, we present the X-ray properties (L_X, L_{bol}, T, M_{gas}, Y_X) of the galaxy clusters and groups detected as extended objects in the eFEDS field in two apertures; core-included ($r < r_{500c}$) and core-excluded ($0.15r_{500c} < r < r_{500c}$). The overdensity radius r_{500c} is obtained from the HSC weak-lensing mass estimates provided in Chiu et al. (2022), allowing our measurements to be free of bias from the hydrostatic equilibrium assumption.

Additionally, we provide the $L - T$, $L - M_{gas}$, $L - Y_X$, and $M_{gas} - T$ scaling relations between these (core-included) X-ray observables for a subsample of clusters. We only consider the extent-selected sample, where we can characterize the selection effects using state-of-the-art simulations. Contamination of the main eFEDS clusters and groups sample by AGNs and false detections due to fluctuations is on the order of 20% (see Liu et al., 2022a, 2021, for details). To reduce the contamination of the sample to under 10%, we applied further cuts on the extent and detection likelihoods: $\mathcal{L}_{det} > 15$ and $\mathcal{L}_{ext} > 15$. Apart from the $\mathcal{L}_{det}$ and $\mathcal{L}_{ext}$ cuts, we have not applied any further cleaning to the sample, such as optical cross-matching. These cuts reduce the sample size to 265 clusters and groups spanning a redshift range of $0.017 < z < 0.94$, a soft-band luminosity range of 8.64×10^{40} erg s^{-1} $< L_X < 3.96 \times 10^{44}$ erg s^{-1}, and a mass range of 6.86×10^{12} M$_\odot$ $< M_{500c} < 7.79 \times 10^{14}$ M$_\odot$. In this sample, we find 68 low-mass galaxy groups with $< 10^{14}$M$_\odot$, which are uniformly selected with the rest of the massive clusters in the sample. We investigated seven relations by taking into account both the selection effects and the cosmological distributions of observables. Fitting was performed twice for each of the seven relations, first with a redshift evolution exponent left free and second with a redshift evolution exponent fixed to the self-similar value. The main conclusions of our analysis are as follows:

- The eFEDS scaling-relation results between X-ray observables, in general, are in good agreement with the recently reported results. However, we find significant tension with the self-similar expectation for all scaling relations studied here. We suggest that these deviations indicate that the non-gravitational effects, such as the feedback mechanisms, play a key, nonnegligible role in shaping the observed physical properties of the clusters, especially in the low-mass group regime. Specifically, the scaling-relation results we present in this Chapter for the $L - T$ relation agree well with the results from the samples that are

similar to the eFEDS sample when the selection function is taken into account (Giles et al., 2016; Lovisari et al., 2015; Eckmiller et al., 2011). Our results for the $L - T$ relation also agree well with the FABLE and MACSIS simulations where they include baryonic feedback (Puchwein et al., 2008; Henden et al., 2019; Biffi et al., 2014; Barnes et al., 2017).

– The largest scatter we measure is for the $L_X - T$ and $L_{bol} - T$ relations. We find $\sigma_{L_X|T} = 0.80 \pm 0.07$, $\sigma_{L_{bol}|T} = 0.76^{+0.07}_{-0.06}$ when we fix the redshift evolution to the self-similar value and $\sigma_{L_X|T} = 0.78^{+0.08}_{-0.07}$, $\sigma_{L_{bol}|T} = 0.70^{+0.07}_{-0.06}$ when the evolution is let free. This intrinsic scatter is mostly driven by the groups. The lowest scatter is measured for the $L_X - Y_X$ and $L_{bol} - Y_X$ relations with $\sigma_{L_{X(bol)}|Y_X} = 0.29(0.28) \pm 0.03(0.02)$. This result shows that in addition to Y_X being a good mass indicator, it is also a good proxy for the X-ray properties of the ICM.

– The redshift evolutions of the seven scaling relations we examined are broadly consistent with the self-similar model. Fixing the redshift evolution exponent to the corresponding self-similar value only changes the best-fit slopes by $< 1\sigma$ from its previous value obtained with a free exponent. Larger samples of clusters and groups are required to constrain the evolution of these relations with redshift.

– We find that the $M_{gas} - T$ relation differs from the previous results in the literature by a factor of approximately two in normalization. This could be driven by the lack of proper consideration of the selection effects in the previously reported results or by the fact that the eFEDS sample contains a much greater number of low-mass clusters and groups than the compared samples. This difference might also partially be due to the lack of a selection function with the M_{gas} flavor. The inclusion of other X-ray observables in the simulations is an ongoing project and will help to understand the effects of such phenomena.

The work presented in this Chapter extends the study of X-ray scaling relations to a sample that is dominated by low-mass clusters and groups. It creates a further avenue by which to study ICM physics for a new population of low-mass clusters and groups, as well as massive clusters at a wide redshift range. These initial results demonstrate the capability of eROSITA to detect the ICM emission out to r_{500c} for a large number of clusters detected at the final depth of the All Sky Survey. We note that this depth is exceeded by the first All Sky Survey for a limited area, allowing the observables to be measured out to r_{500c} or beyond for a subsample of clusters. These measurements will provide access to increasingly stringiest constraints on the mass and redshift evolution of the scaling relations. eFEDS observations not only allow us to put tight constraints on the scaling relation parameters but also allow us to test our selection function, which will be used in future statistical studies with eROSITA.

Chapter 3

The SRG/eROSITA All-Sky Survey: Constraints on AGN Feedback in Galaxy Groups

The intra-group medium retains a historical record of any heating and cooling processes. AGN feedback is the dominant heating mechanism for gas in dark matter haloes at the mass scale of galaxy groups. The energetics of feedback, particularly from AGN, can be constrained by quantifying its impact on the properties of the intra-group medium. eROSITA's instrumental characteristics and observing strategy allow the detection of large samples of galaxy groups and the examination of their X-ray properties. In Chapter 2, we explored the deviations from self-similarity in the scaling relations of integrated X-ray observables for galaxy clusters and groups in the eFEDS field. In this Chapter, we shift our focus to galaxy groups in the eROSITA all-sky survey and constrain the impact of AGN feedback, a major contributor to deviations from self-similarity, on the properties of the intra-group medium. To achieve this, we use a sample of 1178 galaxy groups selected from the eRASS1 survey. We divide the sample into 271 sub-samples based on their physical and statistical properties. Using deeper eROSITA observations (eRASS:4), we then measure the average thermodynamic properties of the subsamples, including characteristic temperature within r_{500c} and entropy at three characteristic radii ($0.15r_{500c}$, r_{2500c} and r_{500c}). The sample used in this Chapter is the largest galaxy group sample studied in X-rays thus far. Using this sample, we put tight constraints on the impact of AGN on the intra-group medium. We also compared our results with the predictions of three modern cosmological hydrodynamic simulations (MillenniumTNG, Magneticum, OWL) and tested different AGN feedback implementations in these simulations. Our measurements will allow future numerical simulations to achieve more realistic AGN feedback implementations. The deeper eROSITA all-sky survey observations will allow constraining AGN feedback in groups at even lower temperatures and will allow the feedback models to be tested in this parameter space.

The results presented in this Chapter have been published in Bahar et al. (2024). I performed the majority of the work and analysis presented in that paper and this Chapter. Dr. Xiaoyuan Zhang calculated the optimum energy band for imaging analysis (see Sect. 3.3.2), Dr. Nicolas Clerc provided the selection function for the group sample, Dr. Boryana Hadzhiyska and Dr.

Rüdiger Pakmor provided the density and temperature profiles of MillenniumTNG haloes (see Sect. 3.6.1), and Dr. Veronica Biffi provided the density and temperature profiles of Magneticum haloes (see Sect. 3.6.2).

3.1 Introduction

In the current understanding of the "bottom–up" structure formation of the Universe in the standard ΛCDM cosmology, small overdensities collapse first, overcoming the cosmological expansion, merging to form larger haloes (Springel, 2005). In this scenario, the gas encapsulated in dark matter haloes forms the first stars and galaxies as it cools and condenses. The effects of tidal forces, mergers, and interactions in their surroundings regulate the galaxy formation and evolution process. The majority of galaxies in the Universe are found in dense environments as galaxy groups and include a large fraction of the universal baryon budget (Mulchaey, 2000). The interaction between galaxies and the intra-group medium (IGrM; the gas encapsulated within the galaxy groups) plays a crucial role in shaping the properties and evolution of galaxies. For instance, the feedback from supernovae, star formation, and central supermassive black holes impacts the evolution of galaxies within the galaxy groups.

As discussed in Sect. 1.4, there is no clear definition of galaxy groups. Dark matter haloes with less than 50 galaxies and/or masses between $5 \times 10^{12} - 10^{14}$ M$_\odot$ are often classified as galaxy groups (Crain et al., 2009). In addition to their member galaxies, galaxy groups contain diffuse baryonic matter in the form of hot plasma with temperatures (T[1]) ranging from 0.1–2 keV, all encapsulated by the potential well provided by dark matter. Groups are further categorized as poor/loose groups, compact groups, and fossil groups depending on their optical properties (Hickson, 1997; Mulchaey and Zabludoff, 1998; Mulchaey, 2000; Voevodkin et al., 2010).

Despite the abundance of galaxy groups and the essential role they play in the assembly process of dark matter haloes in the Universe (Crain et al., 2009), their detection has been challenging due to their low richness, faint X-ray signal, and shallow potential wells. A variety of methods have been employed to search for galaxy groups. In the optical domain, clustering and friends-of-friends (FoF) algorithms are used to catalog groups in spectroscopic or photometric galaxy redshift surveys (e.g., Hickson, 1982; Robotham et al., 2011; Tempel et al., 2017; Gozaliasl et al., 2022). However, due to their relatively low richnesses, group catalogs compiled using optical observations may suffer from large contamination fractions due to random superposition of galaxies along the line-of-sight, otherwise known as projection effects (see Costanzi et al., 2019; Grandis et al., 2021; Myles et al., 2021). On the other hand, in the X-ray domain, the emission from IGrM makes them appear as extended sources in the X-ray sky, where they typically exhibit rapidly increasing X-ray emission profiles from the outskirts of the system to the center. Because of their characteristic surface brightness profiles, if their emission is above the background level, they can be easily identified and do not suffer significantly from projection effects. Aside from being a reliable tool for detecting groups, X-ray observations also enable the

---

[1]Throughout this Chapter, we use the notation T to represent k_BT and express temperature measurements in the units of keV.

measurement of the physical properties of the hot ionized IGrM through imaging and spectral analysis.

As discussed in detail in Sect. 1.4, the effects of the non-thermal astrophysical phenomena governing galaxy formation are easier to study using galaxy groups compared to clusters, as the input energy associated with these phenomena is comparable to the binding energies of groups (Balogh et al., 2001). For investigating the non-thermal phenomena, entropy ($S = T/n_e^{2/3}$) measurements of IGrM are often used, which retains a historical record of the thermodynamic state of the gas and reflects the changes in the cooling and heating processes in galaxy groups (Voit, 2005; Pratt et al., 2010). For example, OverWhelmingly Large Simulations (OWLS, Schaye et al., 2010; McCarthy et al., 2010) showed that the outflows from central active galactic nuclei (AGN) elevate the entropy of the IGrM by mechanically expelling low-entropy gas instead of directly heating it. This process mitigates rapid cooling and prevents excessive star formation (Bryan, 2000; Balogh et al., 2001). On the other hand, the feedback generated by supernova-driven winds associated with galaxies can also increase the entropy of the IGrM through direct heating (see Eckert et al., 2021, for a review).

Another important observational constraint on the non-thermal astrophysical phenomenon is the shape of the stellar mass function (see Sect. 1.3). Observational studies have demonstrated that the stellar mass exhibits a cut-off at $M_\star \sim 10^{11} M_\odot$ (Davidzon et al., 2017). Early studies trying to reproduce the cut-off with stellar feedback (e.g., through the energy and momentum released by supernovae explosions and stellar winds) were unsuccessful. This is because the injected energy is proven to be not enough to prevent cooling and regulate the star formation efficiency (Benson et al., 2003). Therefore, it is commonly agreed that feedback from another source, such as AGN, is needed to reproduce the observed cut-off in the stellar mass function (Harrison, 2017). Moreover, there are further observational constraints on the energy released by the non-gravitational feedback, such as the Si and Fe abundance profiles of the intracluster/intragroup medium. These measurements cannot be reproduced even with the assumption of 100 percent efficient stellar feedback heating (Kravtsov and Yepes, 2000), a scenario that is rejected by the measurements of the galactic outflows (Martin, 1999). Therefore, the total amount of energy that can be injected through stellar feedback on the IGrM is constrained relatively well by the abundant observational data. Consequently, by measuring the thermodynamic properties of galaxy groups, one effectively constrains the energetics of the remaining source of energy, AGN. For the higher mass groups ($M_{500c} > 10^{13.5} M_\odot$), the impact of stellar feedback is at a negligible level, such that entropy measurements put direct constraints on the impact of AGN (Le Brun et al., 2014). For the low mass groups ($M_{500c} < 10^{13} M_\odot$), constraints from multiple observables should be combined to isolate the impact of AGN on its surroundings (e.g., see Altamura et al., 2023).

As shown in Sect. 1.3, AGN heating in galaxy clusters and groups is observationally confirmed by shocks, ripples, and cavities in X-ray (e.g., Fabian et al., 2006; Randall et al., 2011) as well as the detection of radio-loud AGN in a significant proportion of the brightest cluster/group galaxies of the cool core galaxy clusters and groups (e.g., Burns, 1990; Best et al., 2007; Smolčić et al., 2011). Furthermore, deeper radio observations revealed that nearly every central galaxy in X-ray bright groups hosts radio emission (Kolokythas et al., 2019). In fact, radio observations of galaxy groups are highly complementary to the X-ray view of groups for investigating the

impact of AGN on IGrM (Eckert et al., 2021). Simultaneously studying their X-ray and radio properties allows for putting constraints on the radio mode feedback from the central engine (e.g., Pasini et al., 2022; Böckmann et al., 2023). Nevertheless, combining multi-wavelength datasets comes with challenges. For instance, crossmatching X-ray and radio catalogs makes it challenging to have a good handle on the selection effects that is crucial for achieving unbiased conclusions about galaxy groups at the population level. Given the challenges and caveats, in this Chapter, we only focus on putting constraints on the impact of non-gravitational feedback mechanisms through X-ray observations and leave the investigation of the multi-wavelength picture of eRASS1 galaxy groups sample to future work.

Entropy of IGrM can be measured using X-ray observations, where the electron density and temperature measurements can be made using the imaging and spectroscopic capabilities of X-ray telescopes, such as SRG/eROSITA, *XMM-Newton*, and *Chandra*. Ponman et al. (1999) measured the entropy of 25 bright galaxy clusters and groups at a radius of $0.1r_{virial}$[2] using ROSAT and GINGA observations and reported that the entropy measurements at the core lay above the expected power-law relation with temperature for the first time. Subsequently, Lloyd-Davies et al. (2000), Finoguenov et al. (2002) and Ponman et al. (2003) measured the entropy profiles of galaxy clusters and groups using ROSAT and ASCA observations that provided the first hint that in galaxy groups, the excess entropy is not limited only to the core but can also be prominent at larger radii. Voit (2005) formulated a baseline entropy profile that can be used for evaluating the impact of non-gravitational processes for galaxy clusters and groups using four sets of simulations that only include gravitational processes. Using X-ray instruments with a higher spatial and spectral resolution, such as *XMM-Newton* and *Chandra*, significantly improved our understanding of the excess entropy in galaxy groups by accurately measuring their entropy profiles. Johnson et al. (2009) investigated entropy profiles of galaxy groups by analyzing *XMM-Newton* observations of 28 nearby galaxy groups from the Two-Dimensional *XMM-Newton* Group Survey. They divided their sample into two subsamples, cool core, and non-cool core, based on the temperature gradient at the core of their groups and found that the entropy profiles of the groups in their non-cool core sample exhibit less scatter compared to entropy profiles of their cool core sample. Around the same time, Sun et al. (2009, S09 hereafter) conducted a comprehensive study on the thermodynamic gas properties of 43 nearby galaxy groups using the archival *Chandra* observations where they constrained the temperature, electron density, and metallicity profiles of 23 groups out to r_{500c}[3] accurately, thanks to the outstanding imaging capabilities of *Chandra* and the relatively deep archival observations of some systems in their sample. Furthermore, they compared their entropy profiles with the baseline entropy profile of Voit (2005) and found that even though the entropy excess reduces as a function of the radius, it remains significant out to r_{500c}. Subsequently, the detailed analysis of the outskirts of RX J1159+5531, UGC 03957, and Virgo using *Suzaku* observations revealed that the entropy excess can go beyond r_{500c} (Humphrey et al., 2012; Thölken et al., 2016; Simionescu et al., 2017). More recently, Panagoulia et al. (2014) analyzed 66 galaxy groups from the NORAS and REFLEX samples to investigate the properties of

---

[2]r_{virial} is defined as the radius within which a system obeys the virial theorem.
[3]r_{500c} is defined as the radius within which the density of a system is 500 times the critical density of the Universe at the redshift of the system.

IGrM at the core and found that entropy profiles of galaxy groups at the core follow a power-law relation and do not exhibit any entropy floor.

Previous studies in the literature on the thermodynamic properties of galaxy groups have been conducted using relatively small (less than a hundred) and highly incomplete samples that lack well-defined selection functions. eROSITA opens a new window for galaxy group studies by providing the largest pure X-ray-selected sample with a well-defined selection function crucial for achieving robust conclusions that reflect the physical properties of the galaxy group well at the population level. Furthermore, the superb soft X-ray band sensitivity and the scanning observing strategy of eROSITA make it an excellent instrument for investigating the physical properties of the hot gas in galaxy groups, given that the emission of IGrM peaks at the soft X-ray band and the brightest galaxy groups above the detection capabilities of the current instruments are at low redshift and well extended.

In this Chapter, we examine the effect of the feedback on the thermodynamics of galaxy groups detected by eROSITA in its first All-Sky Survey. We accomplish this by performing joint imaging and spectral analysis on the eRASS:4 (the four eROSITA consecutive All-Sky Surveys stacked together) observations of the galaxy groups in our sample. The extended ROentgen Survey with an Imaging Telescope Array (eROSITA), the soft X-ray telescope on board the Spectrum-Roentgen-Gamma (SRG) mission (Sunyaev et al., 2021), was launched on July 13, 2019 (Predehl et al., 2021). The first All-Sky Survey with eROSITA was successfully executed on June 11, 2020, after 184 days of operations. In this first All-Sky Survey (eRASS1), eROSITA detected a total of 12247 optically confirmed galaxy groups and clusters spanning the redshift range $0.003 < z < 1.32$ with a sample purity level of 86% in the Western Galactic half of the survey ($359.9442 \deg > l > 179.9442 \deg$), where the data rights belong to the German eROSITA consortium (Merloni et al., 2024; Bulbul et al., 2024; Kluge et al., 2024).

We combine the imaging and spectroscopic information of 1178 eROSITA-detected galaxy groups and obtain average entropy measurements at $0.15r_{500c}$, r_{2500c} and r_{500c} to investigate the effects of AGN feedback and compare our findings with the state-of-the-art numerical simulations from MillenniumTNG (Hernández-Aguayo et al., 2023; Pakmor et al., 2023), Magneticum (Hirschmann et al., 2014), and OverWhelmingly Large simulations (Schaye et al., 2010; McCarthy et al., 2010). The findings represent the first study of a comprehensive group sample with a well-defined selection function. This Chapter is organized as follows: In Sect. 3.2, we describe the construction of the galaxy groups sample from the primary eRASS1 sample, and in Sect. 3.3, we describe the X-ray data reduction and the analysis of the groups. In Sect. 3.4, we provide a discussion of major systematics and the details of the quantification and incorporation of them in our results, and in Sect. 3.5, we provide our final results on the entropy measurements of the sample and comparisons with the previous measurements. In Sect. 3.6, we provide a comparison between our measurements and the predictions of the state-of-the-art simulations. Lastly, we provide a summary of our findings and list our conclusions in Sect. 3.7.
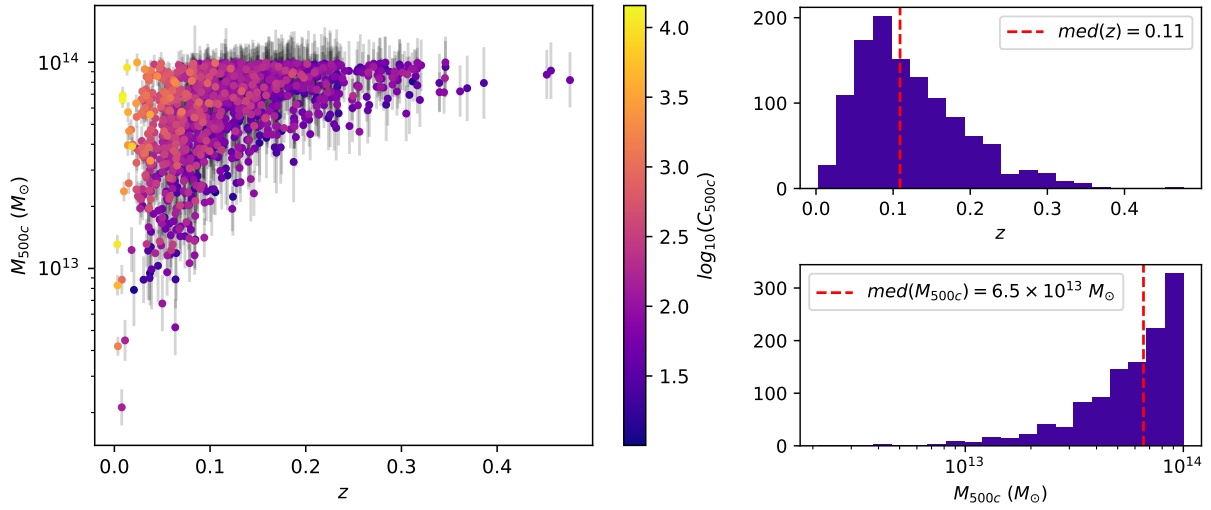
Figure 3.1: *Left:* The mass and redshift distributions of the galaxy group sample used in the work presented in this Chapter consist of 1178 objects where colors of the data points represent the eROSITA counts of the groups in soft X-ray band (0.3 − 1.8 keV) *Right:* Mass and redshift histograms of the group sample where the median redshift (z) is 0.11 and median mass (M_{500c}) is 6.5×10^{13} $M_\odot$.

3.2   Sample of Galaxy Groups

The work presented in this Chapter utilizes a subsample of the X-ray-selected, optically identified primary eRASS1 galaxy cluster and group sample detected in the Western Galactic hemisphere of the first eROSITA All-Sky Survey (Bulbul et al., 2024; Kluge et al., 2024). Below, we briefly describe the detection of galaxy clusters and groups in eRASS1 observations and a brief summary of the optical and X-ray cleaning performed in Bulbul et al. (2024). Subsequently, we provide the details of the additional selection and cleaning applied to the eRASS1 galaxy clusters and groups catalog.

The X-ray emitting celestial objects in the eRASS1 master X-ray catalog (Merloni et al., 2024) are detected using the eROSITA source detection pipeline, which is part of the eROSITA Science Analysis Software System (eSASS, Brunner et al., 2022). The pipeline locates detection candidates and calculates detection and extent likelihood ($\mathcal{L}_{\mathrm{det}}$ and $\mathcal{L}_{\mathrm{ext}}$) parameters by comparing the spatial distribution and the abundance of the photons around the candidate with the local background. To construct the primary galaxy groups and clusters sample (Bulbul et al., 2024), a $\mathcal{L}_{\mathrm{ext}} > 3$ cut is applied to increase the completeness of the galaxy groups and clusters sample (see Bulbul et al., 2022, for the motivation). The DESI Legacy Survey DR9 and DR10 datasets are used in the optical identification processes by the eROMaPPer pipeline, which is based on the matched-filter red-sequence algorithm from redMaPPer (Rykoff et al., 2014, 2016) tailored and optimized for the identification of eROSITA extended sources (Ider Chitham et al., 2020; Kluge et al., 2024). If available, spectroscopic redshifts (z_{spec}) are prioritized over photometric redshift (z_λ) by the eROMaPPer pipeline (see Kluge et al., 2024, for further details). In this primary sam-

ple, 12 705 extended sources in the redshift range of 0.01 to 1.35 are identified as galaxy clusters or groups with a contamination fraction of 14% (Bulbul et al., 2024; Kluge et al., 2024).

To construct a final clean and secure galaxy group sample, we apply further cuts based on the X-ray and optical properties of the primary sample. While the literature lacks a precise definition for galaxy groups, we classify an object as a group if its mass ranges between $5 \times 10^{12} < M_{500c} < 10^{14} M_{\odot}$. The upper end of our group definition ($10^{14} M_{\odot}$) corresponds to a plasma temperature of $T \sim 2$ keV and is commonly used in previous X-ray studies for distinguishing galaxy clusters from galaxy groups (Lovisari et al., 2021). For incorporating this mass criterion, we use the M_{500c} estimates obtained in Sect. 3.3.4 using a Bayesian X-ray observable estimation framework that jointly estimates the soft-band (0.5–2 keV) X-ray luminosity (L_X), temperature (T) and the mass (M_{500c}) of galaxy clusters and groups from their count-rate profiles (see Sect. 3.3.4 for the details of our $L_X - T - M_{500c}$ estimation). After applying a mass cut of $M_{500c} < 10^{14} M_{\odot}$, we select 2526 galaxy group candidates with a median redshift of 0.11.

To further reduce the contamination, we apply other cleaning methods using the deeper eRASS:4 data. Contaminants in the $\mathcal{L}_{ext} > 3$ sample of the eRASS1 clusters and groups catalog can be classified into two categories: misclassified sources (mostly AGN) and spurious sources. Given that our preliminary sample has a median redshift of 0.11, the "real" galaxy groups in our sample are expected to be relatively well extended in the sky, whereas misclassified point sources, by definition, should have a low extent. We make use of this fact and conservatively remove 841 objects that have EXT < 20 arcsec and $\mathcal{L}_{ext} < 5.5$. These cuts remove most point sources, leaving 1685 group candidates in the sample.

Once the misclassified point sources are removed, spurious sources are left to be cleaned from our group sample. We use the count measurements in the $0.3 - 1.8$ keV band (see Sect. 3.3.2 for the details on the choice of the energy band) obtained from eRASS:4 observations as described in Sect. 3.3.3 to clean the spurious sources. We first apply an X-ray count cut of 10. This cut removes 423 objects from our group candidates. Furthermore, we remove 10 more sources from the remaining sample with count measurements 1σ consistent with the background level. This procedure removes most of the spurious sources since one would expect the galaxy groups to be more prominent and bright as the survey gets deeper. On the other hand, the spurious sources are expected to have low counts and be consistent with the background level since they are mostly due to background fluctuations or superpositions of undetected AGN in the eRASS1 observations. Applying these cuts, we remove a large fraction of contaminants in our sample and obtain a highly pure sample with 1252 galaxy groups.

One of the major benefits of the strict cleaning procedure described above is its applicability to simulations. Our cleaning procedure relies upon the detection pipeline outputs (e.g., $\mathcal{L}_{ext}$ and EXT) and therefore the selection process is fully reproducible in the simulations of the eRASS1 digital twin (Comparat et al., 2020; Seppi et al., 2022). This allows us to construct a robust selection function for our sample using the eROSITA's digital twin simulations. We further note that the cleaning applied in this Chapter to remove spurious sources has no impact on the
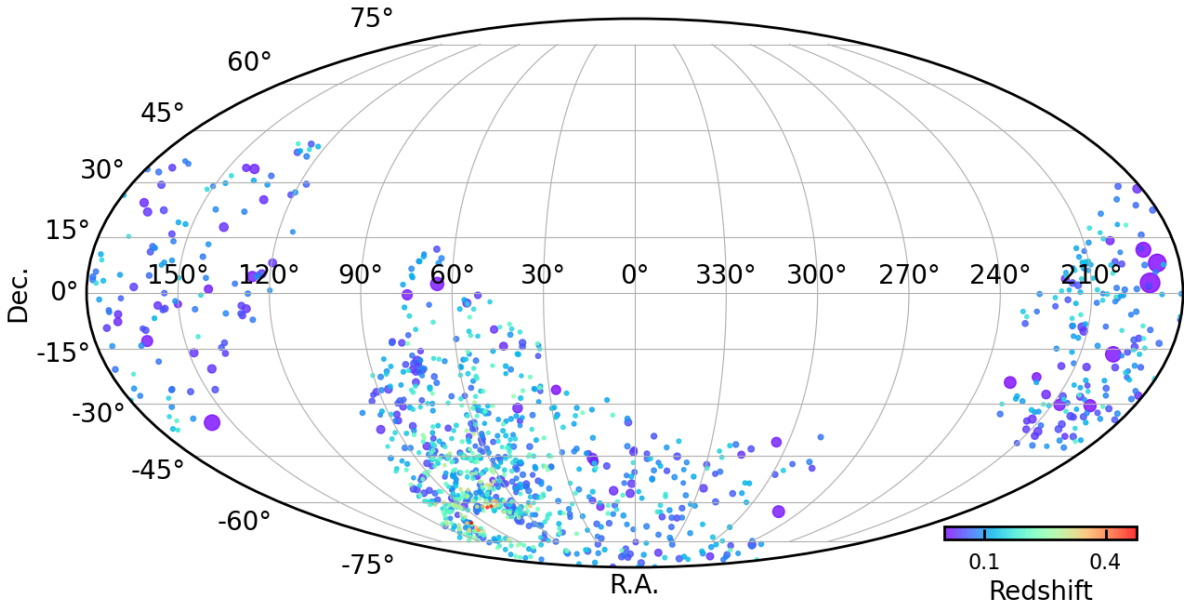
Figure 3.2: The projected locations of the 1178 galaxy groups in the primary catalog in the eROSITA and Legacy Survey DR9N and DR10 13,116 deg^2 common footprints are shown. The redshift confirmed by the follow-up algorithm `eROMaPPer` is color-coded (Kluge et al., 2024), while the sizes of the detections are scaled with the angular sizes (r_{500c}) of the groups (see Sect. 3.3.4 for the r_{500c} estimation procedure). The inhomogeneity of the source density in this figure is due to the exposure variation across the eROSITA-DE X-ray sky (see Fig. 2 in Bulbul et al., 2024).

selection function[4].

Following the cleaning procedure, we visually inspect the groups that are centrally peaked ($r_c < 32$ arcsec)[5] and have low extent likelihoods ($\mathcal{L}_{ext} < 10$) using the eRASS:4 and the Legacy Survey data. As a result of the visual inspection, we further flagged and removed 74 falsely classified point sources from our sample. These objects make a small fraction of our clean sample (6%); therefore, their removal has a negligible impact on the selection function, especially compared to the systematic uncertainties of X-ray simulations at group scales used to construct the selection function. The final sample, consisting of 1178 galaxy groups, has a median redshift of 0.11 and a median mass (M_{500c}) of 6.3×10^{13} M$_\odot$. The redshift and mass distributions of the final sample can be seen in the right panel of Fig. 3.1. Moreover, the 2D projected distribution of these groups in the eROSITA sky is shown in Fig. 3.2. We note that some of the "cleaning" procedures described above (e.g., the EXT and $\mathcal{L}_{ext}$ cuts) not only clean spurious sources but also unavoidably remove some of the faint real groups from the sample according to the expected

---

[4]The selection function, $P(I|O)$, can be seen as the ratio of the number of the detected "real" objects to the number of all the "real" objects within the infinitesimal observable parameter space of $(O, O + dO)$. Removal of confirmed spurious sources does not change this ratio and, therefore, has no impact on $P(I|O)$.

[5]See Eq. 3.1 for the definition of r_c and Sect. 3.3.3 for the details of the imaging analysis.

purity of the eRASS1 cluster sample in the cost of achieving a more secure groups sample. Nevertheless, the resulting extra selection is taken into account in our analysis by incorporating a selection function built for our final sample. After the cleaning procedure described above, our sample ended up having three objects with mass estimates slightly below the lower bound of our group mass definition (5×10^{12} $M_\odot <$ M $_{500c} < 10^{14}$ $M_\odot$). We eventually decided to keep them in our group sample since the removal of three objects has little to no impact on our final results, and their "true" masses may well be within our group mass definition due to the intrinsic scatter of the $L_X - M_{500c}$ relation.

The final galaxy group sample described above is obtained to construct a well-defined selection function using eROSITA's twin simulations. A good handle on selection effects is key for achieving universal conclusions about the properties and the governing physics of studies of groups. The deeper eRASS:4 observations of an unprecedented number of galaxy groups we use in this Chapter are particularly well-suited for studying the baryonic physics in galaxy groups because of the higher statistics allowed by the deeper survey data and large field-of-view necessary to measure the X-ray properties out to large radii. In the next section, we present our eRASS:4 analysis of the galaxy groups in the sample.

3.3 Data Analysis

3.3.1 X-ray Data Reduction and Analysis

Taking advantage of the higher signal-to-noise deeper survey observation, we use the eRASS:4 observations of the eRASS1 selected galaxy groups with the processing version 020 (briefly described in Appendix C of Merloni et al., 2024), that is an updated version of 010 processing used for the first data release (DR1). The main updates on the 020 version (internal catalog version 221031) are the improved boresight correction, low-energy detector noise suppression, improved subpixel resolution, and updated pattern and energy tasks. We further reduce the calibrate event files using the using the eROSITA Science Analysis Software System (eSASS, Brunner et al., 2022)[6] with the version id `eSASSusers_211214` that is the same version used for Bulbul et al. (2024) and Merloni et al. (2024) for DR1. Time variable (solar incident angle dependent) optical light contamination (light leak) is observed in the data from the telescope modules (TMs) 5 and 7, which has a large impact on the calibration of the low-energy band of the spectrum (see Predehl et al., 2021; Coutinho et al., 2022; Merloni et al., 2024, for further details). In this Chapter, we analyze the hot gas properties of galaxy groups whose emission peaks at the soft X-ray band that suffers from the contamination; therefore, we follow a conservative approach and only use the data from TMs 1, 2, 3, 4, and 6, removing the TM5 and 7, suffering from contamination from the optical light leak. Furthermore, we obtain a clean event list by applying the standard flag `0xE000F000` to select all the possible patterns (singles, doubles, triples, and quads) and run the `flaregti` eSASS task to have flare filtered good-time-intervals.

---

[6]https://erosita.mpe.mpg.de/dr1/eSASS4DR1/

3.3.2 Energy band selection for the imaging analysis

We choose the energy band for the imaging analysis by optimizing the signal-to-noise ratio given multiple X-ray foreground and background components. The models we used during this optimization scheme include: 1) a 0.1 keV unabsorbed APEC component for the Local Hot Bubble, whose flux is scaled to 2.3×10^{-13} erg s^{-1} cm^{-2} deg^{-2} in the 0.3–0.7 keV band (Yeung et al., 2023); 2) a 0.18 keV absorbed APEC component for the Galactic Halo, whose absorbed flux is scaled to 1.1×10^{-12} erg s^{-1} cm^{-2} deg^{-2} in the 0.5–2.0 keV band (Henley and Shelton, 2013); 3) a $\Gamma = 1.4$ power law component for the Cosmic X-ray Background component, whose absorbed flux is scaled to 6×10^{-13} erg s^{-1} cm^{-2} deg^{-2} in the 0.5–2.0 keV band, that corresponds to a 10^{-13} erg s^{-1} cm^{-2} point source flux cut; and 4) the instrumental background from eROSITA filter-wheel-closed observations. The foreground HI column density is fixed to 2.7×10^{20} cm^{-2}, which is the averaged value of the sample. With these foreground and background configuration, we find that the signal-to-noise ratio of a $T = 1$ keV APEC source component at the redshift of 0.18 reaches the maximum in the 0.3–1.8 keV band at a source-to-background ratio of 1. We note that the upper boundary of the optimal band could increase if we adopt a higher source-to-background ratio since the $\log N - \log S$ curve of the selected sample is a power low. Nevertheless, we select a source-to-background ratio of 1 and we adopt the 0.3–1.8 keV band for our imaging analysis to maintain high signal-to-noise for the faint sources.

3.3.3 Imaging analysis

For the imaging analysis, we use an energy band of 0.3–1.8 keV to maximize the signal-to-noise ratio (SNR) for a soft X-ray emitting source such as groups (see Sect. 3.3.2 for the details of this optimization scheme). We extract images, vignetted and non-vignetted exposure maps in this band centered around each group in the catalog using the `evtool` and `expmap` tasks in `eSASS` with a standard eROSITA pixel size of 4 arcsec and the `FLAREGTI` option. For the extraction region, we use an image size of $\sim 8r_{500c,\text{eSASS}} \times 8r_{500c,\text{eSASS}}$ that covers well the region from the source center beyond the Virial radius for the local background measurements. The radius, $r_{500c,\text{eSASS}}$, is estimated using the flux reported in column `ML_FLUX_1` of the eRASS1 X-ray catalog (Merloni et al., 2024) and an $L_\text{X} - M_{500c}$ relation of the eROSITA Depth Final Equatorial Survey (eFEDS) clusters and groups (Chiu et al., 2022). These estimates are only used to determine the image size and have a negligible impact on the results. After generating X-ray images and exposure maps, we use the eRASS:4 point source catalog in the 0.2–2.3 keV band to mask or co-fit the point sources in the field of view (FOV) in the rest of the imaging analysis. Following the same procedure in our eFEDS analysis (Chapter 2), we mask the faint point sources with `ML_RATE_1` < 0.1 cnts/s) out to the radii where their emission becomes consistent with the background. On the other hand, we co-fit bright point sources (`ML_RATE_1` > 0.1 cnts/s) in the surface brightness analysis. In addition to the bright point sources, we also model and co-fit the closest extended sources to the central galaxy group to clean the image from contaminating X-ray emission. The remaining ones in the field are conservatively masked out to their $2r_{500c,\text{eSASS}}$. Example eROSITA images of a bright nearby group (1eRASS J024933.9-311126) and a group at the median redshift of our group sample (1eRASS J045547.0-572404) are shown in Fig. 3.3.
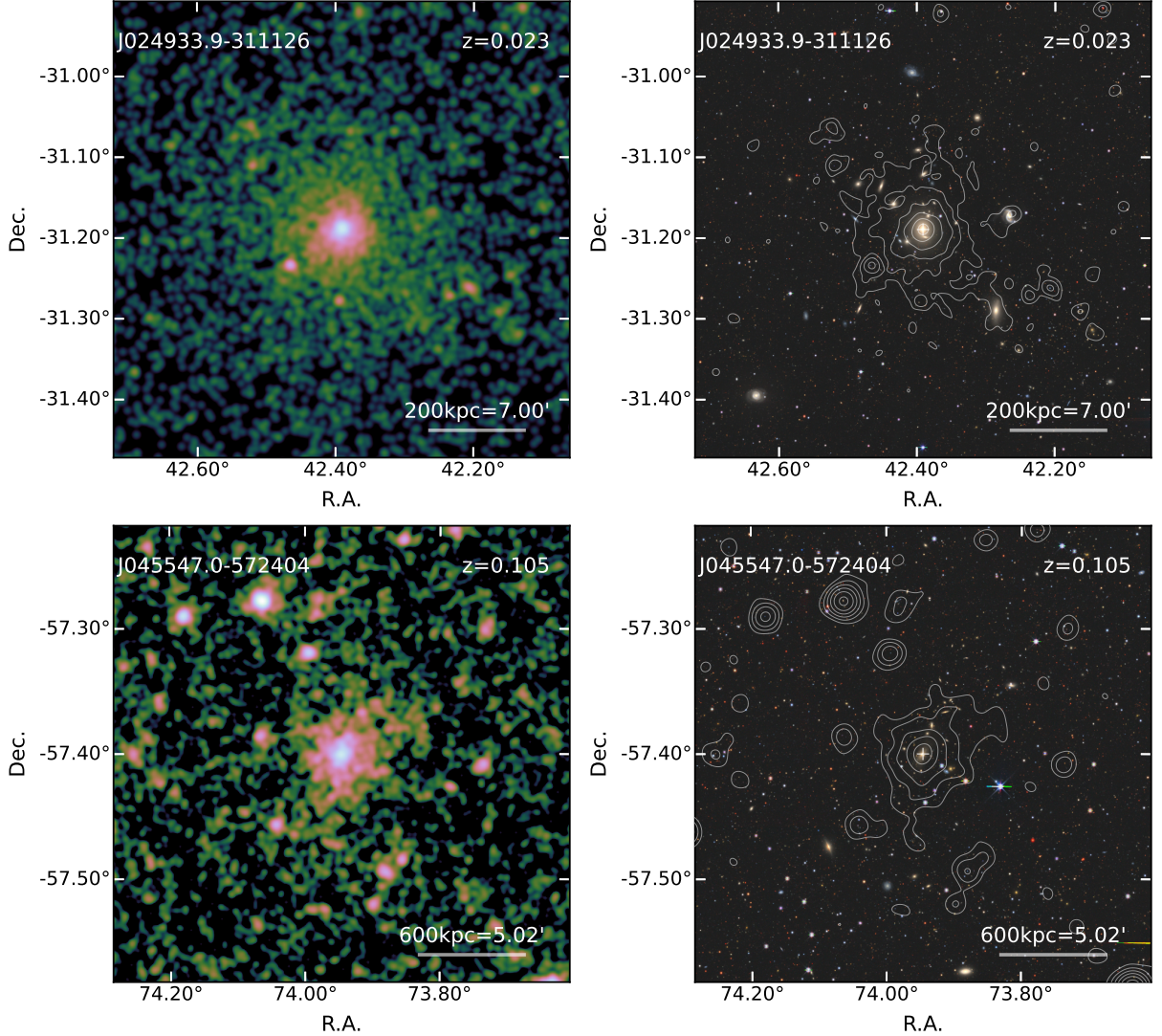
Figure 3.3: *Left:* eRASS:4 soft band 0.3–1.8 keV images of two bright groups (1eRASS J024933.9-311126 and 1eRASS J045547.0-572404) at redshifts 0.023 and 0.105. *Right:* The Legacy Survey DR10 images of the same groups with the eRASS:4 X-ray contours overlayed.

Following a forward modeling approach, we fit the X-ray images using a Bayesian fitting pipeline to deproject the surface brightness emission. We assume a Poisson likelihood for the X-ray counts and sample the likelihood using the `emcee` package (Foreman-Mackey et al., 2013) that employs the Goodman and Weare (2010) Affine Invariant Markov chain Monte Carlo (MCMC) technique. The fit is performed to account for the cross-talk between the emission from the nearby co-fitted extended and point sources. For extended sources, we model emissivity using a modified Vikhlinin et al. (2006) profile:

$$\Lambda_{\rm ep}(T,Z)\, n_{\rm e}^2(r) = N_{\Lambda,n_{\rm e}^2} \left(\frac{r}{r_c}\right)^{-\alpha} \left(1 + \left(\frac{r}{r_c}\right)^2\right)^{-3\beta+\alpha/2} \left(1 + \left(\frac{r}{r_s}\right)^3\right)^{-\epsilon/3}, \tag{3.1}$$

where $\Lambda_{\rm ep}(T,Z)$ is the band-averaged cooling function, Z is the metallicity, and $N_{\Lambda,n_{\rm e}^2}$, r_c, r_s, α, β, ϵ are the free parameters of the emissivity profile, normalization, core radius, scale radius, and the power law exponents, respectively. These parameters are allowed to vary in the fits. At each MCMC step, the profile is projected along the line of sight following the equation:

$$S_X = \frac{1}{4\pi(1+z)^4} \int n_{\rm e} n_{\rm p} \Lambda_{\rm ep}(T,Z) {\rm d}l, \tag{3.2}$$

where the number density of protons ($n_{\rm p}$) are related to the number density of electrons ($n_{\rm e}$) via $n_{\rm p} = n_{\rm e}/1.2$ (Bulbul et al., 2010). Then, the projected count rate is convolved with the eROSITA point spread function (PSF), multiplied with the exposure map, and compared with the masked X-ray image. In addition to the electron density profile parameters, two additional parameters are left free for the central position of the groups, which adds up to eight free parameters for every extended source modeled in the image. For the bright point sources, we only allow the normalization of their profile to vary while keeping the centroids fixed due to the high positional accuracy of eROSITA (Brunner et al., 2022; Merloni et al., 2024). Lastly, for each image, the background count rates are assumed to be constant across the image, and two more parameters are allowed to be free for the vignetted and unvignetted backgrounds.

As an output of this fitting procedure, we obtain the best-fit de-projected emissivity profiles ($\Lambda_{\rm ep}(T,Z)\, n_{\rm e}^2(r)$), count-rate profiles, and the associated uncertainties that include the cross-talk between the co-fitted nearby extended and point sources. We show the performance of our pipeline in Fig. 3.4 for a bright group (1eRASS J045547.0-572404, the second group in Fig. 3.3) with the images before and after subtracting the emission from the modeled extended and point sources on the left. It is clear from the bottom left figure that after the removal of the modeled profiles, the image is free from any X-ray source, and only noise remains. The surface brightness profile of the observed field (in blue) and the best-fit model (in red) are shown on the right panel of the same figure. The PSF convolved best-fit surface brightness model represents the eROSITA data well. The peaked emission at large radii (at 500 and 1000 arcsec) shows the contribution of the modeled point sources to the overall emission, which are successfully modeled and removed from the total source model.

Given the PSF of eROSITA being relatively large, we also ran tests on the robustness of our fitting procedure around the core region ($0.15r_{500c}$) of groups by simulating and fitting synthetic galaxy group observations. The synthetic observations are obtained by first generating galaxy group profiles in a non-parametric way employing a covariance matrix obtained from XXL observations following Comparat et al. (2020)[7]. These profiles are then convolved with the eROSITA PSF, and the X-ray observations are obtained by creating the poison realizations of the PSF convolved surface brightness distributions. Through this procedure, we have fitted 30 simulated groups at a redshift of $z = 0.11$ (the median redshift of our sample) and 30 groups at

---

[7]The covariance matrix used to synthesize galaxy group profiles is publically available in `https://github.com/domeckert/cluster-brightness-profiles`
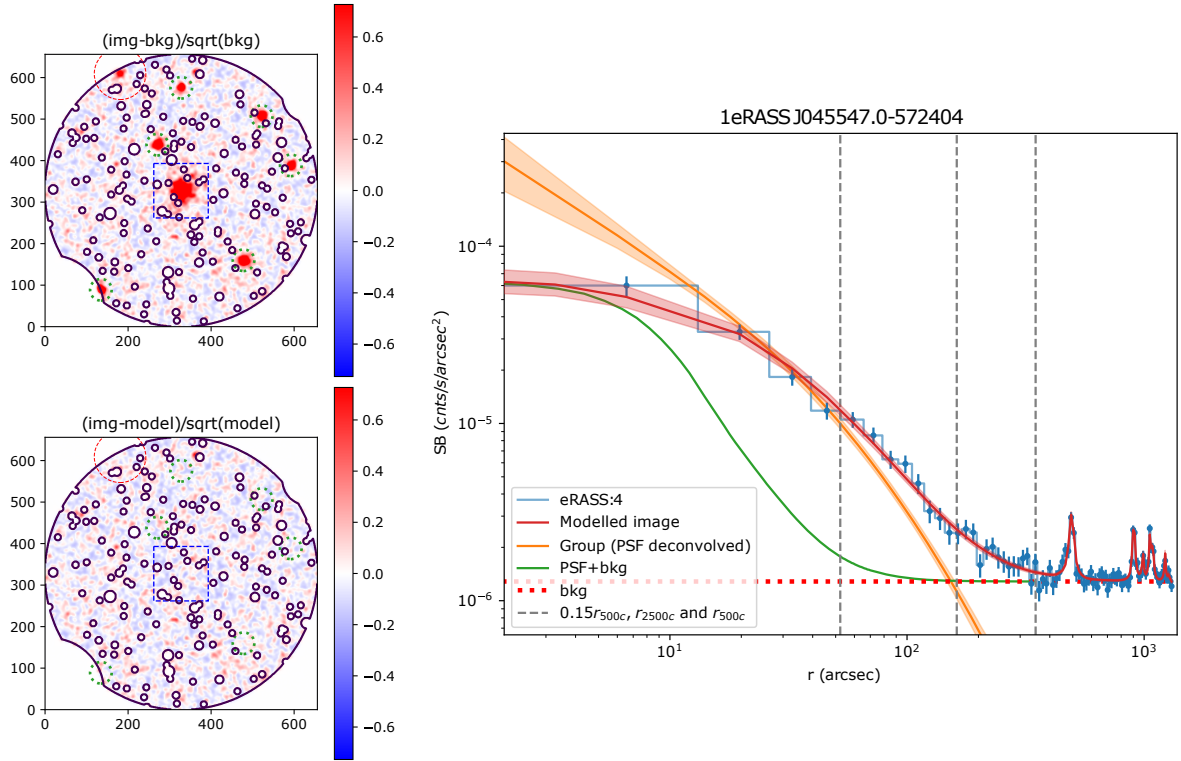
Figure 3.4: An example of the eROSITA imaging analysis for the group 1eRASS J045547.0-572404. *Left:* The residual image of the group before and after subtracting the co-fit extended sources and point sources in the field. Nearby co-fit clusters and groups are shown with red circles, co-fit nearby bright AGN are shown with green circles, and the fitted galaxy group is shown with a blue rectangle. The smooth noise level indicates that the contaminant emission is modeled properly in the analysis. *Right:* Surface brightness profile of the same group. The observed surface brightness profile of the image is plotted in blue, the best-fit model of the image is plotted in red, the PSF profile over the measured background is plotted in green, the PSF deconvolved surface brightness profile of the galaxy group is plotted in orange, the measured background level is shown with a horizontal dashed red line, and three characteristic radii of the group ($0.15r_{500c}$, r_{2500c} and r_{500c} from the core to the outskirt respectively) are shown with dashed grey lines.

a redshift of $z = 0.2$ (85% of the groups in our sample are at $z < 0.2$). As a result of these tests, we found that our fitting procedure is capable of robustly deconvolving the profiles with PSF and recovering the input surface brightness profiles around $0.15r_{500c}$. We also found that because of the PSF smoothing, the recovered profiles of the objects with intrinsically larger surface brightness fluctuations may deviate more from the input simulated profiles; however, at the sample level, these fluctuations cancel out such that our measurements, on average, are unbiased. Furthermore, we have also investigated the possible impact of an undetected central compact source on the surface brightness measurements of the groups in our sample at $0.15r_{500c}$ by comparing the fitted surface brightness profiles of groups with the PSF profile. From this investigation, we find that an undetected point source at the center of a group can only change $n_e(0.15r_{500c})$ a few percent, which is within the total error budget of our n_e measurements that includes statistical and systematic uncertainties (see Sect. 3.4 for details on the systematic uncertainties taken into account in this study). Therefore, we conclude that the galaxy groups we use in this Chapter are well extended in the sky such that an undetected point source at the center of the group has little to no impact on the electron density measurements at $0.15r_{500c}$.

3.3.4 Estimation of X-ray Observables

The shallow nature of the eROSITA survey only allows the measurement of the physical properties of a few nearby bright galaxy groups. The eRASS1 group sample should be binned into smaller samples to achieve sufficient signal-to-noise for reliably constraining the physical properties of the faint galaxy groups through joint spectral analysis (see Sect. 3.3.5). For an optimal binning scheme, a low-scatter temperature estimator should be used such that groups with similar temperatures can be binned together. Moreover, mass estimates of the galaxy groups are needed to extract spectra within a physically motivated scale radii (r_{500c}). For these purposes, we use $L_X - M_{500c}$ and $L_X - T$ scaling relations and calculate the soft-band ($0.5 - 2$ keV) X-ray luminosity (L_X), temperature (T), and mass (M_{500c}) estimates of the galaxy clusters and groups from the count-rate profiles measured in Sect. 3.3.3. For a self-consistent treatment of the eROSITA groups, we employ the $L_X - M_{500c}$ and $L_X - T$ relations calibrated using the eFEDS observations (Chiu et al., 2022; Bahar et al., 2022).

The selection effects and the mass function need to be accounted for to obtain unbiased estimations of the physical properties of an underlying population from intrinsically scattered scaling relations. For this purpose, we built a Bayesian framework that simultaneously estimates the L_X and T, M_{500c} observables from the observed count-rate profiles, $\hat{C}_R(r)$ (see Sect. 3.3.3 for the details of the count-rate profile measurement procedure). The formulation of the Bayesian estimation framework is as follows. To simultaneously estimate L_X, T and M_{500c} observables, the joint probability density function, $P(L_X, T, M_{500c}|D, \theta_{all})$, given the data, D, and a set of model parameters, θ_{all} is needed to be computed. This can be expanded as:

$$P(L_X, T, M_{500c}|D, \theta_{all}) \equiv P(L_X, T, M_{500c}|\hat{C}_{R,500c}, I, z, \mathcal{H}, \theta_{LT}, \theta_{LM}) \tag{3.3}$$

where the count-rate within r_{500c} ($\hat{C}_{R,500c}$), detection information of the galaxy group (I), redshift (z), and sky position ($\mathcal{H}$), represent the data (D); and the scaling relations parameters (θ_{LT} and

θ_{LM}) represent the model parameters (θ_{all}). We note that by definition, the $\hat{C}_{R,500c}$ term has an intrinsic dependence on M_{500c} such that $\hat{C}_{R,500c}$ is different for every M_{500c} in the $L_{\mathrm{X}} - T - M_{500c}$ parameter space. Taking this into account, our framework allows the information of the measured count-rate profiles to be included in our analysis rather than count-rate measurements within fixed radii.

Using the Bayes rule, Eq. 3.3 can be rewritten as

$$P(L_{\mathrm{X}}, T, M_{500c} | \hat{C}_{R,500c}, I, z, \mathcal{H}, \theta_{\mathrm{LT}}, \theta_{\mathrm{LM}}) =$$
$$\frac{P(L_{\mathrm{X}}, T, M_{500c}, \hat{C}_{R,500c}, I | z, \mathcal{H}, \theta_{\mathrm{LT}}, \theta_{\mathrm{LM}})}{\int \int \int P(L_{\mathrm{X}}, T, M_{500c}, \hat{C}_{R,500c}, I | z, \mathcal{H}, \theta_{\mathrm{LT}}, \theta_{\mathrm{LM}}) dL_{\mathrm{X}} dT dM_{500c}}. \tag{3.4}$$

Furthermore, one can expand the common term in the numerator and the denominator as

$$P(L_{\mathrm{X}}, T, M_{500c}, \hat{C}_{R,500c}, I | z, \mathcal{H}, \theta_{\mathrm{LT}}, \theta_{\mathrm{LM}}) \approx$$
$$P(\hat{C}_{R,500c} | L_{\mathrm{X}}, T, M_{500c}, z) P(I | L_{\mathrm{X}}, z, \mathcal{H}) \tag{3.5}$$
$$\times P(L_{\mathrm{X}}, T | M_{500c}, z, \theta_{\mathrm{LT}}, \theta_{\mathrm{LM}}) P(M_{500c} | z)$$

where the first term, $P(\hat{C}_{R,500c} | L_{\mathrm{X}}, T, M_{500c}, z)$, represents for the measurement uncertainty of the count-rate. The conditional probability distribution for this term is obtained by first calculating the true count rate ($C_{R,500c}$) for every point in the $L_{\mathrm{X}} - T$ parameter space by assuming the source emitting an unabsorbed APEC (Smith et al., 2001) spectrum in Xspec (Arnaud, 1996) at a redshift z with an abundance of $0.3Z_{\odot}$, a temperature of T and a luminosity of L_{X}. Then the true count-rates ($C_{R,500c}$) are compared with the observed count-rates calculated ($\hat{C}_{R,500c}$) at every r_{500c} value in the mass parameter space (M_{500c}) and the value of the conditional probability is obtained. The $P(I | L_{\mathrm{X}}, z, \mathcal{H})$ term in Eq. 3.5 is the selection function term that is a function of soft-band X-ray luminosity, redshift, and sky position where the sky position includes the local background surface brightness, exposure, and the neutral hydrogen column density information.

The selection function is obtained by simulating the eROSITA X-ray All-Sky observations using the baryon painting method (Comparat et al., 2019, 2020) and applying the same routines of the eSASS source detection pipeline to construct one-to-one correspondence of the catalogs and selection (Seppi et al., 2022; Clerc et al., 2024). The $P(M_{500c} | z)$ term is the mass function term for which the analytical formulation of Tinker et al. (2008) is used. Lastly, the $P(L_{\mathrm{X}}, T | M_{500c}, z, \theta_{\mathrm{LT}}, \theta_{\mathrm{LM}})$ term is the intrinsically scattered scaling relation term that gives the L_{X} and T distributions at a given mass and redshift.

Ideally, one would use a jointly fit, intrinsically scattered $L_{\mathrm{X}} - T - M_{500c}$ scaling relation for the $P(L_{\mathrm{X}}, T | M_{500c}, z, \theta_{\mathrm{LT}}, \theta_{\mathrm{LM}})$, however, there is no such relation in the literature yet that is calibrated by taking into account the selection effects and covers a similar mass range as eROSITA. For this reason, we expand this term as

$$P(L_{\mathrm{X}}, T | M_{500c}, z, \theta_{\mathrm{LT}}, \theta_{\mathrm{LM}}) \approx P(T | L_{\mathrm{X}}, z, \theta_{\mathrm{LT}}) P(L_{\mathrm{X}} | M_{500c}, z, \theta_{\mathrm{LM}}) \tag{3.6}$$

and use the best-fit $L_{\mathrm{X}} - T$ relation presented in Chapter 2 and the $L_{\mathrm{X}} - M_{500c}$ relation presented in Chiu et al. (2022) that are calibrated for eROSITA by taking into account the selection effects. The $P(T | L_{\mathrm{X}}, z, \theta_{\mathrm{LT}})$ term is obtained from $P(L_{\mathrm{X}} | T, z, \theta_{\mathrm{LT}})$ using Bayes theorem
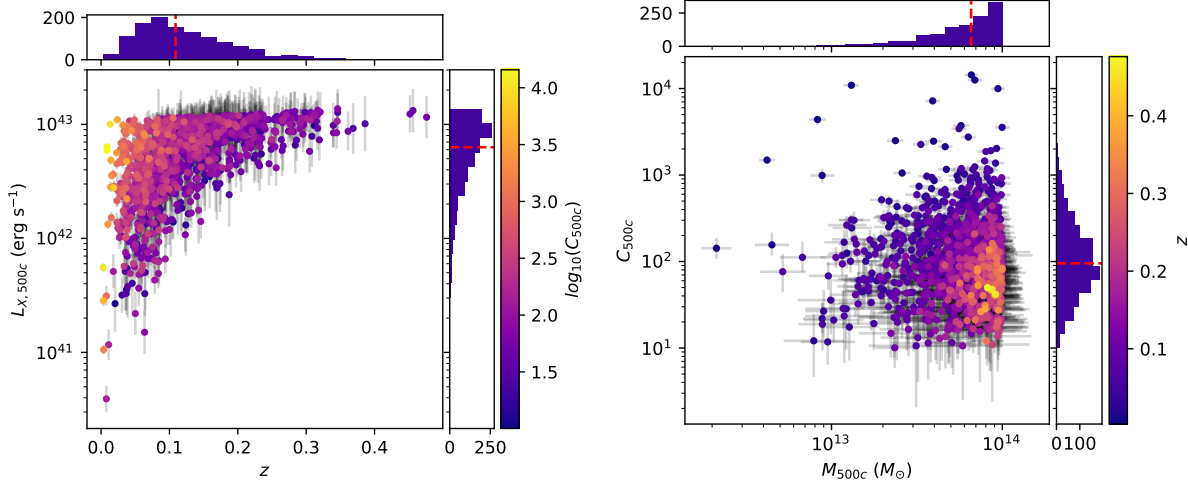
Figure 3.5: *Left:* The soft-band (0.5–2 keV) X-ray luminosity ($L_{X,500c}$) and redshift (z) distributions of the final galaxy group sample used in this Chapter consisting of 1178 objects. Luminosity of the groups cover a range of $3.9 \times 10^{40} - 1.4 \times 10^{43}$ ergs s^{-1} and the redshift span of the sample is $0.003 - 0.48$. *Right:* Count (C_{500c}) and mass (M_{500c}) distributions of the 1178 galaxy groups used in this Chapter. Measured counts of galaxy groups range between $10 - 14380$ and their masses span a range of $2.1 \times 10^{12} - 10^{14}$ $M_\odot$. Median values of the $L_{X,500c}$, z, C_{500c} and M_{500c} observables are 6.3×10^{42} ergs s^{-1}, 0.11, 95, 6.5×10^{13} $M_\odot$ respectively.

$$P(T|L_X, z, \theta_{LT}) = \frac{P(L_X|T, z, \theta_{LT})P(T|z)}{\int P(L_X|T, z, \theta_{LT})P(T|z)dL_X}. \tag{3.7}$$

where self-consistently, the same temperature function is used for the $P(T|z)$ term as in Eq. 2.6 of Chapter 2.

As a final step, we substitute the terms in Eq. 3.5 to Eq. 3.4 and calculate the joint probability density function, $P(L_X, T, M_{500c}|\hat{C}_{R,500c}, I, z, \mathcal{H}, \theta_{LT}, \theta_{LM})$, for each galaxy group. Subsequently, we marginalize over the nuisance parameters and obtain L_X, T, and M_{500c} estimates given the data and the scaling relations parameters[8]. We provide the distributions of mass, temperature, soft-band ($0.5 - 2$ keV) X-ray luminosity estimates obtained through this Bayesian framework along with the distributions of redshift and count ($0.3 - 1.8$ keV) of the final galaxy group sample in Figs. 3.1, 3.5 and 3.6.

The estimated M_{500c} are then converted to r_{500c} and r_{2500c} by assuming an average dark matter concentration of $c_{500c} = r_{500c}/r_{s,NFW} = 4.2$[9] and scaling the r_{500c} estimates accordingly (S09). These characteristic radii are employed to determine the spectral extraction region ($r < r_{500c}$) and serve as characteristic radii ($0.15r_{500c}$, r_{2500c}, r_{500c}) for the entropy measurements.

---

[8]For example, the marginal probability distribution of temperature is calculated as $P(T|\ldots) = \iint P(L_X, T, M_{500c}|\ldots)dL_X dM_{500c}$ and the temperature corresponding to the 50th percentile of the marginal probability distribution is used as the point estimate.

[9]$r_{s,NFW}$ is the characteristic radius of the Navarro–Frenk–White (NFW) profile and a concentration (c_{500c}) of 4.2 corresponds to a r_{2500c}/r_{500c} ratio of 0.465.

The net effect of accounting for selection effects and the mass function when estimating L_X, T, and M_{500c} from scaling relations depends on two factors: the scatter in the scaling relations and the interplay between the selection and mass functions. With zero scatter, there's a one-to-one relationship between observables, allowing straightforward conversions. As the scatter of the relation increases, the scaling relation estimates that ignore the selection effects will be more vulnerable to being biased. Furthermore, the net effect also depends on the shapes of the selection and mass functions. The interplay between the selection function and the mass function across the $L_X - T - M_{500c}$ parameter space is often not trivial, however, to the first order, if we consider X-ray selection as a redshift dependent L_X cut, T and M_{500c} to be overestimated would be overestimated if the selection and mass functions are not accounted for.

3.3.5 Grouping and the Spectral Analysis

Measuring temperature through X-ray spectroscopy requires considerably more photons than measuring surface brightness properties with imaging analysis. Given the shallow nature of the eROSITA All-Sky Survey, the photon counts of most of the galaxy groups in our sample are insufficient for temperature measurements, even though the flux or luminosity of these objects can be reliably measured from X-ray images. For instance, more than half of the groups in the sample, shown on the right panel of Fig. 3.5, have less than 100 counts within the $0.3 - 1.8$ keV band, which is not sufficient for measuring their temperature reliably.

The two canonical ways to overcome the problem of insufficient photon counts for spectral analysis are co-fitting or stacking. A plethora of examples of both techniques exist in the literature. For example, McDonald et al. (2014) co-fit radially extracted spectra of 80 South Pole Telescope (SPT) selected massive clusters, while Bulbul et al. (2014) and Zhang et al. (2024) stacked megaseconds of *XMM-Newton* and eROSITA spectra respectively to achieve a high signal-to-noise level and reveal faint spectral features. In the work presented in this Chapter, we employ the co-fitting technique to maintain the spectral information of individual groups that would be averaged out when stacked. This method is the most suitable for the primary goal of our work. Compared to stacking, this approach is computationally expensive; however, with the recently developed high-performance Central Processing Units (CPUs) and the improvements in parallel computing, we are able to employ the co-fitting technique in our work.

We group the sample such that the IGrM temperatures of the galaxy groups are similar in each bin. Moreover, we require the statistical constraining power (photon counts) of the groups in the same bin to be similar to each other to avoid the source with the highest count biasing the measurements. In other words, we aim to minimize the temperature and photon count variation ($\Delta T_{500c} \sim std(T_{500c})$[10] and $\Delta C_{500c} \sim std(C_{500c})$) in each bin while trying to achieve a sufficient signal-to-noise ratio. To achieve this, we group the sample using the Voronoi binning technique (Cappellari and Copin, 2003). To apply the tessellation technique, we pixelate our temperature proxy $T_{500c,sc}$ (surface brightness inferred temperature estimate; see Sect. 3.3.4 for the details) and count measurements C_{500c} such that each pixel occupied by only one galaxy group. The axes are then re-scaled, and the resulting image is given to the `Vorbin` package, the Python

---

[10]The notation $std(X)$ represents standard deviation of X.
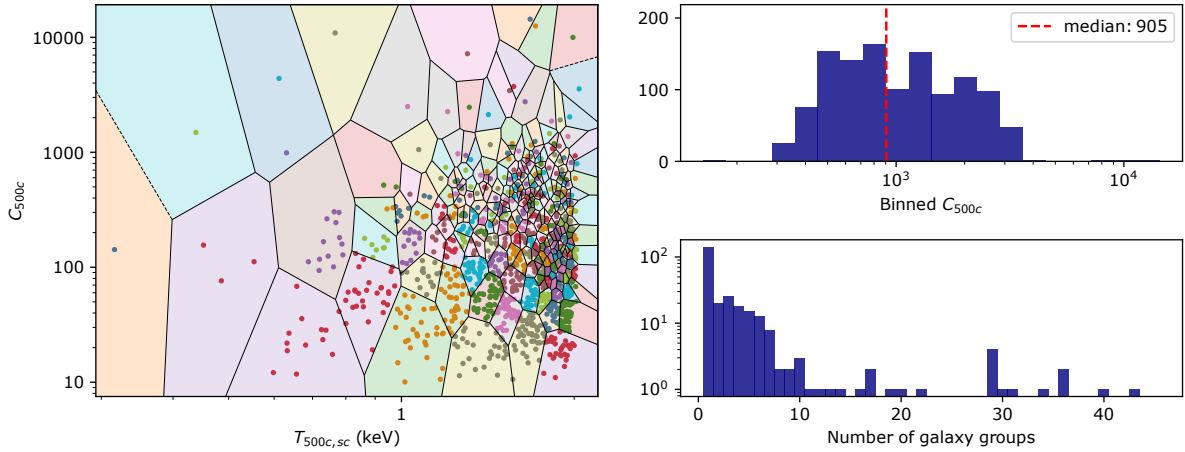
Figure 3.6: *Left:* The Voronoi binning scheme used for grouping the sample obtained from the distribution of count (within r_{500c}) measurements (C_{500c}) and scaling relation based temperature estimates ($T_{500c,sc}$). *Top right:* The histogram of total counts in 271 Voronoi bins with a median of 905 counts. *Bottom right:* The histogram of galaxy groups in Voronoi bins.

implementation of the Voronoi binning technique. The free parameters, namely, the axes scaling factors and the target SNR, are fine-tuned until the temperature variation (ΔT_{500c}) and the photon count variation (ΔC_{500c}) in the Voronoi bins are sufficiently small. The final binning scheme, shown in Fig. 3.6, is achieved using an SNR target, $S/N = 22.36$ (equivalent to 500 counts). We further present the distributions of the total counts and the number of galaxy groups in the Voronoi bins in Fig. 3.6. Using this binning scheme, we obtained 271 bins with a median count of 905, sufficient for obtaining reliable spectroscopic temperature measurements at $T < 2$ keV for each bin. We note that the binning scheme can be slightly different if a different target SNR or axis scaling factors are chosen; however, the impact of the chosen binning scheme is negligible on the final results as long as the resulting ΔT_{500c} and ΔC_{500c} are similar.

After the grouping, the source and local background spectra of the galaxy groups in our sample are extracted using the eSASS task `srctool`. The source spectra are extracted from the circular regions centered around the galaxy group and have a radius of r_{500c} (see Sect. 3.3.4 for the details of the M_{500c}/r_{500c} estimation procedure). Similarly, the local background spectra are extracted from annuli that are centered around the galaxy group and have a radial range of $4r_{500c} < r < 6r_{500c}$. The best-fit count-rate profiles are used to determine the masking radius of the bright point sources and nearby extended objects co-fitted during the imaging analysis. The remaining point sources and nearby extended sources within the extraction region are masked as described in Sect. 3.3.3.

We extract ancillary response files (ARFs) and redistribution matrix files (RMFs) using the `srctool` task for the background and the source region in different settings to be assigned to various components of the source and background models. The ARF assigned to the source component is extracted with the `exttype=BETA` and `psftype=2D_PSF` settings to consider the

energy-dependent PSF and vignetting corrections. Over the extraction regions, the flux distribution of the vignetted X-ray background is assumed to be flat, and the `exttype=TOPHAT` and `psftype=NONE` settings are used for extracting the ARFs assigned to the vignetted X-ray background components of the source and background regions.

Similar to our eFEDS analysis (Chapter 2), the local background model consists of two major components: particle-induced instrumental background (see Bulbul et al., 2020; Freyberg et al., 2020, for further details) and X-ray background including the Galactic foreground, and unresolved point sources in the sky. The total model includes a spectral model component with an absorbed thermal component. The spectral analysis is performed using `PyXspec`, the Python interface of the standard X-ray spectral analysis package `Xspec` (version 12.12.1, Arnaud, 1996), that employs the `AtomDB` atomic database (version 3.0.9, Foster et al., 2012). The `Xspec` model of the X-ray foreground consists of an unabsorbed APEC (Smith et al., 2001) for the local hot bubble (Yeung et al., 2023, $T \sim 0.084$ keV), two absorbed APECs for the hot and cold components of the galactic halo (Ponti et al., 2023; Bulbul et al., 2012, $T \sim 0.49$ and 0.157 keV respectively). To model the cosmic X-ray background, we use an absorbed power-law for the unresolved AGN (Cappelluti et al., 2017, $\Gamma = 1.45$). For the shape of the instrumental background, we use the best-fitting model of Yeung et al. (2023) obtained by calibrating the filter wheel closed (FWC) data (see Appendix A.1. and A.2. of Yeung et al., 2023, for the details of the modeling of FWC data). This instrumental background component is folded with unvignetted ARF (Freyberg et al., 2020), while the cosmic X-ray background and Galactic foreground are folded with the respective vignetted ARF in the fits.

To account for the X-ray absorption, we use the TBABS (Wilms et al., 2000b) interstellar medium (ISM) absorption model in `Xspec` (Arnaud, 1996). We use the HI4PI survey (HI4PI Collaboration et al., 2016) for calculations of the hydrogen column density (n_H). The n_H values at the positions of eRASS1 galaxy groups are relatively low because of their locations at higher Galactic latitudes; therefore, using the total hydrogen column density ($n_{H,tot}$) rather than the neutral hydrogen column density ($n_{H,I}$) has a negligible impact on our results at the sample level[11] as also noted in Bulbul et al. (2024). We use the solar abundances of Asplund et al. (2009) when measuring the metallicity of the groups. We use C-statistic (Cash, 1979) for the statistical interpretation of our spectra, which provides unbiased estimates of the model parameters at the low and high count regimes (Kaastra, 2017). We employ the co-fitting technique for the spectral analysis. This requires us to explore likelihoods with relatively high dimensional parameter space. For this purpose, we have chosen to employ the MCMC fitting technique. `Xspec` has a built-in MCMC sampler; however, the control it allows the user over the priors is limited. For this reason, we employ the widely used MCMC sampler `emcee` (Foreman-Mackey et al., 2013) rather than the built-in `Xspec` sampler to explore high dimensional likelihoods. We achieved this by developing an interface that allows the cross-talk between `PyXspec` and `emcee` and updates the model parameters at every MCMC step accordingly.

Galaxy groups are low-mass objects with relatively low plasma temperatures ($T < 2$ keV) due

---

[11]To confirm this statement, we ran tests to quantify the impact of using $n_{H,tot}$ (Willingale et al., 2013b) instead of $n_{H,I}$ (HI4PI Collaboration et al., 2016) on the sample averaged quantities presented in Sect. 2.4, $S(r)$ and $T(r < r_{500c})$. The tests showed that the choice has overall a negligible impact ($< 3\%$) compared to the systematic error budget of the average quantities (see Sect. 3.4).

to their shallower potential wells. They share this low-temperature parameter space with other background/foreground components, such as the cold ($T \sim 0.157$ keV) and hot ($T \sim 0.49$ keV) components of the galactic halo (Ponti et al., 2023). This results in degeneracies between the source and background/foreground components at the low count regime. At a given energy band, it is relatively easy to separate the source and background components using the 2D distribution of photons through imaging analysis since we expect the local background rate to be relatively flat, whereas the source emission roughly follows a projected Vikhlinin profile (Vikhlinin et al., 2006). In our work, we make use of this fact and combine the spatial and spectral information of photons following a novel approach with the aim of lifting the aforementioned degeneracies as best we can. We achieve this by using the observed count-rates ($0.3 - 1.8$ keV) measured through imaging analysis as priors in the spectral analysis in our pipeline that combines `PyXspec` and `emcee`.

To obtain the average temperatures of the binned galaxy groups (see the first paragraph of this section for the details of the grouping), we only link the temperature parameter of the (APEC) model and co-fit all the source and background spectra of the galaxy groups in each Voronoi bin. In total, $2 \times N_{i,\mathrm{gr}}$ spectra are co-fit (one spectrum for the source region and one for the background region) where $N_{i,\mathrm{gr}}$ is the number of galaxy groups in the i'th Voronoi bin. During the fitting, the temperatures, the normalizations of the X-ray background components, and the normalizations of the unvignetted particle background components are allowed to be free with flat priors in the logarithmic parameter space.

Many studies in the literature show strong degeneracy between the temperature and metallicity measurements for galaxy clusters and groups hosting multi-phase gas. This manifests as the so-called 'Fe bias' (Buote and Fabian, 1998; Buote, 2000; Gastaldello et al., 2021; Mernier et al., 2022) where temperature and abundance measurements change depending on the number of gas components fitted. In our work, we take this effect into account by allowing the metallicities of each galaxy group to be free with a Gaussian prior centered around 0.3 $Z_{\odot}$ with a standard deviation of 0.025 while measuring average temperatures. The normalization of the source emission of each galaxy group and the co-fit temperature are left free with log-uniform priors. Consequently, following the spectral co-fitting analysis procedure described above, we obtained 271 average temperature measurements within r_{500c} for each Voronoi bin shown in Fig. 3.6.

3.3.6 Electron Density, Temperature, and Entropy Profiles

From the imaging analysis described in Sec.3.3.3, we obtain deprojected emissivity profiles of all the 1178 galaxy groups. The spectral analysis, described in Sec.3.3.5, yields average temperature measurements of the 271 galaxy group bin within r_{500c}. The electron number density profile measurements of the IGrM have a non-negligible dependence on the assumptions on the temperature and metallicity profiles. Furthermore, temperature profiles of the galaxy groups are needed for obtaining entropy profiles. For most binned groups, only a single average temperature and metallicity measurement can be achieved within r_{500c} due to low SNR eROSITA data. We overcome this limitation and incorporate the impact of temperature variation on the thermodynamic properties as a function of radius, as described below.

To account for the radial temperature variation, we first determine the average shape of the
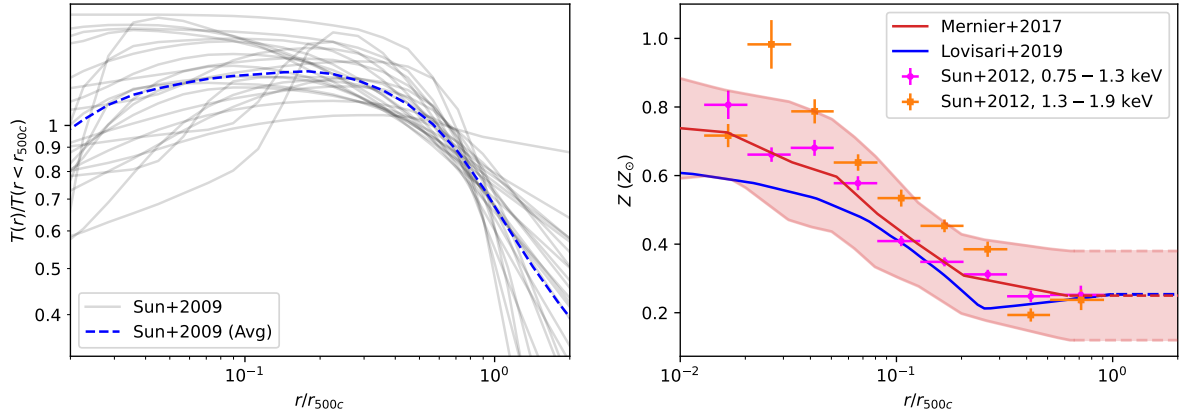
Figure 3.7: *Left:* Normalized temperature profiles, $T(r)/T(r < r_{500c})$, of 23 groups (gray) presented in S09 and their average (blue). The blue dashed line provides an average conversion ratio between the temperature profile, $T(r)$, and the characteristic temperature measurements, $T(r < r_{500c})$. *Right:* Average metalicity profiles of galaxy groups reported by Mernier et al. (2017), Lovisari et al. (2015) and the stacked metallicity profiles of Sun (2012) for galaxy groups in two temperature bins ($T = 0.75 - 1.3$ keV and $0.75 - 1.3$ keV).

3D temperature profile of groups ($T(r)/T(r < r_{500c})$) using the temperature profile measurements of the tier 1 and 2 groups presented in S09 (see Sect. 3.4.1 for the details). The average and individual shapes of the $T(r)/T(r < r_{500c})$ profiles are shown in the left panel of Fig. 3.7. We then rescale the average shape with the integrated temperature measurements and obtain the average temperature profiles for each binned group. The temperature profile measurements presented in S09 for a sample of 43 groups are obtained by analyzing deep *Chandra* observations; therefore, the overall shape of the profiles is relatively well-constrained. Following this procedure, we obtain the average temperature profiles of the 271 galaxy group bins. We note that our approach of obtaining temperature profiles of groups is equivalent to fixing the shape of an assumed temperature profile and fitting spectra by allowing the normalization of the profile to be free. We further note that the observed temperature measurement discrepancy between telescopes (e.g., Liu et al., 2023) does not affect our work given that the temperature measurements of eROSITA for galaxy groups agree very well with the *Chandra* and *XMM-Newton* temperatures (Migkas et al., 2024).

For the metallicity profile, we consider the following studies in the literature that have reasonably large galaxy group samples: Sun (2012), Mernier et al. (2017), and Lovisari and Reiprich (2019). We find that their measurements agree relatively well within the scatter of the metallicity profile reported in Mernier et al. (2017) (see right panel in Fig. 3.7). For this reason, we adopt the median Mernier et al. (2017) metallicity profile (Z_{M17}) for our measurements and consider the scatter of their profile as our systematic uncertainty. We quantify the impact of this uncertainty on the thermodynamic profile measurements ($n_e(r)$ and $S(r)$) and consider the resulting difference as part of the overall error budget (see Sect. 3.4.1 for the details of the assumed metallicity profile and quantification of the impact of this choice).

We then calculate the electron density profiles from our deprojected emissivity measurements

by constructing `APEC` models in `Xspec` (similarly done in Liu et al., 2022a) having the temperatures equal to the temperature profiles of the binned groups and the metallicities equal to the assumed metallicity profile at all radii out to $2r_{500c}$. During the n_{e} profile calculation, in addition to the errors of the imaging analysis, the uncertainties of the average metallicity and temperature measurements are propagated as well using the MCMC chains of the spectral analysis, taking into account the covariances. Then, the electron density profiles of the objects within each Voronoi bin are averaged to get the average electron density profiles of the binned groups.

Lastly, the entropy profiles of the binned groups are obtained by combining the average electron density and the temperature profiles using the equation below.

$$S(r) = T(r)/n_{\mathrm{e}}(r)^{2/3}. \tag{3.8}$$

The entropy profiles are then sampled at three characteristic radii, and the final entropy measurements of 271 galaxy group bins are obtained. The full shape of the entropy profiles of binned groups, along with the other thermodynamic profiles such as electron density and pressure ($P = n_{\mathrm{e}}T$), are presented in Chapter 4.

Besides the systematics resulting from the metallicity profile, we also consider other major systematics that have a non-negligible impact on the thermodynamic properties measured in this Chapter. We discuss and quantify the impact of these systematics on our measurements in Sect. 3.4 and take them into account as part of the total error budget when we draw conclusions in the next section.

3.4 Assumptions, Corrections, and Systematics

Having fair comparisons between the thermodynamic properties of groups observed with different X-ray observatories and simulations is a challenging task. Various systematics should be taken into account in the measurements, such as the systematic uncertainties on the metallicity and temperature profiles, systematic uncertainties on the group masses, the flux calibration mismatches between instruments and the systematics resulting from the use of different atomic database versions. In this section, we provide a list of assumptions, corrections, and systematics taken into account in this Chapter, along with our approach to account for them. We also list a summary of the description and implementation of the assumptions, corrections, and systematics in Table 3.2.

3.4.1 Assumptions on Temperature and Metallicity Profiles

Accounting for the temperature and metallicity radial variation is key to having reliable thermodynamic profiles. Shallow survey observations and low signal-to-noise data of most groups in our sample are insufficient to measure temperature profiles reliably. There are various studies in the literature on the average temperature profile of the hot gas in clusters (e.g., McDonald et al., 2014; Ghirardini et al., 2019), while the studies focusing on the shape of the average temperature profile of groups with a large enough sample are limited. An in-depth study of 43 nearby galaxy
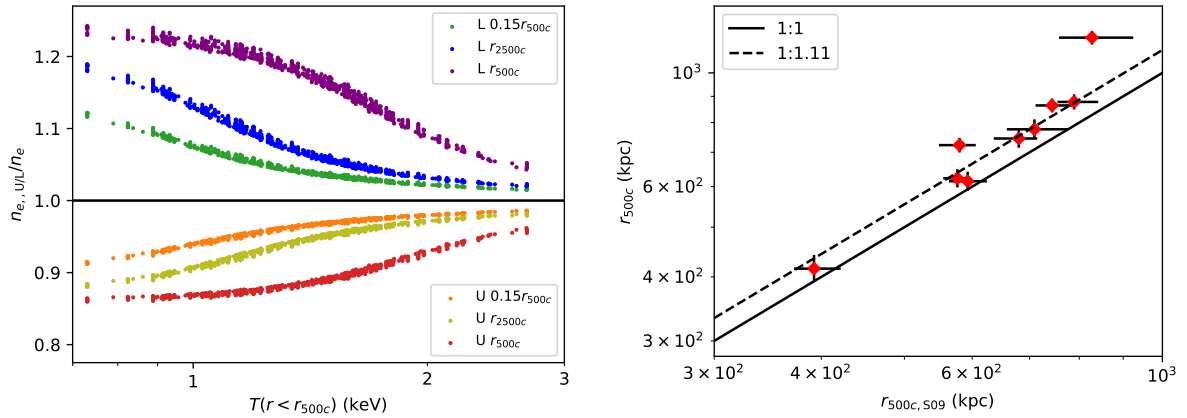
Figure 3.8: *Left:* Ratio of the electron densities obtained by assuming low/up-scattered Mernier et al. (2017) metallicity profiles to the electron densities obtained by the median Mernier et al. (2017) metallicity profile at three radii, $0.15r_{500c}$, r_{2500c} and r_{500c} as a function of characteristic temperature, $T(r < r_{500c})$. Green, blue, and purple data points represent the ratio between the electron densities obtained by assuming the lower envelope ($n_{e,L}$) of the red shared area and the dark red median line (n_e) in the right panel of Fig. 3.7. Orange, yellow, and red data points represent the ratio between the electron densities obtained by assuming the upper envelope of the red shared area ($n_{e,U}$) and the dark red median line (n_e) in the right panel in Fig. 3.7. *Right:* Comparison between the scaling relation based r_{500c} estimates of the cross-matched galaxy groups obtained in our work (y-axis: r_{500c}) with the estimates of S09 (x-axis: $r_{500c,S09}$) obtained by assuming hydrostatic equilibrium.
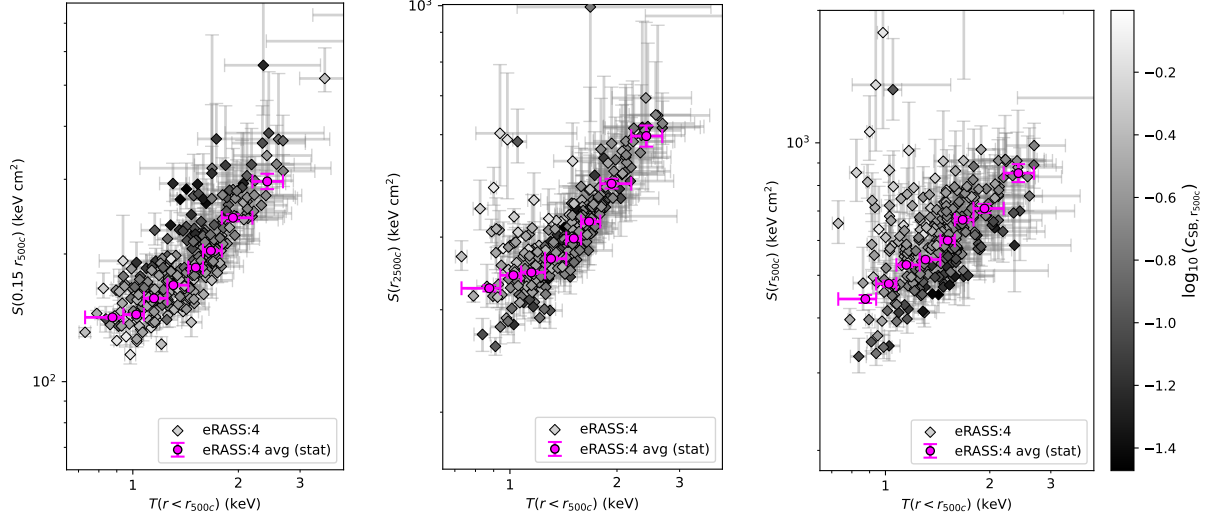
Figure 3.9: Average entropy measurements of binned groups (diamonds) at three radii ($0.15r_{500c}$, r_{2500c}, r_{500c}) as a function of characteristic temperature, $T(r < r_{500c})$. The colors of the diamond data points represent the average concentration ($c_{SB,r_{500c}} = SB(r < 0.1r_{500c})/SB(r < r_{500c})$) of the groups within the corresponding Voronoi bin. Error-weighted averages of the diamond data points are shown in magenta.

groups with deep *Chandra* observations by S09 (among which 23 of them have good temperature constraints out to r_{500c}) is one of the few studies we compared within this Chapter. In our work, we use the temperature profile measurements of the 23 groups presented in S09 to get the average shape of the temperature profile of groups. To get the average shape, we first calculate the characteristic temperatures of the groups, $T(r < r_{500c})$, by projecting and integrating all the temperature profiles within a cylindrical volume of radius r_{500c}. We achieve this following the Mazzotta et al. (2004) weighting and projection formulas

$$w = n_e n_p T^\alpha \tag{3.9}$$

and

$$T_{sl} = \frac{\int wT\,dV}{\int w\,dV} \tag{3.10}$$

where for α we use 0.76 that is calibrated for eROSITA (ZuHone et al., 2023). Furthermore, we use our average group electron density profile for n_e (see Chapter 4). We then divide the temperature profiles with the characteristic temperatures and obtain the normalized temperature profiles, $T(r)/T(r < r_{500c})$. Lastly, we take the average of these profiles and renormalize them to get the average shape of the temperature profiles of groups. The average and individual normalized profiles of 23 groups are shown in the left panel of Fig. 3.7.

Unlike clusters, the band-averaged cooling function of groups has a strong metallicity dependence because of the significant contribution from the line emission at temperatures, $T < 2$ keV.

Table 3.1: Positions, redshifts and r_{500c} estimates of the crossmatched groups with S09

eROSITA ID (1eRASS)	Literature name	RA[*] (deg)	DEC[*] (deg)	z[*]	r_{500c}[†] (kpc)
J120427.3+015346	MKW4	181.114	1.896	0.0203	723
J093325.7+340302	UGC 5088	143.357	34.051	0.0269	415
J120638.9+281024	NGC 4104	181.662	28.173	0.0283	623
J110943.5+214545	A1177	167.432	21.763	0.0322	615
J054006.9-405004	ESO 306-017	85.029	-40.835	0.0368	864
J000313.1-355607	A2717	0.805	-35.935	0.0500	878
J102212.8+383136	RXJ 1022+3830	155.553	38.527	0.0544	745
J231358.6-424338	AS1101	348.494	-42.727	0.0557	1172
J131214.0-005825	A1692	198.059	-0.974	0.0843	776

Notes.
[*] RA, DEC, and z of the listed groups are taken from Bulbul et al. (2024).
[†] Scaling relation based r_{500c} estimates used in this Chapter are obtained by fully accounting for the selection and the mass functions.

Therefore, the radial change in metallicity from the center to the outskirts should be accounted for to calculate electron density profiles accurately.

During the last decade, the shape and the strength of emission lines have significantly changed in most commonly used plasma emission codes (see Sect. 3.4.4) that had a strong influence on the metallicity measurements of groups (e.g., Mernier et al., 2018). For this reason, it is important to use the most recent publications and account for uncertainties in metallicity profiles in the systematics error budget. Among the metallicity profile measurements in the literature, the results presented in Sun (2012), Mernier et al. (2017) and Lovisari and Reiprich (2019) stand out as the most recent studies with moderately large galaxy group samples with sufficiently deep observations. The right panel of Fig. 3.7 presents the stacked metallicity profiles of Sun (2012) and the average metallicity profiles of Mernier et al. (2017) and Lovisari and Reiprich (2019) that are renormalized based on the iron abundance ratio of Asplund et al. (2009). In Sun (2012), the author reports stacked abundance profiles of 39 galaxy groups in three temperature bins ($0.75 - 1.3$, $1.3 - 1.9$ and $1.9 - 2.7$ keV). In this Chapter, we consider only the results of the first two temperature bins ($0.75 - 1.3$ keV and $1.3 - 1.9$ keV), which are relevant to our sample that has a median temperature of $T(r < r_{500c}) = 1.45$ keV.

Overall, the Sun (2012) measurements in the $1.3 - 1.9$ keV temperature bin lie above the Mernier et al. (2017) profile, and the average measurements of Lovisari and Reiprich (2019) lie below the Mernier et al. (2017) profile. When calculating the thermodynamic properties, the differences in metallicity measurements must be accounted for as systematics because of the strong dependence of emissivity on metallicity at group scales. Given the large spread of metallicity measurements, we take the average profile of Mernier et al. (2017) as our default profile and conservatively consider the shaded area as the systematics of the average profile measurements.

To account for the impact of the choice of average metallicity profile, we construct APEC spectra in `Xspec` and obtain deprojected electron density profiles of the 1178 galaxy groups in our sample (similarly done in Liu et al., 2022a) using the scaled temperature profiles and three metallicity profiles (low-scattered, median, and up-scattered Z_{M17} profiles) shown with red in the right panel of Fig. 3.7. We present the ratios of the electron densities in the left panel of Fig. 3.8 that are obtained by using the aforementioned three metallicity profiles (low-scattered Z_{M17}: $n_{e,L}$, median Z_{M17}: n_e, and up-scattered Z_{M17}: $n_{e,U}$) for 1178 groups at the three characteristic radii ($0.15r_{500c}$, r_{2500c} and r_{500c}). The ratios ($n_{e,U}/n_e$ and $n_{e,L}/n_e$) ranging between $0.84 - 1.24$ in the left panel of Fig. 3.8 indicating a non-negligible difference between the electron density measurements. The ratios deviate more from unity as the characteristic temperature decreases, and the measurement radius increases. This is due to line emission, coupled with metalicity, which plays a more important role as the temperature decreases. The procedure described above is followed for the final results, and the radius/temperature dependent systematics due to the choice of metallicity profile are quantified and propagated to our final entropy measurements presented in Sect. 3.5.

3.4.2 Correction for the Flux Discrepancy

A discrepancy of 15% is reported in the luminosity measurements in the soft-band ($0.5-2$ keV) of a subsample of massive galaxy clusters observed with both eROSITA and *Chandra* (Bulbul et al., 2024). The observed flux difference is constant with no flux or luminosity dependence. Some of this difference can be explained by the photon loss in the latest processing due to the higher CCD thresholds (Merloni et al., 2024); however, further investigation is required to understand the observed flux discrepancy, which could be due to various calibration effects. We account for the flux discrepancy while comparing our entropy measurements with those reported in the literature. Among our two main X-ray observables n_e and T, only electron density is impacted by the flux discrepancy since the spectroscopic T measurements are not sensitive to the overall flux normalization. To roughly estimate the impact, we assumed the shape of the measured electron density profile to be the same for different instruments, used the fact that $L \propto n_e^2$, and obtained a ratio of $n_{e,\text{eRO}}/n_{e,\text{Cha}} = 0.85^{0.5} \sim 0.92$ between the electron density measurements of *Chandra* and eROSITA. The 8% underestimation of n_e corresponds to a 5% overestimation of entropy. This fraction is factored in the *Chandra* measurements in S09 when comparing with the eROSITA results in Fig. 3.12.

3.4.3 Systematics Related to Mass Measurements

We note that entropy measurements at overdensity radii, $0.15r_{500c}$, r_{2500c}, and r_{500c} are sensitive to the assumed masses of the galaxy groups. This dependence is due to the entropy profile of galaxy groups being a strong function of the radial distance and the overdensity radius, which is a mass-dependent quantity (e.g. Bulbul et al., 2010; Ghirardini et al., 2019). Therefore, any disagreement in radius and mass may lead to a bias in the measured thermodynamic profiles and their comparisons between different methods. Masses of galaxy groups can be estimated in different ways, such as by assuming hydrostatic equilibrium, using the shear information of the lensed galaxies, or using scaling relations; however, these methods have advantages and

Table 3.2: Summary of assumptions, corrections, and systematics

Assumptions, corrections and systematics	Description and our approach*
Temperature and metallicity profiles	Radial variation of temperature and metallicity need to be accounted for to have reliable thermodynamic profiles of galaxy groups. Given the limited signal-to-noise we have for most of the groups in our sample, we adopt the average shape of the temperature profiles of the galaxy groups presented in S09 and allow its normalization to vary for deriving the average thermodynamic properties of our sample. Furthermore, we adopt the average Mernier et al. (2017) metallicity profile for the main results and conservatively consider the reported scatter as the systematic uncertainty of the profile. We then propagate the systematic uncertainty to our final results and consider its impact as part of the total error budget.
Instrumental calibration	A flux mismatch of 15% is reported in Bulbul et al. (2024) between eROSITA and *Chandra* for galaxy clusters and groups. Assuming the flux mismatch is not a function of radii, this discrepancy corresponds to an 8% difference in n_e and a 5% difference in S. In this Chapter, we take the mismatch into account while comparing our results with the measurements in the literature with other telescopes.
Mass measurements	Obtaining the underlying mass distributions of galaxy groups are challenging and may lead to inconsistencies while comparing measurements. In this Chapter, we account for the mass measurement mismatches while comparing our results with the literature and provide derivatives of our entropy measurements for future work to account for the mass measurement systematic while comparing with our results.
Atomic databases	Spectral models evolve over time as our knowledge of atomic transitions increases. This may result in discrepancies when measurements obtained with different atomic database versions are compared. In this Chapter, we account for this by applying corrections to the measurements in the literature.

Notes.

* See Sect. 3.4 for a more detailed description of the assumptions, corrections, and systematics, along with a more detailed prescription on how they are addressed in this study.

disadvantages along with introduced biases. Comparison of the mass estimation techniques for galaxy groups is beyond the scope of our study; therefore, in this Chapter, we'll only account for the bias while comparing our results with the literature. We find that our scaling relations based r_{500c} estimates are $\sim 11\%$ higher than the hydrostatic equilibrium based r_{500c} estimates in S09 for 9 cross-matched groups. Comparison between our characteristic radii estimates (r_{500c}) and those in the literature ($r_{500c,\text{S09}}$) is provided in the right panel of Fig. 3.8. A discrepancy of $\sim 11\%$ approximately corresponds to a bias of $\sim 37\%$ ($1.11^3 = 1.37$) on M_{500c}. This result is close but slightly below the 45% hydrostatic mass bias observed in galaxy groups (Nagai et al., 2007a), see also Sect. 6.2 of S09. We note that the masses of S09 are obtained with an outdated version of AтомDB. Lovisari et al. (2015) and Sun (2012) independently confirmed that using a more recent AтомDB version (v2.0.1) increases the temperatures by $\sim 15\%$. Such an increase would reduce the mass mismatch to a $\sim 22\%$ level and the radius mismatch to $\sim 7\%$ level.

One should note that constraining hydrostatic mass bias, especially in galaxy groups, is challenging due to our limited knowledge of the magnitude of non-thermal pressure support, magnified in galaxy groups due to powerful AGN feedback compared to galaxy clusters. Moreover, the fraction of discrepancy may be due to other systematics in the measurements, such as the representation of the $L_X - M$ relation with a single power-law spanning a large mass range. We provide the r_{500c} estimates of the 9 cross-matched groups in Table 3.1 along with the slopes of the average entropy profiles of the binned groups at the three characteristic radii in Table 3.3.

The mass estimate dependence is also responsible for the observed scatter in the entropy of the sample. Fig. 3.9 shows a strong correlation between the scatter of the average entropy measurements at a given temperature and the average concentration ($c_{\text{SB},r_{500c}} = SB(r < 0.1r_{500c})/SB(r < r_{500c})$) of the sample (see Sanders et al., in prep. for the concentration measurements). This is expected since the M_{500c} (or r_{500c}) estimates used in this Chapter are obtained using an $L_X - M$ scaling relation. At a given mass, the cool-core galaxy groups with higher luminosity would have higher entropy measurements while the others scatter around the sample's median. The average entropy and temperature measurements of the sample are presented in Fig. 3.9, where the colors of the data points indicating average concentration obtained by averaging the measurements provided in Sanders et al. (in prep.). A few extreme cases with larger concentration, electron number density, and entropy are easily noticeable in Fig. 3.9. By construction, the r_{500c} (or M_{500c}) estimates are, on average, unbiased at the sample scale. Therefore, a small scatter does not significantly impact the conclusions of our work. On average, these effects cancel out such that at all three radii, the error-weighted average entropy plotted in magenta coincides with the intermediate concentration values $\log_{10}(c_{\text{SB},r_{500c}}) \sim -0.7$.

3.4.4 Systematics Related to the Atomic Databases

Over time, our knowledge of the strength of atomic transitions has changed significantly for $T < 2$ keV plasma. The change in our knowledge of the strength and the width of the Fe-L complex is the most relevant to the work presented in this Chapter, given its key role in determining the temperature and metallicity of the IGrM. The change in our knowledge resulted in significant updates on the predictions of the spectral models, APEC (Smith et al., 2001) and CIE (an updated version of the MEKAL model, Mewe et al., 1985, 1986; Liedahl et al., 1995), that retrieves data
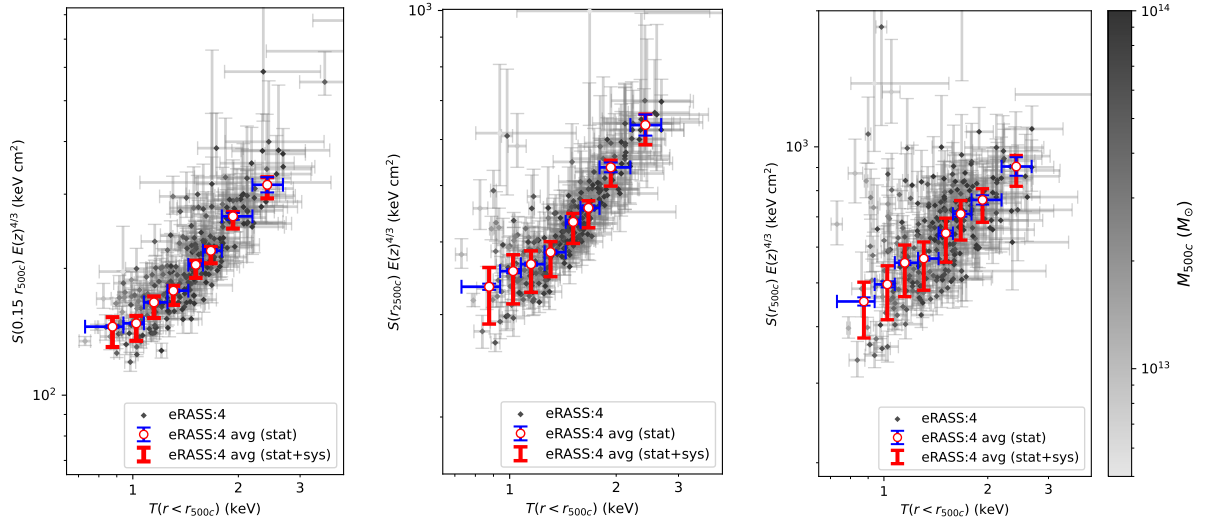
Figure 3.10: Redshift evolution scaled average entropy measurements of binned groups (grey diamonds) at three radii ($0.15r_{500c}$, r_{2500c}, r_{500c}) as a function of characteristic temperature, $T(r < r_{500c})$. The colors of the grey data points represent the average masses (M_{500c}) of the groups within the corresponding Voronoi bin. Error-weighted averages of the data points are plotted as white circles, statistical uncertainties of the averages are shown with blue error bars, and the overall error budget of the average measurements resulting from the statistical and systematic uncertainties are shown with red error bars (see Sect. 3.4 for the details of the accounted systematics).

from atomic databases, `AtomDB` (Foster et al., 2012) and `SPEXACT` (Kaastra et al., 1996, 2020), around the Fe-L complex (e.g., see Fig. 1 in Gastaldello et al., 2021).

These updates may cause measurement mismatches between the studies that employed different versions of the atomic databases. For this reason, the possible impact of using different versions of the atomic databases should be taken into account while comparing results with the literature. In fact, Sun (2012) reports that for the $T < 2$ keV plasma, the temperature measurements presented in S09 increase by $10 - 20\%$ when a more recent `AtomDB` version, v2.0.1, is used instead of the one employed in S09, v1.3.1. The increase in the temperature is also independently confirmed by Lovisari et al. (2015), who found their temperature measurements to be 13% higher than the temperatures of S09 for the seven crossmatched objects. In our study, we take this change into account and apply a 15% correction to the entropy and temperature measurements of S09 to their $T < 2$ keV groups while comparing their results with the eROSITA measurements (e.g., in Fig. 3.12). With this correction, we aim to have the fairest comparison of our results.

Lovisari et al. (2015) further report that in the case of such an update in the atomic database, the normalization of the APEC spectrum reduces $\sim 10\%$ for a group (NGC3402) residing at the low-T parameter space ($T \sim 1$ keV), where the impact of the change is expected to be the most prominent. The density of the plasma scales as the square root of the APEC normalization, which results in a $\sim 3\%$ increase in entropy. Given that the 3% increase in entropy is an upper limit (as explained in section A.3 of Lovisari et al., 2015) and is well within the entropy error bars presented in S09, we did not propagate the impact of this change to the S09 entropy measurements.

Lastly, Sun (2012) reported that abundance measurements drop $\sim 20\%$ after updating the `AtomDB` version (from 1.3.1 to 2.0.1). This reduces the stacked metallicity data points of Sun (2012) by $\sim 20\%$ however, given that we are employing Mernier et al. (2017) profile in our work, our results are not affected by this. We further note that even if we apply such a correction to Sun (2012) measurements, they will be well within our conservative systematic errorbars for the metallicity profile (shaded area in the right panel of Fig. 3.7); therefore, it does not pose any challenge to our measurements.

It can be seen from Fig. 1 of Gastaldello et al. (2021) that the width and the normalization of the Fe-L complex seemed to be converging. However, it is hard to know how far we are from the absolute calibration. Therefore, future work should keep systematics related to the atomic databases in mind while comparing results from the literature.

3.5   Entropy and Characteristic Temperature Measurements

In this Chapter, we constrain the entropy of the IGrM, utilizing the deep eRASS:4 observations of the galaxy groups detected in the eRASS1 survey. In this section, we present our measurements of the characteristic temperature, $T(r < r_{500c})$, and entropy at three overdensity radii, $0.15r_{500c}$, r_{2500c}, and r_{500c}, from the combined analysis of 1178 galaxy groups. We then compare our findings with the previously reported results in the literature.

Following the procedures described in Sects. 3.2 and 3.3, we obtain average entropy and

Table 3.3: Average entropy, and entropy slope measurements of the grouped sample as a function of temperature at the three characteristic radii: $0.15r_{500c}$, r_{2500c}, and r_{500c}.

	$T(r < r_{500c})$ (keV)							
	$0.73 - 0.94$	$0.94 - 1.08$	$1.08 - 1.26$	$1.26 - 1.44$	$1.44 - 1.59$	$1.59 - 1.79$	$1.79 - 2.19$	$2.19 - 2.68$
$S(0.15r_{500c})E(z)^{4/3*}$	$145.4^{+1.1(+7.7)}_{-1.1(-15.3)}$	$148.09^{+0.90(+6.1)}_{-0.89(-13.5)}$	$166.04^{+0.87(+5.5)}_{-0.86(-13.6)}$	$177.0^{+1.2(+4.6)}_{-1.2(-13.2)}$	$203.9^{+1.6(+4.3)}_{-1.6(-14.0)}$	$220.2^{+2.1(+3.9)}_{-2.0(-14.4)}$	$265.8^{+5.0(+3.9)}_{-4.9(-16.5)}$	$316^{+13(+3.6)}_{-13(-18.6)}$
$S(r_{2500c})E(z)^{4/3*}$	$335.0^{+4.1(+26)}_{-4.1(-46)}$	$356.3^{+2.9(+24)}_{-2.9(-43)}$	$366.3^{+2.3(+20)}_{-2.3(-39)}$	$384.0^{+2.7(+16)}_{-2.6(-35)}$	$433.0^{+3.7(+14)}_{-3.7(-35)}$	$457.7^{+4.5(+12)}_{-4.4(-34)}$	$537^{+10(+11)}_{-10(-37)}$	$635^{+27(+9.8)}_{-26(-40.0)}$
$S(r_{500c})E(z)^{4/3*}$	$454.9^{+9.6(+46)}_{-9.4(-77)}$	$496.3^{+7.7(+49)}_{-7.6(-81)}$	$553.9^{+6.1(+52)}_{-6.1(-88)}$	$566.0^{+5.9(+50)}_{-5.9(-84)}$	$644.0^{+8.7(+51)}_{-8.6(-88)}$	$710.6^{+10.1(+49)}_{-9.9(-88)}$	$763^{+18(+41)}_{-18(-80)}$	$905^{+44(+32)}_{-42(-76)}$
$S'(0.15r_{500c})^{\dagger}$	0.76	0.82	0.67	0.71	0.63	0.60	0.61	0.61
$S'(r_{2500c})^{\dagger}$	0.61	0.64	0.68	0.63	0.65	0.65	0.59	0.59
$S'(r_{500c})^{\dagger}$	0.30	0.23	0.37	0.34	0.46	0.59	0.44	0.41

Notes.

* Error-weighted average of the redshift evolution scaled entropy measurements of the grouped sample in units of keV cm^2 within the corresponding temperature bin. The first set of errors above and below the measurements represent the statistical uncertainty, and the errors presented within the parenthesis represent the systematic uncertainty (see Sect. 3.4 for the details of the accounted systematics).

† $S'(r) = \frac{d \log(S(r))}{d \log(r/r_{500c})}$, the slope of the error-weighted average entropy measurements as a function of dimensionless radius in logarithmic space, in units of log(keV cm^2).

temperature measurements of a sample of 1178 eROSITA selected galaxy groups in 271 bins. Our measurements for the average temperature and average entropy at three characteristic radii scaled by the self-similar redshift evolution ($E(z)^{4/3}$) can be seen in Fig. 3.10, where the error-weighted average entropy measurements are shown in white circles, the statistical uncertainties are shown with blue errorbars and the overall error budget resulting from the statistical and systematic (see Sect. 3.4) uncertainties are shown with red error bars. Error-weighted average of the redshift evolution scaled entropy measurements, their statistical uncertainties, and the impact of systematics are also provided in Table 3.3 as a function of IGrM temperature. Besides the average entropy measurements, we provide slopes of the average entropy profiles in Table 3.3 at the three characteristic radii for future work to account for the mass measurement systematic while comparing with our results (see Sect. 3.4.3 for the details of accounting the systematics in mass measurements). We note that the few outlying entropy measurements in Fig. 3.10 are due to the extreme cool-core objects and have negligible impact on our error-weighted entropy measurements (see Sect. 3.4.3 for a more detailed discussion on the outliers and their impact on our final results).

We find that the characteristic temperature measurements of our binned group sample span a range of $\sim 0.73 - 2.68$ keV. Furthermore, we find that the characteristic temperature measurements of the binned groups correlate well with the entropy measurements at the three characteristic radii such that an increase in the characteristic temperature from 0.73 keV to 2.68 keV corresponds to an increase from the redshift scaled entropy levels of 121, 271, 341 keV cm^2 to 404, 722, 1135 keV cm^2 respectively. This trend can also be clearly seen from the error-weighted average measurements (white circles) in Fig. 3.10 such that the error-weighted averages at these three radii increase from the levels of 145, 335, 455 keV cm^2 to 316, 635, 905 keV cm^2 respectively. It can further be noticed that as the characteristic temperature of the binned groups
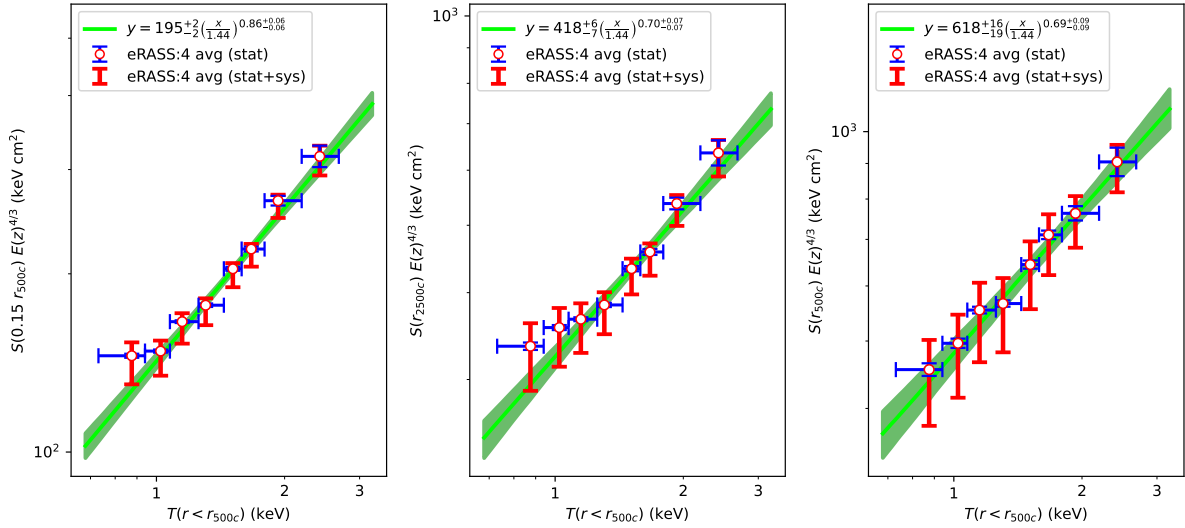
Figure 3.11: $S(r) - T$ relations at $0.15r_{500c}$, r_{2500c} and r_{500c}. The white circles represent redshift evolution scaled average entropy measurements, blue error bars represent statistical uncertainties of the averages, and the red error bars represent the overall error budget of the average measurements resulting from the statistical and systematic uncertainties (see Sect. 3.4 for the details of the accounted systematics). The best-fit power-law models to the data points are plotted as light green lines, and the uncertainties of the best-fit lines are shown with dark green shaded regions.

decreases, the statistical uncertainty of the error-weighted average profiles (blue error bars) decreases. Conversely, the decrease in the temperature corresponds to an increase in the overall error budget (red error bars). This is due to the fact that the line emission from the Fe-L complex at the low-temperature parameter space becomes significant, which provides an additional spectral feature for measuring the temperature and reduces the statistical uncertainty. Meanwhile, at the same parameter space, the systematic uncertainty of the metallicity profile has a very large impact on the electron density measurements, which results in the entropy measurements having large systematic uncertainties. At higher temperatures, the systematic uncertainties of the electron density measurements become smaller due to the reduced line emission, and the less significant Fe-L complex increases the statistical uncertainties.

Furthermore, we find that the redshift scaled average entropy and the average temperature measurements of our sample at the three radii follow power-law relations within the uncertainties. To quantify the normalizations and the slopes of the relations, we fit a power-law model to the measurements of the form $S(r)E(z)^{4/3} = A(T/T_{\mathrm{piv}})^B$ where the $S(r)$ term represents entropy measured at three characteristic radii ($0.15r_{500c}$, r_{2500c}, and r_{500c}), the T term represents the characteristic temperature ($T(r < r_{500c})$), T_{piv} term represents the pivot temperature, and the A and B terms stand for the normalization and the slope of the relation respectively. For our galaxy group sample, we took a pivot value of $T_{\mathrm{piv}} = 1.44$ keV and obtained the best-fit power-law models to the average measurements at the three radii as shown in Fig. 3.11. Furthermore, we noticed that the slope of the $S(r) - T$ relations seem to be changing around $T = 1.44$ keV such that the

Table 3.4: Best-fit parameters of the $S(r) - T$ relation.

Relation	A (keV cm^2)	B
All groups ($T = 0.73 - 2.68$ keV, $T_{\mathrm{piv}} = 1.44$ keV)		
$S(0.15r_{500c}) - T(r < r_{500c})$	195^{+2}_{-2}	$0.86^{+0.06}_{-0.06}$
$S(r_{2500c}) - T(r < r_{500c})$	418^{+6}_{-7}	$0.70^{+0.07}_{-0.07}$
$S(r_{500c}) - T(r < r_{500c})$	618^{+16}_{-19}	$0.69^{+0.09}_{-0.09}$
Warm groups ($T = 1.44 - 2.68$ keV, $T_{\mathrm{piv}} = 1.79$ keV)		
$S(0.15r_{500c}) - T(r < r_{500c})$	235^{+4}_{-4}	$0.98^{+0.10}_{-0.10}$
$S(r_{2500c}) - T(r < r_{500c})$	485^{+9}_{-10}	$0.87^{+0.11}_{-0.11}$
$S(r_{500c}) - T(r < r_{500c})$	717^{+24}_{-26}	$0.72^{+0.17}_{-0.17}$
Cool groups ($T = 0.73 - 1.44$ keV, $T_{\mathrm{piv}} = 1.08$ keV)		
$S(0.15r_{500c}) - T(r < r_{500c})$	155^{+3}_{-4}	$0.59^{+0.16}_{-0.16}$
$S(r_{2500c}) - T(r < r_{500c})$	352^{+11}_{-13}	$0.32^{+0.22}_{-0.22}$
$S(r_{500c}) - T(r < r_{500c})$	504^{+21}_{-27}	$0.56^{+0.28}_{-0.28}$

Notes. The fitted relation is of the form $S(r)E(z)^{4/3} = A(T/T_{\mathrm{piv}})^B$ where the $S(r)$ term stands for entropy measured at three characteristic radii ($0.15r_{500c}$, r_{2500c}, and r_{500c}), the T term stands for the characteristic temperature, $T(r < r_{500c})$, and T_{piv} is the pivot temperature value. The relation is fitted to the measurements presented in Table 3.3 by taking into account the statistical and systematic uncertainties. The fitting procedure is executed three times at each radius: first, for all the groups in the sample spanning a temperature range of $0.73 - 2.68$ keV; second, for only the warm groups spanning a temperature range of $1.44 - 2.68$ keV; and third, for only the cool groups spanning a temperature range of $0.73 - 1.44$ keV.

warm/higher-mass groups in our sample ($T = 1.44 - 2.68$ keV) are steeper than the $S(r) - T$ relations of the cool/lower-mass groups ($T = 0.73 - 1.44$ keV). To quantify the difference, we separately fit the average measurements of the warm and cool groups using the same relation, assuming pivot values of $T_{\mathrm{piv}} = 1.79$ and 1.08 keV, respectively. Best-fit parameters of the $S(r) - T$ relation at three radii for all galaxy groups in our sample, along with the best-fit parameters for the warm, and cool groups, are listed in Table 3.4.

As a result of the fitting procedure, we find that for all galaxy groups ($T = 0.73 - 2.68$ keV), the slopes of the $S(r_{2500c}) - T(r < r_{500c})$ and $S(r_{500c}) - T(r < r_{500c})$ relations ($B = 0.70^{+0.07}_{-0.07}$ and $0.69^{+0.09}_{-0.09}$ respectively) are in very good agreement with each other. Whereas we find that the slope of the $S(0.15r_{500c}) - T(r < r_{500c})$ relation ($B = 0.86^{+0.06}_{-0.06}$) is slightly steeper. We also compare our relations with the self-similar predictions presented in Voit (2005). We find that our best-fit normalizations of the $S(r) - T$ relations are $> 5\sigma$ larger than the self-similar predictions at all radii. This agrees well with the previous findings on the entropy excess in galaxy groups and indicates that non-gravitational processes such as AGN feedback and radiative cooling are non-negligible and play an important role in shaping the entropy profiles of galaxy groups. Moreover,

we compare the best-fit slopes of the $S(0.15r_{r500c}) - T(r < r_{500c})$, $S(r_{2500c}) - T(r < r_{500c})$, $S(r_{500c}) - T(r < r_{500c})$ relations for all galaxy groups in our sample with the self-similar prediction ($B_{self} = 1$ at all radii) and find that our slopes are 2.3, 4.3, 3.4σ shallower than the self-similar slope respectively.

Furthermore, we compare the best-fit $S(r) - T$ relations of the warm and cool groups and find that the slopes of the warm/higher-mass groups, $B = 0.98^{+0.10}_{-0.10}$, $0.87^{+0.11}_{-0.11}$ and $0.72^{+0.17}_{-0.17}$, are much steeper than the slopes of the cool/lower-mass groups, $B = 0.59^{+0.16}_{-0.16}$, $0.32^{+0.22}_{-0.22}$ and $0.56^{+0.28}_{-0.28}$ at $0.15r_{500c}$, r_{2500c} and r_{500c} respectively. We then compare our best-fit normalizations of the warm and cool groups with the self-similar predictions presented in Voit (2005) and find that the normalizations for warm and cool groups are $> 5\sigma$ larger than the self-similar predictions at all radii. Moreover, we also compare the slopes of the warm and cool groups with the self-similar prediction and find that the best-fit slopes of the warm/higher-mass groups, $B = 0.98^{+0.10}_{-0.10}$, $0.87^{+0.11}_{-0.11}$ and $0.72^{+0.17}_{-0.17}$, agree much better with the self-similar prediction ($B_{self} = 1$) compared to the slopes of the cool/lower-mass groups, $B = 0.59^{+0.16}_{-0.16}$, $0.32^{+0.22}_{-0.22}$ and $0.56^{+0.28}_{-0.28}$, at $0.15r_{500c}$, r_{2500c}, and r_{500c} respectively. This comparison suggests that even though the non-gravitational processes significantly increase the overall entropy levels of galaxy groups at all temperature/mass scales, they result in the slope of the $S(r) - T$ relation for cool/lower-mass groups deviating more from the self-similar prediction compared to the slope of the warm/higher-mass groups that live at a temperature/mass parameter space closer to clusters.

We note that the observed flattening for the cool groups can also be due to other reasons, such as the selection effects or relatively large systematic uncertainties. The X-ray selection probability of galaxy clusters and groups has a dependency on the emission profile of the cluster and group (Clerc et al., 2024). Therefore, for the most robust calibration of the $S(r) - T$ scaling relation, a selection function that takes entropy at given radii as input should be used, which is currently not implemented in our framework for galaxy groups. In the future, a better understanding of the temperature and metallicity profiles of galaxy groups, along with the use of a profile-dependent selection function for fitting the $S(r) - T$ relation, would make the picture clearer and help us understand the origin of the observed flattening for the cool/lower-mass groups.

Comparing the entropy measurements at the three radii, with the previous measurements in the literature as a function of temperature, $T(r < r_{500c})$, is challenging given the limited number of studies reporting these quantities and the information provided in these studies to account for the discrepancies in the measurement radii being limited across the literature. In this section, we present our findings from the comparison performed between our measurements and the results reported by S09 and Johnson et al. (2009).

To have a fair comparison, we quantify and account for the systematic differences between our results and those presented in S09. The average temperature of galaxy groups in S09 are measured using core-excised apertures ($0.15r_{500c} < r < r_{500c}$), whereas in our study, we measure temperatures including the core out to r_{500c} to maximize the signal-to-noise in our measurements. We convert the core-excised characteristic temperature measurements, $T(0.15r_{500c} < r < r_{500c})$, reported in S09 to the core-included temperatures by applying a conversion factor of $T(r < r_{500c})/T(0.15r_{500c} < r < r_{500c}) = 1.07$. This conversion factor is obtained by projecting the average group temperature profile (see Sect. 3.4.1) using the temperature weighting and projection
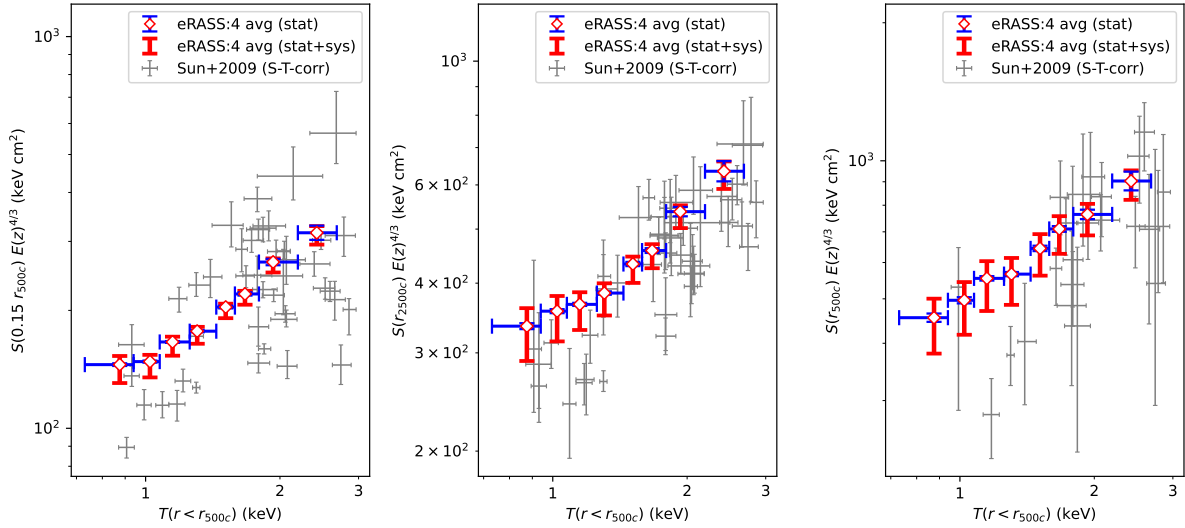
Figure 3.12: Comparison between the redshift evolution scaled average eROSITA entropy measurements (white diamonds) with the *Chandra* measurements of 43 galaxy groups (black error bars) presented in S09 at three radii ($0.15r_{500c}$, r_{2500c}, r_{500c}) as a function of characteristic temperature, $T(r < r_{500c})$. Blue error bars represent the statistical uncertainties of the average measurements, and the red error bars represent the overall error budget resulting from the statistical and systematic uncertainties (see Sect. 3.4 for the details of the accounted systematics). For consistency, core-excised temperatures presented in S09 are converted to core-included temperatures, and the entropy measurements presented in S09 are normalized such that the new data points are measured at the same angular radii with eROSITA flux calibration (see Sect. 3.5 for the details of these corrections).

formulation of ZuHone et al. (2023) calibrated for eROSITA and the average group electron density profile presented in Chapter 4. Additionally, we apply a correction factor to account for the difference in the characteristic radii estimation to the S09 entropies as described in Sect. 3.4.3. The correction factors are obtained by comparing our scaling relations based on r_{500c} estimates with the masses obtained assuming hydrostatic equilibrium (see Sect. 3.4.1) and quantifying the impact of the mismatch on the average entropy measurements at three characteristic radii. Furthermore, we apply a 5% correction to the entropy measurements of S09 to account for the 15% flux discrepancy between *Chandra* and eROSITA (see Sect. 3.4.2) that is reported in Bulbul et al. (2024). Lastly, we applied a 15% correction to the entropy and temperature measurements of the $T < 2$ keV groups in the S09 sample due to the use of an old version of the atomic database `AtomDB` (see Sect. 3.4.4 for the details on the correction).

The comparison between our temperature and entropy measurements with the findings of S09 are shown in Fig. 3.12. After the systematic differences are accounted for, we find our measurements to agree well with the S09 results within $\sim 1\sigma$ confidence at all three radii. Fig. 3.12 shows that our results only deviate from the measurements of S09 at the cooler temperatures with $T(r < r_{500c}) < 1.15$ keV. We argue that this may be due to the completeness of our sample

being much higher than the completeness of the S09 sample at these temperatures. The S09 sample is based on the archival *Chandra* follow-up observations of 43 ROSAT-detected bright groups. For this reason, by construction, the limited number of measurements reported in S09 at the low-temperature parameter space is for bright groups that have relatively high n_e and low S. This effect is visible in Fig. 3.12 such that S09 has only three measurements for $S(r_{500c})$ and 11 for $S(r_{2500c})$ and $S(0.15r_{500c})$ at the cool temperatures end, whereas our sample includes temperature measurements of a sample of 323 galaxy groups binned into 61 groups. Furthermore, we note that the sample studies analyzing individually followed-up systems, such as S09, exclude morphologically disturbed systems. Nevertheless, in our work, with the aim of achieving comprehensive conclusions about galaxy groups, we did not make such a distinction and have analyzed all the galaxy groups in our sample by allowing the centroid of the surface brightness profile to be free. Parallel to having a preferential selection toward bright objects, excluding morphologically disturbed systems can also potentially decrease the average entropy of a sample at a given mass/temperature. That is in agreement with the direction of the slight discrepancy we see in Fig. 3.12 and can possibly explain the mismatch. A more quantitative statement on the relationship between the morphology and gas properties of galaxy clusters and groups, as well as the relationship between the eROSITA selection and the morphology of the extended objects, will be explored in Sanders et al. (in prep.).

Furthermore, Johnson et al. (2009) analyzed *XMM-Newton* observations of 28 nearby galaxy groups and found that the entropy measurements of their sample at the core, $S(0.1r_{500c})$, follow a power-law relation with their core-excluded temperature measurements, $T(0.1r_{500c} < r < 0.3r_{500c})$. They further report that the best-fit slope of their $S(0.1r_{500c}) - T(0.1r_{500c} < r < 0.3r_{500c})$ relation (0.79 ± 0.06) agrees with the slope of a similar relation, $S(0.15r_{500c}) - T(0.15r_{500c} < r < r_{2500c})$, presented in S09, 0.78 ± 0.12. In our work, we measure entropy at the core at a slightly different radius ($0.15r_{500c}$) than the one used in Johnson et al. (2009), and we use core-included temperature measurements rather than the core-excised temperatures. Nevertheless, we compare our most similar relation, $S(0.15r_{500c}) - T(r < r_{500c})$, to the relations fitted in S09 and Johnson et al. (2009) and find that our slope 0.86 ± 0.08 is in good statistical agreement with the slopes of S09 and Johnson et al. (2009). Moreover, we further compare our best-fit slope for the $S(r_{2500c}) - T(r < r_{500c})$ relation with the best-fit slope of another similar relation, $S(r_{2500c}) - T(0.15r_{500c} < r < r_{500c})$, presented in S09 and find that our slope (0.7 ± 0.07) agrees well with the slope reported in S09 (0.76 ± 0.06). Lastly, we compare the best-fit slope of our $S(r_{500c}) - T(r < r_{500c})$ relation with the best-fit slope of S09 for the $S(r_{500c}) - T(0.15r_{500c} < r < r_{500c})$ relation and find that our slope (0.69 ± 0.09) is in good statistical agreement with the slope reported in S09 (0.8 ± 0.2).

3.6 Comparison with the Numerical Simulations

In this section, we compare our results with the state-of-the-art simulations to place constraints on the physics of the AGN feedback. We quantify the agreement or disagreement between our measurements and the predictions of the various AGN feedback models implemented in these cos-

mological hydrodynamical simulations, including MillenniumTNG[12] (Hernández-Aguayo et al., 2023; Pakmor et al., 2023), Magneticum[13] (Hirschmann et al., 2014) and the OverWhelmingly Large Simulations (OWL simulations, Schaye et al., 2010).

We compare our results with the Magneticum, MillenniumTNG, and OWL simulations that include different implementations for AGN feedback. The entropy measurements of the OWL simulations are plotted in Fig. 2 of McCarthy et al. (2010); therefore, we extracted their measurements from their paper and directly used them in our work. In contrast, the entropy and the characteristic temperature profile measurements for MillenniumTNG and Magneticum simulations are not publicly available. For this reason, we extract thermodynamic profiles of the gaseous halos from the MillenniumTNG and Magneticum simulations. A brief description of the MillenniumTNG and Magneticum simulations and the extraction process is as follows.

3.6.1 MillenniumTNG Simulations

The MTNG740 flagship full physics run of the MillenniumTNG project (Pakmor et al., 2023) is used in this Chapter which simulates a 500 Mpc/h cosmological box with the Planck Collaboration et al. (2016) cosmology. Its galaxy formation model is close to the IllustrisTNG model (Weinberger et al., 2017; Pillepich et al., 2018) and includes primordial and metal line cooling, a subgrid model for star formation and the interstellar medium, mass return from stars via AGB stars and supernovae, an effective model for galactic winds, as well as a model for the formation, growth, and feedback from supermassive black holes. At a baryonic mass resolution of $3 \times 10^7 M_\odot$ MTNG740 reproduces well many properties of observed galaxies and galaxy clusters for halos with $M_{500c} > 2.3 \times 10^{12} \, M_\odot$.

The hydrodynamical profiles of groups shown in this Chapter are computed the same way as the galaxy cluster profiles in Pakmor et al. (2023). MTNG outputs a number of useful quantities: gas cell mass (m), electron abundance (x), and internal energy (ϵ). Assuming a primordial hydrogen mass fraction of $X_H = 0.76$, and an adiabatic index of $\gamma = 5/3$, we compute the volume-weighted electron number density, n_e, and temperature T, for each gas particle i as

$$V_i n_{e,i} = x_i m_i \frac{X_H}{m_p} \tag{3.11}$$

$$T_i = (\gamma - 1)\epsilon_i / k \frac{4 m_p}{1 + 3X_H + 4X_H x_i}, \tag{3.12}$$

where m_p the proton mass and k is the Boltzmann constant. We then compute the averages of the two quantities in radial bins $\hat{b}_j$:

$$n_{e,j} = V^{-1}(\hat{b}_j) \sum_{i \in \hat{b}_j} V_i n_{e,i} \tag{3.13}$$

$$T_j = m^{-1}(\hat{b}_j) \sum_{i \in \hat{b}_j} m_i T_i, \tag{3.14}$$

---

[12]https://www.mtng-project.org
[13]http://www.magneticum.org

The radial bins are chosen as 23 logarithmically spaced intervals between 0.001 and 10 r_{200c}, where r_{200c} is the radius from the halo center encompassing 200 times the critical density of the Universe, ρ_c. As a derived quantity, we also compute the entropy as:

$$S(\hat{b}_j) = \frac{T(\hat{b}_j)}{n_e(\hat{b}_j)^{2/3}}, .$$ (3.15)

3.6.2   Magneticum Simulations

The Magneticum simulations used in this study were performed with the TreePM/SPH code P-Gadget3, an extended version of P-Gadget2 (Springel, 2005). In addition to hydrodynamics and gravity, the simulations also account for a variety of physical baryonic processes, including radiative cooling and heating from a time-dependent UV background (Haardt and Madau, 2001), star formation and feedback (Springel and Hernquist, 2003), metal enrichment from stellar evolution (Tornatore et al., 2004, 2007), and black hole growth and gas accretion powering energy feedback from AGN (Springel et al., 2005; Di Matteo et al., 2005; Fabjan et al., 2010). In this study, we consider a sample of 22,254 galaxy groups and clusters with mass $M_{500c} > 5 \times 10^{12} M_\odot$ identified using the SubFind algorithm (Springel et al., 2001; Dolag et al., 2009) in the "Box2_hr" simulation box. This covers a comoving volume of $(352h^{-1}\text{cMpc})^3$ and is resolved with 2×1584^3 particles (which correspond to mass resolutions of $m_{\text{DM}} = 6.9 \times 10^8 h^{-1} M_\odot$ and $m_{\text{gas}} = 1.4 \times 10^8 h^{-1} M_\odot$, for DM and gas respectively). A ΛCDM cosmology with $h = 0.704$, $\Omega_b = 0.0451$, $\Omega_m = 0.272$, $\Omega_\Lambda = 0.728$ and $\sigma_8 = 0.809$ is employed (from the 7-year results of the Wilkinson Microwave Anisotropy Probe Komatsu et al., 2011). See also Biffi et al. (2022) for further details.

We compute gas thermodynamical profiles by selecting the hot, diffuse gas component in each halo of the sample, characterized by temperature higher than $5 \times 10^5 K$ and non-star-forming, representing the X-ray emitting intra cluster and group mediums. The gas mass-weighted temperature and electron density radial profiles are then generated by considering three-dimensional radial bins. The profiles of massive haloes are resolved with 50 linear radial bins up to 1.5 r_{500c}. For smaller systems resolved with fewer gas particles, we instead adopt an equal-particle binning of the radial profiles, to ensure statistically reliable estimates. In all cases, we ensure a minimum of 150 selected gas particles in each radial shell.

3.6.3   OverWhelmingly Large Simulations

The OverWhelmingly Large Simulations (Schaye et al., 2010) used in this Chapter is a cosmological hydrodynamical simulation that was performed using an extended version of the ThreePM/SPH code Gadget3 (Springel, 2005). The simulations include radiative cooling (Wiersma et al., 2009a), star formation (Schaye and Dalla Vecchia, 2008), stellar evolution and chemical enrichment (Wiersma et al., 2009b), kinetic supernovae feedback (Dalla Vecchia and Schaye, 2008) and feedback from supermassive black holes (Springel et al., 2005; Booth and Schaye, 2009). The simulations employ a flat ΛCDM cosmology with parameters $h = 0.73$, $\Omega_b = 0.0418$, $\Omega_m = 0.238$, $\Omega_\Lambda = 0.762$ and $\sigma_8 = 0.74$ that are taken from the analysis of 3-year results of

WMAP (Spergel et al., 2007). The entropy and temperature measurements of galaxy groups in OWL simulations are taken from McCarthy et al. (2010) where ~ 200 galaxy groups are selected by applying a mass criterion of $M_{200c} > 10^{13}$ M$_\odot$. The temperature and electron density profiles are obtained by emission-weighting the gas properties, and the entropy measurements are obtained by combining the temperature and electron density measurements.

They ran their simulations two times. In their first run (AGN run), they included all the sub-grid physics listed above, and in their second run (REF run), they turned off the AGN feedback. Both runs are indistinguishable in all aspects, with the only difference being that the former includes feedback from supermassive black holes as prescribed in (Booth and Schaye, 2009). We refer the reader to Schaye et al. (2010) and McCarthy et al. (2010) for further details on the OWL simulations and the measurements of the thermodynamic properties of the galaxy groups in OWLS.

3.6.4   Comparisons of Observations with OWL, MillenniumTNG and Magneticum Simulations

A fair comparison between simulations and observations is only possible when the compared samples are subject to a similar selection and the simulated temperatures are weighted with a well-calibrated temperature weighting scheme that would reproduce the observed spectroscopic-like temperatures. We achieve this by using the eROSITA selection function that is obtained by applying the same cleaning procedure described in Sect. 3.2 to the mock catalogs from the eROSITA's digital twin (Seppi et al., 2022). The eRASS1 selection function, encapsulating the selection and cleaning information, provides detection probabilities of the group- and cluster-scale dark matter haloes as a function of M_{500c} and z (see Clerc et al., 2024, for details). The selection function obtained through this procedure is applied to the MillenniumTNG and Magneticum clusters and groups, and the entropy profiles of the simulated samples are measured at the three characteristic radii. Furthermore, the spectroscopic-like characteristic temperatures, $T(r < r_{500c})$, are obtained by weighting and projecting the simulated 3D temperature profiles of MillenniumTNG and Magneticum haloes, using the temperature weighting scheme calibrated for eROSITA (ZuHone et al., 2023). Lastly, we compare the entropy and characteristic temperature measurements of simulated groups with the observations.

Before comparing our results with the simulations employing different AGN feedback implementations, we first test the reference (REF) run of the OWL simulations of McCarthy et al. (2010) with the observations. The predictions of the REF run serve as a baseline simulation and can be used to test the overall impact of the AGN feedback on the entropy profiles and characteristic temperatures of groups (Schaye et al., 2010). Their REF run is performed with their full model, identical to their final run, but does not include AGN feedback. To have a fair comparison, we convert the core-excised characteristic temperature measurements in simulations ($T(0.15r_{500c} < r < r_{500c})$) to the core-included temperatures, $T(r < r_{500c})$, following the same approach presented in Sect. 3.5. After the correction, we compare our measurements and the predictions of the REF run of the OWL simulations at the three characteristic radii, as shown in Fig. 3.13. We find that the main visible effect of AGN feedback is to lift the entropy values of
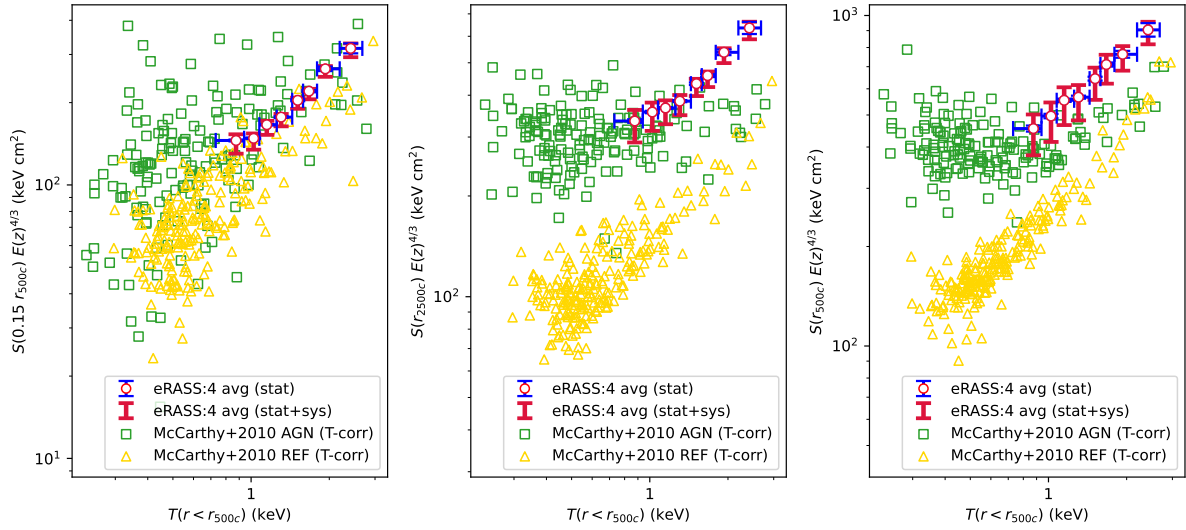
Figure 3.13: Comparison between the redshift evolution scaled average eROSITA entropy measurements (white circles) with the predictions of the REF (AGN feedback off) and AGN (AGN feedback on) runs of OWL simulations (yellow triangles and green squares) presented in McCarthy et al. (2010) at three radii ($0.15r_{500c}$, r_{2500c}, r_{500c}) as a function of characteristic temperature, $T(r < r_{500c})$. Blue error bars represent the statistical uncertainties of the average measurements, and the red error bars represent the overall error budget resulting from the statistical and systematic uncertainties (see Sect. 3.4 for the details of the accounted systematics). For consistency, core-excised temperatures presented in McCarthy et al. (2010) are converted to core-included temperatures (see Sect. 3.6 for the details of the correction).

the groups outside the core (e.g., at r_{2500c} or r_{500c}) for all groups, with a more marked effect at the lowest temperatures. The excess entropy induced by the AGN feedback in observations leads to significant disagreement between our measurements and the predictions of their REF run outside the core. On the other hand, the consistency with the AGN run (the twin simulations of the REF run, but the AGN feedback is turned on) suggests that the observations significantly favor the presence of strong AGN feedback in galaxy groups. It can further be seen from Fig. 3.13 that at the core $0.15r_{500c}$, the data points of McCarthy et al. (2010) for the AGN feedback run are indistinguishable from data points of the reference run, and their results agree well with ours at this radius. Contrarily, outside the core (at r_{2500c} or r_{500c}), the reference and the feedback runs are significantly different at the low-temperature parameter space, indicating the strong AGN feedback imprint. This suggests that the entropy measurements at the core probe the AGN feedback much less efficiently than those outside the core at the group scale haloes, which is also shown in McCarthy et al. (2010) for core-excised quantities. We note that the agreement at the core of groups between the reference and AGN feedback runs are obtained from the OWL simulations, where a thermal AGN feedback model is implemented. It is unclear whether such a conclusion would hold true for simulations implementing a feedback model that includes both kinetic and thermal feedback that leads to significant turbulent stirring in the core, such as MillenniumTNG. Therefore, to verify the universality of the conclusion, further tests are required to be conducted in the future on simulations implementing kinetic and thermal feedback.

After comparing our measurements with the (REF) run of the OWL simulations, we compare our results with the three simulations employing different AGN feedback implementations: Magneticum, MillenniumTNG, and OWL (AGN run). The comparison between our measurements and the predictions of the simulations at the three characteristic radii is shown in Fig. 3.14.

At the cores of groups ($0.15r_{500c}$), we find the eROSITA observations agree relatively well with the OWL simulations between the IGrM temperatures $T = 0.73 - 1.79$ keV whereas at the warmer IGrM temperatures $T = 1.79 - 2.68$ keV the observations fall above their predictions. We further find that the Magneticum and MillenniumTNG simulations overpredict the average entropy for the cool/lower-mass groups ($T = 0.73 - 1.44$ keV), whereas the agreement becomes better in the MillenniumTNG at the warmer IGrM temperatures, close to the cluster ICM temperature range. Even though our measurements disagree with the average entropy predictions of Magneticum and MillenniumTNG, our measurements still lie within the 1σ scatter of the simulated profiles.

At the mid-region of groups (r_{2500c}), the entropy measured by eROSITA agrees well with the Magneticum and OWL simulation for cool/lower-mass groups, whereas the MillenniumTNG simulations underpredict the entropy for the groups in this region at a $\sim 2.5\sigma$ level. We find that our measurements also agree well with the Magneticum simulations for warm/higher-mass groups. Furthermore, we find that as the temperatures/masses of the groups increase ($T > 1.44$ keV) and approach the cluster temperatures/masses, the offset between observations and the predictions of MillenniumTNG and OWL simulations becomes more significant, starting from a statistical disagreement level of 3.5σ at $T = 1.44$ keV and going up to a level of 8.5σ at $T = 2.68$ keV.

At the group outskirts (r_{500c}), we observe an overall agreement between the eROSITA observations and the Magneticum simulations at all temperatures. While the entropy measurements of
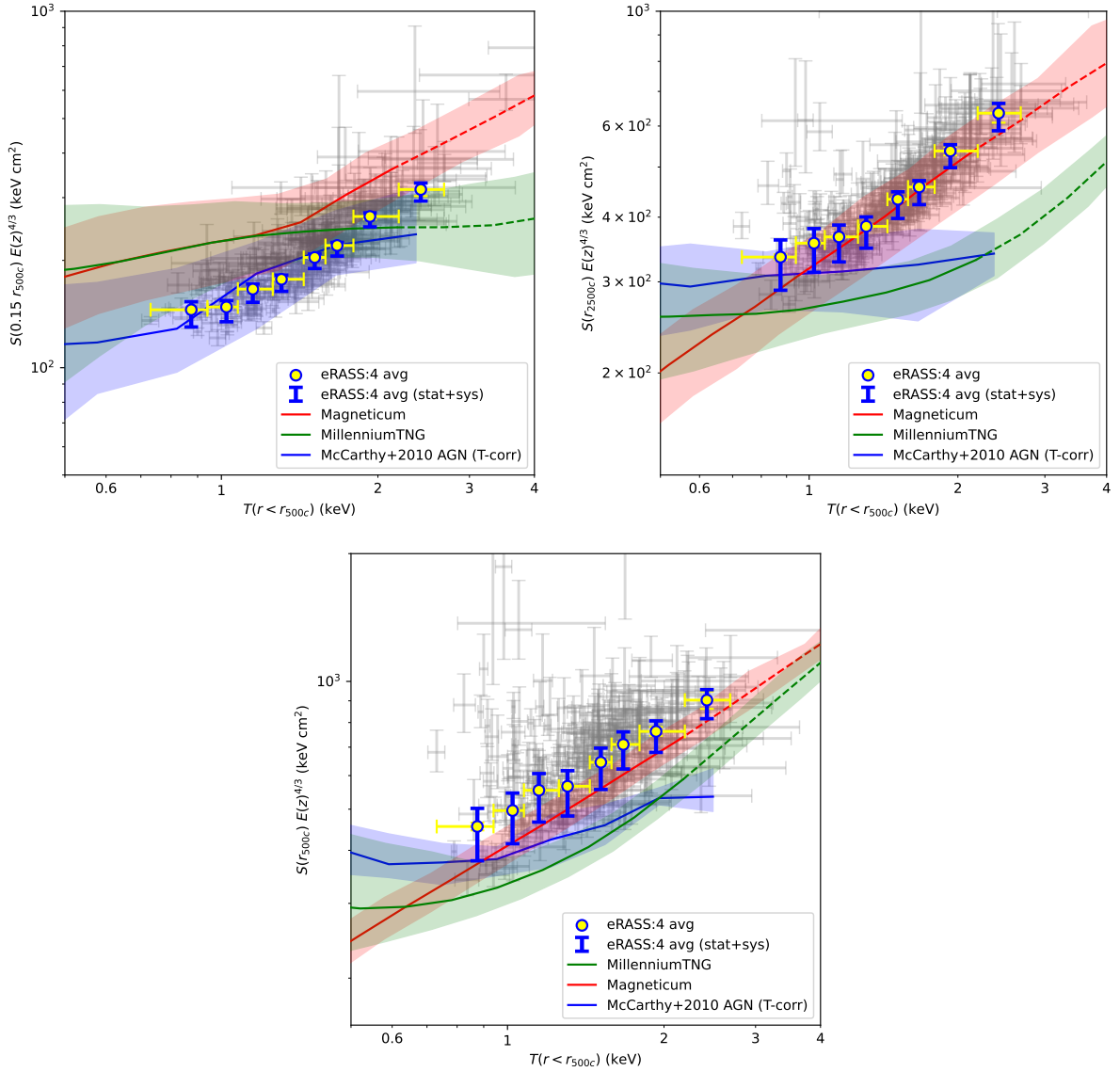
Figure 3.14: Comparison of the redshift evolution scaled average eROSITA entropy measurements (yellow circles) with the predictions of three simulations (Magneticum, MillenniumTNG, and OWL simulations) at $0.15r_{500c}$ (top left), r_{2500c} (top right) and r_{500c} (bottom) as a function of characteristic temperature, $T(r < r_{500c})$. Gray crosses represent the average entropy measurements of the binned groups, and the blue error bars represent the overall error budget of the average measurements resulting from the statistical and systematic uncertainties (see Sect. 3.4 for the details of the accounted systematics). The solid lines represent the predictions of simulations at the group regime ($5 \times 10^{12} < M_{500c} < 10^{14}\ M_{\odot}$), the dashed lines represent the predictions at the low-mass cluster regime ($10^{14} < M_{500c} < 3 \times 10^{14}\ M_{\odot}$) and the shaded regions represent the scatter of the measurements.

galaxy groups in MillenniumTNG simulations are slightly below observations, we find that they are consistent at a 2σ confidence level at all temperatures. Although our measurements are in 1σ agreement with the OWL simulations for cooler/lower-mass groups $T < 1.44$ keV, the departure from observations becomes more significant ($> 2\sigma$) at warmer temperatures, close to the ICM regime.

The AGN feedback implementations in most large-scale simulations are variations of the Springel et al. (2005); Di Matteo et al. (2005) models. Even though similar in spirit, different adaptions and extensions to the original model have been made for the different simulations, leading to a strongly varying impact on the hot gas among the three simulations covered in this Chapter. While the main feature behind the model for the OWL simulation is to achieve an effective AGN feedback by accumulating the injected energy until a ΔT_{heat} is reached, Magneticum and MillenniumTNG introduce a transition from quasar-mode to a stronger radio mode feedback (e.g. see Sijacki et al., 2007; Fabjan et al., 2010) instead. However, while in Magneticum the radio mode feedback is still modeled as a isotropic, thermal feedback with an increased efficiency (e.g., see Hirschmann et al., 2014), in MillenniumTNG it is modeled as a kinetic feedback (e.g., see Pillepich et al., 2018; Weinberger et al., 2017). In addition to these differences, the detailed setting within the individual models can not only significantly change the distribution and properties of gas within galaxies, but also impact the hot gas and especially the entropy within and around clusters and groups (e.g. see figure 3 in Fabjan et al., 2010). Subsequently, in an updated version of the OWL simulations (Le Brun et al., 2014), three different ΔT_{heat} parameters (10^{8}, $10^{8.5}$ and $10^{8.7}$ keV) of the Booth and Schaye (2009) model, coupled with the burstiness and the energeticness of the feedback, are tested. The authors report that ΔT_{heat} can be used to tune the impact of the feedback in the IGrM gas. They further show that for groups, the normalization and slope of the $S - T$ relation (or the $S - M$ relation) does not depend much on ΔT_{heat} at the core ($0.15r_{500c}$). In comparison, an increase in the ΔT_{heat} parameter corresponds to a larger normalization and possibly a different slope at the outskirts (r_{2500c} and r_{500c}) due to the low-entropy gas getting ejected (see Fig. 6 in Le Brun et al., 2014). This can also be seen in Fig. 7 of Le Brun et al. (2014) where the gas gets ejected in the case of more bursty and energetic feedback and results in lower densities at all radii out to $1.6r_{500c}$.

In light of these indications found within simulations, the discrepancy between the observed entropy and the predictions of MillenniumTNG and OWL simulations at the outskirts can be justified by the effectiveness and energetics of the individual AGN feedback models being insufficient to match our observations at the group scale. The weaker AGN feedback found in MillenniumTNG, leading to lower entropy in the outskirts, may also be related to the elimination of the magnetic fields from the TNG physics model, as noted in Pakmor et al. (2023). The agreement between the observations and the Magneticum simulations in the group outskirts suggest that the underlying model is able to effectively treat a broad range in mass, extending the previously reported good agreement of entropy profiles for galaxy clusters (Planelles et al., 2014; Rasia et al., 2015) to group scales.

The agreement between the entropy measurements in eROSITA observations and the numerical simulations at the cores is better than the outskirts. Slightly higher entropy in simulations is harder to explain using the Booth and Schaye (2009) model since the normalization and the shape at the core ($0.15r_{500c}$) do not seem to be affected by the change of the ΔT_{heat} parameter in

the runs presented in Le Brun et al. (2014).

We note that the interpretations above for the OWL simulation assume that the Booth and Schaye (2009) model can reproduce the gas properties by tuning the ΔT_{heat} parameter relatively accurately, which may or may not be the case. Furthermore, as also discussed above, the AGN feedback implementation in MillenniumTNG and Magneticum simulations are even different (among them as well as compared to OWL). For these reasons, a more detailed analysis would be needed to understand better which aspects of the underlying AGN feedback models are driving the differences between the simulations and the eROSITA observations, which is beyond the scope of our study. Furthermore, we note that the selection function we used in this study is a function of mass and redshift, and the use of it significantly improves the robustness of our comparison. In future studies, a profile-dependent selection function can be used that would make the selection procedure applied to the simulations even more realistic. Ultimately, the most accurate comparison would be achieved by producing synthetic eROSITA observations through fully forward modeling cosmological hydrodynamic simulations to which the same detection and data analysis pipeline used for real observations can be applied.

3.7   Conclusions

Our work places the tightest constraints on the impact of AGN feedback on the average thermodynamic properties by populating the low-mass galaxy groups down to cool IGrM temperatures of 0.7 keV. eROSITA's superb sensitivity in the soft X-ray band led to the detection of a large number of galaxy groups with a well-understood selection function. When stacked, the eROSITA data provides unprecedented statistical power for the measurements of X-ray properties of these sources. We use a sample of 1178 galaxy groups to place constraints on the impact of AGN feedback on the thermodynamic properties of the IGrM. We select the galaxy group sample based on the primary sample of the eRASS1 clusters and groups and apply a rigorous selection and cleaning. The cleaning procedure is designed to provide a pure sample with a well-defined selection function while maximizing the sample size. A Bayesian imaging analysis is carried out for all the 1178 galaxy groups in the sample where the nearby clusters and bright point sources are co-fit. The galaxy groups with similar statistical and physical properties, such as count and temperature, are then grouped together into 271 bins. A joint Bayesian spectral fitting is performed on the groups in the same bin to increase the statistical power in each bin with the sources with similar properties.

Constraining baryonic physics at group scales is a highly challenging task. Systematic effects must be considered to achieve a reliable and robust conclusion. We quantify and discuss three major systematics for thermodynamic profile studies and conservatively take them into account for our final measurements and conclusions. Besides the robust thermodynamic property measurements, we also provide a detailed comparison of our findings with the state-of-the-art simulations by accounting for the selection effects. We assess the agreement between our measurements and the simulations employing various AGN feedback implementations to pave the way for a more realistic AGN feedback modeling in numerical simulations.

The study presented in this Chapter is the first in-depth study of galaxy groups with eROSITA

focusing on the impact of AGN feedback on the entropy and temperature measurements within an overdensity radius. The main conclusions of the work presented in this Chapter are as follows:

– With a sample of 1178 galaxy groups and average thermodynamic properties of 271 binned groups, our work stands as the most comprehensive study of the hot gas in galaxy groups in terms of sample size, diversity, and statistics. The selection effects are considered for the first time while comparing the measured thermodynamic profiles of galaxy groups with the numerical simulations.

– Overall, the entropy measurements at three characteristic radii: $0.15r_{500c}$, r_{2500c} and r_{500c} and the characteristic temperature of the galaxy groups detected in the eROSITA first All-Sky Survey observations are in good agreement with the previously reported results in S09 and Johnson et al. (2009) within the uncertainties (see Sect. 3.4). The largest mismatch between the eROSITA measurements presented in our work and the *Chandra* measurements of S09 is at the low-temperature parameter space ($T(r < r_{500c}) < 1.15$ keV). We argue that this is because the completeness and the selection of the two samples being different in this temperature range. The archival sample used in S09 consists mostly of bright and morphologically undisturbed galaxy groups detected in ROSAT observations and followed up by *Chandra*. In contrast, the group sample used in our study has a more uniform and well-defined selection.

– We compare our entropy measurements with the reference (REF) run of OWL simulations that include various non-gravitational processes except the AGN feedback. From this comparison, we conclude that the impact of AGN feedback on the entropy profiles of groups is significant at the outskirts (r_{2500c} and r_{500c}), and less pronounced near the core ($0.15r_{500c}$). This result suggests that for groups, AGN feedback has a larger impact on the outskirts than the core, contrary to its impact on the observed gas properties of clusters of galaxies (Le Brun et al., 2014). Due to their shallower potential wells, the feedback from the central black hole is able to move the low entropy gas to much further radii to the outskirts in galaxy groups.

– Our measurements have significant constraining power on the impact of AGN feedback on the thermodynamic properties of the IGrM gas and serve as a reference for the feedback implementations in numerical simulations and theoretical models. We compare our results with three state-of-the-art cosmological hydrodynamic simulations, MillenniumTNG, Magneticum, and OWL, employing various AGN feedback implementations by accounting for the selection effects. In the cores of the galaxy groups, the entropy agrees well with OWL simulations out to $T = 1.79$ keV. Although the sample averaged entropy from the MillenniumTNG and Magneticum simulations are higher, the measurements within the scatter of the respective simulations. At the outskirts, (r_{2500c} and r_{500c}), the observed entropy agrees well with the Magneticum simulations for groups with IGrM temperatures down to 0.79 keV. In OWL simulations, although we see a similar entropy flattening trend for the cooler groups, the departure from observations becomes significant towards the

galaxy cluster regime at higher temperatures. A similar trend is observed in MillenniumTNG simulations; however, in this case, the entropy offset is relatively significant for all temperature regimes. Overall, the AGN feedback implementation in Magneticum simulations best reproduces our observations at the three characteristic radii.

Our study demonstrates the potential of eROSITA for exploring the baryonic physics at the galaxy groups out to large radii. Deeper data with the eROSITA All-sky Survey survey will allow the detection of a larger sample of galaxy groups pushing down in mass and IGrM temperature floors. Employing these groups in similar future studies with larger statistical power will enable to test hydrodynamical simulations in very cool temperatures below < 0.5 keV, which is currently unreachable with the eRASS1 sample.

Chapter 4

The SRG/eROSITA All-Sky Survey: Thermodynamic Properties of Galaxy Groups

As discussed in previous Chapters, the distribution of the hot plasma in gaseous haloes, as well as its temperature structure, result from the complex interplay between gravity, radiative cooling, and non-gravitational heating (e.g., through AGN feedback). Previous studies suggest that groups exhibit distinctly different thermodynamic profiles compared to clusters, attributed to the shallower potential wells of the former, which make them more sensitive to non-gravitational processes. In this Chapter, we determine the radial thermodynamic profiles of eROSITA-selected galaxy groups using X-ray observations. The work presented in this Chapter builds on that presented in Chapter 3, where we have explored the entropy of the hot gas in groups at three characteristic radii ($0.15r_{500c}$, r_{2500c} and r_{500c}) as a function its characteristic temperature. In this Chapter, we determine the full radial profiles of four thermodynamic properties (namely, density, temperature, entropy, and pressure) relative to their self-similar scales. As in Chapter 3, we measure these observables for 1178 galaxy groups by jointly analyzing their eRASS:4 observations in 271 subsamples. We then normalize their thermodynamic profiles using the predictions of the self-similar model and compare the scaled thermodynamic profiles of our groups with those of clusters. We furthermore compare our measurements with predictions of non-radiative hydrodynamical simulations that serve as baselines to constrain the overall impact of non-gravitational mechanisms. Lastly, we apply the selection function of our sample to two state-of-the-art simulations that have different feedback implementations (Magneticum, MillenniumTNG) and compare their predictions with our measurements. Our profiles establish benchmarks for the impact of non-gravitational processes across a broad radial range and will be instrumental in achieving more realistic cosmological hydrodynamical simulations.

I performed the majority of the work and analysis described in this Chapter. The galaxy group sample and the initial data analysis steps have already been presented in Chapter 3 (see Sect. 4.2 for details), the contents of Chapter 3 were originally published in Bahar et al. (2024).

4.1   Introduction

At $z = 0$, the peak of the halo mass density function falls in the group mass regime (Eckert et al., 2024). This puts galaxy groups in a pivotal place in the hierarchical structure of the universe, making it essential to achieve a good understanding of their astrophysics to achieve an accurate and comprehensive picture of the universe at cosmological scales.

Most of the baryonic matter in galaxy groups is in the form of hot dilute gas called intra-group medium (IGrM), which fills large volumes within the potential well of the group. The processes governing IGrM can be split into two categories: gravitational and non-gravitational, where the former is dictated by the underlying potential well, and the latter arises from the interaction of baryons with each other and their surroundings. As discussed in detail in Sect. 1.4, thermodynamic properties of the IGrM medium serve as a window to the history of heating and cooling processes acting on IGrM, such as cooling through radiation and heating through supernovae, star formation, and AGN feedback. Relatively shallower potential wells of galaxy groups make them ideal laboratories for investigating the dominant heating mechanism for large-scale haloes, active galactic nuclei (AGN) feedback (see Sect. 1.3). The importance of non-gravitational processes for shaping properties of the large-scale structure is well acknowledged such that they are implemented in almost all modern cosmological hydrodynamical simulations. However, the energetics and kinematics of the implementation of AGN feedback vastly vary between simulations (e.g., see Oppenheimer et al., 2021) due to the uncertainties on the total energy output and the interaction of AGN with its surroundings. Measurements of thermodynamic properties of galaxy groups put constraints on these mechanisms that serve as references to tune and improve implementations of these mechanisms in simulations.

Measurements of the integrated gas content of galaxy groups as a function of the total mass revealed that groups appear to be gas depleted within an overdensity radius of r_{500c} compared to the average baryon density of the universe (e.g., Sun et al., 2009; Ettori, 2015; Lovisari et al., 2015). This is argued in the literature to be due to the fact that feedback from AGN pushes away gas in groups more easily out to large radii (beyond r_{500c}) compared to clusters. Thus, the gas mass fraction (f_{gas}) measurements of groups are lower than the ones observed for the clusters (e.g., see Fig. 7 in Eckert et al., 2021). These measurements serve as strong evidence that the impact of AGN feedback on the thermodynamic properties of galaxy groups reaches large radii, even beyond r_{500c}. This is also confirmed by simulations where the gas pushed out from the inner regions is observed to be expelled to very large radii (e.g., see Fig. 3 of Ayromlou et al., 2023). Therefore, accurate measurements of the profiles of thermodynamic properties out to large radii are key to constraining the impact of feedback from AGN and improving our knowledge of feedback energetics and kinematics.

There are a limited number of studies in the literature that investigate profiles of thermodynamic properties of groups with large samples. Sun et al. (2009) stands as the most recent study that investigates thermodynamic profiles of groups with a moderately large sample. Sun et al. (2009) analyzed deep *Chandra* observations of 43 nearby groups and measured electron density (n_{e}), temperature (T[1]), entropy (S), and pressure (P) profiles of them. Through their analysis,

---

[1]Throughout this Chapter, we use the notation T to represent $k_B T$ and express temperature measurements in

they were able to reliably measure profiles of 23 groups in their sample out to r_{500}. They also normalized their entropy profiles with the self-similar scale (see Sect. 4.3.1 for details of the self-similar scale) and compared their scaled entropy measurements with the baseline profiles of Voit (2005) for self-similar clusters obtained from non-radiative hydrodynamical simulations that do not include AGN and stellar feedback. They also normalized their pressure profiles with the self-similar scales and reported them in a follow-up paper (Sun et al., 2011), where they found good agreement with the "universal" pressure profile of Arnaud et al. (2010) for clusters after removing deviations from self-similarity.

Significantly more studies in the literature investigate the scaled thermodynamic properties of galaxy clusters (e.g., Arnaud et al., 2010; Eckert et al., 2012; McDonald et al., 2014; Ghirardini et al., 2019; Sanders et al., 2021). These studies analyze moderately large samples of galaxy clusters and provide scaled[2] "universal" profiles for their thermodynamic properties. A comparison between the scaled profiles of clusters and the scaled profiles of groups reveals the mass evolution of the impact of non-gravitational processes. eROSITA (Predehl et al., 2021) opened a new window for measuring the thermodynamic properties of groups by providing high-quality X-ray observations for large group samples (e.g., see the galaxy group sample introduced in Chapter 3). The large field of view and superb soft band sensitivity of eROSITA make it the ideal instrument for studying low redshift groups that are well-extended in the sky and shine brightly in the soft X-ray band.

The Chapter is organized as follows: In Sect. 4.2, we provide a brief overview of the galaxy group sample used in this study and the X-ray data reduction and analysis procedures employed to obtain their n_e and T profiles. In Sect. 4.3, we provide our measurements for the profiles of thermodynamic properties, and in Sect. 4.3.1, we provide our measurements for the scaled profiles. In Sect. 4.4, we provide a comparison between our measurements and the results in the literature for clusters and groups. In Sect. 4.5, we provide a comparison between our measurements and the predictions of the numerical simulations. Lastly, in Sect. 4.6, we provide a summary of our findings and list our conclusions.

4.2   Galaxy Group Sample and Data Analysis

The work presented in this Chapter uses the galaxy group sample presented in Chapter 3. The sample is made up of 1178 objects and is selected from the eRASS1 galaxy clusters and groups catalog (Bulbul et al., 2024). A comprehensive description of the sample selection and cleaning procedures is presented in Sect. 3.2. The n_e and T profiles presented in this Chapter are measured the same way as presented in Chapter 3. The data analysis and reduction steps to obtain the n_e and T profiles are described in detail in Sect. 3.3. The uncertainties of the n_e and T profiles presented in this Chapter (Chapter 4) include statistical and systematic uncertainties. The major sources of systematics on our measurements, as well as the procedures followed to quantify their impact on our measurements, are presented and discussed in Sect. 3.4. We refer the reader to

---

units of keV.

[2]The thermodynamic profiles are often normalized in the literature with their self-similar scales. See Sect. 4.3.1 for details.

Chapter 3 for detailed information on the group sample used in this study and the data analysis procedures for obtaining the n_e and T profiles.

4.3 Profiles of the Thermodynamic Properties

In this Chapter, a total of four thermodynamic properties are investigated, with a focus on the variation of these properties as a function of radius and mass. The investigated properties include electron density (n_e), temperature (T), entropy (S), and pressure (P), all of which are measured from X-ray observations. The derivation of the first two quantities is described in Sect. 3.3 and the remaining two are derived from n_e and T following the equations

$$S \equiv T/n_e^{2/3} \tag{4.1}$$

and

$$P \equiv Tn_e \tag{4.2}$$

taking into account the covariances. The profiles of thermodynamic properties so determined are shown in the left column of Fig. 4.1. We note that in Fig. 4.1, the temperature profiles are scaled versions of each other. This is due to the fact that we fixed the shape of the temperature profiles to the average shape of the profiles of the Sun et al. (2009) groups (see Sect. 3.4.1 for the details). Therefore, in this Chapter, we put constraints only on the normalization of the temperature profiles, not on their shapes.

It can be seen from the plots in the left column of Fig. 4.1 that the more massive groups appear to have higher normalizations for n_e, T, S, and P. Such an appearance can be explained by the fact that these observables scale with M according to the corresponding scaling relations. This would not be a surprise for T, S, and P since the self-similar model predicts relatively strong correlations with mass for these observables ($T \propto M^{2/3}E(z)^{2/3}$, $S \propto M^{2/3}E(z)^{-2/3}$ and $P \propto M^{2/3}E(z)^{8/3}$). However, the self-similar model does not predict mass evolution for n_e but only predicts redshift evolution: $n_e \propto E(z)^2$. The redshift evolution should also be accounted for to confirm that the observed picture in the left column of Fig. 4.1 is due to deviations from self-similarity. In the next section, we remove the mass and redshift scales introduced by self-similarity and investigate the normalized thermodynamic profiles of groups in our sample.

4.3.1 Scaled Thermodynamic Profiles

As discussed in Chapter 1, in the simple spherical collapse scenario, gaseous halos are expected to be scaled versions of each other. In the absence of non-gravitational mechanisms, this scaling is solely determined by gravity, such that the profiles of galaxy clusters and groups only differ from each other with respect to their intrinsic scales that depend on masses and redshifts of the halos and the underlying cosmology. These are referred to in the literature as the self-similar scales (Kaiser, 1986; Voit, 2005) and can be used to normalize measured thermodynamic profiles and investigate the impact of non-gravitational processes (e.g., radiative cooling, stellar feedback, and AGN feedback). Besides the mass and the redshift of the halo, self-similar scales also vary
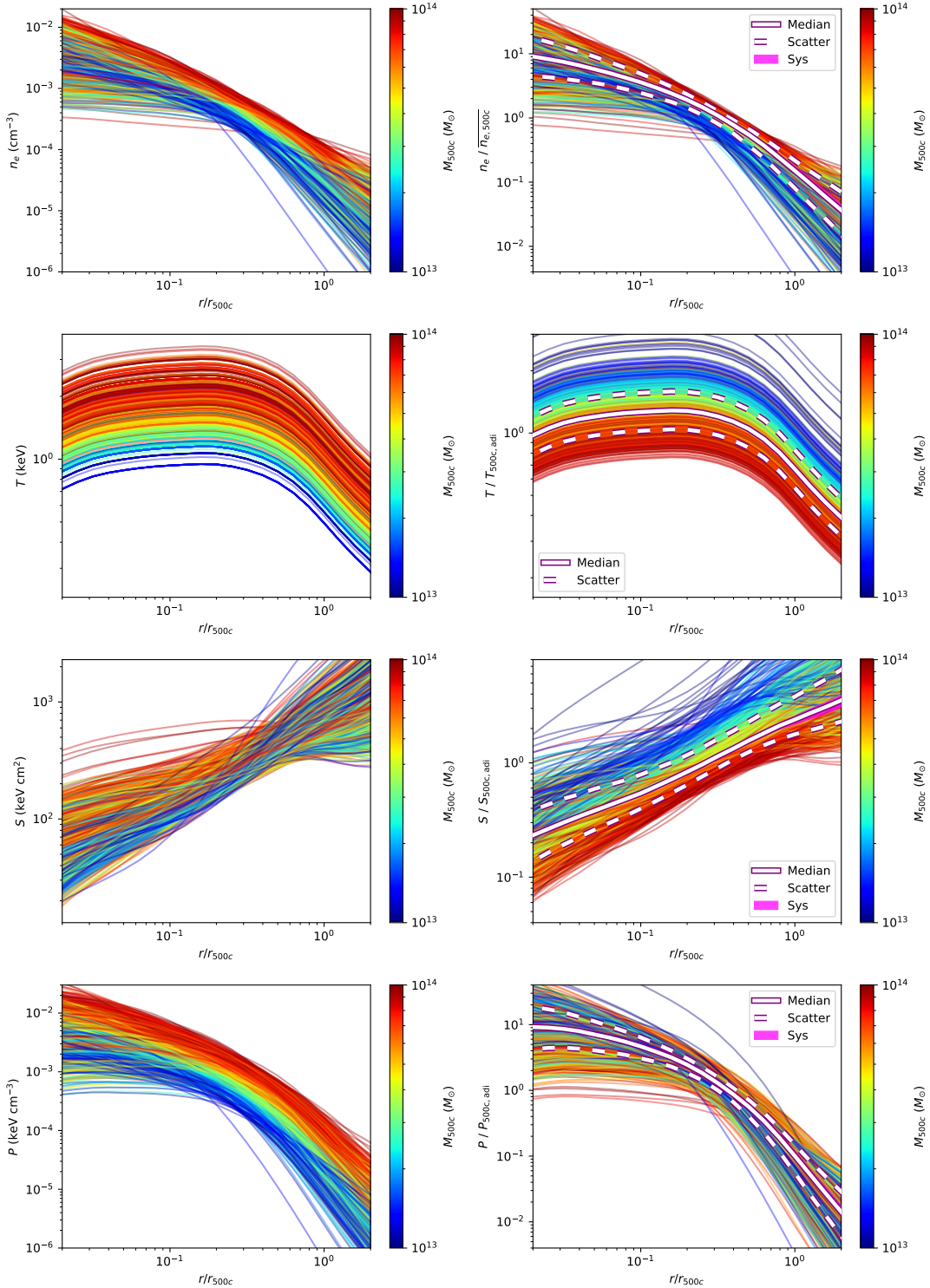
Figure 4.1: *Left:* n_e, T, S and P profiles of the groups in our sample. *Right:* $n_e/\overline{n_{e,\Delta}}$, $T/T_{\Delta,\mathrm{adi}}$, $S/S_{\Delta,\mathrm{adi}}$ and $P/P_{\Delta,\mathrm{adi}}$ profiles. The colors of the lines indicate the masses. The colorbar is cut at $M_{500c} = 10^{13}\,M_\odot$ for visual purposes. Groups with masses lower than $M_{500c} = 10^{13}\,M_\odot$ are shown with dark blue. The median scaled profiles are shown with solid white lines (with purple outline), and the 16th and 84th percentiles of the profiles are shown with dashed white lines (with purple outline). The systematic uncertainties of the median are shown with magenta-shaded areas (see Sect. 3.4 for details of the systematic uncertainties).

as a function of density contrast (Δ) that determines the radius within which the properties are calculated, r_Δ (see Eq. 1.14 for the definitions and the relationship between Δ and r_Δ).

Following the notation in Sun et al. (2009), we denote these cosmological scales as $\overline{n_{e,\Delta}}$, $T_{\Delta,\text{adi}}$[3], $S_{\Delta,\text{adi}}$ and $P_{\Delta,\text{adi}}$ for electron density, temperature, entropy and pressure respectively, to avoid confusion with the measured quantities (e.g., T_{500c}, S_{500c}, P_{500c}). Furthermore, following the derivation for $\overline{n_{e,200c}}$ and $T_{200c,\text{adi}}$ in Voit (2005), we derive formulations of these scales while explicitly keeping the dependencies on various assumed parameters, such as the cosmological constants, density contrast, or mean molecular weights, to allow future work to calculate self-similar scales by using their assumed parameters and consistently compare with our results. The derivation of the self-similar scales for n_e, T, S, and P is as follows.

The average electron density within an overdensity radius r_Δ can be calculated as $\overline{n_{e,\Delta}} \equiv \Delta \rho_c f_b / \mu_e m_p$ where f_b is the baryon fraction, μ_e is the mean molecular weight per electron and m_p is the proton mass. This equation can be further expanded using the definition of critical density (see Footnote 5 in Chapter 1) such that the final form of $\overline{n_{e,\Delta}}$ can be written as

$$\overline{n_{e,\Delta}} \equiv 1.54 \times 10^{-4} \text{ cm}^{-3} E(z)^2 \left(\frac{f_b}{0.16}\right)\left(\frac{\mu_e}{1.14}\right)^{-1}\left(\frac{h}{0.7}\right)^2\left(\frac{\Delta}{200}\right). \tag{4.3}$$

Furthermore, the temperature of a self-similar gaseous halo can be calculated as $T_{\Delta,\text{adi}} \equiv GM_\Delta \mu m_p / 2r_\Delta$ where G is the gravitational constant and μ is the mean molecular weight per particle. This equation can be rewritten using the definition of r_Δ (Eq. 1.14) such that the final form of $T_{\Delta,\text{adi}}$ can be written as

$$T_{\Delta,\text{adi}} \equiv 1.41 \text{ keV} \left(\frac{M_\Delta}{10^{14}M_\odot}\right)^{2/3} E(z)^{2/3}\left(\frac{\mu}{0.6}\right)\left(\frac{h}{0.7}\right)^{2/3}\left(\frac{\Delta}{200}\right)^{1/3}. \tag{4.4}$$

Lastly, the expressions above for $\overline{n_{e,\Delta}}$ and $T_{\Delta,\text{adi}}$ can be combined using Eqs. 4.1 and 4.2 and the self-similar scales for S and P can be obtained as

$$S_{\Delta,\text{adi}} \equiv 489 \text{ keV cm}^2 \left(\frac{M_\Delta}{10^{14}M_\odot}\right)^{2/3} E(z)^{-2/3}\left(\frac{f_b}{0.16}\right)^{-2/3}\left(\frac{\mu}{0.6}\right)\left(\frac{\mu_e}{1.14}\right)^{2/3}\left(\frac{h}{0.7}\right)^{-2/3}\left(\frac{\Delta}{200}\right)^{-1/3} \tag{4.5}$$

and

$$P_{\Delta,\text{adi}} \equiv 2.17 \times 10^{-4} \text{ keV cm}^{-3} \left(\frac{M_\Delta}{10^{14}M_\odot}\right)^{2/3} E(z)^{8/3}\left(\frac{f_b}{0.16}\right)\left(\frac{\mu}{0.6}\right)\left(\frac{\mu_e}{1.14}\right)^{-1}\left(\frac{h}{0.7}\right)^{8/3}\left(\frac{\Delta}{200}\right)^{4/3}. \tag{4.6}$$

In this Chapter, we assume $\{0.5994, 1.1548, 0.6774, 0.1573\}$ for the parameters $\{\mu, \mu_e, h, f_b\}$ respectively (Asplund et al., 2009; Planck Collaboration et al., 2016).

---

[3]The subscript "adi" stands for adiabatic. Non-radiative gaseous haloes that are not subject to non-gravitational heating are often called in the literature "adiabatic clusters".

Scaled n_e, T, S, and P profiles of the galaxy groups in our sample are shown in the right column of Fig. 4.1. It can be seen that the normalizations of the profiles have a mass dependence even after the profiles are scaled with their self-similar predictions. Furthermore, it can be seen that outside the core ($r > 0.2r_{500c}$), the mass dependence is more evident, whereas, at the core ($r < 0.2r_{500c}$), the profiles become more diverse and the dependence on mass appears to be weaker. The reason for the observed diversity at the core is likely due to the fact that, similar to clusters, gas profiles of groups exhibit diverse cool-core/non-cool-core and AGN feedback characteristics in their central regions.

It can be seen in the $n_e/\overline{n_{e,\Delta}}$ plot of Fig. 4.1 that outside the core ($r > 0.2r_{500c}$), normalizations of the scaled density profiles reduce with decreasing mass. Such a dependence indicates that the gas mass fractions of groups ($f_{gas} \equiv M_{gas}/M_{500c}$) decrease as a function of mass. This is in agreement with previous studies reporting that within r_{500c}, low mass haloes (e.g., groups) have lower f_{gas} compared to higher mass haloes (e.g., clusters) (Sun et al., 2009; Lovisari et al., 2015; Ettori, 2015). The current understanding of this phenomenon suggests that gas depletion in lower mass halos (e.g., groups) is primarily driven by AGN feedback that expels gas more efficiently from groups compared to clusters due to their shallower gravitational potential wells (Ayromlou et al., 2023).

Furthermore, it can be noticed by comparing the T and $T/T_{\Delta,\text{adi}}$ profiles in Fig. 4.1 that normalizing temperature profiles with their self-similar predictions inverts the mass dependence such that after the normalization, the lower mass groups lie above and higher mass groups lie below the median. This suggests that the scaling exponent (B_{tm}) of the $T - M_{500c}$ relation ($T \propto (M_{500c})^{B_{tm}}$) for our group sample is lower than the self-similar prediction ($B_{tm,\text{self}} = 2/3$). However, it should be noted that our masses are estimated using an $L_X - M_{500c}$ scaling relation, $L_X \propto (M_{500c})^{1.44}$, which is calibrated using eROSITA observations (Chiu et al., 2022). The M_{500c} term in this equation can be substituted using the general form of the $T - M_{500c}$ relation, and the scaling between L_X and T can be obtained as $L_X \propto (T)^{1.44/B_{tm}}$. Therefore effectively, our finding of $B_{tm} < 2/3$ implies $B_{lt} > 2.16$ where B_{lt} is the the scaling exponent of the $L_X - T$ relation. This is in agreement with recent studies that found a scaling exponent of $B_{lt} \sim 2.9$ (Giles et al., 2016; Molham et al., 2020; Bahar et al., 2022), which is significantly larger than 2.16 and the self-similar prediction for the $L_X - T$ relation for groups ($B_{lt,\text{self}} \sim 1.12$ for $T = 0.7 - 2.0$, Lovisari et al., 2021). Nevertheless, to accurately quantify the deviation of the $L_X - T$ relation of groups from the self-similar prediction, a dedicated scaling relations study should be performed within which the selection effects and the mass function are accounted (e.g., as done in Chapter 2 for eFEDS).

Furthermore, investigating measured entropy profiles (S) and the scaled entropy profiles ($S/S_{\Delta,\text{adi}}$) is particularly interesting for this study since the feedback mechanisms (e.g., AGN and/or stellar feedback) provide excess entropy to the system over the self-similar predictions by heating the gas and pushing it away to larger radii. Even though the self-similar model predicts $S \propto (M_{500c})^{2/3}$, the $S - r/r_{500c}$ plot in Fig. 4.1 shows no clear mass trend for the normalizations of the profiles as observed for n_e, T and P. The lack of mass trend in the entropy profiles results manifests itself as a clear mass trend in the scaled entropy profiles. It can be seen from the $S/S_{500c,adi}$ plot in Fig. 4.1 that the non-gravitational mechanisms raise the scaled entropy profiles of lower mass groups to the values larger than the higher mass ones. This is in agreement
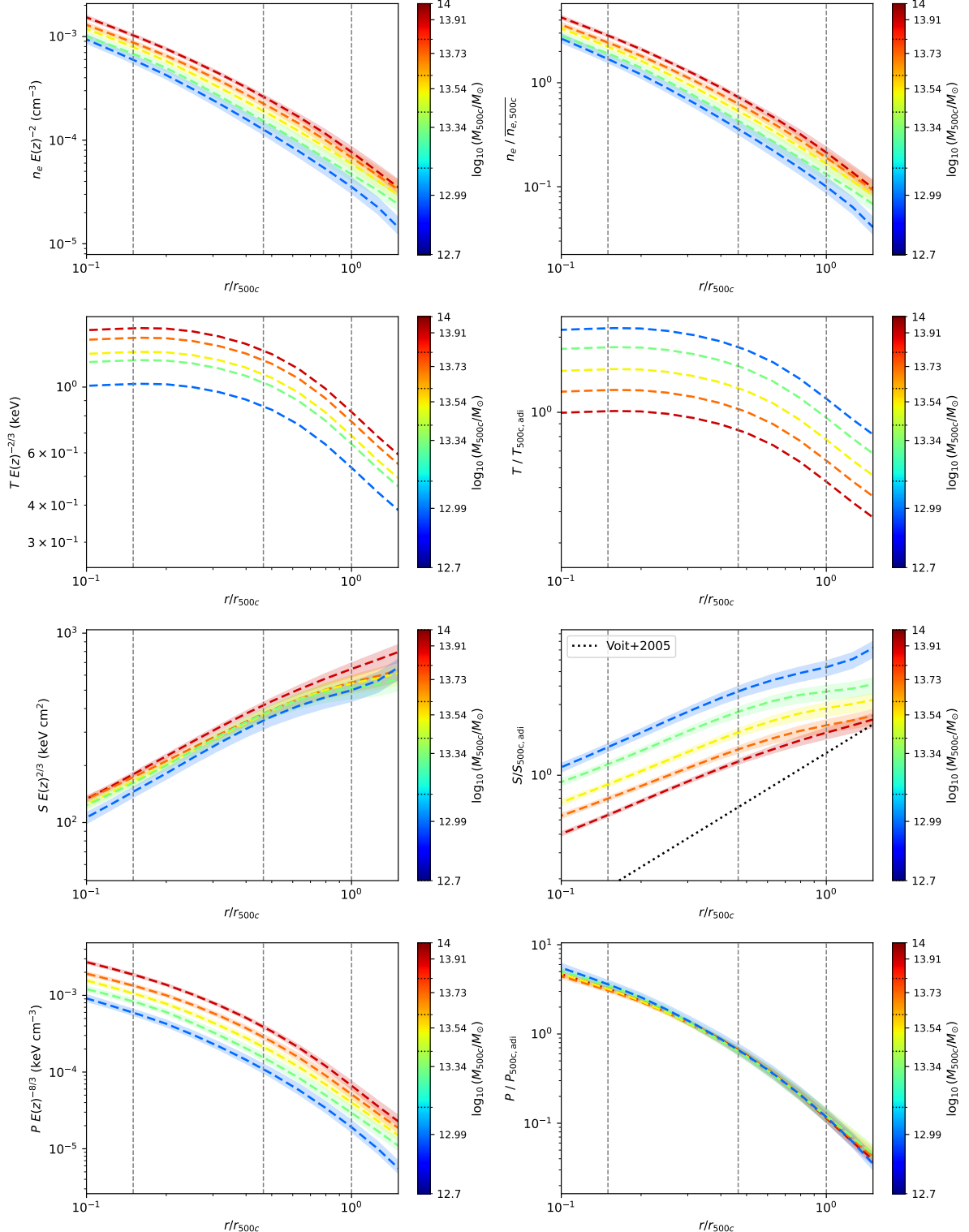
Figure 4.2: Error weighted average thermodynamic profiles of the mass binned groups. Edges of the bins, {12.7, 13.13, 13.42, 13.61, 13.81, 14.0}, are shown as horizontal dotted lines, and the average mass of the bin is marked with ticks. The shaded areas represent the systematic uncertainties of the average profiles (see Sect. 3.4 for the details on the systematic uncertainties). The vertical grey dashed lines indicate the three characteristic radii ($0.15r_{500c}$, r_{2500c} and $0.15r_{500c}$) used in Chapter 3. *Left:* Average $n_e E(z)^{-2}$, $TE(z)^{-2/3}$, $SE(z)^{2/3}$ and $PE(z)^{-8/3}$ profiles of the groups in the mass bins. *Right:* Average $n_e/\overline{n_{e,\Delta}}$, $T/T_{\Delta,\mathrm{adi}}$, $S/S_{\Delta,\mathrm{adi}}$ and $P/P_{\Delta,\mathrm{adi}}$ profiles of the groups in the mass bins.

with the current understanding in the literature suggesting that the gas properties of lower mass haloes, such as groups, should be affected more significantly by AGN feedback than the higher mass haloes, such as clusters (Eckert et al., 2021). This effect is also very evident when we compare our profiles with the literature measurements of clusters in Sect. 4.4 and with simulations in Sect. 4.5.

It can be seen in Fig. 4.1 that once the pressure profiles of the groups in our sample are scaled with their self-similar predictions ($P_{\Delta,\mathrm{adi}}$), the mass trend for the normalizations of the profiles disappears. This indicates that the normalizations of the pressure profiles of galaxy groups scale the same as predicted by the self-similar model ($P \propto (M_{500c})^{2/3}$). This appears to be due to the fact that the mass dependence of the scaled profiles for n_e and T ($n_\mathrm{e}/\overline{n_{\mathrm{e},\Delta}}$ and $T/T_{\Delta,\mathrm{adi}}$) cancel each other out, such that the normaliations of the scaled pressure profiles, $P/P_{\Delta,\mathrm{adi}} = (T/T_{\Delta,\mathrm{adi}})(n_\mathrm{e}/\overline{n_{\mathrm{e},\Delta}})$, has no mass dependence. Nonetheless, it should be noted that the normalizations of the pressure profiles scaling the same as predicted from the self-similar model does not mean the pressure profiles are in agreement with the self-similar pressure profiles (e.g., for groups without radiative cooling, AGN feedback, and stellar feedback). In fact, we found that neither the shapes nor the normalizations of the scaled pressure profiles of groups are in agreement with the self-similar pressure profiles when we compare the profiles with the predictions of non-radiative simulations that do not include feedback mechanisms in Sect. 4.5.

To further investigate the mass dependence of the normalization outside the core ($r > 0.1r_{500c}$), we removed the redshift evolution from the n_e, T, S and P profiles, bin groups according to their masses and obtain (error-weighted) average profiles for each bin. Moreover, we applied the same binning scheme to the scaled profiles and obtained average thermodynamic profiles for the bins. The average profiles obtained from this procedure are presented in Fig. 4.2. The shaded areas shown in this figure represent the total error budget of the averages that include the statistical and systematic uncertainties (see Sect. 3.4). We use a total of five mass bins to investigate the mass dependence of the profiles. The average masses of the five bins are marked with ticks, and the edges of the mass bins are marked with horizontal dotted lines on the color bar. It should be noted that the average masses of the top four bins are roughly equally spaced with each other; however, to have enough groups in the lowest mass bin, we made it larger. This difference should be kept in mind while drawing conclusions from this figure.

The mass trends of the normalizations of the profiles discussed above can also be seen from the binned profiles in Fig. 4.2. The gas depletion, inverted mass dependence of the scaled T profiles, increasing entropy profiles with decreasing mass, and the self-similar appearance of the pressure profiles can easily be seen in the $n_\mathrm{e}/\overline{n_{\mathrm{e},\Delta}}$, $T/T_{\Delta,\mathrm{adi}}$, $S/S_{\Delta,\mathrm{adi}}$ and $P/P_{\Delta,\mathrm{adi}}$ plots. It can be further noticed that the lowest mass bin has a slightly steeper density profile. We argue that this can be explained by the fact that, close to the detection threshold of the survey (e.g., for the faintest, lowest mass haloes), it is easier for the eROSITA detection pipeline to detect groups with peaky profiles. This interpretation is in agreement with the findings of Clerc et al. (2024), where they show that the central emission measure (EM_0) plays a non-negligible role in the detection of clusters and groups with eROSITA. We note that this has a negligible impact on the other results presented in this Chapter since the bulk of our sample is above the detection threshold. For the lowest mass bin, the observed trend can be corrected by using a section function that takes the steepness of the profile also as input (e.g., as will be presented in the Sanders et al., in prep.).

Nonetheless, this does not have a significant impact on the scaled entropy and pressure profiles such that their shape appears to be constant across the probed mass range.

4.4   Comparison with Previous Measurements

In this section, we compare the scaled n_e, T, S, and P profiles of our sample with the latest measurements available in the literature. Comparing our measurements with previous results for groups is challenging due to the limited number of studies reporting profiles of thermodynamic properties for moderately large group samples. Therefore, for galaxy groups, we only compare our results with the scaled entropy ($S/S_{\Delta,\text{adi}}$) and scaled pressure ($P/P_{\Delta,\text{adi}}$) profiles presented in Sun et al. (2009) and Sun et al. (2011) from the analysis of deep *Chandra* observations of 43 groups. Given that the scaled entropy and pressure profiles presented in these studies were obtained from the same analysis (the analysis is described in Sun et al., 2009), we self-consistently combine them and obtain scaled electron density ($n_e/\overline{n_{e,\Delta}}$) and scaled temperature ($T/T_{\Delta,\text{adi}}$) profiles as

$$\frac{n_e}{\overline{n_{e,\Delta}}} = \left(\frac{S}{S_{\Delta,\text{adi}}}\right)^{3/5} \left(\frac{P}{P_{\Delta,\text{adi}}}\right)^{-3/5} \tag{4.7}$$

and

$$\frac{T}{T_{\Delta,\text{adi}}} = \left(\frac{S}{S_{\Delta,\text{adi}}}\right)^{2/5} \left(\frac{P}{P_{\Delta,\text{adi}}}\right)^{3/5}. \tag{4.8}$$

Nevertheless, as also described in Chapter 3, the results reported in these studies cannot be directly compared with ours. This is due to the fact that there are systematic mismatches between studies (e.g., assumed cosmology) that need to be accounted for to make a fair and accurate comparison. Therefore, we applied a set of corrections to the scaled profiles presented in Sun et al. (2009) and Sun et al. (2011) before comparing them with our results. The corrections we applied to these measurements are described below.

It can be seen from Eqs. 4.3, 4.4, 4.6 and 4.5 that the self-similar entropy scales have a strong dependence on cosmology through h and f_b. However, the measurements of these observables have different dependencies on cosmology (e.g., $n_e \propto h^{1/2}$, $S \propto h^{-1/3}$, and $P \propto h^{1/3}$). Therefore the normalizations of the scaled profiles are cosmology dependent. In Sun et al. (2009) and Sun et al. (2011), significantly different cosmological constants ($h = 0.73$ and $f_b = 0.165$) are assumed compared to our study. We brought the Sun et al. (2009) and Sun et al. (2011) results to our cosmology by applying appropriate h and f_b corrections.

Furthermore, the profiles presented in Sun et al. (2009) and Sun et al. (2011) are obtained by using an old version (v1.3.1) of the plasma atomic database, `AtomDB`. It is reported both in Sun (2012) and Lovisari et al. (2015) that the use of a more recent version (v2.0.1) of the atomic database results in a $\sim 15\%$ increase in the temperature measurements of plasma that has $T(r < r_{500c}) < 2$ keV (see Sect. 3.4.4 for the details). This has direct implications for the scaled
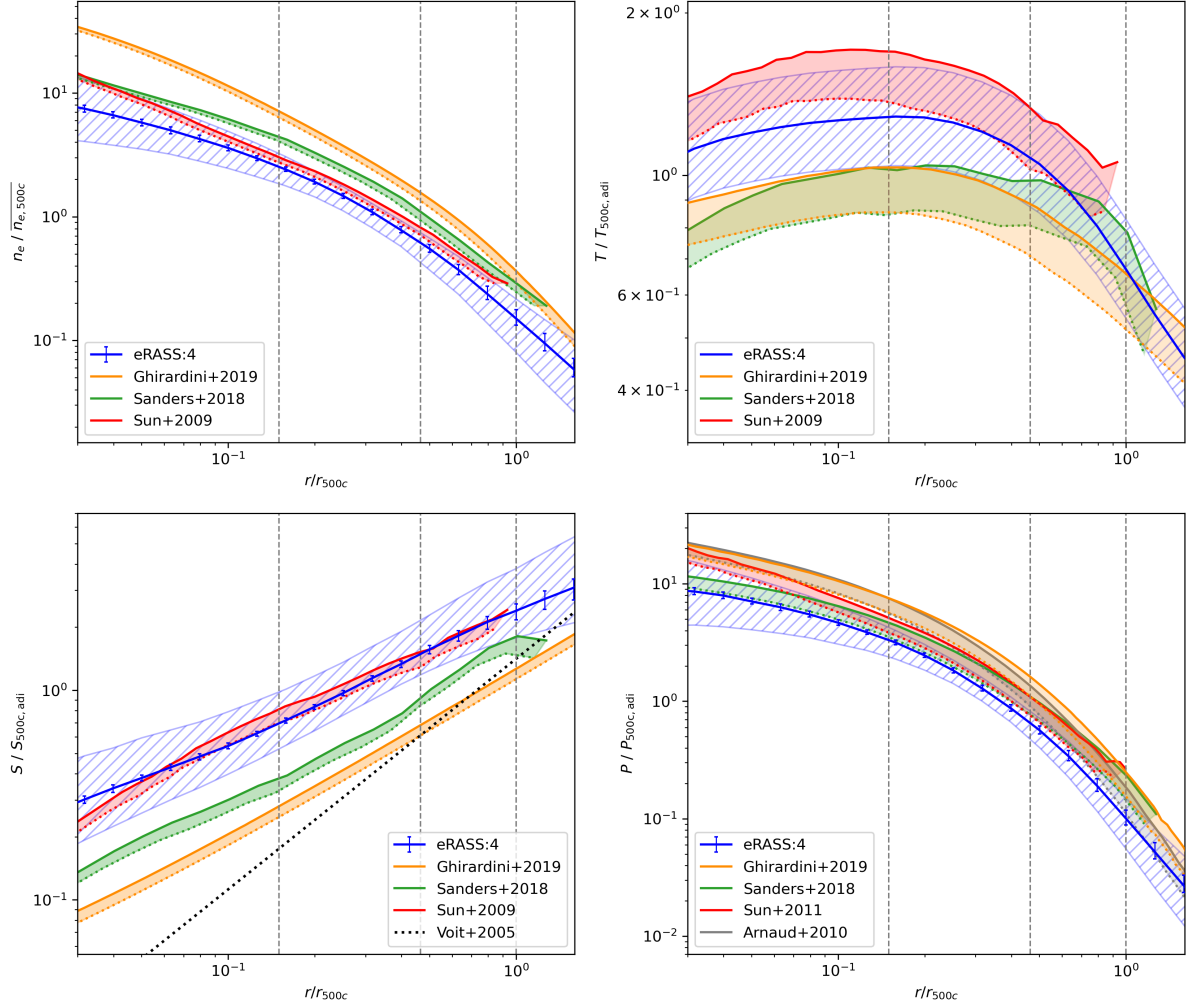
Figure 4.3: Comparison of the median scaled profiles ($n_e/\overline{n_{e,\Delta}}$, $T/T_{\Delta,\text{adi}}$, $S/S_{\Delta,\text{adi}}$ and $P/P_{\Delta,\text{adi}}$) measured in this study (blue) with the results in the literature for groups (red) and clusters (orange and green). The blue error bars represent the systematic uncertainties of the median eRASS:4 profiles (see Sect. 3.4 for the details on the systematic uncertainties), and the blue hatched area represents the scatter. The systematic uncertainty of the literature measurements resulting from hydro-mass bias is shown with red, green, and orange shaded areas. The baseline profile of Voit (2005) is plotted with black dotted lines, and the universal scaled pressure profile of Arnaud et al. (2010) is shown with grey solid and dotted lines. The solid lines for the literature results represent measurements before correcting hydro-mass bias and the dotted colorful lines represent the measurements after correcting hydro-mass bias. The vertical grey dashed lines indicate the three characteristic radii ($0.15r_{500c}$, r_{2500c} and $0.15r_{500c}$) used in Chapter 3.

profiles since the masses measured in Sun et al. (2009) are obtained by using the hydrostatic equilibrium equation where the total mass of the halo scales as $M \propto T$. We found that 19 of the 43 groups analyzed in Sun et al. (2009) has $T(r < r_{500c}) < 2$ keV. This corresponds to the average mass correction of 6% $((1.15 \times 19 + 24)/43 = 1.06)$ that we used to correct the profiles. After this correction, the median mass of the Sun et al. (2009) sample became $M_{500c} = 9 \times 10^{13}$ $M_{\odot}$.

The masses employed in this study are found to be ~ 1.37 times higher than the masses of Sun et al. (2009) for the cross-matched 9 groups (see Sect. 3.4.3 for details). The observed mismatch may arise from the fact that in our work, masses are obtained from weak lensing calibrated scaling relations; however, in Sun et al. (2009), the masses are obtained assuming hydrostatic equilibrium. It is relatively well-established that hydro-masses (mass measurements obtained from hydrostatic equilibrium analysis) are biased low due to non-thermal pressure support by turbulence and bulk motions (see Figs. 10 and 1 in Salvati et al. 2018 and Gianfagna et al. 2021 respectively). Nagai et al. (2007a) reported that the bias for groups is at 45% level (see also Sect. 6.2 of Sun et al., 2009); however, the exact amount of this bias is still under debate. To account for this systematic uncertainty, for the Sun et al. (2009) results, we took the observed mismatch with our sample (37%) as our reference and assumed $1/1.37 < M_{hydro}/M_{true} < 1$. These constraints are then propagated and considered as the systematic error of the scaled profiles presented in Sun et al. (2009) and Sun et al. (2011).

A flux mismatch of 15% is reported in Bulbul et al. (2024) when comparing the soft-band $(0.5 - 2$ keV$)$ X-ray luminosity measurements of a subsample of high mass galaxy clusters observed with both eROSITA and *Chandra*. Given that $L \propto n_e^2$, the 15% flux mismatch corresponds to an n_e mismatch of 8%. As in Chapter 3, we account for this mismatch by applying correction factors to the literature measurements while comparing our results.

For galaxy clusters, we compared our results with the scaled profiles of Ghirardini et al. (2019) and Sanders et al. (2021) that are based on X-COP (Eckert et al., 2017) and X-ray cross-matched SPT-SZ 2500d (Bleem et al., 2015) samples respectively. The samples analyzed in Ghirardini et al. (2019) and Sanders et al. (2021) have median masses of $M_{500c} = 5.9 \times 10^{14}$ $M_{\odot}$ and $M_{500c} = 5.6 \times 10^{14}$ $M_{\odot}$ that are roughly an order of magnitude higher than the median mass of our sample, $M_{500c} = 6.5 \times 10^{13}$ $M_{\odot}$. As for the groups, a cosmology and flux correction is applied to the scaled profiles of Ghirardini et al. (2019) and Sanders et al. (2021). For the hydrostatic mass bias, we assumed $0.75 < M_{hydro}/M_{true} < 1$, which covers a significant proportion of the observational constraints (e.g., see the compilation of the literature results in Fig. 10 of Salvati et al. 2018).

The comparison between our results and the scaled profiles of Sun et al. (2009), Sun et al. (2011), Ghirardini et al. (2019) and Sanders et al. (2021) is shown in Fig. 4.3. We note that the uncertainties of the eRASS:4 measurements (blue error bars) plotted in this figure are due to the systematics quantified and discussed in Sect. 3.4, whereas the uncertainties for the literature measurements (shaded areas) are due to the systematic uncertainty introduced by the hydrostatic mass bias. It can be seen from the $n_e/\overline{n_{e,\Delta}}$ plot that the scaled density measurements of clusters are significantly higher than our results for groups. This is in agreement with the findings in the literature suggesting that galaxy groups are gas depleted within r_{500c} compared to clusters (see Fig. 7 of Eckert et al., 2021, and the references therein). Moreover, this is also in agreement with our finding in Sect. 4.3.1, where we report that the normalization of the scaled profiles decreases

with decreasing total mass (M_{500c}). It can further be seen that, outside the core ($r > 0.1r_{500c}$), the scaled density profiles of the Sun et al. (2009) groups are slightly higher but in agreement with our measurements within the systematic uncertainties. The slight difference outside the core can also be explained by the fact that the median mass of the Sun et al. (2009) sample is a factor of 1.38 higher than the median mass of our sample, which would result in the profiles of our groups, on average, to be more depleted compared to the Sun et al. (2009) sample. Within the core ($r < 0.1r_{500c}$), we find that their sample is significantly more centrally peaked. This is due to the fact that the Sun et al. (2009) sample is based on *Chandra* follow-up observations of ROSAT-detected bright and relaxed groups; however, our sample includes fainter objects and is selected more homogeneously in terms of morphology.

It can be seen from the $T/T_{\Delta,\mathrm{adi}}$ plot that our measurements are in good agreement with the median profiles of the Sun et al. (2009) groups when the mass measurement mismatch is taken into account. This is expected since, in our study, we fix the shape of the temperature profile to the average shape of the temperature profiles of 23 groups in Sun et al. (2009) that have temperature constraints out to r_{500c} (see Sect. 3.4.1 for details). Furthermore, we find that our scaled temperature profiles lie above the profiles of clusters. This is in agreement with the trend observed in our sample, indicating that higher mass groups have lower scaled temperatures (see the $T/T_{\Delta,\mathrm{adi}}$ plot in Fig. 4.1) and confirms our finding in Sect. 4.3.1 that the observed $T - M_{500c}$ relation, deviates from the prediction of the self-similar model ($B_{\mathrm{self}} = 2/3$).

For the scaled entropy ($S/S_{\Delta,\mathrm{adi}}$), we find that our measurements are slightly above but in agreement with the median profiles of the Sun et al. (2009) groups outside the core region within the systematic uncertainties. Furthermore, we find that the scaled entropy profiles of galaxy clusters lie significantly below our entropy measurements and are in much better agreement with the self-similar profile (Voit, 2005) that provides a baseline (see Sect. 3.6 for details). From this comparison, it can be concluded that the impact of non-gravitational feedback (e.g., from AGN) is much more prominent for groups and can increase entropy out to much larger radii (even beyond r_{500c}) compared to clusters. The comparison of our scaled entropy profiles with previous results in the literature is also in agreement with our findings in Sect. 4.3 that suggests that non-gravitational feedback results in an increase of the normalization of the scaled entropy with decreasing mass.

Lastly, we find our measurements for $P/P_{\Delta,\mathrm{adi}}$ to be below but in agreement within 2σ with the scaled pressure profiles presented in Sun et al. (2011) outside the core ($r > 0.3r_{500c}$). We, on the other hand, find that our scaled pressure profiles lie 10σ below the measurements of Ghirardini et al. (2019) for clusters at the core. As the distance from the center increases, the mismatch gradually decreases to the $\sim 2.5\sigma$ level. Nevertheless, we also find that our scaled pressure profiles are surprisingly close (within $\sim 2.5\sigma$) to the profiles reported in Sanders et al. (2021) across all radii. Given the mismatch between Ghirardini et al. (2019) and Sanders et al. (2021) at the core, we compared our measurements with a third study of clusters by Arnaud et al. (2010) that report "universal" pressure profiles of clusters by analyzing clusters in the REXCESS sample (Pratt et al., 2010). We find that our scaled entropy measurements are also significantly below the "universal" pressure profile of Arnaud et al. (2010) at the core (at the $> 5\sigma$ level); however, at the outskirts, our measurements converge to agreement at a 1σ. McDonald et al. (2014) independently analyzed the galaxy cluster sample used in Sanders et al. (2021) and found

a similar mismatch with the "universal" pressure profile of Arnaud (1996) in the core region. The disagreement between the scaled pressure profile measurements of clusters makes it hard to draw a comprehensive conclusion in comparison with groups. However, given that the literature measurements for all clusters lie above the median profiles of our sample beyond $r > 0.4r_{500c}$, we conclude that as the mass of the halo decreases, non-gravitational feedback mechanisms, which are significantly more impactful for lower mass haloes, result in scaled pressure profiles that gradually decrease.

4.5 Comparison with Numerical Simulations

In this section, we compare our scaled profiles with predictions of the cosmological hydrodynamical simulations with the aim of constraining the impact of non-gravitational mechanisms. An overview of the comparisons with simulations we perform in this section is briefly summarized below. We first compare our results with the predictions for self-similar clusters and groups from non-radiative hydrodynamical simulations that do not include stellar and AGN feedback. We then compare our results with various runs of the cosmo-OWL simulations (an extended version of the OWL simulation McCarthy et al., 2010; Le Brun et al., 2014) that are simulated with the same AGN feedback implementation but with different model parameters. Lastly, we apply the eROSITA selection function, constructed for our sample following the selection procedures described in Sect. 4.2, to the MillenniumTNG[4], and (Hernández-Aguayo et al., 2023; Pakmor et al., 2023), Magneticum[5] (Hirschmann et al., 2014) simulations and compare our results with different implementations of AGN feedback in these simulations.

For the baseline scaled entropy profile, we use the self-similar profile of Voit (2005). They showed using non-radiative simulations (two smoothed-particle hydrodynamics and two adaptive-mesh refinement simulations) without stellar and AGN feedback that scaled entropy profiles of gaseous haloes, $S/S_{200c,\text{adi}}$, follow a tight power-law relation in the regime with dimensionless radius, r/r_{200c}, between $0.1r_{200c} < r < r_{200c}$. They found that the power-law relation can be fitted well with the formula $S/S_{200c,\text{adi}} = 1.32(r/r_{200c})^{1.1}$ for their simulated clusters, in a ΛCDM cosmology with $h = 0.7$, Ω_M and $f_b = 0.022h^{-2}/\Omega_M$. In this Chapter, we report a more generalized version of this relation by explicitly keeping the dependencies on various assumed parameters by Voit (2005). The generalized version of the Voit (2005) scaled entropy relation can be formulated as

$$\frac{S}{S_{\Delta,\text{adi}}} = 1.38 \left(\frac{r}{r_\Delta}\right)^{1.1} \left(\frac{r_\Delta}{r_{200c}}\right)^{-0.9} \left(\frac{\Delta}{200}\right)^{-1/3} \left(\frac{f_b}{0.16}\right)^{2/3} \left(\frac{h}{0.7}\right)^{2/3}. \tag{4.9}$$

In our study, we are interested in $S/S_{500c,\text{adi}}$ therefore we take $\Delta = 500$. We also assume $r_{500}/r_{200} = 0.669$ (the average conversion factor for the groups in Sun et al., 2009) and obtain the relation $S/S_{500,\text{adi}} = 1.41(r/r_{500})^{1.1}$ for the cosmology assumed in this thesis ($f_b = 0.157$, $h = 0.677$).

We also compare our results with the scaled thermodynamic profiles of Le Brun et al. (2014) that include (i) a baseline run (NOCOOL) without radiative cooling, AGN feedback, and stellar

---

[4]https://www.mtng-project.org
[5]http://www.magneticum.org
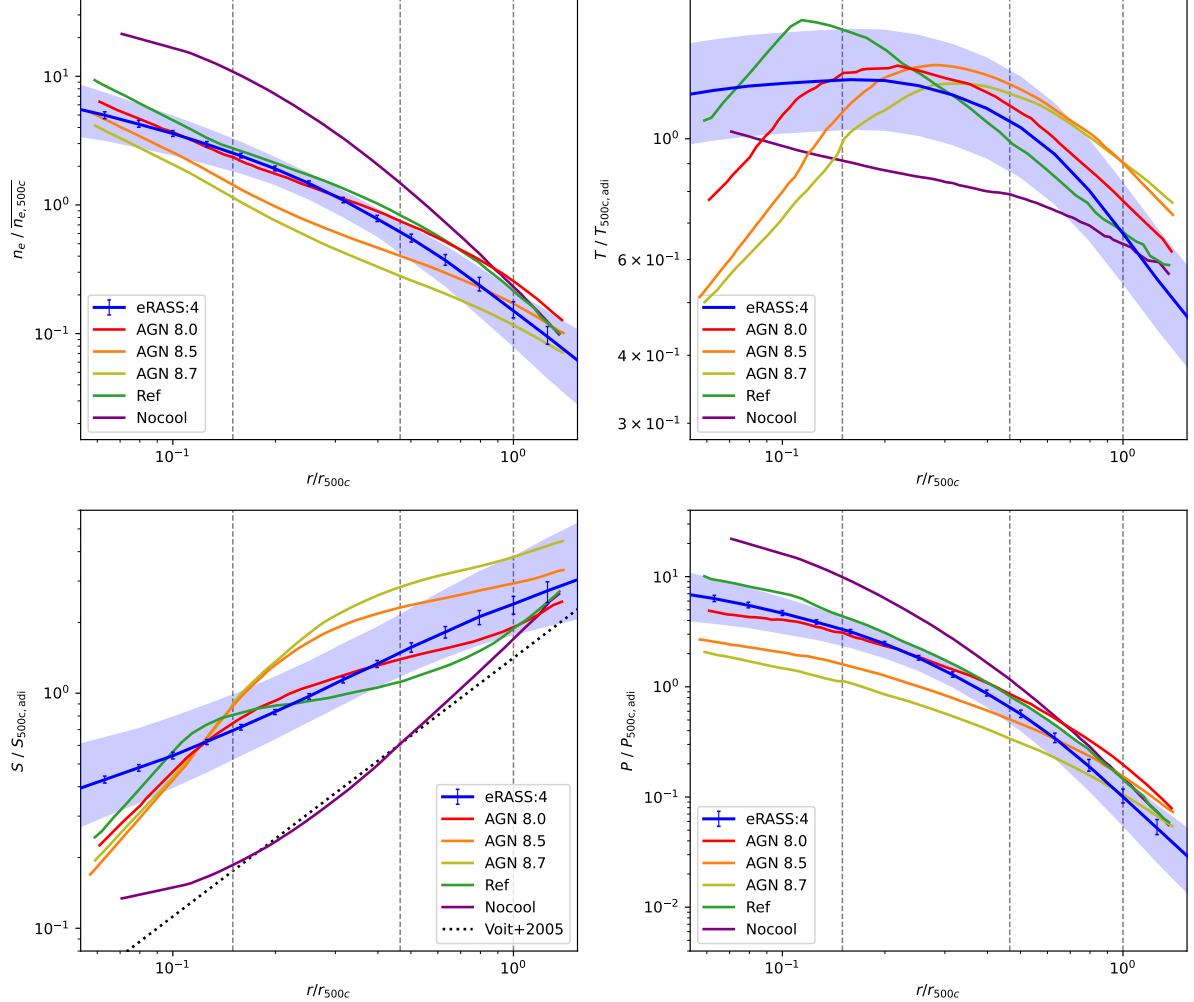
Figure 4.4: Comparison of the median scaled profiles ($n_e/\overline{n_{e,\Delta}}$, $T/T_{\Delta,\mathrm{adi}}$, $S/S_{\Delta,\mathrm{adi}}$ and $P/P_{\Delta,\mathrm{adi}}$) measured in this Chapter (blue) with self-similar scaled entropy profile of Voit (2005) and the REF, NOCOOL and AGN (8.0, 8.5 and 8.7) runs of the cosmo-OWL simulations presented in Le Brun et al. (2014). The blue error bars represent the systematic uncertainties of the median profiles (see Sect. 3.4), and the blue shaded area represents the scatter. The vertical grey dashed lines indicate the three characteristic radii ($0.15r_{500c}$, r_{2500c} and $0.15r_{500c}$) used in Chapter 3.

feedback, (ii) a reference run (REF) without AGN feedback and (iii) three AGN feedback runs (AGN 8.0, AGN 8.5 and AGN 8.7) that has different heating temperature parameters (ΔT_{heat}, see Le Brun et al., 2014, for details). Le Brun et al. (2014) only provide results for the $S_{\text{spec}}/S_{500c,\text{HSE}}-r/r_{500c,\text{HSE}}$ and $\rho_{\text{spec}}/\rho_c-r/r_{500c,\text{HSE}}$ profiles where the subscript "spec" indicates that the quantities are obtained by simulating X-ray spectra and the subscript "HSE" indicates that the quantity is obtained from a hydrostatic mass analysis. To make a fair comparison, we first apply corrections to convert quantities obtained from the hydrostatic mass analysis (e.g., $r_{500c,\text{HSE}}$ and $S_{500c,\text{HSE}}$) to their "true" values by using the hydrostatic equilibrium mass bias Le Brun et al. (2014) report in Fig. B1 for the different runs[6]. After recovering the "true" $S/S_{500c,\text{adi}}$ and ρ/ρ_c profiles, we applied cosmology corrections to the scaled profiles. We then calculate scaled n_{e}, T, and P profiles from the $S/S_{500c,\text{adi}}$ and ρ/ρ_c profiles following the equations

$$\frac{n_e}{n_{\text{e},\Delta}} = \frac{\rho}{\rho_c} \left(3.13 \times 10^{-2} \left(\frac{f_b}{0.16}\right)^{-1} \left(\frac{\Delta}{200}\right)^{-1}\right), \tag{4.10}$$

$$\frac{T}{T_{500c,\text{adi}}} = \left(\frac{n_e}{n_{\text{e},\Delta}}\right)^{2/3} \frac{S}{S_{500c,\text{adi}}}, \tag{4.11}$$

and

$$\frac{P}{P_{500c,\text{adi}}} = \left(\frac{n_e}{n_{\text{e},\Delta}}\right)^{5/3} \frac{S}{S_{500c,\text{adi}}}. \tag{4.12}$$

We note that the NOCOOL run of Le Brun et al. (2014) is similar to Voit (2005) since it does not include non-gravitational processes such as radiative cooling, AGN feedback, and stellar feedback.

The comparison of our profiles with the predictions of Voit (2005) and Le Brun et al. (2014) is shown in Fig. 4.4. First of all, from all the plots in Fig. 4.4, it can easily be seen that the observed profiles are significantly different than the baseline profiles (NOCOOL and the Voit 2005 profiles) that do not include any non-gravitational mechanisms. Furthermore, it can be seen from the $S/S_{500c,\text{adi}}$ plot that our measurements are significantly above the predictions of the self-similar profiles of Voit (2005), and Le Brun et al. (2014) that are shown with dotted black and solid purple lines respectively. It can be concluded from this comparison that the non-gravitational mechanisms that raise the entropy of the IGrM (e.g., AGN and stellar feedback) are more prominent than the mechanisms that lower the entropy (e.g., radiative cooling) such that the measured scaled profiles lie significantly above the self-similar profiles. By comparing our results with the baseline profiles, it can be concluded that overall, the non-gravitational processes result in the gas the in IGrM getting heated (temperature increase), expanding, and being pushed away (density decrease). It can be seen that the impact of non-gravitational processes on temperature is much less prominent compared to their impact on density. This is due to the fact

---

[6]The simulated systems used to create the $S_{\text{spec}}/S_{500c,\text{HSE}}-r/r_{500c,\text{HSE}}$ and $\rho_{\text{spec}}/\rho_c-r/r_{500c,\text{HSE}}$ profiles in Figs. 5 and 7 of Le Brun et al. (2014) are selected to match the median mass of the Sun et al. (2009) group sample. Therefore, to get the value of the hydrostatic mass bias correction from Fig B1, we took the mass of $M_{500c,\text{HSE}} = 8.5 \times 10^{13}\ M_\odot$ as our reference that is the median hydro-mass of the Sun et al. (2009) sample before the ATOMDB correction (see Sects. 3.4.4 and 4.4 for the details on the ATOMDB correction.

that even though the gas gets heated very rapidly around AGN and galaxies through feedback, its temperature also drops relatively fast as it expands, raises to outer layers (because of its increased bouncy), and transfers its energy to its surroundings (see Donahue and Voit, 2022, for a more detailed discussion). By comparing our results with the baseline profiles, we conclude that overall, the non-gravitational mechanisms decrease the scaled density and pressure profiles and increase the scaled temperature and entropy profiles.

After comparing our results with the baseline profiles, we compared our results with the reference (green) and AGN (red, orange, and yellow) runs of the cosmo-OWL simulations. It can be seen in Fig. 4.4 that the green profile (obtained by turning off the AGN feedback) disagrees with our measurements, especially at the outskirts. Therefore, we conclude that our measurements significantly favor the presence of feedback from AGN such that without the energetic feedback from AGN, the remaining non-gravitational processes appear to be insufficient to raise scaled entropy and reduce density beyond $r > 0.2r_{500c}$. Furthermore, from the comparison between the reference and AGN runs, it can be clearly seen that the presence of feedback from AGN has a significant impact on the scaled profiles of groups, and the amount of this impact gets more prominent with increasing heating temperatures (ΔT_{heat}). The normalizations and shapes of the scaled thermodynamic profiles we report in this Chapter put constraints on the implementation and efficiency of the feedback. When we compare our results with the cosmo-OWL runs with different AGN heating temperatures (red, orange, and yellow lines), we find that our measurements agree the best with the AGN 8.0 run. However, it can be seen that the agreement with the predictions of the AGN 8.0 run is only good within $r < 0.4r_{500c}$, and beyond this radius, the entropy excess from feedback appears to be insufficient to reproduce observations. It can further be seen from the $S/S_{500c,\text{adi}}$ plot that the feedback implemented in cosmo-OWLS results in flatter profiles compared to our measurements for all AGN runs. For example, for the AGN 8.0 run, it appears that the high entropy gas produced at the cores of groups cannot be efficiently carried to larger radii with the current feedback implementation in cosmo-OWLS such that the scaled entropy at $0.2r_{500c}$ lie above the observations whereas the scaled entropy at r_{500c} lies below the observations. We argue that this may be due to the fact that the energy released by the effective thermal feedback implemented in cosmo-OWLS dissipates too fast within $r < 0.4r_{500c}$ such that the excess entropy at the core could not be efficiently transferred to larger radii.

It should be noted that the groups selected in Le Brun et al. (2014) to create scaled profiles are not selected the same way as eROSITA selects groups in the X-ray sky. Le Brun et al. (2014) selected groups to match the median mass of Sun et al. (2009) (see Footnote 6). This results in both the median mass and the mass distribution of our sample being different from the groups used in Le Brun et al. (2014) to create the scaled profiles. Such a difference may result in additional systematics that are not accounted for when comparing our results with the scaled profiles of Le Brun et al. (2014).

To make the most accurate comparison between observations and simulations, X-ray observations of cosmological hydrodynamical simulations should be forward-modelled, and the X-ray detection and analysis pipeline ran on "real" observations should also be applied to the forward-modelled "mock" observations. Even though this approach is the most accurate, it is also the most challenging since the forward modeling, detection, and X-ray fitting procedures are required to be repeated for every different simulation. Consequently, in this Chapter, we take a relatively

simpler approach by running the eROSITA detection pipeline on the simulated eRASS1 digital twin (Comparat et al., 2020; Seppi et al., 2022), applying the selection procedure we used to form our group sample to the mock catalogs and obtaining a custom selection function compiled for our sample. The selection function we obtained from this procedure encapsulates the selection and cleaning information and provides detection probabilities of haloes as a function of M_{500c} and z (see Clerc et al., 2024, for details).

To investigate the accuracy of AGN feedback implementations in different simulations, we applied our selection function to the MillenniumTNG and Magneticum simulations and compared our measurements with the properties of the groups in these simulations. By doing so, we aim to achieve a fair comparison with these simulations as we similarly did in Chapter 3. Brief descriptions of these simulations, as well as the extraction of the thermodynamic profiles of their gaseous haloes, are presented in Sect. 3.6. After the profiles are extracted and the eROSITA selection function is applied, the scaled profiles are obtained by normalizing the n_e, T, S, and P profiles of MillenniumTNG and Magneticum groups with their self-similar predictions following Eqs. 4.3, 4.4, 4.5 and 4.6. The comparison between the scaled profiles of MillenniumTNG and Magneticum groups with our measurements is shown in Fig. 4.5.

It can be seen from the $S/S_{500c,\mathrm{adi}}$ plot in Fig. 4.5 that groups in Magneticum have higher scaled entropy profiles at all radii compared to the groups in MillenniumTNG. This indicates that the overall strength of the feedback implemented in the Magneticum simulations is larger than the feedback implemented in MillenniumTNG simulations. It can further be seen that at large radii ($r > r_{500c}$), the scaled entropy profiles of MillenniumTNG groups are close to the baseline profile of (Voit, 2005) whereas, for Magneticum groups, the entropy excess with respect to the baseline profile at outer radii is significantly larger. This can also be seen in the $n_e/\overline{n_{e,\Delta}}$ plot of Fig. 4.5 where the scaled density profiles of MillenniumTNG groups are above the scaled density profiles of Magneticum groups out to $1.5r_{500c}$. Such a mismatch can also be explained by the feedback in Magneticum being more energetic compared to MillenniumTNG, such that the IGrM in Magneticum is expelled to larger radii more efficiently compared to MillenniumTNG. When we compare our scaled entropy and density measurements with the predictions of these simulations, we find that the Magneticum simulations reproduce the observations better outside the core region ($r > 0.3r_{500c}$), with very good agreement starting from the intermediate radii r_{2500c} (second vertical line from the left in Fig. 4.5), whereas MillenniumTNG simulations reproduce the observations better around the core ($r < 0.3r_{500c}$). This is in agreement with our findings in Chapter 3. It can further be seen from the $T/T_{500c,\mathrm{adi}}$ plot that the scaled temperature profiles of MillenniumTNG and Magneticum groups are in relatively good agreement with each other, and our measurements between $0.15r_{500c} < r < r_{500c}$. This confirms that the average shape we assumed for the temperature profiles in our work is relatively robust and does not introduce major systematics. Lastly, we compare our measurements with the scaled pressure profiles of MillenniumTNG and Magneticum in the bottom right panel of Fig. 4.5 and find that our measurements are in remarkable agreement with the pressure profiles of MillenniumTNG within $r < 0.2r_{500c}$. At intermediate radii (around r_{2500c}), our measurements agree much better with the profiles of Magneticum groups, and at the outskirts (around r_{500c}), the predictions of the MillenniumTNG and Magneticum simulations converge and reach to an agreement with our observations at a 2.5σ level.
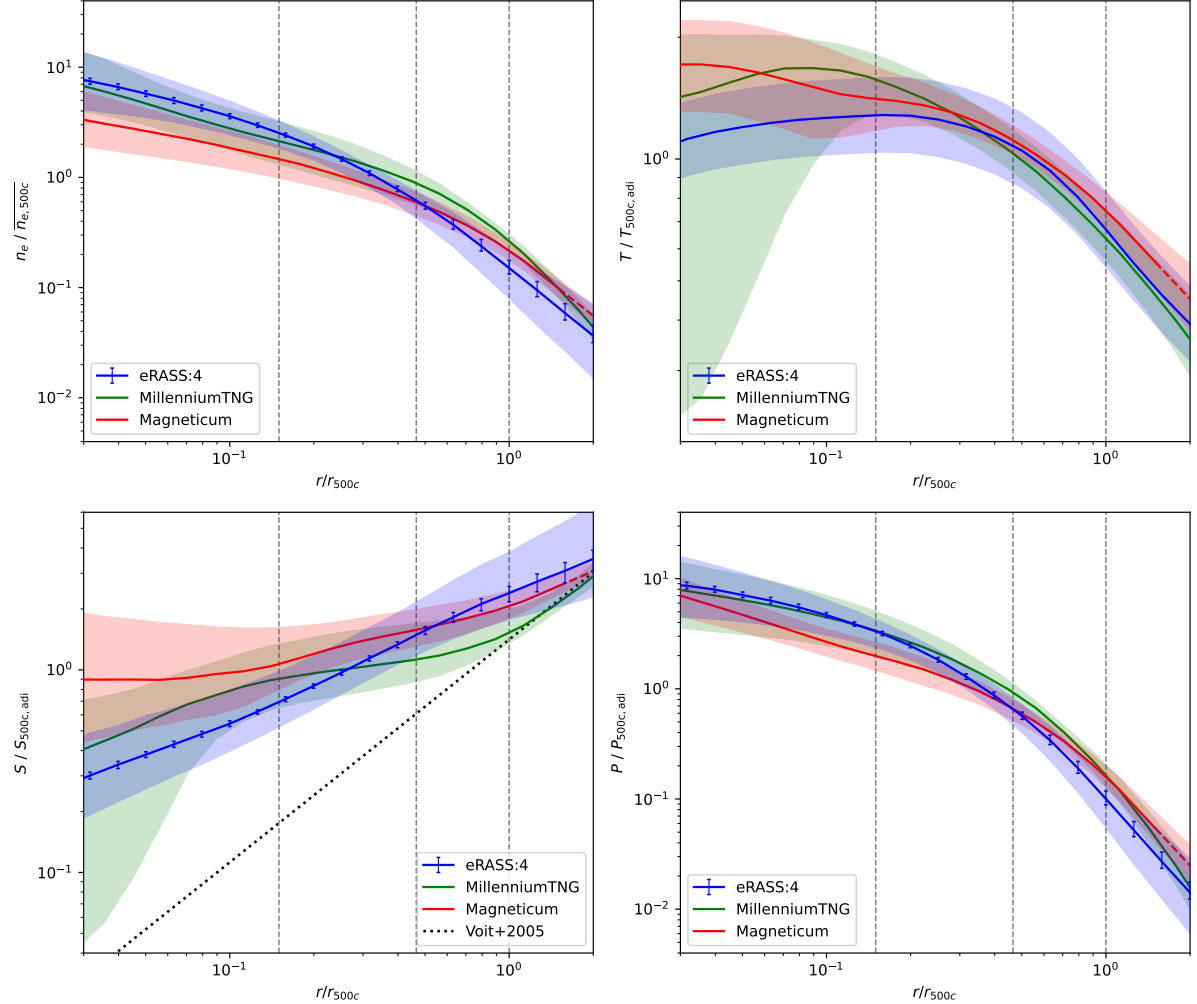
Figure 4.5: Comparison of the median scaled profiles ($n_{\mathrm{e}}/\overline{n_{\mathrm{e},\Delta}}$, $T/T_{\Delta,\mathrm{adi}}$, $S/S_{\Delta,\mathrm{adi}}$ and $P/P_{\Delta,\mathrm{adi}}$) measured in this study (blue) with the predictions of the MillenniumTNG and Magneticum simulations and the self-similar scaled entropy profile of Voit (2005). The blue error bars represent the systematic uncertainties of the median profiles (see Sect. 3.4 for the details on the systematic uncertainties), and the shaded areas represent the scatter. The vertical grey dashed lines indicate the three characteristic radii ($0.15r_{500c}$, r_{2500c} and $0.15r_{500c}$) used in Chapter 3.

Overall, we conclude that both of the simulations fall short of reproducing our measurements at all radii. We find that our measurements around the core region ($r < 0.3r_{500c}$) are reproduced better by MillenniumTNG, whereas our measurements at the intermediate and outer regions ($r > 0.3r_{500c}$) are reproduced better with Magneticum. We argue that the AGN feedback efficiency in MillenniumTNG should be higher to match our profiles at the intermediate radii and outskirts. At the core, we find that our scaled entropy measurements are too low and scaled density measurements are too high compared to simulations. It appears that the excess entropy injected by the central AGN could not be transferred to the outer regions effectively in both of the AGN feedback implementations. We further argue that this may be achieved by improving the directional kinetic feedback from AGN that would create large bubbles and cavities in ICM/IGrM, as seen in X-ray observations (e.g., Bîrzan et al., 2004; Gastaldello et al., 2009; Randall et al., 2011), and efficiently transfer high entropy gas out to larger radii by buoyant forces. As discussed in more detail in Chapter 1, AGN provides feedback to its environment in two forms: (i) quasar mode feedback and (ii) radio mode feedback. The quasar mode feedback is fueled by a radiatively efficient accretion disk, whereas the radiation mode feedback is fueled by a radiatively inefficient accretion disk. The AGN in the quasar mode predominantly emit high levels of radiation and generate winds, whereas AGN in the radio mode produce strong relativistic jets (Hlavacek-Larrondo et al., 2022). Both the MillenniumTNG and Magneticum simulations include a transition from quasar mode to a stronger radio mode feedback (e.g., see Sijacki et al., 2007; Fabjan et al., 2010). In Magneticum, AGN in the radio mode has an increased feedback efficiency compared to the quasar mode; however, it is still implemented as an isotropic, thermal feedback (e.g., see Hirschmann et al., 2014). However, in MillenniumTNG, the radio mode is modeled as kinetic feedback where the AGN in radio mode releases kinetic energy to a random direction for every energy release event (e.g., see Weinberger et al., 2017). Given the mismatch with the observations, we argue that the efficiency and/or the implementation of the feedback in these simulations are required to be tuned/improved. Our measurements put constraints on the impact of the feedback; and serve as a reference point for improving and tuning AGN feedback implementations to achieve more realistic numerical simulations.

4.6 Summary and Conclusions

In this Chapter, we have determined the profiles of thermodynamic properties of 1178 eROSITA-selected galaxy groups. The sample is selected from the eRASS1 galaxy cluster and group catalog (Bulbul et al., 2024) in a way that the selection is reproducible in eRASS1 simulations, and the sample has a well-defined selection function. For the X-ray analysis, deeper eRASS:4 observations are used. Imaging analysis is performed on individual groups, and spectral analysis is performed by co-fitting groups that have similar scaling relation based temperature estimates and signal-to-noise ratios. The results from imaging and spectral analysis are combined, and profiles of thermodynamic properties are obtained. The selection and the X-ray analysis of the sample are described in detail in Chapter 3 and our companion paper Bahar et al. (2024). In this Chapter, we investigate profiles of four X-ray-derived thermodynamic properties: electron density (n_e), temperature (T), entropy (S), and pressure (P). We also normalize these profiles with the pre-

dictions of the self-similar model and provide our results for the self-similar evolution removed, scaled thermodynamic profiles. We compare the scaled thermodynamic profiles with the measurements in the literature for groups and clusters. Additionally, we assess our measurements against predictions from non-radiative hydrodynamic simulations of self-similar clusters without feedback (Voit, 2005; Le Brun et al., 2014). Moreover, we compared our scaled profiles with the predictions of the REF (AGN feedback turned off), AGN 8.0, AGN 8.5, and AGN 8.7 runs of the cosmo-OWL simulations obtained with different model parameters for feedback (Le Brun et al., 2014). Lastly, we applied the eROSITA selection function to two simulations that include different AGN feedback implementations, Magneticum and MillenniumTNG, and compared our results with their predictions. The main conclusions of this Chapter are as follows:

– We have presented the most comprehensive study of the thermodynamic properties of IGrM in terms of sample size and group diversity. By analyzing eROSITA observations of 1178 groups, we were able to put the tightest constraints on the average profiles of their thermodynamic properties. The normalization and shapes of these profiles also stand as the tightest constraints on the impact of non-gravitational processes (radiative cooling, AGN feedback, and stellar feedback) acting on IGrM.

– When we scale our profiles with the predictions of the self-similar model, we find that the normalizations of the scaled profiles have a strong dependence on the masses of the group except the scaled pressure profile. We find that beyond $r > r_{500c}$, the scaled pressure profiles have no mass dependence, whereas the scaled electron density decreases, and the scaled temperature and entropy increase with decreasing mass. This confirms previous findings that suggest the gas mass fractions of galaxy groups decrease with decreasing total mass. Furthermore, increasing scaled entropy with decreasing mass confirms the scenario that the impact of feedback is much more prominent in galaxy groups compared to clusters.

– We compared our scaled profiles with literature results for groups (Sun et al., 2009) and clusters (Arnaud et al., 2010; Ghirardini et al., 2019; Sanders et al., 2021). Overall, we find that our measurements for the scaled profiles agree relatively well with the measurements of Sun et al. (2009) within the systematic uncertainties. Nevertheless, when we compare our profiles with the literature results of clusters, we find that our scaled density profiles are significantly below, and our scaled entropy profiles are significantly above the measurements for clusters. Our measurements, revealing lower scaled density profiles for groups compared to clusters, agree well with the scenario where AGN feedback pushes away gas out to larger radii, and groups appear to be gas-depleted within r_{500c}. Furthermore, our measurements, revealing higher-scaled entropy at all radii compared to clusters, indicate that the excess entropy provided by AGN can reach large radii.

– From the comparison of our results with the baseline profiles of Voit (2005) and Le Brun et al. (2014), we find that our measurements significantly favor the presence of strong feedback that raises the scaled entropy and temperature profiles, and reduces the scaled density

and pressure profiles. We also compared our results with the REF (without AGN feedback) run of the cosmo-OWL simulations and found that the presence of AGN feedback is crucial for reproducing the observed profiles. Furthermore, we compared our results with their AGN ($\Delta T_{\text{heat}} = 10^{8.0}$, $10^{8.5}$ and $10^{8.7}$ K) runs and found that the model parameters, as well as the implementation of the feedback, need to be tuned to match observations. Furthermore, we argue that the shapes of the scaled entropy profiles for all the ΔT_{heat} parameters are too flat at the outskirts, suggesting that the current feedback implementation cannot efficiently transfer the excess entropy from AGN to outer radii.

– We find, from a comparison of our results with the Magneticum and MillenniumTNG simulations, that our measurements at intermediate and large radii are in good agreement with the predictions of the Magneticum simulation. When we compare our results around the core ($r < 0.3r_{500c}$), we find that the MillenniumTNG simulation reproduces the observations better. We further find that the scaled entropies of MillenniumTNG groups lie below observations outside the core ($r > 0.3r_{500c}$). We argue that the efficiency of AGN feedback in MillenniumTNG should be increased to match our observations at larger radii. We further find that the predictions of both of the simulations for the scaled entropy at the core lie significantly above our measurements. We argue that this indicates the need for more realistic feedback implementation that would carry the excess entropy produced by the central AGN to larger radii.

Chapter 5

Summary, Conclusions and Outlook

Galaxy clusters and groups are the cornerstones of the large-scale structure that reside at the nodes of the cosmic web. Their properties can be investigated in various energy bands across the electromagnetic spectrum (e.g., X-ray, optical/infrared, microwave/millimeter-wave, and radio) by analyzing the light directly coming from the baryons hosted in these structures or by studying the background light that gets distorted and/or modified while passing through these objects. They are ideal laboratories for studying cosmological and astrophysical phenomena governing structures at large scales, such as dark matter, dark energy, AGN feedback, stellar feedback, and radiative cooling. X-ray observations have proven to be one of the best mediums for robustly detecting galaxy clusters and groups and studying their dark and baryonic components. The bulk of the baryonic matter residing in these haloes is in the form of hot, X-ray-emitting plasma whose spatial distribution and energetics can be measured using X-ray observations. The eROSITA telescope, optimized for efficiently detecting galaxy clusters and groups, is revolutionizing our understanding of the astrophysics of the large-scale structure by detecting unprecedented amounts of galaxy clusters and groups in diverse dynamical states and providing high-quality X-ray observations for measuring their physical properties.

In this thesis, we first investigate the scaling relations between the X-ray observables of galaxy clusters and groups. Even though the presence of the correlation between X-ray observables of clusters and groups is well established, accurate calibration of these relations with a large sample ($N > 200$) was lacking in the literature due to the lack of a well-defined selection function in most of the previous studies. Calibration of these relations and comparing them with the predictions of the simple spherical collapse scenario allow for constraining the impact of non-gravitational processes. In our study, we calibrated seven X-ray scaling relations by taking into account the selection effects and the mass function using eROSITA observations of galaxy clusters and groups detected in the eFEDS field. A sample of 265 clusters and groups with less than 10% contamination is utilized in the scaling relations analysis that is obtained by applying selection procedures to the main eFEDS catalog that are reproducible in eROSITA simulations of the eFEDS field. A Bayesian framework is constructed to fit the relations within which a custom selection function obtained from simulations and a canonical halo mass function are used to take into account the selection effects and the mass distribution of dark matter haloes. We find that the best-fit slopes significantly deviate from the predictions of the self-similar model, but our results

are nevertheless in good agreement with the simulations that include non-gravitational physics and the recent results that take into account selection effects. We argue that the strong deviations from the self-similar scenario indicate that the non-gravitational effects play an important role in shaping the observed physical state of clusters. Our study extends the scaling relations to the low-mass, low-luminosity galaxy cluster, and group regime using eFEDS observations, demonstrating the ability of eROSITA to measure emission from the intracluster medium out to r_{500c} with survey-depth exposures and constrain the scaling relations in a wide mass-luminosity–redshift range.

Second, we investigate the impact of feedback, particularly from AGN, on the entropy and characteristic temperature measurements of galaxy groups detected in the SRG/eROSITA's first All-Sky Survey (eRASS1) to shed light on the characteristics of the feedback mechanisms and help guide future AGN feedback implementations in numerical simulations. We analyze the eRASS:4 observations of 1178 galaxy groups detected in the eRASS1. The sample is selected from the eRASS1 galaxy clusters and groups catalog, such that the selection is reproducible in eRASS1 simulations and the sample has a well-defined selection function. We measure the count rate and emissivity profiles of groups by fitting their X-ray images following a Bayesian approach. We then divide the sample into 271 subsamples based on their physical and statistical properties and jointly analyze the spectra of the groups sharing the same subsample. As a result of our imaging and spectral analysis, we obtained average thermodynamic properties for the 271 group bins, including electron number density, temperature, and entropy at three characteristic radii (from cores to outskirts) and average integrated temperature within r_{500c}. We also quantify the impact of major systematics in our analysis and consider their impact as part of our total error budget. We report the tightest constraints with unprecedented statistical precision on the impact of AGN feedback through our average entropy and characteristic temperature measurements of the largest group sample used in X-ray studies. We find that entropy shows an increasing trend with temperature in the form of a power-law-like relation at the higher intra-group medium (IGrM) temperatures, while for the low mass groups with cooler IGrM temperatures ($T < 1.44$ keV), a slight flattening is observed on the average entropy. Overall, the observed entropy measurements agree well with the earlier measurements in the literature. We compare our results with the state-of-the-art cosmological hydrodynamic simulations (MillenniumTNG, Magneticum, OWL) after applying the selection function calibrated for our sample and find that the observed entropy profiles at the core are below the predictions of simulations. At the mid-region, the entropy measurements agree well with the Magneticum simulations, whereas the predictions of MillenniumTNG and OWL simulations fall below observations. At the outskirts, the overall agreement between the observations and simulations improves, with Magneticum simulations reproducing the observations the best. Our measurements in this study will pave the way for achieving more realistic AGN feedback implementations in numerical simulations. The future eROSITA Surveys will enable the extension of the entropy measurements in even cooler IGrM temperatures below 0.5 keV, allowing the test of the AGN feedback models in this regime.

Lastly, in this thesis, we investigate the profiles of thermodynamic properties of eROSITA-selected galaxy groups. Previous studies examining a limited number of groups have indicated that the thermodynamic properties of the intragroup medium differ significantly from the properties of the intracluster medium. The difference is argued to be due to the fact that groups are

more vulnerable to non-gravitational processes compared to clusters because of their shallower potential wells. However, to achieve a clear and comprehensive picture, it is necessary to investigate the thermodynamic profiles of groups using larger samples and constrain the impact of non-gravitational processes on the intragroup medium. In our study, we present the density, temperature, entropy, and pressure profiles of 1178 galaxy groups using eROSITA observations. The sample employed in this study is the same as the one used in our second project; therefore, has a well-defined selection function. We also normalize these profiles with the predictions of the self-similar model and obtain tight constraints on the average profiles of thermodynamic properties of X-ray bright groups. We compare the scaled profiles with the previous measurements for clusters and groups and find that the scaled density profiles of groups are significantly below the profiles of clusters, confirming previous studies indicating that groups are baryon depleted within r_{500c}. We further find that the scaled entropy profiles of groups are considerably higher than clusters at all radii. These findings are in agreement with the expectation that the non-gravitational processes, particularly AGN feedback, have a more significant impact on the IGrM than the ICM. We also compare our measurements with the baseline predictions of the non-radiative hydrodynamical simulations that do not include feedback prescriptions. We conclude from this comparison that the non-gravitational mechanisms result in the scaled density and pressure profiles of groups to decrease and the scaled entropy and temperature profiles of groups to increase. Lastly, we apply our selection function to simulations that include different AGN feedback implementations (Magneticum and MillenniumTNG) and compare our findings with their predictions. We find that our measurements are reproduced very well at the intermediate radii and outskirts by Magneticum, whereas at the core, our measurements agree better with MillenniumTNG. We further find that our entropy measurements are below the predictions of simulations at the core and above the predictions at the outskirts. We argue that this indicates the need for a more realistic AGN feedback implementation that would more efficiently transfer the excess entropy produced at the core by the central AGN to larger radii.

The results we presented in this thesis put tight constraints on the non-gravitational processes shaping the properties of the baryons within clusters and groups. Nevertheless, the astrophysics of gaseous haloes in the group regime still remains largely unexplored, with many critical questions yet to be addressed by future research. Some of the key open questions include: Do galaxy groups scale differently than galaxy clusters? Are the metallicity profiles of groups different than clusters? What is the most suitable technique to measure the masses of groups? How biased are the hydro-masses for groups? How do the thermodynamic properties of galaxy groups evolve over time? How much coupling is there between the properties of the central AGN and the host halo? The studies presented in this thesis are among the first to investigate the astrophysics of galaxy clusters and groups using large samples with eROSITA. In these studies, we analyzed gaseous haloes detected in eRASS1 and eFEDS observations. The groups detected in eRASS:4 observations will substantially increase the number of known X-ray bright groups, populating both the higher redshift and lower-mass parameter spaces. Furthermore, follow-up observations of the groups with higher resolution X-ray instruments, such as *XMM-Newton*, will reveal finer features of the IGrM, such as shocks and cavities, that will constrain the energetics of the central engine from different perspectives. Recently, X-ray observations of 49 galaxy groups have been performed as part of a large *XMM-Newton* observing program for groups, X-GAP (Eckert et al.,

2024). These observations will allow revealing the average temperature and metallicity profiles of groups that will shrink the systematic error bars of our measurements presented in Chapters 3 and 4. The next-generation X-ray telescopes equipped with microcalorimeters, such as the recently launched XRISM (XRISM Science Team, 2020) or ESA's flagship mission Athena (Nandra et al., 2013), will allow the velocity structures within ICM/IGrM to be measured and will put constraints on the non-thermal pressure support and the hydrostatic mass bias in clusters and groups. Moreover, Athena will detect groups at high redshift with its next generation, CCD-based Wide Field Imager (WFI, Meidinger, 2018) instrument and will allow probing of the redshift evolution of the thermodynamic properties of galaxy groups. On the optical/infrared front, the next-generation survey telescopes with advanced weak lensing capabilities, such as Euclid (Laureijs et al., 2011), Large Synoptic Survey Telescope (LSST, LSST Science Collaboration et al., 2009) and the Roman Space Telescope (Spergel et al., 2015) will provide high-quality shear maps of the high-mass galaxy groups that will allow measuring masses of large samples of groups. In the microwave/millimeter-wave band, Cosmic Microwave Background Stage 4 (CMB-S4, Abazajian et al., 2016) experiment will push the detection limit to the high-mass end of the group regime, which will allow investigating gaseous haloes at the transition regime from cluster to group at a wide redshift range. Lastly, in the radio band, future large-area radio surveys, such as the Square Kilometre Array Observatory (SKAO, Dewdney et al., 2009) surveys, will allow the investigation of the radio properties of the central AGN (e.g., radio AGN luminosity or jet-fed radio lobes) simultaneously with the X-ray properties of the IGrM medium for large samples. Therefore, observations of galaxy groups with next-generation observatories across the electromagnetic spectrum will continue providing deeper insights into the astrophysical phenomena governing large-scale structures at cosmological scales.

Appendix A

X-ray Properties of eFEDS Clusters and Groups

Table A.1: Best-fit parameters of the eFEDS clusters and groups to the modified Vikhlinin et al. (2006) model: $n_e^2(r) = n_0^2 \left(\frac{r}{r_s}\right)^{-\alpha} \left(1 + \left(\frac{r}{r_s}\right)^2\right)^{-3\beta+\alpha/2} \left(1 + \left(\frac{r}{r_s}\right)^3\right)^{-\epsilon/3}$.

Cluster (eFEDS J+)	ID_SRC	n_0^2 $(10^{-7}\ \text{cm}^{-6})$	r_s (arcsec)	ϵ	β	α
082626.5-003429	28993	$4.0^{+36.4}_{-3.0}$	72^{+65}_{-52}	$2.5^{+1.7}_{-1.7}$	$1.56^{+0.66}_{-0.77}$	$1.09^{+1.01}_{-0.71}$
082751.7-002853	11248	$1.9^{+32.7}_{-1.6}$	72^{+67}_{-46}	$2.6^{+1.6}_{-1.7}$	$1.59^{+0.64}_{-0.77}$	$1.54^{+1.17}_{-0.98}$
082808.7-001003	4800	$0.75^{+3.53}_{-0.50}$	224^{+87}_{-82}	$1.5^{+1.8}_{-1.0}$	$1.16^{+0.90}_{-0.57}$	$1.42^{+0.34}_{-0.71}$
082820.5-000721	4169	$8.9^{+31.8}_{-7.4}$	125^{+72}_{-45}	$3.0^{+1.5}_{-1.8}$	$1.62^{+0.67}_{-0.87}$	$1.12^{+0.53}_{-0.74}$
082840.6-000500	7991	$1.7^{+12.1}_{-1.4}$	123^{+60}_{-47}	$2.6^{+1.6}_{-1.8}$	$1.39^{+0.74}_{-0.70}$	$1.38^{+0.56}_{-0.91}$
082859.9+010756	14973	$0.51^{+0.62}_{-0.22}$	296^{+115}_{-98}	$2.5^{+1.7}_{-1.8}$	$1.49^{+0.72}_{-0.80}$	$0.56^{+0.44}_{-0.37}$
082952.7+002139	7528	$7.4^{+43.9}_{-6.9}$	59^{+41}_{-23}	$2.4^{+1.8}_{-1.7}$	$1.62^{+0.62}_{-0.75}$	$1.53^{+0.77}_{-1.02}$
082955.4+004131	3810	$8.0^{+42.6}_{-7.0}$	110^{+64}_{-42}	$2.5^{+1.8}_{-1.8}$	$1.62^{+0.62}_{-0.76}$	$1.37^{+0.56}_{-0.79}$
083040.7+023219	9837	$6.2^{+45.1}_{-5.5}$	65^{+42}_{-32}	$2.6^{+1.6}_{-1.8}$	$1.63^{+0.61}_{-0.76}$	$1.34^{+0.78}_{-0.87}$
083110.5+015616	5601	$1.4^{+6.1}_{-1.1}$	173^{+93}_{-62}	$2.7^{+1.5}_{-1.6}$	$1.60^{+0.56}_{-0.60}$	$1.16^{+0.50}_{-0.69}$
083120.5+005257	9594	$3.5^{+17.6}_{-3.2}$	90^{+63}_{-40}	$2.4^{+1.9}_{-1.6}$	$1.62^{+0.67}_{-0.82}$	$1.38^{+0.66}_{-0.88}$
083120.5+030949	11134	$1.9^{+71.0}_{-1.5}$	67^{+109}_{-53}	$2.6^{+1.6}_{-1.8}$	$1.49^{+0.68}_{-0.78}$	$1.35^{+1.58}_{-0.93}$
083125.9+015533	2659	$1.9^{+6.8}_{-1.3}$	179^{+52}_{-48}	$2.6^{+1.5}_{-1.5}$	$1.16^{+0.80}_{-0.57}$	$1.42^{+0.43}_{-0.75}$
083137.9+004632	3725	$0.85^{+14.29}_{-0.66}$	111^{+52}_{-54}	$2.0^{+1.8}_{-1.4}$	$1.35^{+0.72}_{-0.76}$	$1.89^{+0.37}_{-0.97}$
083146.7-012849	4403	$1.03^{+11.74}_{-0.81}$	112^{+74}_{-56}	$2.5^{+1.7}_{-1.7}$	$1.42^{+0.72}_{-0.73}$	$1.70^{+0.44}_{-0.78}$
083149.4+005230	5463	13^{+41}_{-10}	59^{+27}_{-22}	$2.3^{+1.6}_{-1.6}$	$1.55^{+0.67}_{-0.77}$	$1.12^{+0.77}_{-0.69}$
083153.6+012530	2600	$0.74^{+4.24}_{-0.54}$	197^{+97}_{-91}	$2.2^{+1.7}_{-1.5}$	$1.37^{+0.75}_{-0.71}$	$1.56^{+0.29}_{-0.60}$
083204.4+041907	3593	$1.14^{+2.22}_{-0.69}$	318^{+97}_{-105}	$2.5^{+1.7}_{-1.6}$	$1.60^{+0.61}_{-0.75}$	$1.07^{+0.32}_{-0.44}$
083228.0-000656	7396	$1.08^{+12.05}_{-0.88}$	95^{+84}_{-57}	$2.8^{+1.5}_{-1.8}$	$1.54^{+0.66}_{-0.75}$	$1.62^{+1.23}_{-0.95}$
083238.8-003200	8565	$2.9^{+7.1}_{-2.4}$	119^{+59}_{-42}	$2.8^{+1.6}_{-1.7}$	$1.72^{+0.55}_{-0.78}$	$0.93^{+0.61}_{-0.59}$
083249.9+031737	10398	$1.06^{+24.28}_{-0.77}$	92^{+145}_{-73}	$2.5^{+1.7}_{-1.6}$	$1.48^{+0.72}_{-0.71}$	$1.21^{+1.61}_{-0.85}$
083310.2+030136	15959	$0.42^{+1.33}_{-0.18}$	310^{+180}_{-250}	$2.7^{+1.6}_{-1.8}$	$1.08^{+0.89}_{-0.55}$	$0.56^{+1.05}_{-0.39}$
083315.5+000623	6869	$0.44^{+3.02}_{-0.30}$	186^{+84}_{-77}	$2.3^{+1.7}_{-1.5}$	$1.45^{+0.71}_{-0.72}$	$1.44^{+0.36}_{-0.70}$
083321.1+012644	2879	$1.02^{+5.93}_{-0.76}$	153^{+67}_{-60}	$2.7^{+1.6}_{-1.7}$	$1.67^{+0.58}_{-0.78}$	$1.73^{+0.31}_{-0.54}$
083322.6-011128	6302	$1.5^{+6.2}_{-1.2}$	134^{+68}_{-51}	$2.6^{+1.6}_{-1.7}$	$1.64^{+0.60}_{-0.70}$	$1.21^{+0.65}_{-0.78}$
083330.4+050427	2528	$0.231^{+0.369}_{-0.087}$	234^{+65}_{-75}	$1.7^{+1.8}_{-1.6}$	$0.91^{+0.83}_{-0.42}$	$1.88^{+0.20}_{-0.24}$
083341.0-002943	6767	$8.2^{+93.9}_{-7.3}$	29^{+26}_{-15}	$1.10^{+1.10}_{-0.78}$	$0.65^{+0.30}_{-0.22}$	$1.6^{+1.2}_{-1.1}$
083345.8+004208	2984	$5.2^{+25.2}_{-4.7}$	97^{+73}_{-38}	$2.7^{+1.6}_{-1.7}$	$1.50^{+0.66}_{-0.78}$	$1.36^{+0.59}_{-0.82}$
083401.5-001337	4258	$0.27^{+0.84}_{-0.15}$	198^{+122}_{-95}	$2.4^{+1.8}_{-1.6}$	$1.55^{+0.67}_{-0.78}$	$0.83^{+0.80}_{-0.58}$
083402.5+023437	6409	$8.1^{+36.5}_{-7.3}$	67^{+41}_{-27}	$2.8^{+1.6}_{-1.8}$	$1.64^{+0.60}_{-0.69}$	$1.21^{+0.73}_{-0.78}$
083403.7+012131	4634	$3.5^{+60.9}_{-3.1}$	68^{+56}_{-42}	$2.7^{+1.6}_{-1.8}$	$1.61^{+0.61}_{-0.70}$	$2.0^{+1.3}_{-1.2}$
083412.7+035856	1092	$0.60^{+3.21}_{-0.45}$	183^{+79}_{-90}	$2.5^{+1.8}_{-1.7}$	$1.55^{+0.65}_{-0.75}$	$1.69^{+0.81}_{-0.84}$
083422.7+034537	3240	$2.5^{+83.5}_{-2.3}$	62^{+64}_{-31}	$2.6^{+1.7}_{-1.8}$	$1.51^{+0.70}_{-0.79}$	$2.15^{+0.50}_{-1.11}$
083427.0-015612	12633	$0.42^{+1.11}_{-0.27}$	224^{+125}_{-76}	$2.9^{+1.4}_{-1.8}$	$1.54^{+0.66}_{-0.77}$	$0.82^{+0.52}_{-0.51}$
083431.0+034208	8206	$0.124^{+0.062}_{-0.028}$	510^{+160}_{-160}	$2.4^{+1.8}_{-1.7}$	$1.59^{+0.63}_{-0.77}$	$0.24^{+0.26}_{-0.17}$
083435.6+050159	4593	$0.39^{+24.30}_{-0.24}$	128^{+284}_{-94}	$2.3^{+1.9}_{-1.7}$	$1.53^{+0.69}_{-0.86}$	$1.15^{+1.56}_{-0.80}$
083457.7+052033	9892	$4.0^{+12.3}_{-3.6}$	88^{+52}_{-35}	$2.6^{+1.7}_{-1.7}$	$1.64^{+0.60}_{-0.79}$	$0.93^{+0.77}_{-0.65}$
083503.2+010756	3874	$0.48^{+1.82}_{-0.32}$	213^{+90}_{-72}	$2.8^{+1.5}_{-1.7}$	$1.50^{+0.69}_{-0.77}$	$1.51^{+0.29}_{-0.54}$
083509.0+001542	1360	30^{+46}_{-22}	91^{+31}_{-26}	$2.6^{+1.7}_{-1.7}$	$1.67^{+0.57}_{-0.75}$	$0.78^{+0.59}_{-0.50}$
083532.5+030911	3198	$0.44^{+5.84}_{-0.31}$	101^{+54}_{-54}	$2.5^{+1.7}_{-1.7}$	$1.41^{+0.77}_{-0.73}$	$2.24^{+0.34}_{-0.50}$
083615.7+024420	12572	$1.04^{+7.54}_{-0.81}$	95^{+65}_{-56}	$2.7^{+1.7}_{-1.8}$	$1.61^{+0.62}_{-0.79}$	$1.39^{+0.89}_{-0.87}$
083626.4+043821	5783	$1.9^{+13.9}_{-1.6}$	100^{+57}_{-39}	$2.7^{+1.7}_{-1.7}$	$1.53^{+0.69}_{-0.69}$	$1.74^{+0.43}_{-0.78}$
083651.3+030002	197	$5.7^{+20.9}_{-3.8}$	112^{+66}_{-52}	$1.25^{+1.11}_{-0.90}$	$0.61^{+0.32}_{-0.19}$	$1.72^{+0.16}_{-0.31}$
083654.6+025954	16471	$5.7^{+20.8}_{-3.8}$	112^{+66}_{-52}	$1.25^{+1.11}_{-0.90}$	$0.61^{+0.32}_{-0.19}$	$1.72^{+0.16}_{-0.31}$

continued.

Cluster (eFEDS J+)	ID_SRC	n_0^2 (10^{-7} cm^{-6})	r_s (arcsec)	ϵ	β	α
083713.3+034110	10475	$3.0^{+20.2}_{-2.4}$	107^{+73}_{-45}	$2.6^{+1.7}_{-1.7}$	$1.70^{+0.58}_{-0.83}$	$1.11^{+0.70}_{-0.74}$
083723.6+012413	4731	$0.63^{+3.45}_{-0.45}$	179^{+82}_{-70}	$2.3^{+1.7}_{-1.6}$	$1.52^{+0.70}_{-0.75}$	$1.57^{+0.33}_{-0.60}$
083743.8-014128	5321	$3.6^{+35.0}_{-3.1}$	108^{+109}_{-57}	$2.3^{+1.8}_{-1.5}$	$1.30^{+0.83}_{-0.66}$	$1.42^{+0.48}_{-0.85}$
083757.1-014217	6303	$1.11^{+22.53}_{-0.83}$	61^{+99}_{-47}	$2.4^{+1.8}_{-1.6}$	$1.53^{+0.67}_{-0.75}$	$1.37^{+1.36}_{-0.94}$
083759.5-003643	2456	$0.193^{+0.390}_{-0.076}$	178^{+52}_{-66}	$1.6^{+2.0}_{-1.2}$	$0.76^{+0.83}_{-0.35}$	$2.28^{+0.19}_{-0.18}$
083802.9+015626	4511	$4.9^{+9.9}_{-3.9}$	126^{+62}_{-48}	$2.5^{+1.8}_{-1.7}$	$1.36^{+0.78}_{-0.76}$	$0.93^{+0.53}_{-0.58}$
083806.9-003600	5386	$0.188^{+0.261}_{-0.072}$	420^{+150}_{-160}	$3.0^{+1.6}_{-2.1}$	$1.55^{+0.62}_{-0.82}$	$0.53^{+0.58}_{-0.37}$
083807.6+002501	19692	$0.34^{+0.47}_{-0.16}$	373^{+99}_{-108}	$2.7^{+1.6}_{-1.7}$	$1.58^{+0.64}_{-0.75}$	$0.76^{+0.35}_{-0.43}$
083809.4-020450	10843	$5.4^{+36.0}_{-4.8}$	66^{+47}_{-36}	$3.1^{+1.5}_{-2.3}$	$1.58^{+0.68}_{-0.94}$	$1.10^{+1.17}_{-0.80}$
083810.1+031520	3035	$0.168^{+0.453}_{-0.063}$	176^{+62}_{-76}	$0.61^{+1.92}_{-0.49}$	$0.458^{+0.498}_{-0.097}$	$2.14^{+0.19}_{-0.20}$
083811.8-015934	53	$7.2^{+19.9}_{-5.1}$	98^{+40}_{-35}	$2.6^{+1.6}_{-1.7}$	$1.57^{+0.65}_{-0.78}$	$2.39^{+0.19}_{-0.21}$
083817.4+041821	6136	$0.173^{+0.340}_{-0.072}$	260^{+84}_{-94}	$2.0^{+1.9}_{-1.4}$	$1.03^{+0.91}_{-0.53}$	$1.68^{+0.21}_{-0.26}$
083817.5-021704	6195	$0.46^{+1.06}_{-0.21}$	252^{+89}_{-88}	$2.1^{+2.0}_{-1.5}$	$1.16^{+0.83}_{-0.60}$	$1.56^{+0.25}_{-0.33}$
083834.1+020643	3905	$2.3^{+7.2}_{-1.7}$	134^{+44}_{-48}	$1.9^{+2.1}_{-1.4}$	$1.31^{+0.81}_{-0.66}$	$1.41^{+0.45}_{-0.57}$
083840.3+044416	8186	$0.41^{+1.84}_{-0.26}$	207^{+94}_{-81}	$2.4^{+1.8}_{-1.6}$	$1.42^{+0.72}_{-0.74}$	$1.28^{+0.36}_{-0.63}$
083840.6-004134	7463	$0.52^{+1.01}_{-0.33}$	231^{+90}_{-78}	$2.5^{+1.6}_{-1.6}$	$1.64^{+0.62}_{-0.80}$	$0.72^{+0.51}_{-0.48}$
083856.9+030743	7902	$3.8^{+20.2}_{-3.5}$	73^{+47}_{-34}	$2.5^{+1.6}_{-1.8}$	$1.66^{+0.61}_{-0.80}$	$1.32^{+0.87}_{-0.96}$
083857.5+020846	1806	$0.76^{+1.86}_{-0.47}$	266^{+95}_{-109}	$2.3^{+2.0}_{-1.6}$	$1.40^{+0.73}_{-0.72}$	$1.49^{+0.23}_{-0.34}$
083858.5-015032	6026	$0.96^{+8.32}_{-0.82}$	84^{+62}_{-44}	$2.4^{+1.9}_{-1.8}$	$1.73^{+0.60}_{-0.94}$	$1.52^{+0.96}_{-1.03}$
083859.3+022841	3315	$2.0^{+15.3}_{-1.7}$	113^{+68}_{-46}	$2.5^{+1.6}_{-1.7}$	$1.59^{+0.63}_{-0.75}$	$1.64^{+0.44}_{-0.87}$
083900.6+020057	736	$4.2^{+10.1}_{-2.6}$	85^{+28}_{-33}	$2.4^{+1.7}_{-1.7}$	$0.80^{+0.89}_{-0.33}$	$2.07^{+0.23}_{-0.32}$
083903.5-011454	7445	$1.05^{+2.34}_{-0.79}$	181^{+79}_{-62}	$2.7^{+1.6}_{-1.8}$	$1.59^{+0.62}_{-0.74}$	$0.89^{+0.65}_{-0.60}$
083914.7-021226	5360	$12.7^{+46.3}_{-9.2}$	34^{+10}_{-10}	$1.56^{+0.50}_{-0.46}$	$0.47^{+0.23}_{-0.10}$	$1.55^{+0.64}_{-0.86}$
083916.7-020552	7669	$5.6^{+6.5}_{-3.0}$	$42.4^{+7.2}_{-6.2}$	$0.61^{+0.26}_{-0.28}$	$0.61^{+0.16}_{-0.11}$	$1.34^{+0.37}_{-0.36}$
083917.9-020839	15489	$0.30^{+1.02}_{-0.18}$	199^{+86}_{-70}	$2.0^{+1.9}_{-1.5}$	$1.68^{+0.57}_{-0.78}$	$1.03^{+0.60}_{-0.65}$
083921.0-014149	12407	$1.9^{+2.7}_{-1.2}$	146^{+45}_{-40}	$2.53^{+1.25}_{-0.98}$	$0.88^{+0.60}_{-0.39}$	$0.80^{+0.57}_{-0.47}$
083927.0-021357	10377	$0.31^{+1.06}_{-0.16}$	190^{+140}_{-120}	$2.9^{+1.5}_{-2.1}$	$1.41^{+0.80}_{-0.81}$	$0.98^{+0.96}_{-0.69}$
083929.0+043001	3677	$1.6^{+13.6}_{-1.4}$	123^{+68}_{-52}	$2.6^{+1.6}_{-1.6}$	$1.48^{+0.69}_{-0.76}$	$1.54^{+0.49}_{-0.93}$
083929.6-015005	15946	$1.18^{+3.86}_{-0.96}$	172^{+84}_{-71}	$2.3^{+2.1}_{-1.6}$	$1.46^{+0.80}_{-0.83}$	$0.86^{+0.69}_{-0.64}$
083930.3-014348	6979	$0.69^{+2.78}_{-0.53}$	147^{+87}_{-55}	$3.1^{+1.4}_{-1.8}$	$1.80^{+0.49}_{-0.76}$	$1.29^{+1.4}_{-0.80}$
083933.8-014044	356	$6.7^{+3.7}_{-2.3}$	159^{+29}_{-27}	$1.74^{+0.96}_{-0.86}$	$0.96^{+0.28}_{-0.21}$	$1.16^{+0.23}_{-0.24}$
083936.0+011445	2898	$1.7^{+51.0}_{-1.6}$	83^{+91}_{-43}	$2.5^{+1.8}_{-1.7}$	$1.32^{+0.77}_{-0.68}$	$1.86^{+0.38}_{-1.11}$
083937.8+014631	7652	$1.4^{+6.7}_{-1.1}$	136^{+64}_{-50}	$2.7^{+1.6}_{-1.7}$	$1.65^{+0.59}_{-0.77}$	$1.31^{+0.50}_{-0.72}$
083940.8+010416	2832	$0.24^{+0.51}_{-0.12}$	247^{+76}_{-83}	$2.5^{+1.7}_{-1.7}$	$1.28^{+0.81}_{-0.64}$	$1.82^{+0.18}_{-0.25}$
083945.5+031556	7213	$5.3^{+57.9}_{-5.1}$	47^{+42}_{-22}	$2.6^{+1.7}_{-1.8}$	$1.67^{+0.58}_{-0.77}$	$1.62^{+0.87}_{-1.08}$
083955.0+022425	3270	$0.62^{+1.85}_{-0.48}$	153^{+97}_{-55}	$2.5^{+1.7}_{-1.6}$	$1.34^{+0.83}_{-0.67}$	$0.80^{+0.62}_{-0.55}$
084000.0-013109	7217	$1.06^{+4.80}_{-0.73}$	150^{+92}_{-80}	$1.6^{+2.1}_{-1.2}$	$0.82^{+0.88}_{-0.39}$	$1.27^{+0.38}_{-0.68}$
084001.6+042452	4839	$0.50^{+4.37}_{-0.35}$	128^{+57}_{-54}	$2.3^{+1.9}_{-1.7}$	$1.49^{+0.66}_{-0.76}$	$1.91^{+0.31}_{-0.70}$
084003.2+003008	2568	$0.68^{+18.55}_{-0.53}$	57^{+111}_{-46}	$2.7^{+1.6}_{-1.7}$	$1.53^{+0.69}_{-0.76}$	$1.33^{+1.54}_{-1.00}$
084004.8+013751	10272	$1.9^{+6.6}_{-1.5}$	98^{+54}_{-39}	$2.7^{+1.6}_{-1.7}$	$1.73^{+0.58}_{-0.84}$	$1.05^{+0.70}_{-0.69}$
084006.1+025913	2388	$1.4^{+6.4}_{-1.1}$	159^{+76}_{-61}	$2.5^{+1.7}_{-1.7}$	$1.67^{+0.59}_{-0.78}$	$1.52^{+0.35}_{-0.62}$
084011.6+034837	5544	12^{+49}_{-11}	60^{+41}_{-26}	$2.4^{+1.6}_{-1.6}$	$1.43^{+0.70}_{-0.72}$	$1.34^{+0.81}_{-0.89}$
084016.6+033951	6282	$5.2^{+26.8}_{-4.7}$	83^{+59}_{-36}	$2.6^{+1.6}_{-1.8}$	$1.64^{+0.59}_{-0.77}$	$1.19^{+0.79}_{-0.77}$
084021.6-022948	5406	$0.134^{+0.158}_{-0.040}$	307^{+113}_{-94}	$2.3^{+1.9}_{-1.8}$	$1.05^{+0.96}_{-0.56}$	$1.42^{+0.27}_{-0.35}$
084021.6+020132	5639	$1.13^{+2.90}_{-0.86}$	181^{+76}_{-63}	$2.6^{+1.6}_{-1.7}$	$1.62^{+0.60}_{-0.73}$	$0.92^{+0.54}_{-0.59}$
084034.5+023638	250	$0.49^{+1.05}_{-0.26}$	156^{+34}_{-45}	$2.0^{+2.0}_{-1.4}$	$0.89^{+0.82}_{-0.37}$	$2.56^{+0.16}_{-0.17}$
084035.8+044036	5844	16^{+110}_{-15}	53^{+45}_{-23}	$2.4^{+1.9}_{-1.8}$	$1.54^{+0.66}_{-0.71}$	$1.64^{+0.86}_{-1.18}$

continued.

Cluster (eFEDS J+)	ID_SRC	n_0^2 (10^{-7} cm^{-6})	r_s (arcsec)	ϵ	β	α
084044.7+024108	8131	$6.1^{+28.2}_{-5.3}$	111^{+75}_{-45}	$2.7^{+1.6}_{-1.9}$	$1.53^{+0.66}_{-0.78}$	$1.23^{+0.57}_{-0.71}$
084051.7+014122	7662	$2.6^{+6.6}_{-2.1}$	142^{+71}_{-47}	$2.8^{+1.5}_{-1.7}$	$1.67^{+0.57}_{-0.78}$	$1.00^{+0.54}_{-0.62}$
084058.4+050407	7625	27^{+176}_{-25}	62^{+36}_{-31}	$2.6^{+1.7}_{-1.8}$	$1.60^{+0.61}_{-0.84}$	$1.30^{+1.04}_{-0.94}$
084102.1+044734	6014	$0.202^{+0.612}_{-0.094}$	237^{+81}_{-88}	$2.1^{+1.9}_{-1.5}$	$1.35^{+0.76}_{-0.72}$	$1.56^{+0.27}_{-0.41}$
084105.5+031639	1906	$0.68^{+2.64}_{-0.51}$	181^{+86}_{-69}	$2.6^{+1.6}_{-1.8}$	$1.53^{+0.63}_{-0.72}$	$1.79^{+0.24}_{-0.42}$
084107.2+050459	4300	17^{+65}_{-15}	38^{+21}_{-14}	$1.32^{+1.01}_{-0.89}$	$0.79^{+0.36}_{-0.29}$	$1.53^{+0.73}_{-0.77}$
084110.8+005200	5702	$2.2^{+39.4}_{-2.0}$	64^{+52}_{-32}	$3.1^{+1.5}_{-2.1}$	$1.79^{+0.52}_{-0.85}$	$1.67^{+0.82}_{-1.22}$
084111.8-001946	7983	$2.7^{+5.8}_{-2.1}$	148^{+66}_{-53}	$2.5^{+1.7}_{-1.6}$	$1.63^{+0.63}_{-0.68}$	$0.75^{+0.64}_{-0.52}$
084116.5+020700	9822	$6.8^{+52.1}_{-5.9}$	53^{+33}_{-31}	$1.47^{+1.01}_{-0.90}$	$0.96^{+0.64}_{-0.44}$	$1.10^{+1.10}_{-0.74}$
084124.1-023350	9149	$0.85^{+5.09}_{-0.65}$	136^{+61}_{-56}	$2.6^{+1.6}_{-1.7}$	$1.56^{+0.63}_{-0.71}$	$1.43^{+0.45}_{-0.75}$
084124.7+004636	6605	$1.9^{+11.4}_{-1.6}$	91^{+42}_{-39}	$2.8^{+1.5}_{-1.8}$	$1.30^{+0.78}_{-0.66}$	$1.65^{+0.54}_{-0.84}$
084129.0+002645	5591	$0.215^{+2.378}_{-0.098}$	163^{+71}_{-115}	$0.25^{+0.57}_{-0.19}$	$0.383^{+0.135}_{-0.037}$	$2.09^{+0.20}_{-0.22}$
084134.1+043503	7544	$0.51^{+3.40}_{-0.34}$	140^{+110}_{-100}	$2.6^{+1.7}_{-1.7}$	$1.52^{+0.69}_{-0.75}$	$0.95^{+0.92}_{-0.66}$
084135.0+010150	1644	$2.3^{+22.8}_{-2.0}$	92^{+51}_{-38}	$2.4^{+1.8}_{-1.6}$	$1.69^{+0.58}_{-0.72}$	$1.98^{+0.39}_{-0.73}$
084135.7-005048	4430	$3.4^{+34.2}_{-2.9}$	58^{+31}_{-24}	$2.5^{+1.7}_{-1.7}$	$1.46^{+0.70}_{-0.72}$	$2.00^{+0.71}_{-0.97}$
084142.9+002841	8433	$0.30^{+2.11}_{-0.19}$	204^{+98}_{-93}	$1.9^{+2.1}_{-1.4}$	$1.32^{+0.73}_{-0.69}$	$1.36^{+0.33}_{-0.82}$
084146.3-021339	18047	$0.61^{+2.48}_{-0.47}$	143^{+88}_{-67}	$2.5^{+1.6}_{-1.7}$	$1.57^{+0.65}_{-0.78}$	$1.09^{+0.54}_{-0.65}$
084146.5+045612	2796	$0.45^{+1.57}_{-0.24}$	240^{+170}_{-140}	$2.2^{+1.9}_{-1.6}$	$1.45^{+0.73}_{-0.80}$	$0.65^{+0.76}_{-0.46}$
084148.1+004911	3008	$2.2^{+63.2}_{-1.9}$	76^{+60}_{-37}	$3.0^{+1.5}_{-2.1}$	$1.26^{+0.93}_{-0.66}$	$2.00^{+0.48}_{-1.35}$
084151.3-003358	3706	$1.07^{+1.72}_{-0.74}$	214^{+64}_{-59}	$3.0^{+1.4}_{-1.9}$	$1.67^{+0.56}_{-0.76}$	$0.73^{+0.52}_{-0.48}$
084151.7+004351	6543	$9.2^{+78.5}_{-8.3}$	49^{+38}_{-30}	$1.8^{+1.8}_{-1.3}$	$2.02^{+0.39}_{-0.85}$	$0.92^{+1.44}_{-0.71}$
084151.9-010156	6071	$5.5^{+13.2}_{-4.7}$	78^{+35}_{-23}	$2.6^{+1.6}_{-1.8}$	$1.57^{+0.66}_{-0.71}$	$0.88^{+0.85}_{-0.63}$
084201.3+040534	6988	$5.6^{+118.3}_{-5.2}$	55^{+53}_{-25}	$2.7^{+1.5}_{-1.8}$	$1.62^{+0.62}_{-0.74}$	$1.80^{+0.69}_{-1.12}$
084201.8+005941	3334	$0.37^{+1.96}_{-0.20}$	88^{+116}_{-65}	$2.6^{+1.6}_{-2.0}$	$1.65^{+0.64}_{-0.95}$	$1.00^{+1.47}_{-0.72}$
084210.5+020558	7967	$0.87^{+22.06}_{-0.70}$	60^{+101}_{-45}	$2.5^{+1.7}_{-1.7}$	$1.58^{+0.62}_{-0.83}$	$1.27^{+1.34}_{-0.88}$
084220.9+013844	3295	$0.52^{+1.22}_{-0.33}$	273^{+92}_{-92}	$2.5^{+1.7}_{-1.7}$	$1.63^{+0.62}_{-0.80}$	$1.41^{+0.27}_{-0.42}$
084223.1+003340	4993	$7.6^{+171.7}_{-6.8}$	63^{+58}_{-38}	$2.7^{+1.6}_{-1.8}$	$1.60^{+0.62}_{-0.74}$	$2.1^{+1.3}_{-1.2}$
084240.7-011643	2859	$0.87^{+73.25}_{-0.76}$	38^{+48}_{-21}	$2.6^{+1.6}_{-1.9}$	$1.68^{+0.61}_{-0.86}$	$2.66^{+0.69}_{-1.22}$
084246.9-000917	4861	$3.2^{+3.9}_{-2.2}$	170^{+54}_{-46}	$3.0^{+1.4}_{-1.9}$	$1.72^{+0.57}_{-0.72}$	$0.58^{+0.50}_{-0.41}$
084253.7+002006	6903	$5.6^{+35.7}_{-5.2}$	57^{+45}_{-22}	$1.9^{+2.2}_{-1.4}$	$1.65^{+0.60}_{-0.79}$	$1.17^{+1.02}_{-0.85}$
084255.6+042332	2475	$0.31^{+0.79}_{-0.16}$	207^{+59}_{-70}	$2.6^{+1.6}_{-1.7}$	$1.38^{+0.75}_{-0.68}$	$2.00^{+0.18}_{-0.24}$
084258.3-004037	4269	$0.158^{+0.247}_{-0.047}$	440^{+230}_{-290}	$2.1^{+1.9}_{-1.5}$	$1.21^{+0.81}_{-0.60}$	$0.32^{+0.60}_{-0.23}$
084301.4+025741	11065	$2.1^{+43.7}_{-1.9}$	58^{+46}_{-30}	$2.6^{+1.6}_{-1.7}$	$1.60^{+0.61}_{-0.72}$	$2.02^{+0.60}_{-1.11}$
084307.1+002839	3336	$3.7^{+11.4}_{-2.9}$	135^{+58}_{-43}	$2.8^{+1.5}_{-1.7}$	$1.57^{+0.64}_{-0.79}$	$1.15^{+0.53}_{-0.70}$
084324.2-001438	9590	$0.71^{+1.89}_{-0.52}$	202^{+91}_{-76}	$2.5^{+1.6}_{-1.6}$	$1.57^{+0.65}_{-0.80}$	$0.96^{+0.58}_{-0.66}$
084346.2+010833	12839	$0.37^{+0.68}_{-0.20}$	224^{+113}_{-74}	$2.4^{+1.3}_{-1.3}$	$1.49^{+0.58}_{-0.59}$	$0.84^{+0.64}_{-0.51}$
084349.1+040404	19985	$6.5^{+9.6}_{-4.3}$	168^{+65}_{-72}	$2.7^{+1.5}_{-1.9}$	$1.52^{+0.70}_{-0.86}$	$0.63^{+0.48}_{-0.42}$
084353.9+031402	19202	$0.98^{+3.57}_{-0.76}$	108^{+62}_{-44}	$2.3^{+1.7}_{-1.5}$	$1.48^{+0.67}_{-0.69}$	$1.03^{+0.62}_{-0.67}$
084412.6-020514	3396	$6.1^{+175.8}_{-4.9}$	71^{+85}_{-53}	$2.6^{+1.6}_{-1.7}$	$1.57^{+0.64}_{-0.80}$	$1.37^{+1.41}_{-0.99}$
084417.9+010415	1812	$3.3^{+9.0}_{-2.4}$	135^{+52}_{-51}	$2.0^{+1.9}_{-1.5}$	$1.28^{+0.88}_{-0.66}$	$1.33^{+0.42}_{-0.63}$
084430.8+021736	3541	$4.3^{+23.2}_{-3.7}$	95^{+46}_{-33}	$2.2^{+1.7}_{-1.4}$	$1.51^{+0.70}_{-0.68}$	$1.58^{+0.56}_{-0.85}$
084434.3+031026	4876	$3.2^{+17.4}_{-2.7}$	111^{+63}_{-68}	$2.7^{+1.6}_{-1.8}$	$1.62^{+0.61}_{-0.76}$	$1.29^{+1.11}_{-0.83}$
084438.5+041946	11610	$2.5^{+7.1}_{-2.1}$	122^{+61}_{-43}	$2.9^{+1.3}_{-1.8}$	$1.60^{+0.64}_{-0.75}$	$0.99^{+0.61}_{-0.65}$
084439.0+043302	5668	$5.2^{+25.4}_{-4.6}$	85^{+45}_{-32}	$3.0^{+1.3}_{-1.7}$	$1.82^{+0.43}_{-0.54}$	$1.21^{+0.76}_{-0.80}$
084441.3+021701	1778	$0.220^{+0.195}_{-0.056}$	233^{+57}_{-56}	$1.9^{+1.7}_{-1.3}$	$0.81^{+0.54}_{-0.31}$	$2.11^{+0.15}_{-0.15}$
084454.0+010021	4436	$0.40^{+5.10}_{-0.27}$	190^{+83}_{-89}	$2.5^{+1.8}_{-1.7}$	$1.50^{+0.72}_{-0.82}$	$1.63^{+0.31}_{-0.90}$
084459.2-011902	4768	$0.29^{+1.59}_{-0.16}$	240^{+100}_{-110}	$2.0^{+1.9}_{-1.5}$	$1.28^{+0.75}_{-0.70}$	$1.54^{+0.25}_{-0.49}$

continued.

Cluster (eFEDS J+)	ID_SRC	n_0^2 (10^{-7} cm^{-6})	r_s (arcsec)	ϵ	β	α
084501.0+012728	1607	$2.4^{+9.6}_{-1.8}$	145^{+61}_{-48}	$2.7^{+1.6}_{-1.9}$	$1.62^{+0.59}_{-0.68}$	$1.35^{+0.47}_{-0.67}$
084528.6+032739	144	$3.6^{+4.5}_{-1.8}$	174^{+67}_{-51}	$1.9^{+1.9}_{-1.3}$	$1.01^{+0.55}_{-0.44}$	$1.67^{+0.13}_{-0.15}$
084531.6+022831	1039	$0.87^{+1.68}_{-0.48}$	269^{+76}_{-87}	$2.4^{+1.7}_{-1.7}$	$1.54^{+0.63}_{-0.69}$	$1.67^{+0.19}_{-0.29}$
084544.3-002914	2214	$3.8^{+10.6}_{-2.3}$	132^{+38}_{-55}	$3.4^{+1.2}_{-1.6}$	$0.62^{+0.34}_{-0.22}$	$1.18^{+0.44}_{-0.60}$
084545.2+005535	3660	$1.5^{+44.8}_{-1.3}$	59^{+104}_{-43}	$2.6^{+1.7}_{-1.8}$	$1.54^{+0.66}_{-0.77}$	$1.6^{+1.5}_{-1.1}$
084552.4+011714	5804	$1.5^{+10.5}_{-1.2}$	124^{+73}_{-76}	$2.7^{+1.6}_{-1.7}$	$1.54^{+0.70}_{-0.81}$	$1.28^{+0.89}_{-0.78}$
084557.6+041103	25781	$0.46^{+1.94}_{-0.31}$	155^{+83}_{-60}	$2.5^{+1.7}_{-1.7}$	$1.72^{+0.55}_{-0.80}$	$0.97^{+0.56}_{-0.66}$
084558.1+012443	9771	$1.29^{+4.01}_{-0.97}$	141^{+68}_{-58}	$2.8^{+1.6}_{-1.9}$	$1.60^{+0.61}_{-0.83}$	$1.04^{+0.81}_{-0.72}$
084559.7+031321	5281	$0.31^{+2.08}_{-0.18}$	164^{+84}_{-75}	$2.2^{+1.8}_{-1.6}$	$1.26^{+0.83}_{-0.68}$	$1.78^{+0.31}_{-0.49}$
084607.6+000651	29318	$1.10^{+4.82}_{-0.82}$	150^{+86}_{-61}	$2.7^{+1.6}_{-1.8}$	$1.51^{+0.66}_{-0.70}$	$0.91^{+0.56}_{-0.60}$
084630.7+024702	13490	$0.200^{+0.784}_{-0.092}$	230^{+110}_{-100}	$2.1^{+1.9}_{-1.5}$	$1.18^{+0.88}_{-0.66}$	$1.25^{+0.39}_{-0.53}$
084637.1-002256	2987	$2.2^{+18.6}_{-1.9}$	114^{+73}_{-51}	$2.7^{+1.6}_{-1.7}$	$1.53^{+0.70}_{-0.69}$	$1.66^{+0.50}_{-1.04}$
084640.3-010423	9948	$3.5^{+23.1}_{-3.1}$	89^{+54}_{-42}	$3.0^{+1.4}_{-1.7}$	$1.61^{+0.61}_{-0.81}$	$1.31^{+0.69}_{-0.87}$
084645.6+014947	6215	$0.264^{+0.344}_{-0.064}$	270^{+100}_{-100}	$0.98^{+2.14}_{-0.76}$	$0.53^{+0.72}_{-0.15}$	$1.67^{+0.22}_{-0.25}$
084647.4+044607	6656	$0.46^{+2.09}_{-0.23}$	185^{+73}_{-81}	$1.7^{+2.0}_{-1.2}$	$0.88^{+0.93}_{-0.41}$	$1.70^{+0.27}_{-0.40}$
084649.0+004946	11018	$1.05^{+6.10}_{-0.81}$	96^{+74}_{-65}	$2.5^{+1.7}_{-1.7}$	$1.63^{+0.61}_{-0.81}$	$1.11^{+1.07}_{-0.76}$
084655.7-003705	3712	$3.5^{+40.4}_{-3.0}$	102^{+61}_{-45}	$2.7^{+1.6}_{-1.8}$	$1.64^{+0.60}_{-0.81}$	$1.63^{+0.76}_{-0.93}$
084657.6-011314	9845	$4.8^{+27.3}_{-4.1}$	86^{+54}_{-38}	$2.7^{+1.7}_{-1.8}$	$1.65^{+0.60}_{-0.77}$	$1.16^{+0.76}_{-0.74}$
084717.7+033421	10507	$1.9^{+24.8}_{-1.6}$	52^{+64}_{-36}	$2.4^{+1.8}_{-1.6}$	$1.61^{+0.60}_{-0.80}$	$1.43^{+1.32}_{-0.99}$
084729.7+013053	5053	$0.72^{+3.65}_{-0.50}$	185^{+82}_{-60}	$2.0^{+2.0}_{-1.5}$	$1.61^{+0.62}_{-0.69}$	$1.40^{+0.38}_{-0.69}$
084751.7+025522	4736	$2.1^{+11.0}_{-1.9}$	96^{+58}_{-33}	$2.7^{+1.6}_{-1.8}$	$1.57^{+0.65}_{-0.74}$	$1.45^{+0.56}_{-0.83}$
084759.1+014903	4709	$2.6^{+48.4}_{-2.1}$	77^{+88}_{-55}	$2.5^{+1.7}_{-1.7}$	$1.61^{+0.64}_{-0.71}$	$1.51^{+1.40}_{-0.97}$
084823.2+041205	2437	$0.89^{+8.46}_{-0.57}$	128^{+57}_{-76}	$1.9^{+2.1}_{-1.4}$	$0.99^{+0.97}_{-0.54}$	$2.29^{+0.26}_{-0.34}$
084833.2-012216	1073	$2.2^{+5.6}_{-1.5}$	177^{+69}_{-64}	$2.5^{+1.7}_{-1.6}$	$1.67^{+0.39}_{-0.73}$	$1.64^{+0.25}_{-0.35}$
084852.9+035939	10165	$5.1^{+27.9}_{-4.5}$	79^{+52}_{-34}	$2.5^{+1.7}_{-1.6}$	$1.59^{+0.64}_{-0.77}$	$1.25^{+0.68}_{-0.82}$
084905.3+021435	7831	$0.48^{+2.45}_{-0.29}$	200^{+130}_{-100}	$2.2^{+2.0}_{-1.6}$	$1.51^{+0.69}_{-0.81}$	$0.98^{+0.84}_{-0.67}$
084910.6+024117	9790	$5.0^{+48.2}_{-4.4}$	70^{+52}_{-40}	$2.4^{+1.7}_{-1.6}$	$1.61^{+0.62}_{-0.80}$	$1.61^{+0.88}_{-0.96}$
084925.4+013840	14327	$1.7^{+4.8}_{-1.3}$	162^{+74}_{-54}	$2.6^{+1.6}_{-1.7}$	$1.58^{+0.64}_{-0.72}$	$1.03^{+0.46}_{-0.61}$
084934.9+014437	32680	$0.40^{+1.47}_{-0.21}$	209^{+115}_{-88}	$2.0^{+1.9}_{-1.5}$	$1.13^{+0.91}_{-0.60}$	$1.16^{+0.41}_{-0.54}$
084939.6-005126	2261	$0.42^{+1.28}_{-0.20}$	205^{+69}_{-85}	$1.9^{+1.9}_{-1.4}$	$1.00^{+0.87}_{-0.50}$	$1.94^{+0.20}_{-0.28}$
084957.4+004524	8524	$5.8^{+115.6}_{-4.9}$	70^{+88}_{-46}	$2.5^{+1.7}_{-1.7}$	$1.47^{+0.72}_{-0.73}$	$1.5^{+1.4}_{-1.0}$
085018.3+020018	5464	$4.2^{+58.4}_{-3.7}$	81^{+61}_{-38}	$2.6^{+1.6}_{-1.7}$	$1.48^{+0.71}_{-0.70}$	$1.78^{+0.51}_{-0.94}$
085020.4+032819	6529	$4.3^{+8.9}_{-3.2}$	127^{+48}_{-36}	$2.8^{+1.6}_{-1.6}$	$1.64^{+0.58}_{-0.64}$	$0.85^{+0.59}_{-0.60}$
085022.2+001607	8602	$0.202^{+0.232}_{-0.065}$	540^{+200}_{-190}	$2.6^{+1.8}_{-1.6}$	$1.40^{+0.82}_{-0.74}$	$0.57^{+0.44}_{-0.37}$
085027.8+001503	1023	$4.1^{+7.8}_{-2.4}$	121^{+66}_{-38}	$0.84^{+0.68}_{-0.58}$	$0.51^{+0.16}_{-0.12}$	$1.31^{+0.25}_{-0.51}$
085030.5+003330	6125	$0.41^{+2.49}_{-0.23}$	184^{+96}_{-105}	$0.66^{+1.38}_{-0.48}$	$0.51^{+0.34}_{-0.12}$	$1.70^{+0.24}_{-0.43}$
085051.8+015331	8679	$1.8^{+8.3}_{-1.4}$	126^{+57}_{-46}	$2.6^{+1.5}_{-1.6}$	$1.67^{+0.55}_{-0.74}$	$1.33^{+0.75}_{-0.86}$
085056.4+005607	3556	$0.85^{+5.42}_{-0.63}$	156^{+88}_{-91}	$2.7^{+1.6}_{-1.7}$	$1.58^{+0.62}_{-0.82}$	$1.27^{+1.09}_{-0.79}$
085119.9+022951	2101	$2.7^{+11.3}_{-2.1}$	166^{+84}_{-66}	$2.3^{+1.8}_{-1.6}$	$1.43^{+0.74}_{-0.76}$	$1.41^{+0.38}_{-0.66}$
085121.2+012856	11156	$1.4^{+6.4}_{-1.1}$	136^{+67}_{-51}	$2.6^{+1.6}_{-1.7}$	$1.58^{+0.63}_{-0.72}$	$1.19^{+0.55}_{-0.76}$
085128.4+011501	7355	$0.57^{+7.57}_{-0.38}$	80^{+135}_{-63}	$2.7^{+1.5}_{-1.7}$	$1.58^{+0.65}_{-0.74}$	$0.93^{+1.30}_{-0.67}$
085130.0-004609	18314	$0.82^{+3.21}_{-0.58}$	171^{+75}_{-59}	$2.7^{+1.7}_{-1.7}$	$1.61^{+0.62}_{-0.81}$	$1.20^{+0.45}_{-0.68}$
085131.0+045239	863	$0.55^{+1.45}_{-0.27}$	224^{+59}_{-77}	$2.5^{+1.7}_{-1.7}$	$1.57^{+0.60}_{-0.70}$	$2.09^{+0.15}_{-0.21}$
085138.2-003537	4508	$0.65^{+2.24}_{-0.46}$	168^{+106}_{-67}	$2.8^{+1.4}_{-1.8}$	$1.50^{+0.72}_{-0.79}$	$0.83^{+0.76}_{-0.58}$
085141.9+021438	7280	$1.14^{+21.88}_{-0.94}$	65^{+77}_{-44}	$2.4^{+1.8}_{-1.7}$	$1.63^{+0.60}_{-0.78}$	$1.5^{+1.3}_{-1.1}$
085204.5+012132	6636	$1.6^{+5.9}_{-1.2}$	171^{+82}_{-66}	$2.4^{+1.8}_{-1.7}$	$1.56^{+0.64}_{-0.83}$	$1.24^{+0.45}_{-0.64}$
085217.0-010131	339	$1.21^{+4.15}_{-0.92}$	240^{+87}_{-79}	$2.4^{+1.8}_{-1.5}$	$1.75^{+0.53}_{-0.76}$	$1.81^{+0.41}_{-0.58}$

continued.

Cluster (eFEDS J+)	ID_SRC	n_0^2 $(10^{-7}\ \mathrm{cm}^{-6})$	r_s (arcsec)	ϵ	β	α
085230.6+002457	2524	$1.05^{+2.54}_{-0.69}$	212^{+80}_{-88}	$2.0^{+1.9}_{-1.4}$	$1.37^{+0.72}_{-0.73}$	$1.38^{+0.31}_{-0.42}$
085231.1-011230	4810	$1.05^{+7.86}_{-0.82}$	142^{+74}_{-64}	$2.4^{+1.8}_{-1.7}$	$1.49^{+0.67}_{-0.78}$	$1.62^{+0.37}_{-0.73}$
085239.6+003240	5477	$2.0^{+38.7}_{-1.7}$	99^{+78}_{-48}	$2.2^{+2.0}_{-1.7}$	$1.53^{+0.69}_{-0.85}$	$1.68^{+0.44}_{-0.99}$
085245.7-020519	5790	$0.65^{+7.35}_{-0.40}$	101^{+61}_{-51}	$2.5^{+1.7}_{-1.8}$	$1.37^{+0.81}_{-0.79}$	$2.20^{+0.38}_{-0.49}$
085255.1-013737	1376	$0.45^{+2.32}_{-0.34}$	199^{+106}_{-77}	$2.6^{+1.6}_{-1.7}$	$1.58^{+0.64}_{-0.80}$	$1.34^{+0.36}_{-0.70}$
085256.8+052741	6642	14^{+130}_{-13}	47^{+33}_{-26}	$2.7^{+1.6}_{-1.7}$	$1.58^{+0.63}_{-0.80}$	$1.83^{+0.95}_{-1.16}$
085325.6+030834	9042	$2.5^{+36.7}_{-2.2}$	67^{+41}_{-27}	$2.8^{+1.5}_{-1.9}$	$1.73^{+0.56}_{-0.74}$	$1.75^{+0.70}_{-1.02}$
085327.2-002117	6003	$0.59^{+2.43}_{-0.41}$	201^{+87}_{-71}	$2.6^{+1.7}_{-1.7}$	$1.52^{+0.66}_{-0.77}$	$1.40^{+0.35}_{-0.63}$
085335.2+032214	8596	$1.5^{+8.1}_{-1.2}$	121^{+60}_{-46}	$2.7^{+1.5}_{-1.8}$	$1.55^{+0.69}_{-0.73}$	$1.36^{+0.51}_{-0.81}$
085340.5+022411	9213	$2.8^{+4.8}_{-2.4}$	140^{+79}_{-50}	$2.2^{+1.9}_{-1.5}$	$1.38^{+0.79}_{-0.82}$	$0.77^{+0.70}_{-0.54}$
085412.8-022123	1458	$1.39^{+5.34}_{-0.93}$	196^{+72}_{-68}	$2.7^{+1.6}_{-1.8}$	$1.53^{+0.68}_{-0.71}$	$1.81^{+0.25}_{-0.49}$
085419.5-000925	1294	$0.49^{+2.01}_{-0.30}$	179^{+71}_{-84}	$0.96^{+1.45}_{-0.70}$	$0.54^{+0.27}_{-0.13}$	$1.97^{+0.18}_{-0.32}$
085433.0+004009	3675	$3.1^{+61.4}_{-2.8}$	37^{+29}_{-16}	$3.4^{+1.1}_{-1.8}$	$1.59^{+0.65}_{-0.75}$	$2.58^{+0.97}_{-1.53}$
085434.5-014038	8094	$0.64^{+2.80}_{-0.46}$	159^{+71}_{-55}	$2.5^{+1.7}_{-1.7}$	$1.44^{+0.70}_{-0.75}$	$1.50^{+0.41}_{-0.67}$
085436.6+003835	328	$10.7^{+9.9}_{-4.5}$	104^{+18}_{-24}	$0.65^{+0.58}_{-0.42}$	$0.57^{+0.11}_{-0.12}$	$1.39^{+0.23}_{-0.25}$
085438.5+001211	5390	$0.58^{+7.43}_{-0.44}$	107^{+95}_{-63}	$2.2^{+1.7}_{-1.5}$	$1.37^{+0.79}_{-0.78}$	$1.53^{+0.64}_{-0.84}$
085440.4-020931	7700	$6.5^{+47.4}_{-6.0}$	57^{+40}_{-25}	$2.5^{+1.7}_{-1.7}$	$1.62^{+0.63}_{-0.69}$	$1.45^{+0.81}_{-0.99}$
085447.0-012132	2079	$2.0^{+5.4}_{-1.4}$	181^{+73}_{-66}	$2.5^{+1.7}_{-1.7}$	$1.59^{+0.65}_{-0.76}$	$1.21^{+0.38}_{-0.50}$
085508.9-003445	2810	$2.0^{+97.9}_{-1.8}$	57^{+42}_{-26}	$2.7^{+1.7}_{-1.7}$	$1.73^{+0.55}_{-0.75}$	$2.33^{+0.52}_{-1.26}$
085517.2+013508	6746	$0.67^{+2.25}_{-0.49}$	263^{+106}_{-94}	$2.6^{+1.4}_{-1.6}$	$1.63^{+0.55}_{-0.67}$	$1.13^{+0.41}_{-0.65}$
085519.1-014315	5909	$0.69^{+10.07}_{-0.56}$	66^{+106}_{-51}	$2.7^{+1.6}_{-1.7}$	$1.56^{+0.66}_{-0.72}$	$1.04^{+1.34}_{-0.74}$
085524.3+015012	23313	$0.24^{+0.39}_{-0.12}$	300^{+130}_{-100}	$2.4^{+1.8}_{-1.7}$	$1.57^{+0.65}_{-0.82}$	$0.82^{+0.44}_{-0.46}$
085530.1-010634	1797	$10.7^{+34.5}_{-9.0}$	108^{+64}_{-41}	$2.6^{+1.6}_{-1.8}$	$1.57^{+0.66}_{-0.81}$	$1.17^{+0.56}_{-0.70}$
085541.2+002740	5589	$0.72^{+5.59}_{-0.54}$	84^{+86}_{-61}	$3.2^{+1.3}_{-2.0}$	$1.70^{+0.57}_{-0.77}$	$1.14^{+1.27}_{-0.81}$
085542.6+032807	8925	$0.96^{+11.49}_{-0.64}$	73^{+113}_{-56}	$2.7^{+1.6}_{-1.8}$	$1.44^{+0.73}_{-0.77}$	$1.10^{+1.35}_{-0.80}$
085547.0+025458	8799	$2.7^{+65.4}_{-2.2}$	53^{+86}_{-36}	$2.3^{+1.9}_{-1.6}$	$1.72^{+0.54}_{-0.86}$	$1.6^{+1.6}_{-1.1}$
085604.8+002520	8826	$0.78^{+1.38}_{-0.50}$	280^{+130}_{-110}	$2.1^{+2.0}_{-1.6}$	$1.02^{+1.01}_{-0.51}$	$0.85^{+0.41}_{-0.54}$
085616.1-013945	8922	$0.85^{+11.41}_{-0.66}$	21^{+38}_{-16}	$3.0^{+1.5}_{-1.9}$	$1.72^{+0.56}_{-0.86}$	$1.02^{+1.70}_{-0.73}$
085620.7+014649	569	$1.08^{+3.52}_{-0.72}$	173^{+62}_{-59}	$2.5^{+1.7}_{-1.8}$	$1.49^{+0.63}_{-0.64}$	$2.09^{+0.20}_{-0.31}$
085623.6-013612	16370	$0.81^{+3.86}_{-0.65}$	139^{+93}_{-68}	$2.7^{+1.6}_{-1.8}$	$1.57^{+0.64}_{-0.81}$	$1.29^{+0.54}_{-0.80}$
085624.3+004632	32576	$2.2^{+5.5}_{-1.8}$	123^{+56}_{-43}	$2.8^{+1.6}_{-1.9}$	$1.74^{+0.55}_{-0.76}$	$0.90^{+0.63}_{-0.64}$
085626.2+021348	5697	$0.183^{+0.344}_{-0.073}$	295^{+90}_{-90}	$2.1^{+1.8}_{-1.5}$	$1.18^{+0.87}_{-0.59}$	$1.53^{+0.22}_{-0.31}$
085627.2+014217	1385	18^{+36}_{-15}	99^{+47}_{-31}	$2.6^{+1.7}_{-1.7}$	$1.55^{+0.64}_{-0.77}$	$0.82^{+0.64}_{-0.58}$
085635.0+031342	24300	$0.76^{+10.36}_{-0.59}$	53^{+87}_{-42}	$2.6^{+1.7}_{-1.7}$	$1.69^{+0.56}_{-0.83}$	$1.28^{+1.58}_{-0.86}$
085650.4-022200	5261	$1.02^{+2.65}_{-0.81}$	162^{+62}_{-48}	$2.6^{+1.6}_{-1.7}$	$1.70^{+0.55}_{-0.73}$	$1.12^{+0.54}_{-0.64}$
085705.9+011453	3128	$1.6^{+4.8}_{-1.2}$	218^{+86}_{-74}	$2.6^{+1.7}_{-1.8}$	$1.48^{+0.76}_{-0.74}$	$1.07^{+0.45}_{-0.68}$
085728.3+032354	6278	$0.81^{+3.52}_{-0.58}$	167^{+75}_{-70}	$2.1^{+1.9}_{-1.5}$	$0.93^{+0.83}_{-0.46}$	$1.25^{+0.44}_{-0.64}$
085740.1-020037	7884	$1.05^{+4.62}_{-0.88}$	155^{+97}_{-56}	$2.5^{+1.7}_{-1.7}$	$1.55^{+0.65}_{-0.71}$	$1.16^{+0.50}_{-0.71}$
085744.0-022448	12696	$0.164^{+0.406}_{-0.092}$	239^{+106}_{-87}	$2.5^{+1.7}_{-1.6}$	$1.55^{+0.66}_{-0.77}$	$1.07^{+0.48}_{-0.63}$
085751.6+031039	108	$23.9^{+13.5}_{-8.0}$	102^{+21}_{-15}	$1.52^{+0.57}_{-0.74}$	$0.50^{+0.15}_{-0.11}$	$1.15^{+0.17}_{-0.20}$
085801.1-004103	11717	$0.58^{+2.09}_{-0.44}$	142^{+62}_{-52}	$2.5^{+1.6}_{-1.7}$	$1.57^{+0.66}_{-0.77}$	$1.32^{+0.49}_{-0.73}$
085805.0+010906	4070	$7.8^{+6.8}_{-3.3}$	72^{+15}_{-13}	$0.92^{+0.38}_{-0.46}$	$0.411^{+0.080}_{-0.054}$	$1.14^{+0.34}_{-0.46}$
085830.0-010656	4297	$0.58^{+1.56}_{-0.42}$	212^{+81}_{-64}	$2.6^{+1.6}_{-1.6}$	$1.69^{+0.59}_{-0.75}$	$1.24^{+0.39}_{-0.60}$
085837.9+012657	8857	$2.7^{+92.4}_{-2.4}$	42^{+67}_{-32}	$2.5^{+1.7}_{-1.7}$	$1.62^{+0.61}_{-0.80}$	$1.5^{+1.5}_{-1.0}$
085841.8-020541	2367	$0.52^{+6.92}_{-0.41}$	126^{+78}_{-59}	$2.6^{+1.6}_{-1.8}$	$1.38^{+0.73}_{-0.67}$	$1.87^{+0.32}_{-0.68}$
085849.8+022800	715	$0.186^{+0.785}_{-0.083}$	241^{+89}_{-120}	$1.6^{+2.1}_{-1.2}$	$0.74^{+0.75}_{-0.31}$	$2.24^{+0.30}_{-0.30}$
085901.1-012025	3527	$7.4^{+30.6}_{-6.7}$	101^{+70}_{-39}	$2.6^{+1.7}_{-1.7}$	$1.60^{+0.65}_{-0.75}$	$1.23^{+0.69}_{-0.79}$

continued.

Cluster (eFEDS J+)	ID_SRC	n_0^2 $(10^{-7}$ cm$^{-6})$	r_s (arcsec)	ϵ	β	α
085901.5+010649	2757	$1.23^{+5.00}_{-0.92}$	151^{+65}_{-50}	$2.4^{+1.7}_{-1.4}$	$1.55^{+0.67}_{-0.65}$	$1.55^{+0.37}_{-0.64}$
085907.3-005056	16320	$0.211^{+0.478}_{-0.098}$	330^{+140}_{-120}	$2.4^{+1.8}_{-1.8}$	$1.34^{+0.88}_{-0.76}$	$0.75^{+0.47}_{-0.52}$
085913.1+031334	485	$0.203^{+0.345}_{-0.092}$	149^{+41}_{-42}	$1.5^{+2.2}_{-1.2}$	$0.67^{+1.22}_{-0.27}$	$2.64^{+0.16}_{-0.13}$
085931.9+030839	360	$0.97^{+1.29}_{-0.51}$	243^{+79}_{-79}	$2.4^{+1.7}_{-1.7}$	$1.46^{+0.70}_{-0.66}$	$1.82^{+0.12}_{-0.14}$
085939.1-004932	6894	$1.28^{+3.47}_{-1.00}$	162^{+75}_{-64}	$2.6^{+1.7}_{-1.8}$	$1.65^{+0.61}_{-0.79}$	$0.98^{+0.55}_{-0.65}$
085948.9+041120	1350	$0.28^{+1.00}_{-0.16}$	204^{+61}_{-84}	$2.3^{+1.9}_{-1.8}$	$1.36^{+0.74}_{-0.75}$	$2.10^{+0.17}_{-0.25}$
085950.1-001221	4539	$0.82^{+4.49}_{-0.65}$	174^{+89}_{-70}	$2.4^{+1.7}_{-1.6}$	$1.56^{+0.64}_{-0.73}$	$1.42^{+0.37}_{-0.71}$
085954.2-013308	13823	$1.9^{+54.2}_{-1.7}$	56^{+73}_{-38}	$2.3^{+1.8}_{-1.6}$	$1.54^{+0.64}_{-0.76}$	$2.0^{+1.1}_{-1.2}$
090004.3+033324	7945	$4.3^{+17.9}_{-3.6}$	91^{+51}_{-32}	$2.6^{+1.8}_{-1.7}$	$1.62^{+0.62}_{-0.71}$	$1.12^{+0.69}_{-0.73}$
090010.4+023631	10878	$0.83^{+3.31}_{-0.64}$	162^{+77}_{-68}	$2.6^{+1.6}_{-1.9}$	$1.46^{+0.68}_{-0.71}$	$1.11^{+0.52}_{-0.63}$
090020.8-002602	1315	$0.88^{+25.63}_{-0.72}$	81^{+101}_{-59}	$2.3^{+1.9}_{-1.7}$	$1.54^{+0.67}_{-0.80}$	$1.4^{+1.4}_{-1.0}$
090033.7+033932	2407	$0.82^{+4.61}_{-0.55}$	180^{+130}_{-110}	$2.4^{+1.8}_{-1.6}$	$1.43^{+0.73}_{-0.74}$	$1.12^{+0.89}_{-0.68}$
090034.1-010649	1652	$0.85^{+2.43}_{-0.66}$	179^{+84}_{-61}	$2.4^{+1.7}_{-1.6}$	$1.69^{+0.56}_{-0.76}$	$1.08^{+0.46}_{-0.59}$
090044.6-011104	8508	$0.32^{+8.25}_{-0.25}$	58^{+61}_{-31}	$2.7^{+1.6}_{-1.8}$	$1.61^{+0.64}_{-0.78}$	$2.27^{+0.71}_{-0.97}$
090051.6-003457	9834	$0.70^{+3.19}_{-0.54}$	133^{+65}_{-61}	$2.9^{+1.5}_{-1.9}$	$1.54^{+0.67}_{-0.71}$	$1.05^{+0.72}_{-0.67}$
090053.0-002837	9310	$1.3^{+5.5}_{-1.2}$	114^{+67}_{-41}	$2.4^{+1.7}_{-1.6}$	$1.55^{+0.66}_{-0.77}$	$1.19^{+0.64}_{-0.80}$
090059.3+035925	983	$1.9^{+12.9}_{-1.6}$	120^{+69}_{-49}	$2.3^{+1.8}_{-1.7}$	$1.50^{+0.67}_{-0.73}$	$1.92^{+0.35}_{-0.52}$
090104.4+011643	3171	$3.9^{+8.8}_{-3.0}$	142^{+67}_{-47}	$2.8^{+1.5}_{-1.8}$	$1.63^{+0.59}_{-0.74}$	$0.96^{+0.50}_{-0.58}$
090105.2-012525	11836	$1.11^{+2.15}_{-0.78}$	169^{+62}_{-59}	$2.7^{+1.5}_{-1.9}$	$1.48^{+0.64}_{-0.70}$	$0.82^{+0.53}_{-0.57}$
090115.3+005040	8881	$2.4^{+4.5}_{-2.0}$	144^{+81}_{-47}	$2.5^{+1.7}_{-1.8}$	$1.55^{+0.64}_{-0.80}$	$0.77^{+0.67}_{-0.53}$
090119.0+030204	7017	$3.4^{+18.1}_{-2.9}$	79^{+53}_{-41}	$1.6^{+2.1}_{-1.0}$	$0.72^{+0.99}_{-0.28}$	$1.36^{+0.76}_{-0.82}$
090121.9-003709	1600	$1.4^{+11.3}_{-1.2}$	117^{+74}_{-51}	$2.3^{+2.0}_{-1.8}$	$1.68^{+0.63}_{-0.96}$	$1.48^{+0.60}_{-1.04}$
090129.1-013853	1104	39^{+32}_{-14}	60^{+13}_{-12}	$0.56^{+0.37}_{-0.36}$	$0.527^{+0.074}_{-0.092}$	$0.49^{+0.49}_{-0.35}$
090131.1+030056	152	$15.3^{+21.8}_{-6.7}$	93^{+14}_{-18}	$1.50^{+0.88}_{-0.83}$	$0.52^{+0.13}_{-0.12}$	$1.27^{+0.31}_{-0.60}$
090133.2+021651	4181	$0.44^{+1.43}_{-0.28}$	214^{+77}_{-76}	$2.6^{+1.6}_{-1.7}$	$1.64^{+0.58}_{-0.72}$	$1.26^{+0.37}_{-0.61}$
090133.5-010540	10870	$0.74^{+6.23}_{-0.64}$	101^{+61}_{-44}	$2.6^{+1.5}_{-1.8}$	$1.53^{+0.67}_{-0.78}$	$1.59^{+0.53}_{-0.86}$
090137.7+030253	15914	$0.56^{+1.57}_{-0.39}$	124^{+79}_{-63}	$2.6^{+1.4}_{-1.8}$	$1.59^{+0.55}_{-0.58}$	$1.01^{+0.60}_{-0.59}$
090140.9-012132	2412	$0.75^{+1.38}_{-0.53}$	241^{+91}_{-68}	$3.1^{+1.4}_{-2.1}$	$1.66^{+0.57}_{-0.65}$	$0.81^{+0.45}_{-0.51}$
090144.7+040827	3199	$1.5^{+11.1}_{-1.1}$	130^{+60}_{-56}	$2.5^{+1.7}_{-1.8}$	$1.43^{+0.76}_{-0.76}$	$1.88^{+0.32}_{-0.61}$
090146.2-013756	4232	$5.8^{+35.6}_{-5.1}$	88^{+45}_{-32}	$2.4^{+1.7}_{-1.5}$	$1.65^{+0.62}_{-0.77}$	$1.56^{+0.61}_{-0.88}$
090153.9-012209	2048	$3.0^{+6.6}_{-1.8}$	123^{+39}_{-40}	$2.5^{+1.8}_{-1.4}$	$1.20^{+0.78}_{-0.52}$	$1.02^{+0.46}_{-0.52}$
090200.5+022339	3800	$0.70^{+2.86}_{-0.47}$	218^{+88}_{-86}	$2.4^{+1.8}_{-1.6}$	$1.43^{+0.74}_{-0.70}$	$1.43^{+0.30}_{-0.60}$
090210.6+032513	431	$0.89^{+11.04}_{-0.68}$	43^{+58}_{-19}	$2.8^{+1.6}_{-1.8}$	$1.53^{+0.66}_{-0.69}$	$3.28^{+0.73}_{-1.90}$
090223.3+015205	6840	$2.7^{+165.1}_{-2.4}$	37^{+33}_{-18}	$2.6^{+1.7}_{-1.8}$	$1.72^{+0.55}_{-0.85}$	$2.55^{+0.73}_{-1.34}$
090224.4-005150	9893	$2.2^{+10.4}_{-1.9}$	94^{+68}_{-37}	$2.6^{+1.7}_{-1.8}$	$1.58^{+0.64}_{-0.78}$	$1.28^{+0.59}_{-0.82}$
090248.5+044005	4121	$2.9^{+14.0}_{-2.4}$	104^{+64}_{-39}	$2.8^{+1.6}_{-1.8}$	$1.56^{+0.65}_{-0.67}$	$1.30^{+0.58}_{-0.76}$
090255.2+030220	5489	$0.73^{+3.02}_{-0.54}$	220^{+110}_{-100}	$2.3^{+1.9}_{-1.6}$	$1.22^{+0.90}_{-0.68}$	$1.19^{+0.40}_{-0.67}$
090255.5+044036	4348	$1.6^{+17.2}_{-1.2}$	125^{+65}_{-65}	$0.97^{+1.33}_{-0.72}$	$1.16^{+0.90}_{-0.61}$	$1.65^{+0.41}_{-0.87}$
090256.2+014625	5655	$0.30^{+0.97}_{-0.18}$	215^{+73}_{-70}	$2.1^{+1.8}_{-1.4}$	$1.58^{+0.62}_{-0.70}$	$1.58^{+0.27}_{-0.49}$
090257.4+004819	1712	$1.8^{+30.4}_{-1.6}$	73^{+59}_{-35}	$2.7^{+1.5}_{-1.8}$	$1.53^{+0.67}_{-0.74}$	$1.98^{+0.49}_{-1.09}$
090323.7+030738	2083	$4.1^{+30.1}_{-3.5}$	103^{+84}_{-61}	$1.5^{+2.3}_{-1.1}$	$0.74^{+1.07}_{-0.30}$	$1.45^{+0.44}_{-0.67}$
090327.2+032545	4771	$0.71^{+15.93}_{-0.56}$	120^{+66}_{-55}	$2.2^{+1.9}_{-1.5}$	$1.54^{+0.68}_{-0.72}$	$1.80^{+0.37}_{-1.12}$
090328.7-013622	4487	$1.7^{+5.9}_{-1.4}$	166^{+73}_{-62}	$2.1^{+1.8}_{-1.5}$	$1.67^{+0.56}_{-0.76}$	$1.18^{+0.55}_{-0.80}$
090333.8+043950	9404	$2.3^{+5.8}_{-1.8}$	136^{+61}_{-45}	$2.5^{+1.7}_{-1.7}$	$1.56^{+0.68}_{-0.76}$	$0.88^{+0.56}_{-0.54}$
090335.0+022006	8941	$1.7^{+13.5}_{-1.5}$	75^{+52}_{-34}	$2.7^{+1.7}_{-1.8}$	$1.66^{+0.59}_{-0.73}$	$1.46^{+0.73}_{-0.89}$
090336.7+033124	12221	$1.5^{+7.3}_{-1.2}$	122^{+55}_{-46}	$3.0^{+1.3}_{-2.1}$	$1.69^{+0.56}_{-0.85}$	$1.37^{+0.59}_{-0.83}$
090408.6+012555	5774	$0.49^{+1.66}_{-0.28}$	200^{+130}_{-110}	$2.5^{+1.7}_{-1.7}$	$1.47^{+0.70}_{-0.73}$	$0.77^{+0.69}_{-0.50}$

continued.

Cluster (eFEDS J+)	ID_SRC	n_0^2 (10^{-7} cm^{-6})	r_s (arcsec)	ϵ	β	α
090409.7+003831	9877	$1.3^{+4.5}_{-1.1}$	143^{+76}_{-54}	$2.6^{+1.7}_{-1.8}$	$1.53^{+0.66}_{-0.73}$	$1.02^{+0.59}_{-0.69}$
090417.0+040439	13330	$0.57^{+1.74}_{-0.39}$	227^{+98}_{-75}	$2.3^{+1.8}_{-1.6}$	$1.61^{+0.63}_{-0.74}$	$1.14^{+0.39}_{-0.60}$
090418.6+020642	3590	16^{+40}_{-14}	84^{+49}_{-30}	$2.6^{+1.5}_{-1.7}$	$1.61^{+0.63}_{-0.76}$	$1.02^{+0.62}_{-0.66}$
090419.1-010436	12660	$0.82^{+3.05}_{-0.65}$	144^{+68}_{-53}	$2.8^{+1.5}_{-1.9}$	$1.68^{+0.56}_{-0.73}$	$1.18^{+0.52}_{-0.70}$
090430.7+042648	1075	$0.92^{+8.69}_{-0.66}$	107^{+47}_{-48}	$2.2^{+1.8}_{-1.5}$	$0.97^{+0.92}_{-0.44}$	$2.39^{+0.22}_{-0.38}$
090452.4+033326	2931	$0.34^{+1.51}_{-0.17}$	228^{+81}_{-104}	$1.9^{+2.0}_{-1.4}$	$0.98^{+0.90}_{-0.52}$	$1.85^{+0.22}_{-0.33}$
090540.0+043440	354	$3.7^{+8.2}_{-2.0}$	194^{+68}_{-75}	$2.8^{+1.6}_{-1.7}$	$1.29^{+0.84}_{-0.59}$	$1.52^{+0.20}_{-0.33}$
090540.7+013219	3585	$7.5^{+14.6}_{-5.7}$	117^{+41}_{-32}	$2.7^{+1.6}_{-1.7}$	$1.70^{+0.57}_{-0.74}$	$0.89^{+0.62}_{-0.61}$
090553.5+002244	5170	$0.50^{+2.41}_{-0.34}$	124^{+51}_{-49}	$2.5^{+1.7}_{-1.7}$	$1.55^{+0.64}_{-0.74}$	$2.05^{+0.30}_{-0.46}$
090600.3-002521	9359	$2.1^{+8.5}_{-1.8}$	110^{+55}_{-39}	$2.4^{+1.7}_{-1.7}$	$1.51^{+0.66}_{-0.76}$	$1.26^{+0.59}_{-0.75}$
090601.0+000055	3259	$0.149^{+0.346}_{-0.051}$	230^{+69}_{-97}	$0.99^{+1.59}_{-0.75}$	$0.59^{+0.47}_{-0.20}$	$1.97^{+0.18}_{-0.19}$
090609.4+042924	11420	$0.67^{+3.54}_{-0.50}$	142^{+67}_{-54}	$2.6^{+1.6}_{-1.7}$	$1.46^{+0.70}_{-0.67}$	$1.42^{+0.45}_{-0.72}$
090614.6-010819	5854	$1.7^{+45.6}_{-1.5}$	82^{+85}_{-45}	$2.7^{+1.6}_{-1.7}$	$1.39^{+0.74}_{-0.75}$	$2.01^{+0.80}_{-1.09}$
090627.5+035846	10162	$0.183^{+0.319}_{-0.083}$	340^{+210}_{-160}	$2.6^{+1.6}_{-1.8}$	$1.37^{+0.79}_{-0.71}$	$0.63^{+0.59}_{-0.39}$
090628.9-012938	2424	$1.3^{+4.5}_{-1.0}$	158^{+69}_{-52}	$2.9^{+1.5}_{-1.8}$	$1.70^{+0.55}_{-0.75}$	$1.44^{+0.36}_{-0.59}$
090634.9+045033	8384	$5.2^{+26.0}_{-4.2}$	106^{+45}_{-37}	$3.0^{+1.4}_{-2.0}$	$1.54^{+0.66}_{-0.74}$	$1.56^{+0.50}_{-0.89}$
090636.9+010852	7086	$2.1^{+12.5}_{-1.8}$	134^{+78}_{-55}	$2.6^{+1.7}_{-1.7}$	$1.58^{+0.63}_{-0.77}$	$1.38^{+0.44}_{-0.79}$
090644.8+011124	5858	$1.00^{+11.06}_{-0.83}$	87^{+40}_{-38}	$3.0^{+1.4}_{-1.8}$	$1.37^{+0.72}_{-0.66}$	$2.12^{+0.44}_{-0.85}$
090656.3+044717	12153	$0.33^{+0.47}_{-0.16}$	460^{+100}_{-120}	$2.3^{+1.8}_{-1.6}$	$1.57^{+0.56}_{-0.64}$	$0.98^{+0.27}_{-0.39}$
090700.7+011032	9463	22^{+124}_{-20}	51^{+33}_{-30}	$1.6^{+1.5}_{-1.1}$	$1.89^{+0.46}_{-0.73}$	$1.27^{+1.11}_{-0.85}$
090703.9+010756	13484	$1.4^{+10.8}_{-1.1}$	42^{+37}_{-28}	$1.6^{+1.4}_{-1.1}$	$2.04^{+0.33}_{-0.67}$	$2.0^{+1.2}_{-1.1}$
090718.6+035258	6439	$8.6^{+15.2}_{-7.1}$	105^{+47}_{-30}	$2.7^{+1.6}_{-1.8}$	$1.70^{+0.54}_{-0.72}$	$0.81^{+0.65}_{-0.55}$
090723.8-011210	2680	$0.21^{+0.47}_{-0.12}$	245^{+78}_{-85}	$2.4^{+1.7}_{-1.6}$	$1.37^{+0.75}_{-0.68}$	$1.78^{+0.17}_{-0.27}$
090734.3-012744	13028	$2.1^{+39.1}_{-1.8}$	54^{+68}_{-40}	$2.6^{+1.6}_{-1.8}$	$1.62^{+0.59}_{-0.80}$	$1.48^{+1.36}_{-0.99}$
090739.7-010633	10976	$0.51^{+4.34}_{-0.42}$	126^{+65}_{-48}	$2.4^{+1.8}_{-1.7}$	$1.74^{+0.54}_{-0.83}$	$1.58^{+0.50}_{-0.96}$
090750.1+025006	4691	$0.60^{+13.47}_{-0.42}$	164^{+75}_{-86}	$2.7^{+1.7}_{-1.8}$	$1.63^{+0.65}_{-0.96}$	$1.72^{+0.32}_{-1.01}$
090751.9+024647	13368	$1.05^{+4.44}_{-0.82}$	157^{+77}_{-58}	$2.7^{+1.7}_{-1.8}$	$1.78^{+0.52}_{-0.82}$	$1.08^{+0.53}_{-0.74}$
090752.9+013407	2074	$0.36^{+1.74}_{-0.25}$	211^{+86}_{-78}	$2.4^{+1.9}_{-1.5}$	$1.46^{+0.75}_{-0.87}$	$1.67^{+0.59}_{-1.22}$
090754.5+005738	5219	$1.14^{+7.31}_{-0.85}$	156^{+74}_{-61}	$2.3^{+1.8}_{-1.6}$	$1.51^{+0.67}_{-0.79}$	$1.56^{+0.36}_{-0.71}$
090757.5+025427	9569	$6.8^{+31.2}_{-6.1}$	92^{+61}_{-41}	$2.7^{+1.6}_{-2.0}$	$1.46^{+0.81}_{-0.88}$	$1.17^{+0.77}_{-0.86}$
090803.8+020045	2234	$0.53^{+2.92}_{-0.37}$	148^{+57}_{-61}	$2.4^{+1.7}_{-1.6}$	$1.53^{+0.64}_{-0.78}$	$2.13^{+0.22}_{-0.36}$
090805.9+011952	7084	$4.4^{+25.1}_{-3.8}$	91^{+50}_{-33}	$2.7^{+1.5}_{-1.8}$	$1.64^{+0.60}_{-0.74}$	$1.33^{+0.63}_{-0.83}$
090806.4+032613	12592	$2.7^{+10.3}_{-2.2}$	96^{+64}_{-40}	$2.5^{+1.8}_{-1.7}$	$1.70^{+0.57}_{-0.73}$	$1.17^{+0.64}_{-0.70}$
090806.9+042351	6554	$0.200^{+0.465}_{-0.099}$	315^{+97}_{-106}	$2.4^{+1.7}_{-1.7}$	$1.36^{+0.78}_{-0.67}$	$1.38^{+0.24}_{-0.37}$
090811.6-014811	3984	$0.67^{+11.22}_{-0.47}$	154^{+73}_{-68}	$3.4^{+1.1}_{-2.1}$	$1.52^{+0.78}_{-0.73}$	$1.81^{+0.33}_{-0.92}$
090816.3+033416	11470	$0.33^{+1.47}_{-0.20}$	178^{+70}_{-70}	$2.4^{+2.0}_{-1.7}$	$1.26^{+0.90}_{-0.67}$	$1.60^{+0.39}_{-0.56}$
090817.2-013034	15548	$0.39^{+1.91}_{-0.29}$	174^{+85}_{-74}	$2.7^{+1.8}_{-1.8}$	$1.53^{+0.68}_{-0.79}$	$1.17^{+0.47}_{-0.72}$
090821.6-014115	16287	$0.49^{+2.53}_{-0.39}$	148^{+87}_{-60}	$2.2^{+2.1}_{-1.6}$	$1.53^{+0.63}_{-0.82}$	$1.35^{+0.48}_{-0.85}$
090821.9+025141	8248	$2.0^{+10.4}_{-1.6}$	130^{+86}_{-60}	$2.8^{+1.6}_{-2.0}$	$1.50^{+0.72}_{-0.81}$	$1.18^{+0.64}_{-0.76}$
090838.0+015226	1479	$0.29^{+0.57}_{-0.17}$	222^{+86}_{-83}	$1.8^{+2.1}_{-1.2}$	$0.86^{+0.86}_{-0.38}$	$1.98^{+0.15}_{-0.20}$
090843.9-013034	4974	$0.40^{+4.05}_{-0.30}$	149^{+81}_{-67}	$1.7^{+2.1}_{-1.3}$	$1.35^{+0.73}_{-0.61}$	$1.32^{+0.57}_{-0.96}$
090849.7+042241	2460	35^{+41}_{-25}	91^{+25}_{-22}	$2.9^{+1.5}_{-1.8}$	$1.80^{+0.50}_{-0.68}$	$0.65^{+0.57}_{-0.43}$
090913.8-001214	885	$0.82^{+1.27}_{-0.46}$	232^{+67}_{-71}	$2.9^{+1.5}_{-1.9}$	$1.67^{+0.58}_{-0.75}$	$1.68^{+0.19}_{-0.23}$
090915.3-010104	2004	$0.57^{+1.55}_{-0.33}$	204^{+66}_{-70}	$2.3^{+1.8}_{-1.6}$	$1.41^{+0.71}_{-0.70}$	$1.96^{+0.19}_{-0.26}$
090916.0-015540	5772	$1.5^{+3.3}_{-1.1}$	161^{+67}_{-48}	$2.8^{+1.5}_{-1.8}$	$1.75^{+0.52}_{-0.80}$	$0.96^{+0.53}_{-0.62}$
090930.6+034055	638	$0.49^{+1.72}_{-0.28}$	108^{+42}_{-42}	$2.3^{+1.8}_{-1.6}$	$1.12^{+0.81}_{-0.55}$	$2.79^{+0.26}_{-0.25}$
090932.5-005020	3523	$2.9^{+26.3}_{-2.3}$	113^{+54}_{-51}	$2.5^{+1.6}_{-1.7}$	$1.51^{+0.67}_{-0.73}$	$1.93^{+0.34}_{-0.64}$

continued.

Cluster (eFEDS J+)	ID_SRC	n_0^2 (10^{-7} cm^{-6})	r_s (arcsec)	ϵ	β	α
090938.1+040816	13180	$0.83^{+3.60}_{-0.66}$	147^{+78}_{-60}	$2.7^{+1.6}_{-1.8}$	$1.48^{+0.69}_{-0.72}$	$1.30^{+0.46}_{-0.68}$
091011.7+013914	13622	$0.42^{+1.69}_{-0.28}$	205^{+86}_{-81}	$2.4^{+1.7}_{-1.6}$	$1.45^{+0.70}_{-0.73}$	$1.30^{+0.34}_{-0.63}$
091032.4+035301	8750	$4.5^{+9.5}_{-3.9}$	103^{+34}_{-30}	$2.6^{+1.7}_{-1.8}$	$1.50^{+0.70}_{-0.85}$	$0.74^{+1.05}_{-0.53}$
091033.8+005100	510	$0.22^{+0.62}_{-0.11}$	171^{+44}_{-58}	$2.3^{+1.7}_{-1.5}$	$1.21^{+0.81}_{-0.66}$	$2.43^{+0.17}_{-0.19}$
091057.2+041730	206	$2.7^{+21.6}_{-2.4}$	105^{+85}_{-46}	$2.6^{+1.6}_{-1.7}$	$1.54^{+0.68}_{-0.80}$	$1.39^{+0.52}_{-0.86}$
091104.1+052237	11694	$1.11^{+6.37}_{-0.89}$	132^{+78}_{-56}	$2.3^{+1.7}_{-1.7}$	$1.36^{+0.77}_{-0.74}$	$1.32^{+0.47}_{-0.79}$
091108.0-015422	5376	23^{+168}_{-21}	43^{+28}_{-20}	$2.5^{+1.6}_{-1.7}$	$1.49^{+0.69}_{-0.72}$	$1.59^{+0.99}_{-1.04}$
091111.0+040015	6021	$1.7^{+5.7}_{-1.4}$	120^{+62}_{-41}	$2.2^{+2.1}_{-1.5}$	$1.68^{+0.63}_{-0.79}$	$1.12^{+0.64}_{-0.78}$
091117.1+030441	15328	$0.199^{+0.276}_{-0.088}$	370^{+110}_{-110}	$2.5^{+1.7}_{-1.7}$	$1.29^{+0.80}_{-0.68}$	$1.05^{+0.28}_{-0.40}$
091135.9+034626	3774	$8.2^{+31.7}_{-6.9}$	114^{+52}_{-42}	$2.4^{+1.6}_{-1.5}$	$1.62^{+0.54}_{-0.57}$	$1.23^{+0.60}_{-0.66}$
091139.3-014144	5511	$4.6^{+20.7}_{-4.0}$	96^{+51}_{-32}	$2.8^{+1.5}_{-1.8}$	$1.71^{+0.57}_{-0.77}$	$1.31^{+0.62}_{-0.73}$
091159.7+031036	9374	$0.27^{+2.48}_{-0.16}$	215^{+86}_{-114}	$2.9^{+1.5}_{-1.7}$	$1.36^{+0.71}_{-0.69}$	$1.49^{+0.35}_{-0.76}$
091213.4-021621	7699	$3.4^{+34.0}_{-3.0}$	81^{+74}_{-59}	$2.9^{+1.4}_{-1.7}$	$1.49^{+0.65}_{-0.73}$	$1.50^{+1.05}_{-0.97}$
091214.1+022443	18040	$0.34^{+1.39}_{-0.22}$	151^{+91}_{-89}	$2.5^{+1.8}_{-1.7}$	$1.59^{+0.62}_{-0.79}$	$1.01^{+0.94}_{-0.67}$
091215.3-021743	626	$3.4^{+5.4}_{-1.8}$	280^{+67}_{-83}	$2.5^{+1.7}_{-1.7}$	$1.67^{+0.57}_{-0.67}$	$1.30^{+0.20}_{-0.29}$
091248.2+002446	11837	$0.30^{+0.93}_{-0.18}$	227^{+109}_{-84}	$2.4^{+1.7}_{-1.6}$	$1.36^{+0.81}_{-0.72}$	$0.99^{+0.44}_{-0.59}$
091254.4+032028	1415	$13.7^{+40.8}_{-9.8}$	93^{+31}_{-26}	$2.7^{+1.6}_{-1.7}$	$1.64^{+0.55}_{-0.69}$	$1.22^{+0.48}_{-0.67}$
091300.9-013152	7531	$2.7^{+22.1}_{-2.4}$	95^{+67}_{-41}	$2.7^{+1.6}_{-1.7}$	$1.56^{+0.65}_{-0.80}$	$1.45^{+0.56}_{-0.90}$
091302.1+035000	1277	$1.8^{+4.8}_{-1.4}$	178^{+83}_{-61}	$2.8^{+1.4}_{-1.9}$	$1.76^{+0.51}_{-0.75}$	$1.05^{+0.52}_{-0.69}$
091305.9+035021	3797	$1.8^{+4.8}_{-1.4}$	178^{+83}_{-61}	$2.8^{+1.4}_{-1.9}$	$1.76^{+0.51}_{-0.75}$	$1.05^{+0.52}_{-0.69}$
091315.0+034850	593	$0.42^{+0.76}_{-0.24}$	216^{+72}_{-70}	$2.0^{+2.0}_{-1.4}$	$0.97^{+0.73}_{-0.40}$	$2.13^{+0.14}_{-0.16}$
091320.3+032834	2977	$1.03^{+14.98}_{-0.84}$	96^{+55}_{-46}	$2.3^{+1.8}_{-1.6}$	$1.51^{+0.66}_{-0.74}$	$2.13^{+0.33}_{-0.64}$
091322.9+040617	9801	$0.201^{+0.225}_{-0.098}$	430^{+110}_{-110}	$2.6^{+1.4}_{-1.5}$	$1.76^{+0.51}_{-0.68}$	$0.71^{+0.41}_{-0.45}$
091331.0+024513	3488	44^{+89}_{-38}	40^{+20}_{-13}	$2.9^{+1.4}_{-1.9}$	$1.73^{+0.54}_{-0.72}$	$0.83^{+0.90}_{-0.60}$
091336.6+031723	5541	$1.5^{+2.5}_{-1.0}$	144^{+59}_{-45}	$0.97^{+1.21}_{-0.69}$	$0.65^{+0.34}_{-0.22}$	$1.04^{+0.49}_{-0.67}$
091351.1-004507	1319	$1.6^{+4.1}_{-1.1}$	182^{+76}_{-71}	$2.4^{+1.6}_{-1.6}$	$1.45^{+0.75}_{-0.68}$	$1.47^{+0.31}_{-0.43}$
091354.7+025323	16902	$0.81^{+3.17}_{-0.63}$	137^{+75}_{-54}	$2.4^{+1.9}_{-1.7}$	$1.48^{+0.67}_{-0.73}$	$1.15^{+0.53}_{-0.69}$
091358.1+025707	940	$1.8^{+8.3}_{-1.6}$	109^{+66}_{-47}	$2.8^{+1.6}_{-1.8}$	$1.35^{+0.75}_{-0.67}$	$1.10^{+0.94}_{-0.77}$
091402.7-010208	5561	$0.57^{+3.99}_{-0.40}$	138^{+62}_{-62}	$2.5^{+1.7}_{-1.7}$	$1.41^{+0.75}_{-0.77}$	$1.80^{+0.33}_{-0.62}$
091403.3+013846	1465	$0.150^{+0.155}_{-0.049}$	284^{+68}_{-74}	$1.8^{+1.9}_{-1.3}$	$0.73^{+0.53}_{-0.27}$	$2.00^{+0.11}_{-0.14}$
091412.6+001856	1844	$0.55^{+1.13}_{-0.30}$	215^{+56}_{-49}	$2.0^{+1.9}_{-1.4}$	$0.89^{+0.63}_{-0.37}$	$1.60^{+0.28}_{-0.47}$
091414.9+022709	1424	$1.7^{+22.3}_{-1.5}$	79^{+48}_{-35}	$1.47^{+1.49}_{-0.93}$	$1.55^{+0.68}_{-0.88}$	$1.90^{+0.56}_{-0.92}$
091417.7+031159	396	$0.108^{+0.225}_{-0.039}$	103^{+40}_{-32}	$2.2^{+2.0}_{-1.5}$	$1.28^{+0.84}_{-0.73}$	$3.02^{+0.28}_{-0.25}$
091423.9+022833	7735	$0.47^{+1.33}_{-0.31}$	226^{+88}_{-78}	$2.0^{+1.9}_{-1.5}$	$1.07^{+0.48}_{-0.44}$	$1.14^{+0.40}_{-0.67}$
091431.6+010910	4637	$1.9^{+57.2}_{-1.7}$	70^{+55}_{-38}	$2.5^{+1.8}_{-1.7}$	$1.47^{+0.70}_{-0.67}$	$2.08^{+0.51}_{-1.03}$
091433.8+022718	3159	$0.195^{+0.800}_{-0.089}$	222^{+77}_{-66}	$3.1^{+1.4}_{-1.6}$	$1.56^{+0.60}_{-0.71}$	$1.84^{+0.25}_{-0.41}$
091439.5-014416	6130	$0.166^{+0.440}_{-0.073}$	242^{+90}_{-87}	$2.1^{+1.9}_{-1.6}$	$1.18^{+0.86}_{-0.65}$	$1.64^{+0.26}_{-0.37}$
091445.7+032755	8636	$0.64^{+2.56}_{-0.46}$	196^{+82}_{-67}	$2.4^{+1.7}_{-1.7}$	$1.61^{+0.63}_{-0.80}$	$1.24^{+0.42}_{-0.69}$
091445.8+042621	13299	71^{+46}_{-30}	70^{+15}_{-15}	$3.64^{+1.00}_{-1.92}$	$0.69^{+0.32}_{-0.22}$	$0.53^{+0.27}_{-0.28}$
091446.1+001047	1917	$0.31^{+0.78}_{-0.16}$	200^{+61}_{-67}	$2.5^{+1.7}_{-1.7}$	$1.39^{+0.74}_{-0.64}$	$2.10^{+0.17}_{-0.22}$
091450.6-022606	2154	$0.47^{+3.36}_{-0.33}$	150^{+66}_{-68}	$2.6^{+1.7}_{-1.7}$	$1.39^{+0.75}_{-0.72}$	$2.04^{+0.23}_{-0.40}$
091453.6+041613	372	$4.9^{+17.0}_{-3.0}$	106^{+38}_{-33}	$0.92^{+0.95}_{-0.60}$	$0.56^{+0.16}_{-0.15}$	$1.93^{+0.42}_{-1.05}$
091509.5+051521	6244	$1.4^{+3.7}_{-1.0}$	250^{+140}_{-110}	$2.0^{+1.8}_{-1.4}$	$1.18^{+0.90}_{-0.62}$	$1.10^{+0.37}_{-0.58}$
091512.2+043506	4253	$6.7^{+40.7}_{-6.2}$	65^{+42}_{-24}	$2.8^{+1.5}_{-1.7}$	$1.61^{+0.62}_{-0.72}$	$1.40^{+0.77}_{-0.86}$
091517.4-005909	13537	$0.33^{+0.69}_{-0.19}$	234^{+95}_{-85}	$2.7^{+1.5}_{-1.8}$	$1.47^{+0.75}_{-0.75}$	$0.78^{+0.54}_{-0.51}$
091520.5+045203	14354	$0.87^{+6.13}_{-0.68}$	116^{+73}_{-55}	$2.2^{+2.0}_{-1.6}$	$1.53^{+0.66}_{-0.88}$	$1.33^{+0.60}_{-0.78}$
091522.5+041201	14525	$1.5^{+7.8}_{-1.2}$	108^{+68}_{-45}	$2.3^{+1.9}_{-1.6}$	$1.72^{+0.57}_{-0.86}$	$1.20^{+0.63}_{-0.72}$

continued.

Cluster (eFEDS J+)	ID_SRC	n_0^2 (10^{-7} cm^{-6})	r_s (arcsec)	ϵ	β	α
091543.5-004944	10164	$5.1^{+41.1}_{-4.8}$	48^{+40}_{-21}	$2.6^{+1.7}_{-1.7}$	$1.62^{+0.63}_{-0.71}$	$1.72^{+0.91}_{-1.09}$
091553.1+040545	12204	$0.63^{+8.07}_{-0.46}$	72^{+55}_{-33}	$3.0^{+1.5}_{-2.0}$	$1.69^{+0.57}_{-0.77}$	$1.92^{+0.76}_{-1.08}$
091555.6-013248	888	$1.5^{+4.8}_{-1.1}$	186^{+93}_{-78}	$2.1^{+1.7}_{-1.5}$	$1.35^{+0.78}_{-0.66}$	$1.69^{+0.24}_{-0.34}$
091601.8+000831	9930	$1.7^{+4.7}_{-1.4}$	147^{+74}_{-50}	$2.6^{+1.6}_{-1.8}$	$1.63^{+0.62}_{-0.75}$	$0.98^{+0.59}_{-0.66}$
091609.4+013519	8107	$0.34^{+1.65}_{-0.21}$	219^{+124}_{-97}	$2.2^{+1.8}_{-1.6}$	$1.42^{+0.73}_{-0.82}$	$1.17^{+0.38}_{-0.61}$
091610.1-002348	534	$13.4^{+7.1}_{-5.2}$	220^{+32}_{-43}	$3.1^{+1.4}_{-1.9}$	$1.91^{+0.42}_{-0.63}$	$0.44^{+0.25}_{-0.24}$
091612.9-015839	6129	$0.30^{+1.38}_{-0.20}$	230^{+88}_{-92}	$2.4^{+1.6}_{-1.6}$	$1.38^{+0.76}_{-0.73}$	$1.44^{+0.32}_{-0.55}$
091631.9-020207	15047	$0.80^{+3.18}_{-0.61}$	122^{+77}_{-56}	$2.6^{+1.6}_{-1.7}$	$1.61^{+0.59}_{-0.79}$	$1.00^{+0.58}_{-0.66}$
091642.3+040634	13204	$3.3^{+4.9}_{-2.5}$	101^{+40}_{-30}	$2.6^{+1.6}_{-1.7}$	$1.65^{+0.60}_{-0.69}$	$0.67^{+0.67}_{-0.46}$
091646.9+015531	8352	$4.3^{+7.9}_{-3.6}$	110^{+54}_{-34}	$2.8^{+1.5}_{-1.7}$	$1.54^{+0.67}_{-0.71}$	$0.80^{+0.66}_{-0.54}$
091648.1+030506	5300	$4.7^{+29.0}_{-4.2}$	89^{+56}_{-37}	$2.5^{+1.6}_{-1.7}$	$1.46^{+0.75}_{-0.78}$	$1.52^{+0.56}_{-0.84}$
091655.7-011158	11550	$1.14^{+8.59}_{-0.93}$	91^{+72}_{-56}	$2.6^{+1.6}_{-1.7}$	$1.44^{+0.74}_{-0.68}$	$1.42^{+1.10}_{-0.89}$
091722.4+010118	1526	$1.3^{+5.1}_{-1.0}$	157^{+77}_{-62}	$2.3^{+1.8}_{-1.9}$	$1.53^{+0.70}_{-0.73}$	$1.73^{+0.29}_{-0.44}$
091741.1+024518	10140	$0.38^{+3.70}_{-0.24}$	170^{+150}_{-110}	$2.6^{+1.7}_{-1.7}$	$1.53^{+0.66}_{-0.77}$	$0.86^{+0.97}_{-0.59}$
091749.4+014621	9976	$0.42^{+1.16}_{-0.27}$	267^{+91}_{-83}	$2.7^{+1.5}_{-1.7}$	$1.64^{+0.59}_{-0.73}$	$1.22^{+0.33}_{-0.57}$
091757.1+050915	1934	22^{+61}_{-20}	110^{+71}_{-38}	$2.7^{+1.6}_{-1.8}$	$1.56^{+0.65}_{-0.77}$	$1.06^{+0.70}_{-0.76}$
091806.0-003228	3910	29^{+111}_{-27}	42^{+27}_{-16}	$2.9^{+1.5}_{-1.8}$	$1.63^{+0.62}_{-0.78}$	$1.09^{+0.96}_{-0.76}$
091842.2+034754	10019	$2.2^{+21.0}_{-1.9}$	76^{+60}_{-40}	$3.0^{+1.4}_{-1.9}$	$1.56^{+0.64}_{-0.81}$	$1.39^{+0.97}_{-0.93}$
091849.0+021204	994	$1.12^{+6.93}_{-0.80}$	250^{+140}_{-140}	$1.7^{+1.8}_{-1.2}$	$1.33^{+0.80}_{-0.71}$	$1.35^{+0.27}_{-0.63}$
091850.7+030942	19979	$0.98^{+3.50}_{-0.66}$	179^{+91}_{-75}	$2.6^{+1.7}_{-1.7}$	$1.68^{+0.58}_{-0.83}$	$1.18^{+0.45}_{-0.64}$
091851.7+021432	4105	$0.42^{+0.93}_{-0.28}$	185^{+108}_{-94}	$2.9^{+1.4}_{-1.9}$	$1.40^{+0.70}_{-0.68}$	$1.05^{+0.65}_{-0.61}$
091855.8+004916	12125	$5.1^{+16.5}_{-4.3}$	99^{+61}_{-36}	$2.7^{+1.5}_{-1.7}$	$1.55^{+0.66}_{-0.74}$	$1.08^{+0.65}_{-0.67}$
091858.0+024946	7194	$0.55^{+1.57}_{-0.38}$	231^{+81}_{-76}	$2.8^{+1.5}_{-1.8}$	$1.56^{+0.64}_{-0.73}$	$1.29^{+0.35}_{-0.57}$
091900.0+035311	5545	$0.52^{+2.23}_{-0.37}$	211^{+95}_{-81}	$2.5^{+1.8}_{-1.7}$	$1.51^{+0.69}_{-0.75}$	$1.46^{+0.31}_{-0.57}$
091925.6-010430	4254	$3.9^{+77.4}_{-3.7}$	76^{+79}_{-39}	$2.4^{+1.7}_{-1.7}$	$1.36^{+0.81}_{-0.76}$	$1.72^{+0.53}_{-1.12}$
091934.6+033941	1892	44^{+195}_{-42}	41^{+31}_{-15}	$2.6^{+1.8}_{-2.0}$	$1.29^{+0.76}_{-0.59}$	$1.27^{+1.07}_{-0.93}$
091936.6+042553	11376	$2.0^{+10.6}_{-1.7}$	77^{+53}_{-32}	$2.5^{+1.8}_{-1.7}$	$1.57^{+0.63}_{-0.73}$	$1.36^{+0.68}_{-0.81}$
091957.7+035012	4131	$7.2^{+23.2}_{-6.1}$	105^{+66}_{-42}	$2.2^{+1.8}_{-1.5}$	$1.38^{+0.80}_{-0.78}$	$0.99^{+0.64}_{-0.66}$
092002.1+010219	150	$1.85^{+2.35}_{-0.89}$	241^{+46}_{-43}	$2.1^{+1.9}_{-1.4}$	$0.78^{+0.54}_{-0.30}$	$2.13^{+0.16}_{-0.19}$
092004.3+010023	11754	16^{+42}_{-11}	81^{+37}_{-37}	$0.39^{+0.73}_{-0.29}$	$1.92^{+0.49}_{-0.77}$	$0.18^{+0.39}_{-0.14}$
092022.0+030106	6534	$1.18^{+28.46}_{-0.98}$	66^{+92}_{-46}	$2.6^{+1.7}_{-1.8}$	$1.51^{+0.70}_{-0.82}$	$1.9^{+1.3}_{-1.2}$
092022.8+045012	5320	$0.249^{+0.378}_{-0.079}$	202^{+68}_{-65}	$1.6^{+2.1}_{-1.2}$	$0.80^{+0.76}_{-0.36}$	$1.96^{+0.22}_{-0.24}$
092023.2+013444	222	$0.75^{+3.46}_{-0.52}$	161^{+62}_{-67}	$2.3^{+2.0}_{-1.6}$	$1.34^{+0.75}_{-0.68}$	$2.44^{+0.15}_{-0.21}$
092031.3+024710	18068	$1.7^{+6.0}_{-1.5}$	98^{+55}_{-44}	$2.3^{+1.8}_{-1.6}$	$1.46^{+0.74}_{-0.75}$	$1.10^{+0.74}_{-0.73}$
092031.8+040621	4115	$4.2^{+30.4}_{-3.9}$	91^{+61}_{-38}	$2.5^{+1.7}_{-1.7}$	$1.60^{+0.59}_{-0.77}$	$1.60^{+0.57}_{-0.88}$
092037.0-011506	5739	$0.36^{+0.87}_{-0.23}$	247^{+85}_{-76}	$2.6^{+1.7}_{-1.7}$	$1.52^{+0.68}_{-0.73}$	$1.39^{+0.29}_{-0.44}$
092037.9+033528	6467	$1.16^{+22.14}_{-0.98}$	74^{+77}_{-49}	$2.6^{+1.6}_{-1.7}$	$1.57^{+0.58}_{-0.70}$	$1.8^{+1.2}_{-1.1}$
092039.1+004725	6669	$0.67^{+4.08}_{-0.51}$	113^{+49}_{-45}	$2.4^{+1.7}_{-1.6}$	$1.38^{+0.76}_{-0.68}$	$1.92^{+0.38}_{-0.62}$
092041.1+041117	10334	$2.7^{+28.5}_{-2.4}$	75^{+65}_{-35}	$2.2^{+1.9}_{-1.5}$	$1.55^{+0.66}_{-0.70}$	$1.55^{+0.62}_{-1.01}$
092046.2+002849	1915	$0.166^{+0.739}_{-0.070}$	259^{+94}_{-137}	$1.10^{+1.98}_{-0.83}$	$0.60^{+0.67}_{-0.19}$	$1.96^{+0.14}_{-0.20}$
092049.5+024513	489	$2.8^{+5.1}_{-1.6}$	153^{+72}_{-55}	$1.34^{+1.43}_{-0.92}$	$0.69^{+0.38}_{-0.22}$	$1.53^{+0.17}_{-0.23}$
092053.4+021125	18194	$0.23^{+0.52}_{-0.13}$	260^{+110}_{-100}	$2.7^{+1.7}_{-1.8}$	$1.53^{+0.66}_{-0.77}$	$0.90^{+0.47}_{-0.52}$
092105.0+004452	6459	$3.4^{+28.6}_{-3.1}$	75^{+54}_{-33}	$3.1^{+1.3}_{-2.1}$	$1.55^{+0.64}_{-0.79}$	$1.46^{+0.71}_{-0.98}$
092121.2+031726	100	26^{+52}_{-21}	93^{+103}_{-32}	$1.11^{+1.15}_{-0.80}$	$0.80^{+0.70}_{-0.27}$	$1.20^{+0.34}_{-0.42}$
092133.2+043431	9512	$1.8^{+7.1}_{-1.5}$	119^{+56}_{-45}	$2.9^{+1.5}_{-1.8}$	$1.65^{+0.58}_{-0.77}$	$1.20^{+0.55}_{-0.73}$
092134.4+015832	810	$0.59^{+3.45}_{-0.46}$	210^{+93}_{-94}	$2.5^{+1.7}_{-1.5}$	$1.39^{+0.76}_{-0.74}$	$1.64^{+0.49}_{-0.83}$
092135.4+005128	7447	$0.72^{+5.53}_{-0.55}$	121^{+95}_{-76}	$2.5^{+1.7}_{-1.7}$	$1.55^{+0.65}_{-0.71}$	$1.37^{+0.94}_{-0.90}$

continued.

Cluster (eFEDS J+)	ID_SRC	n_0^2 (10^{-7} cm^{-6})	r_s (arcsec)	ϵ	β	α
092136.4-001449	4168	$2.0^{+6.4}_{-1.5}$	161^{+80}_{-58}	$2.8^{+1.5}_{-1.9}$	$1.67^{+0.57}_{-0.80}$	$1.18^{+0.48}_{-0.67}$
092202.2+034520	5347	$4.4^{+2.4}_{-1.8}$	128^{+28}_{-27}	$1.8^{+1.4}_{-1.1}$	$0.74^{+0.23}_{-0.20}$	$0.54^{+0.37}_{-0.34}$
092209.3+034628	367	47^{+43}_{-22}	58^{+14}_{-16}	$0.47^{+0.68}_{-0.35}$	$0.60^{+0.12}_{-0.13}$	$0.50^{+0.42}_{-0.33}$
092212.0-002731	857	$0.63^{+0.92}_{-0.38}$	299^{+111}_{-85}	$2.0^{+1.9}_{-1.5}$	$1.46^{+0.69}_{-0.60}$	$1.62^{+0.18}_{-0.21}$
092220.4+034806	4014	$9.0^{+9.8}_{-5.6}$	77^{+18}_{-18}	$1.19^{+1.20}_{-0.84}$	$0.86^{+0.34}_{-0.30}$	$0.56^{+0.66}_{-0.40}$
092235.8-002443	3133	$11.2^{+8.8}_{-4.8}$	97^{+31}_{-21}	$1.12^{+0.50}_{-0.50}$	$0.62^{+0.88}_{-0.23}$	$1.06^{+0.54}_{-0.50}$
092241.9+020719	1535	$1.6^{+5.4}_{-1.3}$	154^{+80}_{-54}	$2.6^{+1.7}_{-1.7}$	$1.61^{+0.64}_{-0.73}$	$1.22^{+0.55}_{-0.66}$
092246.2+034251	2216	$7.3^{+11.0}_{-4.6}$	78^{+23}_{-17}	$1.06^{+0.99}_{-0.74}$	$0.90^{+0.29}_{-0.28}$	$1.04^{+0.68}_{-0.66}$
092246.4+042424	5348	$1.7^{+14.9}_{-1.5}$	109^{+79}_{-47}	$2.3^{+1.7}_{-1.6}$	$1.41^{+0.73}_{-0.71}$	$1.62^{+0.46}_{-0.96}$
092258.2+032041	4833	$4.8^{+26.8}_{-4.4}$	87^{+57}_{-36}	$2.6^{+1.7}_{-1.7}$	$1.54^{+0.63}_{-0.67}$	$1.32^{+0.64}_{-0.79}$
092302.6+034002	9076	$0.26^{+0.62}_{-0.16}$	283^{+112}_{-92}	$2.3^{+1.7}_{-1.6}$	$1.53^{+0.65}_{-0.75}$	$0.95^{+0.44}_{-0.54}$
092312.0+000355	6657	$0.40^{+9.12}_{-0.27}$	77^{+184}_{-64}	$2.5^{+1.7}_{-1.7}$	$1.53^{+0.65}_{-0.74}$	$0.98^{+1.57}_{-0.75}$
092328.2+043107	6063	13^{+24}_{-11}	88^{+41}_{-26}	$2.7^{+1.6}_{-1.7}$	$1.71^{+0.53}_{-0.71}$	$0.70^{+0.74}_{-0.51}$
092333.1-001917	7637	12^{+44}_{-11}	79^{+37}_{-29}	$2.9^{+1.5}_{-1.7}$	$1.58^{+0.62}_{-0.73}$	$1.11^{+0.73}_{-0.73}$
092335.1+012907	4806	$0.49^{+1.02}_{-0.27}$	272^{+116}_{-94}	$2.5^{+1.7}_{-1.7}$	$1.54^{+0.69}_{-0.82}$	$0.80^{+0.45}_{-0.51}$
092339.0+052654	1894	40^{+758}_{-38}	62^{+58}_{-33}	$3.0^{+1.4}_{-1.8}$	$1.64^{+0.60}_{-0.75}$	$2.5^{+1.0}_{-1.4}$
092346.8-005330	11530	$1.22^{+2.80}_{-0.95}$	162^{+68}_{-55}	$2.6^{+1.7}_{-1.8}$	$1.66^{+0.59}_{-0.72}$	$1.00^{+0.53}_{-0.61}$
092402.2+054205	7973	$4.9^{+13.6}_{-3.7}$	142^{+63}_{-52}	$2.6^{+1.7}_{-1.7}$	$1.44^{+0.72}_{-0.72}$	$1.10^{+0.51}_{-0.71}$
092405.0-013059	298	$1.6^{+4.9}_{-1.1}$	163^{+67}_{-66}	$2.4^{+1.7}_{-1.7}$	$1.44^{+0.75}_{-0.67}$	$1.61^{+0.24}_{-0.37}$
092409.4+040057	1437	$0.34^{+0.67}_{-0.19}$	322^{+96}_{-100}	$2.6^{+1.7}_{-1.7}$	$1.62^{+0.64}_{-0.68}$	$1.58^{+0.19}_{-0.32}$
092421.9-005103	8544	$0.47^{+2.86}_{-0.34}$	139^{+67}_{-56}	$2.8^{+1.5}_{-1.8}$	$1.44^{+0.73}_{-0.72}$	$1.66^{+0.40}_{-0.71}$
092454.7+014901	7841	$0.98^{+10.90}_{-0.80}$	96^{+60}_{-47}	$2.7^{+1.6}_{-1.7}$	$1.51^{+0.70}_{-0.75}$	$1.63^{+0.53}_{-0.88}$
092502.6+022612	7060	$2.7^{+19.4}_{-2.4}$	93^{+56}_{-40}	$2.5^{+1.7}_{-1.7}$	$1.65^{+0.58}_{-0.75}$	$1.40^{+0.61}_{-0.87}$
092504.3-005602	11531	$2.2^{+52.3}_{-1.9}$	67^{+64}_{-43}	$2.7^{+1.6}_{-1.7}$	$1.65^{+0.59}_{-0.81}$	$1.6^{+1.2}_{-1.0}$
092510.0-014830	5079	$2.7^{+19.4}_{-2.1}$	78^{+43}_{-32}	$2.9^{+1.3}_{-1.6}$	$1.22^{+0.64}_{-0.54}$	$1.91^{+0.48}_{-0.69}$
092511.8-011436	9471	$0.97^{+4.01}_{-0.82}$	139^{+77}_{-52}	$2.1^{+1.9}_{-1.5}$	$1.68^{+0.60}_{-0.92}$	$1.18^{+0.57}_{-0.79}$
092522.1-013148	6653	$0.90^{+4.08}_{-0.70}$	154^{+74}_{-60}	$2.8^{+1.5}_{-1.8}$	$1.65^{+0.61}_{-0.75}$	$1.37^{+0.40}_{-0.68}$
092533.6-014205	1483	$2.3^{+9.9}_{-1.6}$	115^{+51}_{-53}	$1.7^{+2.0}_{-1.2}$	$1.06^{+0.82}_{-0.54}$	$1.46^{+0.36}_{-0.64}$
092546.3-014347	566	$1.17^{+2.96}_{-0.67}$	224^{+48}_{-60}	$2.2^{+1.5}_{-1.4}$	$1.65^{+0.51}_{-0.49}$	$1.46^{+0.28}_{-0.48}$
092548.9-011725	5488	$0.80^{+2.64}_{-0.63}$	206^{+88}_{-69}	$2.6^{+1.6}_{-1.8}$	$1.64^{+0.60}_{-0.78}$	$1.09^{+0.50}_{-0.65}$
092553.3+015519	991	$0.51^{+3.88}_{-0.36}$	105^{+105}_{-83}	$2.6^{+1.6}_{-1.7}$	$1.50^{+0.71}_{-0.70}$	$0.99^{+1.22}_{-0.68}$
092555.6+004311	6732	$1.7^{+1.9}_{-1.0}$	258^{+81}_{-82}	$2.6^{+1.6}_{-1.8}$	$1.60^{+0.61}_{-0.73}$	$0.62^{+0.41}_{-0.41}$
092619.9+021207	8160	$2.4^{+11.1}_{-2.1}$	113^{+66}_{-40}	$2.8^{+1.5}_{-1.8}$	$1.69^{+0.55}_{-0.81}$	$1.23^{+0.61}_{-0.72}$
092621.3-003356	4366	$1.2^{+12.2}_{-1.0}$	109^{+67}_{-49}	$2.3^{+1.9}_{-1.6}$	$1.46^{+0.68}_{-0.69}$	$1.64^{+0.45}_{-0.87}$
092629.3+032614	2050	$0.141^{+0.276}_{-0.044}$	191^{+52}_{-72}	$0.63^{+1.30}_{-0.50}$	$0.426^{+0.159}_{-0.066}$	$2.25^{+0.15}_{-0.16}$
092631.0+014511	2967	$1.4^{+9.3}_{-1.1}$	132^{+66}_{-53}	$2.5^{+1.7}_{-1.8}$	$1.56^{+0.65}_{-0.75}$	$1.89^{+0.29}_{-0.54}$
092639.7+040733	3560	$0.71^{+7.20}_{-0.53}$	120^{+50}_{-59}	$3.0^{+1.9}_{-2.0}$	$1.01^{+1.00}_{-0.53}$	$2.04^{+0.49}_{-0.85}$
092644.0+040010	9238	$2.0^{+4.0}_{-1.7}$	162^{+77}_{-55}	$3.0^{+1.5}_{-2.0}$	$1.63^{+0.59}_{-0.74}$	$0.79^{+0.72}_{-0.56}$
092647.5+050032	137	70^{+118}_{-53}	60^{+50}_{-22}	$1.12^{+1.38}_{-0.80}$	$0.65^{+0.63}_{-0.22}$	$0.85^{+0.53}_{-0.55}$
092647.5+030946	12965	$1.01^{+2.24}_{-0.78}$	155^{+73}_{-57}	$2.7^{+1.6}_{-1.7}$	$1.62^{+0.61}_{-0.78}$	$0.85^{+0.62}_{-0.60}$
092648.0+050124	6875	$3.0^{+14.7}_{-2.6}$	158^{+101}_{-53}	$2.3^{+1.7}_{-1.5}$	$1.65^{+0.61}_{-0.86}$	$1.40^{+0.48}_{-0.70}$
092650.5+035755	671	$2.1^{+50.9}_{-1.8}$	96^{+56}_{-51}	$2.5^{+1.9}_{-1.8}$	$1.42^{+0.81}_{-0.76}$	$2.22^{+0.32}_{-0.83}$
092711.5+011735	10285	$2.0^{+8.2}_{-1.7}$	117^{+61}_{-45}	$2.7^{+1.5}_{-1.8}$	$1.55^{+0.65}_{-0.72}$	$1.17^{+0.59}_{-0.73}$
092735.3+014423	266	$0.25^{+4.72}_{-0.13}$	217^{+73}_{-57}	$2.7^{+1.5}_{-1.8}$	$1.11^{+0.89}_{-0.61}$	$2.15^{+0.31}_{-1.68}$
092737.7+020607	1924	$4.6^{+9.0}_{-3.3}$	159^{+70}_{-58}	$2.3^{+1.7}_{-1.5}$	$1.50^{+0.69}_{-0.72}$	$0.91^{+0.45}_{-0.53}$
092739.7-010427	2636	$0.67^{+1.87}_{-0.46}$	260^{+94}_{-90}	$2.8^{+1.6}_{-1.7}$	$1.51^{+0.69}_{-0.77}$	$1.14^{+0.42}_{-0.62}$
092740.1-002922	3454	$0.22^{+1.00}_{-0.11}$	160^{+62}_{-66}	$2.3^{+1.7}_{-1.7}$	$1.08^{+0.87}_{-0.57}$	$2.16^{+0.23}_{-0.27}$

continued.

Cluster (eFEDS J+)	ID_SRC	n_0^2 (10^{-7} cm^{-6})	r_s (arcsec)	ϵ	β	α
092740.1+042038	4999	$0.167^{+0.318}_{-0.063}$	300^{+230}_{-190}	$2.8^{+1.5}_{-2.3}$	$1.40^{+0.81}_{-0.80}$	$0.44^{+0.99}_{-0.34}$
092740.7-015320	7063	$0.57^{+3.18}_{-0.42}$	154^{+71}_{-60}	$2.5^{+1.7}_{-1.7}$	$1.52^{+0.67}_{-0.78}$	$1.60^{+0.35}_{-0.59}$
092744.6+045630	17315	$2.0^{+9.8}_{-1.7}$	81^{+54}_{-33}	$2.6^{+1.6}_{-1.7}$	$1.70^{+0.56}_{-0.80}$	$1.30^{+0.66}_{-0.84}$
092755.9+000439	10316	$9.4^{+38.6}_{-8.0}$	86^{+49}_{-31}	$2.8^{+1.5}_{-1.8}$	$1.60^{+0.62}_{-0.75}$	$1.16^{+0.68}_{-0.77}$
092803.4+010953	1527	$0.42^{+1.83}_{-0.27}$	138^{+57}_{-58}	$2.1^{+1.9}_{-1.5}$	$1.29^{+0.78}_{-0.70}$	$2.35^{+0.20}_{-0.23}$
092807.5-001353	13561	$1.11^{+13.17}_{-0.83}$	93^{+48}_{-37}	$2.2^{+1.6}_{-1.5}$	$1.49^{+0.67}_{-0.68}$	$1.76^{+0.71}_{-1.31}$
092807.7-012704	6687	$2.0^{+65.1}_{-1.5}$	80^{+170}_{-62}	$2.5^{+1.8}_{-1.7}$	$1.50^{+0.70}_{-0.79}$	$1.12^{+1.45}_{-0.80}$
092813.0-004508	13305	$1.8^{+3.6}_{-1.4}$	148^{+73}_{-49}	$2.4^{+1.8}_{-1.7}$	$1.49^{+0.69}_{-0.70}$	$0.81^{+0.59}_{-0.54}$
092821.1+041941	7167	$0.45^{+1.85}_{-0.32}$	130^{+140}_{-100}	$2.9^{+1.6}_{-2.0}$	$1.80^{+0.51}_{-0.79}$	$0.82^{+0.90}_{-0.59}$
092821.2+042149	666	$2.4^{+10.0}_{-1.6}$	180^{+75}_{-54}	$1.9^{+2.2}_{-1.3}$	$1.86^{+0.53}_{-1.13}$	$1.46^{+0.33}_{-0.74}$
092828.3-000955	845	$0.93^{+4.51}_{-0.72}$	131^{+69}_{-63}	$2.7^{+1.6}_{-1.7}$	$1.14^{+0.68}_{-0.51}$	$1.26^{+0.71}_{-0.85}$
092832.4+041517	4192	$1.3^{+6.8}_{-1.1}$	114^{+73}_{-56}	$2.2^{+1.8}_{-1.5}$	$1.47^{+0.75}_{-0.70}$	$1.51^{+0.91}_{-0.96}$
092844.0+005318	8858	$1.14^{+3.81}_{-0.92}$	158^{+77}_{-56}	$2.7^{+1.5}_{-1.8}$	$1.62^{+0.61}_{-0.77}$	$1.03^{+0.57}_{-0.67}$
092846.5+000056	10287	$0.76^{+2.05}_{-0.57}$	210^{+91}_{-71}	$2.6^{+1.7}_{-1.8}$	$1.61^{+0.61}_{-0.76}$	$0.99^{+0.45}_{-0.61}$
092859.0+040532	4029	$0.33^{+1.57}_{-0.20}$	265^{+74}_{-90}	$2.5^{+1.6}_{-1.5}$	$1.30^{+0.70}_{-0.58}$	$1.53^{+0.27}_{-0.67}$
092900.0-003920	5593	$0.26^{+1.42}_{-0.13}$	159^{+72}_{-60}	$2.5^{+1.6}_{-1.6}$	$1.37^{+0.59}_{-0.58}$	$1.82^{+0.38}_{-0.96}$
092910.2+022034	5092	11^{+31}_{-10}	76^{+47}_{-26}	$2.7^{+1.7}_{-1.8}$	$1.64^{+0.59}_{-0.75}$	$1.06^{+0.80}_{-0.70}$
092911.0+021118	10090	$1.2^{+26.2}_{-1.0}$	43^{+59}_{-32}	$2.8^{+1.6}_{-1.8}$	$1.66^{+0.58}_{-0.82}$	$1.8^{+1.5}_{-1.2}$
092915.2+002427	8178	$0.77^{+3.39}_{-0.55}$	177^{+77}_{-62}	$2.7^{+1.6}_{-1.7}$	$1.54^{+0.67}_{-0.77}$	$1.34^{+0.40}_{-0.68}$
092915.7-001357	1549	$0.21^{+0.56}_{-0.10}$	178^{+52}_{-62}	$2.0^{+2.1}_{-1.4}$	$1.07^{+0.91}_{-0.56}$	$2.27^{+0.16}_{-0.18}$
092918.3+044925	6602	$4.6^{+8.5}_{-3.6}$	115^{+43}_{-33}	$2.8^{+1.5}_{-1.7}$	$1.71^{+0.56}_{-0.73}$	$0.86^{+0.64}_{-0.57}$
092921.7+040040	609	$2.1^{+15.7}_{-1.8}$	108^{+63}_{-43}	$2.7^{+1.7}_{-1.7}$	$1.56^{+0.63}_{-0.72}$	$2.16^{+0.31}_{-0.51}$
092928.3+042411	3563	$1.3^{+7.9}_{-1.1}$	133^{+72}_{-51}	$2.5^{+1.7}_{-1.7}$	$1.54^{+0.68}_{-0.74}$	$1.59^{+0.42}_{-0.74}$
092941.7+023026	7770	$0.38^{+0.98}_{-0.22}$	260^{+150}_{-100}	$2.2^{+1.8}_{-1.5}$	$1.41^{+0.75}_{-0.73}$	$0.66^{+0.51}_{-0.44}$
092953.5+002801	12565	$0.70^{+1.49}_{-0.51}$	208^{+72}_{-60}	$2.7^{+1.7}_{-1.8}$	$1.65^{+0.60}_{-0.73}$	$0.89^{+0.58}_{-0.64}$
092955.8-003403	1967	$0.204^{+0.288}_{-0.091}$	283^{+78}_{-82}	$2.8^{+1.6}_{-1.7}$	$1.22^{+0.86}_{-0.56}$	$1.88^{+0.16}_{-0.19}$
093003.3+035630	288	$5.9^{+12.1}_{-4.0}$	103^{+26}_{-28}	$2.5^{+1.6}_{-1.5}$	$1.56^{+0.62}_{-0.66}$	$1.89^{+0.28}_{-0.35}$
093009.0+040144	536	14^{+98}_{-12}	78^{+48}_{-42}	$1.9^{+1.8}_{-1.4}$	$1.04^{+0.97}_{-0.50}$	$1.63^{+0.45}_{-0.77}$
093011.2+031648	16215	$2.8^{+56.0}_{-2.5}$	66^{+56}_{-40}	$2.6^{+1.6}_{-1.8}$	$1.50^{+0.69}_{-0.78}$	$1.86^{+0.99}_{-1.09}$
093012.0+030202	7539	$3.1^{+20.0}_{-2.8}$	77^{+48}_{-33}	$2.6^{+1.6}_{-1.8}$	$1.59^{+0.64}_{-0.76}$	$1.47^{+0.69}_{-0.92}$
093022.1+021835	8763	$0.68^{+3.69}_{-0.46}$	163^{+70}_{-65}	$2.9^{+1.4}_{-1.8}$	$1.40^{+0.72}_{-0.64}$	$1.61^{+0.37}_{-0.62}$
093025.3+021714	1003	$0.59^{+1.14}_{-0.34}$	233^{+61}_{-60}	$3.2^{+1.2}_{-1.9}$	$1.58^{+0.58}_{-0.63}$	$1.83^{+0.20}_{-0.29}$
093025.7-020507	1064	$1.23^{+6.40}_{-0.93}$	130^{+60}_{-52}	$2.5^{+1.7}_{-1.6}$	$0.86^{+0.64}_{-0.36}$	$1.38^{+0.45}_{-0.83}$
093049.2-003714	1823	$0.94^{+4.19}_{-0.71}$	198^{+97}_{-85}	$2.3^{+1.8}_{-1.6}$	$1.39^{+0.77}_{-0.71}$	$1.39^{+0.38}_{-0.60}$
093056.9+034825	4579	$0.186^{+0.556}_{-0.071}$	214^{+81}_{-65}	$2.4^{+1.7}_{-1.6}$	$1.18^{+0.82}_{-0.68}$	$1.85^{+0.25}_{-0.37}$
093117.4-015643	11648	$3.8^{+11.0}_{-2.8}$	42^{+16}_{-15}	$1.25^{+0.35}_{-0.35}$	$0.68^{+0.26}_{-0.18}$	$0.97^{+0.63}_{-0.57}$
093138.7-020933	5201	$0.87^{+3.41}_{-0.73}$	161^{+88}_{-62}	$2.7^{+1.7}_{-1.8}$	$1.62^{+0.63}_{-0.86}$	$1.19^{+0.50}_{-0.75}$
093141.2-004717	1705	$0.60^{+6.14}_{-0.46}$	119^{+74}_{-56}	$2.1^{+2.0}_{-1.5}$	$1.52^{+0.70}_{-0.86}$	$2.00^{+0.74}_{-1.01}$
093149.8-020143	6494	$0.143^{+0.505}_{-0.089}$	259^{+106}_{-97}	$3.2^{+1.3}_{-2.0}$	$1.37^{+0.84}_{-0.71}$	$1.35^{+0.30}_{-0.52}$
093151.3-002212	836	$1.28^{+4.79}_{-0.95}$	150^{+69}_{-59}	$2.6^{+1.7}_{-1.8}$	$1.57^{+0.66}_{-0.80}$	$1.91^{+0.24}_{-0.36}$
093207.5-021317	1674	$0.49^{+6.46}_{-0.38}$	108^{+57}_{-53}	$2.3^{+1.9}_{-1.6}$	$1.30^{+0.78}_{-0.68}$	$2.29^{+0.25}_{-0.50}$
093222.0+012412	7346	$1.6^{+74.2}_{-1.4}$	52^{+41}_{-22}	$2.3^{+1.9}_{-1.5}$	$1.62^{+0.59}_{-0.69}$	$2.15^{+0.84}_{-1.43}$
093231.0+010617	4873	11^{+41}_{-10}	86^{+70}_{-33}	$2.8^{+1.6}_{-1.8}$	$1.56^{+0.67}_{-0.79}$	$1.06^{+0.77}_{-0.75}$
093232.8-015152	10734	$0.43^{+1.54}_{-0.31}$	165^{+90}_{-73}	$2.3^{+1.8}_{-1.6}$	$1.59^{+0.63}_{-0.78}$	$1.00^{+0.65}_{-0.62}$
093253.8+025917	5631	$1.17^{+11.85}_{-0.96}$	86^{+61}_{-39}	$2.6^{+1.6}_{-1.8}$	$1.46^{+0.70}_{-0.68}$	$1.60^{+0.62}_{-0.97}$
093301.3+024301	12582	$2.2^{+48.5}_{-1.9}$	64^{+85}_{-40}	$2.4^{+1.8}_{-1.6}$	$1.58^{+0.65}_{-0.81}$	$1.25^{+0.88}_{-0.87}$
093302.7-010145	5763	$2.8^{+5.6}_{-2.1}$	144^{+64}_{-47}	$2.8^{+1.5}_{-1.7}$	$1.47^{+0.70}_{-0.74}$	$0.90^{+0.55}_{-0.58}$

continued.

Cluster (eFEDS J+)	ID_SRC	n_0^2 (10^{-7} cm^{-6})	r_s (arcsec)	ϵ	β	α
093316.6+004619	13784	$0.47^{+3.95}_{-0.33}$	92^{+103}_{-75}	$2.3^{+1.8}_{-1.5}$	$1.54^{+0.70}_{-0.74}$	$0.98^{+1.09}_{-0.71}$
093329.3+000334	5618	$1.7^{+8.1}_{-1.5}$	120^{+69}_{-44}	$2.5^{+1.7}_{-1.7}$	$1.47^{+0.73}_{-0.69}$	$1.38^{+0.49}_{-0.77}$
093332.1+020933	6577	$5.6^{+52.8}_{-5.0}$	71^{+46}_{-35}	$2.5^{+1.7}_{-1.7}$	$1.49^{+0.68}_{-0.68}$	$1.69^{+0.65}_{-0.98}$
093403.5-001422	900	$2.2^{+18.0}_{-1.5}$	129^{+72}_{-74}	$1.8^{+1.9}_{-1.3}$	$0.77^{+0.69}_{-0.30}$	$1.65^{+0.30}_{-0.66}$
093431.3-002309	1641	$0.85^{+3.58}_{-0.56}$	201^{+75}_{-89}	$2.2^{+1.8}_{-1.5}$	$1.16^{+0.83}_{-0.55}$	$1.63^{+0.27}_{-0.48}$
093436.1+051533	9995	$2.7^{+5.7}_{-1.9}$	182^{+70}_{-58}	$2.7^{+1.6}_{-1.8}$	$1.64^{+0.62}_{-0.77}$	$0.92^{+0.51}_{-0.58}$
093456.1+031518	7091	$4.9^{+13.9}_{-4.3}$	94^{+53}_{-32}	$2.5^{+1.8}_{-1.8}$	$1.62^{+0.62}_{-0.76}$	$0.99^{+0.70}_{-0.68}$
093500.7+005417	649	$11.1^{+38.2}_{-7.7}$	113^{+39}_{-43}	$2.4^{+1.8}_{-1.6}$	$1.61^{+0.65}_{-0.82}$	$1.19^{+0.38}_{-0.72}$
093513.0+004757	213	$18.5^{+28.7}_{-9.6}$	111^{+35}_{-29}	$1.49^{+1.22}_{-0.95}$	$0.77^{+0.25}_{-0.24}$	$0.93^{+0.31}_{-0.48}$
093520.7+003448	4394	$0.34^{+1.28}_{-0.20}$	209^{+71}_{-79}	$2.5^{+1.8}_{-1.8}$	$1.40^{+0.75}_{-0.70}$	$1.73^{+0.25}_{-0.48}$
093520.9+023234	82	$3.0^{+3.5}_{-1.3}$	132^{+28}_{-35}	$2.7^{+1.6}_{-1.6}$	$0.87^{+0.52}_{-0.34}$	$2.26^{+0.11}_{-0.13}$
093522.2+032329	1242	$3.7^{+10.9}_{-2.6}$	133^{+59}_{-46}	$2.2^{+1.9}_{-1.5}$	$1.33^{+0.74}_{-0.64}$	$1.34^{+0.38}_{-0.55}$
093525.6+023445	12009	$1.32^{+2.05}_{-0.91}$	201^{+65}_{-67}	$2.7^{+1.6}_{-1.9}$	$1.22^{+0.92}_{-0.63}$	$0.77^{+0.57}_{-0.52}$
093525.9+035101	3773	$4.2^{+48.9}_{-3.4}$	76^{+51}_{-38}	$2.4^{+1.8}_{-1.6}$	$1.50^{+0.69}_{-0.71}$	$1.89^{+0.59}_{-0.94}$
093531.4+022710	2609	$2.1^{+9.4}_{-1.8}$	130^{+70}_{-52}	$2.2^{+1.7}_{-1.6}$	$1.23^{+0.84}_{-0.65}$	$1.40^{+0.54}_{-0.80}$
093544.2-000339	6324	$1.18^{+3.87}_{-0.89}$	164^{+71}_{-52}	$2.8^{+1.3}_{-1.9}$	$1.57^{+0.68}_{-0.76}$	$1.31^{+0.46}_{-0.72}$
093546.3-000115	1761	$0.25^{+0.38}_{-0.10}$	187^{+55}_{-57}	$2.2^{+1.9}_{-1.6}$	$0.99^{+0.89}_{-0.48}$	$2.24^{+0.20}_{-0.20}$
093612.7+001650	4455	$0.56^{+1.72}_{-0.35}$	205^{+69}_{-74}	$2.4^{+1.8}_{-1.5}$	$1.42^{+0.72}_{-0.71}$	$1.56^{+0.29}_{-0.47}$
093630.8+031838	4848	$0.65^{+14.03}_{-0.51}$	50^{+98}_{-40}	$2.8^{+1.6}_{-1.8}$	$1.52^{+0.70}_{-0.73}$	$1.12^{+1.31}_{-0.81}$
093707.4+034831	11748	$0.95^{+3.70}_{-0.78}$	161^{+106}_{-60}	$2.4^{+1.7}_{-1.7}$	$1.43^{+0.76}_{-0.77}$	$1.03^{+0.50}_{-0.68}$
093709.7+014143	6251	$5.6^{+8.0}_{-4.0}$	146^{+51}_{-38}	$2.5^{+1.6}_{-1.6}$	$1.76^{+0.50}_{-0.73}$	$0.68^{+0.56}_{-0.45}$
093712.8+031651	38	$0.68^{+13.59}_{-0.53}$	33^{+21}_{-13}	$2.8^{+1.6}_{-2.0}$	$1.50^{+0.69}_{-0.71}$	$3.95^{+0.51}_{-0.86}$
093742.8+033841	6038	$4.9^{+17.9}_{-4.0}$	106^{+47}_{-36}	$2.8^{+1.6}_{-1.8}$	$1.66^{+0.59}_{-0.70}$	$1.18^{+0.60}_{-0.71}$
093744.1+024536	3372	$1.46^{+8.19}_{-0.87}$	155^{+59}_{-60}	$2.1^{+1.8}_{-1.4}$	$1.31^{+0.82}_{-0.65}$	$2.05^{+0.26}_{-0.35}$
093830.5+041523	10322	$0.21^{+0.58}_{-0.11}$	280^{+110}_{-100}	$2.3^{+1.8}_{-1.6}$	$1.28^{+0.77}_{-0.64}$	$1.26^{+0.29}_{-0.44}$
093938.3+042218	1594	$2.7^{+10.8}_{-2.1}$	139^{+62}_{-53}	$2.5^{+1.7}_{-1.7}$	$1.55^{+0.68}_{-0.76}$	$1.45^{+0.37}_{-0.56}$
094005.9+031329	4689	$6.6^{+98.5}_{-6.1}$	77^{+67}_{-39}	$2.5^{+1.7}_{-1.7}$	$1.52^{+0.69}_{-0.80}$	$1.73^{+0.51}_{-1.06}$
094007.3+035754	11337	$4.0^{+18.1}_{-3.4}$	105^{+65}_{-41}	$2.5^{+1.7}_{-1.7}$	$1.48^{+0.69}_{-0.69}$	$1.08^{+0.62}_{-0.74}$

Notes. Electronic version of the table is available at the CDS. Column 1: cluster name. Column 2: unique source ID presented in the eFEDS source catalog (Brunner et al., 2022). Columns 3, 4, 5, 6, 7: parameters of the Vikhlinin et al. (2006) model, n_0^2, r_s, ϵ, β, α respectively.

Table A.2: X-ray observables of eFEDS clusters measured within R_{500} and between $0.15R_{500} - R_{500}$.

Cluster (eFEDS J+)	ID_SRC	RA (deg)	Dec (deg)	$\mathcal{L}_{ext}$	$\mathcal{L}_{det}$	z	R_{500} (arcmin)	T (keV)	L_X (10^{42} erg s^{-1})	L_{bol} (10^{42} erg s^{-1})	M_{gas} (10^{12} M$_\odot$)	Y_X (10^{12} M$_\odot$ keV)	T_{cex} (keV)	$L_{X,cex}$ (10^{42} erg s^{-1})	$L_{bol,cex}$ (10^{42} erg s^{-1})	t_{exp} (s)
082626.5-003429	28993	126.6108	-0.5748	8.5	5.0	0.161	2.404	$5.1^{+13.4}_{-2.4}$	< 5.7	< 30	< 2.5	< 36	$4.1^{+12.9}_{-2.7}$	< 4.9	< 24	184
082751.7-002853	11248	126.9655	-0.4816	12.8	27.9	0.257	2.620	$1.80^{+2.11}_{-...}$	< 12	< 33	< 5.0	< 15	$1.73^{+2.17}_{-...}$	< 7.0	< 21	707
082808.7-001003	4800	127.0366	-0.1677	28.5	62.5	0.076	5.487	$0.994^{+0.096}_{-0.063}$	$2.40^{+0.48}_{-0.34}$	$4.58^{+0.99}_{-0.62}$	$1.12^{+0.27}_{-0.20}$	$1.13^{+0.31}_{-0.22}$	$1.08^{+0.23}_{-0.26}$	$1.62^{+0.52}_{-0.34}$	$3.22^{+1.12}_{-0.70}$	675
082820.5-000721	4169	127.0856	-0.1228	42.4	81.4	0.845	1.894	$5.5^{+5.0}_{-2.0}$	273^{+43}_{-45}	$990^{+330}_{-...}$	$42.5^{+6.2}_{-6.5}$	233^{+218}_{-84}	$4.9^{+5.74}_{-2.2}$	$232^{+49}_{-...}$	790^{+310}_{-170}	748
082840.6-000500	7991	127.1692	-0.0836	18.4	37.5	0.320	2.504	$8.7^{+11.2}_{-4.9}$	$14.7^{+2.7}_{-...}$	$65^{+44}_{-...}$	$5.7^{+1.7}_{-1.5}$	< 190	$7.0^{+11.4}_{-3.8}$	$8.3^{+3.9}_{-...}$	35^{+26}_{-13}	856
082859.9+010756	14973	127.2500	+1.1323	19.2	14.4	0.354	2.522	$6.9^{+13.3}_{-3.8}$	$27.4^{+7.8}_{-...}$	$115^{+91}_{-...}$	$11.9^{+3.2}_{-2.7}$	< 420	$5.7^{+10.8}_{-3.1}$	$25.9^{+6.9}_{-6.8}$	95^{+69}_{-13}	464
082952.7+002139	7528	127.4697	+0.3611	7.7	38.6	0.420	1.874	$6.3^{+4.0}_{-...}$	$14.3^{+2.8}_{-...}$	$58^{+49}_{-...}$	$3.7^{+1.6}_{-...}$	< 130	$6.0^{+13.6}_{-3.4}$	$7.5^{+4.3}_{-2.6}$	$31^{+27}_{-...}$	1099
082955.4+004131	3810	127.4810	+0.6922	24.2	80.3	0.940	1.555	$5.6^{+8.7}_{-2.1}$	217^{+47}_{-39}	790^{+410}_{-160}	$28.8^{+4.6}_{-4.5}$	152^{+269}_{-66}	$4.1^{+4.1}_{-1.4}$	180^{+43}_{-41}	580^{+160}_{-140}	1020
083040.7+023219	9837	127.6697	+2.5388	11.5	23.7	0.111	3.431	$3.4^{+9.1}_{-...}$	$0.64^{+0.25}_{-0.20}$	$2.01^{+1.89}_{-0.80}$	< 0.48	< 5.1	$3.4^{+11.0}_{-1.8}$	< 0.49	< 1.9	718
083110.5+015616	5601	127.7940	+1.9378	11.8	34.1	0.420	2.172	$11.3^{+14.2}_{-...}$	$37.1^{+8.7}_{-...}$	189^{+128}_{-82}	$13.0^{+2.5}_{-2.2}$	< 540	$7.7^{+16.8}_{-4.5}$	$31.0^{+9.1}_{-8.2}$	137^{+112}_{-49}	1016
083120.5+005257	9594	127.8354	+0.8825	7.0	25.9	0.664	1.510	$3.0^{+6.2}_{-...}$	$33.6^{+10.3}_{-8.8}$	98^{+47}_{-26}	$7.6^{+2.0}_{-1.9}$	$22.6^{+42.8}_{-9.5}$	$2.69^{+4.57}_{-0.86}$	$22.1^{+9.0}_{-8.1}$	63^{+34}_{-24}	1205
083120.5+030949	11134	127.8355	+3.1639	32.8	27.7	0.568	2.243	$1.24^{+0.25}_{-...}$	< 75	< 160	< 23	< 31	$1.24^{+0.30}_{-0.24}$	< 62	< 130	746
083125.9+015533	2659	127.8580	+1.9259	47.5	110.5	0.684	1.930	$2.05^{+0.44}_{-0.15}$	197^{+26}_{-28}	482^{+61}_{-66}	$34.1^{+4.9}_{-4.5}$	71^{+18}_{-14}	$1.95^{+0.71}_{-0.27}$	170^{+25}_{-30}	417^{+56}_{-75}	1095
083137.9+004632	3725	127.9081	+0.7758	17.2	66.1	0.293	2.379	$1.38^{+0.41}_{-0.20}$	$10.4^{+2.2}_{-...}$	$23.0^{+5.9}_{-3.8}$	$3.39^{+0.85}_{-0.59}$	$4.8^{+2.3}_{-1.2}$	$1.45^{+0.66}_{-0.23}$	$5.5^{+2.0}_{-1.4}$	$12.3^{+4.6}_{-3.3}$	1207
083146.7-012849	4403	127.9449	-1.4805	6.0	28.1	0.050	4.405	$4.4^{+7.2}_{-...}$	$0.117^{+0.049}_{-0.034}$	$0.40^{+0.33}_{-...}$	< 0.16	< 1.3	$3.0^{+4.5}_{-0.23}$	< 0.12	< 0.39	1684
083149.4+005230	5463	127.9559	+0.8751	13.1	41.5	0.398	2.204	$1.84^{+1.75}_{-...}$	$12.8^{+3.8}_{-...}$	$30.9^{+10.2}_{-...}$	$2.72^{+0.98}_{-...}$	< 14	$2.4^{+3.5}_{-1.1}$	< 9.3	< 27	1205
083153.6+012530	2600	127.9734	+1.4253	48.4	94.5	0.269	3.209	$2.41^{+1.14}_{-...}$	$25.1^{+2.9}_{-...}$	$64.2^{+11.3}_{-...}$	$10.4^{+1.5}_{-...}$	$25.6^{+12.2}_{-5.7}$	$2.72^{+1.34}_{-...}$	$17.5^{+3.2}_{-3.1}$	$47.1^{+11.4}_{-...}$	1207
083204.4+041907	3593	128.0185	+4.3188	66.0	118.6	0.197	4.511	$2.54^{+0.36}_{-...}$	$40.9^{+4.5}_{-...}$	$105^{+14}_{-...}$	$18.1^{+2.4}_{-...}$	$46.8^{+16.8}_{-...}$	$2.56^{+0.21}_{-...}$	$34.7^{+3.1}_{-...}$	89^{+15}_{-13}	524
083228.0-000656	7396	128.1169	-0.1157	13.6	42.4	0.421	2.026	$3.4^{+1.3}_{-...}$	$18.2^{+5.4}_{-...}$	$53^{+26}_{-...}$	$6.7^{+1.8}_{-2.9}$	$20.9^{+23.5}_{-...}$	$3.7^{+5.8}_{-4.4}$	< 22	< 82	1204
083238.8-003200	8565	128.1617	-0.5336	15.8	32.6	0.399	2.122	$6.2^{+34}_{-...}$	$17.0^{+3.5}_{-2.8}$	66^{+46}_{-20}	$7.4^{+4.3}_{-...}$	< 200	$4.0^{+5.8}_{-1.8}$	$14.0^{+3.5}_{-3.1}$	44^{+23}_{-12}	1213
083249.9+031737	10398	128.2082	+3.2939	7.7	29.0	0.828	1.363	$3.9^{+2.3}_{-...}$	< 76	< 300	$7.5^{+3.3}_{-...}$	< 180	$6.7^{+14.6}_{-3.7}$	< 51	< 260	1166
083310.2+030136	15959	128.2928	+3.0269	6.7	18.4	0.748	1.376	$1.73^{+0.83}_{-...}$	39^{+19}_{-13}	95^{+43}_{-31}	$7.4^{+3.0}_{-2.2}$	$13.1^{+7.8}_{-4.6}$	$1.72^{+0.64}_{-0.34}$	37^{+16}_{-13}	89^{+38}_{-31}	1206
083315.5+000623	6869	128.3148	+0.1065	16.5	42.0	0.470	1.970	$1.03^{+0.39}_{-...}$	$41.3^{+8.3}_{-8.0}$	82^{+16}_{-15}	$10.6^{+2.0}_{-1.8}$	$10.8^{+5.5}_{-2.7}$	$1.19^{+0.40}_{-0.21}$	$33.1^{+7.9}_{-...}$	$68^{+15}_{-...}$	1212
083321.1+012644	2879	128.3382	+1.4456	18.7	43.6	0.566	1.912	$8.2^{+12.2}_{-...}$	$65.7^{+10.9}_{-9.1}$	$284^{+187}_{-...}$	$16.2^{+2.6}_{-2.3}$	< 540	$6.8^{+11.6}_{-3.8}$	$47.0^{+9.7}_{-8.3}$	190^{+133}_{-55}	1214
083322.6-011128	6302	128.3444	-1.1912	11.6	22.5	0.288	2.489	$2.16^{+0.93}_{-...}$	$12.5^{+2.5}_{-...}$	$30.9^{+7.0}_{-...}$	$5.1^{+1.2}_{-1.3}$	$10.9^{+6.2}_{-3.7}$	$2.30^{+1.46}_{-0.70}$	$9.0^{+2.2}_{-2.6}$	$22.8^{+6.8}_{-6.8}$	1185
083330.4+050427	2528	128.3767	+5.0744	50.1	122.2	0.213	3.476	$2.19^{+0.58}_{-...}$	$17.6^{+2.8}_{-2.7}$	$43.4^{+8.8}_{-6.8}$	$7.8^{+1.4}_{-1.2}$	$17.4^{+7.7}_{-4.3}$	$2.27^{+0.93}_{-0.48}$	$12.5^{+3.1}_{-2.1}$	$31.4^{+9.9}_{-5.9}$	891
083341.0-002943	6767	128.4211	-0.4954	7.2	32.3	0.318	2.067	$1.61^{+0.48}_{-...}$	< 19	< 45	< 5.8	< 15	$3.5^{+7.2}_{-2.0}$	< 12	< 43	1187
083345.8+004208	2984	128.4409	+0.7025	29.3	90.5	0.384	2.344	$2.33^{+0.49}_{-...}$	$33.6^{+5.3}_{-5.8}$	85^{+15}_{-16}	$9.5^{+2.2}_{-2.5}$	$21.8^{+9.3}_{-6.8}$	$2.35^{+1.29}_{-0.57}$	$22.9^{+4.4}_{-5.6}$	58^{+13}_{-15}	1204
083401.5-001337	4258	128.5065	-0.2271	8.3	23.2	0.314	0.629	$7.9^{+11.4}_{-...}$	< 6.6	< 34	< 0.73	< 11	$6.2^{+8.1}_{-...}$	< 4.2	< 20	1184
083402.5-023437	6409	128.5155	+2.5772	9.2	36.8	0.362	2.020	$5.0^{+10.0}_{-3.1}$	$11.6^{+2.9}_{-...}$	39^{+32}_{-13}	$2.9^{+1.1}_{-1.0}$	< 76	$3.2^{+6.2}_{-4.0}$	$6.1^{+3.1}_{-3.0}$	$18.1^{+12.3}_{-8.9}$	1205
083403.7+012131	4634	128.5155	+1.3588	15.4	65.4	0.671	1.676	$4.2^{+3.6}_{-...}$	66^{+33}_{-25}	214^{+125}_{-84}	< 21	< 120	$7.5^{+14.4}_{-4.3}$	< 78	< 380	1207
083412.7+035856	1092	128.5530	+3.9825	20.7	20.6	0.201	2.785	$5.8^{+12.1}_{-...}$	$9.9^{+3.3}_{-2.0}$	$40^{+14}_{-...}$	$3.93^{+0.86}_{-0.78}$	23^{+49}_{-11}	$8.6^{+11.5}_{-5.0}$	$6.9^{+1.7}_{-1.5}$	31^{+22}_{-11}	1187
083422.7+034537	3240	128.5946	+3.7603	10.0	77.7	0.338	2.222	$1.50^{+0.42}_{-0.23}$	$14.1^{+2.3}_{-2.0}$	$31.3^{+5.5}_{-5.6}$	< 5.7	< 10	$1.37^{+0.37}_{-0.22}$	< 10	< 23	1193
083427.0-015612	12633	128.6129	-1.9369	13.4	21.8	0.573	1.661	$6.4^{+12.0}_{-...}$	$25.7^{+6.6}_{-...}$	$103^{+69}_{-...}$	$9.1^{+2.0}_{-...}$	< 260	$4.0^{+9.3}_{-2.2}$	$25.0^{+6.6}_{-5.9}$	$81^{+57}_{-...}$	1574
083431.0+034208	8206	128.6296	+3.7023	6.8	18.1	0.215	2.188	$5.0^{+12.0}_{-3.0}$	$3.06^{+1.03}_{-...}$	$11.1^{+10.0}_{-...}$	$1.59^{+0.50}_{-0.39}$	< 49	$5.6^{+14.7}_{-3.2}$	$2.95^{+0.98}_{-0.72}$	$11.2^{+10.7}_{-...}$	1205
083435.6+050159	4593	128.6484	+5.0332	7.7	62.3	0.091	3.805	$2.48^{+1.28}_{-...}$	$0.65^{+0.30}_{-...}$	$1.66^{+1.15}_{-0.80}$	< 1.4	< 3.8	$0.85^{+0.15}_{-0.72}$	< 1.6	< 3.2	1266
083457.7+052033	9892	128.7406	+5.3425	15.4	19.3	0.410	2.103	$2.26^{+1.08}_{-0.57}$	$13.5^{+4.3}_{-3.3}$	$34.3^{+10.3}_{-8.8}$	$5.4^{+1.5}_{-1.6}$	$12.0^{+7.3}_{-4.2}$	$3.1^{+2.8}_{-1.2}$	$9.3^{+3.6}_{-2.6}$	$26.9^{+13.6}_{-8.4}$	985

continued.

Cluster (eFEDS J+)	ID_SRC	RA (deg)	Dec (deg)	$\mathcal{L}_{ext}$	$\mathcal{L}_{det}$	z	R_{500} (arcmin)	T (keV)	L_X (10^{42} erg s^{-1})	L_{bol} (10^{42} erg s^{-1})	M_{gas} (10^{12} M$_\odot$)	Y_X (10^{12} M$_\odot$ keV)	T_{cex} (keV)	$L_{X,cex}$ (10^{42} erg s^{-1})	$L_{bol,cex}$ (10^{42} erg s^{-1})	t_{exp} (s)
083503.2+010756	3874	128.7636	+1.1325	36.9	85.8	0.296	2.696	$4.2^{+8.2}_{-1.8}$	$22.6^{+3.7}_{-2.9}$	74^{+50}_{-17}	$9.4^{+1.6}_{-1.3}$	40^{+82}	$2.28^{+0.67}_{-0.45}$	$18.8^{+3.3}_{-3.1}$	$46.6^{+9.5}_{-7.6}$	1188
083509.0+001542	1360	128.7876	+0.2619	74.8	213.1	0.597	2.239	$2.85^{+0.75}$	153^{+17}	407^{+48}_{-49}	$24.1^{+2.6}_{-3.1}$	68^{+20}_{-18}	$2.93^{+2.93}_{-0.72}$	106^{+17}_{-17}	298^{+71}_{-50}	1192
083532.5+030911	3198	128.8858	+3.1533	10.8	81.0	0.267	2.380	$2.46^{+1.66}_{-0.63}$	$7.8^{+1.8}$	$20.6^{+6.7}$	< 4.5	$6.6^{+5.8}_{-3.2}$	$3.0^{+6.3}$	< 6.9	< 25	1209
083615.7+024420	12572	129.0655	+2.7390	6.3	18.6	0.569	1.514	$11.1^{+9.8}$	$15.3^{+6.1}_{-2.1}$	77^{+52}_{-35}	$5.5^{+1.8}_{-2.5}$	< 190	$11.2^{+10.2}$	< 22	< 140	1196
083626.4+043821	5783	129.1100	+4.6394	17.0	51.6	0.574	1.832	$6.5^{+12.1}$	$42.4^{+10.1}$	172^{+121}	$9.7^{+3.5}$	< 310	$6.0^{+14.0}_{-5.1}$	$26.1^{+11.5}$	104^{+81}_{-40}	1221
083651.3+030002	197	129.2138	+3.0006	153.5	747.9	0.192	4.648	$2.56^{+0.63}$	$51.8^{+2.3}$	$133.0^{+52.0}$	$16.2^{+1.6}$	$41.8^{+10.8}$	$2.32^{+0.36}$	$31.5^{+2.3}$	$79.0^{+6.8}$	1203
083654.6+025954	16471	129.2277	+2.9984	10.9	14.0	0.191	3.550	$2.64^{+0.30}$	$49.0^{+2.2}$	$127.0^{+7.0}_{-8.0}$	$11.5^{+1.3}$	$30.8^{+7.1}$	$2.97^{+0.50}$	$33.2^{+1.9}$	$89.5^{+5.4}$	1197
083713.3+034110	10475	129.3055	+3.6862	6.2	19.4	1.000	1.241	$2.26^{+3.90}$	79^{+24}	219^{+78}	$12.2^{+3.2}$	28^{+38}	$2.8^{+3.56}$	61^{+27}_{-23}	180^{+69}	1206
083723.6+012413	4731	129.3487	+1.4037	27.3	69.3	0.349	2.382	$3.8^{+1.3}$	$30.5^{+4.3}$	92^{+32}	$10.4^{+3.7}$	39^{+14}	$3.2^{+3.1}$	$24.4^{+3.6}$	69^{+21}_{-15}	1184
083743.8-014128	5321	129.4328	-1.6912	11.8	41.9	1.043	1.313	$3.11^{+3.61}$	148^{+58}_{-37}	443^{+109}_{-98}	$19.4^{+3.6}$	61^{+63}_{-19}	$2.77^{+2.72}$	131^{+39}	375^{+100}_{-96}	1374
083757.1-014217	6303	129.4880	-1.7049	8.5	38.9	0.855	1.388	$3.7^{+4.6}_{-1.5}$	< 75	< 240	< 13	< 62	$3.9^{+9.7}$	< 40	< 150	1308
083759.5-003643	2456	129.4981	-0.6121	11.7	118.7	0.451	2.060	$3.09^{+2.36}$	$45.7^{+7.2}$	130^{+35}_{-20}	$11.2^{+2.1}_{-1.7}$	36^{+26}_{-11}	$2.9^{+4.7}$	$28.0^{+7.9}$	83^{+38}	1217
083802.9+015626	4511	129.5124	+1.9407	55.8	94.6	0.360	2.836	$7.1^{+11.1}$	$37.5^{+6.0}$	157^{+103}_{-43}	$15.1^{+2.5}$	108^{+182}_{-51}	$5.4^{+5.9}$	$29.4^{+5.9}$	108^{+70}_{-26}	1186
083806.9-003600	5386	129.5289	-0.6002	8.7	17.5	0.420	2.266	$3.05^{+2.82}$	$25.8^{+8.1}$	74^{+28}_{-29}	$9.9^{+2.8}$	31^{+28}_{-12}	$2.96^{+1.51}$	$24.9^{+7.8}$	69^{+25}	1216
083807.6+002501	19692	129.5321	+0.4171	6.4	15.1	0.080	3.444	$7.8^{+10.5}_{-4.5}$	$1.09^{+0.21}$	$4.6^{+3.3}_{-1.6}$	$0.66^{+0.16}_{-0.13}$	< 20	$7.8^{+13.7}_{-3.9}$	$1.01^{+0.15}_{-0.20}$	$4.5^{+3.4}_{-1.6}$	1205
083809.4-020450	10843	129.5394	-2.0808	9.3	19.8	0.550	1.597	$1.43^{+1.16}_{-0.34}$	< 46	< 110	$5.9^{+2.1}$	$9.0^{+8.0}_{-3.3}$	$1.68^{+1.60}_{-0.47}$	$14.5^{+11.9}_{-7.0}$	34^{+30}_{-17}	1025
083810.1+031520	3035	129.5422	+3.2558	14.5	88.4	0.347	2.265	$1.73^{+0.73}_{-0.35}$	$28.3^{+5.0}$	66^{+14}_{-11}	$8.2^{+1.4}$	$14.6^{+7.0}_{-3.9}$	$1.65^{+5.2}_{-0.28}$	$20.1^{+3.2}$	$46.7^{+13.0}$	1182
083811.8-015934	53	129.5496	-1.9930	163.7	2105.1	0.560	2.926	$4.80^{+1.56}_{-0.80}$	396^{+25}	1320^{+160}	$32.0^{+4.0}$	151^{+55}	$6.9^{+4.8}$	102^{+16}	403^{+131}	1144
083817.4+041821	6136	129.5727	+4.3060	21.1	56.6	0.211	3.028	$3.4^{+6.0}$	$11.3^{+1.4}$	$32.7^{+19.4}$	$5.45^{+0.93}$	$18.5^{+33.3}$	$4.4^{+8.7}$	$8.8^{+1.5}$	$28.8^{+22.1}$	1214
083817.5-021704	6195	129.5732	-2.2845	33.7	71.2	0.565	2.177	$4.6^{+5.3}$	130^{+23}	440^{+198}	$30.1^{+5.0}$	139^{+174}	$3.5^{+3.0}$	117^{+22}	348^{+98}	639
083834.1+020643	3905	129.6425	+2.1121	29.1	67.2	0.457	2.181	$3.7^{+2.9}$	$55.6^{+8.6}$	169^{+51}_{-29}	$15.2^{+2.5}$	57^{+45}_{-18}	$4.6^{+5.2}$	$41.2^{+8.2}$	140^{+53}	1188
083840.3+044416	8186	129.6681	+4.7380	17.9	34.1	0.455	1.946	$2.59^{+1.93}_{-0.77}$	$28.3^{+4.4}$	76^{+21}_{-10}	$10.0^{+1.8}$	$26.4^{+20.8}_{-8.6}$	$2.27^{+2.37}_{-0.77}$	$24.6^{+6.3}$	$63.1^{+21.0}_{-9.3}$	1341
083840.6-004134	7463	129.6694	-0.6930	9.5	36.9	0.462	1.919	$12.5^{+6.3}$	$19.2^{+3.9}$	106^{+67}	$8.3^{+2.3}$	< 310	$13.0^{+14.7}$	$18.0^{+6.5}$	102^{+73}_{-42}	1207
083856.9+030743	7902	129.7372	+3.1287	6.7	31.1	0.241	2.239	$2.3^{+3.4}$	$3.70^{+0.76}$	$9.5^{+4.0}$	$1.17^{+0.58}$	< 10	$5.4^{+17.1}$	< 3.7	< 24	1190
083857.5+020846	1806	129.7398	+2.1464	92.8	192.1	0.360	3.019	$4.3^{+1.3}$	$95.6^{+8.4}$	298^{+54}	$28.5^{+3.4}$	120^{+51}_{-32}	$4.7^{+2.4}$	$77.3^{+9.7}_{-7.8}$	255^{+69}_{-36}	1200
083858.5-015032	6026	129.7441	-1.8424	7.4	49.5	0.135	3.038	$1.18^{+0.39}$	$1.09^{+0.41}$	$2.24^{+0.95}_{-1.08}$	< 1.5	< 1.8	$1.48^{+1.75}_{-0.48}$	< 1.6	< 3.4	1223
083859.3+022841	3315	129.7473	+2.4782	11.5	26.8	0.359	2.122	$4.9^{+2.0}$	$23.6^{+4.3}$	81^{+48}_{-18}	$6.8^{+1.3}$	32^{+52}	$3.9^{+8.48}$	$16.0^{+4.2}$	51^{+35}_{-14}	1187
083900.6+020057	736	129.7527	+2.0159	39.3	313.3	0.359	2.701	$3.46^{+7.36}$	$51.2^{+4.4}$	149^{+26}_{-18}	$9.2^{+1.2}$	$32.2^{+15.1}$	$4.7^{+7.9}$	$20.5^{+5.5}$	72^{+40}_{-17}	1201
083903.5-011454	7445	129.7649	-1.2485	13.0	38.9	0.437	1.883	$4.4^{+8.4}$	$27.1^{+8.1}$	94^{+60}	$9.4^{+1.8}$	41^{+82}	$4.4^{+8.8}$	$24.4^{+6.1}$	82^{+56}_{-23}	1173
083914.7-021226	5360	129.8117	-2.2073	21.4	45.0	0.187	2.850	$1.68^{+0.72}$	$4.0^{+1.3}$	$9.0^{+3.1}$	$1.59^{+0.57}$	$2.5^{+1.8}$	$1.40^{+0.56}_{-0.76}$	< 4.0	< 8.9	1086
083916.7-020552	7669	129.8198	-2.0979	24.9	29.6	0.269	2.508	$1.56^{+0.45}$	$5.6^{+2.7}_{-1.3}$	$12.8^{+6.1}_{-2.8}$	$2.62^{+2.45}$	$4.4^{+2.5}$	$1.55^{+0.29}$	$3.1^{+3.2}_{-1.2}$	$6.9^{+7.1}_{-2.8}$	1223
083917.9-020839	15489	129.8247	-2.1442	18.2	15.0	0.269	2.266	$1.87^{+0.54}$	< 18	< 43	$3.4^{+1.7}$	$6.4^{+4.1}$	$1.81^{+0.45}$	< 17	< 40	1183
083921.0-014149	12407	129.8377	-1.6970	18.5	26.5	0.269	2.990	$3.95^{+1.30}$	$19.9^{+2.6}$	60^{+12}	$9.6^{+1.4}$	$38.1^{+14.0}_{-9.0}$	$4.24^{+1.92}_{-0.77}$	$17.1^{+2.2}_{-2.8}$	54^{+13}_{-11}	1180
083927.0-021357	10377	129.8627	-2.2328	9.3	22.5	0.567	1.767	$2.70^{+0.87}$	$20.1^{+21.6}$	56^{+60}_{-10}	< 15	< 60	$2.67^{+1.66}$	< 47	< 130	1156
083929.0+043001	3677	129.8711	+4.5003	20.1	76.6	0.249	2.582	$1.86^{+0.67}$	$11.4^{+1.4}$	$26.8^{+4.0}$	$3.90^{+0.79}_{-0.93}$	$7.2^{+3.3}_{-2.2}$	$2.00^{+1.31}_{-0.51}$	$7.5^{+1.7}$	$18.3^{+5.5}_{-3.8}$	1216
083929.6-015005	15946	129.8736	-1.8348	16.4	21.3	0.575	1.907	$5.7^{+6.7}_{-3.1}$	$39.1^{+7.8}$	142^{+76}	$14.2^{+3.7}$	< 290	$7.8^{+14.5}$	$35.1^{+7.7}_{-7.0}$	151^{+115}_{-47}	1198
083930.3-014348	6979	129.8763	-1.7302	7.8	22.5	0.271	2.243	$1.93^{+0.41}$	$6.8^{+3.9}_{-2.7}$	$16.1^{+9.9}_{-6.3}$	$2.5^{+2.1}_{-1.2}$	< 14	$1.79^{+0.36}_{-0.21}$	< 15	< 35	1178
083933.8-014044	356	129.8909	-1.6790	245.8	663.7	0.272	4.501	$3.73^{+0.60}$	$130.0^{+11.0}_{-7.0}$	386^{+43}_{-35}	$38.0^{+3.3}$	142^{+29}_{-25}	$3.56^{+0.57}_{-0.73}$	$90.8^{+10.2}$	265^{+36}_{-28}	1126
083936.0+011445	2898	129.9001	+1.2459	7.4	42.1	0.149	2.836	$1.72^{+0.58}_{-0.27}$	$1.78^{+0.68}_{-0.59}$	$4.2^{+1.6}_{-1.4}$	$0.49^{+0.45}_{-0.23}$	< 2.7	$1.44^{+0.69}_{-0.37}$	< 1.7	< 3.8	1216

continued.

Cluster (eFEDS J+)	ID_SRC	RA (deg)	Dec (deg)	$\mathcal{L}_{ext}$	$\mathcal{L}_{det}$	z	R_{500} (arcmin)	T (keV)	L_X (10^{42} erg s^{-1})	L_{bol} (10^{42} erg s^{-1})	M_{gas} (10^{12} M$_\odot$)	Y_X (10^{12} M$_\odot$ keV)	T_{cex} (keV)	$L_{X,cex}$ (10^{42} erg s^{-1})	$L_{bol,cex}$ (10^{42} erg s^{-1})	t_{exp} (s)
083937.8+014631	7652	129.9079	+1.7754	17.6	38.0	0.389	2.088	$2.73^{+4.44}_{-0.88}$	$22.6^{+4.0}_{-4.8}$	62^{+27}	$7.7^{+1.6}$	$21.5^{+33.5}$	$2.07^{+2.39}_{-0.61}$	$17.5^{+4.4}_{-4.8}$	44^{+14}_{-12}	1213
083940.8+010416	2832	129.9201	+1.0714	27.3	84.0	0.157	3.349	$2.57^{+1.89}$	$7.20^{+1.12}$	$19.2^{+4.6}$	$3.30^{+0.56}_{-0.48}$	$8.6^{+6.0}_{-2.5}$	$3.7^{+3.1}_{-1.0}$	$5.3^{+1.0}_{-1.0}$	$15.6^{+6.2}_{-3.7}$	1206
083945.5+031556	7213	129.9396	+3.2657	11.0	32.9	0.425	1.859	$0.90^{+0.31}_{-0.66}$	$9.0^{+3.7}$	$17.3^{+7.6}$	<3.6	<4.0	$1.01^{+0.43}_{-...}$	<7.9	<16	1193
083955.0+022425	3270	129.9793	+2.4071	9.0	12.3	0.189	3.258	$1.22^{+0.16}_{-0.19}$	$3.34^{+1.03}_{-...}$	$7.0^{+2.6}$	$1.97^{+0.84}_{-0.62}$	$2.49^{+1.74}_{-0.92}$	$1.30^{+0.33}_{-0.21}$	$2.28^{+1.17}$	$4.9^{+3.0}$	1215
084000.0-013109	7217	130.0002	-1.5194	26.2	53.8	0.266	3.130	$1.70^{+0.50}$	$19.0^{+2.7}$	$44.0^{+8.8}$	$9.2^{+0.6}$	$16.0^{+5.5}$	$1.73^{+0.21}_{-...}$	$14.7^{+3.9}$	$34.6^{+8.9}$	1096
084001.6+042452	4839	130.0070	+4.4145	14.8	51.2	0.259	2.452	$3.2^{+2.4}$	$8.0^{+1.3}$	$22.4^{+9.1}_{-5.0}$	$2.96^{+0.75}_{-1.19}$	$9.1^{+7.6}_{-3.9}$	$3.9^{+3.8}_{-...}$	$4.4^{+1.3}_{-1.7}$	$13.3^{+6.6}_{-4.8}$	1221
084003.2+003008	2568	130.0137	+0.5023	19.1	104.0	0.385	2.223	$4.6^{+1.5}$	<15	<55	<7.3	<36	$7.2^{+10.7}$	<7.2	<31	1211
084004.8+013751	10272	130.0203	+1.6309	13.1	17.4	0.342	2.210	$2.6^{+1.3}$	$5.0^{+1.4}$	$13.4^{+9.5}$	$2.63^{+0.78}_{-0.67}$	<37	$3.2^{+5.1}$	$2.9^{+1.5}_{-1.0}$	$8.9^{+8.5}$	1213
084006.1+025913	2388	130.0258	+2.9871	41.9	117.5	0.456	2.307	$3.76^{+2.95}_{-0.97}$	$61.5^{+8.6}_{-7.1}$	189^{+31}	$17.4^{+2.7}$	67^{+50}_{-20}	$6.7^{+5.8}_{-3.2}$	$44.4^{+9.3}$	172^{+74}	1208
084011.6+034837	5544	130.0487	+3.8104	12.5	39.3	0.825	1.469	$9.1^{+12.3}_{-6.0}$	$45.3^{+7.9}$	211^{+132}_{-71}	$9.7^{+2.4}$	<350	$11.4^{+11.3}$	$27^{+7.3}_{-11}$	131^{+93}	1215
084016.6+033951	6282	130.0695	+3.6644	9.4	35.5	0.805	1.443	$17.1^{+10.5}_{-8.9}$	46^{+13}	300^{+140}_{-110}	$11.8^{+2.9}$	<470	$14.1^{+7.0}_{-6.8}$	37^{+13}_{-14}	217^{+134}_{-89}	1199
084021.6-022948	5406	130.0901	-2.4967	12.5	29.3	0.184	2.978	$2.65^{+1.58}_{-0.62}$	$7.2^{+1.2}$	$19.1^{+4.2}$	$3.70^{+0.69}$	$10.1^{+5.7}_{-3.0}$	$2.31^{+1.10}_{-0.51}$	$6.29^{+0.92}$	$15.9^{+3.5}_{-3.0}$	1290
084021.6+020132	5639	130.0903	+2.0256	31.1	17.7	0.357	0.565	$0.76^{+1.98}_{-0.40}$	$7.7^{+3.8}$	$17.3^{+15.3}_{-5.9}$	$0.54^{+0.31}$	$0.37^{+1.20}_{-0.14}$	$0.73^{+0.35}_{-0.29}$	$7.2^{+3.0}_{-2.0}$	$14.5^{+9.6}_{-4.2}$	1215
084034.5+023638	250	130.1441	+2.6108	114.6	661.8	0.049	7.565	$0.849^{+0.032}_{-0.033}$	$0.952^{+0.108}_{-0.091}$	$1.74^{+0.17}$	$0.222^{+0.131}_{-0.097}$	$0.188^{+0.112}_{-0.082}$	$9.2^{+9.0}_{-8.3}$	$0.154^{+0.084}_{-0.072}$	<2.0	1217
084035.8+044036	5844	130.1493	+4.6768	8.6	39.8	0.793	1.448	$3.3^{+3.4}_{-1.4}$	43^{+22}_{-15}	130^{+63}_{-46}	$2.7^{+5.0}_{-1.1}$	<51	$3.4^{+3.4}_{-1.4}$	<53	<160	1320
084044.7+024108	8131	130.1863	+2.6858	8.6	19.8	1.104	1.220	$2.9^{+7.2}_{-1.2}$	167^{+62}_{-43}	510^{+180}_{-110}	$19.0^{+3.9}_{-3.1}$	55^{+113}_{-19}	$3.1^{+5.7}_{-1.3}$	141^{+52}_{-36}	432^{+144}_{-98}	1216
084051.7+014122	7662	130.2156	+1.6895	32.6	54.3	0.411	2.263	$14.2^{+17.4}_{-7.7}$	$31.6^{+4.6}_{-5.7}$	188^{+89}_{-69}	$12.7^{+2.1}_{-1.9}$	<500	$15.9^{+8.6}_{-9.0}$	$26.1^{+4.5}_{-4.9}$	160^{+67}_{-59}	1215
084058.4+050407	7625	130.2434	+5.0688	7.3	26.6	1.265	1.209	$13.5^{+8.5}$	<300	<2100	<30	<680	$10.0^{+14.5}_{-6.4}$	<260	<1500	776
084102.1+044734	6014	130.2591	+4.7930	22.7	50.5	0.203	2.972	$1.75^{+1.2}_{-1.0}$	$7.3^{+1.2}_{-1.0}$	$17.3^{+3.5}_{-2.7}$	$4.01^{+0.72}_{-0.62}$	$7.2^{+2.9}_{-1.6}$	$1.66^{+0.25}_{-0.22}$	$5.87^{+1.29}_{-0.92}$	$13.5^{+3.3}_{-2.3}$	1195
084105.5+031639	1906	130.2731	+3.2777	32.3	146.2	0.337	2.597	$3.38^{+4.02}_{-0.99}$	$37.2^{+4.5}_{-4.0}$	107^{+41}	$11.5^{+1.8}_{-2.2}$	37^{+45}_{-12}	$3.10^{+2.72}_{-0.92}$	$25.8^{+4.4}_{-4.5}$	74^{+21}_{-15}	1204
084107.2+050459	4300	130.2801	+5.0832	8.1	56.1	0.288	2.435	$13.3^{+8.9}$	$8.8^{+1.7}$	50^{+22}_{-15}	$2.58^{+1.19}_{-0.78}$	<91	$12.7^{+10.4}_{-7.1}$	$3.4^{+2.1}_{-1.6}$	<49	730
084110.8+005200	5702	130.2953	+0.8668	7.1	39.4	0.415	1.796	$3.6^{+6.2}_{-2.8}$	$9.9^{+2.8}$	31^{+17}	<6.0	<46	$4.8^{+5.8}_{-2.1}$	<11	<44	1179
084111.8-001946	7983	130.2994	-0.3297	10.9	18.9	0.703	1.959	$6.2^{+1.6}_{-2.5}$	66^{+16}_{-13}	249^{+135}_{-47}	$20.8^{+3.5}_{-3.6}$	<470	$6.9^{+13.4}_{-3.0}$	55^{+14}_{-13}	222^{+161}_{-66}	1110
084116.5+020700	9822	130.3191	+2.1168	10.1	25.1	0.580	1.574	$7.1^{+1.08}$	$15.5^{+6.3}$	65^{+27}	<8.9	<120	$7.3^{+13.0}$	<23	<110	1214
084124.1-023350	9149	130.3505	-2.5641	15.6	30.4	0.204	2.792	$3.9^{+3.2}_{-2.2}$	$4.65^{+1.21}_{-0.95}$	$14.2^{+5.9}_{-3.8}$	$2.45^{+0.82}_{-0.56}$	$9.3^{+9.3}_{-4.1}$	$8.8^{+12.0}$	$3.15^{+1.31}_{-0.99}$	$14.1^{+12.6}$	1341
084124.7+004636	6605	130.3530	+0.7768	10.0	41.8	0.407	1.997	$4.6^{+15.6}$	$16.0^{+3.2}_{-4.5}$	56^{+58}	5.2^{+12}	<190	$5.0^{+8.5}$	$9.5^{+4.9}$	35^{+24}	1157
084129.0+002645	5591	130.3708	+0.4460	10.2	56.2	0.402	2.156	$1.92^{+0.56}$	$41.8^{+3.8}$	99^{+15}	$11.2^{+1.7}$	$21.7^{+7.7}$	$1.59^{+0.34}$	$34.0^{+6.0}$	78^{+16}	1134
084134.1+043503	7544	130.3925	+4.5844	11.2	40.9	0.560	1.815	$1.59^{+0.45}$	$20.2^{+8.4}$	46^{+10}	$8.1^{+2.3}$	$12.9^{+5.9}$	$1.74^{+1.02}$	$17.8^{+7.3}$	43^{+19}	1320
084135.0+010150	1644	130.3958	+1.0306	16.5	139.6	0.507	2.110	$3.0^{+3.6}$	$44.2^{+10.0}$	125^{+52}	$8.7^{+2.4}$	26^{+36}_{-12}	$1.32^{+2.76}_{-0.33}$	$23.7^{+9.4}_{-7.1}$	55^{+23}_{-17}	1171
084135.7-005048	4430	130.3988	-0.8468	6.0	60.0	0.328	2.178	$3.7^{+1.6}$	$10.5^{+3.3}$	34^{+34}	<3.8	<61	$9.7^{+14.0}_{-6.8}$	<9.5	<54	1061
084142.9+002841	8433	130.4292	+0.4782	19.2	33.9	0.206	2.802	$1.43^{+0.44}_{-0.20}$	$5.42^{+0.82}$	$11.9^{+2.4}_{-2.2}$	$2.88^{+0.57}_{-0.52}$	$4.1^{+1.8}_{-1.1}$	$1.23^{+0.21}_{-0.13}$	$4.00^{+0.79}_{-0.78}$	$8.3^{+1.8}_{-1.8}$	1135
084146.3-021339	18047	130.4432	-2.2278	11.8	12.9	0.428	1.719	$1.34^{+0.29}_{-0.18}$	$13.5^{+4.5}$	$29.0^{+10.0}_{-8.1}$	$4.9^{+1.3}$	$6.6^{+2.8}_{-3.2}$	$1.32^{+0.31}_{-0.16}$	$11.7^{+4.4}_{-3.9}$	$24.9^{+9.5}_{-8.4}$	1961
084146.5+045612	2796	130.4438	+4.9369	12.1	85.0	0.636	1.746	$4.9^{+9.2}_{-2.0}$	41^{+35}_{-14}	156^{+151}	<18	<200	$3.0^{+3.8}_{-1.0}$	<66	<220	941
084148.1+004911	3008	130.4507	+0.8198	16.8	80.9	0.078	4.330	$0.88^{+0.12}_{-0.11}$	$0.67^{+0.17}_{-0.14}$	$1.25^{+0.33}_{-0.23}$	$0.133^{+0.193}_{-0.059}$	$0.125^{+0.171}_{-0.061}$	$3.2^{+3.5}_{-1.0}$	<0.47	<1.6	1144
084151.3-003358	3706	130.4640	-0.5661	6.0	12.9	0.250	2.632	$4.5^{+12.1}_{-2.0}$	$12.5^{+2.7}$	42^{+37}_{-13}	$6.1^{+1.1}$	27^{+79}	$5.4^{+9.2}_{-2.8}$	$11.0^{+2.5}_{-2.8}$	39^{+28}_{-12}	1062
084151.7+004351	6543	130.4656	+0.7311	12.5	25.5	0.237	2.312	$15.6^{+11.5}$	1.92^{+132}	<34	<2.2	<36	$5.2^{+9.3}$	<3.0	<11	1133
084151.9-010156	6071	130.4665	-1.0323	9.1	36.8	0.270	2.240	$9.3^{+13.9}$	$4.9^{+1.3}$	$23.1^{+17.7}_{-8.9}$	$2.03^{+0.44}_{-0.48}$	<80	$14.0^{+12.4}_{-7.6}$	$3.20^{+0.90}_{-1.08}$	$17.9^{+11.5}_{-7.2}$	1603
084201.3+040534	6988	130.5056	+4.0928	6.6	36.5	0.758	1.432	$6.1^{+10.7}$	39^{+13}_{-11}	153^{+99}_{-49}	$6.8^{+2.5}_{-3.2}$	<180	$4.4^{+5.6}_{-3.2}$	<46	<160	1208
084201.8+005941	3334	130.5076	+0.9950	7.5	9.9	0.087	1.940	$5.6^{+12.9}_{-3.2}$	<0.45	<1.7	<0.23	2.4	$6.4^{+10.2}_{-3.7}$	0.38	<1.5	1137

continued.

Cluster (eFEDS J+)	ID_SRC	RA (deg)	Dec (deg)	$\mathcal{L}_{ext}$	$\mathcal{L}_{det}$	z	R_{500} (arcmin)	T (keV)	L_X (10^{42} erg s^{-1})	L_{bol} (10^{42} erg s^{-1})	M_{gas} (10^{12} M$_\odot$)	Y_X (10^{12} M$_\odot$ keV)	T_{cex} (keV)	$L_{X,cex}$ (10^{42} erg s^{-1})	$L_{bol,cex}$ (10^{42} erg s^{-1})	t_{exp} (s)
084210.5+020558	7967	130.5439	+2.0997	6.8	28.0	0.421	1.748	$3.4^{+7.4}$	<12	<43	<5.9	<27	$3.4^{+3.5}$	<9.8	<29	1199
084220.9+013844	3295	130.5875	+1.6457	27.7	64.5	0.421	0.498	$7.9^{+8.4}_{-5.1}$	$13.5^{+3.9}_{-3.9}$	57^{+36}_{-20}	$0.73^{+0.30}_{-0.17}$	<22	$5.8^{+8.9}_{-1.7}$	$12.8^{+3.6}_{-2.6}$	48^{+32}_{-15}	1157
084223.1+003340	4993	130.5963	+0.5613	11.0	55.3	1.077	1.317	$3.2^{+2.8}$	247^{+138}	720^{+410}_{-280}	<33	<150	$2.60^{+2.49}$	<350	<950	1092
084240.7-011643	2859	130.6698	-1.2787	18.5	16.5	0.210	0.876	$0.392^{+0.117}_{-0.079}$	$1.29^{+0.53}$	$3.1^{+1.6}$	$0.148^{+0.086}_{-0.062}$	$0.060^{+0.041}_{-0.026}$	$0.371^{+0.064}$	$0.38^{+0.42}_{-0.19}$	<3.4	2096
084246.9-000917	4861	130.6956	-0.1548	31.3	45.7	0.420	2.485	$6.8^{+11.4}$	$43.8^{+6.1}$	167^{+48}	$17.4^{+2.3}_{-2.2}$	<570	$6.7^{+6.1}_{-3.3}$	$37.6^{+5.4}$	148^{+106}_{-41}	1074
084253.7+002006	6903	130.7238	+0.3350	6.6	29.7	0.345	1.970	$3.0^{+1.9}$	$6.9^{+3.8}$	$21.2^{+20.5}$	<6.3	<53	2.6	$3.4^{+4.6}$	<38	1064
084255.6+042332	2475	130.7317	+4.3924	32.3	129.4	0.484	2.202	$2.34^{+1.22}$	$67.1^{+7.6}_{-7.4}$	172^{+24}_{-19}	$17.3^{+2.2}$	$41.4^{+19.7}_{-9.3}$	$2.37^{+1.37}$	$46.3^{+7.1}$	120^{+23}	1327
084258.3-004037	4269	130.7432	-0.6772	7.7	55.4	0.407	1.986	$2.24^{+0.47}$	$16.5^{+6.3}_{-5.7}$	43^{+20}_{-17}	$4.4^{+1.3}_{-1.1}$	$10.3^{+8.9}_{-3.8}$	$2.80^{+0.65}$	$15.3^{+6.3}_{-7.1}$	45^{+30}_{-21}	1132
084301.4+025741	11065	130.7560	+2.9615	7.8	31.3	0.539	1.613	$2.08^{+0.68}$	$18.6^{+5.7}$	47^{+16}	<7.9	<28	$2.37^{+2.40}$	<20	<55	1199
084307.1+002839	3336	130.7797	+0.4777	28.1	87.0	0.264	2.866	$8.9^{+6.9}$	$20.9^{+3.4}$	98^{+39}_{-30}	$8.0^{+1.4}$	<290	$9.3^{+11.3}_{-4.5}$	$15.3^{+3.0}_{-3.7}$	72^{+44}_{-23}	1057
084324.2-001438	9590	130.8511	-0.2441	16.3	31.7	0.330	2.191	$4.1^{+9.8}$	$14.8^{+4.0}$	47^{+14}	$6.4^{+1.3}$	26^{+64}_{-11}	$3.2^{+2.6}$	$13.4^{+3.5}$	38^{+13}_{-10}	1135
084346.2+010833	12839	130.9425	+1.1425	11.2	21.1	0.342	2.095	$3.8^{+5.6}$	$12.6^{+4.5}_{-3.3}$	40^{+21}_{-13}	$5.8^{+1.5}_{-1.2}$	$21.9^{+31.7}_{-9.0}$	$3.4^{+6.0}$	$11.0^{+5.1}_{-2.8}$	35^{+23}_{-12}	1062
084349.1+040404	19985	130.9547	+4.0678	12.0	18.2	0.213	2.716	$3.0^{+3.0}$	<31	<110	<9.5	<59	$3.3^{+4.3}$	<26	<110	1215
084353.9+031402	19202	130.9747	+3.2341	7.7	11.1	0.374	1.919	$2.62^{+4.85}$	$6.9^{+3.6}_{-2.6}$	$19.8^{+11.8}_{-8.4}$	$3.3^{+1.3}_{-1.4}$	<38	$2.48^{+3.28}_{-0.84}$	<11	<34	1176
084412.6-020514	3396	131.0526	-2.0874	6.8	80.1	0.382	2.894	$5.0^{+9.6}$	<180	<710	<25	<200	$9.1^{+8.8}$	<63	<320	187
084417.9+010415	1812	131.0748	+1.0711	26.0	94.6	0.340	2.586	$3.5^{+2.7}$	$45.2^{+3.7}_{-4.2}$	131^{+37}_{-17}	$12.9^{+1.6}_{-1.7}$	44^{+36}_{-14}	$4.6^{+5.7}_{-2.0}$	$32.1^{+4.9}$	105^{+55}_{-23}	1085
084430.8+021736	3541	131.1285	+2.2935	27.5	79.3	0.050	5.678	$0.852^{+0.084}_{-0.089}$	$0.320^{+0.046}_{-0.041}$	$0.590^{+0.122}_{-0.078}$	$0.090^{+0.026}_{-0.028}$	$0.076^{+0.027}_{-0.024}$	$5.0^{+7.8}_{-2.0}$	$0.074^{+0.030}_{-0.029}$	$0.25^{+0.019}_{-9.10}$	1085
084434.3+031026	4876	131.1430	+3.1739	9.9	48.9	0.724	1.560	$2.05^{+0.89}$	91^{+56}_{-36}	222^{+280}_{-86}	<22	<56	$2.27^{+1.65}_{-0.63}$	55^{+28}	145^{+73}_{-70}	1136
084438.5+041946	11610	131.1606	+4.3295	18.7	28.2	0.577	1.726	$4.2^{+9.4}$	$34.9^{+8.2}$	115^{+91}	$10.5^{+2.1}$	43^{+95}_{-19}	$4.9^{+17.0}$	$27.6^{+8.2}$	100^{+94}_{-70}	1315
084439.0+043302	5668	131.1625	+4.5507	11.9	47.6	0.517	1.839	$2.9^{+1.8}$	$27.3^{+7.0}$	79^{+31}	$6.6^{+2.0}$	$20.3^{+27.4}$	$3.9^{+9.2}$	$17.3^{+9.7}$	56^{+37}_{-22}	1209
084441.3+021701	1778	131.1723	+2.2839	22.1	146.1	0.651	1.913	$6.2^{+9.1}$	141^{+10}	540^{+310}	$26.3^{+3.9}_{-3.6}$	159^{+86}	$7.7^{+13.2}$	103^{+57}	450^{+300}	1064
084454.0-010021	4436	131.2253	+1.0059	17.1	59.7	0.295	2.314	$2.70^{+2.22}$	$17.7^{+2.8}$	$47.9^{+12.3}$	$6.4^{+1.1}$	$17.5^{+14.5}$	$4.2^{+4.9}$	$13.7^{+2.9}$	43^{+11}	1160
084459.2-011902	4768	131.2471	-1.3174	48.2	93.5	0.447	2.517	$5.7^{+8.8}$	$53.6^{+9.0}$	198^{+119}	$20.1^{+3.2}$	112^{+185}	$7.0^{+10.2}$	$45.4^{+8.7}$	180^{+124}	1566
084501.0+012728	1607	131.2542	+1.4578	29.0	78.1	0.420	2.350	$3.08^{+3.11}$	$58.2^{+9.2}$	165^{+51}	$16.1^{+2.2}$	50^{+50}_{-16}	$4.3^{+8.0}$	$43.6^{+8.6}$	140^{+84}	1127
084528.6+032739	144	131.3695	+3.4609	316.7	1183.0	0.334	3.872	$6.7^{+2.2}_{-1.7}$	$219^{+11.0}$	860^{+150}_{-120}	$49.9^{+3.7}$	335^{+120}	$6.7^{+2.5}$	$149.0^{+9.0}$	585^{+192}	1093
084531.6+022831	1039	131.3818	+2.4753	98.9	275.7	0.076	6.064	$1.460^{+0.090}_{-0.090}$	$3.85^{+0.28}$	$8.51^{+0.61}$	$1.65^{+0.14}$	$2.43^{+0.35}_{-0.27}$	$1.42^{+0.15}$	$2.17^{+0.27}$	$4.74^{+0.61}_{-0.50}$	1077
084544.3-002914	2214	131.4349	-0.4874	33.5	103.1	0.156	3.745	$2.33^{+0.87}$	$13.0^{+1.0}$	$32.4^{+4.4}$	$4.78^{+0.50}_{-0.49}$	$11.1^{+4.8}$	$3.12^{+2.93}$	$9.0^{+1.5}$	$25.5^{+9.2}_{-4.7}$	1021
084545.2+005535	3660	131.4384	+0.9265	10.7	26.4	0.293	2.122	$6.5^{+4.0}$	<8.7	<44	<4.6	<44	$9.0^{+15.2}$	<6.4	<33	1182
084552.4+011714	5804	131.4684	+1.2872	12.8	47.6	0.668	1.596	$3.01^{+3.13}$	44^{+25}_{-18}	130^{+78}_{-53}	<18	<92	$4.5^{+5.2}$	<68	<250	1185
084557.6+041103	25781	131.4901	+4.1843	13.2	13.0	0.284	2.432	$7.0^{+10.5}$	$4.7^{+2.2}$	<51	$2.9^{+1.7}$	<87	$6.9^{+10.2}$	<8.4	<45	1211
084558.1+012443	9771	131.4924	+1.4120	11.2	34.3	0.350	2.135	$3.3^{+8.7}$	$18.1^{+5.8}$	58^{+39}_{-17}	$5.8^{+2.0}$	$19.8^{+45.9}_{-9.2}$	$3.3^{+3.9}$	$12.2^{+3.7}$	36^{+16}_{-14}	1179
084559.7+031321	5281	131.4988	+3.2227	11.4	32.0	0.391	2.014	$4.4^{+9.2}$	$23.4^{+6.0}$	78^{+58}_{-25}	$7.8^{+1.7}$	<180	$5.4^{+13.9}$	$18.0^{+5.5}_{-5.3}$	63^{+61}_{-24}	1063
084607.6+000651	29318	131.5318	+0.1143	6.1	11.0	0.229	2.561	$0.47^{+0.73}_{-0.20}$	$5.9^{+2.4}$	$20.3^{+19.0}$	$3.6^{+1.0}$	$1.65^{+32.45}_{-0.56}$	$0.42^{+8.42}_{-0.20}$	$5.0^{+2.3}_{-1.8}$	$17.2^{+19.3}_{-7.5}$	1060
084630.7+024702	13490	131.6281	+2.7839	8.4	15.6	0.206	2.353	$1.60^{+0.40}_{-0.23}$	$4.9^{+1.2}$	$11.0^{+2.8}$	$2.26^{+0.55}_{-0.46}$	$3.66^{+1.40}_{-0.95}$	$1.60^{+0.46}_{-0.26}$	$3.98^{+1.25}_{-0.95}$	$9.1^{+3.0}_{-2.3}$	1123
084637.1-002256	2987	131.6546	-0.3824	32.9	63.6	0.256	3.499	$4.5^{+8.5}$	$14.0^{+4.9}$	48^{+36}	<11	<130	$4.5^{+6.7}$	<15	<55	901
084640.3-010423	9948	131.6681	-1.0733	8.8	19.7	0.244	2.261	$0.91^{+10.99}_{-0.71}$	$6.6^{+5.9}$	$19.8^{+82.2}$	$2.55^{+2.41}_{-0.89}$	<74	$0.38^{+0.36}_{-0.30}$	$5.4^{+39.0}_{-2.3}$	<52000	933
084645.6+014947	6215	131.6902	+1.8298	12.4	39.2	0.051	5.077	$2.51^{+1.86}_{-0.81}$	$0.92^{+0.14}_{-0.12}$	$2.41^{+0.86}_{-0.42}$	$0.515^{+0.101}_{-0.087}$	$1.32^{+1.02}_{-0.66}$	$2.32^{+1.25}$	$0.76^{+0.14}_{-0.13}$	$1.96^{+0.52}_{-0.39}$	1173
084647.4+044607	6656	131.6975	+4.7688	19.6	48.8	0.245	3.468	$3.7^{+3.0}$	$20.1^{+4.2}$	61^{+25}_{-13}	$9.7^{+2.0}_{-1.6}$	36^{+33}_{-13}	$3.5^{+3.0}$	$14.5^{+4.1}_{-3.1}$	44^{+18}_{-12}	531
084649.0+004946	11018	131.7045	+0.8295	8.4	18.8	0.416	1.781	$1.90^{+1.47}_{-0.43}$	<25	<63	<6.7	<20	$2.16^{+1.36}_{-0.62}$	<16	<43	1073

continued.

Cluster (eFEDS J+)	ID_SRC	RA (deg)	Dec (deg)	$\mathcal{L}_{ext}$	$\mathcal{L}_{det}$	z	R_{500} (arcmin)	T (keV)	L_X (10^{42} erg s^{-1})	L_{bol} (10^{42} erg s^{-1})	M_{gas} ($10^{12}\,M_\odot$)	Y_X ($10^{12}\,M_\odot$ keV)	T_{cex} (keV)	$L_{X,cex}$ (10^{42} erg s^{-1})	$L_{bol,cex}$ (10^{42} erg s^{-1})	t_{exp} (s)
084655.7-003705	3712	131.7322	-0.6181	21.6	70.1	0.365	2.348	$2.49^{+1.79}_{-0.71}$	$37.7^{+10.8}_{-8.0}$	99^{+37}_{-22}	$9.6^{+3.2}_{-2.7}$	$24.2^{+19.1}_{-9.3}$	$2.8^{+8.3}_{-2.7}$	$23.1^{+10.1}_{-7.2}$	70^{+47}_{-26}	863
084657.6-011314	9845	131.7403	-1.2206	6.6	21.4	0.804	1.370	$5.5^{+12.6}_{-3.0}$	$45^{+8.0}_{-2.4}$	167^{+127}_{-79}	$10.1^{+3.5}_{-4.1}$	<290	$7.1^{+15.2}_{-4.2}$	<73	<430	1085
084717.7+033421	10507	131.8241	+3.5725	6.4	21.6	0.716	1.451	$12.0^{+10.7}_{-4.1}$	<24	<150	<8.4	<140	$13.0^{+12.6}_{-4.2}$	<18	<110	1124
084729.7+013053	5053	131.8740	+1.5149	26.4	55.7	0.351	2.524	$4.5^{+8.3}_{-2.2}$	$27.2^{+4.4}_{-4.0}$	88^{+55}_{-20}	$10.3^{+1.6}_{-1.7}$	44^{+85}_{-19}	$6.1^{+7.8}_{-2.8}$	$19.7^{+4.4}_{-4.0}$	72^{+44}_{-42}	1080
084751.7+025522	4736	131.9656	+2.9230	17.1	58.7	0.269	2.426	$0.937^{+0.113}_{-0.113}$	$9.6^{+2.6}_{-2.0}$	$18.1^{+3.7}_{-3.7}$	$2.44^{+0.57}_{-0.65}$	$2.28^{+0.67}_{-0.63}$	$0.98^{+0.14}_{-0.14}$	$4.9^{+1.9}_{-1.6}$	$9.2^{+3.7}_{-3.0}$	1178
084759.1+014903	4709	131.9966	+1.8178	17.8	54.6	0.576	1.853	$2.67^{+2.8}_{-0.8}$	37^{+28}_{-20}	101^{+44}_{-44}	<16	<58	$2.40^{+2.93}_{-0.84}$	<44	<120	1043
084823.2+041205	2437	132.0971	+4.2015	23.8	118.2	0.872	1.608	$3.8^{+1.2}_{-0.9}$	196^{+46}_{-39}	620^{+180}_{-120}	$21.8^{+5.5}_{-5.0}$	84^{+84}_{-31}	$2.85^{+0.93}_{-0.66}$	119^{+39}_{-38}	340^{+110}_{-120}	1204
084833.2-012216	1073	132.1385	-1.3712	91.2	253.7	0.629	2.291	$17.0^{+10.4}_{-8.3}$	187^{+18}_{-17}	1260^{+450}_{-390}	$41.6^{+9.2}_{-4.5}$	<1600	$14.3^{+11.5}_{-5.6}$	142^{+18}_{-17}	870^{+370}_{-220}	1191
084852.9+035939	10165	132.2205	+3.9944	10.9	21.9	0.688	1.611	$7.7^{+21}_{-5.2}$	$37.5^{+12.4}_{-10.0}$	155^{+54}_{-54}	$9.8^{+2.5}_{-3.5}$	<300	$7.2^{+12.5}_{-4.6}$	27^{+11}_{-11}	109^{+49}_{-86}	1242
084905.3+021435	7831	132.2723	+2.2433	8.4	43.0	0.395	2.036	$1.55^{+1.30}_{-0.33}$	$24.0^{+11.1}_{-6.3}$	58^{+34}_{-17}	$7.5^{+2.1}_{-2.8}$	<420	$1.41^{+1.03}_{-0.27}$	$18.2^{+7.6}_{-9.0}$	41^{+19}_{-19}	961
084910.6+024117	9790	132.2943	+2.6882	9.8	17.5	0.830	1.535	18^{+10}_{-10}	<96	<700	<20	<24	$14.3^{+13.8}_{-9.9}$	<67	<410	1016
084925.4+013840	14327	132.3562	+1.6447	15.0	12.6	0.506	0.434	$7.4^{+12.3}_{-5.0}$	$10.2^{+4.7}_{-2.8}$	44^{+38}_{-18}	$0.61^{+0.32}_{-0.16}$	<280	$9.7^{+14.1}_{-7.3}$	$9.6^{+5.5}_{-2.6}$	50^{+44}_{-22}	861
084934.9+014437	32680	132.3958	+1.7438	13.9	15.8	0.325	2.849	$6.4^{+10.6}_{-3.5}$	$18.1^{+7.2}_{-5.0}$	72^{+58}_{-28}	$9.3^{+3.7}_{-3.9}$	210^{+280}_{-100}	$6.7^{+11.0}_{-3.6}$	$13.5^{+8.0}_{-6.2}$	<150	857
084939.6-005126	2261	132.4151	-0.8573	29.0	108.8	0.613	2.004	$8.3^{+10.0}_{-3.8}$	121^{+54}_{-17}	540^{+300}_{-140}	$25.8^{+4.1}_{-3.4}$	<760	$7.2^{+10.1}_{-3.5}$	93^{+23}_{-16}	380^{+230}_{-100}	868
084957.4+004524	8524	132.4894	+0.7567	11.0	37.4	1.066	1.360	$14.0^{+10.8}_{-7.2}$	<360	<2300	<33	<15	$11.0^{+12.9}_{-6.2}$	<260	<1500	857
085018.3+020018	5464	132.5764	+2.0053	8.2	48.4	0.421	2.084	$4.3^{+10.0}_{-2.1}$	33^{+10}_{-16}	108^{+87}_{-49}	<15	<160	$7.7^{+14.1}_{-5.0}$	<39	<220	856
085020.4+030218	6529	132.5850	+3.0384	26.4	47.3	0.294	2.822	$4.4^{+7.1}_{-1.7}$	$19.0^{+2.6}_{-1.6}$	60^{+38}_{-13}	$7.2^{+1.7}_{-1.8}$	30^{+56}_{-14}	$4.2^{+5.2}_{-1.5}$	$13.4^{+3.0}_{-3.0}$	43^{+21}_{-11}	965
085022.2+001607	8602	132.5927	+0.2687	13.4	18.2	0.196	3.001	$3.86^{+0.87}_{-0.67}$	$11.0^{+3.4}_{-3.3}$	34^{+13}_{-13}	$4.4^{+1.4}_{-1.4}$	$17.5^{+12.6}_{-5.9}$	$4.3^{+1.36}_{-1.36}$	$10.6^{+3.1}_{-3.1}$	34^{+11}_{-11}	862
085027.8+001503	1023	132.6160	+0.2509	128.7	280.4	0.197	4.560	$3.31^{+3.4}_{-0.87}$	$55.8^{+3.4}_{-3.4}$	155^{+15}_{-14}	$20.5^{+2.5}_{-2.3}$	68^{+17}_{-17}	$3.21^{+1.36}_{-0.62}$	$44.8^{+2.9}_{-2.9}$	125^{+19}_{-13}	860
085030.5+003330	6125	132.6272	+0.5584	29.2	62.1	0.192	3.291	$5.2^{+2.3}_{-0.4}$	$14.8^{+3.8}_{-3.3}$	52^{+32}_{-13}	$6.28^{+7.18}_{-0.97}$	32^{+43}_{-14}	$5.3^{+9.5}_{-2.5}$	$11.8^{+3.3}_{-3.4}$	43^{+27}_{-11}	852
085051.8+015331	8679	132.7161	+1.8921	9.8	22.0	0.268	2.270	$14.4^{+10.4}_{-7.9}$	$10.7^{+1.5}_{-1.9}$	61^{+39}_{-29}	$3.7^{+1.1}_{-1.1}$	<150	$14.2^{+10.0}_{-10.0}$	$6.6^{+3.5}_{-3.5}$	<94	862
085056.4+005607	3556	132.7354	+0.9353	9.9	83.5	0.295	2.459	$2.5^{+2.9}_{-0.8}$	$16.4^{+4.6}_{-3.2}$	42^{+25}_{-14}	$6.3^{+1.5}_{-1.3}$	<58	$0.93^{+0.46}_{-0.16}$	$13.4^{+3.9}_{-3.9}$	$25.4^{+8.0}_{-7.8}$	851
085119.9+022951	2101	132.8333	+2.4977	54.7	133.3	0.381	2.664	$2.25^{+0.54}_{-0.50}$	95^{+10}_{-10}	233^{+29}_{-27}	$22.7^{+3.2}_{-2.9}$	51^{+14}_{-12}	$2.58^{+0.95}_{-0.64}$	$70.9^{+11.2}_{-11.2}$	184^{+37}_{-28}	853
085121.2+012856	11156	132.8384	+1.4825	10.2	25.2	0.327	2.217	$14.2^{+10.9}_{-9.9}$	$13.7^{+4.2}_{-3.5}$	78^{+50}_{-34}	$6.2^{+1.6}_{-1.8}$	<260	$9.3^{+14.5}_{-5.8}$	$10.9^{+4.0}_{-4.2}$	51^{+41}_{-23}	860
085128.4+011501	7355	132.8685	+1.2505	6.9	48.0	0.197	2.817	$9.6^{+5.1}_{-4.0}$	<3.0	<17	<2.9	<37	$7.0^{+11.9}_{-4.0}$	<2.3	<11	861
085130.0-004609	18314	132.8750	-0.7693	12.3	23.7	0.484	1.950	$1.78^{+0.72}_{-0.41}$	$35.6^{+8.7}_{-8.5}$	84^{+20}_{-20}	$11.3^{+2.3}_{-2.2}$	$20.3^{+9.0}_{-6.1}$	$2.05^{+1.55}_{-0.51}$	$29.8^{+7.7}_{-7.9}$	75^{+21}_{-21}	1010
085131.0+045239	863	132.8795	+4.8778	28.0	117.4	0.395	2.566	$2.63^{+1.50}_{-0.60}$	117^{+15}_{-16}	311^{+66}_{-48}	$22.4^{+3.4}_{-4.8}$	58^{+34}_{-19}	$2.53^{+1.99}_{-0.57}$	74^{+13}_{-13}	199^{+53}_{-50}	827
085138.2-003537	4508	132.9096	-0.5938	6.6	40.1	0.458	1.862	$16.2^{+6.1}_{-6.4}$	$17.3^{+6.7}_{-6.4}$	110^{+66}_{-50}	$7.5^{+2.4}_{-2.5}$	<310	$12.0^{+12.9}_{-5.5}$	$15.7^{+6.4}_{-5.5}$	87^{+60}_{-38}	1007
085141.9+021438	7280	132.9248	+2.2440	9.1	39.3	0.107	3.689	$1.01^{+0.16}_{-0.13}$	<1.3	<2.6	<0.98	<1.0	$0.115^{+0.975}_{-0.083}$	<1.5	<1200000	859
085204.5+012132	6636	133.0188	+1.3590	27.9	54.1	0.401	2.530	$12.7^{+12.0}_{-7.4}$	$43.2^{+7.6}_{-7.6}$	238^{+129}_{-87}	$16.0^{+3.1}_{-2.4}$	<630	$12.3^{+10.4}_{-7.8}$	$33.7^{+7.4}_{-7.1}$	182^{+98}_{-71}	867
085217.0-010131	339	133.0709	-1.0254	209.0	405.9	0.460	3.097	$9.7^{+7.4}_{-3.9}$	232^{+20}_{-20}	1120^{+370}_{-250}	$53.6^{+5.1}_{-4.8}$	520^{+370}_{-210}	$12.8^{+9.9}_{-6.2}$	163^{+16}_{-16}	910^{+380}_{-270}	1133
085230.6+002457	2524	133.1275	+0.4159	64.5	140.4	0.270	3.364	$2.39^{+1.06}_{-0.44}$	$37.1^{+3.3}_{-3.3}$	$94.1^{+12.9}_{-9.6}$	$14.8^{+1.9}_{-1.7}$	$35.8^{+16.0}_{-16.0}$	$2.57^{+1.11}_{-0.58}$	$29.4^{+3.1}_{-3.1}$	77^{+12}_{-10}	967
085231.1-011230	4810	133.1296	-1.2084	25.9	69.7	0.546	1.949	$3.3^{+4.3}_{-1.5}$	$50.8^{+9.5}_{-9.3}$	150^{+48}_{-28}	$14.2^{+2.2}_{-2.2}$	48^{+53}_{-21}	$12.8^{+12.4}_{-8.9}$	$36.4^{+6.8}_{-6.8}$	198^{+113}_{-79}	1172
085239.6+003240	5477	133.1652	+0.5446	11.6	40.7	0.452	1.921	$4.0^{+6.7}_{-2.0}$	$31.9^{+7.6}_{-6.9}$	99^{+59}_{-28}	$8.9^{+1.9}_{-3.9}$	30^{+61}_{-15}	$3.3^{+5.7}_{-1.4}$	$22.4^{+7.5}_{-10.4}$	67^{+37}_{-30}	968
085245.7-020519	5790	133.1905	-2.0888	8.2	44.6	0.761	1.497	$2.40^{+3.27}_{-0.61}$	64^{+22}_{-20}	175^{+65}_{-54}	<18	<74	$3.4^{+3.0}_{-1.3}$	<78	<240	1059
085255.1-013737	1376	133.2297	-1.6271	7.4	14.9	0.343	0.586	$4.9^{+9.4}_{-2.9}$	$5.3^{+1.7}_{-1.1}$	$18.7^{+13.8}_{-6.2}$	$0.51^{+0.23}_{-0.10}$	<14	$3.7^{+6.8}_{-1.3}$	$5.0^{+1.5}_{-1.0}$	$15.5^{+10.6}_{-4.5}$	1668
085256.8+052741	6642	133.2370	+5.4615	8.2	29.0	0.273	2.401	$10.8^{+14.0}_{-9.6}$	$8.4^{+2.9}_{-2.0}$	41^{+34}_{-18}	$1.43^{+0.83}_{-0.58}$	<65	$7.1^{+13.2}_{-5.6}$	<7.2	<39	545
085325.6+030834	9042	133.3570	+3.1430	7.1	29.7	0.335	2.074	$6.3^{+4.3}_{-1.8}$	$7.5^{+1.8}_{-1.8}$	28^{+10}_{-8}	$1.83^{+0.88}_{-0.86}$	<57	$8.7^{+15.6}_{-3.7}$	<7.0	<52	862
085327.2-002117	6003	133.3634	-0.3549	17.5	52.7	0.193	2.894	$6.8^{+17.3}_{-3.5}$	$7.5^{+1.8}_{-1.5}$	$29.1^{+17.3}_{-8.7}$	$3.61^{+0.86}_{-0.70}$	90	$6.8^{+11.4}_{-3.7}$	$6.1^{+1.4}_{-1.7}$	$23.8^{+18.9}_{-8.5}$	1171

continued.

Cluster (eFEDS J+)	ID_SRC	RA (deg)	Dec (deg)	$\mathcal{L}_{ext}$	$\mathcal{L}_{det}$	z	R_{500} (arcmin)	T (keV)	L_X (10^{42} erg s^{-1})	L_{bol} (10^{42} erg s^{-1})	M_{gas} (10^{12} M$_\odot$)	Y_X (10^{12} M$_\odot$ keV)	T_{cex} (keV)	$L_{X,cex}$ (10^{42} erg s^{-1})	$L_{bol,cex}$ (10^{42} erg s^{-1})	t_{exp} (s)
085335.2+032214	8596	133.3967	+3.3708	12.0	33.7	0.295	2.421	$12.6^{+12.1}_{-7.5}$	$10.6^{+2.7}_{-2.9}$	57^{+35}_{-23}	$4.8^{+1.5}_{-1.8}$	<190	$12.7^{+10.9}_{-7.8}$	$7.4^{+2.8}_{-3.2}$	38^{+28}_{-19}	854
085340.5+022411	9213	133.4191	+2.4032	31.2	48.5	0.196	3.367	$1.73^{+0.91}_{-...}$	$7.8^{+1.1}_{-1.1}$	$18.1^{+3.6}_{-3.6}$	$3.93^{+0.85}_{-0.77}$	$6.9^{+4.0}_{-2.1}$	$1.55^{+0.64}_{-0.28}$	$5.8^{+1.2}_{-1.2}$	$12.9^{+3.4}_{-2.8}$	883
085412.8-022123	1458	133.5536	-2.3566	12.7	61.0	0.377	3.233	$8.1^{+11.2}_{-4.8}$	118^{+16}_{-16}	510^{+330}_{-160}	$31.7^{+4.4}_{-4.1}$	<1000	$6.5^{+13.1}_{-3.3}$	76^{+16}_{-16}	303^{+251}_{-88}	312
085419.5-000925	1294	133.5814	-0.1572	56.0	110.0	0.282	3.324	$1.83^{+0.43}_{-0.33}$	$47.1^{+3.5}_{-...}$	$110.0^{+10.0}_{-8.0}$	$16.8^{+2.2}_{-1.9}$	$31.4^{+8.2}_{-5.7}$	$1.89^{+0.42}_{-0.35}$	$35.0^{+3.4}_{-2.7}$	$82.9^{+8.7}_{-7.6}$	1196
085433.0+004009	3675	133.6376	+0.6693	10.3	46.5	0.109	3.878	$2.79^{+0.33}_{-...}$	$0.63^{+0.25}_{-0.25}$	$1.68^{+0.66}_{-...}$	<0.33	<0.87	$2.60^{+0.35}_{-0.35}$	<0.20	<0.51	1166
085434.5-014038	8094	133.6438	-1.6774	13.6	38.7	0.595	1.698	$1.81^{+0.40}_{-...}$	47^{+11}_{-11}	112^{+26}_{-26}	$11.9^{+2.2}_{-2.0}$	$21.9^{+11.2}_{-7.0}$	$2.02^{+0.35}_{-0.35}$	38^{+12}_{-12}	93^{+31}_{-27}	1554
085436.6+003835	328	133.6526	+0.6431	242.8	688.6	0.106	6.414	$2.68^{+0.46}_{-0.37}$	$19.30^{+1.30}_{-1.00}$	$50.4^{+4.1}_{-3.8}$	$8.13^{+0.97}_{-0.88}$	$21.9^{+4.8}_{-3.9}$	$2.45^{+0.44}_{-0.31}$	$12.50^{+1.20}_{-0.80}$	$32.2^{+3.2}_{-2.7}$	1175
085438.5+001211	5390	133.6608	+0.2032	6.2	21.4	0.178	3.375	$3.8^{+7.8}_{-...}$	$2.1^{+1.0}_{-1.0}$	<19	<4.1	<29	$5.5^{+12.5}_{-...}$	<3.9	<19	1199
085440.4-020931	7700	133.6686	-2.1588	7.0	32.4	0.472	1.787	$5.8^{+18.6}_{-3.5}$	$13.0^{+4.4}_{-4.1}$	50^{+53}_{-20}	$3.1^{+1.7}_{-1.5}$	<140	$5.0^{+17.3}_{-3.0}$	<14	<72	967
085447.0-012132	2079	133.6962	-1.3591	81.5	153.9	0.353	3.015	$1.99^{+0.50}_{-0.36}$	$57.5^{+5.0}_{-5.2}$	137^{+15}_{-13}	$19.5^{+2.3}_{-2.1}$	$39.0^{+11.4}_{-8.1}$	$2.05^{+0.95}_{-0.45}$	$43.8^{+4.6}_{-5.1}$	107^{+15}_{-13}	1204
085508.9-003445	2810	133.7874	-0.5793	9.2	103.6	0.174	2.974	$1.29^{+0.40}_{-...}$	$2.76^{+0.66}_{-0.54}$	$5.8^{+1.5}_{-1.3}$	<1.1	<1.5	$1.9^{+1.5}_{-1.3}$	<1.2	<3.0	1201
085517.2+013508	6746	133.8219	+1.5857	36.4	55.0	0.324	2.548	$2.40^{+0.59}_{-...}$	$36.5^{+4.2}_{-4.0}$	94^{+14}_{-12}	$12.8^{+1.9}_{-1.8}$	$30.9^{+13.3}_{-7.6}$	$2.62^{+1.38}_{-0.49}$	$32.2^{+3.9}_{-4.3}$	85^{+14}_{-12}	1148
085519.1-014315	5909	133.8296	-1.7211	12.9	42.5	0.365	2.029	$2.32^{+2.02}_{-...}$	<13	<37	<5.2	<18	$2.38^{+3.66}_{-...}$	<14	<39	1305
085524.3+015012	23313	133.8516	+1.8368	8.2	10.7	0.264	2.181	$9.7^{+13.5}_{-...}$	$8.2^{+2.7}_{-2.0}$	40^{+30}_{-16}	$3.83^{+1.02}_{-0.84}$	<150	$9.9^{+12.4}_{-7.3}$	$7.7^{+1.9}_{-1.9}$	35^{+27}_{-15}	1134
085530.1-010634	1797	133.8756	-1.1097	40.6	74.3	0.754	1.987	$8.0^{+13.1}_{-3.9}$	177^{+25}_{-22}	760^{+520}_{-180}	$32.6^{+42}_{-5.0}$	250^{+440}_{-120}	$12.4^{+9.8}_{-7.4}$	134^{+22}_{-22}	730^{+320}_{-250}	1201
085541.2+002740	5589	133.9219	+0.4611	6.9	47.0	0.170	2.662	$10.4^{+10.7}_{-...}$	<2.5	<15	<1.6	<28	$12.0^{+14.3}_{-...}$	<1.5	<9.6	1206
085542.6+032807	8925	133.9279	+3.4687	7.0	20.7	0.738	1.454	$2.04^{+4.37}_{-...}$	<58	<170	<13	<65	$1.68^{+1.44}_{-...}$	<54	<140	963
085547.0+025458	8799	133.9458	+2.9162	7.3	27.8	0.970	1.388	$8.3^{+13.3}_{-5.2}$	<150	<680	<17	<160	$11.0^{+11.1}_{-7.3}$	<64	<320	1054
085604.8+002520	8826	134.0202	+0.4223	25.8	43.6	0.168	3.549	$2.10^{+0.52}_{-0.31}$	$13.6^{+1.7}_{-1.2}$	$33.2^{+4.5}_{-3.5}$	$6.08^{+1.02}_{-0.87}$	$12.9^{+4.0}_{-2.7}$	$2.05^{+0.56}_{-0.39}$	$12.2^{+1.6}_{-1.2}$	$29.7^{+4.6}_{-3.3}$	1207
085616.1-013945	8922	134.0672	-1.6626	10.6	22.5	0.514	2.046	$1.17^{+4.83}_{-...}$	<4.4	<12	<3.3	<5.0	$0.78^{+1.19}_{-...}$	<2.3	<5.6	1308
085620.7+014649	569	134.0865	+1.7805	51.7	309.1	0.724	2.027	$5.8^{+1.9}_{-1.6}$	269^{+37}_{-32}	1000^{+320}_{-170}	$37.7^{+5.8}_{-4.7}$	$219^{+174}_{-...}$	$7.0^{+0.8}_{-0.8}$	174^{+33}_{-32}	700^{+260}_{-170}	1199
085623.6-013612	16370	134.0984	-1.6036	11.9	17.7	0.425	2.104	$2.06^{+2.14}_{-...}$	$18.6^{+26.8}_{-...}$	$49^{+64}_{-...}$	$8.3^{+4.9}_{-...}$	$19.1^{+76.9}_{-8.6}$	$2.42^{+2.31}_{-...}$	$15.0^{+23.7}_{-...}$	45^{+61}_{-28}	1220
085624.3+004632	32576	134.1016	+0.7757	8.5	11.9	0.319	2.498	$4.6^{+2.4}_{-...}$	$9.8^{+3.2}_{-...}$	$32.8^{+9.0}_{-...}$	$5.31^{+1.12}_{-0.99}$	<150	$6.2^{+16.7}_{-3.8}$	$7.3^{+1.9}_{-...}$	29^{+28}_{-10}	1204
085626.2+021348	5697	134.1094	+2.2302	21.5	51.9	0.125	3.589	$1.33^{+0.18}_{-0.12}$	$4.09^{+0.39}_{-...}$	$8.8^{+1.4}_{-...}$	$2.09^{+0.37}_{-0.34}$	$2.79^{+0.81}_{-0.56}$	$1.31^{+0.21}_{-0.14}$	$3.37^{+0.52}_{-0.54}$	$7.1^{+1.2}_{-...}$	1181
085627.2+014217	1385	134.1134	+1.7050	26.8	92.8	0.732	2.311	$8.9^{+8.6}_{-...}$	173^{+29}_{-24}	800^{+390}_{-200}	$38.4^{+6.0}_{-6.1}$	330^{+370}_{-150}	$9.8^{+10.2}_{-4.2}$	128^{+24}_{-22}	630^{+320}_{-170}	1192
085635.0+031342	24300	134.1459	+3.2284	8.1	10.5	0.390	2.203	$9.0^{+11.5}_{-5.6}$	<9.7	<47	<7.6	<97	$15.2^{+12.2}_{-9.8}$	<8.0	<49	1108
085650.4-022200	5261	134.2101	-2.3669	36.2	70.2	0.318	2.723	$1.18^{+0.12}_{-...}$	$15.6^{+2.9}_{-2.3}$	$32.5^{+7.6}_{-5.2}$	$7.0^{+1.2}_{-1.1}$	$8.4^{+4.9}_{-...}$	$1.010^{+0.130}_{-0.079}$	$12.0^{+2.5}_{-2.5}$	$23.1^{+4.9}_{-4.6}$	1490
085705.9+011453	3128	134.2749	+1.2482	53.7	119.3	0.106	5.101	$1.40^{+0.60}_{-...}$	$4.76^{+0.32}_{-0.32}$	$10.3^{+1.4}_{-...}$	$2.35^{+0.53}_{-0.55}$	$3.34^{+1.68}_{-0.93}$	$1.38^{+0.34}_{-0.22}$	$3.35^{+0.43}_{-0.64}$	$7.2^{+1.2}_{-1.4}$	1201
085728.3+032354	6278	134.3680	+3.3984	23.2	41.0	0.200	2.951	$2.94^{+2.54}_{-...}$	$8.4^{+1.7}_{-...}$	$23.6^{+7.7}_{-5.1}$	$4.18^{+0.72}_{-...}$	$12.4^{+11.4}_{-3.7}$	$2.80^{+2.56}_{-0.70}$	$6.8^{+1.4}_{-1.5}$	$18.9^{+5.4}_{-4.6}$	1165
085740.1-020037	7884	134.4172	-2.0103	19.8	34.0	0.717	1.587	$18.3^{+9.0}_{-...}$	$40.3^{+9.7}_{-...}$	$280^{+110}_{-...}$	$12.9^{+2.4}_{-2.1}$	<510	$15.5^{+8.6}_{-10.0}$	$34.8^{+9.9}_{-...}$	213^{+101}_{-82}	2272
085744.0-022448	12696	134.4337	-2.4134	9.3	20.1	0.162	2.803	$1.27^{+0.53}_{-...}$	$1.98^{+0.61}_{-...}$	$4.2^{+1.4}_{-...}$	$1.36^{+0.37}_{-0.36}$	$1.71^{+1.07}_{-0.57}$	$1.30^{+0.47}_{-...}$	$1.72^{+0.50}_{-0.56}$	$3.6^{+1.2}_{-...}$	1859
085751.6+031039	108	134.4653	+3.1775	742.2	2053.9	0.201	6.278	$5.68^{+0.37}_{-...}$	$163.0^{+6.0}_{-...}$	590^{+70}_{-45}	$49.3^{+4.7}_{-4.0}$	285^{+72}_{-47}	$5.13^{+1.63}_{-0.96}$	$106.0^{+5.0}_{-6.0}$	367^{+55}_{-38}	1204
085801.1-004103	11717	134.5048	-0.6842	12.4	21.5	0.245	2.479	$1.02^{+0.60}_{-...}$	$5.8^{+1.1}_{-...}$	$11.6^{+2.8}_{-...}$	$2.85^{+0.60}_{-0.50}$	$2.89^{+2.22}_{-0.95}$	$1.10^{+0.95}_{-0.51}$	$4.45^{+1.16}_{-...}$	$9.2^{+3.3}_{-...}$	1203
085805.0+010906	4070	134.5209	+1.1517	39.7	90.8	0.071	5.196	$2.59^{+1.22}_{-0.74}$	$2.74^{+0.30}_{-...}$	$6.9^{+2.1}_{-...}$	$1.31^{+0.28}_{-0.28}$	$3.4^{+1.8}_{-...}$	$1.79^{+0.38}_{-...}$	$2.13^{+0.30}_{-0.94}$	$4.83^{+0.83}_{-2.10}$	1206
085830.0-010656	4297	134.6251	-1.1157	19.5	70.5	0.224	2.902	$5.1^{+12.2}_{-2.5}$	$9.1^{+1.1}_{-...}$	$31.2^{+28.4}_{-8.1}$	$4.97^{+0.89}_{-0.73}$	24^{+63}_{-12}	$7.5^{+10.6}_{-4.0}$	$7.3^{+1.3}_{-1.3}$	31^{+26}_{-10}	1912
085837.9+012657	8857	134.6581	+1.4494	7.8	18.9	0.750	1.403	$2.8^{+4.2}_{-...}$	<47	<140	<9.2	<39	$2.00^{+3.13}_{-...}$	<26	<66	1198
085841.8-020541	2367	134.6744	-2.0948	15.5	42.0	0.575	1.555	$1.47^{+0.67}_{-...}$	$32.5^{+7.1}_{-...}$	73^{+16}_{-14}	$7.4^{+1.6}_{-1.4}$	$11.0^{+5.6}_{-3.0}$	$1.65^{+0.90}_{-0.39}$	$22.9^{+6.7}_{-...}$	53^{+16}_{-15}	2301
085849.8+022800	715	134.7076	+2.4668	92.3	304.5	0.215	3.648	$1.76^{+0.16}_{-0.17}$	$29.3^{+3.1}_{-...}$	$67.5^{+9.2}_{-7.2}$	$9.8^{+1.3}_{-...}$	$17.2^{+3.4}_{-2.9}$	$1.65^{+0.19}_{-0.18}$	$16.9^{+5.9}_{-2.2}$	$38.4^{+5.9}_{-5.3}$	1207
085901.1-012025	3527	134.7547	-1.3406	8.7	30.1	1.301	1.239	$10.9^{+7.4}_{-6.4}$	147^{+30}_{-31}	720^{+300}_{-200}	$19.3^{+3.3}_{-3.1}$	<540	$17.3^{+10.1}_{-7.7}$	111^{+29}_{-26}	760^{+290}_{-250}	2203

continued.

Cluster (eFEDS J+)	ID_SRC	RA (deg)	Dec (deg)	$\mathcal{L}_{ext}$	$\mathcal{L}_{det}$	z	R_{500} (arcmin)	T (keV)	L_X (10^{42} erg s^{-1})	L_{bol} (10^{42} erg s^{-1})	M_{gas} (10^{12} M$_\odot$)	Y_X (10^{12} M$_\odot$ keV)	T_{cex} (keV)	$L_{X,cex}$ (10^{42} erg s^{-1})	$L_{bol,cex}$ (10^{42} erg s^{-1})	t_{exp} (s)
085901.5+010649	2757	134.7564	+1.1137	33.6	97.4	0.162	3.365	$2.79^{+2.53}_{-0.70}$	$5.55^{+0.92}_{-0.74}$	$15.4^{+5.2}_{-2.9}$	$2.36^{+0.71}_{-0.40}$	$7.0^{+7.0}_{-2.4}$	$3.9^{+9.4}_{-1.7}$	$3.43^{+0.92}_{-0.63}$	$11.2^{+9.6}_{-3.2}$	1208
085907.3-005056	16320	134.7808	-0.8489	7.3	11.6	0.623	1.689	$11.5^{+11.6}$	$26.3^{+8.9}$	144^{+85}	$9.0^{+2.7}$	<340	$10.2^{+15.7}$	$25.5^{+8.6}_{-0.63}$	130^{+94}	1989
085913.1+031334	485	134.8048	+3.2263	15.9	16.8	0.189	2.980	$2.34^{+3.25}$	$13.1^{+2.1}$	$34.1^{+13.1}$	$3.79^{+0.74}_{-0.66}$	$9.2^{+12.1}$	$1.78^{+0.84}$	$6.7^{+1.3}$	$15.6^{+4.1}$	1210
085931.9+030839	360	134.8830	+3.1443	175.1	617.4	0.196	4.648	$2.50^{+0.31}$	$41.3^{+2.3}$	$106.0^{+8.0}$	$14.4^{+1.1}$	$36.0^{+9.0}$	$2.69^{+0.90}_{-0.30}$	$24.8^{+2.0}$	$65.1^{+9.2}$	1211
085939.1-004932	6894	134.9133	-0.8258	10.9	8.2	0.812	1.369	$1.24^{+0.76}$	63^{+38}	138^{+66}	$11.8^{+3.1}$	$14.3^{+10.6}$	$1.22^{+0.91}$	57^{+31}	124^{+44}	2238
085948.9+041120	1350	134.9539	+4.1889	22.6	43.0	0.208	3.177	$1.69^{+0.22}$	$13.7^{+1.5}$	$31.6^{+2.0}$	$4.84^{+0.81}$	$8.4^{+2.9}_{-1.7}$	$1.58^{+0.42}_{-0.32}$	$7.8^{+1.3}$	$17.8^{+3.2}$	1212
085950.1-001221	4539	134.9589	-0.2058	16.9	35.1	0.427	0.494	$5.1^{+2.6}$	$11.8^{+2.0}$	41^{+22}	$0.73^{+0.33}_{-0.13}$	<15	$13.7^{+12.2}$	$10.3^{+2.6}_{-1.7}$	61^{+33}_{-26}	1306
085954.2-013308	13823	134.9758	-1.5524	6.5	16.4	0.577	1.464	$10.2^{+11.1}$	$15.6^{+5.6}$	76^{+59}_{-33}	<5.4	<64	$8.8^{+13.4}_{-3.9}$	<12	<60	2033
090004.3+033324	7945	135.0183	+3.5568	11.8	30.8	0.698	1.570	$4.5^{+6.3}$	$47.9^{+12.2}$	164^{+95}_{-40}	$12.3^{+2.1}$	55^{+86}_{-24}	$6.8^{+13.9}$	$37.9^{+11.5}$	151^{+114}_{-49}	1203
090010.4+023631	10878	135.0435	+2.6086	12.9	23.6	0.200	2.781	$2.29^{+0.56}$	$4.59^{+0.98}$	$11.7^{+3.9}_{-2.7}$	$2.69^{+0.72}$	$6.4^{+3.6}_{-2.1}$	$3.1^{+4.2}_{-1.2}$	$3.61^{+1.22}_{-0.95}$	$10.5^{+5.7}_{-3.3}$	1211
090020.8-002602	1315	135.0867	-0.4340	17.9	184.8	0.490	2.091	$2.96^{+2.74}$	<41	<120	<12	<50	$3.6^{+5.5}_{-1.4}$	<25	<89	1476
090033.7+033932	2407	135.1408	+3.6591	25.2	119.6	0.809	1.690	$3.5^{+2.9}_{-1.0}$	73^{+29}_{-28}	225^{+99}_{-87}	$17.3^{+4.9}_{-5.2}$	59^{+43}_{-21}	$3.09^{+1.85}_{-0.82}$	68^{+27}_{-25}	198^{+78}_{-71}	1207
090034.1-010649	1652	135.1422	-1.1137	15.4	29.8	0.273	2.651	$2.94^{+1.99}_{-0.88}$	$11.1^{+1.3}$	$30.2^{+7.6}$	$5.94^{+0.85}_{-0.75}$	$17.4^{+12.2}_{-5.4}$	$3.2^{+3.4}_{-1.9}$	$9.1^{+1.2}$	$26.0^{+9.9}_{-4.5}$	3253
090044.6-011104	8508	135.1862	-1.1845	8.1	6.3	0.430	1.825	$16.5^{+6.1}$	$3.0^{+1.3}$	$19.4^{+12.7}$	<3.1	<55	$21.7^{+6.7}_{-10.1}$	<2.6	<19	3240
090051.6-003457	9834	135.2152	-0.5826	6.0	13.7	0.350	1.787	$3.2^{+4.0}$	$7.5^{+2.7}$	$22.3^{+13.5}_{-8.6}$	$3.53^{+0.89}$	$11.4^{+15.5}_{-4.9}$	$4.2^{+5.8}_{-2.0}$	$6.1^{+2.6}_{-1.5}$	$20.5^{+13.9}_{-6.8}$	1585
090053.0-002837	9310	135.2212	-0.4772	15.8	27.0	0.295	2.190	$1.21^{+0.19}_{-0.12}$	$7.2^{+1.9}$	$15.0^{+4.1}$	$2.97^{+0.74}$	$3.63^{+1.36}_{-0.94}$	$1.29^{+0.38}_{-0.22}$	$5.2^{+1.5}$	$11.0^{+3.7}$	1571
090059.3+035925	983	135.2471	+3.9905	43.2	230.7	0.412	2.490	$11.0^{+?}_{-4.9}$	$49.8^{+5.8}$	257^{+110}_{-67}	$11.9^{+2.8}$	126^{+114}_{-58}	$10.5^{+13.4}_{-6.0}$	$26.7^{+5.3}$	130^{+85}_{-44}	1202
090104.4+011643	3171	135.2686	+1.2788	38.0	62.8	0.251	3.247	$2.75^{+?}_{-0.69}$	$19.2^{+2.1}$	$51.1^{+11.2}_{-7.0}$	$8.2^{+1.2}$	$22.7^{+15.8}$	$2.27^{+1.59}_{-0.50}$	$14.3^{+1.8}$	$36.5^{+8.2}_{-5.5}$	1230
090105.2-012525	11836	135.2718	-1.4237	17.8	29.4	0.405	2.178	$8.2^{+?}$	$18.0^{+2.3}$	79^{+51}_{-24}	$9.0^{+1.5}$	<300	$7.6^{+11.5}_{-3.4}$	$15.9^{+2.1}$	68^{+43}_{-19}	2274
090115.3+005040	8881	135.3140	+0.8445	10.1	28.9	0.312	2.077	$2.39^{+1.02}_{-0.52}$	$15.3^{+2.1}$	$39.4^{+7.5}_{-6.1}$	$5.68^{+0.36}_{-0.86}$	$13.8^{+6.5}_{-3.7}$	$3.2^{+2.7}_{-1.0}$	$13.1^{+2.3}_{-2.1}$	$37.3^{+11.6}_{-6.9}$	1371
090119.0+030204	7017	135.3294	+3.0345	24.7	22.7	0.193	2.660	$4.3^{+?}$	<9.4	<33	<4.7	<23	$4.1^{+5.3}$	<8.0	<30	1203
090121.9-003709	1600	135.3414	-0.6194	9.8	24.8	0.555	1.778	$15.5^{+12.6}$	$36.8^{+18.3}$	237^{+154}	$9.7^{+2.8}$	<420	$14.5^{+?}$	<54	<350	1611
090129.1-013853	1104	135.3715	-1.6483	86.6	274.4	0.311	3.794	$6.1^{+2.8}$	167^{+14}	630^{+290}_{-120}	$44.9^{+5.2}$	271^{+295}	$8.3^{+?}_{-2.1}$	$135.0^{+8.0}$	590^{+250}_{-130}	967
090131.1+030056	152	135.3800	+3.0157	373.9	1266.7	0.193	5.184	$4.12^{+2.65}$	$71.3^{+5.3}$	219^{+28}	$23.1^{+1.8}$	95^{+27}	$4.20^{+3.38}_{-0.73}$	$45.8^{+5.0}$	145^{+36}_{-26}	1210
090133.2+021651	4181	135.3886	+2.2809	28.2	31.2	0.354	2.168	$3.1^{+?}$	$19.4^{+3.3}$	56^{+18}_{-11}	$7.8^{+1.4}$	$24.6^{+23.0}$	$4.2^{+?}_{-1.7}$	$16.3^{+3.1}$	53^{+13}	1210
090133.5-010540	10870	135.3898	-1.0946	11.8	28.3	0.270	2.016	$2.42^{+4.02}$	$3.80^{+1.24}_{-0.93}$	$10.2^{+4.9}_{-2.9}$	$1.92^{+0.59}_{-0.61}$	$4.7^{+7.5}_{-2.0}$	$2.39^{+2.56}_{-1.94}$	$2.52^{+1.33}_{-0.93}$	$6.8^{+4.1}_{-2.7}$	2655
090137.7+030253	15914	135.4072	+3.0483	6.4	11.0	0.188	2.730	$5.0^{+1.3}$	<3.7	<13	<2.8	<15	$4.52^{+1.94}$	<3.2	<10	1204
090140.9-012132	2412	135.4207	-1.3591	20.4	43.8	0.295	2.511	$2.20^{+0.63}_{-0.40}$	$17.6^{+2.0}$	$43.4^{+5.7}_{-5.8}$	$7.9^{+1.2}_{-1.1}$	$17.6^{+5.6}_{-4.0}$	$2.08^{+0.90}_{-0.34}$	$15.7^{+1.8}_{-2.4}$	$38.4^{+5.7}$	2149
090144.7+040827	3199	135.4366	+4.1408	22.8	92.6	0.844	1.606	$3.1^{+1.8}$	138^{+25}	389^{+84}	$21.3^{+3.8}_{-3.3}$	65^{+42}_{-22}	$2.21^{+1.04}_{-0.41}$	106^{+26}	266^{+66}_{-67}	1211
090146.2-013756	4232	135.4427	-1.6322	22.3	63.0	0.295	2.983	$1.82^{+0.51}$	$18.7^{+3.3}$	$43.4^{+8.6}$	$4.7^{+1.5}$	$8.2^{+4.9}$	$1.73^{+1.33}_{-0.37}$	<14	<35	605
090153.9-012209	2048	135.4748	-1.3694	87.9	163.9	0.295	2.858	$2.17^{+0.58}_{-0.37}$	$19.8^{+2.5}$	$48.9^{+6.8}$	$7.67^{+0.85}_{-0.78}$	$16.9^{+4.8}_{-3.1}$	$2.14^{+0.58}_{-0.33}$	$13.6^{+2.9}_{-2.5}$	$33.7^{+6.9}$	2016
090200.5+022339	3800	135.5024	+2.3943	36.2	95.4	0.202	3.222	$2.62^{+3.04}$	$14.3^{+1.1}$	$37.2^{+4.1}$	$5.99^{+0.75}_{-0.69}$	$15.8^{+6.6}_{-3.8}$	$2.51^{+1.18}_{-0.54}$	$10.6^{+1.0}_{-1.2}$	$27.5^{+4.9}_{-3.7}$	1211
090210.6+032513	431	135.5445	+3.4204	10.0	14.8	0.535	1.600	$13.6^{+1.3}$	<64	<470	<3.5	<45	$11.0^{+11.7}$	<4.8	<23	1205
090223.3+015205	6840	135.5974	+1.8682	6.7	43.2	0.561	1.657	$4.8^{+14.6}_{-2.6}$	$16.2^{+6.2}$	58^{+50}_{-20}	<4.3	<60	$1.75^{+9.05}_{-0.84}$	<11	33^{+27}_{-15}	1376
090224.4-005150	9893	135.6020	-0.8641	11.4	24.0	0.409	1.979	$16.1^{+9.5}$	$11.3^{+3.9}$	69^{+40}_{-32}	$5.0^{+1.7}$	<210	$7.7^{+11.8}_{-4.8}$	$7.6^{+4.5}$	$8.1^{+5.8}_{-3.3}$	1560
090248.5+044005	4121	135.7022	+4.6681	52.1	83.7	0.226	3.405	$2.42^{+0.63}$	$6.5^{+2.1}_{-1.3}$	$16.7^{+5.3}$	$2.35^{+1.20}_{-0.84}$	$5.8^{+3.4}_{-2.8}$	$3.11^{+4.43}_{-0.74}$	$2.6^{+1.8}$	33^{+27}	1033
090255.2+030220	5489	135.7300	+3.0389	48.9	66.8	0.200	3.406	$1.74^{+0.46}$	$12.9^{+1.1}$	$29.8^{+3.3}$	$6.41^{+0.87}_{-0.69}$	$11.3^{+3.2}_{-0.74}$	$1.96^{+0.26}$	$10.40^{+1.40}_{-0.81}$	$25.1^{+3.7}$	1217
090255.5+044036	4348	135.7317	+4.6767	7.8	40.2	0.484	1.912	$4.1^{+4.2}$	56^{+10}	176^{+73}	$13.4^{+2.4}_{-1.8}$	54^{+60}_{-18}	$4.8^{+7.3}_{-2.6}$	$42.2^{+8.4}$	144^{+73}	1004
090256.2+014625	5655	135.7345	+1.7737	13.3	37.9	0.118	3.248	$2.16^{+0.24}_{-0.43}$	$1.94^{+0.24}_{-0.36}$	$4.76^{+0.80}_{-0.90}$	$1.02^{+0.24}_{-0.20}$	$2.24^{+0.94}_{-0.65}$	$2.22^{+1.89}_{-0.49}$	$1.39^{+0.27}_{-0.30}$	$3.49^{+0.78}_{-0.82}$	1497

continued.

Cluster (eFEDS J+)	ID_SRC	RA (deg)	Dec (deg)	$\mathcal{L}_{ext}$	$\mathcal{L}_{det}$	z	R_{500} (arcmin)	T (keV)	L_X (10^{42} erg s^{-1})	L_{bol} (10^{42} erg s^{-1})	M_{gas} (10^{12} M$_\odot$)	Y_X (10^{12} M$_\odot$ keV)	T_{cex} (keV)	$L_{X,cex}$ (10^{42} erg s^{-1})	$L_{bol,cex}$ (10^{42} erg s^{-1})	t_{exp} (s)
090257.4+004819	1712	135.7395	+0.8055	11.6	47.6	0.521	0.424	$2.16^{+4.94}$	$16.1^{+4.7}_{-3.4}$	42^{+19}	$0.80^{+0.26}_{-0.15}$	$1.81^{+3.89}$	$1.71^{+1.06}_{-0.42}$	$12.8^{+3.9}$	$30.2^{+9.5}_{-9.0}$	1598
090323.7+030738	2083	135.8489	+3.1273	44.7	118.6	0.407	2.490	$6.5^{+7.2}$	$60.3^{+6.6}$	234^{+118}	$18.4^{+2.2}$	118^{+144}	$4.4^{+5.7}$	$46.9^{+5.8}$	152^{+70}_{-30}	1279
090327.2+032545	4771	135.8634	+3.4294	14.6	47.9	0.364	2.238	$1.54^{+0.45}$	$19.9^{+2.9}$	$44.3^{+7.1}$	$6.2^{+1.2}$	$9.6^{+3.7}$	$1.46^{+0.48}_{-0.26}$	$12.8^{+2.8}$	$28.0^{+7.0}_{-6.2}$	1242
090328.7-013622	4487	135.8697	-1.6062	70.8	99.5	0.443	2.781	$5.1^{+5.8}$	41^{+22}	148^{+103}	$17.9^{+6.5}$	<310	$4.3^{+4.0}$	<70	<280	923
090333.8+043950	9404	135.8909	+4.6640	24.2	24.6	0.222	2.840	$1.80^{+1.25}$	$7.44^{+0.91}$	$17.3^{+3.9}$	$3.30^{+0.70}_{-0.79}$	<16	$1.24^{+0.86}$	$5.6^{+1.1}_{-1.3}$	$11.8^{+3.1}_{-3.0}$	946
090335.0+022006	8941	135.8959	+2.3351	6.4	15.4	0.345	1.835	$7.5^{+12.7}$	$5.3^{+2.2}$	22^{+20}	<4.6	<82	$6.7^{+12.4}$	<8.2	<47	1502
090336.7-033124	12221	135.9033	+3.5235	13.1	26.1	0.617	1.769	$9.8^{+13.6}$	$38.5^{+9.3}$	181^{+120}	$12.7^{+2.6}$	<460	$10.2^{+9.1}$	$32.1^{+9.6}_{-8.8}$	151^{+90}_{-54}	1255
090408.6+012555	5774	136.0360	+1.4320	9.4	40.5	0.841	1.402	5.6^{+30}_{-30}	32^{+12}	130^{+85}	$8.9^{+3.0}$	<240	$9.8^{+12.8}_{-6.0}$	29^{+11}	141^{+102}_{-59}	1552
090409.7+003831	9877	136.0404	+0.6421	12.2	18.6	0.311	2.644	$2.79^{+0.87}$	$13.1^{+2.0}$	$35.5^{+6.7}$	$7.2^{+2.2}$	$20.5^{+14.6}_{-6.9}$	$2.2^{+2.6}_{-1.3}$	$10.7^{+1.8}$	$26.0^{+10.5}_{-5.9}$	1400
090417.0+040439	13330	136.0712	+4.0776	10.9	19.8	0.536	1.819	$12.7^{+11.1}$	$43.8^{+8.7}$	237^{+125}	$13.6^{+2.2}$	<510	$14.3^{+12.3}$	$38.9^{+6.2}_{-8.2}$	226^{+116}_{-78}	1341
090418.6-020642	3590	136.0778	+2.1117	32.9	78.5	0.808	1.611	$3.81^{+2.20}$	124^{+19}	375^{+71}	$20.0^{+3.6}$	77^{+38}_{-22}	$3.5^{+2.4}$	95^{+19}	278^{+81}_{-78}	1595
090419.1-010436	12660	136.0796	-1.0767	13.6	23.6	0.306	2.266	$2.2^{+4.7}$	$8.7^{+2.0}$	$22.2^{+6.1}$	$4.1^{+1.0}$	<47	$3.2^{+10.2}$	$6.6^{+2.0}_{-2.2}$	$19.8^{+18.0}_{-7.4}$	1537
090430.7-042648	1075	136.1282	+4.4468	37.7	209.8	0.457	2.308	$5.9^{+9.0}$	$59.0^{+5.7}$	217^{+61}	$11.7^{+2.3}$	66^{+112}_{-26}	$7.1^{+12.0}$	$23.6^{+5.4}_{-5.7}$	98^{+65}_{-30}	1192
090452.4-033326	2931	136.2187	+3.5574	18.8	66.3	0.808	1.677	$4.2^{+3.6}$	159^{+28}	522^{+155}	$26.0^{+3.1}$	111^{+91}_{-32}	$4.2^{+4.5}$	131^{+24}_{-21}	428^{+151}_{-71}	1490
090540.0-043440	354	136.4171	+4.5780	231.4	678.2	0.236	4.608	$3.73^{+0.79}$	$93.3^{+3.9}_{-3.1}$	274^{+24}	$25.9^{+2.4}$	95^{+25}_{-20}	$3.46^{+1.10}_{-0.69}$	$58.8^{+4.2}_{-3.8}$	171^{+23}_{-17}	1048
090540.7+013219	3585	136.4199	+1.5388	28.1	79.6	0.644	1.973	$6.2^{+6.9}$	96^{+17}_{-15}	366^{+178}	$22.9^{+3.7}$	139^{+172}_{-64}	$5.9^{+11.7}_{-2.8}$	76^{+16}	285^{+193}_{-74}	1273
090553.5-002244	5170	136.4732	+0.3791	10.8	69.4	0.367	2.168	$14.6^{+12.6}$	$15.1^{+2.9}$	92^{+46}	$5.7^{+1.0}$	<240	18^{+11}_{-10}	$8.9^{+2.6}_{-2.2}$	59^{+31}_{-24}	1205
090600.3-002521	9359	136.5016	-0.4226	18.7	41.7	0.299	2.507	$2.25^{+0.96}$	$11.9^{+2.5}$	$29.6^{+6.2}$	$4.4^{+1.4}$	$9.7^{+6.3}_{-3.6}$	$1.82^{+0.61}$	$8.0^{+2.2}_{-2.1}$	$18.1^{+5.4}_{-4.9}$	1212
090601.0+000055	3259	136.5043	+0.0154	18.6	92.2	0.200	2.876	$2.63^{+0.64}$	$12.5^{+1.6}$	$32.9^{+6.5}$	$4.83^{+0.82}$	$12.9^{+6.6}_{-3.2}$	$2.13^{+1.10}_{-0.45}$	$9.9^{+1.4}_{-1.3}$	$24.6^{+4.2}_{-3.7}$	1208
090609.4+042924	11420	136.5392	+4.4901	7.8	19.4	0.406	2.010	$4.9^{+6.8}$	$17.4^{+3.1}$	60^{+36}	$7.1^{+1.4}$	34^{+53}_{-15}	$3.8^{+3.9}_{-3.5}$	$14.3^{+3.5}_{-4.0}$	44^{+18}_{-13}	1286
090614.6-010819	5854	136.5612	-1.1389	16.9	15.5	0.894	1.602	$14.8^{+11.7}$	80^{+24}	490^{+250}	<27	<680	$8.5^{+15.7}_{-5.0}$	<110	<600	1521
090627.5-035846	10162	136.6148	+3.9795	7.4	24.6	0.463	2.032	$3.1^{+3.6}$	$19.7^{+7.4}$	58^{+28}	$7.6^{+2.2}$	$24.1^{+29.8}_{-9.7}$	$2.49^{+1.92}_{-0.88}$	$19.5^{+5.3}_{-4.7}$	52^{+17}_{-13}	1634
090628.9-012938	2424	136.6207	-1.4941	46.1	119.0	0.431	2.235	$3.10^{+2.40}$	$44.2^{+4.4}$	125^{+32}	$14.0^{+1.8}$	44^{+37}_{-13}	$3.14^{+0.93}_{-0.83}$	$34.5^{+4.4}_{-3.4}$	98^{+25}_{-13}	2120
090634.9-045033	8384	136.6454	+4.8427	10.6	42.7	0.884	1.605	$4.4^{+1.8}$	163^{+21}_{-10}	580^{+310}	$24.6^{+4.6}_{-3.6}$	108^{+120}_{-46}	$4.2^{+1.9}_{-0.9}$	123^{+48}	420^{+210}_{-110}	695
090636.9+010852	7086	136.6542	+1.1479	29.6	53.7	0.786	1.723	$7.1^{+12.0}_{-3.9}$	91^{+19}	370^{+240}	$20.9^{+9.6}_{-3.4}$	<660	$5.0^{+12.2}_{-2.3}$	74^{+22}_{-17}	271^{+189}_{-78}	1214
090644.8+011124	5858	136.6867	+1.1902	9.8	60.3	0.441	1.919	$4.6^{+4.4}$	$17.3^{+7.8}$	58^{+33}	<8.8	<66	$9.4^{+14.6}$	<24	<130	1209
090656.3+044717	12153	136.7347	+4.7882	29.0	32.2	0.120	4.349	$1.70^{+0.37}$	$8.16^{+0.95}$	$18.6^{+2.6}$	$4.23^{+0.75}_{-0.66}$	$7.2^{+2.4}_{-1.6}$	$1.64^{+0.47}_{-0.17}$	$7.38^{+0.81}_{-0.82}$	$16.8^{+2.4}_{-2.0}$	864
090700.7-011032	9463	136.7531	+1.1757	10.3	23.1	0.799	1.391	$4.6^{+15.9}$	35^{+15}	137^{+112}	<16	<180	$3.9^{+7.0}$	<78	<250	1216
090703.9-010756	13484	136.7663	+1.1323	7.9	12.6	0.307	2.121	$7.2^{+12.2}$	<4.4	<21	<1.7	<19	$10.9^{+10.9}$	<1.7	<9.1	1212
090718.6+035258	6439	136.8278	+3.8829	23.3	50.3	0.729	1.691	$13.0^{+12.5}$	71^{+14}	400^{+210}	$17.5^{+3.0}$	<700	$11.5^{+12.0}$	58^{+14}	300^{+170}_{-100}	1464
090723.8-011210	2680	136.8494	-1.2029	32.5	107.9	0.251	2.855	$2.31^{+0.94}$	$15.7^{+1.7}$	$39.1^{+6.1}$	$6.84^{+1.09}_{-0.99}$	$16.0^{+6.7}_{-3.8}$	$2.37^{+1.47}_{-0.49}$	$11.9^{+1.7}_{-2.6}$	$30.5^{+6.1}_{-7.0}$	1685
090734.3-012744	13028	136.8930	-1.4625	10.2	20.0	0.922	1.234	$2.15^{+4.88}$	<72	<200	<11	<45	$3.2^{+8.2}$	<47	<150	2000
090739.7-010633	10976	136.9157	-1.1094	6.5	29.7	0.218	2.482	$0.99^{+0.17}$	$4.46^{+1.00}_{-0.96}$	$8.6^{+2.0}$	$1.81^{+0.52}_{-0.44}$	$1.76^{+0.69}_{-0.53}$	$1.13^{+0.21}_{-0.18}$	$2.97^{+1.07}_{-0.79}$	$6.0^{+2.3}_{-1.7}$	1207
090750.1+025006	4691	136.9591	+2.8351	22.6	54.0	0.648	1.738	$6.6^{+10.2}$	70^{+12}	273^{+190}	$16.4^{+2.7}$	<480	$8.7^{+12.3}$	$55.6^{+9.9}_{-9.9}$	244^{+167}_{-77}	1205
090751.9+024647	13368	136.9666	+2.7797	7.5	21.1	0.618	1.507	$3.1^{+7.0}$	$25.9^{+24.0}_{-9.3}$	89^{+61}	$8.8^{+3.5}$	29^{+56}_{-13}	$2.00^{+2.32}_{-0.51}$	$25.2^{+23.8}_{-12.3}$	66^{+58}_{-24}	1212
090752.9+013407	2074	136.9705	+1.5687	9.4	17.9	0.163	3.444	$2.38^{+1.75}$	$6.4^{+1.2}$	$16.2^{+4.4}$	$3.46^{+0.89}_{-1.05}$	$8.4^{+5.8}_{-3.3}$	$3.0^{+5.5}$	$5.0^{+1.6}_{-2.5}$	$14.1^{+8.0}_{-7.0}$	1215
090754.5-005738	5219	136.9772	+0.9607	16.6	58.4	0.738	1.650	$10.4^{+7.9}$	91^{+16}	460^{+190}	$19.3^{+3.0}$	198^{+173}_{-94}	$7.4^{+13.3}$	76^{+15}_{-25}	325^{+217}_{-89}	1210
090757.5-025427	9569	136.9900	+2.9077	9.2	32.3	0.798	1.436	$7.0^{+8.0}$	79^{+16}	319^{+166}	$14.7^{+2.3}$	<360	$4.2^{+6.1}$	66^{+11}_{-15}	213^{+96}_{-38}	1208
090803.8+020045	2234	137.0162	+2.0127	15.4	117.4	0.468	2.118	$7.1^{+3.5}$	$47.9^{+4.6}_{-6.1}$	198^{+131}_{-54}	$11.9^{+2.9}$	<360	$6.7^{+2.8}_{-3.6}$	$28.6^{+6.8}_{-7.2}$	112^{+38}_{-37}	1209

continued.

Cluster (eFEDS J+)	ID_SRC	RA (deg)	Dec (deg)	$\mathcal{L}_{ext}$	$\mathcal{L}_{det}$	z	R_{500} (arcmin)	T (keV)	L_X (10^{42} erg s^{-1})	L_{bol} (10^{42} erg s^{-1})	M_{gas} (10^{12} M$_\odot$)	Y_X (10^{12} M$_\odot$ keV)	T_{cex} (keV)	$L_{X,cex}$ (10^{42} erg s^{-1})	$L_{bol,cex}$ (10^{42} erg s^{-1})	t_{exp} (s)
090805.9+011952	7084	137.0250	+1.3314	10.6	34.9	0.659	1.593	$8.9^{+10.4}_{-5.2}$	$44.1^{+10.3}_{-8.5}$	200^{+109}_{-64}	$10.1^{+2.3}_{-2.4}$	<300	$6.0^{+8.7}_{-2.8}$	$32.4^{+11.3}_{-8.7}$	124^{+73}_{-42}	1214
090806.4+032613	12592	137.0270	+3.4370	7.1	18.6	0.740	1.468	$3.0^{+8.6}_{-1.3}$	37^{+14}_{-13}	116^{+59}_{-42}	$10.1^{+2.5}_{-2.3}$	30^{+79}	$1.94^{+1.89}_{-0.72}$	35^{+17}_{-13}	89^{+42}_{-32}	1214
090806.9+042351	6554	137.0289	+4.3977	33.2	56.7	0.205	3.255	$2.91^{+2.94}_{-1.32}$	$11.8^{+1.5}_{-1.3}$	$32.4^{+4.9}_{-4.2}$	$6.31^{+0.99}_{-0.92}$	$18.6^{+17.7}_{-5.0}$	$2.80^{+1.44}_{-0.68}$	$10.1^{+1.4}_{-1.2}$	$27.3^{+5.9}_{-4.2}$	1337
090811.6-014811	3984	137.0486	-1.8032	13.4	72.5	0.040	5.725	$0.367^{+0.257}_{-0.064}$	$0.135^{+0.036}_{-0.029}$	$0.33^{+0.15}_{-0.10}$	$0.054^{+0.060}_{-0.016}$	$0.0229^{+0.0215}_{-0.0077}$	$0.314^{+0.086}_{-0.043}$	$0.039^{+0.038}_{-0.016}$	$0.120^{+0.132}_{-0.060}$	1959
090816.3+033416	11470	137.0681	+3.5713	7.9	22.8	0.137	2.828	$4.5^{+4.3}_{-2.0}$	$2.18^{+0.45}_{-0.32}$	$7.4^{+3.3}_{-1.0}$	$1.17^{+0.24}_{-0.21}$	$5.3^{+5.9}_{-2.0}$	$6.7^{+15.8}$	$1.60^{+0.32}$	$6.1^{+6.6}_{-2.2}$	1214
090817.2-013034	15548	137.0717	-1.5096	14.1	18.2	0.331	2.042	$10.7^{+14.5}_{-?}$	$7.3^{+0.84}_{-?}$	$35^{+18}_{-?}$	$4.10^{+0.30}_{-?}$	<170	$10.9^{+16.2}_{-?}$	$6.1^{+2.8}_{-?}$	$30^{+58}_{-?}$	2019
090821.6-014115	16287	137.0903	-1.6876	8.6	18.4	0.200	2.267	$1.42^{+0.31}_{-?}$	$3.05^{+0.50}_{-0.82}$	$6.6^{+1.5}_{-?}$	$1.56^{+0.56}_{-0.43}$	$2.25^{+1.56}_{-?}$	$1.58^{+0.25}_{-0.33}$	$2.60^{+0.55}_{-1.12}$	$5.8^{+?}_{-2.5}$	2150
090821.9+025141	8248	137.0913	+2.8615	7.7	17.9	0.812	1.602	$1.68^{+1.43}_{-?}$	$89^{+36}_{-?}$	$202^{+72}_{-?}$	$15.8^{+5.7}_{-?}$	$26^{+12}_{-?}$	$1.66^{+?}_{-0.37}$	<130	<310	1211
090838.0+015226	1479	137.1585	+1.8741	42.9	183.6	0.264	2.962	$2.87^{+1.43}_{-?}$	$29.8^{+3.1}_{-?}$	81^{+15}_{-10}	$10.4^{+1.3}_{-?}$	$30.1^{+15.1}_{-6.9}$	$3.06^{+1.36}_{-0.84}$	$22.1^{+2.9}_{-?}$	61^{+14}_{-11}	1215
090843.9-013034	4974	137.1831	-1.5095	6.9	44.8	0.255	2.124	$12.2^{+15.1}_{-7.5}$	$4.02^{+0.78}_{-0.62}$	$22.3^{+8.8}_{-?}$	$2.44^{+0.55}_{-0.49}$	<110	$8.9^{+14.4}_{-4.1}$	$3.34^{+0.78}_{-0.74}$	$16.1^{+11.5}_{-?}$	2073
090849.7+042241	2460	137.2072	+4.3783	45.6	128.3	0.796	1.860	$3.22^{+2.55}_{-?}$	$201^{+29}_{-?}$	583^{+114}_{-81}	$29.4^{+3.6}_{-?}$	96^{+70}_{-25}	$2.73^{+1.39}_{-0.70}$	158^{+27}_{-25}	$421^{+64}_{-?}$	1241
090913.8-001214	885	137.3079	-0.2040	67.6	243.9	0.310	3.477	$3.87^{+1.28}_{-0.92}$	$60.2^{+4.2}_{-?}$	179^{+28}_{-20}	$21.1^{+2.4}_{-?}$	80^{+31}_{-20}	$3.8^{+1.1}_{-?}$	$42.0^{+3.7}_{-?}$	125^{+32}_{-18}	1212
090915.3-010104	2004	137.3139	-1.0178	28.8	130.7	0.822	1.731	$4.1^{+2.8}_{-?}$	212^{+33}_{-31}	670^{+160}_{-110}	$31.4^{+4.6}_{-2.2}$	125^{+91}_{-41}	$3.9^{+2.9}_{-1.4}$	163^{+33}_{-28}	507^{+128}_{-92}	1214
090916.0-015540	5772	137.3168	-1.9280	30.1	58.6	0.326	2.406	$5.3^{+6.1}_{-2.6}$	$17.2^{+2.9}_{-?}$	$60^{+14}_{-?}$	$7.9^{+1.2}_{-1.1}$	41^{+52}_{-19}	$4.9^{+9.9}_{-2.2}$	$14.6^{+2.7}_{-2.5}$	50^{+37}_{-22}	1617
090930.6+034055	638	137.3775	+3.6822	10.3	15.2	0.740	1.804	$4.6^{+14.8}_{-2.7}$	174^{+27}_{-35}	590^{+540}_{-140}	$21.5^{+4.6}_{-5.2}$	<720	$4.3^{+10.2}_{-2.6}$	78^{+39}_{-29}	260^{+170}_{-110}	1210
090932.5-005020	3523	137.3857	-0.8390	12.8	75.5	1.134	1.369	$5.2^{+12.3}_{-2.3}$	$230^{+47}_{-?}$	850^{+540}_{-170}	$25.0^{+4.3}_{-?}$	127^{+289}_{-53}	$5.5^{+7.9}_{-2.8}$	170^{+59}_{-47}	630^{+260}_{-180}	1210
090938.1+040816	13180	137.4089	+4.1380	14.3	23.5	0.170	2.896	$1.74^{+0.64}_{-?}$	$3.08^{+0.95}_{-0.71}$	$7.3^{+1.8}_{-?}$	$1.77^{+0.51}_{-0.50}$	$3.2^{+1.7}_{-?}$	$1.79^{+1.75}_{-0.42}$	$2.23^{+0.91}_{-0.71}$	$5.5^{+2.7}_{-1.9}$	1210
091011.7+013914	13622	137.5491	+1.6541	14.7	23.8	0.290	2.385	$2.27^{+1.34}_{-?}$	$14.0^{+2.0}_{-?}$	$35.5^{+7.3}_{-?}$	$6.2^{+1.1}_{-?}$	$14.5^{+9.0}_{-3.9}$	$2.02^{+1.08}_{-0.40}$	$12.1^{+2.0}_{-?}$	$29.9^{+5.9}_{-5.3}$	1199
091032.4-053301	8750	137.6354	+3.8837	17.4	35.7	0.357	2.778	$6.5^{+14.8}_{-3.1}$	$15.6^{+3.0}_{-?}$	63^{+57}_{-19}	$6.3^{+1.3}_{-?}$	<240	$10.0^{+12.2}_{-6.0}$	$12.0^{+2.6}_{-?}$	57^{+38}_{-22}	1214
091033.8+005100	510	137.6409	+0.8501	45.6	416.8	0.366	2.770	$2.35^{+0.73}_{-0.41}$	$45.4^{+8.6}_{-?}$	116^{+22}_{-21}	$12.1^{+2.8}_{-?}$	$28.5^{+11.2}_{-8.8}$	$2.47^{+1.15}_{-0.54}$	$20.8^{+3.6}_{-?}$	$54^{+18}_{-?}$	1212
091057.2+041730	206	137.7384	+4.2918	20.4	53.8	0.468	2.034	$12.9^{+11.4}_{-?}$	$30.0^{+6.7}_{-?}$	157^{+101}_{-58}	$9.0^{+3.7}_{-2.8}$	<390	$9.1^{+13.6}_{-?}$	$22.0^{+6.8}_{-?}$	103^{+68}_{-38}	1217
091104.1+052237	11694	137.7671	+5.3770	13.5	24.6	0.159	3.268	$5.7^{+6.7}_{-2.9}$	$3.3^{+1.1}_{-?}$	$12.0^{+7.4}_{-?}$	$2.09^{+0.68}_{-0.85}$	<43	$4.8^{+12.6}_{-?}$	$2.4^{+1.0}_{-1.1}$	$8.3^{+7.8}_{-4.0}$	905
091108.0-015422	5376	137.7836	-1.9063	7.1	24.3	1.202	1.143	$13.7^{+13.6}_{-?}$	$61^{+31}_{-?}$	$350^{+250}_{-?}$	<17	<370	$13.4^{+13.5}_{-?}$	<95	<580	1421
091111.0+040015	6021	137.7960	+4.0043	12.3	19.9	0.503	1.905	$11.7^{+8.1}_{-?}$	$20.0^{+8.9}_{-?}$	$99^{+44}_{-?}$	$8.2^{+3.1}_{-?}$	<280	$12.1^{+13.6}_{-?}$	<34	<220	1212
091117.1+030441	15328	137.8216	+3.0782	15.2	19.2	0.213	2.699	$4.0^{+2.2}_{-?}$	$11.3^{+1.6}_{-?}$	$34.5^{+9.6}_{-?}$	$4.83^{+1.07}_{-?}$	$18.9^{+12.3}_{-?}$	$4.5^{+3.7}_{-?}$	$10.4^{+1.5}_{-?}$	$33.8^{+12.3}_{-?}$	1180
091135.9+034626	3774	137.8997	+3.7741	12.7	72.9	0.927	1.502	$1.98^{+1.21}_{-?}$	$201^{+41}_{-?}$	499^{+81}_{-76}	$26.0^{+4.1}_{-?}$	$54^{+13}_{-?}$	$1.75^{+0.92}_{-?}$	$179^{+57}_{-?}$	430^{+120}_{-100}	1220
091139.3-014144	5511	137.9141	-1.6958	23.8	53.7	0.589	1.881	$3.00^{+2.35}_{-?}$	$52.2^{+9.7}_{-?}$	$146^{+44}_{-?}$	$13.0^{+2.4}_{-?}$	39^{+32}_{-12}	$2.38^{+0.74}_{-?}$	$39.2^{+8.7}_{-?}$	$98^{+24}_{-?}$	1531
091159.7+031036	9374	137.9988	+3.1768	10.7	29.1	0.243	2.370	$7.7^{+11.1}_{-4.2}$	$8.4^{+1.7}_{-?}$	35^{+25}_{-12}	$3.99^{+0.82}_{-0.88}$	<130	$6.6^{+13.3}_{-?}$	$7.0^{+1.7}_{-?}$	$27.8^{+25.3}_{-9.3}$	1193
091213.4-021621	7699	138.0559	-2.2726	10.5	9.2	0.160	4.087	$2.60^{+0.99}_{-?}$	<10	<28	<4.5	<13	$3.03^{+0.87}_{-0.71}$	<5.9	<17	533
091214.1+022443	18040	138.0589	+2.4122	6.8	17.1	0.181	2.430	$1.07^{+0.44}_{-?}$	<4.0	<8.2	<2.0	<2.9	$1.13^{+1.31}_{-?}$	<3.4	<8.0	1102
091215.3-021743	626	138.0641	-2.2956	120.3	435.9	0.159	5.791	$2.10^{+0.55}_{-?}$	$65.5^{+5.4}_{-5.7}$	159^{+15}_{-16}	$19.7^{+1.5}_{-2.0}$	$41.5^{+11.4}_{-6.7}$	$1.92^{+0.30}_{-?}$	$44.5^{+4.1}_{-?}$	105^{+11}_{-12}	496
091248.2+002446	11837	138.2011	+0.4130	7.1	17.4	0.308	2.602	$3.2^{+3.7}_{-?}$	$12.2^{+3.1}_{-?}$	$35.2^{+15.1}_{-?}$	$7.1^{+1.6}_{-1.4}$	$22.3^{+26.1}_{-?}$	$2.86^{+1.73}_{-?}$	$10.9^{+3.0}_{-2.8}$	$29.7^{+10.0}_{-8.2}$	1211
091254.4+032028	1415	138.2270	+3.3414	48.5	199.3	0.619	2.191	$3.45^{+1.48}_{-0.80}$	$136^{+17}_{-?}$	$395^{+62}_{-?}$	$23.9^{+4.5}_{-?}$	$83^{+42}_{-?}$	$3.2^{+3.8}_{-?}$	$89^{+19}_{-?}$	263^{+75}_{-52}	1216
091300.9-013152	7531	138.2538	-1.5311	14.0	33.4	0.592	1.715	$4.0^{+5.1}_{-?}$	$41.6^{+9.8}_{-?}$	129^{+57}_{-47}	$10.1^{+3.9}_{-?}$	<130	$4.5^{+9.9}_{-?}$	$30^{+16}_{-?}$	101^{+69}_{-39}	1218
091302.1+035000	1277	138.2590	+3.8336	11.4	18.7	0.455	2.168	$5.7^{+10.3}_{-2.9}$	$64.5^{+8.9}_{-?}$	234^{+177}_{-54}	$18.3^{+2.8}_{-?}$	$101^{+207}_{-?}$	$3.7^{+3.7}_{-?}$	$56.7^{+8.1}_{-?}$	$172^{+62}_{-?}$	1215
091305.9+035021	3797	138.2747	+3.8394	15.7	25.6	0.456	2.352	$3.26^{+1.88}_{-?}$	$70.4^{+8.0}_{-?}$	$203^{+42}_{-?}$	$20.8^{+3.1}_{-?}$	$68^{+40}_{-?}$	$4.8^{+3.8}_{-?}$	$57.4^{+8.2}_{-?}$	$191^{+?}_{-?}$	1213
091315.0+034850	593	138.3125	+3.8139	88.3	393.5	0.453	2.666	$4.8^{+2.3}_{-?}$	$133^{+12}_{-?}$	$439^{+92}_{-?}$	$30.7^{+3.7}_{-?}$	$145^{+75}_{-?}$	$5.7^{+6.3}_{-?}$	$89^{+10}_{-?}$	$330^{+141}_{-?}$	1218
091320.3+032834	2977	138.3348	+3.4763	9.3	84.6	0.399	2.082	$2.74^{+1.75}_{-0.80}$	$24.3^{+4.8}_{-?}$	$66^{+13}_{-?}$	$5.4^{+2.4}_{-?}$	$14.9^{+12.0}_{-?}$	$2.39^{+1.32}_{-?}$	$12.0^{+5.3}_{-?}$	$31^{+16}_{-?}$	1220
091322.9+040617	9801	138.3454	+4.1050	9.6	26.9	0.088	3.752	$0.868^{+0.010}_{-0.085}$	$1.74^{+0.45}_{-0.34}$	$3.24^{+0.85}_{-0.63}$	$0.86^{+0.13}_{-0.16}$	$0.74^{+0.19}_{-0.16}$	$0.884^{+0.063}_{-0.079}$	$1.60^{+0.38}_{-0.29}$	$2.99^{+0.70}_{-0.55}$	1214

continued.

Cluster (eFEDS J+)	ID_SRC	RA (deg)	Dec (deg)	$\mathcal{L}_{ext}$	$\mathcal{L}_{det}$	z	R_{500} (arcmin)	T (keV)	L_X (10^{42} erg s^{-1})	L_{bol} (10^{42} erg s^{-1})	M_{gas} (10^{12} M$_\odot$)	Y_X (10^{12} M$_\odot$ keV)	T_{cex} (keV)	$L_{X,cex}$ (10^{42} erg s^{-1})	$L_{bol,cex}$ (10^{42} erg s^{-1})	t_{exp} (s)
091331.0+024513	3488	138.3792	+2.7537	15.4	61.0	0.156	2.953	$0.825^{+0.074}_{-0.088}$	$2.03^{+0.43}_{-0.43}$	$3.70^{+0.79}_{-0.79}$	$0.25^{+0.12}_{-0.11}$	$0.197^{+0.110}_{-0.086}$	$0.84^{+0.19}_{-0.17}$	< 0.88	< 1.8	1202
091336.6+031723	5541	138.4026	+3.2899	54.9	82.7	0.142	4.335	$1.74^{+0.58}_{-0.56}$	$7.09^{+0.99}_{-1.08}$	$16.5^{+2.7}_{-2.7}$	$4.32^{+0.67}_{-0.60}$	$7.7^{+3.0}_{-1.7}$	$1.78^{+1.00}_{-0.30}$	$5.49^{+0.85}_{-0.91}$	$13.2^{+2.7}_{-2.5}$	1220
091351.1-004507	1319	138.4632	-0.7520	64.6	113.1	0.294	3.285	$2.30^{+0.66}_{-0.66}$	$44.2^{+4.6}_{-4.8}$	111^{+14}_{-14}	$15.1^{+1.8}_{-1.8}$	$34.9^{+11.0}_{-11.0}$	$2.36^{+0.38}_{-0.38}$	$31.6^{+4.1}_{-4.1}$	79^{+11}_{-11}	1218
091354.7+025323	16902	138.4782	+2.8898	6.3	15.4	0.423	1.912	$3.8^{+9.3}_{-3.0}$	$11.2^{+3.4}_{-3.4}$	36^{+26}_{-12}	$5.4^{+1.5}_{-1.8}$	$21.0^{+52.0}_{-8.5}$	$4.7^{+9.3}_{-0.48}$	$8.6^{+3.8}_{-4.4}$	31^{+22}_{-12}	1217
091358.1+025707	940	138.4924	+2.9521	17.2	21.8	0.417	2.256	$9.6^{+14.3}_{-5.5}$	$17.4^{+6.6}_{-5.6}$	82^{+66}_{-35}	$8.1^{+2.3}_{-1.1}$	< 310	$14.2^{+12.4}_{-2.4}$	$13.5^{+5.0}_{-2.6}$	74^{+56}_{-36}	1216
091402.7-010208	5561	138.5116	-1.0358	9.7	48.7	0.516	1.858	$2.66^{+4.14}_{-0.83}$	$32.3^{+3.7}_{-3.2}$	91^{+35}_{-35}	$9.3^{+3.2}_{-2.2}$	$25.2^{+37.5}_{-7.5}$	$2.06^{+9.33}_{-0.5}$	$23.9^{+8.0}_{-3.0}$	59^{+32}_{-36}	1213
091403.3+013846	1465	138.5140	+1.6464	42.7	185.2	0.168	4.597	$6.0^{+2.0}_{-2.0}$	$14.5^{+1.5}_{-1.5}$	53^{+24}_{-24}	$8.4^{+7.4}_{-1.4}$	50^{+18}_{-18}	$9.1^{+12.8}_{-1.2}$	$10.1^{+8.4}_{-1.5}$	48^{+15}_{-22}	1210
091412.6+001856	1844	138.5528	+0.3158	55.0	87.3	0.165	3.985	$2.84^{+1.62}_{-0.79}$	$13.0^{+1.9}_{-1.9}$	$35.2^{+7.7}_{-5.7}$	$6.16^{+1.09}_{-0.79}$	$17.9^{+10.5}_{-5.1}$	$2.21^{+1.24}_{-0.49}$	$9.8^{+1.9}_{-1.7}$	$25.1^{+5.6}_{-4.9}$	1217
091414.9+022709	1424	138.5623	+2.4527	10.2	22.6	0.348	2.315	$2.39^{+1.57}_{-0.59}$	$12.1^{+4.1}_{-4.1}$	32^{+17}_{-11}	< 8.1	< 24	$2.25^{+1.69}_{-0.44}$	< 15	< 39	1214
091417.7+031159	396	138.5740	+3.1998	16.7	26.9	0.231	3.183	$1.02^{+0.30}_{-0.18}$	$10.7^{+3.3}_{-3.3}$	$21.1^{+10.1}_{-4.4}$	< 6.7	< 6.7	$1.04^{+0.25}_{-0.23}$	< 9.7	< 19	1219
091423.9+022833	7735	138.5999	+2.4759	14.3	32.7	0.319	2.356	$2.40^{+1.08}_{-1.08}$	$25.0^{+4.7}_{-4.3}$	64^{+14}_{-12}	$9.2^{+1.7}_{-1.5}$	$22.3^{+12.3}_{-6.7}$	$1.81^{+0.64}_{-0.29}$	$23.8^{+4.3}_{-4.2}$	56^{+11}_{-10}	1219
091431.6+010910	4637	138.6318	+1.1528	10.9	55.2	0.543	1.751	$2.30^{+2.36}_{-0.64}$	$30.1^{+9.6}_{-6.6}$	79^{+28}_{-30}	< 13	< 38	$4.3^{+10.7}_{-1.9}$	< 32	< 120	1214
091433.8+022718	3159	138.6411	+2.4550	38.1	99.6	0.316	2.657	$3.7^{+5.1}_{-1.5}$	$24.5^{+5.1}_{-5.1}$	74^{+35}_{-22}	$9.2^{+2.1}_{-2.5}$	33^{+50}_{-15}	$2.58^{+2.41}_{-0.79}$	$18.3^{+5.3}_{-8.0}$	49^{+18}_{-21}	1212
091439.5-014416	6130	138.6648	-1.7380	11.3	39.7	0.484	1.765	$3.7^{+3.3}_{-1.3}$	$35.2^{+5.8}_{-2.8}$	107^{+33}_{-22}	$9.8^{+1.7}_{-1.7}$	36^{+34}_{-13}	$4.0^{+5.6}_{-1.7}$	$30.2^{+5.6}_{-5.9}$	94^{+41}_{-21}	1569
091445.7+032755	8636	138.6906	+3.4655	8.7	17.7	0.122	4.059	$7.2^{+17.4}_{-4.4}$	$1.94^{+0.36}_{-0.39}$	$8.2^{+8.6}_{-3.2}$	$1.52^{+0.40}_{-0.36}$	< 68	$6.9^{+14.1}_{-3.8}$	$1.38^{+0.38}_{-0.51}$	$5.4^{+5.0}_{-2.1}$	1214
091445.8+042621	13299	138.6909	+4.4394	14.8	17.7	0.348	2.375	$1.45^{+0.63}_{-0.26}$	144^{+24}_{-15}	325^{+64}_{-42}	$19.0^{+2.1}_{-2.0}$	$27.8^{+13.6}_{-6.7}$	$1.45^{+0.84}_{-0.24}$	110^{+21}_{-12}	249^{+53}_{-33}	1221
091446.1+001047	1917	138.6925	+0.1799	25.2	156.6	0.533	2.104	$3.7^{+3.1}_{-1.3}$	87^{+11}_{-10}	262^{+73}_{-40}	$18.4^{+2.7}_{-2.9}$	69^{+56}_{-24}	$2.61^{+2.81}_{-0.77}$	57^{+11}_{-11}	155^{+46}_{-33}	1219
091450.6-022606	2154	138.7110	-2.4351	44.3	121.9	0.504	2.045	$25.0^{+4.8}_{-4.8}$	$40.4^{+5.7}_{-5.7}$	341^{+75}_{-107}	$13.3^{+2.2}_{-2.2}$	320^{+150}_{-150}	$15.0^{+17.0}_{-7.9}$	$27.3^{+3.6}_{-5.3}$	166^{+79}_{-58}	1684
091453.6-041613	372	138.7235	+4.2704	123.9	398.6	0.143	5.827	$2.77^{+1.68}_{-0.68}$	$25.5^{+2.8}_{-2.8}$	$67.5^{+9.4}_{-9.4}$	$11.3^{+1.4}_{-1.4}$	$31.5^{+8.7}_{-5.9}$	$2.48^{+0.65}_{-0.65}$	$15.8^{+1.5}_{-1.9}$	$40.5^{+5.2}_{-4.9}$	1216
091509.5+051521	6244	138.7897	+5.2560	48.0	70.0	0.249	3.720	$2.47^{+0.46}_{-0.46}$	$50.4^{+6.0}_{-6.0}$	129^{+67}_{-67}	$19.6^{+2.7}_{-2.5}$	49^{+11}_{-11}	$3.35^{+1.51}_{-1.51}$	$41.8^{+5.5}_{-4.6}$	119^{+25}_{-17}	577
091512.2+043506	4253	138.8012	+4.5851	11.6	59.8	0.361	2.138	$2.41^{+0.70}_{-0.70}$	$11.6^{+2.4}_{-2.4}$	$29.8^{+1.4}_{-1.4}$	< 4.6	$6.9^{+3.6}_{-3.3}$	$1.96^{+0.39}_{-0.39}$	< 9.1	< 22	1326
091517.4-005909	13537	138.8229	-0.9860	6.2	24.8	0.405	1.822	$3.7^{+6.4}_{-2.6}$	$13.0^{+4.9}_{-4.9}$	42^{+24}_{-14}	$5.4^{+1.5}_{-1.2}$	$20.0^{+36.4}_{-9.1}$	$3.4^{+4.9}_{-1.2}$	$11.8^{+4.3}_{-3.3}$	36^{+22}_{-14}	1220
091520.5+045203	14354	138.8357	+4.8676	10.5	11.8	0.149	3.013	$3.3^{+1.7}_{-0.8}$	$1.41^{+0.57}_{-0.57}$	$4.4^{+4.1}_{-1.7}$	$0.96^{+0.45}_{-0.39}$	< 24	$3.4^{+6.6}_{-1.2}$	$0.87^{+0.61}_{-0.40}$	$2.6^{+2.4}_{-1.3}$	1233
091522.5+041201	14525	138.8438	+4.2003	7.6	10.2	0.460	1.932	$3.7^{+3.3}_{-1.7}$	$17.3^{+5.5}_{-5.5}$	53^{+25}_{-25}	$7.2^{+2.1}_{-2.0}$	26^{+30}_{-12}	$3.4^{+14}_{-1.2}$	$13.4^{+7.0}_{-7.0}$	43^{+33}_{-17}	1219
091543.5-004944	10164	138.9316	-0.8291	6.3	23.7	0.296	1.948	$11.4^{+13.0}_{-7.9}$	$3.28^{+0.89}_{-0.89}$	$16.4^{+11.9}_{-7.7}$	$0.90^{+0.27}_{-0.27}$	< 38	$9.9^{+11.0}_{-7.9}$	$1.10^{+0.82}_{-0.54}$	< 16	1260
091553.1+040545	12204	138.9715	+4.0961	6.4	23.4	0.567	1.560	$8.0^{+12.1}_{-4.9}$	$12.6^{+3.2}_{-3.2}$	55^{+40}_{-40}	$4.5^{+1.6}_{-1.6}$	< 160	$5.1^{+16.2}_{-3.0}$	$8.2^{+4.5}_{-3.4}$	31^{+29}_{-15}	1215
091555.6-013248	888	138.9820	-1.5468	86.6	275.5	0.490	2.957	$7.3^{+12.1}_{-2.6}$	151^{+14}_{-15}	630^{+430}_{-130}	$42.4^{+5.4}_{-4.8}$	310^{+530}_{-120}	$6.2^{+6.7}_{-2.6}$	111^{+13}_{-14}	418^{+198}_{-91}	1168
091601.8+000831	9930	139.0078	+0.1420	12.9	32.0	0.563	1.760	$6.8^{+6.8}_{-3.2}$	$36.3^{+8.5}_{-8.5}$	144^{+70}_{-43}	$11.5^{+2.3}_{-2.2}$	74^{+85}_{-35}	$7.4^{+11.5}_{-3.8}$	$31.1^{+7.4}_{-7.0}$	128^{+89}_{-44}	1222
091609.4+013519	8107	139.0393	+1.5888	37.4	33.0	0.454	2.322	$5.6^{+7.9}_{-2.2}$	$28.1^{+7.7}_{-7.7}$	102^{+63}_{-32}	$12.9^{+2.8}_{-2.5}$	69^{+109}_{-34}	$14.8^{+10.0}_{-8.0}$	$24.5^{+7.0}_{-7.0}$	136^{+88}_{-57}	1215
091610.1-002348	534	139.0423	-0.3969	282.2	623.3	0.322	4.189	$4.14^{+0.81}_{-0.81}$	$203.0^{+9.0}_{-9.0}$	623^{+56}_{-56}	$54.5^{+3.6}_{-3.7}$	225^{+47}_{-34}	$3.91^{+1.36}_{-0.81}$	$166.0^{+10.0}_{-10.0}$	502^{+76}_{-48}	1247
091612.9-015839	6129	139.0540	-1.9776	13.5	40.4	0.160	3.358	$5.2^{+10.2}_{-3.0}$	$4.66^{+0.54}_{-0.54}$	$15.7^{+12.5}_{-4.6}$	$2.88^{+0.56}_{-0.47}$	< 74	$5.7^{+10.9}_{-0.81}$	$3.68^{+0.53}_{-0.78}$	$13.0^{+11.5}_{-4.0}$	1833
091631.9-020207	15047	139.1331	-2.0355	6.9	13.4	0.326	2.136	$7.8^{+10.9}_{-4.8}$	$5.4^{+1.7}_{-1.5}$	$23.5^{+17.2}_{-9.3}$	$3.65^{+0.90}_{-0.90}$	< 120	$4.2^{+3.5}_{-1.7}$	$4.6^{+1.6}_{-1.3}$	$14.9^{+8.1}_{-5.4}$	1485
091642.3-040634	13204	139.1764	+4.1095	20.7	20.5	0.312	2.429	$0.68^{+1.06}_{-0.25}$	$8.4^{+2.8}_{-2.8}$	$17.3^{+8.8}_{-4.6}$	$3.7^{+1.1}_{-1.0}$	$2.33^{+4.08}_{-0.76}$	$1.51^{+3.02}_{-0.96}$	$5.8^{+2.3}_{-2.1}$	$13.8^{+5.4}_{-5.1}$	1218
091646.9-015531	8352	139.1957	+1.9255	36.7	41.8	0.259	2.957	$18.1^{+9.4}_{-9.4}$	$8.2^{+1.5}_{-1.5}$	55^{+25}_{-23}	$4.7^{+1.0}_{-1.0}$	< 200	$15.6^{+9.3}_{-9.3}$	$5.5^{+1.6}_{-1.2}$	35^{+14}_{-14}	1219
091648.1+030506	5300	139.2007	+3.0851	16.4	58.2	0.620	1.752	$4.2^{+8.1}_{-1.7}$	54^{+15}_{-0}	176^{+106}_{-40}	$11.5^{+2.6}_{-3.0}$	48^{+94}_{-20}	$5.2^{+7.4}_{-2.7}$	$34.8^{+11.7}_{-9.4}$	126^{+69}_{-42}	1220
091655.7-011158	11550	139.2324	-1.1996	9.3	21.4	0.314	2.086	$0.50^{+0.90}_{-0.15}$	$7.2^{+3.7}_{-2.5}$	$15.9^{+12.3}_{-5.9}$	< 5.6	< 4.4	$0.61^{+3.19}_{-0.21}$	< 8.9	< 23	1410
091722.4+010118	1526	139.3435	+1.0218	56.4	187.8	0.359	2.785	$3.05^{+1.28}_{-0.75}$	$48.5^{+4.8}_{-4.8}$	133^{+22}_{-22}	$14.2^{+2.0}_{-2.0}$	43^{+21}_{-11}	$2.91^{+1.56}_{-0.91}$	$32.3^{+4.3}_{-4.3}$	87^{+18}_{-15}	1220
091741.1+024518	10140	139.4215	+2.7551	8.7	28.3	0.486	1.836	$6.2^{+12.5}_{-2.9}$	$13.4^{+6.7}_{-6.7}$	54^{+48}_{-17}	$6.3^{+2.2}_{-2.0}$	< 210	$9.1^{+12.0}_{-5.7}$	$12.3^{+5.8}_{-5.8}$	< 150	1222
091749.4+014621	9976	139.4560	+1.7728	21.4	42.6	0.355	2.335	$3.8^{+3.3}_{-1.2}$	$31.1^{+3.6}_{-3.6}$	94^{+32}_{-15}	$11.3^{+1.9}_{-1.7}$	42^{+41}_{-14}	$5.9^{+11.3}_{-3.0}$	$26.9^{+3.2}_{-3.2}$	98^{+76}_{-25}	1219

continued.

Cluster (eFEDS J+)	ID_SRC	RA (deg)	Dec (deg)	$\mathcal{L}_{ext}$	$\mathcal{L}_{det}$	z	R_{500} (arcmin)	T (keV)	L_X (10^{42} erg s^{-1})	L_{bol} (10^{42} erg s^{-1})	M_{gas} (10^{12} M$_\odot$)	Y_X (10^{12} M$_\odot$ keV)	T_{cex} (keV)	$L_{X,cex}$ (10^{42} erg s^{-1})	$L_{bol,cex}$ (10^{42} erg s^{-1})	t_{exp} (s)
091757.1+050915	1934	139.4881	+5.1542	23.9	61.4	0.586	2.744	$1.58^{+0.70}$	291^{+52}_{-52}	660^{+110}_{-120}	49^{+11}_{-11}	78^{+40}	$1.56^{+1.13}_{-0.35}$	202^{+40}_{-44}	459^{+92}_{-101}	388
091806.0-003228	3910	139.5253	-0.5413	10.6	60.9	0.223	2.423	$2.40^{+2.64}_{-0.39}$	$2.99^{+0.74}$	$8.0^{+2.9}_{-2.0}$	$0.49^{+0.23}_{-0.20}$	$1.26^{+1.55}_{-0.61}$	$5.2^{+14.3}_{-2.9}$	< 1.4	< 6.7	1574
091842.2+034754	10019	139.6759	+3.7985	11.5	22.4	0.452	1.807	$2.40^{+3.89}_{-0.96}$	$12.2^{+4.8}$	$32.5^{+19.8}_{-9.5}$	< 7.2	< 32	$1.72^{+1.03}_{-0.33}$	< 15	< 37	1218
091849.0+021204	994	139.7042	+2.2013	94.8	245.3	0.283	3.428	$4.5^{+2.7}$	$75.4^{+3.8}$	243^{+60}	$24.2^{+2.8}_{-2.5}$	109^{+66}	$4.7^{+3.1}_{-1.4}$	$62.4^{+4.7}$	208^{+59}_{-30}	1220
091850.7+030942	19979	139.7113	+3.1619	12.8	14.7	0.838	1.462	$5.1^{+8.9}$	70^{+24}_{-19}	259^{+136}	$15.2^{+3.3}_{-2.5}$	75^{+134}	$5.3^{+5.4}_{-2.6}$	63^{+22}_{-16}	229^{+104}_{-66}	1220
091851.7+021432	4105	139.7155	+2.2423	10.0	19.0	0.283	2.389	$5.5^{+6.5}$	< 24	$48^{+?}$	$6.1^{+1.9}$	33^{+61}_{-36}	$5.9^{+7.0}$	< 22	< 100	1220
091855.8+004916	12125	139.7326	+0.8211	12.1	19.4	0.845	1.382	$2.8^{+2.4}_{-1.1}$	76^{+24}	219^{+56}	$13.8^{+2.9}_{-2.0}$	39^{+45}	$2.8^{+3.2}$	63^{+21}_{-18}	179^{+70}_{-48}	1495
091858.0+024946	7194	139.7418	+2.8295	26.3	46.3	0.199	3.204	$1.71^{+0.85}_{-0.29}$	$10.6^{+2.0}$	$24.8^{+5.1}$	$5.24^{+0.90}_{-0.78}$	$9.2^{+4.5}$	$1.88^{+0.72}_{-0.37}$	$8.9^{+1.8}_{-1.5}$	$21.2^{+5.3}_{-3.8}$	1223
091900.0-035311	5545	139.7503	-3.8864	25.3	53.8	0.403	2.258	$2.11^{+0.43}_{-0.28}$	$39.9^{+4.8}$	98^{+37}	$12.9^{+2.1}_{-1.7}$	$27.9^{+9.6}_{-6.3}$	$1.94^{+0.41}_{-4.5}$	$32.9^{+4.7}$	79^{+14}_{-11}	1221
091925.6-010430	4254	139.8567	-1.0752	9.2	55.6	0.513	1.734	$7.7^{+3.4}$	$28.3^{+6.1}$	124^{+73}	< 12	< 180	$11.9^{+11.3}_{-7.1}$	< 32	< 210	1433
091934.6+033941	1892	139.8943	+3.6615	20.8	126.9	0.223	2.788	$1.26^{+0.15}_{-0.17}$	$7.8^{+1.3}$	$16.4^{+3.0}_{-2.4}$	$1.14^{+0.89}_{-0.51}$	$1.42^{+1.17}_{-0.65}$	$1.13^{+0.15}_{-0.15}$	< 4.3	< 8.6	1224
091936.6-042553	11376	139.9028	-4.4314	9.3	21.3	0.179	2.567	$1.57^{+0.64}_{-0.53}$	$1.13^{+0.64}$	$2.6^{+1.7}$	$0.41^{+0.37}_{-0.20}$	< 2.8	$1.79^{+1.76}_{-0.61}$	< 1.4	< 3.4	1313
091957.7+035012	4131	139.9908	+3.8369	38.5	74.3	0.525	2.211	$2.01^{+1.23}_{-0.51}$	$75.2^{+9.4}$	182^{+27}	$18.3^{+3.4}_{-3.4}$	38^{+10}_{-12}	$2.32^{+2.62}_{-0.81}$	56^{+10}_{-12}	145^{+39}_{-30}	1221
092002.1+010219	150	140.0090	+1.0389	179.6	1049.6	0.017	15.354	$0.86^{+0.24}_{-0.11}$	$0.295^{+0.075}_{-0.032}$	$0.69^{+0.26}_{-0.21}$	$0.102^{+0.096}_{-0.041}$	< 0.85	$1.03^{+7.91}_{-0.40}$	$0.067^{+0.079}_{-0.029}$	< 0.75	1572
092004.3-010023	11754	140.0183	+1.0066	20.0	35.9	0.033	7.193	$0.779^{+0.018}_{-0.018}$	< 0.17	< 0.31	$0.0145^{+0.0103}_{-0.0069}$	$0.0114^{+0.0083}_{-0.0056}$	$0.782^{+0.019}_{-0.023}$	< 0.03	< 0.06	1570
092022.0+030106	6534	140.0918	+3.0186	12.0	14.1	0.481	1.608	$2.8^{+6.6}$	$9.0^{+11.2}$	< 97	< 9.6	< 39	$3.0^{+9.4}$	< 27	< 82	1304
092022.8+045012	5320	140.0954	+4.8369	12.0	60.2	0.270	2.774	$4.2^{+7.8}_{-1.9}$	$23.7^{+4.1}$	76^{+51}_{-19}	$8.7^{+1.7}_{-1.5}$	36^{+71}_{-17}	$4.1^{+4.9}_{-2.1}$	$16.7^{+4.9}_{-3.5}$	55^{+43}_{-17}	695
092023.1+034444	222	140.0967	+1.5789	88.4	719.6	0.708	2.178	$3.20^{+0.77}_{-0.55}$	315^{+30}	869^{+86}_{-89}	$36.5^{+4.5}_{-3.8}$	116^{+31}_{-22}	$2.87^{+0.79}_{-0.55}$	157^{+63}_{-25}	414^{+63}_{-57}	1547
092031.3+024710	18068	140.1306	+2.7863	11.6	11.7	0.278	2.406	$2.36^{+1.58}_{-0.74}$	$4.0^{+2.6}$	$10.6^{+6.8}_{-3.2}$	$2.25^{+1.40}_{-0.92}$	$5.6^{+5.9}_{-2.7}$	$2.8^{+3.5}_{-1.1}$	$2.17^{+2.55}_{-0.79}$	$6.6^{+7.0}_{-2.8}$	1377
092031.8+040621	4115	140.1329	+4.1059	12.5	53.2	0.575	1.755	$7.7^{+14.1}$	$46.0^{+0.5}$	196^{+145}_{-58}	$10.8^{+2.1}_{-1.9}$	< 390	$9.4^{+8.5}$	$31.5^{+8.8}_{-9.5}$	142^{+83}_{-49}	1224
092037.0-011506	5739	140.1545	-1.2519	34.3	63.0	0.154	3.760	$1.26^{+0.20}_{-0.13}$	$6.06^{+0.77}$	$12.7^{+1.8}_{-1.7}$	$3.28^{+0.52}_{-0.45}$	$4.18^{+1.09}_{-0.84}$	$1.110^{+0.120}_{-0.070}$	$4.64^{+0.79}_{-0.71}$	$9.2^{+1.7}_{-1.4}$	1354
092037.9+033528	6467	140.1580	+3.5913	6.8	44.8	0.362	1.984	$3.3^{+2.5}$	$8.1^{+0.50}$	$23^{+1.8}_{-1.7}$	< 6.0	< 28	$5.1^{+6.3}$	< 11	< 44	1247
092039.1+004725	6669	140.1632	+0.7904	8.8	45.1	0.472	1.766	$9.6^{+4.6}_{-1.62}$	$20.3^{+3.9}$	100^{+76}_{-32}	$6.8^{+1.4}_{-2.1}$	< 300	$10.4^{+10.3}_{-7.6}$	$14.5^{+4.0}_{-5.6}$	67^{+44}_{-28}	1496
092041.1+041117	10334	140.1716	+4.1883	10.8	23.6	0.580	1.632	$2.53^{+1.53}_{-0.84}$	$20.9^{+8.1}$	55^{+22}_{-18}	$5.7^{+1.9}_{-1.6}$	$13.8^{+9.6}_{-6.7}$	$4.0^{+7.6}_{-1.9}$	< 29	< 100	1329
092046.2+002849	1915	140.1926	+0.4803	40.0	69.6	0.413	2.716	$2.54^{+0.84}_{-0.48}$	$74.9^{+7.8}$	193^{+27}	$22.5^{+3.4}_{-3.4}$	57^{+22}_{-13}	$2.68^{+1.17}_{-0.88}$	$57.3^{+7.9}_{-7.1}$	152^{+25}_{-23}	1422
092049.5+024513	489	140.2063	+2.7538	142.1	514.2	0.284	3.708	$3.16^{+0.73}_{-0.53}$	$105.0^{+5.0}$	290^{+25}	$30.6^{+3.0}_{-3.0}$	97^{+24}_{-21}	$3.25^{+0.88}_{-0.64}$	$81.2^{+4.6}_{-4.8}$	226^{+19}_{-23}	1439
092053.4+021125	18194	140.2228	+2.1905	12.8	17.4	0.280	2.488	$2.10^{+1.54}_{-0.52}$	$7.7^{+2.5}$	$19.4^{+4.73}$	$4.68^{+1.19}_{-0.94}$	$10.3^{+7.7}_{-3.6}$	$1.97^{+1.02}_{-0.59}$	$6.8^{+2.5}_{-2.4}$	$16.6^{+6.7}_{-4.4}$	1540
092105.0+004452	6459	140.2710	+0.7480	7.3	33.9	0.159	2.680	$11.5^{+8.1}$	$1.68^{+0.43}$	$8.4^{+5.6}$	$0.69^{+0.47}_{-0.24}$	< 29	$12.6^{+13.9}$	$0.82^{+0.45}_{-0.34}$	< 12	1419
092121.2+031726	100	140.3385	+3.2906	478.6	1729.7	0.333	4.068	$5.51^{+1.08}_{-0.92}$	$251.0^{+10.0}$	887^{+86}_{-78}	$53.1^{+4.3}_{-3.8}$	292^{+64}_{-53}	$5.20^{+1.50}_{-0.93}$	163^{+10}_{-9}	565^{+81}_{-61}	1437
092133.2+043431	9512	140.3885	+4.5754	14.1	24.9	0.417	2.021	$1.94^{+1.47}_{-0.48}$	$19.4^{+5.1}$	47^{+13}	$6.8^{+1.5}_{-1.4}$	$13.4^{+9.7}_{-4.6}$	$3.1^{+4.2}_{-1.4}$	$13.3^{+4.4}_{-2.7}$	42^{+14}_{-14}	1066
092134.4+015832	810	140.3936	+1.9757	56.1	133.2	0.290	3.175	$3.7^{+4.5}$	$30.6^{+5.6}$	94^{+39}	$12.3^{+1.5}_{-1.4}$	44^{+54}_{-14}	$6.1^{+8.5}$	$21.2^{+2.5}_{-3.0}$	79^{+48}_{-19}	1537
092135.4+005128	7447	140.3977	+0.8580	7.4	35.0	0.488	1.780	$2.62^{+3.16}_{-0.68}$	$14.6^{+8.4}$	41^{+31}	< 9.5	< 47	$2.76^{+7.84}_{-0.84}$	< 22	< 76	1355
092136.4-001449	4168	140.4020	-0.2471	37.9	80.2	0.313	2.780	$4.0^{+3.2}$	$26.8^{+3.9}$	82^{+30}	$10.4^{+1.7}_{-1.5}$	40^{+38}_{-14}	$5.6^{+9.1}_{-2.5}$	$20.3^{+4.0}_{-3.0}$	75^{+53}_{-20}	1184
092202.2+034520	5347	140.5095	+3.7557	43.4	66.6	0.270	3.155	$4.40^{+1.13}_{-0.77}$	$44.9^{+9.8}$	143^{+34}	$15.8^{+3.0}_{-3.2}$	69^{+23}_{-17}	$4.35^{+1.09}_{-0.93}$	$39.7^{+9.6}_{-14.8}$	128^{+32}_{-45}	1440
092209.3+034628	367	140.5391	+3.7746	369.0	783.1	0.270	4.315	$4.83^{+0.90}_{-0.87}$	95^{+23}	319^{+70}	$30.4^{+5.7}_{-5.5}$	145^{+41}_{-32}	$4.50^{+1.27}_{-0.90}$	66^{+19}_{-17}	217^{+62}_{-54}	1469
092212.0-002731	857	140.5503	-0.4586	165.1	361.5	0.321	3.647	$5.1^{+2.6}$	$115.0^{+7.0}$	390^{+91}	$36.6^{+4.2}_{-3.8}$	187^{+103}_{-53}	$4.8^{+3.3}$	$91.5^{+5.8}_{-7.1}$	303^{+88}_{-40}	1135
092220.4+034806	4014	140.5852	+3.8017	24.1	48.9	0.267	0.719	$1.51^{+0.71}$	$8.6^{+2.1}$	$19.4^{+5.2}_{-4.9}$	$0.72^{+0.82}_{-0.32}$	$1.20^{+0.82}_{-0.50}$	$1.74^{+0.73}_{-0.32}$	$8.0^{+2.0}_{-3.5}$	$18.8^{+5.3}_{-4.0}$	1494
092235.8-002443	3133	140.6494	-0.4120	30.2	49.4	0.055	6.929	$2.64^{+0.51}_{-0.31}$	$1.24^{+0.38}$	$3.21^{+1.08}_{-0.87}$	$0.57^{+0.30}_{-0.13}$	$1.54^{+0.88}_{-0.36}$	$2.97^{+0.62}_{-0.42}$	$0.53^{+0.27}_{-0.14}$	$1.44^{+0.80}_{-0.36}$	1124
092241.9+020719	1535	140.6749	+2.1222	32.5	52.2	0.198	3.310	$1.38^{+0.21}_{-0.15}$	$8.9^{+1.2}$	$19.3^{+3.6}_{-2.7}$	$3.97^{+0.49}_{-0.75}$	$5.5^{+1.2}$	$1.29^{+0.14}_{-0.14}$	$6.3^{+1.0}$	$13.2^{+2.4}_{-2.2}$	1392

continued.

Cluster (eFEDS J+)	ID_SRC	RA (deg)	Dec (deg)	$\mathcal{L}_{ext}$	$\mathcal{L}_{det}$	z	R_{500} (arcmin)	T (keV)	L_X (10^{42} erg s^{-1})	L_{bol} (10^{42} erg s^{-1})	M_{gas} (10^{12} M$_\odot$)	Y_X (10^{12} M$_\odot$ keV)	T_{cex} (keV)	$L_{X,cex}$ (10^{42} erg s^{-1})	$L_{bol,cex}$ (10^{42} erg s^{-1})	t_{exp} (s)
092246.2+034251	2216	140.6928	+3.7143	27.2	65.5	0.269	2.759	$2.06^{+0.93}_{-0.93}$	$19.0^{+2.6}_{-2.5}$	$46.0^{+7.9}_{-7.9}$	$6.59^{+0.78}_{-0.67}$	$13.7^{+6.6}_{-3.5}$	$1.91^{+0.66}_{-0.32}$	$13.0^{+2.0}_{-1.8}$	$31.1^{+5.3}_{-4.7}$	1536
092246.4+042424	5348	140.6936	+4.4067	12.5	55.0	0.346	2.180	$1.80^{+0.38}_{-0.27}$	$17.5^{+3.3}_{-3.4}$	$40.9^{+8.3}_{-6.3}$	$5.8^{+1.3}_{-1.1}$	$10.5^{+3.3}_{-3.3}$	$1.94^{+0.74}_{-0.39}$	$11.9^{+3.4}_{-2.8}$	$28.4^{+8.7}_{-4.7}$	1377
092258.2+032041	4833	140.7426	+3.3449	14.4	51.1	0.575	1.762	$3.5^{+3.5}_{-3.5}$	$34.4^{+8.6}_{-8.6}$	102^{+37}_{-37}	$8.2^{+2.2}_{-2.2}$	28^{+27}_{-11}	$3.9^{+5.2}_{-0.39}$	$21.9^{+7.8}_{-2.8}$	69^{+38}_{-20}	1543
092302.6+034002	9076	140.7611	+3.6673	7.9	13.7	0.269	2.211	$2.60^{+2.05}_{-1.3}$	$10.2^{+2.0}_{-2.0}$	$26.9^{+20}_{-6.1}$	$4.34^{+1.07}_{-0.87}$	$11.2^{+9.3}_{-4.2}$	$1.97^{+1.71}_{-0.34}$	$9.7^{+1.8}_{-2.1}$	$24.1^{+6.0}_{-5.3}$	1556
092312.0+000355	6657	140.8003	+0.0655	7.4	46.9	0.321	2.107	$5.4^{+10.8}_{-3.0}$	< 8.4	< 35	< 4.5	< 50	$6.4^{+10.0}_{-3.0}$	< 5.8	< 29	1133
092328.2+043107	6063	140.8678	+4.5187	7.9	26.0	0.663	1.656	$3.48^{+4.27}_{-2.04}$	64^{+15}_{-15}	198^{+66}_{-66}	$13.1^{+2.8}_{-2.2}$	48^{+49}_{-29}	$3.5^{+5.4}_{-1.0}$	49^{+15}_{-15}	152^{+66}_{-41}	1262
092333.1-001917	7637	140.8879	-0.3216	10.2	42.5	0.813	1.539	$3.4^{+1.2}_{-1.2}$	78^{+24}_{-24}	245^{+106}_{-68}	$13.8^{+3.7}_{-3.7}$	48^{+76}_{-19}	$3.2^{+1.3}_{-1.4}$	54^{+12}_{-12}	172^{+15}_{-60}	1127
092335.1+012907	4806	140.8965	+1.4853	6.8	19.4	0.687	1.559	$16.5^{+9.3}_{-9.3}$	48^{+12}_{-12}	310^{+110}_{-110}	$12.7^{+3.1}_{-2.7}$	< 500	$10.9^{+13.5}_{-7.0}$	46^{+14}_{-12}	238^{+156}_{-91}	1186
092339.0+052654	1894	140.9129	+5.4486	30.3	158.3	0.373	3.264	$6.4^{+8.8}_{-3.1}$	280^{+58}_{-58}	1150^{+400}_{-400}	< 18	< 190	$9.9^{+12.7}_{-5.7}$	< 29	< 170	258
092346.8-005330	11530	140.9452	-0.8918	20.1	28.7	0.358	2.517	$5.1^{+5.2}_{-2.2}$	$18.9^{+4.0}_{-3.7}$	66^{+17}_{-17}	$9.7^{+1.9}_{-1.8}$	50^{+56}_{-23}	$4.4^{+7.5}_{-1.8}$	$15.9^{+4.2}_{-3.6}$	53^{+33}_{-15}	1143
092402.2+054205	7973	141.0094	+5.7016	13.8	33.3	0.488	2.788	$18.5^{+8.5}_{-8.5}$	90^{+19}_{-19}	610^{+290}_{-230}	$28.7^{+8.4}_{-7.3}$	< 1200	$16.4^{+10.9}_{-10.9}$	64^{+28}_{-19}	420^{+250}_{-170}	224
092405.0-013059	298	141.0211	-1.5165	196.6	576.5	0.337	3.119	$2.77^{+0.8}_{-0.8}$	$53.0^{+4.4}_{-4.1}$	140^{+13}_{-13}	$17.0^{+1.8}_{-1.8}$	$47.2^{+9.0}_{-7.6}$	$3.56^{+1.86}_{-0.99}$	$34.9^{+3.5}_{-3.9}$	102^{+21}_{-15}	2202
092409.4+040057	1437	141.0393	+4.0160	122.1	238.5	0.084	6.175	$1.020^{+0.070}_{-0.044}$	$3.83^{+0.26}_{-0.25}$	$7.43^{+0.56}_{-0.53}$	$1.99^{+0.28}_{-0.27}$	$2.04^{+0.34}_{-0.30}$	$0.923^{+0.054}_{-0.063}$	$2.52^{+0.32}_{-0.32}$	$4.71^{+0.48}_{-0.59}$	1528
092421.9-005103	8544	141.0914	-0.8510	6.3	33.2	0.276	2.158	$3.2^{+3.4}_{-3.4}$	$6.5^{+1.8}_{-1.3}$	$19.6^{+5.1}_{-5.1}$	$2.95^{+0.81}_{-0.60}$	$9.9^{+3.8}_{-3.8}$	$2.76^{+1.83}_{-0.60}$	$4.7^{+2.0}_{-1.5}$	$12.9^{+5.8}_{-4.3}$	1175
092454.7+014901	7841	141.2280	+1.8170	7.7	21.8	0.177	2.615	$1.39^{+0.70}_{-0.27}$	$2.15^{+0.89}_{-0.66}$	$4.7^{+2.1}_{-1.5}$	< 2.2	< 3.9	$1.46^{+0.84}_{-0.40}$	< 3.1	< 7.2	1140
092502.6-022612	7060	141.2608	+2.4367	10.6	39.4	0.390	2.118	$14.4^{+17.4}_{-7.1}$	$14.2^{+3.0}_{-2.5}$	86^{+30}_{-30}	$5.5^{+1.7}_{-2.0}$	< 220	$15.9^{+10.8}_{-8.5}$	$9.1^{+3.2}_{-3.2}$	55^{+34}_{-24}	1165
092504.3-005602	11531	141.2682	-0.9339	9.7	19.4	0.280	2.343	$2.03^{+2.80}_{-0.58}$	$5.2^{+3.3}_{-2.5}$	$13.9^{+9.6}_{-9.6}$	< 3.7	< 9.0	$1.75^{+1.90}_{-0.42}$	< 6.6	< 16	1211
092510.0-014830	5079	141.2918	-1.8085	7.3	71.0	0.863	1.401	$12.1^{+1.8}_{-1.8}$	61^{+14}_{-11}	340^{+180}_{-110}	$10.6^{+2.1}_{-1.8}$	< 430	$7.3^{+13.2}_{-4.0}$	$38.4^{+14.4}_{-9.8}$	162^{+104}_{-56}	1819
092511.8-011436	9471	141.2993	-1.2436	12.3	24.7	0.419	1.893	$2.68^{+2.91}_{-0.93}$	$12.5^{+4.2}_{-2.1}$	$35.0^{+15.2}_{-7.7}$	$5.25^{+1.46}_{-0.97}$	$15.0^{+15.6}_{-6.0}$	$3.5^{+5.3}_{-1.6}$	$8.8^{+4.9}_{-2.0}$	$27.9^{+21.3}_{-8.4}$	1767
092522.1-013148	6653	141.3423	-1.5301	26.3	49.7	0.445	1.940	$1.61^{+0.46}_{-0.24}$	$27.3^{+4.4}_{-4.4}$	$62.3^{+10.6}_{-7.7}$	$9.0^{+1.4}_{-1.4}$	$14.9^{+5.3}_{-5.3}$	$1.59^{+0.67}_{-0.21}$	$21.7^{+4.4}_{-4.4}$	$49.1^{+10.4}_{-6.3}$	2192
092533.6-014205	1483	141.3903	-1.7016	51.0	150.6	0.229	0.815	$2.97^{+2.4}_{-1.7}$	$7.65^{+1.23}_{-0.83}$	$21.2^{+7.4}_{-3.3}$	$0.73^{+0.27}_{-0.27}$	$2.31^{+2.39}_{-0.80}$	$2.62^{+1.81}_{-1.21}$	$6.86^{+1.02}_{-0.82}$	$18.3^{+4.9}_{-1.8}$	2065
092546.3-014347	566	141.4432	-1.7298	197.1	480.2	0.228	3.813	$2.88^{+0.83}_{-0.74}$	$33.4^{+3.9}_{-3.8}$	$89.8^{+11.2}_{-10.1}$	$12.3^{+1.9}_{-1.5}$	$36.0^{+9.2}_{-9.4}$	$2.87^{+0.95}_{-0.55}$	$23.3^{+4.0}_{-3.9}$	$62.5^{+7.8}_{-8.4}$	2008
092548.9-011725	5488	141.4539	-1.2903	12.0	18.4	0.337	2.390	$2.25^{+0.74}_{-0.37}$	$23.8^{+3.6}_{-3.4}$	$59.6^{+10.1}_{-8.9}$	$9.6^{+1.6}_{-1.4}$	$22.3^{+9.7}_{-5.0}$	$2.37^{+0.83}_{-0.40}$	$20.6^{+3.4}_{-3.6}$	$52.3^{+9.7}_{-9.7}$	1718
092553.3+015519	991	141.4724	+1.9220	11.3	33.3	0.231	3.126	$2.58^{+0.24}_{-0.82}$	< 4.4	< 15	< 4.0	< 18	$2.9^{+6.4}_{-0.0}$	< 3.0	< 9.8	1129
092555.6-004311	6732	141.4820	+0.7199	64.5	88.9	0.255	3.279	$4.2^{+1.1}_{-1.1}$	$33.2^{+3.6}_{-2.8}$	106^{+49}_{-17}	$14.5^{+2.1}_{-2.0}$	61^{+75}_{-18}	$4.5^{+3.1}_{-1.6}$	$29.7^{+3.6}_{-2.5}$	96^{+34}_{-17}	1184
092619.9+021207	8160	141.5830	+2.2022	23.4	32.5	0.493	2.104	$11.1^{+12.7}_{-7.9}$	$30.5^{+6.3}_{-6.3}$	154^{+99}_{-61}	$12.0^{+2.1}_{-2.1}$	< 470	$5.9^{+10.5}_{-3.0}$	$24.7^{+5.3}_{-4.9}$	92^{+62}_{-28}	1131
092621.3-003356	4366	141.5890	-0.5657	10.1	63.4	0.340	2.118	$3.6^{+9.0}_{-1.2}$	$12.5^{+2.9}_{-2.9}$	40^{+29}_{-29}	$4.5^{+1.2}_{-1.0}$	$17.0^{+42.0}_{-7.3}$	$4.9^{+9.7}_{-1.5}$	$7.8^{+3.0}_{-2.3}$	27^{+10}_{-10}	1229
092629.3+032614	2050	141.6225	+3.4374	19.7	117.5	0.088	4.336	$1.020^{+0.060}_{-0.068}$	$2.45^{+0.36}_{-0.43}$	$4.74^{+0.73}_{-0.85}$	$1.07^{+0.21}_{-0.20}$	$1.08^{+0.25}_{-0.22}$	$1.10^{+0.23}_{-0.11}$	$1.62^{+0.36}_{-0.42}$	$3.26^{+0.83}_{-0.85}$	1152
092631.0-014511	2967	141.6295	+1.7533	31.8	100.0	0.761	1.834	$9.2^{+4.6}_{-4.6}$	124^{+21}_{-18}	580^{+350}_{-150}	$24.8^{+3.5}_{-3.0}$	220^{+320}_{-110}	$13.4^{+10.7}_{-10.7}$	84^{+18}_{-15}	470^{+230}_{-160}	1152
092639.7+040733	3560	141.6655	+4.1260	7.7	34.5	0.245	2.290	$6.2^{+15.5}_{-3.5}$	$11.2^{+2.3}_{-2.3}$	44^{+42}_{-15}	$3.8^{+1.0}_{-1.0}$	< 140	$16.2^{+9.3}_{-9.7}$	< 13	< 100	1184
092644.0+040010	9238	141.6834	+4.0029	11.1	29.5	0.347	2.128	$2.59^{+2.39}_{-0.85}$	$20.0^{+4.0}_{-4.0}$	$54.0^{+21.2}_{-8.9}$	$7.6^{+1.5}_{-1.1}$	$20.4^{+20.5}_{-2.6}$	$3.6^{+5.1}_{-1.5}$	$17.0^{+4.0}_{-2.6}$	52^{+31}_{-11}	1171
092647.5-050032	137	141.6980	+5.0091	505.4	1395.7	0.455	3.422	$6.5^{+1.7}_{-1.6}$	319^{+26}_{-24}	1220^{+190}_{-190}	$61.3^{+5.7}_{-5.5}$	400^{+126}_{-120}	$7.3^{+3.1}_{-3.1}$	205^{+26}_{-25}	840^{+210}_{-140}	1330
092647.5+030946	12965	141.6981	+3.1630	16.2	16.0	0.226	2.851	$3.2^{+3.7}_{-3.7}$	$5.0^{+1.9}_{-1.9}$	$14.7^{+7.5}_{-7.5}$	$3.16^{+0.89}_{-0.97}$	$10.0^{+13.7}_{-4.6}$	$3.2^{+2.9}_{-2.9}$	$3.9^{+1.3}_{-1.6}$	$11.0^{+8.5}_{-4.5}$	1135
092648.0+050124	6875	141.7002	+5.0234	16.0	26.5	0.454	2.542	$6.2^{+2.0}_{-1.3}$	115^{+37}_{-37}	442^{+144}_{-144}	$27.8^{+5.2}_{-4.4}$	174^{+66}_{-66}	$5.4^{+1.5}_{-1.5}$	88^{+27}_{-19}	312^{+97}_{-74}	1331
092650.5-035755	671	141.7106	+3.9654	33.0	304.8	0.377	2.594	$2.27^{+0.52}_{-0.43}$	$45.1^{+10.1}_{-5.0}$	111^{+25}_{-14}	$7.4^{+3.6}_{-2.3}$	$16.8^{+9.4}_{-6.0}$	$2.37^{+1.78}_{-0.56}$	$14.7^{+9.1}_{-5.3}$	39^{+26}_{-15}	1166
092711.5+011735	10285	141.7981	+1.2933	7.5	25.8	0.613	1.558	$12.5^{+12.5}_{-7.1}$	$33.4^{+7.2}_{-7.1}$	190^{+102}_{-50}	$10.1^{+1.9}_{-1.9}$	< 400	$11.1^{+12.8}_{-5.3}$	$29.1^{+6.7}_{-6.7}$	149^{+95}_{-53}	1209
092735.3+014423	266	141.8974	+1.7399	32.9	43.2	0.149	4.171	$4.7^{+8.0}_{-2.9}$	$8.2^{+1.0}_{-1.0}$	$27.0^{+20.5}_{-2.6}$	$4.42^{+0.56}_{-0.52}$	$20.6^{+40.4}_{-9.8}$	$4.8^{+8.7}_{-2.4}$	$6.06^{+1.13}_{-0.80}$	$20.8^{+15.6}_{-5.4}$	1205
092737.7+020607	1924	141.9074	+2.1021	106.4	191.5	0.419	2.793	$3.7^{+2.7}_{-2.2}$	$90.2^{+8.1}_{-8.1}$	266^{+85}_{-85}	$27.5^{+3.9}_{-3.4}$	101^{+33}_{-33}	$3.7^{+2.4}_{-2.4}$	$74.7^{+7.6}_{-7.6}$	221^{+51}_{-51}	1191
092739.7-010427	2636	141.9158	-1.0743	34.8	47.3	0.329	2.747	$18.0^{+9.2}_{-9.0}$	$34.0^{+4.6}_{-3.6}$	242^{+83}_{-87}	$15.4^{+3.0}_{-2.2}$	< 610	$15.0^{+11.4}_{-7.4}$	$29.9^{+4.7}_{-3.3}$	190^{+81}_{-65}	1232

continued.

Cluster (eFEDS J+)	ID_SRC	RA (deg)	Dec (deg)	$\mathcal{L}_{ext}$	$\mathcal{L}_{det}$	z	R_{500} (arcmin)	T (keV)	L_X (10^{42} erg s^{-1})	L_{bol} (10^{42} erg s^{-1})	M_{gas} (10^{12} M$_\odot$)	Y_X (10^{12} M$_\odot$ keV)	T_{cex} (keV)	$L_{X,cex}$ (10^{42} erg s^{-1})	$L_{bol,cex}$ (10^{42} erg s^{-1})	t_{exp} (s)
092740.1-002922	3454	141.9171	-0.4897	11.4	77.7	0.138	3.308	$1.88^{+0.76}_{-1.3}$	$3.25^{+0.63}_{-0.44}$	$7.8^{+1.9}_{-1.3}$	$1.62^{+0.34}_{-0.30}$	$3.07^{+1.67}_{-0.98}$	$2.19^{+2.22}_{-0.58}$	$1.91^{+0.60}_{-0.50}$	$4.9^{+2.0}_{-1.4}$	1230
092740.1+042038	4999	141.9173	+4.3440	6.2	21.4	0.275	2.929	$1.82^{+0.94}_{-0.46}$	$8.9^{+3.6}_{-3.6}$	$21.2^{+9.3}_{-8.4}$	$5.9^{+1.6}_{-1.3}$	$11.0^{+6.5}_{-3.2}$	$2.16^{+1.17}_{-0.43}$	$8.3^{+3.5}_{-3.3}$	$21.0^{+9.4}_{-8.4}$	1151
092740.7-015320	7063	141.9196	-1.8889	16.1	41.4	0.332	2.362	$10.4^{+11.9}$	$12.5^{+2.3}_{-1.8}$	63^{+37}_{-24}	$5.9^{+1.2}_{-1.0}$	<210	$10.7^{+12.1}_{-7.3}$	$8.7^{+2.1}_{-1.7}$	43^{+29}_{-18}	1443
092744.6+045630	17315	141.9360	+4.9418	11.3	9.6	0.355	2.192	$1.32^{+1.14}$	$6.3^{+2.7}$	$14.1^{+6.3}$	<5.3	<11	$1.18^{+0.69}$	<8.7	<19	1281
092755.9+000439	10316	141.9829	+0.0778	10.9	21.9	0.983	1.384	$1.53^{+1.78}$	126^{+85}	300^{+149}	$17.6^{+4.4}$	$26.8^{+18.9}_{-8.9}$	$2.3^{+3.3}_{-0.20}$	84^{+51}	231^{+106}	1229
092803.4+010953	1527	142.0142	+1.1648	13.0	163.7	0.552	1.987	$2.59^{+2.50}_{-9.57}$	$70.4^{+12.8}$	191^{+35}	$13.2^{+4.0}_{-3.0}$	35^{+53}_{-12}	$3.0^{+5.1}$	$34.3^{+13.9}_{-9.2}$	101^{+56}_{-30}	1228
092807.5-001353	13561	142.0314	-0.2316	9.5	25.9	0.771	1.390	$1.24^{+0.95}$	48^{+31}	104^{+47}	<15	<25	$1.45^{+1.14}_{-1.64}$	<99	<210	1228
092807.7-012704	6687	142.0323	-1.4512	6.8	28.9	1.304	1.145	$10.4^{+14.4}$	<150	<810	<17	<310	$10.9^{+6.9}_{-10.6}$	<110	<590	1543
092813.0-004508	13305	142.0544	-0.7524	7.8	16.9	0.318	1.942	$3.1^{+2.6}_{-1.0}$	$13.6^{+2.4}_{-2.5}$	$38.9^{+16.6}_{-8.5}$	$5.04^{+1.07}_{-0.86}$	$15.6^{+21.8}_{-5.8}$	$3.5^{+1.3}$	$11.7^{+2.4}_{-2.4}$	$35.9^{+21.8}_{-9.2}$	1228
092821.1+041941	7167	142.0880	+4.3283	8.3	20.4	0.157	2.929	$3.26^{+0.89}$	<3.5	<10	<2.3	<8.5	$3.30^{+1.46}$	<3.1	<8.6	1135
092821.2+042149	666	142.0884	+4.3637	113.0	375.3	0.235	3.863	$2.21^{+0.33}_{-0.26}$	$43.4^{+3.6}_{-4.2}$	$106.0^{+10.0}_{-10.7}$	$14.4^{+1.6}_{-1.5}$	$31.6^{+6.3}_{-5.5}$	$2.08^{+3.7}_{-0.22}$	$29.2^{+3.7}_{-5.3}$	$70.8^{+9.5}_{-12.4}$	1136
092828.3-000955	845	142.1180	-0.1653	7.1	22.9	0.509	1.703	$16.4^{+8.9}$	$23.9^{+8.9}$	149^{+84}_{-59}	$8.7^{+2.5}_{-2.1}$	<340	$15.5^{+10.8}$	$20.1^{+10.8}_{-6.0}$	127^{+82}_{-53}	1229
092832.4-041517	4192	142.1354	+4.2548	16.4	53.8	0.440	2.053	$17.9^{+8.0}$	$20.9^{+9.5}$	141^{+87}	$8.3^{+2.1}$	<330	$18.5^{+8.5}_{-8.5}$	<27	<210	1136
092844.0+005318	8858	142.1835	+0.8885	8.9	26.9	0.318	2.018	$2.38^{+1.68}_{-0.87}$	$13.1^{+2.5}_{-2.2}$	$33.5^{+6.6}$	$4.97^{+1.04}_{-0.90}$	$11.9^{+8.5}_{-4.7}$	$2.20^{+4.09}_{-0.75}$	$11.0^{+2.7}_{-2.3}$	$28.9^{+14.2}_{-7.1}$	1225
092846.5+000056	10287	142.1940	+0.0157	19.8	38.4	0.344	2.650	$1.45^{+0.41}_{-0.88}$	$25.6^{+5.0}$	56^{+13}_{-19}	$11.0^{+2.1}$	$16.5^{+11.2}$	$2.6^{+2.7}$	$21.3^{+4.3}$	56^{+20}_{-12}	1226
092859.0+040532	4029	142.2462	+4.0923	52.6	113.0	0.259	3.325	$4.0^{+3.8}$	$24.8^{+2.3}$	76^{+24}_{-14}	$11.8^{+1.8}$	48^{+44}_{-17}	$4.7^{+7.3}$	$20.0^{+4.8}$	65^{+39}_{-12}	1152
092900.0-003920	5593	142.2502	-0.6557	6.1	44.5	0.503	1.722	12.1^{+13}	$20.0^{+7.0}$	113^{+70}_{-45}	$7.1^{+2.2}$	<290	$15.7^{+18.2}_{-9.5}$	$13.9^{+3.9}$	89^{+66}_{-40}	1232
092910.2-022034	5092	142.2925	+2.3429	19.0	57.9	0.440	2.178	$11.7^{+6.3}$	$25.1^{+5.6}_{-4.5}$	129^{+79}_{-47}	$6.6^{+1.6}_{-1.9}$	<260	$12.4^{+12.7}_{-8.0}$	$14.4^{+4.8}_{-4.7}$	74^{+51}_{-31}	1229
092911.0+021118	10090	142.2960	+2.1885	13.2	23.9	0.469	1.813	$3.6^{+12.4}$	<14	<54	<6.1	<34	$4.9^{+10.8}_{-2.6}$	<8.0	<31	1228
092915.2+002427	8178	143.2135	+0.4077	13.2	31.1	0.458	2.022	$3.2^{+2.1}$	$37.4^{+7.4}$	106^{+28}_{-21}	$12.0^{+2.2}_{-1.9}$	38^{+26}_{-13}	$3.2^{+10.6}$	$30.9^{+7.1}_{-7.0}$	95^{+70}_{-24}	1224
092915.7-001357	1549	143.3158	-0.2327	31.5	181.0	0.322	2.609	$1.70^{+0.52}$	$30.7^{+3.2}$	$70.4^{+8.5}$	$9.5^{+1.3}$	$16.4^{+5.0}_{-3.4}$	$1.54^{+0.53}_{-0.25}$	$18.7^{+7.0}$	$41.9^{+7.3}_{-6.8}$	1229
092918.3+044925	6602	143.3266	+4.8237	27.2	53.2	0.352	2.428	$3.3^{+3.2}$	$22.1^{+3.0}$	$64^{+8.6}$	$8.3^{+1.3}$	27^{+30}	$2.24^{+1.66}$	$17.5^{+2.8}$	$44.1^{+9.5}$	1238
092921.7+040040	609	143.3408	+4.0112	51.8	297.4	0.501	2.442	$5.3^{+1.3}$	91^{+12}	322^{+169}	$15.5^{+2.9}$	81^{+18}_{-34}	$4.8^{+7.9}$	$39.0^{+3.3}$	134^{+88}	1173
092928.3+042411	3563	142.3679	+4.4032	31.1	80.8	0.278	2.626	$2.49^{+4.76}_{-1.21}$	$15.4^{+2.1}$	$39.9^{+9.2}$	$5.5^{+1.2}$	$14.0^{+10.1}_{-4.8}$	$2.43^{+4.84}$	$9.9^{+2.2}_{-2.1}$	$26.5^{+15.2}$	1157
092941.7+023026	7770	142.4238	+2.5072	7.3	26.3	0.544	1.620	$8.2^{+14.1}_{-4.3}$	$27.5^{+6.6}$	125^{+91}	$8.3^{+2.0}$	<300	$10.1^{+12.9}$	25.8^{+62}	128^{+83}	1228
092953.5+002801	12565	142.4732	+0.4670	8.4	22.4	0.147	2.829	$1.77^{+1.10}$	$2.81^{+0.36}$	$6.6^{+1.4}$	$1.56^{+0.32}$	$2.82^{+1.79}$	$2.43^{+2.02}$	$2.39^{+0.42}$	$6.3^{+3.1}$	1227
092955.8-003403	1967	142.4829	-0.5676	39.4	137.1	0.150	3.765	$2.23^{+0.78}$	$8.51^{+0.83}$	$21.1^{+3.1}$	$3.88^{+0.64}$	$8.9^{+3.95}$	$2.05^{+0.88}$	$6.0^{+1.1}$	$14.6^{+2.9}$	1234
093003.3+035630	288	142.5140	+3.9417	82.1	593.1	0.327	3.151	$3.47^{+2.34}$	$60.8^{+5.0}_{-4.8}$	177^{+43}	$10.8^{+3.8}$	39^{+27}	$4.2^{+2.5}$	$23.6^{+5.2}_{-4.2}$	74^{+24}_{-16}	1210
093009.0+040144	536	142.5376	+4.0289	76.4	376.0	0.328	2.977	$4.0^{+1.4}$	$50.0^{+6.1}$	156^{+102}	$10.5^{+3.4}$	42^{+76}	$7.4^{+10.8}$	$21.0^{+7.2}_{-5.5}$	91^{+64}_{-33}	1210
093011.2+031648	16215	142.5470	+3.2801	23.3	18.4	0.724	1.692	$5.0^{+10.5}_{-2.9}$	36^{+19}	130^{+95}	<16	<140	$3.9^{+7.9}$	<52	<170	1231
093012.0+030202	7539	142.5503	+3.0340	11.1	29.2	0.223	2.408	$3.6^{+13.4}_{-1.9}$	$3.12^{+1.48}$	$10.9^{+10.6}$	$1.24^{+0.54}_{-0.52}$	<35	$4.1^{+10.1}_{-3.6}$	<3.5	<16	1232
093022.1+021835	8763	142.5921	+2.3100	7.4	26.2	0.547	1.736	$6.9^{+9.9}_{-2.2}$	57^{+15}_{-22}	236^{+119}	$13.5^{+3.2}$	90^{+114}_{-39}	$6.3^{+6.6}$	<77	<370	1229
093025.3+021714	1003	142.6055	+2.2872	77.5	252.3	0.546	2.446	$6.8^{+6.5}_{-17}$	156^{+16}	630^{+240}_{-110}	$35.7^{+4.4}_{-5.3}$	243^{+232}_{-77}	$6.5^{+6.5}$	116^{+16}_{-13}	452^{+193}_{-83}	1231
093025.7-020507	1064	142.6072	-2.0856	34.6	80.4	0.220	2.916	$11.3^{+10.9}$	$8.87^{+0.97}$	46^{+26}	$4.71^{+0.70}_{-0.59}$	<170	$14.4^{+14.0}$	$7.00^{+1.45}_{-0.97}$	41^{+22}_{-17}	1789
093049.2-003714	1823	142.7052	-0.6207	30.1	78.2	0.334	2.714	$4.1^{+3.8}$	$39.4^{+5.0}$	125^{+45}	$14.0^{+1.9}$	58^{+55}_{-18}	$4.0^{+5.4}$	$31.0^{+5.1}$	98^{+47}_{-20}	1229
093056.9+034825	4579	142.7372	+3.8072	12.3	55.6	0.090	3.965	$1.37^{+0.26}_{-0.25}$	$1.55^{+0.39}_{-0.25}$	$3.31^{+0.87}_{-0.88}$	$0.84^{+0.20}_{-0.22}$	$1.12^{+0.46}_{-0.34}$	$0.99^{+0.59}_{-0.36}$	$1.05^{+0.36}_{-0.37}$	$2.09^{+0.74}_{-0.74}$	1233
093117.4-015643	11648	142.8228	-1.9455	13.3	18.6	0.199	2.397	$2.9^{+2.7}_{-1.0}$	$0.76^{+0.64}$	$2.19^{+1.87}_{-0.96}$	$0.64^{+0.41}_{-0.24}$	<6.3	$5.5^{+6.4}$	<1.5	<5.7	2240
093138.7-020933	5201	142.9115	-2.1593	42.7	62.5	0.245	2.631	$1.92^{+0.86}_{-0.33}$	$7.5^{+1.3}_{-1.5}$	$18.1^{+4.1}_{-3.6}$	$3.68^{+0.43}_{-0.69}$	$7.3^{+3.9}$	$2.00^{+1.18}_{-0.5}$	$5.6^{+1.3}_{-1.4}$	$13.7^{+3.9}_{-3.6}$	2462
093141.2-004717	1705	142.9219	-0.7883	13.7	30.5	0.093	4.644	$1.02^{+0.28}_{-0.21}$	$1.27^{+0.39}_{-0.41}$	$2.51^{+0.85}_{-0.85}$	<1.3	<1.3	$1.11^{+0.29}_{-0.26}$	<1.3	<2.6	1230

continued.

Cluster (eFEDS J+)	ID_SRC	RA (deg)	Dec (deg)	$\mathcal{L}_{ext}$	$\mathcal{L}_{det}$	z	R_{500} (arcmin)	T (keV)	L_X (10^{42} erg s^{-1})	L_{bol} (10^{42} erg s^{-1})	M_{gas} (10^{12} M$_\odot$)	Y_X (10^{12} M$_\odot$ keV)	T_{cex} (keV)	$L_{X,cex}$ (10^{42} erg s^{-1})	$L_{bol,cex}$ (10^{42} erg s^{-1})	t_{exp} (s)
093149.8-020143	6494	142.9576	-2.0289	27.5	39.9	0.134	3.094	$1.040^{+0.100}_{-0.067}$	$2.15^{+0.36}_{-0.41}$	$4.21^{+0.76}_{-0.81}$	$1.18^{+0.26}_{-0.24}$	$1.24^{+0.32}_{-0.29}$	$1.05^{+0.17}_{-0.13}$	$1.76^{+0.36}_{-0.43}$	$3.45^{+0.78}_{-0.85}$	2483
093151.3-002212	836	142.9638	-0.3701	54.0	307.1	0.336	2.824	$2.27^{+0.67}_{-0.61}$	$48.1^{+4.2}_{-4.3}$	119^{+12}_{-12}	$12.2^{+2.4}_{-2.2}$	$27.8^{+8.6}_{-8.6}$	$2.02^{+0.47}_{-0.28}$	$27.6^{+4.1}_{-4.3}$	66^{+11}_{-11}	1236
093207.5-021317	1674	143.0316	-2.2215	36.1	133.5	0.666	1.648	$3.00^{+4.40}_{-0.38}$	$49.0^{+10.0}_{-4.5}$	141^{+12}_{-30}	$10.7^{+2.0}_{-2.3}$	32^{+43}_{-12}	$3.3^{+3.2}_{-0.28}$	$29.7^{+9.9}_{-13.2}$	85^{+37}_{-36}	2463
093222.0+012412	7346	143.0918	+1.4035	6.1	32.0	0.536	1.613	$6.9^{+11.2}_{-0.90}$	$13.6^{+3.0}_{-3.5}$	56^{+47}_{-30}	< 6.8	< 76	$8.2^{+12.3}_{-5.7}$	< 20	< 85	1230
093231.0+010617	4873	143.1293	+1.1050	22.2	56.4	0.644	1.772	$2.60^{+1.77}_{-0.98}$	72^{+12}_{-12}	189^{+41}_{-41}	$13.9^{+3.3}_{-3.3}$	36^{+23}_{-12}	$3.0^{+3.7}_{-5.2}$	50^{+12}_{-12}	141^{+51}_{-34}	1230
093232.8-015152	10734	143.1367	-1.8647	8.0	24.9	0.553	1.516	$5.6^{+14}_{-3.4}$	$14.2^{+5.7}_{-5.8}$	52^{+39}_{-22}	$5.3^{+3.5}_{-1.8}$	< 160	$10.7^{+10.5}_{-6.7}$	$11.0^{+4.4}_{-5.3}$	< 150	2134
093253.8+025917	5631	143.2244	+2.9882	7.2	23.7	0.093	4.279	8.9^{+51}_{-116}	$0.194^{+0.164}_{-0.093}$	< 2.8	< 0.31	< 3.8	$8.3^{+0.8}_{-0.8}$	< 0.19	< 0.91	1234
093301.3+024301	12582	143.2558	+2.7170	10.4	16.2	0.838	1.345	$12.0^{+8.3}_{-11.9}$	$21.4^{+10.3}_{-9.4}$	108^{+84}_{-52}	< 11	< 260	$10.6^{+15.1}_{-5.1}$	< 38	< 240	1234
093302.7-010145	5763	143.2616	-1.0292	45.3	66.4	0.356	2.676	$3.8^{+1.5}_{-5.2}$	$28.1^{+5.4}_{-4.0}$	87^{+47}_{-18}	$12.0^{+2.1}_{-1.7}$	45^{+74}_{-17}	$3.6^{+6.4}_{-1.3}$	$22.4^{+5.0}_{-3.9}$	69^{+38}_{-15}	1232
093316.6+004619	13784	143.3195	+0.7721	9.2	21.2	0.347	2.457	$5.5^{+14.3}_{-3.5}$	< 8.2	< 39	< 6.3	< 66	$8.1^{+15.6}_{-5.4}$	< 6.3	< 33	1230
093329.3+000334	5618	143.3725	+0.0596	14.3	43.6	0.395	2.104	$3.2^{+2.5}_{-3.5}$	$21.7^{+3.6}_{-3.9}$	63^{+31}_{-13}	$7.6^{+1.5}_{-1.5}$	$24.0^{+41.7}_{-8.5}$	$5.0^{+3.3}_{-2.6}$	$16.2^{+3.3}_{-3.7}$	54^{+38}_{-15}	1230
093332.1+020933	6577	143.3841	+2.1594	6.7	24.9	0.838	1.373	$8.8^{+11.4}_{-5.4}$	61^{+25}_{-20}	270^{+180}_{-100}	$10.7^{+3.4}_{-3.4}$	< 350	$10.6^{+11.7}_{-5.1}$	40^{+19}_{-19}	189^{+147}_{-91}	1231
093403.5-001422	900	143.5148	-0.2397	79.7	279.5	0.240	3.533	$2.13^{+0.62}_{-0.27}$	$31.7^{+4.7}_{-3.2}$	$78.1^{+9.0}_{-9.0}$	$11.2^{+1.5}_{-1.2}$	$24.5^{+7.2}_{-4.7}$	$2.48^{+1.48}_{-0.61}$	$20.8^{+3.5}_{-2.9}$	$54.4^{+12.9}_{-9.0}$	1226
093431.3-002309	1641	143.6304	-0.3860	35.5	87.4	0.342	2.815	$4.7^{+11.5}_{-1.8}$	$57.0^{+5.6}_{-5.2}$	187^{+173}_{-35}	$18.1^{+2.5}_{-2.2}$	82^{+228}_{-32}	$4.7^{+7.7}_{-2.2}$	$44.7^{+5.6}_{-5.4}$	147^{+96}_{-32}	1103
093436.1+051533	9995	143.6508	+5.2594	22.6	36.6	0.341	3.141	$9.3^{+10.2}_{-4.8}$	$48.3^{+8.6}_{-8.6}$	223^{+137}_{-72}	$19.5^{+3.8}_{-3.7}$	< 640	$10.5^{+13.1}_{-6.9}$	$38.3^{+8.4}_{-9.0}$	183^{+133}_{-73}	336
093456.1+031518	7091	143.7340	+3.2552	16.6	32.9	0.085	4.207	$0.61^{+0.24}_{-0.25}$	$0.645^{+0.141}_{-0.090}$	$1.31^{+0.50}_{-0.25}$	$0.206^{+0.059}_{-0.049}$	$0.116^{+0.057}_{-0.036}$	$0.61^{+0.46}_{-0.27}$	$0.250^{+0.087}_{-0.076}$	$0.59^{+0.45}_{-0.22}$	1238
093500.7+005417	649	143.7532	+0.9048	104.4	330.3	0.361	2.973	$3.10^{+0.91}_{-0.54}$	$77.8^{+6.7}_{-6.7}$	214^{+27}_{-23}	$17.4^{+2.5}_{-2.1}$	54^{+18}_{-11}	$4.1^{+2.6}_{-1.0}$	$46.5^{+6.5}_{-6.0}$	145^{+39}_{-24}	1243
093513.0+004757	213	143.8046	+0.7994	332.8	836.9	0.356	4.104	$7.3^{+3.6}_{-3.6}$	249^{+37}_{-94}	980^{+330}_{-330}	$62.7^{+7.4}_{-7.1}$	420^{+260}_{-260}	$5.6^{+3.0}_{-1.5}$	187^{+79}_{-79}	650^{+180}_{-260}	1233
093520.7+003448	4394	143.8363	+0.5802	15.3	65.7	0.355	2.308	$2.15^{+1.13}_{-1.13}$	$28.8^{+4.4}_{-4.0}$	72^{+14}_{-10}	$9.8^{+1.6}_{-1.4}$	$21.6^{+10.7}_{-4.9}$	$2.43^{+1.49}_{-0.59}$	$22.7^{+4.6}_{-4.4}$	59^{+14}_{-12}	1174
093520.9+023234	82	143.8374	+2.5429	175.9	1645.8	0.516	2.977	$4.45^{+1.47}_{-1.47}$	373^{+26}_{-25}	1190^{+170}_{-110}	$54.2^{+5.4}_{-5.3}$	237^{+85}_{-85}	$7.0^{+3.5}_{-3.5}$	185^{+24}_{-24}	740^{+210}_{-130}	1236
093522.2+032329	1242	143.8427	+3.3915	86.3	248.3	0.324	3.120	$2.43^{+0.67}_{-0.43}$	$49.2^{+4.1}_{-4.1}$	125^{+15}_{-10}	$15.4^{+2.0}_{-2.0}$	$37.6^{+12.4}_{-12.4}$	$2.71^{+0.70}_{-0.70}$	$33.4^{+2.1}_{-2.1}$	88^{+14}_{-14}	1237
093525.6+023445	12009	143.8570	+2.5793	35.4	39.7	0.503	2.272	$2.87^{+0.80}_{-0.66}$	$58.3^{+10.5}_{-8.2}$	156^{+33}_{-23}	$19.7^{+3.5}_{-3.5}$	56^{+27}_{-14}	$3.05^{+0.93}_{-0.91}$	$51.7^{+10.2}_{-7.0}$	143^{+30}_{-21}	1236
093525.9+035101	3773	143.8580	+3.8503	6.2	31.6	1.261	1.162	$2.8^{+1.5}_{-1.5}$	162^{+85}_{-85}	490^{+200}_{-200}	$16.7^{+3.4}_{-3.4}$	47^{+34}_{-19}	$1.85^{+1.93}_{-1.93}$	151^{+69}_{-69}	400^{+210}_{-210}	1241
093531.4+022710	2609	143.8811	+2.4530	36.6	95.3	0.225	2.976	$3.05^{+1.78}_{-0.84}$	$12.7^{+1.3}_{-1.3}$	$34.6^{+18.2}_{-8.5}$	$5.21^{+0.97}_{-0.77}$	$15.7^{+10.6}_{-5.1}$	$3.7^{+4.3}_{-1.4}$	$8.8^{+1.3}_{-1.3}$	$26.7^{+12.7}_{-5.6}$	1241
093544.2-000339	6324	143.9342	-0.0609	20.5	51.9	0.347	2.565	$5.0^{+2.9}_{-0.89}$	$27.6^{+6.5}_{-5.6}$	95^{+52}_{-25}	$10.7^{+2.5}_{-2.5}$	52^{+66}_{-23}	$5.0^{+7.4}_{-2.2}$	$20.9^{+7.4}_{-5.6}$	76^{+47}_{-24}	829
093546.3-000115	1761	143.9433	-0.0211	19.8	146.8	0.339	2.611	$4.7^{+4.2}_{-1.7}$	$43.8^{+10.2}_{-7.3}$	144^{+59}_{-35}	$12.3^{+2.3}_{-2.3}$	57^{+59}_{-23}	$5.9^{+8.0}_{-2.6}$	$26.0^{+7.5}_{-7.1}$	98^{+58}_{-31}	833
093612.7+001650	4455	144.0529	+0.2807	17.0	58.5	0.358	2.402	$1.82^{+1.71}_{-0.33}$	$38.1^{+5.3}_{-5.4}$	92^{+19}_{-14}	$11.9^{+1.8}_{-1.7}$	$22.6^{+20.0}_{-5.7}$	$1.92^{+2.01}_{-0.44}$	$30.3^{+5.7}_{-5.0}$	75^{+20}_{-14}	802
093630.8+031838	4848	144.1287	+3.3106	11.5	57.1	0.405	2.203	$2.38^{+2.68}_{-0.90}$	< 14	< 38	< 8.6	< 30	$2.39^{+4.19}_{-0.92}$	< 12	< 33	1242
093707.4+034831	11748	144.2810	+3.8089	12.6	28.7	0.279	2.503	$3.5^{+5.7}_{-1.5}$	$10.4^{+1.6}_{-1.8}$	$30.7^{+17.2}_{-6.8}$	$5.21^{+0.99}_{-1.00}$	$18.1^{+30.4}_{-8.0}$	$2.40^{+6.63}_{-0.77}$	$8.6^{+1.6}_{-1.9}$	$23.0^{+14.8}_{-5.6}$	1239
093709.7+014143	6251	144.2908	+1.6954	27.9	50.0	0.377	2.428	$1.80^{+0.66}_{-0.39}$	$51.1^{+6.1}_{-6.1}$	119^{+16}_{-16}	$15.2^{+2.0}_{-1.9}$	$28.1^{+10.8}_{-7.4}$	$2.62^{+2.90}_{-0.77}$	$41.6^{+5.1}_{-6.3}$	110^{+30}_{-18}	1042
093712.8+031651	38	144.3036	+3.2810	19.7	26.0	0.247	2.469	$3.3^{+12.9}_{-4.3}$	$12.7^{+2.2}_{-2.2}$	$37.1^{+47.4}_{-8.5}$	$0.25^{+0.25}_{-0.11}$	< 7.9	$2.11^{+3.62}_{-0.52}$	< 0.47	< 1.3	1238
093742.8+033841	6038	144.4285	+3.6450	19.4	48.0	0.620	1.767	$1.63^{+1.16}_{-3.0}$	69^{+17}_{-15}	159^{+36}_{-36}	$13.7^{+3.0}_{-3.3}$	$22.9^{+15.7}_{-8.1}$	$1.69^{+0.85}_{-0.54}$	52^{+17}_{-14}	118^{+38}_{-31}	1247
093744.1+024536	3372	144.4341	+2.7600	11.8	66.6	0.024	8.111	$0.282^{+0.144}_{-0.038}$	$0.071^{+0.016}_{-0.015}$	$0.25^{+0.15}_{-0.11}$	< 0.10	< 0.03	$0.269^{+0.083}_{-0.036}$	< 0.04	< 0.19	1187
093830.5+041523	10322	144.6272	+4.2564	20.8	37.7	0.262	2.559	$3.4^{+5.0}_{-2.0}$	$13.0^{+2.0}_{-2.1}$	$37.0^{+20.6}_{-8.0}$	$6.08^{+1.13}_{-0.98}$	$19.8^{+33.5}_{-9.6}$	$3.4^{+6.7}_{-1.7}$	$11.5^{+1.9}_{-1.7}$	$34.1^{+21.2}_{-8.4}$	1366
093938.3+042218	1594	144.9096	+4.3717	65.2	164.9	0.369	2.717	$3.9^{+4.4}_{-4.3}$	$50.1^{+4.8}_{-4.8}$	153^{+63}_{-17}	$14.6^{+2.2}_{-1.9}$	57^{+69}_{-17}	$4.3^{+4.4}_{-1.5}$	$34.3^{+5.1}_{-4.6}$	111^{+42}_{-21}	1188
094005.9+031329	4689	145.0246	+3.2247	16.2	62.0	0.470	2.210	$5.4^{+16.4}_{-3.1}$	41^{+13}_{-10}	154^{+151}_{-54}	$7.9^{+3.4}_{-2.8}$	< 300	$5.8^{+11.4}_{-3.2}$	$17.3^{+12.0}_{-8.2}$	< 190	578
094007.3-035754	11337	145.0307	+3.9652	8.5	25.7	0.666	1.637	$3.8^{+8.6}_{-1.8}$	56^{+16}_{-13}	179^{+103}_{-46}	$13.7^{+2.7}_{-3.1}$	50^{+108}_{-23}	$2.52^{+4.46}_{-0.81}$	49^{+15}_{-14}	139^{+57}_{-42}	928

Notes. Electronic version of the table is available at the CDS. Column 1: cluster name. Column 2: unique source ID presented in the eFEDS source catalog (Brunner et al., 2022). Columns 3 and 4: RA and Dec. Columns 5 and 6: extent and detection likelihoods. Column 7: redshift. Column 8: R_{500} estimates calculated from the M_{500} measurements presented in (Chiu et al., 2022). Column 9: temperature measured within R_{500}. Column 10: soft band (0.5–2 keV) luminosity measured within R_{500}. Column 11: bolometric (0.01–100 keV) luminosity measured within R_{500}. Column 12: gas mass measured within R_{500}. Column 13: X-ray analog of integrated Compton-y parameter measured within R_{500}. Column 14: core-excised temperature measured between $0.15R_{500} - R_{500}$. Column 15: soft band (0.5–2 keV) core-excised luminosity measured between $0.15R_{500} - R_{500}$. Column 16: bolometric (0.01–100 keV) core-excised luminosity measured between $0.15R_{500} - R_{500}$. Column 17: unvignetted exposure time measured at the X-ray center of the cluster. X-ray observable measurements $< 2\sigma$ are presented as 2σ upper limits except T and T_{cex}.

Bibliography

K. N. Abazajian, P. Adshead, Z. Ahmed, S. W. Allen, D. Alonso, K. S. Arnold, C. Baccigalupi, J. G. Bartlett, N. Battaglia, B. A. Benson, C. A. Bischoff, J. Borrill, V. Buza, E. Calabrese, R. Caldwell, J. E. Carlstrom, C. L. Chang, T. M. Crawford, F.-Y. Cyr-Racine, F. De Bernardis, T. de Haan, S. di Serego Alighieri, J. Dunkley, C. Dvorkin, J. Errard, G. Fabbian, S. Feeney, S. Ferraro, J. P. Filippini, R. Flauger, G. M. Fuller, V. Gluscevic, D. Green, D. Grin, E. Grohs, J. W. Henning, J. C. Hill, R. Hlozek, G. Holder, W. Holzapfel, W. Hu, K. M. Huffenberger, R. Keskitalo, L. Knox, A. Kosowsky, J. Kovac, E. D. Kovetz, C.-L. Kuo, A. Kusaka, M. Le Jeune, A. T. Lee, M. Lilley, M. Loverde, M. S. Madhavacheril, A. Mantz, D. J. E. Marsh, J. McMahon, P. D. Meerburg, J. Meyers, A. D. Miller, J. B. Munoz, H. N. Nguyen, M. D. Niemack, M. Peloso, J. Peloton, L. Pogosian, C. Pryke, M. Raveri, C. L. Reichardt, G. Rocha, A. Rotti, E. Schaan, M. M. Schmittfull, D. Scott, N. Sehgal, S. Shandera, B. D. Sherwin, T. L. Smith, L. Sorbo, G. D. Starkman, K. T. Story, A. van Engelen, J. D. Vieira, S. Watson, N. Whitehorn, and W. L. Kimmy Wu. CMB-S4 Science Book, First Edition. arXiv e-prints, art. arXiv:1610.02743, Oct. 2016. doi: 10.48550/arXiv.1610.02743.

G. O. Abell. The Distribution of Rich Clusters of Galaxies. ApJS, 3:211, May 1958. doi: 10.1086/190036.

G. O. Abell, J. Corwin, Harold G., and R. P. Olowin. A Catalog of Rich Clusters of Galaxies. ApJS, 70:1, May 1989. doi: 10.1086/191333.

H. Aihara, N. Arimoto, R. Armstrong, S. Arnouts, N. A. Bahcall, S. Bickerton, J. Bosch, K. Bundy, P. L. Capak, J. H. H. Chan, M. Chiba, J. Coupon, E. Egami, M. Enoki, F. Finet, H. Fujimori, S. Fujimoto, H. Furusawa, J. Furusawa, T. Goto, A. Goulding, J. P. Greco, J. E. Greene, J. E. Gunn, T. Hamana, Y. Harikane, Y. Hashimoto, T. Hattori, M. Hayashi, Y. Hayashi, K. G. Hełminiak, R. Higuchi, C. Hikage, P. T. P. Ho, B.-C. Hsieh, K. Huang, S. Huang, H. Ikeda, M. Imanishi, A. K. Inoue, K. Iwasawa, I. Iwata, A. T. Jaelani, H.-Y. Jian, Y. Kamata, H. Karoji, N. Kashikawa, N. Katayama, S. Kawanomoto, I. Kayo, J. Koda, M. Koike, T. Kojima, Y. Komiyama, A. Konno, S. Koshida, Y. Koyama, H. Kusakabe, A. Leauthaud, C.-H. Lee, L. Lin, Y.-T. Lin, R. H. Lupton, R. Mandelbaum, Y. Matsuoka, E. Medezinski, S. Mineo, S. Miyama, H. Miyatake, S. Miyazaki, R. Momose, A. More, S. More, Y. Moritani, T. J. Moriya, T. Morokuma, S. Mukae, R. Murata, H. Murayama, T. Nagao, F. Nakata, M. Niida, H. Niikura, A. J. Nishizawa, Y. Obuchi, M. Oguri, Y. Oishi, N. Okabe, S. Okamoto, Y. Okura, Y. Ono, M. Onodera, M. Onoue, K. Osato, M. Ouchi, P. A. Price, T.-S. Pyo, M. Sako,

M. Sawicki, T. Shibuya, K. Shimasaku, A. Shimono, M. Shirasaki, J. D. Silverman, M. Simet, J. Speagle, D. N. Spergel, M. A. Strauss, Y. Sugahara, N. Sugiyama, Y. Suto, S. H. Suyu, N. Suzuki, P. J. Tait, M. Takada, T. Takata, N. Tamura, M. M. Tanaka, M. Tanaka, M. Tanaka, Y. Tanaka, T. Terai, Y. Terashima, Y. Toba, N. Tominaga, J. Toshikawa, E. L. Turner, T. Uchida, H. Uchiyama, K. Umetsu, F. Uraguchi, Y. Urata, T. Usuda, Y. Utsumi, S.-Y. Wang, W.-H. Wang, K. C. Wong, K. Yabe, Y. Yamada, H. Yamanoi, N. Yasuda, S. Yeh, A. Yonehara, and S. Yuma. The Hyper Suprime-Cam SSP Survey: Overview and survey design. PASJ, 70:S4, Jan. 2018. doi: 10.1093/pasj/psx066.

S. W. Allen, A. E. Evrard, and A. B. Mantz. Cosmological Parameters from Observations of Galaxy Clusters. ARA&A, 49(1):409–470, Sept. 2011. doi: 10.1146/annurev-astro-081710-102514.

E. Altamura, S. T. Kay, R. G. Bower, M. Schaller, Y. M. Bahé, J. Schaye, J. Borrow, and I. Towler. EAGLE-like simulation models do not solve the entropy core problem in groups and clusters of galaxies. MNRAS, 520(2):3164–3186, Apr. 2023. doi: 10.1093/mnras/stad342.

F. Andrade-Santos, G. W. Pratt, J.-B. Melin, M. Arnaud, C. Jones, W. R. Forman, E. Pointecouteau, I. Bartalucci, A. Vikhlinin, S. S. Murray, P. Mazzotta, S. Borgani, L. Lovisari, R. J. van Weeren, R. P. Kraft, L. P. David, and S. Giacintucci. Chandra Observations of the Planck Early Sunyaev-Zeldovich Sample: A Reexamination of Masses and Mass Proxies. ApJ, 914 (1):58, June 2021. doi: 10.3847/1538-4357/abf73e.

L. Arcangeli, G. Borghi, H. Bräuninger, O. Citterio, I. Ferrario, P. Friedrich, G. Grisoni, F. Marioni, P. Predehl, M. Rossi, A. Ritucci, G. Valsecchi, and D. Vernani. The eROSITA X-ray mirrors: technology and qualification aspects of the production of mandrels, shells and mirror modules. In Society of Photo-Optical Instrumentation Engineers (SPIE) Conference Series, volume 10565 of Society of Photo-Optical Instrumentation Engineers (SPIE) Conference Series, page 1056558, Nov. 2017. doi: 10.1117/12.2309182.

K. A. Arnaud. XSPEC: The First Ten Years. In G. H. Jacoby and J. Barnes, editors, Astronomical Data Analysis Software and Systems V, volume 101 of Astronomical Society of the Pacific Conference Series, page 17, Jan. 1996.

M. Arnaud, E. Pointecouteau, and G. W. Pratt. Calibration of the galaxy cluster $M\{500\}$-$Y\{X\}$ relation with XMM-Newton. A&A, 474(3):L37–L40, Nov. 2007. doi: 10.1051/0004-6361: 20078541.

M. Arnaud, G. W. Pratt, R. Piffaretti, H. Böhringer, J. H. Croston, and E. Pointecouteau. The universal galaxy cluster pressure profile from a representative sample of nearby systems (REXCESS) and the Y_{SZ} - M_{500} relation. A&A, 517:A92, July 2010. doi: 10.1051/0004-6361/200913416.

Y. Ascasibar, R. Sevilla, G. Yepes, V. Müller, and S. Gottlöber. Adiabatic scaling relations of galaxy clusters. MNRAS, 371(1):193–203, Sept. 2006. doi: 10.1111/j.1365-2966.2006.10596.x.

M. Asplund, N. Grevesse, A. J. Sauval, and P. Scott. The Chemical Composition of the Sun. ARA&A, 47:481–522, Sept. 2009. doi: 10.1146/annurev.astro.46.060407.145222.

M. Ayromlou, D. Nelson, and A. Pillepich. Feedback reshapes the baryon distribution within haloes, in halo outskirts, and beyond: the closure radius from dwarfs to massive clusters. MNRAS, 524(4):5391–5410, Oct. 2023. doi: 10.1093/mnras/stad2046.

A. Babul, M. L. Balogh, G. F. Lewis, and G. B. Poole. Physical implications of the X-ray properties of galaxy groups and clusters. MNRAS, 330(2):329–343, Feb. 2002. doi: 10.1046/j.1365-8711.2002.05044.x.

Y. E. Bahar, E. Bulbul, N. Clerc, V. Ghirardini, A. Liu, K. Nandra, F. Pacaud, I. N. Chiu, J. Comparat, J. Ider-Chitham, M. Klein, T. Liu, A. Merloni, K. Migkas, N. Okabe, M. E. Ramos-Ceja, T. H. Reiprich, J. S. Sanders, and T. Schrabback. The eROSITA Final Equatorial-Depth Survey (eFEDS). X-ray properties and scaling relations of galaxy clusters and groups. A&A, 661: A7, May 2022. doi: 10.1051/0004-6361/202142462.

Y. E. Bahar, E. Bulbul, V. Ghirardini, J. S. Sanders, X. Zhang, A. Liu, N. Clerc, E. Artis, F. Balzer, V. Biffi, S. Bose, J. Comparat, K. Dolag, C. Garrel, B. Hadzhiyska, C. Hernández-Aguayo, L. Hernquist, M. Kluge, S. Krippendorf, A. Merloni, K. Nandra, R. Pakmor, P. Popesso, M. Ramos-Ceja, R. Seppi, V. Springel, J. Weller, and S. Zelmer. The SRG/eROSITA All-Sky Survey: Constraints on AGN Feedback in Galaxy Groups. arXiv e-prints, art. arXiv:2401.17276, Jan. 2024. doi: 10.48550/arXiv.2401.17276.

M. L. Balogh, F. R. Pearce, R. G. Bower, and S. T. Kay. Revisiting the cosmic cooling crisis. MNRAS, 326(4):1228–1234, Oct. 2001. doi: 10.1111/j.1365-2966.2001.04667.x.

D. J. Barnes, S. T. Kay, M. A. Henson, I. G. McCarthy, J. Schaye, and A. Jenkins. The redshift evolution of massive galaxy clusters in the MACSIS simulations. MNRAS, 465(1):213–233, Feb. 2017. doi: 10.1093/mnras/stw2722.

P. Behroozi, R. H. Wechsler, A. P. Hearin, and C. Conroy. UNIVERSEMACHINE: The correlation between galaxy growth and dark matter halo assembly from z = 0-10. MNRAS, 488(3): 3143–3194, Sept. 2019. doi: 10.1093/mnras/stz1182.

A. J. Benson, R. G. Bower, C. S. Frenk, C. G. Lacey, C. M. Baugh, and S. Cole. What Shapes the Luminosity Function of Galaxies? ApJ, 599(1):38–49, Dec. 2003. doi: 10.1086/379160.

B. A. Benson, T. de Haan, J. P. Dudley, C. L. Reichardt, K. A. Aird, K. Andersson, R. Armstrong, M. L. N. Ashby, M. Bautz, M. Bayliss, G. Bazin, L. E. Bleem, M. Brodwin, J. E. Carlstrom, C. L. Chang, H. M. Cho, A. Clocchiatti, T. M. Crawford, A. T. Crites, S. Desai, M. A. Dobbs, R. J. Foley, W. R. Forman, E. M. George, M. D. Gladders, A. H. Gonzalez, N. W. Halverson, N. Harrington, F. W. High, G. P. Holder, W. L. Holzapfel, S. Hoover, J. D. Hrubes, C. Jones, M. Joy, R. Keisler, L. Knox, A. T. Lee, E. M. Leitch, J. Liu, M. Lueker, D. Luong-Van, A. Mantz, D. P. Marrone, M. McDonald, J. J. McMahon, J. Mehl, S. S. Meyer, L. Mocanu, J. J. Mohr, T. E. Montroy, S. S. Murray, T. Natoli, S. Padin, T. Plagge, C. Pryke, A. Rest, J. Ruel,

J. E. Ruhl, B. R. Saliwanchik, A. Saro, J. T. Sayre, K. K. Schaffer, L. Shaw, E. Shirokoff, J. Song, H. G. Spieler, B. Stalder, Z. Staniszewski, A. A. Stark, K. Story, C. W. Stubbs, R. Suhada, A. van Engelen, K. Vanderlinde, J. D. Vieira, A. Vikhlinin, R. Williamson, O. Zahn, and A. Zenteno. Cosmological Constraints from Sunyaev-Zel'dovich-selected Clusters with X-Ray Observations in the First 178 deg^2 of the South Pole Telescope Survey. ApJ, 763(2): 147, Feb. 2013. doi: 10.1088/0004-637X/763/2/147.

P. N. Best, A. von der Linden, G. Kauffmann, T. M. Heckman, and C. R. Kaiser. On the prevalence of radio-loud active galactic nuclei in brightest cluster galaxies: implications for AGN heating of cooling flows. MNRAS, 379(3):894–908, Aug. 2007. doi: 10.1111/j.1365-2966.2007.11937.x.

S. Bhattacharya, T. Di Matteo, and A. Kosowsky. Effects of quasar feedback in galaxy groups. MNRAS, 389(1):34–44, Sept. 2008. doi: 10.1111/j.1365-2966.2008.13555.x.

V. Biffi, F. Sembolini, M. De Petris, R. Valdarnini, G. Yepes, and S. Gottlöber. The MUSIC of galaxy clusters - II. X-ray global properties and scaling relations. MNRAS, 439(1):588–603, Mar. 2014. doi: 10.1093/mnras/stu018.

V. Biffi, K. Dolag, T. H. Reiprich, A. Veronica, M. E. Ramos-Ceja, E. Bulbul, N. Ota, and V. Ghirardini. The eROSITA view of the Abell 3391/95 field: Case study from the Magneticum cosmological simulation. A&A, 661:A17, May 2022. doi: 10.1051/0004-6361/202141107.

J. Binney and G. Tabor. Evolving cooling flows. MNRAS, 276:663–678, Sept. 1995. doi: 10.1093/mnras/276.2.663.

L. Bîrzan, D. A. Rafferty, B. R. McNamara, M. W. Wise, and P. E. J. Nulsen. A Systematic Study of Radio-induced X-Ray Cavities in Clusters, Groups, and Galaxies. ApJ, 607(2):800–809, June 2004. doi: 10.1086/383519.

A. Blanchard, D. Valls-Gabaud, and G. A. Mamon. The origin of the galaxy luminosity function and the thermal evolution of the intergalactic medium. A&A, 264:365–378, Oct. 1992.

E. L. Blanton, S. W. Randall, T. E. Clarke, C. L. Sarazin, B. R. McNamara, E. M. Douglass, and M. McDonald. A Very Deep Chandra Observation of A2052: Bubbles, Shocks, and Sloshing. ApJ, 737(2):99, Aug. 2011. doi: 10.1088/0004-637X/737/2/99.

M. R. Blanton, M. A. Bershady, B. Abolfathi, F. D. Albareti, C. Allende Prieto, A. Almeida, J. Alonso-García, F. Anders, S. F. Anderson, B. Andrews, E. Aquino-Ortíz, A. Aragón-Salamanca, M. Argudo-Fernández, E. Armengaud, E. Aubourg, V. Avila-Reese, C. Badenes, S. Bailey, K. A. Barger, J. Barrera-Ballesteros, C. Bartosz, D. Bates, F. Baumgarten, J. Bautista, R. Beaton, T. C. Beers, F. Belfiore, C. F. Bender, A. A. Berlind, M. Bernardi, F. Beutler, J. C. Bird, D. Bizyaev, G. A. Blanc, M. Blomqvist, A. S. Bolton, M. Boquien, J. Borissova, R. van den Bosch, J. Bovy, W. N. Brandt, J. Brinkmann, J. R. Brownstein, K. Bundy, A. J. Burgasser, E. Burtin, N. G. Busca, M. Cappellari, M. L. Delgado Carigi, J. K. Carlberg, A. Carnero Rosell, R. Carrera, N. J. Chanover, B. Cherinka, E. Cheung, Y. Gómez

Maqueo Chew, C. Chiappini, P. D. Choi, D. Chojnowski, C.-H. Chuang, H. Chung, R. F. Cirolini, N. Clerc, R. E. Cohen, J. Comparat, L. da Costa, M.-C. Cousinou, K. Covey, J. D. Crane, R. A. C. Croft, I. Cruz-Gonzalez, D. Garrido Cuadra, K. Cunha, G. J. Damke, J. Darling, R. Davies, K. Dawson, A. de la Macorra, F. Dell'Agli, N. De Lee, T. Delubac, F. Di Mille, A. Diamond-Stanic, M. Cano-Díaz, J. Donor, J. J. Downes, N. Drory, H. du Mas des Bourboux, C. J. Duckworth, T. Dwelly, J. Dyer, G. Ebelke, A. D. Eigenbrot, D. J. Eisenstein, E. Emsellem, M. Eracleous, S. Escoffier, M. L. Evans, X. Fan, E. Fernández-Alvar, J. G. Fernandez-Trincado, D. K. Feuillet, A. Finoguenov, S. W. Fleming, A. Font-Ribera, A. Fredrickson, G. Freischlad, P. M. Frinchaboy, C. E. Fuentes, L. Galbany, R. Garcia-Dias, D. A. García-Hernández, P. Gaulme, D. Geisler, J. D. Gelfand, H. Gil-Marín, B. A. Gillespie, D. Goddard, V. Gonzalez-Perez, K. Grabowski, P. J. Green, C. J. Grier, J. E. Gunn, H. Guo, J. Guy, A. Hagen, C. Hahn, M. Hall, P. Harding, S. Hasselquist, S. L. Hawley, F. Hearty, J. I. Gonzalez Hernández, S. Ho, D. W. Hogg, K. Holley-Bockelmann, J. A. Holtzman, P. H. Holzer, J. Huehnerhoff, T. A. Hutchinson, H. S. Hwang, H. J. Ibarra-Medel, G. da Silva Ilha, I. I. Ivans, K. Ivory, K. Jackson, T. W. Jensen, J. A. Johnson, A. Jones, H. Jönsson, E. Jullo, V. Kamble, K. Kinemuchi, D. Kirkby, F.-S. Kitaura, M. Klaene, G. R. Knapp, J.-P. Kneib, J. A. Kollmeier, I. Lacerna, R. R. Lane, D. Lang, D. R. Law, D. Lazarz, Y. Lee, J.-M. Le Goff, F.-H. Liang, C. Li, H. Li, J. Lian, M. Lima, L. Lin, Y.-T. Lin, S. Bertran de Lis, C. Liu, M. A. C. de Icaza Lizaola, D. Long, S. Lucatello, B. Lundgren, N. K. MacDonald, A. Deconto Machado, C. L. MacLeod, S. Mahadevan, M. A. Geimba Maia, R. Maiolino, S. R. Majewski, E. Malanushenko, V. Malanushenko, A. Manchado, S. Mao, C. Maraston, R. Marques-Chaves, T. Masseron, K. L. Masters, C. K. McBride, R. M. McDermid, B. McGrath, I. D. McGreer, N. Medina Peña, M. Melendez, A. Merloni, M. R. Merrifield, S. Meszaros, A. Meza, I. Minchev, D. Minniti, T. Miyaji, S. More, J. Mulchaey, F. Müller-Sánchez, D. Muna, R. R. Munoz, A. D. Myers, P. Nair, K. Nandra, J. Correa do Nascimento, A. Negrete, M. Ness, J. A. Newman, R. C. Nichol, D. L. Nidever, C. Nitschelm, P. Ntelis, J. E. O'Connell, R. J. Oelkers, A. Oravetz, D. Oravetz, Z. Pace, N. Padilla, N. Palanque-Delabrouille, P. Alonso Palicio, K. Pan, J. K. Parejko, T. Parikh, I. Pâris, C. Park, A. Y. Patten, S. Peirani, M. Pellejero-Ibanez, S. Penny, W. J. Percival, I. Perez-Fournon, P. Petitjean, M. M. Pieri, M. Pinsonneault, A. Pisani, R. Poleski, F. Prada, A. Prakash, A. B. d. A. Queiroz, M. J. Raddick, A. Raichoor, S. Barboza Rembold, H. Richstein, R. A. Riffel, R. Riffel, H.-W. Rix, A. C. Robin, C. M. Rockosi, S. Rodríguez-Torres, A. Roman-Lopes, C. Román-Zúñiga, M. Rosado, A. J. Ross, G. Rossi, J. Ruan, R. Ruggeri, E. S. Rykoff, S. Salazar-Albornoz, M. Salvato, A. G. Sánchez, D. S. Aguado, J. R. Sánchez-Gallego, F. A. Santana, B. X. Santiago, C. Sayres, R. P. Schiavon, J. da Silva Schimoia, E. F. Schlafly, D. J. Schlegel, D. P. Schneider, M. Schultheis, W. J. Schuster, A. Schwope, H.-J. Seo, Z. Shao, S. Shen, M. Shetrone, M. Shull, J. D. Simon, D. Skinner, M. F. Skrutskie, A. Slosar, V. V. Smith, J. S. Sobeck, F. Sobreira, G. Somers, D. Souto, D. V. Stark, K. Stassun, F. Stauffer, M. Steinmetz, T. Storchi-Bergmann, A. Streblyanska, G. S. Stringfellow, G. Suárez, J. Sun, N. Suzuki, L. Szigeti, M. Taghizadeh-Popp, B. Tang, C. Tao, J. Tayar, M. Tembe, J. Teske, A. R. Thakar, D. Thomas, B. A. Thompson, J. L. Tinker, P. Tissera, R. Tojeiro, H. Hernandez Toledo, S. de la Torre, C. Tremonti, N. W. Troup, O. Valenzuela, I. Martinez Valpuesta, J. Vargas-González, M. Vargas-Magaña, J. A. Vazquez, S. Villanova, M. Vivek, N. Vogt, D. Wake, R. Walterbos, Y. Wang, B. A. Weaver,

A.-M. Weijmans, D. H. Weinberg, K. B. Westfall, D. G. Whelan, V. Wild, J. Wilson, W. M. Wood-Vasey, D. Wylezalek, T. Xiao, R. Yan, M. Yang, J. E. Ybarra, C. Yèche, N. Zakamska, O. Zamora, P. Zarrouk, G. Zasowski, K. Zhang, G.-B. Zhao, Z. Zheng, Z. Zheng, X. Zhou, Z.-M. Zhou, G. B. Zhu, M. Zoccali, and H. Zou. Sloan Digital Sky Survey IV: Mapping the Milky Way, Nearby Galaxies, and the Distant Universe. AJ, 154(1):28, July 2017. doi: 10.3847/1538-3881/aa7567.

L. E. Bleem, B. Stalder, T. de Haan, K. A. Aird, S. W. Allen, D. E. Applegate, M. L. N. Ashby, M. Bautz, M. Bayliss, B. A. Benson, S. Bocquet, M. Brodwin, J. E. Carlstrom, C. L. Chang, I. Chiu, H. M. Cho, A. Clocchiatti, T. M. Crawford, A. T. Crites, S. Desai, J. P. Dietrich, M. A. Dobbs, R. J. Foley, W. R. Forman, E. M. George, M. D. Gladders, A. H. Gonzalez, N. W. Halverson, C. Hennig, H. Hoekstra, G. P. Holder, W. L. Holzapfel, J. D. Hrubes, C. Jones, R. Keisler, L. Knox, A. T. Lee, E. M. Leitch, J. Liu, M. Lueker, D. Luong-Van, A. Mantz, D. P. Marrone, M. McDonald, J. J. McMahon, S. S. Meyer, L. Mocanu, J. J. Mohr, S. S. Murray, S. Padin, C. Pryke, C. L. Reichardt, A. Rest, J. Ruel, J. E. Ruhl, B. R. Saliwanchik, A. Saro, J. T. Sayre, K. K. Schaffer, T. Schrabback, E. Shirokoff, J. Song, H. G. Spieler, S. A. Stanford, Z. Staniszewski, A. A. Stark, K. T. Story, C. W. Stubbs, K. Vanderlinde, J. D. Vieira, A. Vikhlinin, R. Williamson, O. Zahn, and A. Zenteno. Galaxy Clusters Discovered via the Sunyaev-Zel'dovich Effect in the 2500-Square-Degree SPT-SZ Survey. ApJS, 216(2):27, Feb. 2015. doi: 10.1088/0067-0049/216/2/27.

K. Böckmann, M. Brüggen, B. Koribalski, A. Veronica, T. H. Reiprich, E. Bulbul, Y. E. Bahar, F. Balzer, J. Comparat, C. Garrel, V. Ghirardini, G. Gürkan, M. Kluge, D. Leahy, A. Merloni, A. Liu, M. E. Ramos-Ceja, M. Salvato, J. Sanders, S. Shabala, and X. Zhang. Central radio galaxies in galaxy clusters: Joint surveys by eROSITA and ASKAP. A&A, 677:A188, Sept. 2023. doi: 10.1051/0004-6361/202346912.

S. Bocquet, J. P. Dietrich, T. Schrabback, L. E. Bleem, M. Klein, S. W. Allen, D. E. Applegate, M. L. N. Ashby, M. Bautz, M. Bayliss, B. A. Benson, M. Brodwin, E. Bulbul, R. E. A. Canning, R. Capasso, J. E. Carlstrom, C. L. Chang, I. Chiu, H. M. Cho, A. Clocchiatti, T. M. Crawford, A. T. Crites, T. de Haan, S. Desai, M. A. Dobbs, R. J. Foley, W. R. Forman, G. P. Garmire, E. M. George, M. D. Gladders, A. H. Gonzalez, S. Grandis, N. Gupta, N. W. Halverson, J. Hlavacek-Larrondo, H. Hoekstra, G. P. Holder, W. L. Holzapfel, Z. Hou, J. D. Hrubes, N. Huang, C. Jones, G. Khullar, L. Knox, R. Kraft, A. T. Lee, A. von der Linden, D. Luong-Van, A. Mantz, D. P. Marrone, M. McDonald, J. J. McMahon, S. S. Meyer, L. M. Mocanu, J. J. Mohr, R. G. Morris, S. Padin, S. Patil, C. Pryke, D. Rapetti, C. L. Reichardt, A. Rest, J. E. Ruhl, B. R. Saliwanchik, A. Saro, J. T. Sayre, K. K. Schaffer, E. Shirokoff, B. Stalder, S. A. Stanford, Z. Staniszewski, A. A. Stark, K. T. Story, V. Strazzullo, C. W. Stubbs, K. Vanderlinde, J. D. Vieira, A. Vikhlinin, R. Williamson, and A. Zenteno. Cluster Cosmology Constraints from the 2500 deg^2 SPT-SZ Survey: Inclusion of Weak Gravitational Lensing Data from Magellan and the Hubble Space Telescope. ApJ, 878(1):55, June 2019. doi: 10.3847/1538-4357/ab1f10.

S. Bocquet, S. Grandis, L. E. Bleem, M. Klein, J. J. Mohr, T. Schrabback, T. M. C. Abbott,

P. A. R. Ade, M. Aguena, A. Alarcon, S. Allam, S. W. Allen, O. Alves, A. Amon, A. J. Anderson, J. Annis, B. Ansarinejad, J. E. Austermann, S. Avila, D. Bacon, M. Bayliss, J. A. Beall, K. Bechtol, M. R. Becker, A. N. Bender, B. A. Benson, G. M. Bernstein, S. Bhargava, F. Bianchini, M. Brodwin, D. Brooks, L. Bryant, A. Campos, R. E. A. Canning, J. E. Carlstrom, A. Carnero Rosell, M. Carrasco Kind, J. Carretero, F. J. Castander, R. Cawthon, C. L. Chang, C. Chang, P. Chaubal, R. Chen, H. C. Chiang, A. Choi, T.-L. Chou, R. Citron, C. Corbett Moran, J. Cordero, M. Costanzi, T. M. Crawford, A. T. Crites, L. N. da Costa, M. E. S. Pereira, C. Davis, T. M. Davis, J. DeRose, S. Desai, T. de Haan, H. T. Diehl, M. A. Dobbs, S. Dodelson, C. Doux, A. Drlica-Wagner, K. Eckert, J. Elvin-Poole, S. Everett, W. Everett, I. Ferrero, A. Ferté, A. M. Flores, J. Frieman, J. Gallicchio, J. García-Bellido, M. Gatti, E. M. George, G. Giannini, M. D. Gladders, D. Gruen, R. A. Gruendl, N. Gupta, G. Gutierrez, N. W. Halverson, I. Harrison, W. G. Hartley, K. Herner, S. R. Hinton, G. P. Holder, D. L. Hollowood, W. L. Holzapfel, K. Honscheid, J. D. Hrubes, N. Huang, J. Hubmayr, E. M. Huff, D. Huterer, K. D. Irwin, D. J. James, M. Jarvis, G. Khullar, K. Kim, L. Knox, R. Kraft, E. Krause, K. Kuehn, N. Kuropatkin, F. Kéruzoré, O. Lahav, A. T. Lee, P. F. Leget, D. Li, H. Lin, A. Lowitz, N. MacCrann, G. Mahler, A. Mantz, J. L. Marshall, J. McCullough, M. McDonald, J. J. McMahon, J. Mena-Fernández, F. Menanteau, S. S. Meyer, R. Miquel, J. Montgomery, J. Myles, T. Natoli, A. Navarro-Alsina, J. P. Nibarger, G. I. Noble, V. Novosad, R. L. C. Ogando, Y. Omori, S. Padin, S. Pandey, P. Paschos, S. Patil, A. Pieres, A. A. Plazas Malagón, A. Porredon, J. Prat, C. Pryke, M. Raveri, C. L. Reichardt, J. Roberson, R. P. Rollins, C. Romero, A. Roodman, J. E. Ruhl, E. S. Rykoff, B. R. Saliwanchik, L. Salvati, C. Sánchez, E. Sanchez, D. Sanchez Cid, A. Saro, K. K. Schaffer, L. F. Secco, I. Sevilla-Noarbe, K. Sharon, E. Sheldon, T. Shin, C. Sievers, G. Smecher, M. Smith, T. Somboonpanyakul, M. Sommer, B. Stalder, A. A. Stark, J. Stephen, V. Strazzullo, E. Suchyta, G. Tarle, C. To, M. A. Troxel, C. Tucker, I. Tutusaus, T. N. Varga, T. Veach, J. D. Vieira, A. Vikhlinin, A. von der Linden, G. Wang, N. Weaverdyck, J. Weller, N. Whitehorn, W. L. K. Wu, B. Yanny, V. Yefremenko, B. Yin, M. Young, J. A. Zebrowski, Y. Zhang, H. Zohren, and J. Zuntz. SPT Clusters with DES and HST Weak Lensing. II. Cosmological Constraints from the Abundance of Massive Halos. arXiv e-prints, art. arXiv:2401.02075, Jan. 2024. doi: 10.48550/arXiv.2401.02075.

H. Boehringer and N. Werner. X-ray Spectroscopy of Galaxy Clusters. arXiv e-prints, art. arXiv:0907.4277, July 2009. doi: 10.48550/arXiv.0907.4277.

H. Böhringer, K. Dolag, and G. Chon. Modelling self-similar appearance of galaxy clusters in X-rays. A&A, 539:A120, Mar. 2012. doi: 10.1051/0004-6361/201118000.

C. M. Booth and J. Schaye. Cosmological simulations of the growth of supermassive black holes and feedback from active galactic nuclei: method and tests. MNRAS, 398(1):53–74, Sept. 2009. doi: 10.1111/j.1365-2966.2009.15043.x.

S. Borgani, F. Governato, J. Wadsley, N. Menci, P. Tozzi, T. Quinn, J. Stadel, and G. Lake. The effect of non-gravitational gas heating in groups and clusters of galaxies. MNRAS, 336(2): 409–424, Oct. 2002. doi: 10.1046/j.1365-8711.2002.05746.x.

S. Borgani, G. Murante, V. Springel, A. Diaferio, K. Dolag, L. Moscardini, G. Tormen, L. Torna-tore, and P. Tozzi. X-ray properties of galaxy clusters and groups from a cosmological hydro-dynamical simulation. MNRAS, 348(3):1078–1096, Mar. 2004. doi: 10.1111/j.1365-2966.2004.07431.x.

R. G. Bower, A. J. Benson, C. G. Lacey, C. M. Baugh, S. Cole, and C. S. Frenk. The impact of galaxy formation on the X-ray evolution of clusters. MNRAS, 325(2):497–508, Aug. 2001. doi: 10.1046/j.1365-8711.2001.04382.x.

H. Brunner, T. Liu, G. Lamer, A. Georgakakis, A. Merloni, M. Brusa, E. Bulbul, K. Dennerl, S. Friedrich, A. Liu, C. Maitra, K. Nandra, M. E. Ramos-Ceja, J. S. Sanders, I. M. Stewart, T. Boller, J. Buchner, N. Clerc, J. Comparat, T. Dwelly, D. Eckert, A. Finoguenov, M. Frey-berg, V. Ghirardini, A. Gueguen, F. Haberl, I. Kreykenbohm, M. Krumpe, S. Osterhage, F. Pacaud, P. Predehl, T. H. Reiprich, J. Robrade, M. Salvato, A. Santangelo, T. Schrabback, A. Schwope, and J. Wilms. The eROSITA Final Equatorial Depth Survey (eFEDS). X-ray catalogue. A&A, 661:A1, May 2022. doi: 10.1051/0004-6361/202141266.

G. L. Bryan. Explaining the Entropy Excess in Clusters and Groups of Galaxies without Addi-tional Heating. ApJ, 544(1):L1–L5, Nov. 2000. doi: 10.1086/317289.

E. Bulbul, M. Markevitch, A. Foster, R. K. Smith, M. Loewenstein, and S. W. Randall. Detection of an Unidentified Emission Line in the Stacked X-Ray Spectrum of Galaxy Clusters. ApJ, 789(1):13, July 2014. doi: 10.1088/0004-637X/789/1/13.

E. Bulbul, S. W. Randall, M. Bayliss, E. Miller, F. Andrade-Santos, R. Johnson, M. Bautz, E. L. Blanton, W. R. Forman, C. Jones, R. Paterno-Mahler, S. S. Murray, C. L. Sarazin, R. K. Smith, and C. Ezer. Probing the Outskirts of the Early-Stage Galaxy Cluster Merger A1750. ApJ, 818(2):131, Feb. 2016. doi: 10.3847/0004-637X/818/2/131.

E. Bulbul, I. N. Chiu, J. J. Mohr, M. McDonald, B. Benson, M. W. Bautz, M. Bayliss, L. Bleem, M. Brodwin, S. Bocquet, R. Capasso, J. P. Dietrich, B. Forman, J. Hlavacek-Larrondo, W. L. Holzapfel, G. Khullar, M. Klein, R. Kraft, E. D. Miller, C. Reichardt, A. Saro, K. Sharon, B. Stalder, T. Schrabback, and A. Stanford. X-Ray Properties of SPT-selected Galaxy Clusters at $0.2 < z < 1.5$ Observed with XMM-Newton. ApJ, 871(1):50, Jan. 2019. doi: 10.3847/1538-4357/aaf230.

E. Bulbul, R. Kraft, P. Nulsen, M. Freyberg, E. D. Miller, C. Grant, M. W. Bautz, D. N. Bur-rows, S. Allen, T. Eraerds, V. Fioretti, F. Gastaldello, V. Ghirardini, D. Hall, N. Meidinger, S. Molendi, A. Rau, D. Wilkins, and J. Wilms. Characterization of the Particle-induced Back-ground of XMM-Newton EPIC-pn: Short- and Long-term Variability. ApJ, 891(1):13, Mar. 2020. doi: 10.3847/1538-4357/ab698a.

E. Bulbul, A. Liu, T. Pasini, J. Comparat, D. N. Hoang, M. Klein, V. Ghirardini, M. Salvato, A. Merloni, R. Seppi, J. Wolf, S. F. Anderson, Y. E. Bahar, M. Brusa, M. Brüggen, J. Buchner, T. Dwelly, H. Ibarra-Medel, J. Ider Chitham, T. Liu, K. Nandra, M. E. Ramos-Ceja, J. S.

Sanders, and Y. Shen. The eROSITA Final Equatorial-Depth Survey (eFEDS). Galaxy clusters and groups in disguise. A&A, 661:A10, May 2022. doi: 10.1051/0004-6361/202142460.

E. Bulbul, A. Liu, M. Kluge, X. Zhang, J. S. Sanders, Y. E. Bahar, V. Ghirardini, E. Artis, R. Seppi, C. Garrel, M. E. Ramos-Ceja, J. Comparat, F. Balzer, K. Böckmann, M. Brüggen, N. Clerc, K. Dennerl, K. Dolag, M. Freyberg, S. Grandis, D. Gruen, F. Kleinebreil, S. Krippendorf, G. Lamer, A. Merloni, K. Migkas, K. Nandra, F. Pacaud, P. Predehl, T. H. Reiprich, T. Schrabback, A. Veronica, J. Weller, and S. Zelmer. The SRG/eROSITA All-Sky Survey: The first catalog of galaxy clusters and groups in the Western Galactic Hemisphere. arXiv e-prints, art. arXiv:2402.08452, Feb. 2024. doi: 10.48550/arXiv.2402.08452.

G. E. Bulbul, N. Hasler, M. Bonamente, and M. Joy. An Analytic Model of the Physical Properties of Galaxy Clusters. ApJ, 720(2):1038–1044, Sept. 2010. doi: 10.1088/0004-637X/720/2/1038.

G. E. Bulbul, R. K. Smith, A. Foster, J. Cottam, M. Loewenstein, R. Mushotzky, and R. Shafer. High-resolution XMM-Newton Spectroscopy of the Cooling Flow Cluster A3112. ApJ, 747 (1):32, Mar. 2012. doi: 10.1088/0004-637X/747/1/32.

D. A. Buote. Iron Gradients in Cooling Flow Galaxies and Groups. ApJ, 539(1):172–186, Aug. 2000. doi: 10.1086/309224.

D. A. Buote and A. C. Fabian. X-ray spectral analysis of elliptical galaxies from ASCA: the Fe abundance in a multiphase medium. MNRAS, 296(4):977–994, June 1998. doi: 10.1046/j.1365-8711.1998.01478.x.

J. O. Burns. The Radio Properties of cD Galaxies in Abell Clusters. I. an X-ray Selected Sample. AJ, 99:14, Jan. 1990. doi: 10.1086/115307.

E. T. Byram, T. A. Chubb, and H. Friedman. Cosmic X-Ray Sources-Galactic and Extragalactic. AJ, 71:379, Aug. 1966. doi: 10.1086/109934.

M. G. Campitiello, S. Ettori, L. Lovisari, I. Bartalucci, D. Eckert, E. Rasia, M. Rossetti, F. Gastaldello, G. W. Pratt, B. Maughan, E. Pointecouteau, M. Sereno, V. Biffi, S. Borgani, F. De Luca, M. De Petris, M. Gaspari, S. Ghizzardi, P. Mazzotta, and S. Molendi. CHEX-MATE: Morphological analysis of the sample. A&A, 665:A117, Sept. 2022. doi: 10.1051/0004-6361/202243470.

P. R. Capelo, P. S. Coppi, and P. Natarajan. The polytropic approximation and X-ray scaling relations: constraints on gas and dark matter profiles for galaxy groups and clusters. MNRAS, 422(1):686–703, May 2012. doi: 10.1111/j.1365-2966.2012.20648.x.

M. Cappellari and Y. Copin. Adaptive spatial binning of integral-field spectroscopic data using Voronoi tessellations. MNRAS, 342(2):345–354, June 2003. doi: 10.1046/j.1365-8711.2003.06541.x.

N. Cappelluti, Y. Li, A. Ricarte, B. Agarwal, V. Allevato, T. Tasnim Ananna, M. Ajello, F. Civano, A. Comastri, M. Elvis, A. Finoguenov, R. Gilli, G. Hasinger, S. Marchesi, P. Natarajan, F. Pacucci, E. Treister, and C. M. Urry. The Chandra COSMOS Legacy Survey: Energy Spectrum of the Cosmic X-Ray Background and Constraints on Undetected Populations. ApJ, 837(1):19, Mar. 2017. doi: 10.3847/1538-4357/aa5ea4.

W. Cash. Parameter estimation in astronomy through application of the likelihood ratio. ApJ, 228:939–947, Mar. 1979. doi: 10.1086/156922.

A. Cavaliere and R. Fusco-Femiano. X-rays from hot plasma in clusters of galaxies. A&A, 49: 137–144, May 1976.

A. G. Cavaliere, H. Gursky, and W. H. Tucker. Extragalactic X-ray Sources and Associations of Galaxies. Nature, 231(5303):437–438, June 1971. doi: 10.1038/231437a0.

I. Chiu, J. J. Mohr, M. McDonald, S. Bocquet, S. Desai, M. Klein, H. Israel, M. L. N. Ashby, A. Stanford, B. A. Benson, M. Brodwin, T. M. C. Abbott, F. B. Abdalla, S. Allam, J. Annis, M. Bayliss, A. Benoit-Lévy, E. Bertin, L. Bleem, D. Brooks, E. Buckley-Geer, E. Bulbul, R. Capasso, J. E. Carlstrom, A. C. Rosell, J. Carretero, F. J. Castander, C. E. Cunha, C. B. D'Andrea, L. N. da Costa, C. Davis, H. T. Diehl, J. P. Dietrich, P. Doel, A. Drlica-Wagner, T. F. Eifler, A. E. Evrard, B. Flaugher, J. García-Bellido, G. Garmire, E. Gaztanaga, D. W. Gerdes, A. Gonzalez, D. Gruen, R. A. Gruendl, J. Gschwend, N. Gupta, G. Gutierrez, J. Hlavacek-L, K. Honscheid, D. J. James, T. Jeltema, R. Kraft, E. Krause, K. Kuehn, S. Kuhlmann, N. Kuropatkin, O. Lahav, M. Lima, M. A. G. Maia, J. L. Marshall, P. Melchior, F. Menanteau, R. Miquel, S. Murray, B. Nord, R. L. C. Ogando, A. A. Plazas, D. Rapetti, C. L. Reichardt, A. K. Romer, A. Roodman, E. Sanchez, A. Saro, V. Scarpine, R. Schindler, M. Schubnell, K. Sharon, R. C. Smith, M. Smith, M. Soares-Santos, F. Sobreira, B. Stalder, C. Stern, V. Strazzullo, E. Suchyta, M. E. C. Swanson, G. Tarle, V. Vikram, A. R. Walker, J. Weller, and Y. Zhang. Baryon content in a sample of 91 galaxy clusters selected by the South Pole Telescope at 0.2 <z < 1.25. MNRAS, 478(3):3072–3099, Aug. 2018. doi: 10.1093/mnras/sty1284.

I. N. Chiu, V. Ghirardini, A. Liu, S. Grandis, E. Bulbul, Y. E. Bahar, J. Comparat, S. Bocquet, N. Clerc, M. Klein, T. Liu, X. Li, H. Miyatake, J. Mohr, S. More, M. Oguri, N. Okabe, F. Pacaud, M. E. Ramos-Ceja, T. H. Reiprich, T. Schrabback, and K. Umetsu. The eROSITA Final Equatorial-Depth Survey (eFEDS). X-ray observable-to-mass-and-redshift relations of galaxy clusters and groups with weak-lensing mass calibration from the Hyper Suprime-Cam Subaru Strategic Program survey. A&A, 661:A11, May 2022. doi: 10.1051/0004-6361/202141755.

K. T. E. Chua, A. Pillepich, M. Vogelsberger, and L. Hernquist. Shape of dark matter haloes in the Illustris simulation: effects of baryons. MNRAS, 484(1):476–493, Mar. 2019. doi: 10.1093/mnras/sty3531.

O. Chwolson. Über eine mögliche Form fiktiver Doppelsterne. Astronomische Nachrichten, 221: 329, June 1924. doi: 10.1002/asna.19242212003.

L. Ciotti and J. P. Ostriker. Cooling Flows and Quasars: Different Aspects of the Same Phenomenon? I. Concepts. ApJ, 487(2):L105–L108, Oct. 1997. doi: 10.1086/310902.

N. Clerc, M. E. Ramos-Ceja, J. Ridl, G. Lamer, H. Brunner, F. Hofmann, J. Comparat, F. Pacaud, F. Käfer, T. H. Reiprich, A. Merloni, C. Schmid, T. Brand, J. Wilms, P. Friedrich, A. Finoguenov, T. Dauser, and I. Kreykenbohm. Synthetic simulations of the extragalactic sky seen by eROSITA. I. Pre-launch selection functions from Monte-Carlo simulations. A&A, 617:A92, Sept. 2018. doi: 10.1051/0004-6361/201732119.

N. Clerc, J. Comparat, R. Seppi, E. Artis, Y. E. Bahar, F. Balzer, E. Bulbul, T. Dauser, C. Garrel, V. Ghirardini, S. Grandis, C. Kirsch, M. Kluge, A. Liu, F. Pacaud, M. E. Ramos-Ceja, T. H. Reiprich, J. S. Sanders, J. Wilms, and X. Zhang. The SRG/eROSITA All-Sky Survey: X-ray selection function models for the eRASS1 galaxy cluster cosmology. arXiv e-prints, art. arXiv:2402.08457, Feb. 2024. doi: 10.48550/arXiv.2402.08457.

J. Comparat, A. Merloni, M. Salvato, K. Nandra, T. Boller, A. Georgakakis, A. Finoguenov, T. Dwelly, J. Buchner, A. Del Moro, N. Clerc, Y. Wang, G. Zhao, F. Prada, G. Yepes, M. Brusa, M. Krumpe, and T. Liu. Active galactic nuclei and their large-scale structure: an eROSITA mock catalogue. MNRAS, 487(2):2005–2029, Aug. 2019. doi: 10.1093/mnras/stz1390.

J. Comparat, D. Eckert, A. Finoguenov, R. Schmidt, J. S. Sanders, D. Nagai, E. T. Lau, F. Kafer, F. Pacaud, N. Clerc, T. H. Reiprich, E. Bulbul, J. I. Chitham, C.-H. Chiang, V. Ghirardini, V. Gonzalez-Perez, G. Gozaliasl, C. C. Fitzpatrick, A. Klypin, A. Merloni, K. Nandra, T. Liu, F. Prada, M. Ramos-Ceja, M. Salvato, R. Seppi, E. Tempel, and G. Yepes. Full-sky photon simulation of clusters and active galactic nuclei in the soft X-rays for eROSITA. The Open Journal of Astrophysics, 3(1):13, Dec. 2020. doi: 10.21105/astro.2008.08404.

M. Costanzi, E. Rozo, E. S. Rykoff, A. Farahi, T. Jeltema, A. E. Evrard, A. Mantz, D. Gruen, R. Mandelbaum, J. DeRose, T. McClintock, T. N. Varga, Y. Zhang, J. Weller, R. H. Wechsler, and M. Aguena. Modelling projection effects in optically selected cluster catalogues. MNRAS, 482(1):490–505, Jan. 2019. doi: 10.1093/mnras/sty2665.

D. Coutinho, M. E. Ramos-Ceja, K. Dennerl, F. Haberl, N. Meidinger, A. Merloni, P. Predehl, I. Stewart, M. Freyberg, W. Bornemann, H. Brunner, V. Burwitz, S. Czesla, J. Eder, S. Friedrich, R. Gaida, A. Gueguen, G. Hartner, W. Kink, I. Kreykenbohm, G. Lamer, C. Maitra, T. Mernik, S. Mueller, P. Nandra, E. Pfeffermann, and J. Robrade. SRG/eROSITA status and operations during the first four all-sky surveys. In J.-W. A. den Herder, S. Nikzad, and K. Nakazawa, editors, Society of Photo-Optical Instrumentation Engineers (SPIE) Conference Series, volume 12181 of Society of Photo-Optical Instrumentation Engineers (SPIE) Conference Series, page 121811A, Aug. 2022. doi: 10.1117/12.2628946.

R. A. Crain, T. Theuns, C. Dalla Vecchia, V. R. Eke, C. S. Frenk, A. Jenkins, S. T. Kay, J. A. Peacock, F. R. Pearce, J. Schaye, V. Springel, P. A. Thomas, S. D. M. White, and R. P. C. Wiersma. Galaxies-intergalactic medium interaction calculation - I. Galaxy formation as a

function of large-scale environment. MNRAS, 399(4):1773–1794, Nov. 2009. doi: 10.1111/j.1365-2966.2009.15402.x.

J. H. Croston, G. W. Pratt, H. Böhringer, M. Arnaud, E. Pointecouteau, T. J. Ponman, A. J. R. Sanderson, R. F. Temple, R. G. Bower, and M. Donahue. Galaxy-cluster gas-density distributions of the representative XMM-Newton cluster structure survey (REXCESS). A&A, 487(2): 431–443, Aug. 2008. doi: 10.1051/0004-6361:20079154.

D. J. Croton, V. Springel, S. D. M. White, G. De Lucia, C. S. Frenk, L. Gao, A. Jenkins, G. Kauffmann, J. F. Navarro, and N. Yoshida. The many lives of active galactic nuclei: cooling flows, black holes and the luminosities and colours of galaxies. MNRAS, 365(1):11–28, Jan. 2006. doi: 10.1111/j.1365-2966.2005.09675.x.

C. Dalla Vecchia and J. Schaye. Simulating galactic outflows with kinetic supernova feedback. MNRAS, 387(4):1431–1444, July 2008. doi: 10.1111/j.1365-2966.2008.13322.x.

T. Dauser, S. Falkner, M. Lorenz, C. Kirsch, P. Peille, E. Cucchetti, C. Schmid, T. Brand, M. Oertel, R. Smith, and J. Wilms. SIXTE: a generic X-ray instrument simulation toolkit. A&A, 630: A66, Sept. 2019. doi: 10.1051/0004-6361/201935978.

I. Davidzon, O. Ilbert, C. Laigle, J. Coupon, H. J. McCracken, I. Delvecchio, D. Masters, P. Capak, B. C. Hsieh, O. Le Fèvre, L. Tresse, M. Bethermin, Y. Y. Chang, A. L. Faisst, E. Le Floc'h, C. Steinhardt, S. Toft, H. Aussel, C. Dubois, G. Hasinger, M. Salvato, D. B. Sanders, N. Scoville, and J. D. Silverman. The COSMOS2015 galaxy stellar mass function . Thirteen billion years of stellar mass assembly in ten snapshots. A&A, 605:A70, Sept. 2017. doi: 10.1051/0004-6361/201730419.

K. Dennerl, R. Andritschke, H. Bräuninger, W. Burkert, V. Burwitz, V. Emberger, M. Freyberg, P. Friedrich, R. Gaida, S. Granato, G. Hartner, A. von Kienlin, N. Meidinger, B. Menz, and P. Predehl. The calibration of eROSITA on SRG. In J.-W. A. den Herder, S. Nikzad, and K. Nakazawa, editors, Space Telescopes and Instrumentation 2020: Ultraviolet to Gamma Ray, volume 11444 of Society of Photo-Optical Instrumentation Engineers (SPIE) Conference Series, page 114444Q, Dec. 2020. doi: 10.1117/12.2562330.

P. E. Dewdney, P. J. Hall, R. T. Schilizzi, and T. J. L. W. Lazio. The Square Kilometre Array. IEEE Proceedings, 97(8):1482–1496, Aug. 2009. doi: 10.1109/JPROC.2009.2021005.

A. Dey, D. J. Schlegel, D. Lang, R. Blum, K. Burleigh, X. Fan, J. R. Findlay, D. Finkbeiner, D. Herrera, S. Juneau, M. Landriau, M. Levi, I. McGreer, A. Meisner, A. D. Myers, J. Moustakas, P. Nugent, A. Patej, E. F. Schlafly, A. R. Walker, F. Valdes, B. A. Weaver, C. Yèche, H. Zou, X. Zhou, B. Abareshi, T. M. C. Abbott, B. Abolfathi, C. Aguilera, S. Alam, L. Allen, A. Alvarez, J. Annis, B. Ansarinejad, M. Aubert, J. Beechert, E. F. Bell, S. Y. BenZvi, F. Beutler, R. M. Bielby, A. S. Bolton, C. Briceño, E. J. Buckley-Geer, K. Butler, A. Calamida, R. G. Carlberg, P. Carter, R. Casas, F. J. Castander, Y. Choi, J. Comparat, E. Cukanovaite, T. Delubac, K. DeVries, S. Dey, G. Dhungana, M. Dickinson, Z. Ding, J. B. Donaldson,

Y. Duan, C. J. Duckworth, S. Eftekharzadeh, D. J. Eisenstein, T. Etourneau, P. A. Fagrelius, J. Farihi, M. Fitzpatrick, A. Font-Ribera, L. Fulmer, B. T. Gänsicke, E. Gaztanaga, K. George, D. W. Gerdes, S. G. A. Gontcho, C. Gorgoni, G. Green, J. Guy, D. Harmer, M. Hernandez, K. Honscheid, L. W. Huang, D. J. James, B. T. Jannuzi, L. Jiang, R. Joyce, A. Karcher, S. Karkar, R. Kehoe, J.-P. Kneib, A. Kueter-Young, T.-W. Lan, T. R. Lauer, L. Le Guillou, A. Le Van Suu, J. H. Lee, M. Lesser, L. Perreault Levasseur, T. S. Li, J. L. Mann, R. Marshall, C. E. Martínez-Vázquez, P. Martini, H. du Mas des Bourboux, S. McManus, T. G. Meier, B. Ménard, N. Metcalfe, A. Muñoz-Gutiérrez, J. Najita, K. Napier, G. Narayan, J. A. Newman, J. Nie, B. Nord, D. J. Norman, K. A. G. Olsen, A. Paat, N. Palanque-Delabrouille, X. Peng, C. L. Poppett, M. R. Poremba, A. Prakash, D. Rabinowitz, A. Raichoor, M. Rezaie, A. N. Robertson, N. A. Roe, A. J. Ross, N. P. Ross, G. Rudnick, S. Safonova, A. Saha, F. J. Sánchez, E. Savary, H. Schweiker, A. Scott, H.-J. Seo, H. Shan, D. R. Silva, Z. Slepian, C. Soto, D. Sprayberry, R. Staten, C. M. Stillman, R. J. Stupak, D. L. Summers, S. Sien Tie, H. Tirado, M. Vargas-Magaña, A. K. Vivas, R. H. Wechsler, D. Williams, J. Yang, Q. Yang, T. Yapici, D. Zaritsky, A. Zenteno, K. Zhang, T. Zhang, R. Zhou, and Z. Zhou. Overview of the DESI Legacy Imaging Surveys. AJ, 157(5):168, May 2019. doi: 10.3847/1538-3881/ab089d.

T. Di Matteo, V. Springel, and L. Hernquist. Energy input from quasars regulates the growth and activity of black holes and their host galaxies. Nature, 433:604–607, Feb. 2005. doi: 10.1038/nature03335.

K. Dolag, S. Borgani, G. Murante, and V. Springel. Substructures in hydrodynamical cluster simulations. MNRAS, 399(2):497–514, Oct. 2009. doi: 10.1111/j.1365-2966.2009.15034.x.

M. Donahue and G. M. Voit. Baryon cycles in the biggest galaxies. Phys. Rep., 973:1–109, Aug. 2022. doi: 10.1016/j.physrep.2022.04.005.

S. P. Driver, P. Norberg, I. K. Baldry, S. P. Bamford, A. M. Hopkins, J. Liske, J. Loveday, J. A. Peacock, D. T. Hill, L. S. Kelvin, A. S. G. Robotham, N. J. G. Cross, H. R. Parkinson, M. Prescott, C. J. Conselice, L. Dunne, S. Brough, H. Jones, R. G. Sharp, E. van Kampen, S. Oliver, I. G. Roseboom, J. Bland-Hawthorn, S. M. Croom, S. Ellis, E. Cameron, S. Cole, C. S. Frenk, W. J. Couch, A. W. Graham, R. Proctor, R. De Propris, I. F. Doyle, E. M. Edmondson, R. C. Nichol, D. Thomas, S. A. Eales, M. J. Jarvis, K. Kuijken, O. Lahav, B. F. Madore, M. Seibert, M. J. Meyer, L. Staveley-Smith, S. Phillipps, C. C. Popescu, A. E. Sansom, W. J. Sutherland, R. J. Tuffs, and S. J. Warren. GAMA: towards a physical understanding of galaxy formation. Astronomy and Geophysics, 50(5):5.12–5.19, Oct. 2009. doi: 10.1111/j.1468-4004.2009.50512.x.

H. Ebeling, A. C. Edge, H. Bohringer, S. W. Allen, C. S. Crawford, A. C. Fabian, W. Voges, and J. P. Huchra. The ROSAT Brightest Cluster Sample - I. The compilation of the sample and the cluster log N-log S distribution. MNRAS, 301(4):881–914, Dec. 1998. doi: 10.1046/j.1365-8711.1998.01949.x.

D. Eckert, S. Molendi, and S. Paltani. The cool-core bias in X-ray galaxy cluster samples. I.

Method and application to HIFLUGCS. A&A, 526:A79, Feb. 2011. doi: 10.1051/0004-6361/201015856.

D. Eckert, F. Vazza, S. Ettori, S. Molendi, D. Nagai, E. T. Lau, M. Roncarelli, M. Rossetti, S. L. Snowden, and F. Gastaldello. The gas distribution in the outer regions of galaxy clusters. A&A, 541:A57, May 2012. doi: 10.1051/0004-6361/201118281.

D. Eckert, S. Ettori, J. Coupon, F. Gastaldello, M. Pierre, J. B. Melin, A. M. C. Le Brun, I. G. McCarthy, C. Adami, L. Chiappetti, L. Faccioli, P. Giles, S. Lavoie, J. P. Lefèvre, M. Lieu, A. Mantz, B. Maughan, S. McGee, F. Pacaud, S. Paltani, T. Sadibekova, G. P. Smith, and F. Ziparo. The XXL Survey. XIII. Baryon content of the bright cluster sample. A&A, 592:A12, June 2016. doi: 10.1051/0004-6361/201527293.

D. Eckert, S. Ettori, E. Pointecouteau, S. Molendi, S. Paltani, and C. Tchernin. The XMM cluster outskirts project (X- COP). Astronomische Nachrichten, 338(293):293–298, Mar. 2017. doi: 10.1002/asna.201713345.

D. Eckert, V. Ghirardini, S. Ettori, E. Rasia, V. Biffi, E. Pointecouteau, M. Rossetti, S. Molendi, F. Vazza, F. Gastaldello, M. Gaspari, S. De Grandi, S. Ghizzardi, H. Bourdin, C. Tchernin, and M. Roncarelli. Non-thermal pressure support in X-COP galaxy clusters. A&A, 621:A40, Jan. 2019. doi: 10.1051/0004-6361/201833324.

D. Eckert, M. Gaspari, F. Gastaldello, A. M. C. Le Brun, and E. O'Sullivan. Feedback from Active Galactic Nuclei in Galaxy Groups. Universe, 7(5):142, May 2021. doi: 10.3390/universe7050142.

D. Eckert, F. Gastaldello, E. O'Sullivan, A. Finoguenov, M. Brienza, and the X-GAP collaboration. Galaxy groups as the ultimate probe of AGN feedback. arXiv e-prints, art. arXiv:2403.17145, Mar. 2024. doi: 10.48550/arXiv.2403.17145.

H. J. Eckmiller, D. S. Hudson, and T. H. Reiprich. Testing the low-mass end of X-ray scaling relations with a sample of Chandra galaxy groups. A&A, 535:A105, Nov. 2011. doi: 10.1051/0004-6361/201116734.

J. Einasto. On the Construction of a Composite Model for the Galaxy and on the Determination of the System of Galactic Parameters. Trudy Astrofizicheskogo Instituta Alma-Ata, 5:87–100, Jan. 1965.

A. Einstein. Die Grundlage der allgemeinen Relativitätstheorie. Annalen der Physik, 354(7):769–822, Jan. 1916. doi: 10.1002/andp.19163540702.

T. A. Ensslin, P. L. Biermann, U. Klein, and S. Kohle. Cluster radio relics as a tracer of shock waves of the large-scale structure formation. A&A, 332:395–409, Apr. 1998. doi: 10.48550/arXiv.astro-ph/9712293.

S. Ettori. β-model and cooling flows in X-ray clusters of galaxies. MNRAS, 318(4):1041–1046, Nov. 2000. doi: 10.1046/j.1365-8711.2000.03664.x.

S. Ettori. The physics inside the scaling relations for X-ray galaxy clusters: gas clumpiness, gas mass fraction and slope of the pressure profile. MNRAS, 446(3):2629–2639, Jan. 2015. doi: 10.1093/mnras/stu2292.

S. Ettori, A. Donnarumma, E. Pointecouteau, T. H. Reiprich, S. Giodini, L. Lovisari, and R. W. Schmidt. Mass Profiles of Galaxy Clusters from X-ray Analysis. Space Sci. Rev., 177(1-4): 119–154, Aug. 2013. doi: 10.1007/s11214-013-9976-7.

A. C. Fabian, J. S. Sanders, S. W. Allen, C. S. Crawford, K. Iwasawa, R. M. Johnstone, R. W. Schmidt, and G. B. Taylor. A deep Chandra observation of the Perseus cluster: shocks and ripples. MNRAS, 344(3):L43–L47, Sept. 2003. doi: 10.1046/j.1365-8711.2003.06902.x.

A. C. Fabian, J. S. Sanders, G. B. Taylor, S. W. Allen, C. S. Crawford, R. M. Johnstone, and K. Iwasawa. A very deep Chandra observation of the Perseus cluster: shocks, ripples and conduction. MNRAS, 366(2):417–428, Feb. 2006. doi: 10.1111/j.1365-2966.2005.09896.x.

D. Fabjan, S. Borgani, L. Tornatore, A. Saro, G. Murante, and K. Dolag. Simulating the effect of active galactic nuclei feedback on the metal enrichment of galaxy clusters. MNRAS, 401(3): 1670–1690, Jan. 2010. doi: 10.1111/j.1365-2966.2009.15794.x.

L. Ferrarese and D. Merritt. A Fundamental Relation between Supermassive Black Holes and Their Host Galaxies. ApJ, 539(1):L9–L12, Aug. 2000. doi: 10.1086/312838.

A. Finoguenov, C. Jones, H. Böhringer, and T. J. Ponman. ASCA Observations of Groups at Radii of Low Overdensity: Implications for the Cosmic Preheating. ApJ, 578(1):74–89, Oct. 2002. doi: 10.1086/342472.

A. Finoguenov, T. J. Ponman, J. P. F. Osmond, and M. Zimer. XMM-Newton study of 0.012 < z < 0.024 groups - I. Overview of the IGM thermodynamics. MNRAS, 374(2):737–760, Jan. 2007. doi: 10.1111/j.1365-2966.2006.11194.x.

A. Finoguenov, M. Ruszkowski, C. Jones, M. Brüggen, A. Vikhlinin, and E. Mandel. In-Depth Chandra Study of the AGN Feedback in Virgo Elliptical Galaxy M84. ApJ, 686(2):911–917, Oct. 2008. doi: 10.1086/591662.

A. Finoguenov, C. L. Sarazin, K. Nakazawa, D. R. Wik, and T. E. Clarke. XMM-Newton Observation of the Northwest Radio Relic Region in A3667. ApJ, 715(2):1143–1151, June 2010. doi: 10.1088/0004-637X/715/2/1143.

A. Finoguenov, M. Tanaka, M. Cooper, V. Allevato, N. Cappelluti, A. Choi, C. Heymans, F. E. Bauer, F. Ziparo, P. Ranalli, J. Silverman, W. N. Brandt, Y. Q. Xue, J. Mulchaey, L. Howes, C. Schmid, D. Wilman, A. Comastri, G. Hasinger, V. Mainieri, B. Luo, P. Tozzi, P. Rosati, P. Capak, and P. Popesso. Ultra-deep catalog of X-ray groups in the Extended Chandra Deep Field South. A&A, 576:A130, Apr. 2015. doi: 10.1051/0004-6361/201323053.

D. Foreman-Mackey, D. W. Hogg, D. Lang, and J. Goodman. emcee: The MCMC Hammer. PASP, 125:306, Mar. 2013. doi: 10.1086/670067.

A. R. Foster, L. Ji, R. K. Smith, and N. S. Brickhouse. Updated Atomic Data and Calculations for X-Ray Spectroscopy. ApJ, 756(2):128, Sept. 2012. doi: 10.1088/0004-637X/756/2/128.

M. Freyberg, E. Perinati, F. Pacaud, T. Eraerds, E. Churazov, K. Dennerl, P. Predehl, A. Merloni, N. Meidinger, E. Bulbul, S. Friedrich, M. Gilfanov, C. Tenzer, C. Pommranz, D. Eckert, J. Schmitt, M. Brusa, and A. Santangelo. SRG/eROSITA in-flight background at L2. In Society of Photo-Optical Instrumentation Engineers (SPIE) Conference Series, volume 11444 of Society of Photo-Optical Instrumentation Engineers (SPIE) Conference Series, page 114441O, Dec. 2020. doi: 10.1117/12.2562709.

P. Friedrich, H. Bräuninger, B. Budau, W. Burkert, J. Eder, M. J. Freyberg, G. Hartner, M. Mühlegger, P. Predehl, M. Erhard, S. Gutruf, D. Jugler, D. Kampf, G. Borghi, O. Citterio, M. Rossi, G. Valsecchi, D. Vernani, and M. Zimmermann. Design and development of the eROSITA x-ray mirrors. In M. J. L. Turner and K. A. Flanagan, editors, Space Telescopes and Instrumentation 2008: Ultraviolet to Gamma Ray, volume 7011 of Society of Photo-Optical Instrumentation Engineers (SPIE) Conference Series, page 70112T, July 2008. doi: 10.1117/12.788948.

M. Gaspari, M. Ruszkowski, and P. Sharma. Cause and Effect of Feedback: Multiphase Gas in Cluster Cores Heated by AGN Jets. ApJ, 746(1):94, Feb. 2012. doi: 10.1088/0004-637X/746/1/94.

F. Gastaldello, D. A. Buote, P. Temi, F. Brighenti, W. G. Mathews, and S. Ettori. X-Ray Cavities, Filaments, and Cold Fronts in the Core of the Galaxy Group NGC 5044. ApJ, 693(1):43–55, Mar. 2009. doi: 10.1088/0004-637X/693/1/43.

F. Gastaldello, A. Simionescu, F. Mernier, V. Biffi, M. Gaspari, K. Sato, and K. Matsushita. The Metal Content of the Hot Atmospheres of Galaxy Groups. Universe, 7(7):208, June 2021. doi: 10.3390/universe7070208.

K. Gebhardt, R. Bender, G. Bower, A. Dressler, S. M. Faber, A. V. Filippenko, R. Green, C. Grillmair, L. C. Ho, J. Kormendy, T. R. Lauer, J. Magorrian, J. Pinkney, D. Richstone, and S. Tremaine. A Relationship between Nuclear Black Hole Mass and Galaxy Velocity Dispersion. ApJ, 539(1):L13–L16, Aug. 2000. doi: 10.1086/312840.

A. Gelman, J. B. Carlin, H. S. Stern, D. B. Dunson, A. Vehtari, and D. B. Rubin. Bayesian Data Analysis. 2014.

V. Ghirardini, D. Eckert, S. Ettori, E. Pointecouteau, S. Molendi, M. Gaspari, M. Rossetti, S. De Grandi, M. Roncarelli, H. Bourdin, P. Mazzotta, E. Rasia, and F. Vazza. Universal thermodynamic properties of the intracluster medium over two decades in radius in the X-COP sample. A&A, 621:A41, Jan. 2019. doi: 10.1051/0004-6361/201833325.

V. Ghirardini, E. Bulbul, D. N. Hoang, M. Klein, N. Okabe, V. Biffi, M. Brüggen, M. E. Ramos-Ceja, J. Comparat, M. Oguri, T. W. Shimwell, K. Basu, A. Bonafede, A. Botteon, G. Brunetti, R. Cassano, F. de Gasperin, K. Dennerl, E. Gatuzz, F. Gastaldello, H. Intema, A. Merloni,

K. Nandra, F. Pacaud, P. Predehl, T. H. Reiprich, J. Robrade, H. Röttgering, J. Sanders, R. J. van Weeren, and W. L. Williams. Discovery of a supercluster in the eROSITA Final Equatorial Depth Survey: X-ray properties, radio halo, and double relics. A&A, 647:A4, Mar. 2021. doi: 10.1051/0004-6361/202039554.

V. Ghirardini, Y. E. Bahar, E. Bulbul, A. Liu, N. Clerc, F. Pacaud, J. Comparat, T. Liu, M. E. Ramos-Ceja, D. Hoang, J. Ider-Chitham, M. Klein, A. Merloni, K. Nandra, N. Ota, P. Predehl, T. H. Reiprich, J. Sanders, and T. Schrabback. The eROSITA Final Equatorial-Depth Survey (eFEDS). Characterization of morphological properties of galaxy groups and clusters. A&A, 661:A12, May 2022. doi: 10.1051/0004-6361/202141639.

V. Ghirardini, E. Bulbul, E. Artis, N. Clerc, C. Garrel, S. Grandis, M. Kluge, A. Liu, Y. E. Bahar, F. Balzer, I. Chiu, J. Comparat, D. Gruen, F. Kleinebreil, S. Krippendorf, A. Merloni, K. Nandra, N. Okabe, F. Pacaud, P. Predehl, M. E. Ramos-Ceja, T. H. Reiprich, J. S. Sanders, T. Schrabback, R. Seppi, S. Zelmer, X. Zhang, W. Bornemann, H. Brunner, V. Burwitz, D. Coutinho, K. Dennerl, M. Freyberg, S. Friedrich, R. Gaida, A. Gueguen, F. Haberl, W. Kink, G. Lamer, X. Li, T. Liu, C. Maitra, N. Meidinger, S. Mueller, H. Miyatake, S. Miyazaki, J. Robrade, A. Schwope, and I. Stewart. The SRG/eROSITA All-Sky Survey: Cosmology Constraints from Cluster Abundances in the Western Galactic Hemisphere. arXiv e-prints, art. arXiv:2402.08458, Feb. 2024. doi: 10.48550/arXiv.2402.08458.

S. Ghizzardi, S. Molendi, R. van der Burg, S. De Grandi, I. Bartalucci, F. Gastaldello, M. Rossetti, V. Biffi, S. Borgani, D. Eckert, S. Ettori, M. Gaspari, V. Ghirardini, and E. Rasia. Iron in X-COP: Tracing enrichment in cluster outskirts with high accuracy abundance profiles. A&A, 646:A92, Feb. 2021. doi: 10.1051/0004-6361/202038501.

G. Gianfagna, M. De Petris, G. Yepes, F. De Luca, F. Sembolini, W. Cui, V. Biffi, F. Kéruzoré, J. Macías-Pérez, F. Mayet, L. Perotto, E. Rasia, and F. Ruppin. Exploring the hydrostatic mass bias in MUSIC clusters: application to the NIKA2 mock sample. MNRAS, 502(4): 5115–5133, Apr. 2021. doi: 10.1093/mnras/stab308.

P. A. Giles, B. J. Maughan, F. Pacaud, M. Lieu, N. Clerc, M. Pierre, C. Adami, L. Chiappetti, J. Démoclés, S. Ettori, J. P. Le Févre, T. Ponman, T. Sadibekova, G. P. Smith, J. P. Willis, and F. Ziparo. The XXL Survey. III. Luminosity-temperature relation of the bright cluster sample. A&A, 592:A3, June 2016. doi: 10.1051/0004-6361/201526886.

S. Giodini, L. Lovisari, E. Pointecouteau, S. Ettori, T. H. Reiprich, and H. Hoekstra. Scaling Relations for Galaxy Clusters: Properties and Evolution. Space Sci. Rev., 177(1-4):247–282, Aug. 2013. doi: 10.1007/s11214-013-9994-5.

J. Goodman and J. Weare. Ensemble samplers with affine invariance. Communications in Applied Mathematics and Computational Science, 5(1):65–80, Jan. 2010. doi: 10.2140/camcos.2010.5.65.

F. Govoni, L. Feretti, G. Giovannini, H. Böhringer, T. H. Reiprich, and M. Murgia. Radio and X-ray diffuse emission in six clusters of galaxies. A&A, 376:803–819, Sept. 2001. doi: 10.1051/0004-6361:20011016.

G. Gozaliasl, A. Finoguenov, M. Tanaka, K. Dolag, F. Montanari, C. C. Kirkpatrick, E. Vardoulaki, H. G. Khosroshahi, M. Salvato, C. Laigle, H. J. McCracken, O. Ilbert, N. Cappelluti, E. Daddi, G. Hasinger, P. Capak, N. Z. Scoville, S. Toft, F. Civano, R. E. Griffiths, M. Balogh, Y. Li, J. Ahoranta, S. Mei, A. Iovino, B. M. B. Henriques, and G. Erfanianfar. VizieR Online Data Catalog: X-ray centres of COSMOS galaxy groups (Gozaliasl+, 2019). VizieR Online Data Catalog, art. J/MNRAS/483/3545, July 2022.

I. S. Gradshteyn and I. M. Ryzhik. Table of integrals, series and products. 1980.

S. Grandis, J. J. Mohr, M. Costanzi, A. Saro, S. Bocquet, M. Klein, M. Aguena, S. Allam, J. Annis, B. Ansarinejad, D. Bacon, E. Bertin, L. Bleem, D. Brooks, D. L. Burke, A. Carnero Rosel, M. Carrasco Kind, J. Carretero, F. J. Castander, A. Choi, L. N. da Costa, J. De Vincente, S. Desai, H. T. Diehl, J. P. Dietrich, P. Doel, T. F. Eifler, S. Everett, I. Ferrero, B. Floyd, P. Fosalba, J. Frieman, J. García-Bellido, E. Gaztanaga, D. Gruen, R. A. Gruendl, J. Gschwend, N. Gupta, G. Gutierrez, S. R. Hinton, D. L. Hollowood, K. Honscheid, D. J. James, T. Jeltema, K. Kuehn, O. Lahav, C. Lidman, M. Lima, M. A. G. Maia, M. March, J. L. Marshall, P. Melchior, F. Menanteau, R. Miquel, R. Morgan, J. Myles, R. Ogando, A. Palmese, F. Paz-Chinchón, A. A. Plazas, C. L. Reichardt, A. K. Romer, E. Sanchez, V. Scarpine, S. Serrano, I. Sevilla-Noarbe, P. Singh, M. Smith, E. Suchyta, M. E. C. Swanson, G. Tarle, D. Thomas, C. To, J. Weller, R. D. Wilkinson, and H. Wu. Exploring the contamination of the DES-Y1 cluster sample with SPT-SZ selected clusters. MNRAS, 504(1):1253–1272, June 2021. doi: 10.1093/mnras/stab869.

S. Grandis, G. Aricò, A. Schneider, and L. Linke. Determining the baryon impact on the matter power spectrum with galaxy clusters. MNRAS, 528(3):4379–4392, Mar. 2024a. doi: 10.1093/mnras/stae259.

S. Grandis, V. Ghirardini, S. Bocquet, C. Garrel, J. J. Mohr, A. Liu, M. Kluge, L. Kimmig, T. H. Reiprich, A. Alarcon, A. Amon, E. Artis, Y. E. Bahar, F. Balzer, K. Bechtol, M. R. Becker, G. Bernstein, E. Bulbul, A. Campos, A. Carnero Rosell, M. Carrasco Kind, R. Cawthon, C. Chang, R. Chen, I. Chiu, A. Choi, N. Clerc, J. Comparat, J. Cordero, C. Davis, J. Derose, H. T. Diehl, S. Dodelson, C. Doux, A. Drlica-Wagner, K. Eckert, J. Elvin-Poole, S. Everett, A. Ferte, M. Gatt, G. Giannini, P. Giles, D. Gruen, R. A. Gruendl, I. Harrison, W. G. Hartley, K. Herner, E. M. Huf, F. Kleinebreil, N. Kuropatkin, P. F. Leget, N. Maccrann, J. Mccullough, A. Merloni, J. Myles, K. Nandra, A. Navarro-Alsina, N. Okabe, F. Pacaud, S. Pandey, J. Prat, P. Predehl, M. Ramos, M. Raveri, R. P. Rollins, A. Roodman, A. J. Ross, E. S. Rykoff, C. Sanchez, J. Sanders, T. Schrabback, L. F. Secco, R. Seppi, I. Sevilla-Noarbe, E. Sheldon, T. Shin, M. Troxel, I. Tutusaus, T. N. Varga, H. Wu, B. Yanny, B. Yin, X. Zhang, Y. Zhang, O. Alves, S. Bhargava, D. Brooks, D. L. Burke, J. Carretero, M. Costanzi, L. N. da Costa, M. E. S. Pereira, J. De Vicente, S. Desai, P. Doel, I. Ferrero, B. Flaugher, D. Friedel, J. Frieman, J. García-Bellido, G. Gutierrez, S. R. Hinton, D. L. Hollowood, K. Honscheid, D. J.

James, N. Jeffrey, O. Lahav, S. Lee, J. L. Marshall, F. Menanteau, R. L. C. Ogando, A. Pieres, A. A. Plazas Malagón, A. K. Romer, E. Sanchez, M. Schubnell, M. Smith, E. Suchyta, M. E. C. Swanson, G. Tarle, N. Weaverdyck, and J. Weller. The SRG/eROSITA All-Sky Survey: Dark Energy Survey Year 3 Weak Gravitational Lensing by eRASS1 selected Galaxy Clusters. arXiv e-prints, art. arXiv:2402.08455, Feb. 2024b. doi: 10.48550/arXiv.2402.08455.

H. Gursky, E. Kellogg, S. Murray, C. Leong, H. Tananbaum, and R. Giacconi. A Strong X-Ray Source in the Coma Cluster Observed by UHURU. ApJ, 167:L81, Aug. 1971. doi: 10.1086/180765.

F. Haardt and P. Madau. Modelling the UV/X-ray cosmic background with CUBA. In D. M. Neumann and J. T. V. Tran, editors, Clusters of Galaxies and the High Redshift Universe Observed in X-rays, page 64, Jan. 2001.

C. M. Harrison. Impact of supermassive black hole growth on star formation. Nature Astronomy, 1:0165, July 2017. doi: 10.1038/s41550-017-0165.

C. M. Harrison and C. Ramos Almeida. Observational Tests of Active Galactic Nuclei Feedback: An Overview of Approaches and Interpretation. Galaxies, 12(2):17, Apr. 2024. doi: 10.3390/galaxies12020017.

N. A. Henden, E. Puchwein, S. Shen, and D. Sijacki. The FABLE simulations: a feedback model for galaxies, groups, and clusters. MNRAS, 479(4):5385–5412, Oct. 2018. doi: 10.1093/mnras/sty1780.

N. A. Henden, E. Puchwein, and D. Sijacki. The redshift evolution of X-ray and Sunyaev-Zel'dovich scaling relations in the FABLE simulations. MNRAS, 489(2):2439–2470, Oct. 2019. doi: 10.1093/mnras/stz2301.

D. B. Henley and R. L. Shelton. An XMM-Newton Survey of the Soft X-Ray Background. III. The Galactic Halo X-Ray Emission. ApJ, 773(2):92, Aug. 2013. doi: 10.1088/0004-637X/773/2/92.

C. Hernández-Aguayo, V. Springel, R. Pakmor, M. Barrera, F. Ferlito, S. D. M. White, L. Hernquist, B. Hadzhiyska, A. M. Delgado, R. Kannan, S. Bose, and C. Frenk. The MillenniumTNG Project: high-precision predictions for matter clustering and halo statistics. MNRAS, 524(2):2556–2578, Sept. 2023. doi: 10.1093/mnras/stad1657.

W. Herschel. On the Construction of the Heavens. Philosophical Transactions of the Royal Society of London Series I, 75:213–266, Jan. 1785.

W. Herschel. Catalogue of 500 New Nebulae, Nebulous Stars, Planetary Nebulae, and Clusters of Stars; With Remarks on the Construction of the Heavens. Philosophical Transactions of the Royal Society of London Series I, 92:477–528, Jan. 1802.

HI4PI Collaboration, N. Ben Bekhti, L. Flöer, R. Keller, J. Kerp, D. Lenz, B. Winkel, J. Bailin, M. R. Calabretta, L. Dedes, H. A. Ford, B. K. Gibson, U. Haud, S. Janowiecki, P. M. W. Kalberla, F. J. Lockman, N. M. McClure-Griffiths, T. Murphy, H. Nakanishi, D. J. Pisano, and L. Staveley-Smith. HI4PI: A full-sky H I survey based on EBHIS and GASS. A&A, 594: A116, Oct. 2016. doi: 10.1051/0004-6361/201629178.

P. Hickson. Systematic properties of compact groups of galaxies. ApJ, 255:382–391, Apr. 1982. doi: 10.1086/159838.

P. Hickson. Compact Groups of Galaxies. ARA&A, 35:357–388, Jan. 1997. doi: 10.1146/ annurev.astro.35.1.357.

M. Hilton, A. K. Romer, S. T. Kay, N. Mehrtens, E. J. Lloyd-Davies, P. A. Thomas, C. J. Short, J. A. Mayers, P. J. Rooney, J. P. Stott, C. A. Collins, C. D. Harrison, B. Hoyle, A. R. Liddle, R. G. Mann, C. J. Miller, M. Sahlén, P. T. P. Viana, M. Davidson, M. Hosmer, R. C. Nichol, K. Sabirli, S. A. Stanford, and M. J. West. The XMM Cluster Survey: evidence for energy injection at high redshift from evolution of the X-ray luminosity-temperature relation. MNRAS, 424(3):2086–2096, Aug. 2012. doi: 10.1111/j.1365-2966.2012.21359.x.

M. Hilton, C. Sifón, S. Naess, M. Madhavacheril, M. Oguri, E. Rozo, E. Rykoff, T. M. C. Abbott, S. Adhikari, M. Aguena, S. Aiola, S. Allam, S. Amodeo, A. Amon, J. Annis, B. Ansarinejad, C. Aros-Bunster, J. E. Austermann, S. Avila, D. Bacon, N. Battaglia, J. A. Beall, D. T. Becker, G. M. Bernstein, E. Bertin, T. Bhandarkar, S. Bhargava, J. R. Bond, D. Brooks, D. L. Burke, E. Calabrese, M. Carrasco Kind, J. Carretero, S. K. Choi, A. Choi, C. Conselice, L. N. da Costa, M. Costanzi, D. Crichton, K. T. Crowley, R. Dünner, E. V. Denison, M. J. Devlin, S. R. Dicker, H. T. Diehl, J. P. Dietrich, P. Doel, S. M. Duff, A. J. Duivenvoorden, J. Dunkley, S. Everett, S. Ferraro, I. Ferrero, A. Ferté, B. Flaugher, J. Frieman, P. A. Gallardo, J. García-Bellido, E. Gaztanaga, D. W. Gerdes, P. Giles, J. E. Golec, M. B. Gralla, S. Grandis, D. Gruen, R. A. Gruendl, J. Gschwend, G. Gutierrez, D. Han, W. G. Hartley, M. Hasselfield, J. C. Hill, G. C. Hilton, A. D. Hincks, S. R. Hinton, S. P. P. Ho, K. Honscheid, B. Hoyle, J. Hubmayr, K. M. Huffenberger, J. P. Hughes, A. T. Jaelani, B. Jain, D. J. James, T. Jeltema, S. Kent, K. Knowles, B. J. Koopman, K. Kuehn, O. Lahav, M. Lima, Y. T. Lin, M. Lokken, S. I. Loubser, N. MacCrann, M. A. G. Maia, T. A. Marriage, J. Martin, J. McMahon, P. Melchior, F. Menanteau, R. Miquel, H. Miyatake, K. Moodley, R. Morgan, T. Mroczkowski, F. Nati, L. B. Newburgh, M. D. Niemack, A. J. Nishizawa, R. L. C. Ogando, J. Orlowski-Scherer, L. A. Page, A. Palmese, B. Partridge, F. Paz-Chinchón, P. Phakathi, A. A. Plazas, N. C. Robertson, A. K. Romer, A. Carnero Rosell, M. Salatino, E. Sanchez, E. Schaan, A. Schillaci, N. Sehgal, S. Serrano, T. Shin, S. M. Simon, M. Smith, M. Soares-Santos, D. N. Spergel, S. T. Staggs, E. R. Storer, E. Suchyta, M. E. C. Swanson, G. Tarle, D. Thomas, C. To, H. Trac, J. N. Ullom, L. R. Vale, J. Van Lanen, E. M. Vavagiakis, J. De Vicente, R. D. Wilkinson, E. J. Wollack, Z. Xu, and Y. Zhang. The Atacama Cosmology Telescope: A Catalog of >4000 Sunyaev-Zel'dovich Galaxy Clusters. ApJS, 253(1):3, Mar. 2021. doi: 10.3847/1538-4365/abd023.

M. Hirschmann, K. Dolag, A. Saro, L. Bachmann, S. Borgani, and A. Burkert. Cosmological

simulations of black hole growth: AGN luminosities and downsizing. MNRAS, 442(3):2304–2324, Aug. 2014. doi: 10.1093/mnras/stu1023.

Hitomi Collaboration, F. Aharonian, H. Akamatsu, F. Akimoto, S. W. Allen, L. Angelini, M. Audard, H. Awaki, M. Axelsson, A. Bamba, M. W. Bautz, R. Blandford, L. W. Brenneman, G. V. Brown, E. Bulbul, E. M. Cackett, M. Chernyakova, M. P. Chiao, P. S. Coppi, E. Costantini, J. de Plaa, J.-W. den Herder, C. Done, T. Dotani, K. Ebisawa, M. E. Eckart, T. Enoto, Y. Ezoe, A. C. Fabian, C. Ferrigno, A. R. Foster, R. Fujimoto, Y. Fukazawa, A. Furuzawa, M. Galeazzi, L. C. Gallo, P. Gandhi, M. Giustini, A. Goldwurm, L. Gu, M. Guainazzi, Y. Haba, K. Hagino, K. Hamaguchi, I. M. Harrus, I. Hatsukade, K. Hayashi, T. Hayashi, K. Hayashida, J. S. Hiraga, A. Hornschemeier, A. Hoshino, J. P. Hughes, Y. Ichinohe, R. Iizuka, H. Inoue, Y. Inoue, M. Ishida, K. Ishikawa, Y. Ishisaki, M. Iwai, J. Kaastra, T. Kallman, T. Kamae, J. Kataoka, S. Katsuda, N. Kawai, R. L. Kelley, C. A. Kilbourne, T. Kitaguchi, S. Kitamoto, T. Kitayama, T. Kohmura, M. Kokubun, K. Koyama, S. Koyama, P. Kretschmar, H. A. Krimm, A. Kubota, H. Kunieda, P. Laurent, S.-H. Lee, M. A. Leutenegger, O. Limousine, M. Loewenstein, K. S. Long, D. Lumb, G. Madejski, Y. Maeda, D. Maier, K. Makishima, M. Markevitch, H. Matsumoto, K. Matsushita, D. McCammon, B. R. McNamara, M. Mehdipour, E. D. Miller, J. M. Miller, S. Mineshige, K. Mitsuda, I. Mitsuishi, T. Miyazawa, T. Mizuno, H. Mori, K. Mori, K. Mukai, H. Murakami, R. F. Mushotzky, T. Nakagawa, H. Nakajima, T. Nakamori, S. Nakashima, K. Nakazawa, K. K. Nobukawa, M. Nobukawa, H. Noda, H. Odaka, T. Ohashi, M. Ohno, T. Okajima, N. Ota, M. Ozaki, F. Paerels, S. Paltani, R. Petre, C. Pinto, F. S. Porter, K. Pottschmidt, C. S. Reynolds, S. Safi-Harb, S. Saito, K. Sakai, T. Sasaki, G. Sato, K. Sato, R. Sato, M. Sawada, N. Schartel, P. J. Serlemitsos, H. Seta, M. Shidatsu, A. Simionescu, R. K. Smith, Y. Soong, L. Stawarz, Y. Sugawara, S. Sugita, A. Szymkowiak, H. Tajima, H. Takahashi, T. Takahashi, S. Takeda, Y. Takei, T. Tamagawa, T. Tamura, T. Tanaka, Y. Tanaka, Y. T. Tanaka, M. S. Tashiro, Y. Tawara, Y. Terada, Y. Terashima, F. Tombesi, H. Tomida, Y. Tsuboi, M. Tsujimoto, H. Tsunemi, T. Go Tsuru, H. Uchida, H. Uchiyama, Y. Uchiyama, S. Ueda, Y. Ueda, S. Uno, C. M. Urry, E. Ursino, C. P. de Vries, S. Watanabe, N. Werner, D. R. Wik, D. R. Wilkins, B. J. Williams, S. Yamada, H. Yamaguchi, K. Yamaoka, N. Y. Yamasaki, M. Yamauchi, S. Yamauchi, T. Yaqoob, Y. Yatsu, D. Yonetoku, I. Zhuravleva, and A. Zoghbi. Solar abundance ratios of the iron-peak elements in the Perseus cluster. Nature, 551(7681):478–480, Nov. 2017. doi: 10.1038/nature24301.

J. Hlavacek-Larrondo, S. W. Allen, G. B. Taylor, A. C. Fabian, R. E. A. Canning, N. Werner, J. S. Sanders, C. K. Grimes, S. Ehlert, and A. von der Linden. Probing the Extreme Realm of Active Galactic Nucleus Feedback in the Massive Galaxy Cluster, RX J1532.9+3021. ApJ, 777(2):163, Nov. 2013. doi: 10.1088/0004-637X/777/2/163.

J. Hlavacek-Larrondo, Y. Li, and E. Churazov. AGN Feedback in Groups and Clusters of Galaxies. In C. Bambi and A. Sangangelo, editors, Handbook of X-ray and Gamma-ray Astrophysics, page 5. 2022. doi: 10.1007/978-981-16-4544-0_122-1.

H. Hoekstra, M. Bartelmann, H. Dahle, H. Israel, M. Limousin, and M. Meneghetti. Masses of

Galaxy Clusters from Gravitational Lensing. Space Sci. Rev., 177(1-4):75–118, Aug. 2013. doi: 10.1007/s11214-013-9978-5.

D. W. Hogg. Distance measures in cosmology. arXiv e-prints, May 1999.

D. W. Hogg, I. K. Baldry, M. R. Blanton, and D. J. Eisenstein. The K correction. arXiv e-prints, art. astro-ph/0210394, Oct. 2002. doi: 10.48550/arXiv.astro-ph/0210394.

P. F. Hopkins, L. Hernquist, T. J. Cox, T. Di Matteo, B. Robertson, and V. Springel. A Unified, Merger-driven Model of the Origin of Starbursts, Quasars, the Cosmic X-Ray Background, Supermassive Black Holes, and Galaxy Spheroids. ApJS, 163(1):1–49, Mar. 2006. doi: 10. 1086/499298.

E. Hubble and M. L. Humason. The Velocity-Distance Relation among Extra-Galactic Nebulae. ApJ, 74:43, July 1931. doi: 10.1086/143323.

E. P. Hubble. Extragalactic nebulae. ApJ, 64:321–369, Dec. 1926. doi: 10.1086/143018.

J. P. Huchra, L. M. Macri, K. L. Masters, T. H. Jarrett, P. Berlind, M. Calkins, A. C. Crook, R. Cutri, P. Erdoğdu, E. Falco, T. George, C. M. Hutcheson, O. Lahav, J. Mader, J. D. Mink, N. Martimbeau, S. Schneider, M. Skrutskie, S. Tokarz, and M. Westover. The 2MASS Redshift Survey—Description and Data Release. ApJS, 199(2):26, Apr. 2012. doi: 10.1088/0067-0049/199/2/26.

P. J. Humphrey, D. A. Buote, F. Brighenti, H. M. L. G. Flohic, F. Gastaldello, and W. G. Mathews. Tracing the Gas to the Virial Radius (R_{100}) in a Fossil Group. ApJ, 748(1):11, Mar. 2012. doi: 10.1088/0004-637X/748/1/11.

J. Ider Chitham, J. Comparat, A. Finoguenov, N. Clerc, C. Kirkpatrick, S. Damsted, A. Kukkola, R. Capasso, K. Nandra, A. Merloni, E. Bulbul, E. S. Rykoff, D. P. Schneider, and J. R. Brownstein. Cosmological constraints from CODEX galaxy clusters spectroscopically confirmed by SDSS-IV/SPIDERS DR16. MNRAS, 499(4):4768–4784, Dec. 2020. doi: 10.1093/mnras/staa3044.

J. Iljenkarevic, T. H. Reiprich, F. Pacaud, A. Veronica, B. Whelan, J. Aschersleben, K. Migkas, E. Bulbul, J. S. Sanders, M. E. Ramos-Ceja, T. Liu, V. Ghirardini, A. Liu, and T. Boller. EROSITA Spectro-Imaging Analysis of the Abell 3408 Galaxy Cluster. arXiv e-prints, art. arXiv:2106.14544, June 2021.

R. Johnson, T. J. Ponman, and A. Finoguenov. A statistical analysis of the Two-Dimensional XMM-Newton Group Survey: the impact of feedback on group properties. MNRAS, 395(3): 1287–1308, May 2009. doi: 10.1111/j.1365-2966.2009.14644.x.

J. S. Kaastra. On the use of C-stat in testing models for X-ray spectra. A&A, 605:A51, Sept. 2017. doi: 10.1051/0004-6361/201629319.

J. S. Kaastra, R. Mewe, and H. Nieuwenhuijzen. SPEX: a new code for spectral analysis of X & UV spectra. In UV and X-ray Spectroscopy of Astrophysical and Laboratory Plasmas, pages 411–414, Jan. 1996.

J. S. Kaastra, F. B. S. Paerels, F. Durret, S. Schindler, and P. Richter. Thermal Radiation Processes. Space Sci. Rev., 134(1-4):155–190, Feb. 2008. doi: 10.1007/s11214-008-9310-y.

J. S. Kaastra, A. J. J. Raassen, J. de Plaa, and L. Gu. SPEX X-ray spectral fitting package, Dec. 2020.

N. Kaiser. Evolution and clustering of rich clusters. MNRAS, 222:323–345, Sept. 1986. doi: 10.1093/mnras/222.2.323.

W. J. Karzas and R. Latter. Electron Radiative Transitions in a Coulomb Field. ApJS, 6:167, May 1961. doi: 10.1086/190063.

S. T. Kay, P. A. Thomas, and T. Theuns. The impact of galaxy formation on X-ray groups. MNRAS, 343(2):608–618, Aug. 2003. doi: 10.1046/j.1365-8711.2003.06711.x.

E. Kellogg, H. Gursky, H. Tananbaum, R. Giacconi, and K. Pounds. The Extended X-Ray Source at M87. ApJ, 174:L65, June 1972. doi: 10.1086/180950.

E. Kellogg, J. R. Baldwin, and D. Koch. Studies of cluster X-ray sources. Energy spectra for the Perseus, Virgo, and Coma clusters. ApJ, 199:299–306, July 1975. doi: 10.1086/153692.

K. Kettula, S. Giodini, E. van Uitert, H. Hoekstra, A. Finoguenov, M. Lerchster, T. Erben, C. Heymans, H. Hildebrandt, T. D. Kitching, A. Mahdavi, Y. Mellier, L. Miller, M. Mirkazemi, L. Van Waerbeke, J. Coupon, E. Egami, L. Fu, M. J. Hudson, J. P. Kneib, K. Kuijken, H. J. McCracken, M. J. Pereira, B. Rowe, T. Schrabback, M. Tanaka, and M. Velander. CFHTLenS: weak lensing calibrated scaling relations for low-mass clusters of galaxies. MNRAS, 451(2): 1460–1481, Aug. 2015. doi: 10.1093/mnras/stv923.

D.-W. Kim. Metal Abundances in the Hot ISM of Elliptical Galaxies. In D.-W. Kim and S. Pellegrini, editors, Astrophysics and Space Science Library, volume 378 of Astrophysics and Space Science Library, page 121, Jan. 2012. doi: 10.1007/978-1-4614-0580-1_5.

A. King. Black Holes, Galaxy Formation, and the M_{BH}-σ Relation. ApJ, 596(1):L27–L29, Oct. 2003. doi: 10.1086/379143.

I. King. The structure of star clusters. I. an empirical density law. AJ, 67:471, Oct. 1962. doi: 10.1086/108756.

C. C. Kirkpatrick, M. Gitti, K. W. Cavagnolo, B. R. McNamara, L. P. David, P. E. J. Nulsen, and M. W. Wise. Direct Evidence for Outflow of Metal-Enriched Gas Along the Radio Jets of Hydra A. ApJ, 707(1):L69–L72, Dec. 2009. doi: 10.1088/0004-637X/707/1/L69.

M. Klein, M. Oguri, J. J. Mohr, S. Grandis, V. Ghirardini, T. Liu, A. Liu, E. Bulbul, J. Wolf, J. Comparat, M. E. Ramos-Ceja, J. Buchner, I. Chiu, N. Clerc, A. Merloni, H. Miyatake, S. Miyazaki, N. Okabe, N. Ota, F. Pacaud, M. Salvato, and S. P. Driver. The eROSITA Final Equatorial-Depth Survey (eFEDS). Optical confirmation, redshifts, and properties of the cluster and group catalog. A&A, 661:A4, May 2022. doi: 10.1051/0004-6361/202141123.

F. Kleinebreil, S. Grandis, T. Schrabback, V. Ghirardini, I.-N. Chiu, A. Liu, M. Kluge, T. H. Reiprich, E. Artis, E. Bahar, F. Balzer, E. Bulbul, N. Clerc, J. Comparat, C. Garrel, D. Gruen, X. Li, H. Miyatake, S. Miyazaki, M. E. Ramos-Ceja, J. Sanders, R. Seppi, N. Okabe, and X. Zhang. The SRG/eROSITA All-Sky Survey: Weak-Lensing of eRASS1 Galaxy Clusters in KiDS-1000 and Consistency Checks with DES Y3 & HSC-Y3. arXiv e-prints, art. arXiv:2402.08456, Feb. 2024. doi: 10.48550/arXiv.2402.08456.

M. Kluge, J. Comparat, A. Liu, F. Balzer, E. Bulbul, J. Ider Chitham, V. Ghirardini, C. Garrel, Y. E. Bahar, E. Artis, R. Bender, N. Clerc, T. Dwelly, M. H. Fabricius, S. Grandis, D. Hernández-Lang, G. J. Hill, J. Joshi, G. Lamer, A. Merloni, K. Nandra, F. Pacaud, P. Predehl, M. E. Ramos-Ceja, T. H. Reiprich, M. Salvato, J. S. Sanders, T. Schrabback, R. Seppi, S. Zelmer, A. Zenteno, and X. Zhang. The First SRG/eROSITA All-Sky Survey: Optical Identification and Properties of Galaxy Clusters and Groups in the Western Galactic Hemisphere. arXiv e-prints, art. arXiv:2402.08453, Feb. 2024. doi: 10.48550/arXiv.2402.08453.

K. Kolokythas, E. O'Sullivan, H. Intema, S. Raychaudhury, A. Babul, S. Giacintucci, and M. Gitti. The complete local volume groups sample - III. Characteristics of group central radio galaxies in the Local Universe. MNRAS, 489(2):2488–2504, Oct. 2019. doi: 10.1093/mnras/stz2082.

E. Komatsu, K. M. Smith, J. Dunkley, C. L. Bennett, B. Gold, G. Hinshaw, N. Jarosik, D. Larson, M. R. Nolta, L. Page, D. N. Spergel, M. Halpern, R. S. Hill, A. Kogut, M. Limon, S. S. Meyer, N. Odegard, G. S. Tucker, J. L. Weiland, E. Wollack, and E. L. Wright. Seven-year Wilkinson Microwave Anisotropy Probe (WMAP) Observations: Cosmological Interpretation. ApJS, 192(2):18, Feb. 2011. doi: 10.1088/0067-0049/192/2/18.

A. V. Kravtsov and S. Borgani. Formation of Galaxy Clusters. ARA&A, 50:353–409, Sept. 2012. doi: 10.1146/annurev-astro-081811-125502.

A. V. Kravtsov and G. Yepes. On the supernova heating of the intergalactic medium. MNRAS, 318(1):227–238, Oct. 2000. doi: 10.1046/j.1365-8711.2000.03771.x.

A. V. Kravtsov, A. Vikhlinin, and D. Nagai. A New Robust Low-Scatter X-Ray Mass Indicator for Clusters of Galaxies. ApJ, 650(1):128–136, Oct. 2006. doi: 10.1086/506319.

E. T. Lau, A. V. Kravtsov, and D. Nagai. Residual Gas Motions in the Intracluster Medium and Bias in Hydrostatic Measurements of Mass Profiles of Clusters. ApJ, 705(2):1129–1138, Nov. 2009. doi: 10.1088/0004-637X/705/2/1129.

R. Laureijs, J. Amiaux, S. Arduini, J. L. Auguères, J. Brinchmann, R. Cole, M. Cropper, C. Dabin, L. Duvet, A. Ealet, B. Garilli, P. Gondoin, L. Guzzo, J. Hoar, H. Hoekstra, R. Holmes, T. Kitching, T. Maciaszek, Y. Mellier, F. Pasian, W. Percival, J. Rhodes, G. Saavedra Criado, M. Sauvage, R. Scaramella, L. Valenziano, S. Warren, R. Bender, F. Castander, A. Cimatti, O. Le Fèvre, H. Kurki-Suonio, M. Levi, P. Lilje, G. Meylan, R. Nichol, K. Pedersen, V. Popa, R. Rebolo Lopez, H. W. Rix, H. Rottgering, W. Zeilinger, F. Grupp, P. Hudelot, R. Massey, M. Meneghetti, L. Miller, S. Paltani, S. Paulin-Henriksson, S. Pires, C. Saxton, T. Schrabback, G. Seidel, J. Walsh, N. Aghanim, L. Amendola, J. Bartlett, C. Baccigalupi, J. P. Beaulieu, K. Benabed, J. G. Cuby, D. Elbaz, P. Fosalba, G. Gavazzi, A. Helmi, I. Hook, M. Irwin, J. P. Kneib, M. Kunz, F. Mannucci, L. Moscardini, C. Tao, R. Teyssier, J. Weller, G. Zamorani, M. R. Zapatero Osorio, O. Boulade, J. J. Foumond, A. Di Giorgio, P. Guttridge, A. James, M. Kemp, J. Martignac, A. Spencer, D. Walton, T. Blümchen, C. Bonoli, F. Bortoletto, C. Cerna, L. Corcione, C. Fabron, K. Jahnke, S. Ligori, F. Madrid, L. Martin, G. Morgante, T. Pamplona, E. Prieto, M. Riva, R. Toledo, M. Trifoglio, F. Zerbi, F. Abdalla, M. Douspis, C. Grenet, S. Borgani, R. Bouwens, F. Courbin, J. M. Delouis, P. Dubath, A. Fontana, M. Frailis, A. Grazian, J. Koppenhöfer, O. Mansutti, M. Melchior, M. Mignoli, J. Mohr, C. Neissner, K. Noddle, M. Poncet, M. Scodeggio, S. Serrano, N. Shane, J. L. Starck, C. Surace, A. Taylor, G. Verdoes-Kleijn, C. Vuerli, O. R. Williams, A. Zacchei, B. Altieri, I. Escudero Sanz, R. Kohley, T. Oosterbroek, P. Astier, D. Bacon, S. Bardelli, C. Baugh, F. Bellagamba, C. Benoist, D. Bianchi, A. Biviano, E. Branchini, C. Carbone, V. Cardone, D. Clements, S. Colombi, C. Conselice, G. Cresci, N. Deacon, J. Dunlop, C. Fedeli, F. Fontanot, P. Franzetti, C. Giocoli, J. Garcia-Bellido, J. Gow, A. Heavens, P. Hewett, C. Heymans, A. Holland, Z. Huang, O. Ilbert, B. Joachimi, E. Jennins, E. Kerins, A. Kiessling, D. Kirk, R. Kotak, O. Krause, O. Lahav, F. van Leeuwen, J. Lesgourgues, M. Lombardi, M. Magliocchetti, K. Maguire, E. Majerotto, R. Maoli, F. Marulli, S. Maurogordato, H. McCracken, R. McLure, A. Melchiorri, A. Merson, M. Moresco, M. Nonino, P. Norberg, J. Peacock, R. Pello, M. Penny, V. Pettorino, C. Di Porto, L. Pozzetti, C. Quercellini, M. Radovich, A. Rassat, N. Roche, S. Ronayette, E. Rossetti, B. Sartoris, P. Schneider, E. Semboloni, S. Serjeant, F. Simpson, C. Skordis, G. Smadja, S. Smartt, P. Spano, S. Spiro, M. Sullivan, A. Tilquin, R. Trotta, L. Verde, Y. Wang, G. Williger, G. Zhao, J. Zoubian, and E. Zucca. Euclid Definition Study Report. arXiv e-prints, art. arXiv:1110.3193, Oct. 2011. doi: 10.48550/arXiv.1110.3193.

A. M. C. Le Brun, I. G. McCarthy, J. Schaye, and T. J. Ponman. Towards a realistic population of simulated galaxy groups and clusters. MNRAS, 441(2):1270–1290, June 2014. doi: 10.1093/mnras/stu608.

H. Liang, R. W. Hunstead, M. Birkinshaw, and P. Andreani. A Powerful Radio Halo in the Hottest Known Cluster of Galaxies 1E 0657-56. ApJ, 544(2):686–701, Dec. 2000. doi: 10.1086/317223.

D. A. Liedahl, A. L. Osterheld, and W. H. Goldstein. New Calculations of Fe L-Shell X-Ray Spectra in High-Temperature Plasmas. ApJ, 438:L115, Jan. 1995. doi: 10.1086/187729.

A. Liu, E. Bulbul, V. Ghirardini, T. Liu, M. Klein, N. Clerc, Y. Özsoy, M. E. Ramos-Ceja, F. Pacaud, J. Comparat, N. Okabe, Y. E. Bahar, V. Biffi, H. Brunner, M. Brüggen, J. Buchner, J. Ider Chitham, I. Chiu, K. Dolag, E. Gatuzz, J. Gonzalez, D. N. Hoang, G. Lamer, A. Merloni, K. Nandra, M. Oguri, N. Ota, P. Predehl, T. H. Reiprich, M. Salvato, T. Schrabback, J. S. Sanders, R. Seppi, and Q. Thibaud. The eROSITA Final Equatorial-Depth Survey (eFEDS). Catalog of galaxy clusters and groups. A&A, 661:A2, May 2022a. doi: 10.1051/0004-6361/202141120.

A. Liu, E. Bulbul, M. E. Ramos-Ceja, J. S. Sanders, V. Ghirardini, Y. E. Bahar, M. Yeung, E. Gatuzz, M. Freyberg, C. Garrel, X. Zhang, A. Merloni, and K. Nandra. X-ray analysis of JWST's first galaxy cluster lens SMACS J0723.3−7327. A&A, 670:A96, Feb. 2023. doi: 10.1051/0004-6361/202245118.

T. Liu, A. Merloni, J. Comparat, K. Nandra, J. S. Sanders, G. Lamer, J. Buchner, T. Dwelly, M. Freyberg, A. Malyali, A. Georgakakis, M. Salvato, H. Brunner, M. Brusa, M. Klein, V. Ghirardini, N. Clerc, F. Pacaud, E. Bulbul, A. Liu, A. Schwope, J. Robrade, J. Wilms, T. Dauser, M. E. Ramos-Ceja, T. H. Reiprich, T. Boller, and J. Wolf. Establishing the X-ray Source Detection Strategy for eROSITA with Simulations. arXiv e-prints, art. arXiv:2106.14528, June 2021.

T. Liu, J. Buchner, K. Nandra, A. Merloni, T. Dwelly, J. S. Sanders, M. Salvato, R. Arcodia, M. Brusa, J. Wolf, A. Georgakakis, T. Boller, M. Krumpe, G. Lamer, S. Waddell, T. Urrutia, A. Schwope, J. Robrade, J. Wilms, T. Dauser, J. Comparat, Y. Toba, K. Ichikawa, K. Iwasawa, Y. Shen, and H. I. Medel. The eROSITA Final Equatorial-Depth Survey (eFEDS). The AGN catalog and its X-ray spectral properties. A&A, 661:A5, May 2022b. doi: 10.1051/0004-6361/202141643.

W. Liu, M. Sun, P. Nulsen, T. Clarke, C. Sarazin, W. Forman, M. Gaspari, S. Giacintucci, D. V. Lal, and T. Edge. AGN feedback in galaxy group 3C 88: cavities, shock, and jet reorientation. MNRAS, 484(3):3376–3392, Apr. 2019. doi: 10.1093/mnras/stz229.

E. J. Lloyd-Davies, T. J. Ponman, and D. B. Cannon. The entropy and energy of intergalactic gas in galaxy clusters. MNRAS, 315(4):689–702, July 2000. doi: 10.1046/j.1365-8711.2000.03380.x.

L. Lovisari and B. J. Maughan. Scaling Relations of Clusters and Groups and Their Evolution. In Handbook of X-ray and Gamma-ray Astrophysics, page 65. 2022. doi: 10.1007/978-981-16-4544-0_118-1.

L. Lovisari and T. H. Reiprich. The non-uniformity of galaxy cluster metallicity profiles. MNRAS, 483(1):540–557, Feb. 2019. doi: 10.1093/mnras/sty3130.

L. Lovisari, T. H. Reiprich, and G. Schellenberger. Scaling properties of a complete X-ray selected galaxy group sample. A&A, 573:A118, Jan. 2015. doi: 10.1051/0004-6361/201423954.

L. Lovisari, G. Schellenberger, M. Sereno, S. Ettori, G. W. Pratt, W. R. Forman, C. Jones, F. Andrade-Santos, S. Randall, and R. Kraft. X-Ray Scaling Relations for a Representative Sample of Planck-selected Clusters Observed with XMM-Newton. ApJ, 892(2):102, Apr. 2020. doi: 10.3847/1538-4357/ab7997.

L. Lovisari, S. Ettori, M. Gaspari, and P. A. Giles. Scaling Properties of Galaxy Groups. Universe, 7(5):139, May 2021. doi: 10.3390/universe7050139.

LSST Science Collaboration, P. A. Abell, J. Allison, S. F. Anderson, J. R. Andrew, J. R. P. Angel, L. Armus, D. Arnett, S. J. Asztalos, T. S. Axelrod, S. Bailey, D. R. Ballantyne, J. R. Bankert, W. A. Barkhouse, J. D. Barr, L. F. Barrientos, A. J. Barth, J. G. Bartlett, A. C. Becker, J. Becla, T. C. Beers, J. P. Bernstein, R. Biswas, M. R. Blanton, J. S. Bloom, J. J. Bochanski, P. Boeshaar, K. D. Borne, M. Bradac, W. N. Brandt, C. R. Bridge, M. E. Brown, R. J. Brunner, J. S. Bullock, A. J. Burgasser, J. H. Burge, D. L. Burke, P. A. Cargile, S. Chandrasekharan, G. Chartas, S. R. Chesley, Y.-H. Chu, D. Cinabro, M. W. Claire, C. F. Claver, D. Clowe, A. J. Connolly, K. H. Cook, J. Cooke, A. Cooray, K. R. Covey, C. S. Culliton, R. de Jong, W. H. de Vries, V. P. Debattista, F. Delgado, I. P. Dell'Antonio, S. Dhital, R. Di Stefano, M. Dickinson, B. Dilday, S. G. Djorgovski, G. Dobler, C. Donalek, G. Dubois-Felsmann, J. Durech, A. Eliasdottir, M. Eracleous, L. Eyer, E. E. Falco, X. Fan, C. D. Fassnacht, H. C. Ferguson, Y. R. Fernandez, B. D. Fields, D. Finkbeiner, E. E. Figueroa, D. B. Fox, H. Francke, J. S. Frank, J. Frieman, S. Fromenteau, M. Furqan, G. Galaz, A. Gal-Yam, P. Garnavich, E. Gawiser, J. Geary, P. Gee, R. R. Gibson, K. Gilmore, E. A. Grace, R. F. Green, W. J. Gressler, C. J. Grillmair, S. Habib, J. S. Haggerty, M. Hamuy, A. W. Harris, S. L. Hawley, A. F. Heavens, L. Hebb, T. J. Henry, E. Hileman, E. J. Hilton, K. Hoadley, J. B. Holberg, M. J. Holman, S. B. Howell, L. Infante, Z. Ivezic, S. H. Jacoby, B. Jain, R, Jedicke, M. J. Jee, J. Garrett Jernigan, S. W. Jha, K. V. Johnston, R. L. Jones, M. Juric, M. Kaasalainen, Styliani, Kafka, S. M. Kahn, N. A. Kaib, J. Kalirai, J. Kantor, M. M. Kasliwal, C. R. Keeton, R. Kessler, Z. Knezevic, A. Kowalski, V. L. Krabbendam, K. S. Krughoff, S. Kulkarni, S. Kuhlman, M. Lacy, S. Lepine, M. Liang, A. Lien, P. Lira, K. S. Long, S. Lorenz, J. M. Lotz, R. H. Lupton, J. Lutz, L. M. Macri, A. A. Mahabal, R. Mandelbaum, P. Marshall, M. May, P. M. McGehee, B. T. Meadows, A. Meert, A. Milani, C. J. Miller, M. Miller, D. Mills, D. Minniti, D. Monet, A. S. Mukadam, E. Nakar, D. R. Neill, J. A. Newman, S. Nikolaev, M. Nordby, P. O'Connor, M. Oguri, J. Oliver, S. S. Olivier, J. K. Olsen, K. Olsen, E. W. Olszewski, H. Oluseyi, N. D. Padilla, A. Parker, J. Pepper, J. R. Peterson, C. Petry, P. A. Pinto, J. L. Pizagno, B. Popescu, A. Prsa, V. Radcka, M. J. Raddick, A. Rasmussen, A. Rau, J. Rho, J. E. Rhoads, G. T. Richards, S. T. Ridgway, B. E. Robertson, R. Roskar, A. Saha, A. Sarajedini, E. Scannapieco, T. Schalk, R. Schindler, S. Schmidt, S. Schmidt, D. P. Schneider, G. Schumacher, R. Scranton, J. Sebag, L. G. Seppala, O. Shemmer, J. D. Simon, M. Sivertz, H. A. Smith, J. Allyn Smith, N. Smith, A. H. Spitz, A. Stanford, K. G. Stassun, J. Strader, M. A. Strauss, C. W. Stubbs, D. W. Sweeney, A. Szalay, P. Szkody, M. Takada, P. Thorman, D. E. Trilling, V. Trimble, A. Tyson, R. Van Berg, D. Vanden Berk, J. VanderPlas, L. Verde, B. Vrsnak, L. M. Walkowicz, B. D. Wandelt, S. Wang, Y. Wang, M. Warner, R. H. Wechsler, A. A. West, O. Wiecha, B. F. Williams, B. Willman, D. Wittman, S. C. Wolff, W. M. Wood-Vasey, P. Wozniak, P. Young, A. Zentner,

and H. Zhan. LSST Science Book, Version 2.0. arXiv e-prints, art. arXiv:0912.0201, Dec. 2009. doi: 10.48550/arXiv.0912.0201.

J. Magorrian, S. Tremaine, D. Richstone, R. Bender, G. Bower, A. Dressler, S. M. Faber, K. Gebhardt, R. Green, C. Grillmair, J. Kormendy, and T. Lauer. The Demography of Massive Dark Objects in Galaxy Centers. AJ, 115(6):2285–2305, June 1998. doi: 10.1086/300353.

A. Mahdavi, A. Finoguenov, H. Böhringer, M. J. Geller, and J. P. Henry. XMM-Newton and Gemini Observations of Eight RASSCALS Galaxy Groups. ApJ, 622(1):187–204, Mar. 2005. doi: 10.1086/427916.

G. Mahler, M. Jauzac, J. Richard, B. Beauchesne, H. Ebeling, D. Lagattuta, P. Natarajan, K. Sharon, H. Atek, A. Claeyssens, B. Clément, D. Eckert, A. Edge, J.-P. Kneib, and A. Niemiec. Precision Modeling of JWST's First Cluster Lens SMACS J0723.3-7327. ApJ, 945(1):49, Mar. 2023. doi: 10.3847/1538-4357/acaea9.

A. Mantz, S. W. Allen, H. Ebeling, D. Rapetti, and A. Drlica-Wagner. The observed growth of massive galaxy clusters - II. X-ray scaling relations. MNRAS, 406(3):1773–1795, Aug. 2010a. doi: 10.1111/j.1365-2966.2010.16993.x.

A. Mantz, S. W. Allen, D. Rapetti, and H. Ebeling. The observed growth of massive galaxy clusters - I. Statistical methods and cosmological constraints. MNRAS, 406(3):1759–1772, Aug. 2010b. doi: 10.1111/j.1365-2966.2010.16992.x.

A. B. Mantz. Coping with selection effects: a Primer on regression with truncated data. MNRAS, 485(4):4863–4872, June 2019. doi: 10.1093/mnras/stz320.

A. B. Mantz, A. von der Linden, S. W. Allen, D. E. Applegate, P. L. Kelly, R. G. Morris, D. A. Rapetti, R. W. Schmidt, S. Adhikari, M. T. Allen, P. R. Burchat, D. L. Burke, M. Cataneo, D. Donovan, H. Ebeling, S. Shandera, and A. Wright. Weighing the giants - IV. Cosmology and neutrino mass. MNRAS, 446(3):2205–2225, Jan. 2015. doi: 10.1093/mnras/stu2096.

A. B. Mantz, S. W. Allen, R. G. Morris, A. von der Linden, D. E. Applegate, P. L. Kelly, D. L. Burke, D. Donovan, and H. Ebeling. Weighing the giants- V. Galaxy cluster scaling relations. MNRAS, 463(4):3582–3603, Dec. 2016. doi: 10.1093/mnras/stw2250.

A. B. Mantz, R. G. Morris, S. W. Allen, R. E. A. Canning, L. Baumont, B. Benson, L. E. Bleem, S. R. Ehlert, B. Floyd, R. Herbonnet, P. L. Kelly, S. Liang, A. von der Linden, M. McDonald, D. A. Rapetti, R. W. Schmidt, N. Werner, and A. Wright. Cosmological constraints from gas mass fractions of massive, relaxed galaxy clusters. MNRAS, 510(1):131–145, Feb. 2022. doi: 10.1093/mnras/stab3390.

C. L. Martin. Properties of Galactic Outflows: Measurements of the Feedback from Star Formation. ApJ, 513(1):156–160, Mar. 1999. doi: 10.1086/306863.

B. J. Maughan. The L_X-Y_X Relation: Using Galaxy Cluster X-Ray Luminosity as a Robust, Low-Scatter Mass Proxy. ApJ, 668(2):772–780, Oct. 2007. doi: 10.1086/520831.

B. J. Maughan, C. Jones, W. Forman, and L. Van Speybroeck. Images, Structural Properties, and Metal Abundances of Galaxy Clusters Observed with Chandra ACIS-I at 0.1 < z < 1.3. ApJS, 174(1):117–135, Jan. 2008. doi: 10.1086/521225.

B. J. Maughan, P. A. Giles, S. W. Randall, C. Jones, and W. R. Forman. Self-similar scaling and evolution in the galaxy cluster X-ray luminosity-temperature relation. MNRAS, 421(2): 1583–1602, Apr. 2012. doi: 10.1111/j.1365-2966.2012.20419.x.

P. Mazzotta, E. Rasia, L. Moscardini, and G. Tormen. Comparing the temperatures of galaxy clusters from hydrodynamical N-body simulations to Chandra and XMM-Newton observations. MNRAS, 354(1):10–24, Oct. 2004. doi: 10.1111/j.1365-2966.2004.08167.x.

I. G. McCarthy, J. Schaye, T. J. Ponman, R. G. Bower, C. M. Booth, C. Dalla Vecchia, R. A. Crain, V. Springel, T. Theuns, and R. P. C. Wiersma. The case for AGN feedback in galaxy groups. MNRAS, 406(2):822–839, Aug. 2010. doi: 10.1111/j.1365-2966.2010.16750.x.

M. McDonald, B. A. Benson, A. Vikhlinin, B. Stalder, L. E. Bleem, T. de Haan, H. W. Lin, K. A. Aird, M. L. N. Ashby, M. W. Bautz, M. Bayliss, S. Bocquet, M. Brodwin, J. E. Carlstrom, C. L. Chang, H. M. Cho, A. Clocchiatti, T. M. Crawford, A. T. Crites, S. Desai, M. A. Dobbs, J. P. Dudley, R. J. Foley, W. R. Forman, E. M. George, D. Gettings, M. D. Gladders, A. H. Gonzalez, N. W. Halverson, F. W. High, G. P. Holder, W. L. Holzapfel, S. Hoover, J. D. Hrubes, C. Jones, M. Joy, R. Keisler, L. Knox, A. T. Lee, E. M. Leitch, J. Liu, M. Lueker, D. Luong-Van, A. Mantz, D. P. Marrone, J. J. McMahon, J. Mehl, S. S. Meyer, E. D. Miller, L. Mocanu, J. J. Mohr, T. E. Montroy, S. S. Murray, D. Nurgaliev, S. Padin, T. Plagge, C. Pryke, C. L. Reichardt, A. Rest, J. Ruel, J. E. Ruhl, B. R. Saliwanchik, A. Saro, J. T. Sayre, K. K. Schaffer, E. Shirokoff, J. Song, R. Šuhada, H. G. Spieler, S. A. Stanford, Z. Staniszewski, A. A. Stark, K. Story, A. van Engelen, K. Vanderlinde, J. D. Vieira, R. Williamson, O. Zahn, and A. Zenteno. The Growth of Cool Cores and Evolution of Cooling Properties in a Sample of 83 Galaxy Clusters at 0.3 < z < 1.2 Selected from the SPT-SZ Survey. ApJ, 774(1):23, Sept. 2013. doi: 10.1088/0004-637X/774/1/23.

M. McDonald, B. A. Benson, A. Vikhlinin, K. A. Aird, S. W. Allen, M. Bautz, M. Bayliss, L. E. Bleem, S. Bocquet, M. Brodwin, J. E. Carlstrom, C. L. Chang, H. M. Cho, A. Clocchiatti, T. M. Crawford, A. T. Crites, T. de Haan, M. A. Dobbs, R. J. Foley, W. R. Forman, E. M. George, M. D. Gladders, A. H. Gonzalez, N. W. Halverson, J. Hlavacek-Larrondo, G. P. Holder, W. L. Holzapfel, J. D. Hrubes, C. Jones, R. Keisler, L. Knox, A. T. Lee, E. M. Leitch, J. Liu, M. Lueker, D. Luong-Van, A. Mantz, D. P. Marrone, J. J. McMahon, S. S. Meyer, E. D. Miller, L. Mocanu, J. J. Mohr, S. S. Murray, S. Padin, C. Pryke, C. L. Reichardt, A. Rest, J. E. Ruhl, B. R. Saliwanchik, A. Saro, J. T. Sayre, K. K. Schaffer, E. Shirokoff, H. G. Spieler, B. Stalder, S. A. Stanford, Z. Staniszewski, A. A. Stark, K. T. Story, C. W. Stubbs, K. Vanderlinde, J. D. Vieira, R. Williamson, O. Zahn, and A. Zenteno. The Redshift Evolution of the Mean Temperature, Pressure, and Entropy Profiles in 80 SPT-Selected Galaxy Clusters. ApJ, 794(1):67, Oct. 2014. doi: 10.1088/0004-637X/794/1/67.

M. McDonald, B. R. McNamara, R. J. van Weeren, D. E. Applegate, M. Bayliss, M. W. Bautz, B. A. Benson, J. E. Carlstrom, L. E. Bleem, M. Chatzikos, A. C. Edge, A. C. Fabian, G. P. Garmire, J. Hlavacek-Larrondo, C. Jones-Forman, A. B. Mantz, E. D. Miller, B. Stalder, S. Veilleux, and J. A. ZuHone. Deep Chandra, HST-COS, and Megacam Observations of the Phoenix Cluster: Extreme Star Formation and AGN Feedback on Hundred Kiloparsec Scales. ApJ, 811(2):111, Oct. 2015. doi: 10.1088/0004-637X/811/2/111.

M. McDonald, S. W. Allen, M. Bayliss, B. A. Benson, L. E. Bleem, M. Brodwin, E. Bulbul, J. E. Carlstrom, W. R. Forman, J. Hlavacek-Larrondo, G. P. Garmire, M. Gaspari, M. D. Gladders, A. B. Mantz, and S. S. Murray. The Remarkable Similarity of Massive Galaxy Clusters from z ~ 0 to z ~ 1.9. ApJ, 843(1):28, July 2017. doi: 10.3847/1538-4357/aa7740.

B. R. McNamara, P. E. J. Nulsen, M. W. Wise, D. A. Rafferty, C. Carilli, C. L. Sarazin, and E. L. Blanton. The heating of gas in a galaxy cluster by X-ray cavities and large-scale shock fronts. Nature, 433(7021):45–47, Jan. 2005. doi: 10.1038/nature03202.

J. F. Meekins, G. Fritz, T. A. Chubb, and H. Friedman. Physical Sciences: X-rays from the Coma Cluster of Galaxies. Nature, 231(5298):107–108, May 1971. doi: 10.1038/231107a0.

N. Meidinger. The Wide Field Imager instrument for Athena. Contributions of the Astronomical Observatory Skalnate Pleso, 48(3):498–505, July 2018. doi: 10.48550/arXiv.1702.01079.

N. Menci and A. Cavaliere. The history of cosmic baryons: X-ray emission versus star formation rate. MNRAS, 311(1):50–62, Jan. 2000. doi: 10.1046/j.1365-8711.2000.03048.x.

A. Merloni, P. Predehl, W. Becker, H. Böhringer, T. Boller, H. Brunner, M. Brusa, K. Dennerl, M. Freyberg, P. Friedrich, A. Georgakakis, F. Haberl, G. Hasinger, N. Meidinger, J. Mohr, K. Nandra, A. Rau, T. H. Reiprich, J. Robrade, M. Salvato, A. Santangelo, M. Sasaki, A. Schwope, J. Wilms, and t. German eROSITA Consortium. eROSITA Science Book: Mapping the Structure of the Energetic Universe. arXiv e-prints, art. arXiv:1209.3114, Sept. 2012.

A. Merloni, G. Lamer, T. Liu, M. E. Ramos-Ceja, H. Brunner, E. Bulbul, K. Dennerl, V. Doroshenko, M. J. Freyberg, S. Friedrich, E. Gatuzz, A. Georgakakis, F. Haberl, Z. Igo, I. Kreykenbohm, A. Liu, C. Maitra, A. Malyali, M. G. F. Mayer, K. Nandra, P. Predehl, J. Robrade, M. Salvato, J. S. Sanders, I. Stewart, D. Tubín-Arenas, P. Weber, J. Wilms, R. Arcodia, E. Artis, J. Aschersleben, A. Avakyan, C. Aydar, Y. E. Bahar, F. Balzer, W. Becker, K. Berger, T. Boller, W. Bornemann, M. Brüggen, M. Brusa, J. Buchner, V. Burwitz, F. Camilloni, N. Clerc, J. Comparat, D. Coutinho, S. Czesla, S. M. Dannhauer, L. Dauner, T. Dauser, J. Dietl, K. Dolag, T. Dwelly, K. Egg, E. Ehl, S. Freund, P. Friedrich, R. Gaida, C. Garrel, V. Ghirardini, A. Gokus, G. Grünwald, S. Grandis, I. Grotova, D. Gruen, A. Gueguen, S. Hämmerich, N. Hamaus, G. Hasinger, K. Haubner, D. Homan, J. Ider Chitham, W. M. Joseph, A. Joyce, O. König, D. M. Kaltenbrunner, A. Khokhriakova, W. Kink, C. Kirsch, M. Kluge, J. Knies, S. Krippendorf, M. Krumpe, J. Kurpas, P. Li, Z. Liu, N. Locatelli, M. Lorenz, S. Müller, E. Magaudda, C. Mannes, H. McCall, N. Meidinger, M. Michailidis, K. Migkas, D. Muñoz-Giraldo, B. Musiimenta, N. T. Nguyen-Dang, Q. Ni, A. Olechowska, N. Ota, F. Pacaud, T. Pasini,

E. Perinati, A. M. Pires, C. Pommranz, G. Ponti, K. Poppenhaeger, G. Pühlhofer, A. Rau, M. Reh, T. H. Reiprich, W. Roster, S. Saeedi, A. Santangelo, M. Sasaki, J. Schmitt, P. C. Schneider, T. Schrabback, N. Schuster, A. Schwope, R. Seppi, M. M. Serim, S. Shreeram, E. Sokolova-Lapa, H. Starck, B. Stelzer, J. Stierhof, V. Suleimanov, C. Tenzer, I. Traulsen, J. Trümper, K. Tsuge, T. Urrutia, A. Veronica, S. G. H. Waddell, R. Willer, J. Wolf, M. C. H. Yeung, A. Zainab, F. Zangrandi, X. Zhang, Y. Zhang, and X. Zheng. The SRG/eROSITA all-sky survey. First X-ray catalogues and data release of the western Galactic hemisphere. A&A, 682:A34, Feb. 2024. doi: 10.1051/0004-6361/202347165.

F. Mernier, J. de Plaa, J. S. Kaastra, Y. Y. Zhang, H. Akamatsu, L. Gu, P. Kosec, J. Mao, C. Pinto, T. H. Reiprich, J. S. Sanders, A. Simionescu, and N. Werner. Radial metal abundance profiles in the intra-cluster medium of cool-core galaxy clusters, groups, and ellipticals. A&A, 603: A80, July 2017. doi: 10.1051/0004-6361/201630075.

F. Mernier, J. de Plaa, N. Werner, J. S. Kaastra, A. J. J. Raassen, L. Gu, J. Mao, I. Urdampilleta, N. Truong, and A. Simionescu. Mass-invariance of the iron enrichment in the hot haloes of massive ellipticals, groups, and clusters of galaxies. MNRAS, 478(1):L116–L121, July 2018. doi: 10.1093/mnrasl/sly080.

F. Mernier, N. Werner, K. Lakhchaura, J. de Plaa, L. Gu, J. S. Kaastra, J. Mao, A. Simionescu, and I. Urdampilleta. How do atomic code uncertainties affect abundance measurements in the intracluster medium? Astronomische Nachrichten, 341(2):203–209, Feb. 2020. doi: 10.1002/asna.202023779.

F. Mernier, N. Werner, Y. Su, C. Pinto, R. Grossová, A. Simionescu, E. Iodice, M. Sarzi, and A. Görgei. The cycle of metals in the infalling elliptical galaxy NGC 1404. MNRAS, 511(3): 3159–3178, Apr. 2022. doi: 10.1093/mnras/stac253.

C. Messier. Catalogue des Nébuleuses et des Amas d'Étoiles (Catalog of Nebulae and Star Clusters). Connoissance des Temps ou des Mouvements Célestes, for 1784, p. 227-267, Jan. 1781.

R. Mewe, E. H. B. M. Gronenschild, and G. H. J. van den Oord. Calculated X-Radiation from Optically Thin Plasmas - Part Five. A&AS, 62:197, Nov. 1985.

R. Mewe, J. R. Lemen, and G. H. J. van den Oord. Calculated X-radiation from optically thin plasmas. VI - Improved calculations for continuum emission and approximation formulae for nonrelativistic average Gaunt actors. A&AS, 65:511–536, Sept. 1986.

K. Migkas, G. Schellenberger, T. H. Reiprich, F. Pacaud, M. E. Ramos-Ceja, and L. Lovisari. Probing cosmic isotropy with a new X-ray galaxy cluster sample through the L_X-T scaling relation. A&A, 636:A15, Apr. 2020. doi: 10.1051/0004-6361/201936602.

K. Migkas, D. Kox, G. Schellenberger, A. Veronica, F. Pacaud, T. H. Reiprich, Y. E. Bahar, F. Balzer, E. Bulbul, J. Comparat, K. Dennerl, M. Freyberg, C. Garrel, V. Ghirardini, S. Grandis, M. Kluge, A. Liu, M. E. Ramos-Ceja, J. Sanders, and X. Zhang. The SRG/eROSITA

All-Sky Survey: SRG/eROSITA cross-calibration with Chandra and XMM-Newton using galaxy cluster gas temperatures. arXiv e-prints, art. arXiv:2401.17297, Jan. 2024. doi: 10.48550/arXiv.2401.17297.

R. J. Mitchell, J. C. Ives, and J. L. Culhane. The X-ray temperatures of eight clusters of galaxies and their relationship to other cluster properties. MNRAS, 181:25P–32P, Oct. 1977. doi: 10.1093/mnras/181.1.25P.

R. J. Mitchell, R. J. Dickens, S. J. B. Burnell, and J. L. Culhane. The X-ray spectra of clusters of galaxies and their relationship to other cluster properties. MNRAS, 189:329–361, Nov. 1979. doi: 10.1093/mnras/189.2.329.

M. Molham, N. Clerc, A. Takey, T. Sadibekova, A. B. Morcos, S. Yousef, Z. M. Hayman, M. Lieu, S. Raychaudhury, and E. R. Gaynullina. X-ray properties of the X-CLASS-redMaPPer galaxy cluster sample: the luminosity-temperature relation. MNRAS, 494(1): 161–177, May 2020. doi: 10.1093/mnras/staa677.

A. Monna, S. Seitz, I. Balestra, P. Rosati, C. Grillo, A. Halkola, S. H. Suyu, D. Coe, G. B. Caminha, B. Frye, A. Koekemoer, A. Mercurio, M. Nonino, M. Postman, and A. Zitrin. Precise strong lensing mass profile of the CLASH galaxy cluster MACS 2129. MNRAS, 466(4): 4094–4106, Apr. 2017. doi: 10.1093/mnras/stx015.

J. S. Mulchaey. X-ray Observations of Poor Groups. In M. J. Valtonen and C. Flynn, editors, IAU Colloq. 174: Small Galaxy Groups, volume 209 of Astronomical Society of the Pacific Conference Series, page 174, Jan. 2000.

J. S. Mulchaey and A. I. Zabludoff. The Properties of Poor Groups of Galaxies. II. X-Ray and Optical Comparisons. ApJ, 496(1):73–92, Mar. 1998. doi: 10.1086/305356.

R. F. Mushotzky. X-ray emission from clusters of galaxies. Physica Scripta Volume T, 7:157–162, Jan. 1984. doi: 10.1088/0031-8949/1984/T7/036.

J. Myles, D. Gruen, A. B. Mantz, S. W. Allen, R. G. Morris, E. Rykoff, M. Costanzi, C. To, J. DeRose, R. H. Wechsler, E. Rozo, T. Jeltema, E. R. Carrasco, A. Kremin, and R. Kron. Spectroscopic quantification of projection effects in the SDSS redMaPPer galaxy cluster catalogue. MNRAS, 505(1):33–44, July 2021. doi: 10.1093/mnras/stab1243.

D. Nagai, A. V. Kravtsov, and A. Vikhlinin. Effects of Galaxy Formation on Thermodynamics of the Intracluster Medium. ApJ, 668(1):1–14, Oct. 2007a. doi: 10.1086/521328.

D. Nagai, A. Vikhlinin, and A. V. Kravtsov. Testing X-Ray Measurements of Galaxy Clusters with Cosmological Simulations. ApJ, 655(1):98–108, Jan. 2007b. doi: 10.1086/509868.

K. Nandra, D. Barret, X. Barcons, A. Fabian, J.-W. den Herder, L. Piro, M. Watson, C. Adami, J. Aird, J. M. Afonso, D. Alexander, C. Argiroffi, L. Amati, M. Arnaud, J.-L. Atteia,

M. Audard, C. Badenes, J. Ballet, L. Ballo, A. Bamba, A. Bhardwaj, E. Stefano Battistelli, W. Becker, M. De Becker, E. Behar, S. Bianchi, V. Biffi, L. Bîrzan, F. Bocchino, S. Bogdanov, L. Boirin, T. Boller, S. Borgani, K. Borm, N. Bouché, H. Bourdin, R. Bower, V. Braito, E. Branchini, G. Branduardi-Raymont, J. Bregman, L. Brenneman, M. Brightman, M. Brüggen, J. Buchner, E. Bulbul, M. Brusa, M. Bursa, A. Caccianiga, E. Cackett, S. Campana, N. Cappelluti, M. Cappi, F. Carrera, M. Ceballos, F. Christensen, Y.-H. Chu, E. Churazov, N. Clerc, S. Corbel, A. Corral, A. Comastri, E. Costantini, J. Croston, M. Dadina, A. D'Ai, A. Decourchelle, R. Della Ceca, K. Dennerl, K. Dolag, C. Done, M. Dovciak, J. Drake, D. Eckert, A. Edge, S. Ettori, Y. Ezoe, E. Feigelson, R. Fender, C. Feruglio, A. Finoguenov, F. Fiore, M. Galeazzi, S. Gallagher, P. Gandhi, M. Gaspari, F. Gastaldello, A. Georgakakis, I. Georgantopoulos, M. Gilfanov, M. Gitti, R. Gladstone, R. Goosmann, E. Gosset, N. Grosso, M. Guedel, M. Guerrero, F. Haberl, M. Hardcastle, S. Heinz, A. Alonso Herrero, A. Hervé, M. Holmstrom, K. Iwasawa, P. Jonker, J. Kaastra, E. Kara, V. Karas, J. Kastner, A. King, D. Kosenko, D. Koutroumpa, R. Kraft, I. Kreykenbohm, R. Lallement, G. Lanzuisi, J. Lee, M. Lemoine-Goumard, A. Lobban, G. Lodato, L. Lovisari, S. Lotti, I. McCharthy, B. McNamara, A. Maggio, R. Maiolino, B. De Marco, D. de Martino, S. Mateos, G. Matt, B. Maughan, P. Mazzotta, M. Mendez, A. Merloni, G. Micela, M. Miceli, R. Mignani, J. Miller, G. Miniutti, S. Molendi, R. Montez, A. Moretti, C. Motch, Y. Nazé, J. Nevalainen, F. Nicastro, P. Nulsen, T. Ohashi, P. O'Brien, J. Osborne, L. Oskinova, F. Pacaud, F. Paerels, M. Page, I. Papadakis, G. Pareschi, R. Petre, P.-O. Petrucci, E. Piconcelli, I. Pillitteri, C. Pinto, J. de Plaa, E. Pointecouteau, T. Ponman, G. Ponti, D. Porquet, K. Pounds, G. Pratt, P. Predehl, D. Proga, D. Psaltis, D. Rafferty, M. Ramos-Ceja, P. Ranalli, E. Rasia, A. Rau, G. Rauw, N. Rea, A. Read, J. Reeves, T. Reiprich, M. Renaud, C. Reynolds, G. Risaliti, J. Rodriguez, P. Rodriguez Hidalgo, M. Roncarelli, D. Rosario, M. Rossetti, A. Rozanska, E. Rovilos, R. Salvaterra, M. Salvato, T. Di Salvo, J. Sanders, J. Sanz-Forcada, K. Schawinski, J. Schaye, A. Schwope, S. Sciortino, P. Severgnini, F. Shankar, D. Sijacki, S. Sim, C. Schmid, R. Smith, A. Steiner, B. Stelzer, G. Stewart, T. Strohmayer, L. Strüder, M. Sun, Y. Takei, V. Tatischeff, A. Tiengo, F. Tombesi, G. Trinchieri, T. G. Tsuru, A. Ud-Doula, E. Ursino, L. Valencic, E. Vanzella, S. Vaughan, C. Vignali, J. Vink, F. Vito, M. Volonteri, D. Wang, N. Webb, R. Willingale, J. Wilms, M. Wise, D. Worrall, A. Young, L. Zampieri, J. In't Zand, S. Zane, A. Zezas, Y. Zhang, and I. Zhuravleva. The Hot and Energetic Universe: A White Paper presenting the science theme motivating the Athena+ mission. arXiv e-prints, art. arXiv:1306.2307, June 2013. doi: 10.48550/arXiv.1306.2307.

J. F. Navarro, C. S. Frenk, and S. D. M. White. The Structure of Cold Dark Matter Halos. ApJ, 462:563, May 1996. doi: 10.1086/177173.

J. F. Navarro, C. S. Frenk, and S. D. M. White. A Universal Density Profile from Hierarchical Clustering. ApJ, 490(2):493–508, Dec. 1997. doi: 10.1086/304888.

Y. Ni, S. Genel, D. Anglés-Alcázar, F. Villaescusa-Navarro, Y. Jo, S. Bird, T. Di Matteo, R. Croft, N. Chen, N. S. M. de Santi, M. Gebhardt, H. Shao, S. Pandey, L. Hernquist, and R. Dave. The CAMELS Project: Expanding the Galaxy Formation Model Space with New ASTRID and 28-

parameter TNG and SIMBA Suites. ApJ, 959(2):136, Dec. 2023. doi: 10.3847/1538-4357/ad022a.

P. E. J. Nulsen, D. C. Hambrick, B. R. McNamara, D. Rafferty, L. Birzan, M. W. Wise, and L. P. David. The Powerful Outburst in Hercules A. ApJ, 625(1):L9–L12, May 2005. doi: 10.1086/430945.

M. Oguri, M. Takada, N. Okabe, and G. P. Smith. Direct measurement of dark matter halo ellipticity from two-dimensional lensing shear maps of 25 massive clusters. MNRAS, 405(4): 2215–2230, July 2010. doi: 10.1111/j.1365-2966.2010.16622.x.

N. Okabe, G. P. Smith, K. Umetsu, M. Takada, and T. Futamase. LoCuSS: The Mass Density Profile of Massive Galaxy Clusters at z = 0.2. ApJ, 769(2):L35, June 2013. doi: 10.1088/2041-8205/769/2/L35.

B. D. Oppenheimer, A. Babul, Y. Bahé, I. S. Butsky, and I. G. McCarthy. Simulating Groups and the IntraGroup Medium: The Surprisingly Complex and Rich Middle Ground between Clusters and Galaxies. Universe, 7(7):209, June 2021. doi: 10.3390/universe7070209.

D. E. Osterbrock. Astrophysics of gaseous nebulae. 1974.

E. O'Sullivan, S. Giacintucci, A. Babul, S. Raychaudhury, T. Venturi, C. Bildfell, A. Mahdavi, J. B. R. Oonk, N. Murray, H. Hoekstra, and M. Donahue. A Giant Metrewave Radio Telescope/Chandra view of IRAS 09104+4109: a type 2 QSO in a cooling flow. MNRAS, 424(4): 2971–2993, Aug. 2012. doi: 10.1111/j.1365-2966.2012.21459.x.

F. Pacaud, M. Pierre, C. Adami, B. Altieri, S. Andreon, L. Chiappetti, A. Detal, P. A. Duc, G. Galaz, A. Gueguen, J. P. Le Fèvre, G. Hertling, C. Libbrecht, J. B. Melin, T. J. Ponman, H. Quintana, A. Refregier, P. G. Sprimont, J. Surdej, I. Valtchanov, J. P. Willis, D. Alloin, M. Birkinshaw, M. N. Bremer, O. Garcet, C. Jean, L. R. Jones, O. Le Fèvre, D. Maccagni, A. Mazure, D. Proust, H. J. A. Röttgering, and G. Trinchieri. The XMM-LSS survey: the Class 1 cluster sample over the initial 5 deg^2 and its cosmological modelling. MNRAS, 382 (3):1289–1308, Dec. 2007. doi: 10.1111/j.1365-2966.2007.12468.x.

F. Pacaud, M. Pierre, J. B. Melin, C. Adami, A. E. Evrard, S. Galli, F. Gastaldello, B. J. Maughan, M. Sereno, S. Alis, B. Altieri, M. Birkinshaw, L. Chiappetti, L. Faccioli, P. A. Giles, C. Horellou, A. Iovino, E. Koulouridis, J. P. Le Fèvre, C. Lidman, M. Lieu, S. Maurogordato, L. Moscardini, M. Plionis, B. M. Poggianti, E. Pompei, T. Sadibekova, I. Valtchanov, and J. P. Willis. The XXL Survey. XXV. Cosmological analysis of the C1 cluster number counts. A&A, 620:A10, Nov. 2018. doi: 10.1051/0004-6361/201834022.

R. Pakmor, V. Springel, J. P. Coles, T. Guillet, C. Pfrommer, S. Bose, M. Barrera, A. M. Delgado, F. Ferlito, C. Frenk, B. Hadzhiyska, C. Hernández-Aguayo, L. Hernquist, R. Kannan, and S. D. M. White. The MillenniumTNG Project: the hydrodynamical full physics simulation and a first look at its galaxy clusters. MNRAS, 524(2):2539–2555, Sept. 2023. doi: 10.1093/mnras/stac3620.

E. K. Panagoulia, A. C. Fabian, and J. S. Sanders. A volume-limited sample of X-ray galaxy groups and clusters - I. Radial entropy and cooling time profiles. MNRAS, 438(3):2341–2354, Mar. 2014. doi: 10.1093/mnras/stt2349.

T. Pasini, M. Brüggen, D. N. Hoang, V. Ghirardini, E. Bulbul, M. Klein, A. Liu, T. W. Shimwell, M. J. Hardcastle, W. L. Williams, A. Botteon, F. Gastaldello, R. J. van Weeren, A. Merloni, F. de Gasperin, Y. E. Bahar, F. Pacaud, and M. Ramos-Ceja. The eROSITA Final Equatorial-Depth Survey (eFEDS). LOFAR view of brightest cluster galaxies and AGN feedback. A&A, 661:A13, May 2022. doi: 10.1051/0004-6361/202141211.

M. Pavlinsky, A. Tkachenko, V. Levin, N. Alexandrovich, V. Arefiev, V. Babyshkin, O. Batanov, Y. Bodnar, A. Bogomolov, A. Bubnov, M. Buntov, R. Burenin, I. Chelovekov, C. T. Chen, T. Drozdova, S. Ehlert, E. Filippova, S. Frolov, D. Gamkov, S. Garanin, M. Garin, A. Glushenko, A. Gorelov, S. Grebenev, S. Grigorovich, P. Gureev, E. Gurova, R. Ilkaev, I. Katasonov, A. Krivchenko, R. Krivonos, F. Korotkov, M. Kudelin, M. Kuznetsova, V. Lazarchuk, I. Lomakin, I. Lapshov, V. Lipilin, A. Lutovinov, I. Mereminskiy, S. Molkov, V. Nazarov, V. Oleinikov, E. Pikalov, B. D. Ramsey, I. Roiz, A. Rotin, A. Ryadov, E. Sankin, S. Sazonov, D. Sedov, A. Semena, N. Semena, D. Serbinov, A. Shirshakov, A. Shtykovsky, A. Shvetsov, R. Sunyaev, D. A. Swartz, V. Tambov, V. Voron, and A. Yaskovich. The ART-XC telescope on board the SRG observatory. A&A, 650:A42, June 2021. doi: 10.1051/0004-6361/202040265.

J. R. Peterson, S. M. Kahn, F. B. S. Paerels, J. S. Kaastra, T. Tamura, J. A. M. Bleeker, C. Ferrigno, and J. G. Jernigan. High-Resolution X-Ray Spectroscopic Constraints on Cooling-Flow Models for Clusters of Galaxies. ApJ, 590(1):207–224, June 2003. doi: 10.1086/374830.

M. Pierre, F. Pacaud, J. B. Juin, J. B. Melin, P. Valageas, N. Clerc, and P. S. Corasaniti. Precision cosmology with a wide area XMM cluster survey. MNRAS, 414(2):1732–1746, June 2011. doi: 10.1111/j.1365-2966.2011.18511.x.

A. Pillepich, C. Porciani, and T. H. Reiprich. The X-ray cluster survey with eRosita: forecasts for cosmology, cluster physics and primordial non-Gaussianity. MNRAS, 422(1):44–69, May 2012. doi: 10.1111/j.1365-2966.2012.20443.x.

A. Pillepich, V. Springel, D. Nelson, S. Genel, J. Naiman, R. Pakmor, L. Hernquist, P. Torrey, M. Vogelsberger, R. Weinberger, and F. Marinacci. Simulating galaxy formation with the IllustrisTNG model. MNRAS, 473(3):4077–4106, Jan. 2018. doi: 10.1093/mnras/stx2656.

Planck Collaboration, P. A. R. Ade, N. Aghanim, M. Arnaud, M. Ashdown, J. Aumont, C. Baccigalupi, A. J. Banday, R. B. Barreiro, J. G. Bartlett, N. Bartolo, E. Battaner, R. Battye, K. Benabed, A. Benoît, A. Benoit-Lévy, J. P. Bernard, M. Bersanelli, P. Bielewicz, J. J. Bock, A. Bonaldi, L. Bonavera, J. R. Bond, J. Borrill, F. R. Bouchet, F. Boulanger, M. Bucher, C. Burigana, R. C. Butler, E. Calabrese, J. F. Cardoso, A. Catalano, A. Challinor, A. Chamballu, R. R. Chary, H. C. Chiang, J. Chluba, P. R. Christensen, S. Church, D. L. Clements, S. Colombi, L. P. L. Colombo, C. Combet, A. Coulais, B. P. Crill, A. Curto, F. Cuttaia,

L. Danese, R. D. Davies, R. J. Davis, P. de Bernardis, A. de Rosa, G. de Zotti, J. Delabrouille, F. X. Désert, E. Di Valentino, C. Dickinson, J. M. Diego, K. Dolag, H. Dole, S. Donzelli, O. Doré, M. Douspis, A. Ducout, J. Dunkley, X. Dupac, G. Efstathiou, F. Elsner, T. A. Enßlin, H. K. Eriksen, M. Farhang, J. Fergusson, F. Finelli, O. Forni, M. Frailis, A. A. Fraisse, E. Franceschi, A. Frejsel, S. Galeotta, S. Galli, K. Ganga, C. Gauthier, M. Gerbino, T. Ghosh, M. Giard, Y. Giraud-Héraud, E. Giusarma, E. Gjerløw, J. González-Nuevo, K. M. Górski, S. Gratton, A. Gregorio, A. Gruppuso, J. E. Gudmundsson, J. Hamann, F. K. Hansen, D. Hanson, D. L. Harrison, G. Helou, S. Henrot-Versillé, C. Hernández-Monteagudo, D. Herranz, S. R. Hildebrandt, E. Hivon, M. Hobson, W. A. Holmes, A. Hornstrup, W. Hovest, Z. Huang, K. M. Huffenberger, G. Hurier, A. H. Jaffe, T. R. Jaffe, W. C. Jones, M. Juvela, E. Keihänen, R. Keskitalo, T. S. Kisner, R. Kneissl, J. Knoche, L. Knox, M. Kunz, H. Kurki-Suonio, G. Lagache, A. Lähteenmäki, J. M. Lamarre, A. Lasenby, M. Lattanzi, C. R. Lawrence, J. P. Leahy, R. Leonardi, J. Lesgourgues, F. Levrier, A. Lewis, M. Liguori, P. B. Lilje, M. Linden-Vørnle, M. López-Caniego, P. M. Lubin, J. F. Macías-Pérez, G. Maggio, D. Maino, N. Mandolesi, A. Mangilli, A. Marchini, M. Maris, P. G. Martin, M. Martinelli, E. Martínez-González, S. Masi, S. Matarrese, P. McGehee, P. R. Meinhold, A. Melchiorri, J. B. Melin, L. Mendes, A. Mennella, M. Migliaccio, M. Millea, S. Mitra, M. A. Miville-Deschênes, A. Moneti, L. Montier, G. Morgante, D. Mortlock, A. Moss, D. Munshi, J. A. Murphy, P. Naselsky, F. Nati, P. Natoli, C. B. Netterfield, H. U. Nørgaard-Nielsen, F. Noviello, D. Novikov, I. Novikov, C. A. Oxborrow, F. Paci, L. Pagano, F. Pajot, R. Paladini, D. Paoletti, B. Partridge, F. Pasian, G. Patanchon, T. J. Pearson, O. Perdereau, L. Perotto, F. Perrotta, V. Pettorino, F. Piacentini, M. Piat, E. Pierpaoli, D. Pietrobon, S. Plaszczynski, E. Pointecouteau, G. Polenta, L. Popa, G. W. Pratt, G. Prézeau, S. Prunet, J. L. Puget, J. P. Rachen, W. T. Reach, R. Rebolo, M. Reinecke, M. Remazeilles, C. Renault, A. Renzi, I. Ristorcelli, G. Rocha, C. Rosset, M. Rossetti, G. Roudier, B. Rouillé d'Orfeuil, M. Rowan-Robinson, J. A. Rubiño-Martín, B. Rusholme, N. Said, V. Salvatelli, L. Salvati, M. Sandri, D. Santos, M. Savelainen, G. Savini, D. Scott, M. D. Seiffert, P. Serra, E. P. S. Shellard, L. D. Spencer, M. Spinelli, V. Stolyarov, R. Stompor, R. Sudiwala, R. Sunyaev, D. Sutton, A. S. Suur-Uski, J. F. Sygnet, J. A. Tauber, L. Terenzi, L. Toffolatti, M. Tomasi, M. Tristram, T. Trombetti, M. Tucci, J. Tuovinen, M. Türler, G. Umana, L. Valenziano, J. Valiviita, F. Van Tent, P. Vielva, F. Villa, L. A. Wade, B. D. Wandelt, I. K. Wehus, M. White, S. D. M. White, A. Wilkinson, D. Yvon, A. Zacchei, and A. Zonca. Planck 2015 results. XIII. Cosmological parameters. A&A, 594:A13, Sept. 2016. doi: 10.1051/0004-6361/201525830.

Planck Collaboration, N. Aghanim, Y. Akrami, M. Ashdown, J. Aumont, C. Baccigalupi, M. Ballardini, A. J. Banday, R. B. Barreiro, N. Bartolo, S. Basak, R. Battye, K. Benabed, J. P. Bernard, M. Bersanelli, P. Bielewicz, J. J. Bock, J. R. Bond, J. Borrill, F. R. Bouchet, F. Boulanger, M. Bucher, C. Burigana, R. C. Butler, E. Calabrese, J. F. Cardoso, J. Carron, A. Challinor, H. C. Chiang, J. Chluba, L. P. L. Colombo, C. Combet, D. Contreras, B. P. Crill, F. Cuttaia, P. de Bernardis, G. de Zotti, J. Delabrouille, J. M. Delouis, E. Di Valentino, J. M. Diego, O. Doré, M. Douspis, A. Ducout, X. Dupac, S. Dusini, G. Efstathiou, F. Elsner, T. A. Enßlin, H. K. Eriksen, Y. Fantaye, M. Farhang, J. Fergusson, R. Fernandez-Cobos, F. Finelli, F. Forastieri, M. Frailis, A. A. Fraisse, E. Franceschi, A. Frolov, S. Galeotta, S. Galli,

K. Ganga, R. T. Génova-Santos, M. Gerbino, T. Ghosh, J. González-Nuevo, K. M. Górski, S. Gratton, A. Gruppuso, J. E. Gudmundsson, J. Hamann, W. Handley, F. K. Hansen, D. Herranz, S. R. Hildebrandt, E. Hivon, Z. Huang, A. H. Jaffe, W. C. Jones, A. Karakci, E. Keihänen, R. Keskitalo, K. Kiiveri, J. Kim, T. S. Kisner, L. Knox, N. Krachmalnicoff, M. Kunz, H. Kurki-Suonio, G. Lagache, J. M. Lamarre, A. Lasenby, M. Lattanzi, C. R. Lawrence, M. Le Jeune, P. Lemos, J. Lesgourgues, F. Levrier, A. Lewis, M. Liguori, P. B. Lilje, M. Lilley, V. Lindholm, M. López-Caniego, P. M. Lubin, Y. Z. Ma, J. F. Macías-Pérez, G. Maggio, D. Maino, N. Mandolesi, A. Mangilli, A. Marcos-Caballero, M. Maris, P. G. Martin, M. Martinelli, E. Martínez-González, S. Matarrese, N. Mauri, J. D. McEwen, P. R. Meinhold, A. Melchiorri, A. Mennella, M. Migliaccio, M. Millea, S. Mitra, M. A. Miville-Deschênes, D. Molinari, L. Montier, G. Morgante, A. Moss, P. Natoli, H. U. Nørgaard-Nielsen, L. Pagano, D. Paoletti, B. Partridge, G. Patanchon, H. V. Peiris, F. Perrotta, V. Pettorino, F. Piacentini, L. Polastri, G. Polenta, J. L. Puget, J. P. Rachen, M. Reinecke, M. Remazeilles, A. Renzi, G. Rocha, C. Rosset, G. Roudier, J. A. Rubiño-Martín, B. Ruiz-Granados, L. Salvati, M. Sandri, M. Savelainen, D. Scott, E. P. S. Shellard, C. Sirignano, G. Sirri, L. D. Spencer, R. Sunyaev, A. S. Suur-Uski, J. A. Tauber, D. Tavagnacco, M. Tenti, L. Toffolatti, M. Tomasi, T. Trombetti, L. Valenziano, J. Valiviita, B. Van Tent, L. Vibert, P. Vielva, F. Villa, N. Vittorio, B. D. Wandelt, I. K. Wehus, M. White, S. D. M. White, A. Zacchei, and A. Zonca. Planck 2018 results. VI. Cosmological parameters. A&A, 641:A6, Sept. 2020. doi: 10.1051/0004-6361/201833910.

S. Planelles, S. Borgani, D. Fabjan, M. Killedar, G. Murante, G. L. Granato, C. Ragone-Figueroa, and K. Dolag. On the role of AGN feedback on the thermal and chemodynamical properties of the hot intracluster medium. MNRAS, 438(1):195–216, Feb. 2014. doi: 10.1093/mnras/stt2141.

E. Pointecouteau, M. Arnaud, and G. W. Pratt. The structural and scaling properties of nearby galaxy clusters. I. The universal mass profile. A&A, 435(1):1–7, May 2005. doi: 10.1051/0004-6361:20042569.

T. J. Ponman, D. B. Cannon, and J. F. Navarro. The thermal imprint of galaxy formation on X-ray clusters. Nature, 397(6715):135–137, Jan. 1999. doi: 10.1038/16410.

T. J. Ponman, A. J. R. Sanderson, and A. Finoguenov. The Birmingham-CfA cluster scaling project - III. Entropy and similarity in galaxy systems. MNRAS, 343(1):331–342, July 2003. doi: 10.1046/j.1365-8711.2003.06677.x.

G. Ponti, X. Zheng, N. Locatelli, S. Bianchi, Y. Zhang, K. Anastasopoulou, J. Comparat, K. Dennerl, M. Freyberg, F. Haberl, A. Merloni, T. H. Reiprich, M. Salvato, J. Sanders, M. Sasaki, A. Strong, and M. C. H. Yeung. Abundance and temperature of the outer hot circumgalactic medium. The SRG/eROSITA view of the soft X-ray background in the eFEDS field. A&A, 674:A195, June 2023. doi: 10.1051/0004-6361/202243992.

G. W. Pratt, J. H. Croston, M. Arnaud, and H. Böhringer. Galaxy cluster X-ray luminosity scaling relations from a representative local sample (REXCESS). A&A, 498(2):361–378, May 2009. doi: 10.1051/0004-6361/200810994.

G. W. Pratt, M. Arnaud, R. Piffaretti, H. Böhringer, T. J. Ponman, J. H. Croston, G. M. Voit, S. Borgani, and R. G. Bower. Gas entropy in a representative sample of nearby X-ray galaxy clusters (REXCESS): relationship to gas mass fraction. A&A, 511:A85, Feb. 2010. doi: 10.1051/0004-6361/200913309.

G. W. Pratt, M. Arnaud, A. Biviano, D. Eckert, S. Ettori, D. Nagai, N. Okabe, and T. H. Reiprich. The Galaxy Cluster Mass Scale and Its Impact on Cosmological Constraints from the Cluster Population. Space Sci. Rev., 215(2):25, Feb. 2019. doi: 10.1007/s11214-019-0591-0.

P. Predehl, R. Andritschke, V. Arefiev, V. Babyshkin, O. Batanov, W. Becker, H. Böhringer, A. Bogomolov, T. Boller, K. Borm, W. Bornemann, H. Bräuninger, M. Brüggen, H. Brunner, M. Brusa, E. Bulbul, M. Buntov, V. Burwitz, W. Burkert, N. Clerc, E. Churazov, D. Coutinho, T. Dauser, K. Dennerl, V. Doroshenko, J. Eder, V. Emberger, T. Eraerds, A. Finoguenov, M. Freyberg, P. Friedrich, S. Friedrich, M. Fürmetz, A. Georgakakis, M. Gilfanov, S. Granato, C. Grossberger, A. Gueguen, P. Gureev, F. Haberl, O. Hälker, G. Hartner, G. Hasinger, H. Huber, L. Ji, A. v. Kienlin, W. Kink, F. Korotkov, I. Kreykenbohm, G. Lamer, I. Lomakin, I. Lapshov, T. Liu, C. Maitra, N. Meidinger, B. Menz, A. Merloni, T. Mernik, B. Mican, J. Mohr, S. Müller, K. Nandra, V. Nazarov, F. Pacaud, M. Pavlinsky, E. Perinati, E. Pfeffermann, D. Pietschner, M. E. Ramos-Ceja, A. Rau, J. Reiffers, T. H. Reiprich, J. Robrade, M. Salvato, J. Sanders, A. Santangelo, M. Sasaki, H. Scheuerle, C. Schmid, J. Schmitt, A. Schwope, A. Shirshakov, M. Steinmetz, I. Stewart, L. Strüder, R. Sunyaev, C. Tenzer, L. Tiedemann, J. Trümper, V. Voron, P. Weber, J. Wilms, and V. Yaroshenko. The eROSITA X-ray telescope on SRG. A&A, 647:A1, Mar. 2021. doi: 10.1051/0004-6361/202039313.

E. Puchwein, D. Sijacki, and V. Springel. Simulations of AGN Feedback in Galaxy Clusters and Groups: Impact on Gas Fractions and the L_X-T Scaling Relation. ApJ, 687(2):L53, Nov. 2008. doi: 10.1086/593352.

S. W. Randall, W. R. Forman, S. Giacintucci, P. E. J. Nulsen, M. Sun, C. Jones, E. Churazov, L. P. David, R. Kraft, M. Donahue, E. L. Blanton, A. Simionescu, and N. Werner. Shocks and Cavities from Multiple Outbursts in the Galaxy Group NGC 5813: A Window to Active Galactic Nucleus Feedback. ApJ, 726(2):86, Jan. 2011. doi: 10.1088/0004-637X/726/2/86.

S. W. Randall, P. E. J. Nulsen, C. Jones, W. R. Forman, E. Bulbul, T. E. Clarke, R. Kraft, E. L. Blanton, L. David, N. Werner, M. Sun, M. Donahue, S. Giacintucci, and A. Simionescu. A Very Deep Chandra Observation of the Galaxy Group NGC 5813: AGN Shocks, Feedback, and Outburst History. ApJ, 805(2):112, June 2015. doi: 10.1088/0004-637X/805/2/112.

E. Rasia, S. Borgani, G. Murante, S. Planelles, A. M. Beck, V. Biffi, C. Ragone-Figueroa, G. L. Granato, L. K. Steinborn, and K. Dolag. Cool Core Clusters from Cosmological Simulations. ApJ, 813(1):L17, Nov. 2015. doi: 10.1088/2041-8205/813/1/L17.

J. C. Raymond and B. W. Smith. Soft X-ray spectrum of a hot plasma. ApJS, 35:419–439, Dec. 1977. doi: 10.1086/190486.

A. Renzini and S. Andreon. Chemical evolution on the scale of clusters of galaxies: a conundrum? MNRAS, 444(4):3581–3591, Nov. 2014. doi: 10.1093/mnras/stu1689.

A. S. G. Robotham, P. Norberg, S. P. Driver, I. K. Baldry, S. P. Bamford, A. M. Hopkins, J. Liske, J. Loveday, A. Merson, J. A. Peacock, S. Brough, E. Cameron, C. J. Conselice, S. M. Croom, C. S. Frenk, M. Gunawardhana, D. T. Hill, D. H. Jones, L. S. Kelvin, K. Kuijken, R. C. Nichol, H. R. Parkinson, K. A. Pimbblet, S. Phillipps, C. C. Popescu, M. Prescott, R. G. Sharp, W. J. Sutherland, E. N. Taylor, D. Thomas, R. J. Tuffs, E. van Kampen, and D. Wijesinghe. Galaxy and Mass Assembly (GAMA): the GAMA galaxy group catalogue (G^3Cv1). MNRAS, 416 (4):2640–2668, Oct. 2011. doi: 10.1111/j.1365-2966.2011.19217.x.

A. K. Romer, P. T. P. Viana, A. R. Liddle, and R. G. Mann. A Serendipitous Galaxy Cluster Survey with XMM: Expected Catalog Properties and Scientific Applications. ApJ, 547(2): 594–608, Feb. 2001. doi: 10.1086/318382.

M. Rossetti, F. Gastaldello, D. Eckert, M. Della Torre, G. Pantiri, P. Cazzoletti, and S. Molendi. The cool-core state of Planck SZ-selected clusters versus X-ray-selected samples: evidence for cool-core bias. MNRAS, 468(2):1917–1930, June 2017. doi: 10.1093/mnras/stx493.

H. R. Russell, A. C. Fabian, J. S. Sanders, R. M. Johnstone, K. M. Blundell, W. N. Brandt, and C. S. Crawford. The X-ray luminous cluster underlying the bright radio-quiet quasar H1821+643. MNRAS, 402(3):1561–1579, Mar. 2010. doi: 10.1111/j.1365-2966.2009.16027. x.

E. S. Rykoff, E. Rozo, M. T. Busha, C. E. Cunha, A. Finoguenov, A. Evrard, J. Hao, B. P. Koester, A. Leauthaud, B. Nord, M. Pierre, R. Reddick, T. Sadibekova, E. S. Sheldon, and R. H. Wechsler. redMaPPer. I. Algorithm and SDSS DR8 Catalog. ApJ, 785(2):104, Apr. 2014. doi: 10.1088/0004-637X/785/2/104.

E. S. Rykoff, E. Rozo, D. Hollowood, A. Bermeo-Hernandez, T. Jeltema, J. Mayers, A. K. Romer, P. Rooney, A. Saro, C. Vergara Cervantes, R. H. Wechsler, H. Wilcox, T. M. C. Abbott, F. B. Abdalla, S. Allam, J. Annis, A. Benoit-Lévy, G. M. Bernstein, E. Bertin, D. Brooks, D. L. Burke, D. Capozzi, A. Carnero Rosell, M. Carrasco Kind, F. J. Castander, M. Childress, C. A. Collins, C. E. Cunha, C. B. D'Andrea, L. N. da Costa, T. M. Davis, S. Desai, H. T. Diehl, J. P. Dietrich, P. Doel, A. E. Evrard, D. A. Finley, B. Flaugher, P. Fosalba, J. Frieman, K. Glazebrook, D. A. Goldstein, D. Gruen, R. A. Gruendl, G. Gutierrez, M. Hilton, K. Honscheid, B. Hoyle, D. J. James, S. T. Kay, K. Kuehn, N. Kuropatkin, O. Lahav, G. F. Lewis, C. Lidman, M. Lima, M. A. G. Maia, R. G. Mann, J. L. Marshall, P. Martini, P. Melchior, C. J. Miller, R. Miquel, J. J. Mohr, R. C. Nichol, B. Nord, R. Ogando, A. A. Plazas, K. Reil, M. Sahlén, E. Sanchez, B. Santiago, V. Scarpine, M. Schubnell, I. Sevilla-Noarbe, R. C. Smith, M. Soares-Santos, F. Sobreira, J. P. Stott, E. Suchyta, M. E. C. Swanson, G. Tarle, D. Thomas, D. Tucker, S. Uddin, P. T. P. Viana, V. Vikram, A. R. Walker, Y. Zhang, and DES Collaboration. The RedMaPPer Galaxy Cluster Catalog From DES Science Verification Data. ApJS, 224(1):1, May 2016. doi: 10.3847/0067-0049/224/1/1.

L. Salvati, M. Douspis, and N. Aghanim. Constraints from thermal Sunyaev-Zel'dovich cluster counts and power spectrum combined with CMB. A&A, 614:A13, June 2018. doi: 10.1051/0004-6361/201731990.

D. J. Sand, T. Treu, and R. S. Ellis. The Dark Matter Density Profile of the Lensing Cluster MS 2137-23: A Test of the Cold Dark Matter Paradigm. ApJ, 574(2):L129–L133, Aug. 2002. doi: 10.1086/342530.

J. S. Sanders and A. C. Fabian. A deeper X-ray study of the core of the Perseus galaxy cluster: the power of sound waves and the distribution of metals and cosmic rays. MNRAS, 381(4): 1381–1399, Nov. 2007. doi: 10.1111/j.1365-2966.2007.12347.x.

J. S. Sanders, A. C. Fabian, G. B. Taylor, H. R. Russell, K. M. Blundell, R. E. A. Canning, J. Hlavacek-Larrondo, S. A. Walker, and C. K. Grimes. A very deep Chandra view of metals, sloshing and feedback in the Centaurus cluster of galaxies. MNRAS, 457(1):82–109, Mar. 2016. doi: 10.1093/mnras/stv2972.

J. S. Sanders, V. Biffi, M. Brüggen, E. Bulbul, K. Dennerl, K. Dolag, T. Erben, M. Freyberg, E. Gatuzz, V. Ghirardini, D. N. Hoang, M. Klein, A. Liu, A. Merloni, F. Pacaud, M. E. Ramos-Ceja, T. H. Reiprich, and J. A. ZuHone. Studying the merging cluster Abell 3266 with eROSITA. arXiv e-prints, art. arXiv:2106.14534, June 2021.

J. S. Sanders, . X., and et al. The SRG/eROSITA All-Sky Survey: The morphological Properties of eRASS1 Clusters. in prep.

C. L. Sarazin. X-ray emission from clusters of galaxies. Reviews of Modern Physics, 58(1): 1–115, Jan. 1986. doi: 10.1103/RevModPhys.58.1.

J. Schaye and C. Dalla Vecchia. On the relation between the Schmidt and Kennicutt-Schmidt star formation laws and its implications for numerical simulations. MNRAS, 383(3):1210–1222, Jan. 2008. doi: 10.1111/j.1365-2966.2007.12639.x.

J. Schaye, C. Dalla Vecchia, C. M. Booth, R. P. C. Wiersma, T. Theuns, M. R. Haas, S. Bertone, A. R. Duffy, I. G. McCarthy, and F. van de Voort. The physics driving the cosmic star formation history. MNRAS, 402(3):1536–1560, Mar. 2010. doi: 10.1111/j.1365-2966.2009.16029.x.

G. Schellenberger and T. H. Reiprich. HICOSMO - cosmology with a complete sample of galaxy clusters - I. Data analysis, sample selection and luminosity-mass scaling relation. MNRAS, 469(3):3738–3761, Aug. 2017. doi: 10.1093/mnras/stx1022.

G. Schellenberger, T. H. Reiprich, L. Lovisari, J. Nevalainen, and L. David. XMM-Newton and Chandra cross-calibration using HIFLUGCS galaxy clusters . Systematic temperature differences and cosmological impact. A&A, 575:A30, Mar. 2015. doi: 10.1051/0004-6361/201424085.

R. Seppi, J. Comparat, K. Nandra, E. Bulbul, F. Prada, A. Klypin, A. Merloni, P. Predehl, and J. Ider Chitham. The mass function dependence on the dynamical state of dark matter haloes. A&A, 652:A155, Aug. 2021. doi: 10.1051/0004-6361/202039123.

R. Seppi, J. Comparat, E. Bulbul, K. Nandra, A. Merloni, N. Clerc, T. Liu, V. Ghirardini, A. Liu, M. Salvato, J. S. Sanders, J. Wilms, T. Dwelly, T. Dauser, O. König, M. E. Ramos-Ceja, C. Garrel, and T. H. Reiprich. Detecting clusters of galaxies and active galactic nuclei in an eROSITA all-sky survey digital twin. A&A, 665:A78, Sept. 2022. doi: 10.1051/0004-6361/202243824.

P. R. Shapiro, I. T. Iliev, and A. C. Raga. A model for the post-collapse equilibrium of cosmological structure: truncated isothermal spheres from top-hat density perturbations. MNRAS, 307(1):203–224, July 1999. doi: 10.1046/j.1365-8711.1999.02609.x.

C. J. Short, P. A. Thomas, O. E. Young, F. R. Pearce, A. Jenkins, and O. Muanwong. The evolution of galaxy cluster X-ray scaling relations. MNRAS, 408(4):2213–2233, Nov. 2010. doi: 10.1111/j.1365-2966.2010.17267.x.

A. Siemiginowska, D. J. Burke, T. L. Aldcroft, D. M. Worrall, S. Allen, J. Bechtold, T. Clarke, and C. C. Cheung. High-redshift X-ray Cooling-core Cluster Associated with the Luminous Radio-loud Quasar 3C 186. ApJ, 722(1):102–111, Oct. 2010. doi: 10.1088/0004-637X/722/1/102.

D. Sijacki, V. Springel, T. Di Matteo, and L. Hernquist. A unified model for AGN feedback in cosmological simulations of structure formation. MNRAS, 380(3):877–900, Sept. 2007. doi: 10.1111/j.1365-2966.2007.12153.x.

J. Silk and M. J. Rees. Quasars and galaxy formation. A&A, 331:L1–L4, Mar. 1998. doi: 10.48550/arXiv.astro-ph/9801013.

A. Simionescu, N. Werner, A. Mantz, S. W. Allen, and O. Urban. Witnessing the growth of the nearest galaxy cluster: thermodynamics of the Virgo Cluster outskirts. MNRAS, 469(2):1476–1495, Aug. 2017. doi: 10.1093/mnras/stx919.

A. Simionescu, S. Nakashima, H. Yamaguchi, K. Matsushita, F. Mernier, N. Werner, T. Tamura, K. Nomoto, J. de Plaa, S. C. Leung, A. Bamba, E. Bulbul, M. E. Eckart, Y. Ezoe, A. C. Fabian, Y. Fukazawa, L. Gu, Y. Ichinohe, M. N. Ishigaki, J. S. Kaastra, C. Kilbourne, T. Kitayama, M. Leutenegger, M. Loewenstein, Y. Maeda, E. D. Miller, R. F. Mushotzky, H. Noda, C. Pinto, F. S. Porter, S. Safi-Harb, K. Sato, T. Takahashi, S. Ueda, and S. Zha. Constraints on the chemical enrichment history of the Perseus Cluster of galaxies from high-resolution X-ray spectroscopy. MNRAS, 483(2):1701–1721, Feb. 2019. doi: 10.1093/mnras/sty3220.

R. K. Smith, N. S. Brickhouse, D. A. Liedahl, and J. C. Raymond. Collisional Plasma Models with APEC/APED: Emission-Line Diagnostics of Hydrogen-like and Helium-like Ions. ApJ, 556:L91–L95, Aug. 2001. doi: 10.1086/322992.

S. Smith. The Mass of the Virgo Cluster. ApJ, 83:23, Jan. 1936. doi: 10.1086/143697.

V. Smolčić, A. Finoguenov, G. Zamorani, E. Schinnerer, M. Tanaka, S. Giodini, and N. Scoville. On the occupation of X-ray-selected galaxy groups by radio active galactic nuclei since z = 1.3. MNRAS, 416(1):L31–L35, Sept. 2011. doi: 10.1111/j.1745-3933.2011.01092.x.

D. Spergel, N. Gehrels, C. Baltay, D. Bennett, J. Breckinridge, M. Donahue, A. Dressler, B. S. Gaudi, T. Greene, O. Guyon, C. Hirata, J. Kalirai, N. J. Kasdin, B. Macintosh, W. Moos, S. Perlmutter, M. Postman, B. Rauscher, J. Rhodes, Y. Wang, D. Weinberg, D. Benford, M. Hudson, W. S. Jeong, Y. Mellier, W. Traub, T. Yamada, P. Capak, J. Colbert, D. Masters, M. Penny, D. Savransky, D. Stern, N. Zimmerman, R. Barry, L. Bartusek, K. Carpenter, E. Cheng, D. Content, F. Dekens, R. Demers, K. Grady, C. Jackson, G. Kuan, J. Kruk, M. Melton, B. Nemati, B. Parvin, I. Poberezhskiy, C. Peddie, J. Ruffa, J. K. Wallace, A. Whipple, E. Wollack, and F. Zhao. Wide-Field InfrarRed Survey Telescope-Astrophysics Focused Telescope Assets WFIRST-AFTA 2015 Report. arXiv e-prints, art. arXiv:1503.03757, Mar. 2015. doi: 10.48550/arXiv.1503.03757.

D. N. Spergel, R. Bean, O. Doré, M. R. Nolta, C. L. Bennett, J. Dunkley, G. Hinshaw, N. Jarosik, E. Komatsu, L. Page, H. V. Peiris, L. Verde, M. Halpern, R. S. Hill, A. Kogut, M. Limon, S. S. Meyer, N. Odegard, G. S. Tucker, J. L. Weiland, E. Wollack, and E. L. Wright. Three-Year Wilkinson Microwave Anisotropy Probe (WMAP) Observations: Implications for Cosmology. ApJS, 170(2):377–408, June 2007. doi: 10.1086/513700.

J. Spitzer, Lyman and J. L. Greenstein. Continuous Emission from Planetary Nebulae. ApJ, 114: 407, Nov. 1951. doi: 10.1086/145480.

V. Springel. The cosmological simulation code GADGET-2. MNRAS, 364(4):1105–1134, Dec. 2005. doi: 10.1111/j.1365-2966.2005.09655.x.

V. Springel and L. Hernquist. Cosmological smoothed particle hydrodynamics simulations: a hybrid multiphase model for star formation. MNRAS, 339(2):289–311, Feb. 2003. doi: 10.1046/j.1365-8711.2003.06206.x.

V. Springel, S. D. M. White, G. Tormen, and G. Kauffmann. Populating a cluster of galaxies - I. Results at [formmu2]z=0. MNRAS, 328(3):726–750, Dec. 2001. doi: 10.1046/j.1365-8711.2001.04912.x.

V. Springel, T. Di Matteo, and L. Hernquist. Modelling feedback from stars and black holes in galaxy mergers. MNRAS, 361(3):776–794, Aug. 2005. doi: 10.1111/j.1365-2966.2005.09238.x.

M. Sun. Hot gas in galaxy groups: recent observations. New Journal of Physics, 14(4):045004, Apr. 2012. doi: 10.1088/1367-2630/14/4/045004.

M. Sun, G. M. Voit, M. Donahue, C. Jones, W. Forman, and A. Vikhlinin. Chandra Studies of the X-Ray Gas Properties of Galaxy Groups. ApJ, 693(2):1142–1172, Mar. 2009. doi: 10.1088/0004-637X/693/2/1142.

M. Sun, N. Sehgal, G. M. Voit, M. Donahue, C. Jones, W. Forman, A. Vikhlinin, and C. Sarazin. The Pressure Profiles of Hot Gas in Local Galaxy Groups. ApJ, 727(2):L49, Feb. 2011. doi: 10.1088/2041-8205/727/2/L49.

R. Sunyaev, V. Arefiev, V. Babyshkin, A. Bogomolov, K. Borisov, M. Buntov, H. Brunner, R. Burenin, E. Churazov, D. Coutinho, J. Eder, N. Eismont, M. Freyberg, M. Gilfanov, P. Gureyev, G. Hasinger, I. Khabibullin, V. Kolmykov, S. Komovkin, R. Krivonos, I. Lapshov, V. Levin, I. Lomakin, A. Lutovinov, P. Medvedev, A. Merloni, T. Mernik, E. Mikhailov, V. Molodtsov, P. Mzhelsky, S. Müller, K. Nandra, V. Nazarov, M. Pavlinsky, A. Poghodin, P. Predehl, J. Robrade, S. Sazonov, H. Scheuerle, A. Shirshakov, A. Tkachenko, and V. Voron. SRG X-ray orbital observatory. Its telescopes and first scientific results. A&A, 656:A132, Dec. 2021. doi: 10.1051/0004-6361/202141179.

R. A. Sunyaev and Y. B. Zeldovich. Small-Scale Fluctuations of Relic Radiation. Ap&SS, 7(1): 3–19, Apr. 1970. doi: 10.1007/BF00653471.

R. A. Sunyaev and Y. B. Zeldovich. The Observations of Relic Radiation as a Test of the Nature of X-Ray Radiation from the Clusters of Galaxies. Comments on Astrophysics and Space Physics, 4:173, Nov. 1972.

E. Tempel, T. Tuvikene, R. Kipper, and N. I. Libeskind. Merging groups and clusters of galaxies from the SDSS data. The catalogue of groups and potentially merging systems. A&A, 602: A100, June 2017. doi: 10.1051/0004-6361/201730499.

S. Thölken, L. Lovisari, T. H. Reiprich, and J. Hasenbusch. X-ray analysis of the galaxy group UGC 03957 beyond R_{200} with Suzaku. A&A, 592:A37, July 2016. doi: 10.1051/0004-6361/201527608.

J. Tinker, A. V. Kravtsov, A. Klypin, K. Abazajian, M. Warren, G. Yepes, S. Gottlöber, and D. E. Holz. Toward a Halo Mass Function for Precision Cosmology: The Limits of Universality. ApJ, 688(2):709–728, Dec. 2008. doi: 10.1086/591439.

L. Tornatore, S. Borgani, F. Matteucci, S. Recchi, and P. Tozzi. Simulating the metal enrichment of the intracluster medium. MNRAS, 349(1):L19–L24, Mar. 2004. doi: 10.1111/j.1365-2966.2004.07689.x.

L. Tornatore, S. Borgani, K. Dolag, and F. Matteucci. Chemical enrichment of galaxy clusters from hydrodynamical simulations. MNRAS, 382(3):1050–1072, Dec. 2007. doi: 10.1111/j.1365-2966.2007.12070.x.

P. Tozzi and C. Norman. The Evolution of X-Ray Clusters and the Entropy of the Intracluster Medium. ApJ, 546(1):63–84, Jan. 2001. doi: 10.1086/318237.

G. R. Tremblay, F. Combes, J. B. R. Oonk, H. R. Russell, M. A. McDonald, M. Gaspari, B. Husemann, P. E. J. Nulsen, B. R. McNamara, S. L. Hamer, C. P. O'Dea, S. A. Baum, T. A. Davis, M. Donahue, G. M. Voit, A. C. Edge, E. L. Blanton, M. N. Bremer, E. Bulbul,

T. E. Clarke, L. P. David, L. O. V. Edwards, D. Eggerman, A. C. Fabian, W. Forman, C. Jones, N. Kerman, R. P. Kraft, Y. Li, M. Powell, S. W. Randall, P. Salomé, A. Simionescu, Y. Su, M. Sun, C. M. Urry, A. N. Vantyghem, B. J. Wilkes, and J. A. ZuHone. A Galaxy-scale Fountain of Cold Molecular Gas Pumped by a Black Hole. ApJ, 865(1):13, Sept. 2018. doi: 10.3847/1538-4357/aad6dd.

J. Truemper. The ROSAT mission. Advances in Space Research, 2(4):241–249, Jan. 1982. doi: 10.1016/0273-1177(82)90070-9.

N. Truong, E. Rasia, P. Mazzotta, S. Planelles, V. Biffi, D. Fabjan, A. M. Beck, S. Borgani, K. Dolag, M. Gaspari, G. L. Granato, G. Murante, C. Ragone-Figueroa, and L. K. Steinborn. Cosmological hydrodynamical simulations of galaxy clusters: X-ray scaling relations and their evolution. MNRAS, 474(3):4089–4111, Mar. 2018. doi: 10.1093/mnras/stx2927.

D. J. Turner, P. A. Giles, A. K. Romer, R. Wilkinson, E. W. Upsdell, S. Bhargava, C. A. Collins, M. Hilton, R. G. Mann, M. Sahl, J. P. Stott, and P. T. P. Viana. The XMM Cluster Survey: An independent demonstration of the fidelity of the eFEDS galaxy cluster data products and implications for future studies. arXiv e-prints, art. arXiv:2109.11807, Sept. 2021.

K. Umetsu, M. Sereno, S.-I. Tam, I. N. Chiu, Z. Fan, S. Ettori, D. Gruen, T. Okumura, E. Medezinski, M. Donahue, M. Meneghetti, B. Frye, A. Koekemoer, T. Broadhurst, A. Zitrin, I. Balestra, N. Benítez, Y. Higuchi, P. Melchior, A. Mercurio, J. Merten, A. Molino, M. Nonino, M. Postman, P. Rosati, J. Sayers, and S. Seitz. The Projected Dark and Baryonic Ellipsoidal Structure of 20 CLASH Galaxy Clusters. ApJ, 860(2):104, June 2018. doi: 10.3847/1538-4357/aac3d9.

R. Valdarnini. Iron abundances and heating of the intracluster medium in hydrodynamical simulations of galaxy clusters. MNRAS, 339(4):1117–1134, Mar. 2003. doi: 10.1046/j.1365-8711. 2003.06163.x.

R. J. van Weeren, F. de Gasperin, H. Akamatsu, M. Brüggen, L. Feretti, H. Kang, A. Stroe, and F. Zandanel. Diffuse Radio Emission from Galaxy Clusters. Space Sci. Rev., 215(1):16, Feb. 2019. doi: 10.1007/s11214-019-0584-z.

A. Veronica, Y. Su, V. Biffi, T. H. Reiprich, F. Pacaud, P. E. J. Nulsen, R. P. Kraft, J. S. Sanders, A. Bogdan, M. Kara, K. Dolag, J. Kerp, B. S. Koribalski, T. Erben, E. Bulbul, E. Gatuzz, V. Ghirardini, A. M. Hopkins, A. Liu, K. Migkas, and T. Vernstrom. The eROSITA View of the Abell 3391/95 Field: The Northern Clump – The Largest Infalling Structure in the Longest Known Gas Filament Observed with eROSITA, XMM-Newton, Chandra. arXiv e-prints, art. arXiv:2106.14543, June 2021.

A. Vikhlinin, A. Kravtsov, W. Forman, C. Jones, M. Markevitch, S. S. Murray, and L. Van Speybroeck. Chandra Sample of Nearby Relaxed Galaxy Clusters: Mass, Gas Fraction, and Mass-Temperature Relation. ApJ, 640(2):691–709, Apr. 2006. doi: 10.1086/500288.

A. Vikhlinin, R. A. Burenin, H. Ebeling, W. R. Forman, A. Hornstrup, C. Jones, A. V. Kravtsov, S. S. Murray, D. Nagai, H. Quintana, and A. Voevodkin. Chandra Cluster Cosmology Project. II. Samples and X-Ray Data Reduction. ApJ, 692(2):1033–1059, Feb. 2009. doi: 10.1088/0004-637X/692/2/1033.

A. Voevodkin, K. Borozdin, K. Heitmann, S. Habib, A. Vikhlinin, A. Mescheryakov, A. Hornstrup, and R. Burenin. Fossil Systems in the 400d Cluster Catalog. ApJ, 708(2):1376–1387, Jan. 2010. doi: 10.1088/0004-637X/708/2/1376.

G. M. Voit. Tracing cosmic evolution with clusters of galaxies. Reviews of Modern Physics, 77 (1):207–258, Apr. 2005. doi: 10.1103/RevModPhys.77.207.

S. A. Walker, A. C. Fabian, J. S. Sanders, and M. R. George. Galaxy cluster outskirts: a universal entropy profile for relaxed clusters? MNRAS, 427(1):L45–L49, Nov. 2012. doi: 10.1111/j.1745-3933.2012.01342.x.

D. Walsh, R. F. Carswell, and R. J. Weymann. 0957+561 A, B: twin quasistellar objects or gravitational lens? Nature, 279:381–384, May 1979. doi: 10.1038/279381a0.

R. H. Wechsler and J. L. Tinker. The Connection Between Galaxies and Their Dark Matter Halos. ARA&A, 56:435–487, Sept. 2018. doi: 10.1146/annurev-astro-081817-051756.

R. Weinberger, V. Springel, L. Hernquist, A. Pillepich, F. Marinacci, R. Pakmor, D. Nelson, S. Genel, M. Vogelsberger, J. Naiman, and P. Torrey. Simulating galaxy formation with black hole driven thermal and kinetic feedback. MNRAS, 465(3):3291–3308, Mar. 2017. doi: 10.1093/mnras/stw2944.

N. Werner, A. Simionescu, E. T. Million, S. W. Allen, P. E. J. Nulsen, A. von der Linden, S. M. Hansen, H. Böhringer, E. Churazov, A. C. Fabian, W. R. Forman, C. Jones, J. S. Sanders, and G. B. Taylor. Feedback under the microscope-II. Heating, gas uplift and mixing in the nearest cluster core. MNRAS, 407(4):2063–2074, Oct. 2010. doi: 10.1111/j.1365-2966.2010.16755.x.

N. Werner, B. R. McNamara, E. Churazov, and E. Scannapieco. Hot Atmospheres, Cold Gas, AGN Feedback and the Evolution of Early Type Galaxies: A Topical Perspective. Space Sci. Rev., 215(1):5, Jan. 2019. doi: 10.1007/s11214-018-0571-9.

B. Whelan, T. H. Reiprich, F. Pacaud, E. Bulbul, M. E. Ramos-Ceja, J. S. Sanders, J. Aschersleben, J. Iljenkarevic, A. Veronica, K. Migkas, M. Freyberg, K. Dennerl, M. Kara, A. Liu, V. Ghirardini, and N. Ota. X-Ray Studies of the Abell 3158 Galaxy Cluster with eROSITA. arXiv e-prints, art. arXiv:2106.14545, June 2021.

R. P. C. Wiersma, J. Schaye, and B. D. Smith. The effect of photoionization on the cooling rates of enriched, astrophysical plasmas. MNRAS, 393(1):99–107, Feb. 2009a. doi: 10.1111/j.1365-2966.2008.14191.x.

R. P. C. Wiersma, J. Schaye, T. Theuns, C. Dalla Vecchia, and L. Tornatore. Chemical enrichment in cosmological, smoothed particle hydrodynamics simulations. MNRAS, 399(2):574–600, Oct. 2009b. doi: 10.1111/j.1365-2966.2009.15331.x.

R. Willingale, R. L. C. Starling, A. P. Beardmore, N. R. Tanvir, and P. T. O'Brien. Calibration of X-ray absorption in our Galaxy. MNRAS, 431:394–404, May 2013a. doi: 10.1093/mnras/stt175.

R. Willingale, R. L. C. Starling, A. P. Beardmore, N. R. Tanvir, and P. T. O'Brien. Calibration of X-ray absorption in our Galaxy. MNRAS, 431(1):394–404, May 2013b. doi: 10.1093/mnras/stt175.

M. A. G. Willson. Radio observations of the cluster of galaxies in Coma Berenices - the 5C4 survey. MNRAS, 151:1, Jan. 1970. doi: 10.1093/mnras/151.1.1.

J. Wilms, A. Allen, and R. McCray. On the Absorption of X-Rays in the Interstellar Medium. ApJ, 542:914–924, Oct. 2000a. doi: 10.1086/317016.

J. Wilms, A. Allen, and R. McCray. On the Absorption of X-Rays in the Interstellar Medium. ApJ, 542(2):914–924, Oct. 2000b. doi: 10.1086/317016.

H. Wolter. Spiegelsysteme streifenden Einfalls als abbildende Optiken für Röntgenstrahlen. Annalen der Physik, 445(1):94–114, Jan. 1952. doi: 10.1002/andp.19524450108.

XRISM Science Team. Science with the X-ray Imaging and Spectroscopy Mission (XRISM). arXiv e-prints, art. arXiv:2003.04962, Mar. 2020. doi: 10.48550/arXiv.2003.04962.

M. C. H. Yeung, M. J. Freyberg, G. Ponti, K. Dennerl, M. Sasaki, and A. Strong. SRG/eROSITA X-ray shadowing study of giant molecular clouds. A&A, 676:A3, Aug. 2023. doi: 10.1051/0004-6361/202345867.

Z. S. Yuan, J. L. Han, and Z. L. Wen. The Scaling Relations and the Fundamental Plane for Radio Halos and Relics of Galaxy Clusters. ApJ, 813(1):77, Nov. 2015. doi: 10.1088/0004-637X/813/1/77.

X. Zhang, E. Bulbul, N. Malavasi, V. Ghirardini, J. Comparat, M. Kluge, A. Liu, A. Merloni, Y. Zhang, Y. E. Bahar, E. Artis, J. Sanders, C. Garrel, F. Balzer, M. Brüggen, M. Freyberg, E. Gatuzz, S. Grandis, S. Krippendorf, K. Nandra, G. Ponti, M. Ramos-Ceja, P. Predehl, T. H. Reiprich, A. Veronica, M. C. H. Yeung, and S. Zelmer. The SRG/eROSITA all-sky survey. X-ray emission from the warm-hot phase gas in long cosmic filaments. arXiv e-prints, art. arXiv:2406.00105, May 2024. doi: 10.48550/arXiv.2406.00105.

Y. Y. Zhang, A. Finoguenov, H. Böhringer, J. P. Kneib, G. P. Smith, R. Kneissl, N. Okabe, and H. Dahle. LoCuSS: comparison of observed X-ray and lensing galaxy cluster scaling relations with simulations. A&A, 482(2):451–472, May 2008. doi: 10.1051/0004-6361:20079103.

Y. Y. Zhang, H. Andernach, C. A. Caretta, T. H. Reiprich, H. Böhringer, E. Puchwein, D. Sijacki, and M. Girardi. HIFLUGCS: Galaxy cluster scaling relations between X-ray luminosity, gas mass, cluster radius, and velocity dispersion. A&A, 526:A105, Feb. 2011. doi: 10.1051/0004-6361/201015830.

S. Zou, B. J. Maughan, P. A. Giles, A. Vikhlinin, F. Pacaud, R. Burenin, and A. Hornstrup. The X-ray luminosity-temperature relation of a complete sample of low-mass galaxy clusters. MNRAS, 463(1):820–831, Nov. 2016. doi: 10.1093/mnras/stw1992.

J. ZuHone, Y. E. Bahar, V. Biffi, K. Dolag, J. Sanders, E. Bulbul, T. Liu, T. Dauser, O. König, X. Zhang, and V. Ghirardini. Effects of multiphase gas and projection on X-ray observables in simulated galaxy clusters as seen by eROSITA. A&A, 675:A150, July 2023. doi: 10.1051/0004-6361/202245749.

F. Zwicky. Die Rotverschiebung von extragalaktischen Nebeln. Helvetica Physica Acta, 6:110–127, Jan. 1933.

Acknowledgments

First and foremost, I would like to express my deep gratitude to my supervisor, Esra, for recognizing my scientific efforts in Turkey before my arrival at MPE and for providing the opportunity to achieve one of young Emre's dreams: conducting cutting-edge research. I also want to acknowledge the support I received from her as she selflessly and devotedly helped me to become a successful scientist.

A special thanks to Paul for the "Friday Quarantinis" Zoom gatherings during the pandemic, which provided a much-needed and refreshing start to my PhD journey. I would like to further express my gratitude to him for allowing me to be part of the scientifically rich and stimulating environment of the high-energy group at MPE.

I am deeply appreciative of the past and present postdocs in our group—Vittorio, Ang, Christian, Emmanuel, Xiaoyuan, Matthias, and Nicola—for their patience in addressing my questions and comments. I owe particular thanks to Vittorio and Ang, who were there throughout my PhD and consistently available to assist with my inquiries.

Jeremy Sanders deserves a special mention for the frequent and engaging discussions about science that have greatly enriched my journey.

I am sincerely grateful to Birgit and Harald for their tireless support and assistance to everyone at the institute, including myself.

I am grateful to Sophia and Raphael for their help with improving the English of my thesis, and to Matthias for translating the English abstract into German.

My appreciation extends to my office mates Francesco and Ania for making the office environment more comfortable when they are around.

Thanks to my housemate, Yusuf, for being a relaxed and easygoing housemate, which has made my life in Munich more enjoyable.

I thank all members of the Cineclub for sharing a passion for discussing cinema, which has added a unique and enjoyable dimension to my PhD experience.

Thanks are also due to Alain, Alena, Ana, Catarina, David, Isabelle, Michael, Martin, Pietro, Robert, Safiye, Silas, Toska, Yi, and Zsofi for making lunch breaks and coffee böreks more pleasant and enjoyable.

A special thanks to the members of the "Not So Secret Santa" group—Soumya, Riccardo, Sophia, Francesco, Fulvio, and James—for adding significant value to my PhD journey through their close friendship and support.

Ailem Ahmet Sina, Mehmet ve Meral'e kalbimin en temiz yerinden teşekkürlerimi sunuyorum. Doktora yolculuğum boyunca desteklerini her zaman arkamda hissettim ve karşılık bek-

lemeden verdikleri sevgi moralimi daha yüksek, keyfimi daha yerinde ve mental ve fiziksel sağlığımı daha dinç tuttu. Benim için çok değerlisiniz.

Son olarak, doktora boyunca bana sevgi, güç, neşe, arkadaşlık, mutluluk ve tezimin teşekkür bölümüne sığamayacak sayısız güzellikler vermiş olan partnerim Ebrar'a teşekkür ediyorum. Ebrar, iyi ki varsın. Benim için değerini anlatmam imkansız. Seni en saf duygularımla seviyor ve bu tezi sana ve kavuşmaya çalışma sürecimizde yaşadığımız zorluklara ithaf ediyorum.